

Table of Contents

Scientific program..... 5

Papers: Oral presentations..... 11

Presentation 1: Richard Ketcham, University of Texas, USA	13
Presentation 2: Seth Parker, University of Kentucky, USA	15
Presentation 3: Magdalena Tomanik, University of Science and Technology, Poland	17
Presentation 4: Greetje Vande Velde, KULeuven, Belgium	22
Presentation 5: Gerard van Dalen, Unilever, the Netherlands	26
Presentation 6: Alexander Ivanov, St. Petersburg State University, Russia	31
Presentation 7: Danieli Moura Brasil, University of Campinas, Brasil	37
Presentation 8: Alix Cornish, Campen BRI, UK	41
Presentation 9: David Habberthür, University of Bern, Switzerland	45
Presentation 10: Rob van't Hof, University of Liverpool, UK	47
Presentation 11: Samuele Ciattini, University of Florence, Italy	53
Presentation 12: Constantine Tarasenko, PIN RAS Moscow, Russia	60
Presentation 13: David Shepherd, University of Cambridge, UK	66
Presentation 14: Barry Quinn, King's College London, UK	69
Presentation 15: Teresa Molina, Pontificia Universidad Católica, Chile	77
Presentation 16: Iara Mantovani, Federal University of Santa Catarina, Brasil	83
Presentation 17: Daniel Chappard, Université d'Angers, France	87
Presentation 18: Simone Tassani, Universitat Pompeu Fabra, Spain	90
Presentation 19: Frederik Doerr, Strathclyde University, UK	97
Presentation 20: Frantisek Spoutil, Institute of Molecular Genetics, Czech Republic	101
Presentation 21: Anneleen Foubert, University of Fribourg, Switzerland	103
Presentation 22: Menelia Vasilopoulou-Kampitsi, University of Antwerp, Belgium	105
Presentation 23: Gareth Deering, Sensata Technologies, UK	110
Presentation 24: Maria Candas, University of Santiago de Compostela, Spain	112
Presentation 25: Carlos Santos, Repsol Technology Center, Spain	117
Presentation 26: Annapaola Parrilli, Rizzoli Orthopaedic institute, Italy	124
Presentation 27: Barbara Satola, University of Oldenburg, Germany	128
Presentation 28: Jardel Chaves, University of Ribeirão Preto, Brazil	133
Presentation 29: Jana Goyens, University of Antwerp, Belgium	137
Presentation 30: Łukasz Skarżyński, Gdansk University of Technology, Poland	141
Presentation 31: Javier Alba-Tercedor, University of Granada, Spain	147
Presentation 32: Giulia Ricci, Ca' Foscari University of Venice, Italy	168
Presentation 33: Dane Gerneke, University of Auckland, New Zealand	172
Presentation 34: Sebastien de Bournonville, KULeuven, Belgium	177
Presentation 35: Christos Bikis, University of Basel, Switzerland	183
Presentation 36: Nicholas Nestle, BASF, Germany	185

Papers: Poster presentations.....193

Poster 1: Gina Roque-Torres, State University of Campinas, Brazil	195
Poster 2: Ruslan Hlushchuk, University of Bern, Switzerland	200
Poster 3: Nicole Bakker, Osteo-Pharma, The Netherlands	202
Poster 4: Stella Pastore, Institute of Crystallography, Italy	204
Poster 5: Christoph Schürmann, Goethe University Frankfurt, Germany	207
Poster 6: Ali Keles, Ondokuz Mayıs University, Turkey	208
Poster 7: Mariana Maloste Butezloff, University of Ribeirão Preto, Brazil	211
Poster 8: Maria Candas, University of Santiago de Compostela, Spain	216
Poster 9: Ariane Zamarioli, University of Ribeirão Preto, Brazil	222
Poster 10: Patrina Poh, Technical University of Munich	227
Poster 11: Bartosz Leszczynski, Jagiellonian University, Poland	229
Poster 12: Susanne Reimann, University of Bonn, Germany	232
Poster 13: Ashok Kumar, Indian Institute of Technology Kanpur, India	234
Poster 14: Simone Tassani, University Pompeu Fabra, Spain	241
Poster 15: Marie-Josée Beaulieu, Laval University, Canada	248
Poster 16: Aida Rajic, University of Suffolk, UK	251
Poster 17: Gaurav Gupta, University of Oldenburg, Germany	254
Poster 18: Athina Mavridou, KULeuven, Belgium	259
Poster 19: Behzad Javaheri, Royal Veterinary College, UK	261
Poster 20: Greet Kerckhofs, KULeuven, Belgium	263
Poster 21: Andrew Chantry, University of Sheffield, UK	267
Poster 22: Javier Alba-Tercedor, University of Granada, Spain	270
Poster 23: Fabiana Kühne, university fo Campinas, Brazil	286
Poster 24: Ingrid Contardo, Pontificia Universidad Católica, Chile	290
Poster 25: Konstantinos Verdelis, University of Pittsburgh, USA	296
Poster 26: Martin Bartos, Charles University of Prague, Czech Republic	298
Poster 27: Amy Voong, University of Birmingham, UK	304
Poster 28: Laura Chelazzi, University of Florence, Italy	307
Poster 29: Lakshana Mohee, University of Cambridge, UK	311
Poster 30: Michal Spanko, Charles University of Prague, Czech Republic	313
Poster 31: Natalia Piskunova, Institute of Geology Komi SC UB, Russia	319
Poster 32: Anderson Camargo Moreira, Universidade federal de Santa Catarina, Brazil	321
Poster 33: Myriam Oger, IRBA, France	325
Poster 34: Sandra Schneider, Technical University of Munich, Germany	329
Poster 35: Aleksey Khomyak, Moscow State University, Russia	332
Poster 36: Alexey Pakhnevich, Russian Academy of Sciences, Russia	335
Poster 37: Benita Putlitz, University of Lausanne, Switzerland	342
Poster 38: Vladimir Mendoza Lavaniegos, Mexican Center of Innovation, Mexico	344
Poster 39: Alexey Pakhnevich, Russian Academy of Sciences, Russia	351
Poster 40: Jenny Shepherd, University of Cambridge, UK	360
Poster 41: Ricardo Tadeu Lopes, Federal university of Rio de Janeiro, Brazil	363
Poster 42: Magdalena Wojtkow, University of Wroclaw, Poland	367
Poster 43: Sylvie Chevalier, ONIRIS, France	370

Poster 44: Lyudmila Kryuchkova, St Petersburg State University, Russia	374
Poster 45: Alexander Kulkov, St Petersburg State University, Russia	381
Poster 46: Yulia Plotkina, St Petersburg State University, Russia	388
Poster 47: Jose Ramirez-GarciaLuna, McGill University, Canada	391

Micro-CT User Meeting 2017: Scientific Program

Royal Belgian Institute of Natural Science, Brussels

Tuesday 13 June, 2017

08:30-09:00	Registration and coffee/tea	
09:00-09:20	Welcome	
09:20-10:00	Invited speaker: Richard Ketcham, University of Texas, USA	13
	<i>"Petrography in 3D: Why isn't everybody doing it?"</i>	
10:00-10:20	Seth Parker, University of Kentucky, USA	15
	<i>"Enhanced CT Analysis Using Volume Flattening"</i>	
10:20-10:40	Magdalena Tomanik, University of Science and Technology, Poland	17
	<i>"Bone diagenesis phenomena - Morphometric evaluation"</i>	
10:40-11:20	COFFEE/TEA break + POSTER VIEWING EVEN NR	
11:20-11:40	Greetje Vande Velde, KULeuven, Belgium	22
	<i>"Brain, bones and cognition: low-dose microCT in the search for treating Down syndrome"</i>	
11:40-12:00	Gerard van Dalen, Unilever, the Netherlands	26
	<i>"Micro-CT as a 3D reverse engineering tool to study emulsification processing"</i>	
12:00-12:20	Alexander Ivanov, Politecnico di Milano, Italy	31
	<i>"Investigation of internal structure in the scales of Palaeozoic cartilaginous fishes using micro-CT"</i>	
12:20-12:40	Danieli Moura Brasil, University of Campinas, Brasil	37
	<i>"Morphometric and content assessment of the bone repair in rats treated with Guar Gum and X-ray irradiation"</i>	
12:40 – 14:00	LUNCH	
14:00-14:30	Bruker microCT Software team	
	<i>"Update Nrecon, CTVOx, CTAn"</i>	
14:30-14:50	Alix Cornish, Campden BRI, UK	41
	<i>"Structure-texture relationships in bakery products"</i>	
14:50-15:10	David Habberthür, University of Bern, Switzerland	45
	<i>"Quantitative assessment of brain tumor radiation treatment reveals decrease in tumor-supporting vessels"</i>	
15:10-16:00	COFFEE/TEA break + Q&A for Bruker microCT Software team	

16:00-16:20	Rob van't Hof, University of Liverpool, UK <i>"Investigating Zoledronate Treatment as a Preventative Strategy for Paget's Disease of Bone"</i>	47
16:20-16:40	Samuele Ciattini, University of Florence, Italy <i>"Determining the concentration of diamond powder deposited on a textile yarn: a multitechnique approach"</i>	53
16:40-17:00	Constantine Tarásenko, PIN RAS Moscow, Russia <i>"Survey of petrosal bone of the inner ear of Late Miocene baleen & toothed whales from Northwest Caucasus through tomography (First experience)"</i>	60
18:00	Bruker microCT social event	

Wednesday 14 June, 2017

08:30-09:00	Registration and coffee/tea	
09:00-09:20	David Shepherd, University of Cambridge, UK	66
	<i>"Tracking Cells in vitro using Micro CT"</i>	
09:20-09:40	Barry Quinn, King's College London, UK	69
	<i>"Using MicroCT Scanning Techniques to Assess the Performance of Dental Students' Tooth Cavity Preparation Skills"</i>	
09:40-10:00	Teresa Molina, Pontificia Universidad Católica, Chile	77
	<i>"A 3D analysis of how oil absorption of fried dough is affected by freezing conditions using X-ray micro-CT"</i>	
10:00-10:20	Iara Mantovani, Federal University of Santa Catarina, Brasil	83
	<i>"Multiscale Characterization of Heterogeneous Porous Media by Means of Micro-CT Images"</i>	
10:20-11:00	COFFEE/TEA break + POSTER VIEWING ODD NR	
11:00-11:20	Daniel Chappard, Université d'Angers, France	87
	<i>"Long term quantitative evaluation of muscle and bone wasting induced by botulinum toxin in mice using microCT"</i>	
11:20-11:40	Simone Tassani, Universitat Pompeu Fabra, Spain	90
	<i>"Independent Active Contours Segmentation"</i>	
11:40-12:00	Frederik Doerr, Strathclyde University, UK	97
	<i>"Morphological Characterisation of Solid Pharmaceutical Products using X-ray tomography"</i>	
12:00-12:20	Frantisek Spoutil, Institute of Molecular Genetics, Czech Republic	101
	<i>"The Youngest Tasmanian Wolf: Scanned"</i>	
12:20 – 13:40	LUNCH	
13:40-14:00	Anneleen Foubert, University of Fribourg, Switzerland	103
	<i>"Insights in the spatial and temporal heterogeneity of biofilm lithification"</i>	
14:00-14:20	Menelia Vasilopoulou-Kampitsi, University of Antwerp, Belgium	105
	<i>"Scaling and morphological analysis of the lizards vestibular system, using micro CT scanning"</i>	
14:20-14:40	Gareth Deering, Sensata Technologies, UK	110
	<i>"Micro-CT application within Automotive R&D: Optimising Metal Weld joints in automotive sensors"</i>	
14:40-15:00	Maria Candas, University of Santiago de Compostela, Spain	112
	<i>"First steps in morphological analysis of the reproductive system of Doto pinnatifida (Montagu, 1804)"</i>	
15:00-15:40	COFFEE/TEA break + Q&A for Bruker microCT Software team	

15:40-16:00	Carlos Santos, Repsol Technology Center, Spain	117
	<i>"Time Effective Reservoir Properties Estimation by Digital Rock Physics Protocols"</i>	
16:00-16:20	Annapaola Parrilli, Rizzoli Orthopaedic institute, Italy	124
	<i>"Longitudinal in vivo analysis of nanostructured hydroxyapatite-functionalized gelatins osteoinductive properties in relation to endogenous or human mesenchymal stromal cells"</i>	
16:20-16:40	Barbara Satola, University of Oldenburg, Germany	128
	<i>"Application of X-Ray Computed Tomography Imaging in the Evaluation of Aging Effects of Batteries and Fuel Cell Components"</i>	
16:40-17:00	Jardel Chaves, University of Ribeirão Preto, Brazil	133
	<i>"The use of microcomputed tomography to evaluate the cervical barrier in internal tooth bleaching"</i>	
17:00	walk to THON hotel	
18:00	Social event	

Thursday 15 June, 2017

08:30-09:00	Registration	
09:00-09:20	Jana Goyens, University of Antwerp, Belgium	137
	<i>"Comparison of conventional and synchrotron X-ray microCT scanning of thin membranes in the inner ear"</i>	
09:20-09:40	Łukasz. Skarżyński, Gdansk University of Technology, Poland	141
	<i>"X-ray micro-CT as a base for Discrete Element Method modelling of fracture phenomenon in various materials"</i>	
09:40-10:00	Javier Alba-Tercedor, University of Granada, Spain	148
	<i>"Comparing micro-CT results of insects with classical anatomical studies: The European honey bee (Apis mellifera Linnaeus, 1758) as a benchmark (Insecta: Hymenoptera, Apidae)"</i>	
10:00-10:20	Giulia Ricci, Ca'Foscari University of Venice, Italy	169
	<i>"Experimental analyses by X-ray μ-CT for the study of the effects of firing temperature on the ceramic body morphology"</i>	
10:20-11:00	COFFEE/TEA break	
11:00-11:20	Dane Gerneke, University of Auckland, New Zealand	173
	<i>"Solving the Challenges of Submicron MicroCT (NanoCT) for Delicate samples."</i>	
11:20-11:40	Sebastien de Bournonville, KULeuven, Belgium	177
	<i>"3D morphological characterization of polymeric microcarriers for stem cell expansion"</i>	
11:40-12:00	Christos Bikis, University of Basel, Switzerland	183
	<i>"Micro-CT for the visualization of the mouse brain"</i>	
12:00-12:20	Nicholaus Nestle, BASF, Germany	185
	<i>"Swelling and drying of non-treated and treated spruce wood during and after exposure to liquid water"</i>	
12:20 – 14:00	LUNCH	
14:00-14:20	Announcement winner of oral, poster, picture and movie awards	
14:20-16:00	Parallel sessions Life Science & Material Science Applications	
	<i>The afternoon is reserved for interactive parallel sessions where Bruker microCT application scientists will update you on newest hardware features, novel methods in the SkyScan software, and answer questions sent in by users.</i>	
16:00	Wrap-up and end of User Meeting	

ORAL PRESENTATIONS

Petrography in 3D: Why isn't everybody doing it?

R.A. Ketcham¹, R.D. Hanna¹, S.A. Eckley¹

¹University of Texas High-Resolution X-ray CT Facility (UTCT), Jackson School of Geosciences, University of Texas, Austin, TX, 78712 USA

Aims

An early critique of X-ray CT for geological applications was that it only produced “pretty pictures,” and subsequently great effort has been expended developing computational tools to extract quantitative data from voxel data sets. However, within those “pretty pictures” lie underexplored opportunities for changing the way we do geoscience by helping us to think in new ways. This talk will discuss two examples of the power of high-resolution X-ray CT for amplifying geological intuition, for understanding asteroid surface processes and deciphering the origin of carbonado diamonds.

The meteorite CM Murchison is a classic “carbonaceous chondrite,” with organic molecules that could be building blocks for life. Murchison is also a regolith breccia, basically consolidated rubble from the surface of an asteroid, and is known to have undergone some degree of hydrous alteration while still on its parent body.

Carbonado is a polycrystalline variety of diamond found only in Brazil and the Central African Republic. Its unique structure, of 10-100 μm diamonds sintered together by $\sim 1 \mu\text{m}$ diamonds, making it the hardest substance in nature. Carbonado has a number of other unique and enigmatic features, including a fully connected pore network, light carbon isotopes suggesting an organic source, and inclusions rich in uranium and rare earth elements and reflective of crustal rather than mantle pressure and temperature conditions.

Method

Several specimens of carbonado diamond were CT scanned – a 27-carat specimen, and several 5-10 carat specimens. Scans were taken from 40-140 kV, and dual-energy scanning was used to locate the high-Z components within the volume and distinguish them from iron-rich ones. Volumes of interest identified during lower-resolution scout scans (10-30 μm) were re-imaged at 2-6 μm to examine inclusions and pore structures in greater detail.

A single specimen of the Murchison meteorite was acquired on loan from the Smithsonian Institution. The entire volume was imaged, and close-in scans were taken of specimen corners for greater resolution. CT images were used to select regions for sectioning for subsequent petrographic, chemical and crystallographic analysis.

For both projects, visualization was done using Avizo software, and 3D measurements of individual objects and bulk fabrics were taken using Blob3D¹ and Quant3D².

Results

Initial scans of the Murchison sample revealed a subtle flattening fabric in its chondrules that had not been previously quantified. In sum, particle shapes exhibited flattening with a preferred orientation within the flattening plane. Estimates of bulk strain under end-member assumptions of compressible and incompressible chondrules resulted in an estimate of 31-59% porosity loss in the matrix due to compression, providing a partial explanation for the phenomenon of meteorites found on Earth tending to be considerably less porous than their parent bodies. Follow-up micro-analysis indicates multiple episodes of fracturing and hydrous

mineralization, and few indications of plastic deformation, indicating that most deformation was brittle and was likely the result of repeated impacts.³

Additional work has concentrated on the fine-grained rims of the chondrules, whose origin remains debated between the solar nebula and local processes on the asteroid surface. Careful analysis of the rim shapes and volumes reveal that they conform closely to predictions based on a model of moderate turbulence in the solar nebula, while other analyses compositional comparison of rims to various core types appear to rule out alteration on the asteroid surface as a reasonable mechanism.

The 27-carat carbonado scan revealed many never-before-seen textural clues, such as dodecahedral pseudomorphs after an original but now-absent phase, and grading and preferred orientation of irregular pores suggesting vapor- or fluid-filled bubbles deformed during a deformation event likely associated with crystallization of the 1- μ m diamond phase⁴. Subsequent scans of additional specimens show the strong preferred orientation of pores to be a pervasive feature of carbonados, and additional pseudomorphs that appear to have diamond ingrowths may document a second original phase that may have started resorbing prior to the end of the diamond crystallization event.

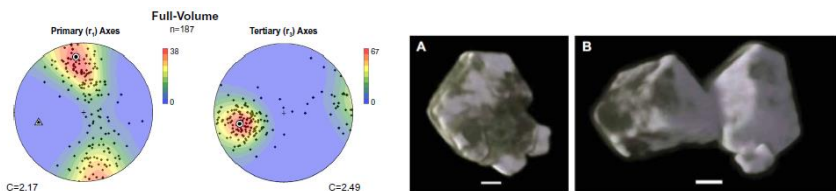


Figure 1: (left) Chondrule orientations in meteorite Murchison CM. (right) Pseudomorphs in carbonado diamond; scale bars are 50 μ m.

None of the original results of these studies were anticipated before scanning began. In both cases the original scans were exploratory, and only during extensive follow-up visualization and contemplation did meaningful patterns become apparent, which in turn led to further scanning and quantitative analysis. In both cases, study continues to this day.

Conclusion

These examples of the power of 3D observation combined with simple geological insight and imagination point to the tremendous potential for scientific discovery with more widespread dissemination and utilization of CT data, and the importance of lowering the technical, educational, and financial barriers to it.

References:

1. Ketcham, R.A., "Computational methods for quantitative analysis of three-dimensional features in geological specimens", *Geosphere*, 1, 32-41, 2005.
2. Ketcham, R.A., Ryan, T.M., "Quantification and visualization of anisotropy in trabecular bone", *Journal of Microscopy*, 213, 158-171, 2004.
3. Hanna, R.D., Ketcham, R.A., Zolensky, M., Behr, W.M., "Impact-induced brittle deformation, porosity loss, and aqueous alteration in the Murchison CM chondrite", *Geochimica et Cosmochimica Acta*, 171, 256-282, 2015.
4. Ketcham, R.A., Koeberl, C., "New textural evidence on the origin of carbonado diamond: An example of 3-D petrography using X-ray computed tomography", 9, 1336-1347.

Enhanced CT Analysis Using Volume Flattening

C.S. Parker¹, W.B. Seales¹

¹University of Kentucky, 329 Rose Street, Lexington, KY, 40506

Aims

Systematic analysis of complex CT scan data can be very difficult. Volumetric rendering is effective, but analysis is viewpoint dependent and locating features of interest in 3D can be difficult. In such circumstances, a simplification of the dataset into a flattened representation can help drive analysis. We present a technique for volumetric flattening and resampling as part of our Virtual Unwrapping pipeline and discuss how this technique can be used in areas other than document preservation.

Method

The Virtual Unwrapping pipeline is a volumetric analysis pipeline built to non-invasively open and read damaged textual documents. Through the steps of Segmentation, Flattening, and Texturing, this pipeline is able to take CT scans of highly damaged and distorted documents and produce readable images suitable for textual scholarship. Our volumetric flattening and resampling technique makes use of the first two stages of this pipeline, but replaces the Texturing phase with a Resampling phase.

In the Segmentation phase, we generate a representation of the document's surface as a triangular mesh. In the Flattening stage, this mesh is flattened using a choice of geometric parameterization (aka flattening) algorithms, producing a new 2D mesh. In the Resampling phase, we warp the original CT volume into a new, flattened representation by mapping volume coordinates through the transformation generated by flattening. This resampled volume can then be used for analysis that otherwise would be impossible.

Results

We applied this technique to a CT scan of a papyrus scroll constructed for document imaging experiments (Fig. 1). The papyrus needed to be curved to fit into our scanner, but we wanted to analyze the writing on its surface using volume rendering. The induced curvature made analysis using the original CT data difficult.

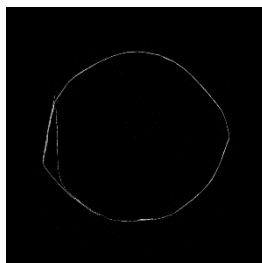


Figure 1: Slice from a CT scan of a papyrus scroll

The resulting resampled volume (Fig. 2) shows some artifacts at the edges of the volume, but these are mostly due to errors in the construction of the original 3D mesh. A “face-on” reslice of the flattened volume (Fig. 3) demonstrates the clarity of the resampled volume.

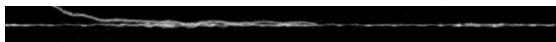


Figure 2: Flattened, resampled version of the papyrus scroll scan data (cropped for scale)

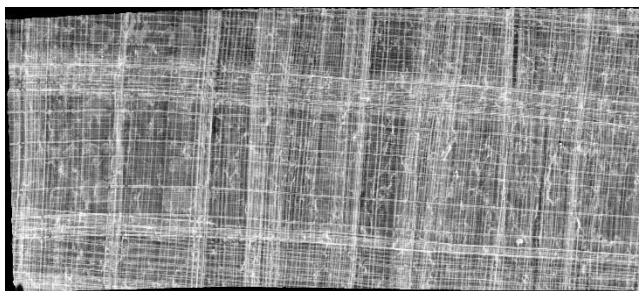


Figure 3: "Face-on" reslice of the resampled, flattened volume

We also analyzed how the choice of flattening algorithm affected the quality of the Texturing and Resampling phases of our pipeline using data from a previously analyzed scroll, the En-Gedi Scroll. Not all surfaces can be mapped to a 2D plane without introducing some sort of distortion, and different algorithms minimize different types of distortions. While the effects of these distortions are often small, our results show that care must be taken in selecting a flattening algorithm suited to the surface being analyzed (Fig. 4).

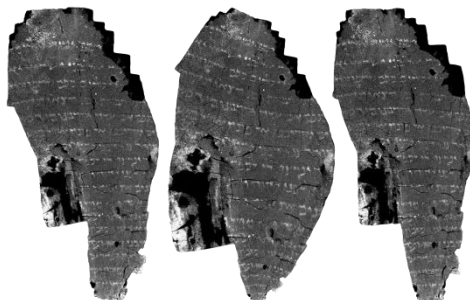


Figure 4: A surface from the En-Gedi scroll, flattened using different methods: Angle-based Flattening (left), Least Squares Conformal Maps (middle), and Cloth Modeling (right). Note the extreme distortion introduced by Least Squares Conformal Maps.

Conclusion

Our volume resampling technique is simple and provides a useful tool for analyzing objects with complex surfaces. While we here applied the technique to documents, it is a small leap to consider how it might be adapted to other fields. In the textile industry, this technique could be used for CT analysis of fabric fiber structures. In medicine, CT scans of arterial walls could be flattened in order to detect problems in the circulatory system. Further work is required to develop systems tailored to the unique needs of industries, but we believe that volumetric flattening and resampling is a tool worth exploring.

Bone diagenesis phenomena - Morphometric evaluation

M.Tomanik¹, M.Wojtków¹, C. Pezowicz¹, A.Lacel²

¹ Department of Biomedical Engineering, Mechatronics and Theory of Mechanisms, Wrocław University of Science and Technology, Poland.

² MAD Engineering Wrocław, Poland

Aims

The vast amount of palaeobiological, bio-archaeological and also numerous forensic studies are focused mainly on bones as often the only available material [10,14,20]. Post-mortem bone undergoes many changes which may lead to either its preservation or complete damage. It is now acknowledged that the processes taking place in the buried bone are so complex, that even slight changes might decide about the outcome. Also, the timing of particular modifications might be highly differentiated. Thus, the preservation of the excavated material can be accidental [9] even within a single bone [11].

The phenomenon of overall alterations inducing the transition of organic remains into fossils is called diagenesis. The diagenetic processes are conditioned by vast number of factors, however just three basic pathways of diagenetic bone modifications can be distinguished:

- I. Bone weathering: physical destruction of the bone with cracking of its surface, enabling further decomposition and involving the influence of physical factors (scavengers, UV radiation, temperature, soil type, etc.) [12,21];
- II. Chemical decomposition: chemical changes of the organic bone compound and/or chemical changes of the mineral compound [6,8];
- III. Microbial decomposition, involving collagen and other proteins hydrolysis by soil fungi and bacteria and acidic demineralization by microbial metabolites [5,13].

The general course of diagenesis is well known, however an analysis of archaeologically preserved bone does not always explain which pathways took place and when. Also, the reverse analysis - foreseeing the dominating pathway or outcome of diagenesis, especially in different depositional environments, seems almost impossible, partly because there is little data giving detailed information on the specific actions and interactions of particular diagenetic factors.

In the past, the attempts have been undertaken at developing a model allowing at least partial and controlled reconstruction of the course of diagenesis [3,16,17]. However, previous research seem not to give all the answers. It is mainly a consequence of the lack of standardization, repeatability and comparability of the experimental conditions. Thus, many questions remain unanswered. In order to gain further and fuller understanding of the diagenetic processes, it became a necessity to create a standardized, controlled experimental environment, where only the influence of selected factors would be investigated - a situation hardly applicable in real-life conditions.

Micro-CT scanning, as a non-destructive method has found wide application in archaeology, paleo-sciences and forensics [18]. It has been used for scanning and virtually unrolling ancient papyrus scrolls [1], evaluating the fossilized or mummified specimen [22], analyzing the structure of prehistoric pottery [15] or identifying engravings on fragile bone or antler archaeological specimen [4].

It is a common knowledge, that micro CT scanning can be a useful tool giving good results when evaluating the overall bone microstructure. It seems only natural that the recent research encourage using the micro-CT to evaluate also the diagenetic alterations to the bone [2,7,19].

The aim of the study was to evaluate time-related early taphonomic changes to the bone incubated in defined and controlled environmental, and expressed as the morphometric parameters, using micro CT.

Method

The vertebrae from clinically healthy pigs, Polish Landrace breed, were used. Bones were cleaned of most of surrounding soft tissues, labelled and used for the study:

1. A group of freshly harvested vertebrae was separated and kept in the freezer at the temperature of -25°C.
2. The remaining vertebrae were incubated for 113, 290 and 935 days respectively in light, acidic soil (pH 4,8).

The bones were kept in the defined environmental conditions in FITOTRON® Plant Growth Room with: constant temperature (25°C), constant soil humidity (60%) and constant air humidity of (60%). The vertebrae were incubated in identical large containers, at the same depth, with the same overall amount of soil in each container.

After 113, 290, and 935 days of incubation respectively, the vertebrae were carefully removed from the soils, brushed and evaluated. Fresh and incubated vertebral bodies with end-plates were separated from the vertebrae and scanned using SkyScan 1172 Bruker micro-CT. In order to investigate the bone degradation phenomena all the specimens were scanned with X-ray tube parameters such as 65 kV, 153 μ A, camera pixel size 13,5 μ m with rotation step 0.2. For 3D morphological analysis a cylindrical sub-volume of the originally scanned data was selected. The volume of interest (VOI) was located in the center of the bone as well on the right and left side (in 45degree angle from the axis of symmetry) with dimensions: h=6mm, r=5mm. Moreover, the VOIs were isolated on three levels: upper, middle and bottom part of vertebrae.



Fig.1. Vertebrae excavated from the soil cover



Fig. 2. Cleaned vertebra prepared for microCT scan, 290 days of incubation

Results

One may expect that as the decomposition progresses the bone volume will decrease and hence the total porosity calculated for the bone will increase. Following that trend, at first we concentrated on the two most common morphological parameters: BV/TV and Po(tot) (Fig.3.). Surprisingly after calculation we have not found any statistically significant differences between any groups what suggest that neither parameter have potential as an incubation time indicator.

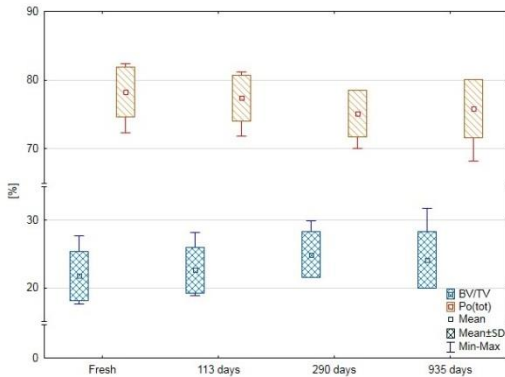


Fig.3. Graph showing the dependence of the BV/TV and Po(tot) with progressive incubation time

Therefore, we started to searching for other parameters may be taken under consideration. The idea was to find parameters that will have statistically significant differences between the fresh and incubated groups, after analyzing the date the following parameters met the requirements: Obj.N, BS/BV, Conn., Conn. Dn as well Tb.Th. As previously assumed, along with prolonged incubation the value decrees, the dependence for chosen parameters is shown on figure (Fig.4). However it should be mention that in the contrary the Tb.Th value increases with bone incubation time what initially may be easily misunderstood, this phenomena is strictly connected with the way the parameter is defined in CTAn.

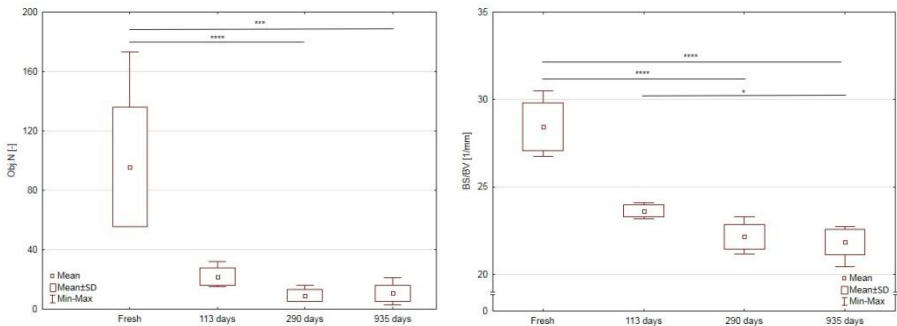


Fig.4. Exemplary graphs for potential parameters suited to be incubation time indicators
* $p < 0,05$, *** $p < 0,001$, **** $p < 0,0001$

As the results of the morphometric analyzes the software will provide user with a single mean value of bone Tb.Th from a trabecular bone site what may faultily indicate that bone elements instead of degrade are actually enhance. Though the explanation can be found in trabecula thickness distribution which shows that with time the thinner elements are absorbed while thicker objects remains giving the false positive of the value.

Moreover, during analyzing the cross-sections obtained for each vertebrae, it was observed that degradation is intensified in middle section of the bone overlapping with vertebral body arterial supply system which provides a natural channels for water and speeding up the process. For the specimens which had undergone 935 days of control in-ground degradation the lack of approximately 1/3 of the anterior cortical bone can be noticed followed by substantial regions of degraded bone tissue, figure (Fig.5) shows the depredated structure of the vertebra.

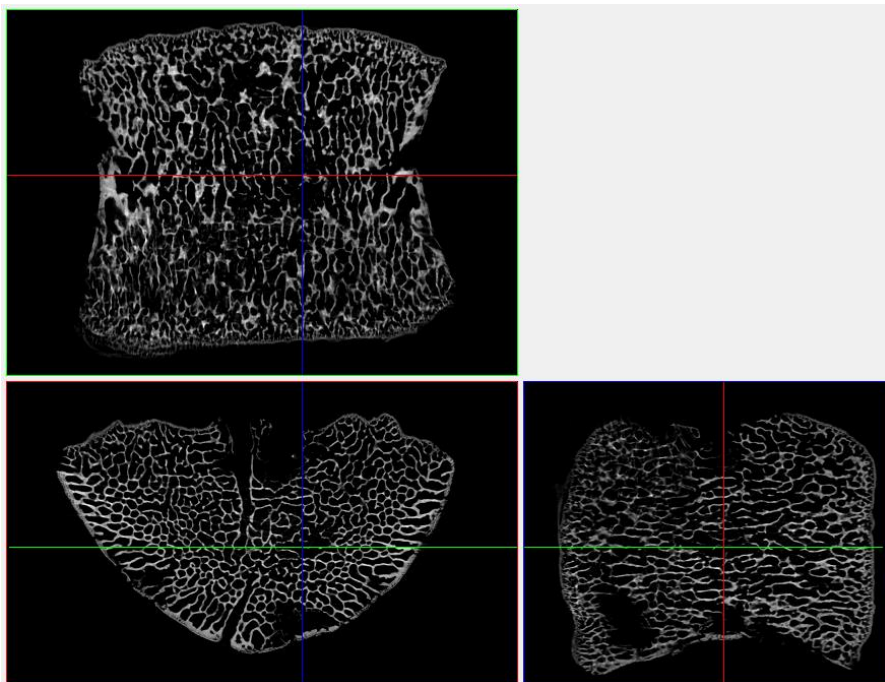


Fig.5. 3D viewing of the vertebra after 935 days of decomposition in the soil with visible regions of total bone degradation

Conclusion

Micro CT scanning of the diagenetically altered bone shows great potential in the analysis and interpretation of the time-related taphonomic changes. The resolution of the images is accrued for the occurring changes. However while interpreting the date one should take into account not only the obtained values but also fully understand the algorithms used for its calculation.

References:

1. Baumann R., Carr Porter D., Seales W.B., "The Use of micro-Ct in the study of archaeological artifacts", 9th International Conference on NDT of Art, Jerusalem Israel, 2008
2. Beck L., Cuif J.-P., Pichon L., Vaubailon S., et al., "Checking collagen preservation in archaeological bone by non-destructive studies (Micro-CT and IBA)", Nuclear Instruments and Methods in Physics Research, B 273:203–207, 2012
3. Bell L.S., Skinner M.F., Jones S.J., "The speed of post mortem change to the human skeleton and its taphonomic significance", Forensic Science International, 82:129–140, 1996
4. Bello S.M., De Groote I., Delbarre G., "Application of 3-dimensional microscopy and micro-CT scanning to the analysis of Magdalenian portable art on bone and antler", Journal of Archaeological Science, 40(5):2464-2476, 2013

5. Child A.M., "Towards an understanding of the microbial decomposition of archaeological bone in the burial environment", *Journal of Archaeological Science*, 22, pp. 165–174, 1995
6. Collins M.J., Nielsen-Marsh C.M., Hiller J., et al., "The survival of organic matter in bone: a review", *Archaeometry*, 44(3):383-394, 2002
7. Dal Sasso G., Maritana L., Usai D., et al., "Bone diagenesis at the micro-scale: Bone alteration patterns during multiple burial phases at Al Khiday (Khartoum, Sudan) between the Early Holocene and the II century AD", *Palaeogeography, Palaeoclimatology, Palaeoecology*, 416:30–42, 2014
8. Dauphin Y., Massard P., Quantin, C., et al., "Experimental in vitro dissolution of the dentine of teeth of *Sus scrofa* (Mammalia, Suidae): chemistry and microstructural alterations*", *Archaeometry*, 55:134–147, 2013
9. Fernandez-Jalvo Y., Andrews P., Pesquero D., et al., "Early bone diagenesis in temperate environments. Part I: Surface features and histology", *Palaeogeography, Palaeoclimatology, Palaeoecology*, 288(1-4):62-81, 2010
10. Garrido Varas C., Intrigo Leiva M., "Managing commingled remains from mass graves: Considerations, implications and recommendations from a human rights case in Chile", *Forensic Science International* 219(1):19-24, 2012
11. Goodwin M. B., Grant P. G., Bench G., et al., "Elemental composition and diagenetic alteration of dinosaur bone: Distinguishing micron-scale spatial and compositional heterogeneity using PIXE", *Palaeogeography, Palaeoclimatology, Palaeoecology*, 253:458–476, 2007
12. Janjua, M. A., Rogers, T. L., "Bone weathering patterns of metatarsal v. femur and the postmortem interval in Southern Ontario", *Forensic Science International*, 178(1):16 -23, 2008
13. Jans, M.M.E., "Microbial bioerosion of bone - a review", pp. 397–413, 2008, In: *Current Developments in Bioerosion*, M. Wisshak and L. Tapanila (Eds.), Erlangen Earth Conference Series, Springer-Verlag, Berlin
14. Jans, M.M.E., Nielsen-Marsh, C.M., Smith, C.I., et al. "Characterisation of microbial attack on archaeological bone". *Journal of Archaeological Science*, 31:87–95, 2004
15. Kahl W.-A., Ramminger B., Helfert M., "X-ray microtomography: a non-destructive tool to visualise different links in the production chain of ancient pottery", *European Mineralogical Conference*, Vol. 1, EMC2012-280, 2012
16. Nicholson R.A., "Bone Degradation, Burial Medium and Species Representation: Debunking the Myths, an Experiment-based Approach", *Journal of Archaeological Science*, 23:513–533, 1996
17. Nicholson R.A., "Bone Degradation in a Compost Heap", *Journal of Archaeological Science*, 25:393–403, 1998
18. Robson Brown K., Silver I.A., Musgrave J.H., et al., "The use of mCT technology to identify skull fracture in a case involving blunt force trauma", *Forensic Science International*, 206:e8–e11, 2011
19. Scherf H., "Computed tomography in paleoanthropology — an overview", *Archaeological and Anthropological Sciences*, 5:205–214, 2013
20. Schweitzer MH, Avci R., Collier T., et al., "Microscopic, chemical and molecular methods for examining fossil specimens", *Palevol*, 7:159-184, 2008
21. Trueman C.N.G., Behrensmeyer A.K., Tuross N., et al., "Mineralogical and compositional changes in bones exposed on soil surfaces in Amboseli National Park, Kenya: diagenetic mechanisms and the role of sediment pore fluids", *Journal of Archaeological Science*, 31(6):721–739, 2004
22. Wanek J, Szekeely G, Ruhli FJ., "X-ray absorption-based imaging and its limitation in differentiation of ancient mummified tissue", *Skeletal Radiology*, 40:595–601, 2011

Brain, bones and cognition: low-dose microCT in the search for treating Down syndrome

Neus Martínez-Abadías^{1,2,3}, Julia Albaigès^{1,2}, Rubèn González^{1,2}, Jorge Roldán³, Sergi Llambrich^{1,2}, Willy Gsell⁴, James Sharpe^{1,2,5}, Uwe Himmelreich⁴, Mara Dierssen^{2,3}, Greetje Vande Velde⁴

¹Center for Genomic Regulation (CRG), The Barcelona Institute of Science and Technology, Barcelona, Spain. ²Universitat Pompeu Fabra (UPF), Barcelona, Spain. ³Departament de Biologia Evolutiva, Ecologia i Ciències Ambientals, Universitat de Barcelona, Barcelona, Spain. ⁴Biomedical MRI unit/ Molecular Small Animal Imaging Center (MoSAIC), Department of Imaging and Pathology, KU Leuven, Flanders, Belgium. ⁵Institució Catalana de Recerca i Estudis Avançats (ICREA), Barcelona, Spain.

Aims

Brain and bones: the integration of two developing systems. Brain malformations lead to cognitive impairment and are associated with malformation of other systems, such as the face. The brain and the face are integrated intimately, indeed, and this linked development has important implications for vertebrate and human evolution, as well as for clinical medicine¹⁻³. Brain and craniofacial malformations co-occur in many congenital diseases, such as holoprosencephaly, cleft lip and palate, micro- and macrocephaly, Apert, Pfeiffer and Crouzon craniosynostosis syndromes and Down syndrome (DS). Although it is not known exactly how (mal-)formation of brain and face influence each other, it is clear that the interaction between common signaling pathways in neural and skeletal development underlie the tight link between the brain, the face and the skull^{3,4}. It is likely that this close developmental relationship is not only restricted to these structures but also can be extended to other elements of the skeletal system, such as the bones of the appendicular skeleton. This integrated view of development is critical to understand diseases such as DS, with a complex and multisystemic phenotype involving cognitive, brain, craniofacial and skeletal malformations.

Down syndrome as a neuro-skeletal disorder. DS is a genetic condition caused by trisomy of chromosome 21, in which gene overexpression alters many systems and results in cognitive impairment, immunodeficiency, congenital heart diseases, skeletal and craniofacial dysmorphologies⁵. Cognitive impairment in DS is the result from altered neural development and can be directly related to brain malformations⁶. Reciprocally, the skull shape is significantly altered in DS, showing a typical shape with shorter, wider and rounder skulls and a flattened face⁷. Besides cranial and facial bones, long bones also show an altered pattern of skeletal development in individuals with DS, with reduced bone mineral density and abnormal bone remodeling and growth, which in adults results in osteopenia and osteoporosis⁸. Extensive research has identified genes and molecular mechanisms underlying the cognitive impairment associated with DS⁶, but we know little about how trisomic genes affect bone maintenance and homeostasis. We still need to understand how the same signaling pathways are involved in both neurogenesis and skeletal development and how these interactions are altered in DS.

Integrated development, integrated treatment? Epigallocatechin-3-gallate (EGCG), a green tea flavonoid, is a strong candidate for pharmacotherapy in DS⁹⁻¹³, possibly through normalization of the overexpression of *Dyrk1A*^{9,11}, a candidate gene for skeletal and brain co-development that lies in the DS critical region of chromosome 21^{6,8,14-17}. Interestingly, the beneficial effects of EGCG may not be limited to neural and cognitive phenotypes, but may

extend to skeletal phenotypes^{8,10,18-21} - although high doses of EGCG may have the contrary effect, suppressing bone formation and exacerbating skeletal defects^{19,20}.

Longitudinal evaluation of the integrated development of the skeleton, the skull and the brain. One of the main challenges to analyze the integration patterns between the skeleton and the brain is to follow their developmental trajectory on the same individuals, from birth to adulthood. Low-dose μ CT is able to provide anatomical images from live, free-breathing animals in three dimensions with excellent resolution and contrast. The properties of μ CT can be extended using diffusible iodine-based contrast-enhanced CT (diceCT), a staining technique that combines the assets of good soft tissue contrast for evaluation of brain anatomy with excellent visualization of bony structures versus soft and aerated tissues, and that is more cost-effective than MRI²². We propose non-invasive imaging to assess longitudinal changes in a preclinical study of the integration of skeletal, neural and cognitive development in DS and to explore the potential for EGCG treatment to ameliorate simultaneously neural and skeletal development from early in development into adulthood.

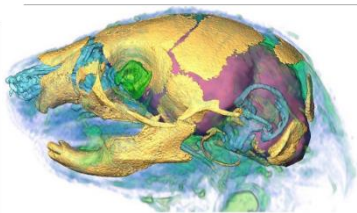


Figure 1: Superimposition of different scans to visualize the head of a P0 mouse and highlight the integration of the skull (yellow) and the brain (purple). From Martínez-Abadías et al (2013).

Method

We bred trisomic (Ts65Dn) mice and administered EGCG (30 mg/kg/ day) to half of the litters, starting when both the face and the brain start developing (embryonic day 9), and continued the treatment up to postnatal day 29. The mice were genotyped by quantitative PCR and distributed in four groups: euploid (WT) and trisomic (TS), treated and untreated. We followed the postnatal development of the skull and the brain by repeatedly scanning each mouse with both *in vivo* μ CT (SkyScan1278) and MRI (9.4T, Bruker Biospin) at postnatal days (PD) 3 (infantile), 14 (juvenile) and 29 (early adult) with optimized scan settings per time point, and *ex vivo* diceCT after the last *in vivo* time point. We also assessed the psychomotor and neurobehavioral development of the mice. We segmented the MR images and estimated the volume of the whole brain, the four brain ventricles and the cerebellum. We also recorded 3D coordinates of landmarks located in these structures. From the μ CT data, we estimated bone mineral density (BMD) in the humerus and performed volumetric and 3D morphometric analyses of the upper limb bones and skull to compare the skeletal development and skull morphometry among groups.

Results

EGCG treatment rescued the TS mice for some brain morphology and psychomotor measurements, such as normalized ventriculomegaly of the lateral ventricles and pivoting behavior. For the rest of measurements we analyzed, the EGCG treatment did not show any effect (i.e. volumes of the third and fourth ventricles, as well as blast response or tactile orientation) or even indicated a worsening of the DS phenotype, such as of walking behavior and bone development (Figure 2). The μ CT scans showed that upon EGCG treatment, both euploid and trisomic mice presented a delay in bone growth, with overall lower BMD and obvious bone defects (Figure 2A-B). Statistical testing revealed that TS mice were smaller than WT and the EGCG significantly reduced skull size in both groups. The comparative analyses of skull shape revealed significant differences between trisomic and euploid mice that are evident from birth and increase with time (Figure 2C). In comparison to euploid mice, trisomic mice present flatter faces with more globular, brachycephalic skulls, which correspond

to the most common craniofacial traits in DS individuals. Unexpectedly, the EGCG treatment caused an exacerbation of the DS craniofacial traits, in both WT and TS mice. These severe effects suggest that over-inhibition of *Dyrk1A*-activity by EGCG treatment can have deleterious effects on bone development and growth. To look deeper into these effects, more volumetric and morphometric brain analyses, as well as systematic assessments of BMD on skull and long bones, are ongoing.

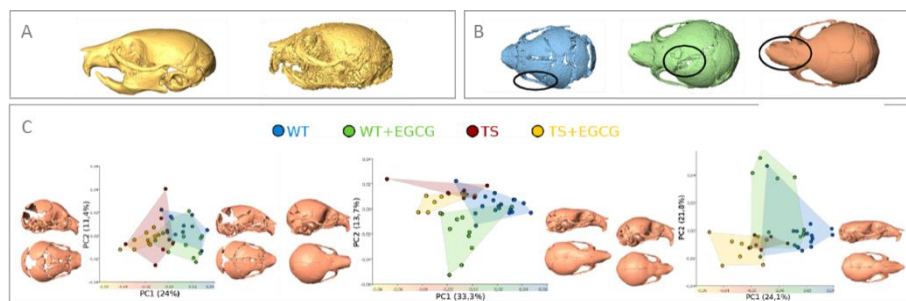


Figure 2: Skull shape and bone development assessment. A) Qualitative comparison showing lack of bone mineralization in EGCG treated mice. The same threshold was used to reconstruct the skulls, which reveals lower bone density in the EGCG treated case (right). B) Examples of abnormal skeletal development in EGCG treated mice. C) Skull morphometric analysis based on Principal Component analyses performed using the 3D coordinates of 27 anatomical landmarks recorded throughout the skulls of the same mice in the four groups of mice (WT, TS, WT+EGCG, TS+EGCG) at PD3 (left), PD14 (middle), PD29 (right). Convex hull shaded areas represent the range of variation of each group of mice, whereas 3D reconstructions depict the skull shape of groups lying at the extremes of variation associated with the first principal component, which explains the largest percentage of morphological variation.

Conclusion

Our results underscore the urgent need to test the effect of the EGCG at different concentrations with the aim to optimize the beneficial over the detrimental effects of this treatment. Our results clearly evidence that EGCG treatment can have pleiotropic effects and that at certain concentrations EGCG can have more negative than positive impact on bone, face and brain development. This is especially relevant when considering that in humans there is suggestive evidence that the EGCG treatment can have a positive impact on facial morphology and that many people are already taking green tea based treatments, which are freely commercially available. It is crucial to establish as soon as possible the efficiency and dose-effect of the treatment, aiming to identify the optimal EGCG dosage that provides maximal therapeutic effect while minimizing potential side effects.

References

1. Lieberman, D.E., Hallgr msson, B., Liu, W., Parsons, T.E. & Jamniczky, H.A. Spatial packing, cranial base angulation, and craniofacial shape variation in the mammalian skull: testing a new model using mice. *Journal of anatomy* 212, 720-735 (2008).
2. Boeckx, C. & Benitez-Burraco, A. Osteogenesis and neurogenesis: a robust link also for language evolution. *Frontiers in cellular neuroscience* 9, 291 (2015).
3. Marcucio, R.S., Young, N.M., Hu, D. & Hallgr msson, B. Mechanisms that underlie co-variation of the brain and face. *Genesis* 49, 177-189 (2011).

4. Richtsmeier, J.T. & Flaherty, K. Hand in glove: brain and skull in development and dysmorphogenesis. *Acta neuropathologica* 125, 469-489 (2013).
5. Wiseman, F.K., Alford, K.A., Tybulewicz, V.L. & Fisher, E.M. Down syndrome--recent progress and future prospects. *Human molecular genetics* 18, R75-83 (2009).
6. Lott, I.T. & Dierssen, M. Cognitive deficits and associated neurological complications in individuals with Down's syndrome. *The Lancet. Neurology* 9, 623-633 (2010).
7. Richtsmeier, J.T., Baxter, L.L. & Reeves, R.H. Parallels of craniofacial maldevelopment in Down syndrome and Ts65Dn mice. *Developmental dynamics : an official publication of the American Association of Anatomists* 217, 137-145 (2000).
8. Blazek, J.D., Abeysekera, I., Li, J. & Roper, R.J. Rescue of the abnormal skeletal phenotype in Ts65Dn Down syndrome mice using genetic and therapeutic modulation of trisomic Dyrk1a. *Human molecular genetics* 24, 5687-5696 (2015).
9. de la Torre, R., et al. Safety and efficacy of cognitive training plus epigallocatechin-3-gallate in young adults with Down's syndrome (TESDAD): a double-blind, randomised, placebo-controlled, phase 2 trial. *The Lancet Neurology* 15, 801-810 (2016).
10. Abeysekera, I., et al. Differential effects of Epigallocatechin-3-gallate containing supplements on correcting skeletal defects in a Down syndrome mouse model. *Molecular nutrition & food research* 60, 717-726 (2016).
11. De la Torre, R., et al. Epigallocatechin-3-gallate, a DYRK1A inhibitor, rescues cognitive deficits in Down syndrome mouse models and in humans. *Molecular nutrition & food research* 58, 278-288 (2014).
12. Guedj, F., et al. Green tea polyphenols rescue of brain defects induced by overexpression of DYRK1A. *PLoS one* 4, e4606 (2009).
13. Bain, J., McLauchlan, H., Elliott, M. & Cohen, P. The specificities of protein kinase inhibitors: an update. *The Biochemical journal* 371, 199-204 (2003).
14. Rahmani, Z., et al. Critical role of the D21S55 region on chromosome 21 in the pathogenesis of Down syndrome. *Proceedings of the National Academy of Sciences of the United States of America* 86, 5958-5962 (1989).
15. Dahmane, N., et al. Transcriptional map of the 2.5-Mb CBR-ERG region of chromosome 21 involved in Down syndrome. *Genomics* 48, 12-23 (1998).
16. Dierssen, M., Herault, Y. & Estivill, X. Aneuploidy: from a physiological mechanism of variance to Down syndrome. *Physiological reviews* 89, 887-920 (2009).
17. Nissen, R.M., Amsterdam, A. & Hopkins, N. A zebrafish screen for craniofacial mutants identifies wdr68 as a highly conserved gene required for endothelin-1 expression. *BMC developmental biology* 6, 28 (2006).
18. Kamon, M., Zhao, R. & Sakamoto, K. Green tea polyphenol (-)-epigallocatechin gallate suppressed the differentiation of murine osteoblastic MC3T3-E1 cells. *Cell biology international* 34, 109-116 (2010).
19. Logsdon, A.L., et al. Exposure to green tea extract alters the incidence of specific cyclophosphamide-induced malformations. *Birth defects research. Part B, Developmental and reproductive toxicology* 95, 231-237 (2012).
20. Rodriguez, R., et al. Implantation of green tea catechin alpha-tricalcium phosphate combination enhances bone repair in rat skull defects. *Journal of biomedical materials research. Part B, Applied biomaterials* 98, 263-271 (2011).
21. McEliea, S.D., et al. Influence of prenatal EGCG treatment and Dyrk1a dosage reduction on craniofacial features associated with Down syndrome. *Human molecular genetics* 25, 4856-4869 (2016).
22. Anderson, R. & Maga, A.M. A Novel Procedure for Rapid Imaging of Adult Mouse Brains with MicroCT Using Iodine-Based Contrast. *PLoS one* 10, e0142974 (2015).

Micro-CT as a 3D reverse engineering tool to study emulsification processing

G. van Dalen¹, T. Kroon, H. Kroon

¹ Unilever Research & Development, Imaging & Spectroscopy, Olivier van Noortlaan 120, 3133AT Vlaardingen, the Netherlands

Introduction

The goal of reverse engineering is to reproduce, duplicate, or enhance products and systems based on the study of an original object/system without drawings, documentation, or a computer model¹. It's also called back engineering and is used in many application areas, such as manufacturing, industrial design, digital archiving, electronics, dental or surgical prosthetics and competitor analysis. In emulsion manufacturing two immiscible liquids are mixed using in-line high shear rotor-stator mixers. They are used for products such as shampoos, deodorants, salad dressings and sauces. The droplet size of these products influences the stability and rheological properties of these products. Generally, the smaller the average particle size and the tighter the size distribution, the more stable the emulsion. Sufficient mixing energy is required in order to create small droplets in an emulsion. These mixers consist of a rotor and stator that have concentric rows of intermeshing teeth². This rotor-stator combination is called the mill head. The product enters at the centre of the stator and moves outward through radial channels in the rotor/stator teeth. The combination of high tip speed and extremely close tolerances subjects the product to intense shear in every pass. The gap between adjacent surfaces of the rotor and stator is adjustable for fine-tuning shear levels and flow rates. Knowledge is needed of the detailed geometry of rotor-stator mixers to obtain hydrodynamic insight in the emulsification process. The geometric size and shape or complete 3D geometric models can be used as input for computational fluid dynamic (CFD) studies³. Reverse engineering often involves disassembling and analysing its components and workings in detail. In this study X-ray microtomography (micro-CT)⁴ is used for the non-invasive visualisation and analysis of the size and shape of rotors and stators. To prevent disassembling, micro-CT images were made of silicone "negatives" (or "moulds") of the rotors and stators. The results were compared to those obtained by profilometry of the original object.

Method

A silicon mould was made of a mill head using the following procedure:

- A silicone-based lubricant was sprayed onto the rotor/stator head, which produces a very thin layer.
- Then a "negative" or "mould" of the rotor/stator was made by filling it with pourable silicone (2-component Silicone RTV 664, <https://www.momentive.com/products/show-technical-datasheet.aspx?id=26640>) and letting this solidify overnight in an oven at 70 °C.
- After solidification of the silicone, the mould was carefully removed. Then a representative piece was cut out that fits the sample holder of the micro-CT (Figure 1). Plastic cylindrical sample holders with an inner diameter of 27 mm were used. The upper part of the sample holder consist of a removable open tube with a length of ~60 mm.

This mould was imaged using a Skyscan 1172 desktop micro-CT system with a 100kV X-ray source (10W, 20-100kV, 0-250 μ A, < 5 μ spot size) and a 10 Mp X-ray detector (4000 * 2096 pixels). Power settings of 95kV and 104 μ A were used. Images were acquired using a aluminium beam filter, step size of 0.23° over 180 degrees and frame averaging of 3. Scans with pixel sizes of 7.92 μ m were made. The total scanning time (1800 images) was 6:16 hours/scan. The sample was scanned using 3 scans, connected in the vertical direction to increase the axial field-of-view (oversized scan) and subsequently merged together during the reconstruction. A stack of 5342 horizontal cross sections with a pixel size of 4000x4000 was obtained after tomographic reconstruction of the projection images. A beam hardening correction of 40% and ring artefact correction of 20 and smoothing of 4 were selected.

For quantitative analysis and visualisation in 3D space of the micro-CT images the AvizoFire 8.1.1 software from the FEI Visualization Sciences Group was used. The sizes were analysed using interactive measurement tools.

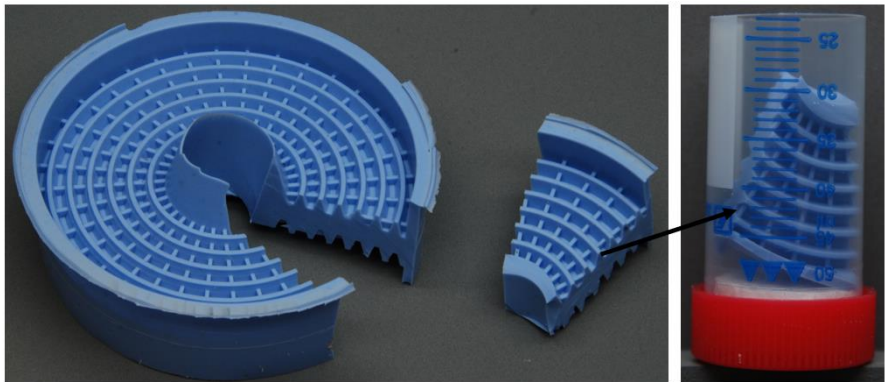


Figure 1 Sampling of a silicon mould of a rotor-stator mixer.

Profilometry was performed at the “Zeiss Measuring House” in Best (The Netherlands). Stylus profilometry refers to scanning the surface or profile of an object in order to specify/quantify its shape. The traditional way is to carefully move a probe (“stylus”) across the surface in order to determine the 3D location of a series of points with respect to a chosen reference. The analysis was performed on a rotor and a stator (the original part, not the mould).

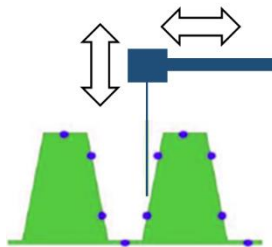


Figure 2 Schematic view of stylus profilometry of a mill head.

Results

Horizontal cross sections with 3D visualisations of micro-CT image of moulds of mill heads are shown in Figure 3. The mould is clearly visible as a dark object (white = low absorption coefficient) within the light grey sample holder. An example of the measurements of the width of the teeth and width of the gaps between the teeth (at their base and top) using a radial micro-CT cross section is shown in Figure 4. The measured values are constant over the total mill head (independent of the ring no). To calculate the actual dimensions, it has to be taken into account that the mould is the negative of the original object (Figure 5). The results of the analysis of a micro-CT image of a rotor are compared to those obtained by profilometry of the original rotor in Figure 6. The values for b , b' , $B + B'$, $b + b'$ and H are within 2% relative. However larger deviations are seen for B and B' . For the latter cases, we have to realise that the measurements are made on the silicone moulds, so translated to that geometry the largest deviation is found in the top width B' of the mould teeth. This is the location where one would expect the largest effect of relaxation of residual elastic stresses in the mould after removal and/or the largest effect of shrinkage during curing. According to the RTV664 silicone information available on the Internet, this material has low shrinkage when cured at room temperature. All in all, we can thus conclude that the micro-CT values can be trusted quite well, although the individual values of B and particularly B' have to be used with some care. In order to develop this method further it would be worthwhile to spend some effort on the elimination of stress relaxation and shrinkage, by changing the curing temperature and/or by selecting a different type of mould material.

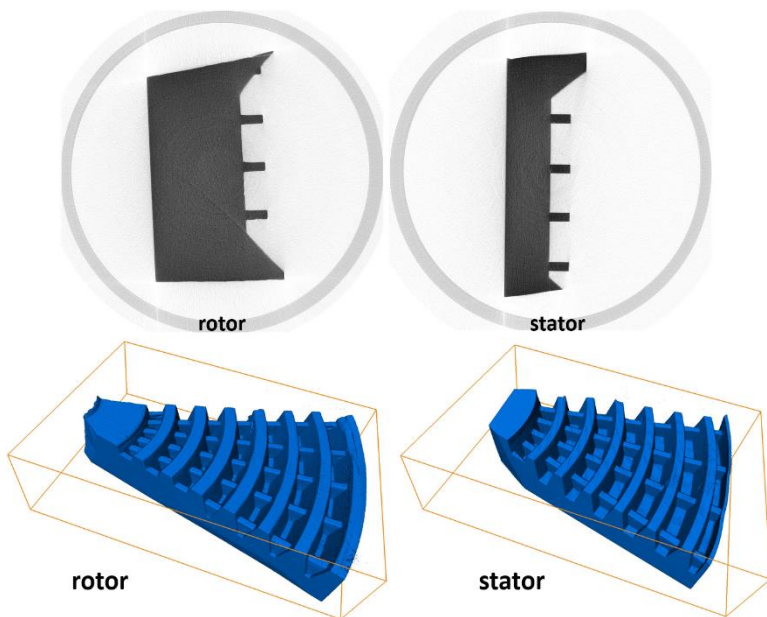


Figure 3 Horizontal cross sections (top) of micro-CT images of moulds of a rotor and stator (inner diameter of sample holder = 27 mm) with 3D visualisations (bottom: box size = 9mm x 26mm x 37mm).

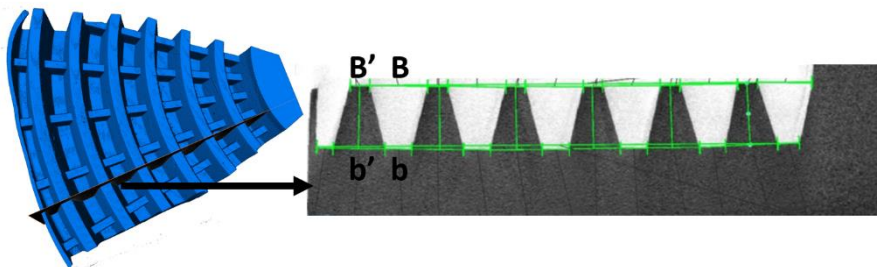


Figure 4 Example showing the measurement in the tangential direction of the mould of a stator).

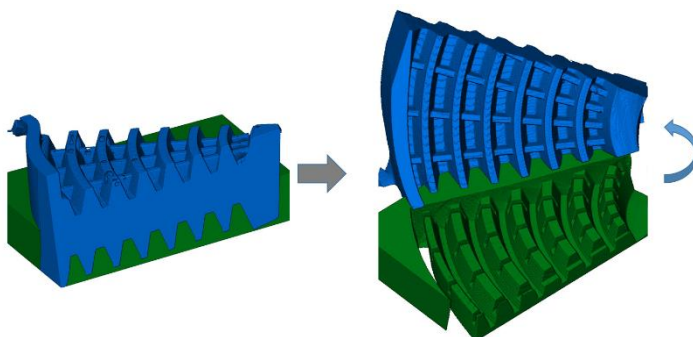


Figure 5 3D visualisation of the mould (blue) and the recalculated original (green).

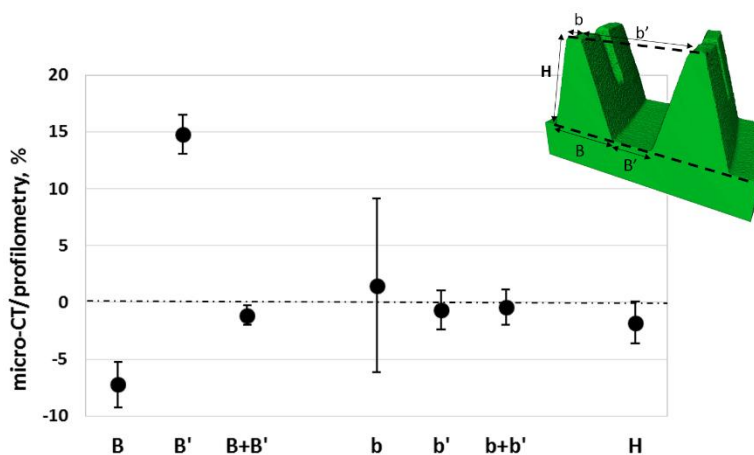


Figure 6 Comparison between the dimensions of a rotor measured by micro-CT and profilometry.

Conclusion

Micro-CT proved to be a very useful technique for non-destructive reverse engineering of complex objects such as stator-rotor mixers. Scanning a silicon mould of the original object is an effective method for accurate and precise 3D geometrical measurement. The results were for the most part well in agreement with profilometry of the original object. Remaining deviations can likely be explained from minor distortions to the mould during its solidification or after removal. Beside extracting the dimensions of the object also a complete 3D model can be generated which can be used as input for 3D modelling or 3D printing.

-
- 1 Raja, V. (2008) Introduction to Reverse Engineering, in Reverse Engineering An Industrial Perspective (ed Editors: Raja, V., Fernandes, K. J.), Springer, 1-9
 - 2 Pacek, A. W., Hall, S., Cooke, M. and Kowalski, A. J. (2013) Emulsification in Rotor–Stator Mixers, in Emulsion Formation and Stability (ed T. F. Tadros), Wiley-VCH Verlag GmbH & Co. KGaA, Weinheim, Germany. doi: 10.1002/9783527647941.ch5
 - 3 Janssen, J.J.M. and Mayer, M. (2016) Computational Fluid Dynamics (CFD)-Based Droplet Size Estimates in Emulsification Equipment, Processes, 4, 50; doi:10.3390/pr4040050
 - 4 Dalen, G. van and Koster, M.W. (2012) 2D & 3D particle size analysis of micro-CT images, Bruker micro-CT Meeting, 3 April 2012, Brussels, Belgium

Investigation of internal structure in the scales of Palaeozoic cartilaginous fishes using micro-CT

A.O. Ivanov^{1,2}, S.P. Nilov¹

¹ Institute of Earth Sciences, St. Petersburg State University, St. Petersburg, Russia,

² Kazan Federal University, Kazan, Republic of Tatarstan, Russia

Aims

The records of early fishes in the Ordovician – Devonian are often represented by isolated body exoskeletal elements such as the scales and spines. The large number of chondrichthyan taxa occurred in this interval has been described based on isolated scales. The internal structure of scales in the recent and some fossil chondrichthyan fishes was studied based on cross sections utilized the optical microscope since 19th century (Agassiz, 1833-1843). This traditional method allows to research the details of skeletal tissues but the specimens were destroyed. The utilization of micro-CT with visualization software allows examination of the internal structure and reconstruction of the 3D model of canal system in the exoskeletal elements such as chondrichthyan teeth and scales without destroying the specimen (Abel et al., 2012). The canal (vascularization) system is poorly studied in the scales of the Palaeozoic chondrichthyans.

The scales of chondrichthyans occur growing and non-growing (Reif, 1978). The morphogenetic types of the scales are distinguished on simple monodontodia, complex monodontodia and polyodontodia depending on the structure and arrangement of odontodes (Karatajute-Talimaa, 1992). In this investigation the scale internal structure included the vascularization system was studied in the scales of different morphogenetic types and groups of the Palaeozoic chondrichthyans.

Method

The following specimens were studied utilized micro-CT: scale of *Cladolepis* from the Mazalovskiy Kitat Regional Stage, Givetian, Middle Devonian of Alchedat River, Kuznetsk Basin, Russia; scale of *Karksilepis* from the Burtneki Regional Stage, Givetian, Middle Devonian of Karksi outcrop, Estonia; scales of orodontid and ctenacanthid types from the Steshev Regional Stage, Serpukhovian, Early Carboniferous of Zabor'e quarry, Moscow Region, Russia; euselachian scale from the Sterlitamak Regional Stage, Sakmarian, Early Permian of road cut outcrop in the Chelyabinsk Region, Russia.

The internal structure of the chondrichthyan scales was reconstructed utilising a SkyScan 1172 Bruker-microCT (Center for Geo-Environmental Research and Modeling "GEOMODEL", Research park of St. Petersburg State University). The specimens were scanned at a voltage of 55 - 96 kV and 104 - 167 mA, with a aluminium/copper or aluminium filter for a rotation of 180° at the highest camera resolution, with an average rotation step of 0.4°. The virtual cross-section images were generated from the 3D reconstruction used to achieve 3D volume rendering with the software InstaRecon, DataViewer, CTAn and CTVox. The reconstruction of canal system was used the transparent mode of skeletal tissues.

Abbreviations: abc – ascending base canal, acc – ascending crown canal, b – scale base; c – scale crown; fbc – foramen of canal in the base, fcc – foramen of canal in the crown, fnc – foramen of canal in the scale neck; hbc – horizontal base canal, hcc – horizontal crown canal,

hnc – horizontal neck canal; inc – inclined neck canal; n – scale neck; od – odontode, pc – pulp canal, pca – pulp cavity.

Results

The scale of *Cladolepis* is flat, rhomboid in shape, with slightly convex base. The scale has a crown containing the odontodes placed at the different distance from each other (Fig. 1A). The odontodes are elongated, with concave middle part. The base is composed of compact lamelline tissue, missing the vascular canals (Fig. 1E). The foramina of canals are penetrated the crown surface between odontodes and around the odontode field. The network of horizontal vascular canals and their ramifications is concentrated in the crown especially in the posterior part where the odontodes are placed densely (Fig. 1B, C). The short ascending canals are connected this network with the small pulp canals of the odontodes (Fig. 1F). The scale of *Cladolepis* is growing, polyodontodia type.

The scales of *Karksilepis* possess the shape from rhomboid with convex base and long odontodes (Märss et al., 2008) to polygonal tessera-like with flat base and short odontodes (Fig. 2A, D). The scale base consists of lamellar tissue with bone cell lacunae (Märss et al., 2008). The tessera-like scale has a narrow, spiniform odontodes, inclined posteriorly and arranged at the sizeable distance from each other. The foramina of vascular canals are located at all edges of the base and on the basal side (Fig. 2D). The canal system in the scale base consists of sinuous main horizontal canals connecting by the small branches and ascending short canals penetrating the scale base (Fig. 2D, C, F). Some horizontal canals interconnect the pulp canals of odontodes (Fig. 2E). The *Karksilepis* scales are polyodontodia type with non-growing base.

The orodontid scale possesses the flat crown with compact odontocomplex, the low neck and the convex base compounded of lamelline. The central primordial odontode is surrounded the elongated additional odontodes (Fig. 3A, B). The scale neck bears the numerous foramina of neck canals opening on the lateral and posterior sides (Fig. 3D, E). The rows of foramina are located on the boundary between the odontodes (Fig. 3B). The network of vascular canals includes the meandering horizontal and ascending basal canals, as well as the branched neck canals rising to the crown (Fig. 3C, F). The orodontid scales are growing with complex polyodontodia crown.

The ctenacanthid scales possess the polyodontode complex crown, narrow neck and low, flat base (Fig. 4A-C). The odontodes are spine-like, inclined and incurved posteriorly, closely spaced and separated by narrow and deep grooves, partly fused, bearing distinct, branching carinae. The most part of odontode is composed of osteodentine. The additional odontodes diverge from the prominent primordial odontode placed in the center of the crown. The small foramina of vascular canals open in the anterior surface of the neck and base, in the basal surface of the base (Fig. 4A) but the large foramina are penetrated the posterior face of the scale neck (Fig. 4B). The very complicate network of canals is distributed within the entire scale. The ascending canals are started from the basal side of the base and continued through the neck to each odontode in the crown merged to the pulp canal (Fig. 4D-F). The ascending canals are connected each other by short horizontal or inclined branches. The inclined neck canals are formed the dense network with the ascending canals in the lower part of the crown (Fig. 4G). The ctenacanthid scales are regularly growing scales of complex polyodontodia type.

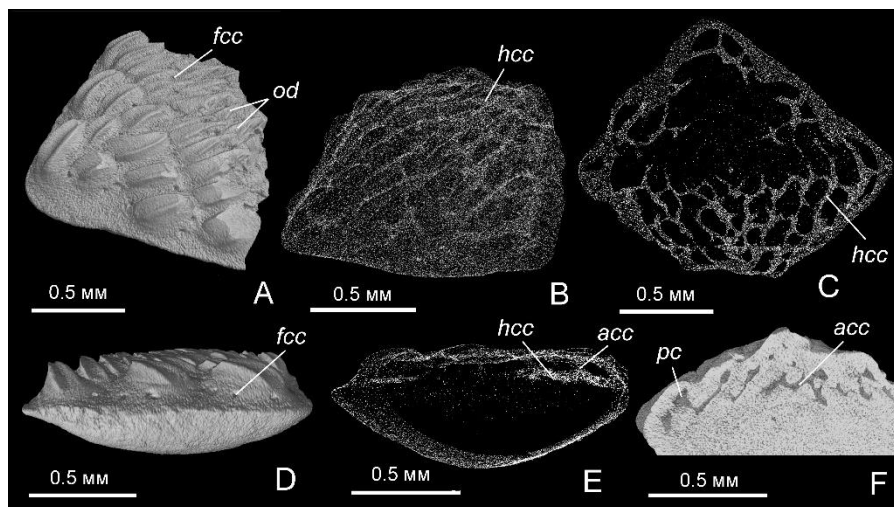


Figure 1: Scale of *Cladolepis*. A – scale in oblique crown view; B – scale in transparent mode, same view; C – virtual longitudinal section of the scale crown; D – scale in lateral view; E – virtual transversal section of the scale; F – section of the odontode group.

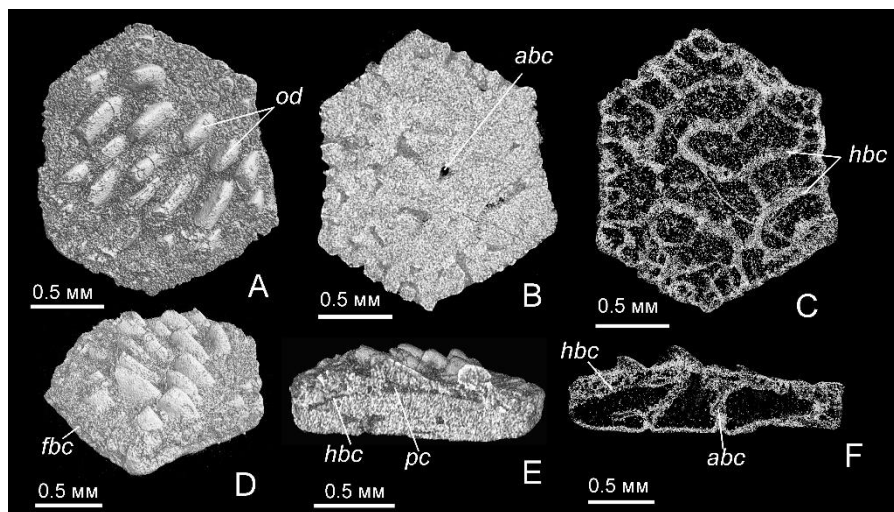


Figure 2: Scale of *Karksilepis*. A – scale in crown view; B – virtual longitudinal section of the scale base; C – virtual longitudinal section of the scale base, transparent mode; D – scale in oblique crown view; E – virtual transversal section of the scale; F – virtual transversal section of the scale, transparent mode.

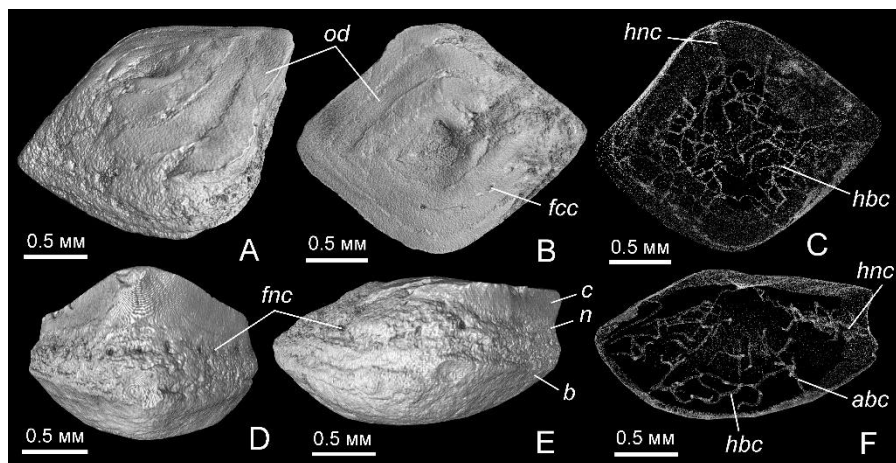


Figure 3: Orodontid scale. A, B – scale in oblique lateral and crown views; C – virtual longitudinal section of the scale base, transparent mode; D, E – scale in posterior and lateral views; F – virtual transversal section of the scale, transparent mode.

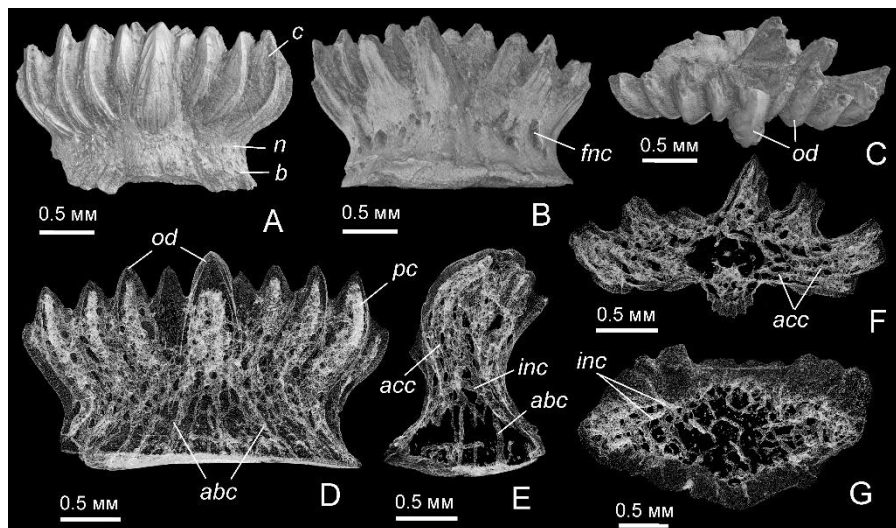


Figure 4: Ctenacanthid scale. A, B, C – scale in anterior, posterior and crown views; D–G – virtual sections of the scale in transparent mode; D – longitudinal section of the scale; E – transversal section of the scale; F – transversal section of the crown; G – transversal section of the scale neck.

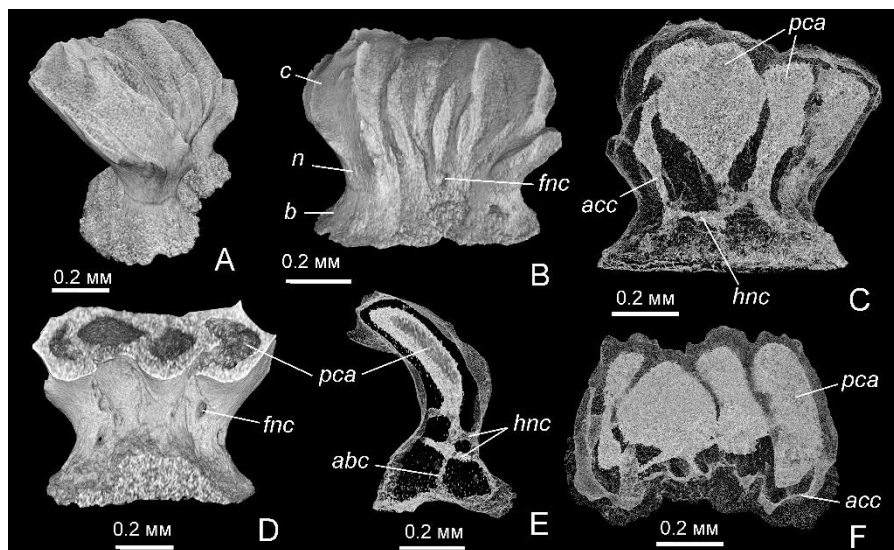


Figure 5: Euselachian scale. A, B – scale in oblique lateral and anterior views; B – virtual longitudinal section of the scale; D – scale in posterior view with virtual section of posterior parts of the crown and base; E – virtual transversal section of the scale, transparent mode; F – virtual transversal section of the crown, transparent mode.

The studied euselachian scale from the Early Permian possesses the flattened, inclined crown bearing the strong ridges, narrow neck and small flat base (Fig. 5A, B). A few foramina are penetrated the basal surface of the base, the anterior and posterior sides of the neck (Fig. 5B, D). The ascending canals run from the base to the crown where they pass into the large, pulp cavities expanded upward (Fig. 5C, F). The short horizontal neck canals are connected with the ascending ones (Fig. 5E). Such scales are probably non-growing type.

Conclusion

The studied scales of the Paleozoic chondrichthyans demonstrate the diverse internal structures: canal system and odontodes. The most complicate system of canals is observed in the growing polyodontode scales such as ctenacanthid in contrast to what was considered before. The scales with non-growing base possess the branching network of basal canals. The large pulp cavities occur only in the probably non-growing euselachian scales. The investigation of fossil scales utilizing micro-CT allows to reconstruct the morphogenesis of squamation in various groups of chondrichthyans

Acknowledgements

The study was partly supported by a grant from Saint-Petersburg State University No. 0.38.292.2015. The work is performed according to the Russian Government Program of Competitive Growth of Kazan Federal University. Scientific researches were performed at the Center for Geo-Environmental Research and Modeling (GEOMODEL) of Research park of St. Petersburg State University.

References:

1. Abel R.L., Laurini C.R. and Richter M., A palaeobiologist's guide to 'virtual' micro-CT preparation. *Palaeontologica Electronica* 15(2), 1-17, 2012.
2. Agassiz J.L.R., Recherches sur les Poissons Fossiles. Neuchâtel (Nicolet), Imprimerie de Petitpierre, 5 vols, 1420 p., 1833-1843.
3. Karatajute-Talimaa V.N. The early stages of the dermal skeleton formation in chondrichthyans. In: Mark-Kurik E, ed. Fossil fishes as living animals. Tallinn: Institute of Geology, 223-231, 1992.
4. Märss T., Kleesment A. and Niit M. *Karksilepis parva* gen. et sp. nov. (Chondrichthyes) from the Burtnieki Regional Stage, Middle Devonian of Estonia. *Estonian Journal of Earth Sciences*, 57, 219-230, 2008.
5. Reif W.E. Types of morphogenesis of the dermal skeleton in fossil sharks. *Paläontologische Zeitschrift* 52:110-128, 1978.

Morphometric and content assessment of the bone repair in rats treated with Guar Gum and X-ray irradiation

D.M. Brasil¹, G.D.Roque-Torres², A.I.V. Silva³, H.W.P. Carvalho⁴, V.C.C. Girão⁵, S.M. Almeida⁶.

^{1,6}Department of Oral Diagnosis, Piracicaba Dental School, State University of Campinas, Piracicaba, SP, Brazil,

²Micro Imaging Research Laboratory, School of Dentistry, Loma Linda University, USA,

³Department of Oral Radiology, School of Dentistry, Pontifical Catholic University of Minas Gerais, Belo Horizonte, Brazil,

³Laboratory of Nuclear Instrumentation, Nuclear power center in Agriculture – *Luiz de Queiroz*, São Paulo University, Piracicaba, SP, Brazil,

⁵Department of Morphology, Faculty of Medicine, Federal University of Ceará, Fortaleza, Brazil,

Aims

Bone tissue has high regenerative capacity, and in general, is able to recover from a damage without the need of major interventions. It involves inflammatory mediators and growth factors, as well as modulating protein from osteoclasts and osteoblasts. However, there are cases in which bone loss occurs, which, depending on the extension, could compromise bone repair. Thus, the use of bone graft is an alternative to provide matrix, allowing osteoblasts migration to form the organic matrix and, consequently, bone tissue repair. Materials that assist in the development of a healthy bone matrix have been studied to be used as graft, such as the polysaccharide derived from Guar Gum (PGG), which is a type of proteoglycan. Proteoglycans are connected with glycosaminoglycans (GAGs) that seems to affect the differentiation of progenitor mesenchymal cells into osteoblasts. It was observed that the osteoblasts treatment with GAG suppressed the ability of these cells to support the osteoclast differentiation, as well as their bone reabsorption activity. Natural polysaccharides with GAG structure have an effect on the inflammatory response. A PGG which reproduces the glycosaminoglycan structure of the extracellular matrix of articular cartilage and has protective properties of the cartilaginous tissue in the experimentally induced osteoarthritis has been developed and patented by UFC (02/09/2010 – nº PI1003401-3). The study of the effect of PGG application may represent the development of a new matrix to accelerate and optimize the repair of bone damages. The treatment used for bone neoplasia, in many cases, involves radiotherapy as an additional method. Despite of the high rates of success of this therapy, it must be highlighted the deleterious effects of radiation on the bone repair process. Studies have found that radiation induces an increase in osteoclastic activity, promoting substantial changes in morphology and bone strength and delayed bone repair. Considering that the search for materials that help in the bone regeneration process is very valuable, the aim of this study was to evaluate the effect of local administration of a polysaccharide derived from Guar Gum (PGG) solution on the repair process of bone defects in tibiae of irradiated rats.

Method

Forty rats (*Rattus norvegicus*, Wistar Albinus), adults, males were divided into 4 groups based on treatment and on the use of irradiation (n=10): Control (Group 1), PGG administration (Group 2), Irradiation nontreated (Group 3), Irradiation + PGG administration (Group 4). Bone defects were produced on the right tibiae, with a round carbide drill #8 at low speed and PGG solution was administrated in these defects. Three days before the bone defect execution, the

animals on groups 3 and 4 were submitted to a single dose of 15 Gy of X-radiation. Twenty-one days after irradiation, all rats were sacrificed and their tibiae were removed.

The tibiae were scanned into a cylindrical plastic tube filled with water by Skyscan 1174 microCT system (Bruker, Belgium) using an aluminum filter of 0.5 mm, X-ray voltage of 50 kV, X-ray current of 800 μ A, 0.5° rotation step, averaging (frames) of 2, 180° scanning and 6,4 μ m of pixel size in a way that the defect was centralized in the scanned bone region. The acquired images were reconstructed by NRecon software (Bruker) and analyzed by CTAn software (Bruker). The volume was standardized on 400 axial images which fitted the repair region in the same amount in the upper and lower direction from the center of the repair (Figure 1A). The ROI was standardized in 2.3 mm of width and 0.8 mm of height based on the size of the bone defect preparation (Figure 1B) ensuring that all repair region was into the ROI. So, a rectangular VOI including the region of repair was created. Then, the morphometric parameters were analyzed. The analysis of the samples' mineral content was done by two-dimensional mapping using X-ray microfluorescence (μ XRF). The results of morphometric parameters were statistically analyzed using ANOVA test and *post hoc* Tukey test. The level of significance was set at 5%.

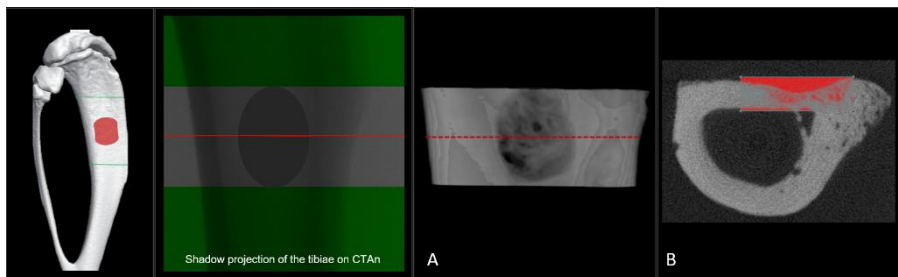


Figure 1: Shadow projection of the tibiae on CTAn. A. Volume composed by 400 axial images. B. Region of Interest.

Results

The PGG group presented better morphometric parameters regarding the bone repair process (Figure 2).

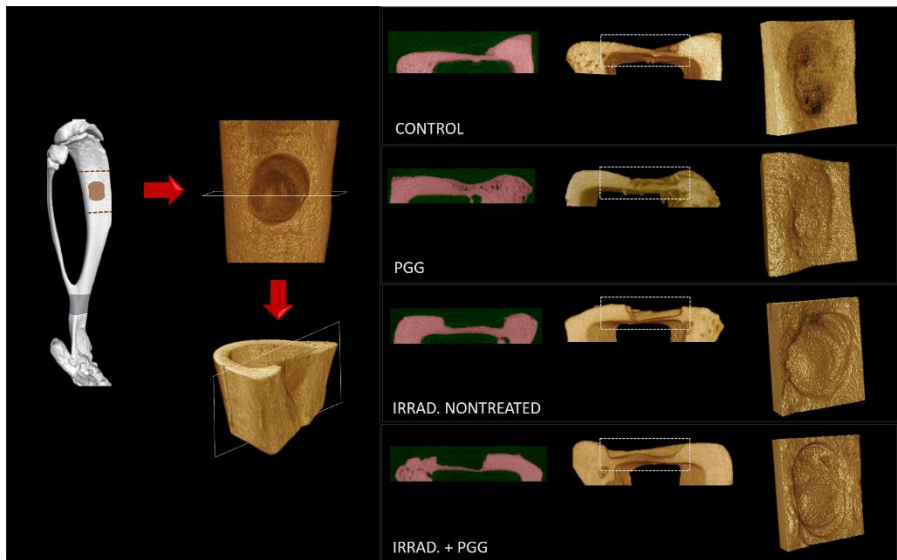


Figure 2: Slices, rendered volumes of repair regions and final VOI assessed for each group.

The PGG group presented statistically significant higher bone volume and number of closed pores ($p < 0.05$) compared with control, irradiated nontreated and irradiated + PGG groups. Bone surface density was statistically significant lower on PGG group compared with control group ($p < 0.05$) (Figure 3).

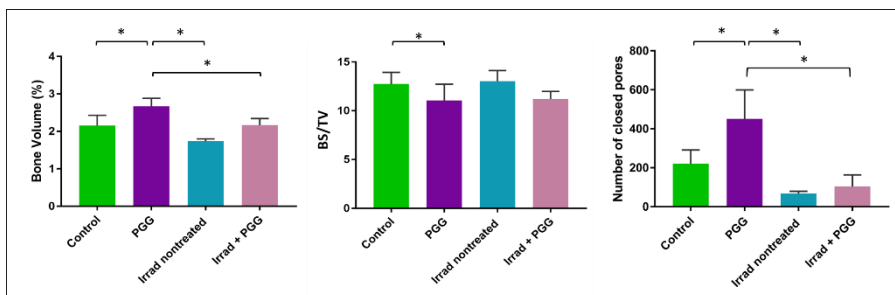


Figure 3: Graphs showing Bone Volume (%), Bone surface density and Number of closed pores for each group. An asterisk (*) indicates statistically significant difference between groups.

The mineral content mapping by μ XRF from control and PGG groups showed that the elements calcium and phosphor presented higher concentration in the center of the repair region in PGG group. It was also possible to notice that the potassium distribution is homogeneous in both groups (Figure 4).

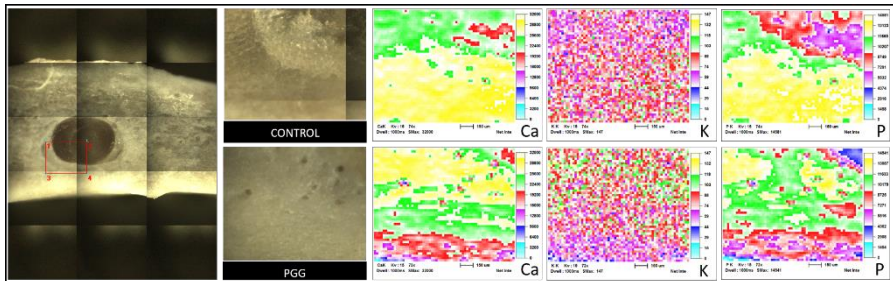


Figure 4: Calcium, Potassium and Phosphor mapping by μ XRF from control and PGG groups.

Conclusion

We concluded that PGG improves the bone regeneration process in non irradiated rats.

References:

1. CASTRO R. R, FEITOSA J. L. A., CUNHA P. L. R., ROCHA F. A. C. Analgesic activity of a polysaccharide in experimental osteoarthritis in rats. *ClinRheumatol.* v. 26, p. 1312–1319, 2007.
2. FAZZALARI N. L., KULIWABA J. S., ATKINS G. J., FORWOOD M. R., FINDLAY D. M. The ratio of messenger RNA levels of receptor activator of nuclear factor Kappa B ligand to osteoprotegerin. *J Bone Miner Res.* v.16, n. 6, p.1015-27, 2001.
3. GANDHI N. S., MANCERA R. L. The structure of glycosaminoglycans and their interactions with proteins. *ChemBiol Drug Des.* v. 72, n. 6, p. 455-482, 2008.
4. KONDO H., SEARBY N. D., MOJARRAB R., PHILLIPS J., ALWOOD J., YUMOTO K., ALMEIDA E. A., LIMOLI C. L., GLOBUS R. K. Total-body irradiation of postpubertal mice with (137) Cs acutely compromises the microarchitecture of cancellous bone and increases osteoclasts. *Radiat Res.* v. 171, n. 3, p. 283-9, 2009.
5. ROTHWELL, B. R. Prevention and treatment of the orofacial complications of radiotherapy. *J Am Dent Assoc.* v. 114, n. 3, p. 316-322, 1987.
6. SALBACH-HIRSCH J. et al. Sulfated glycosaminoglycans support osteoblast function sandc on currently suppressosteoclasts. *J Cell Biochem.* v. 115, n. 6, p. 1101-11, 2014.
7. STEVENS C. T., TEN DUIS H. J. Plate osteosynthesis of simple forearm fractures: LCP versus DC plates. *ActaOrthop Belg.* v. 74, n. 2, p. 180-3. 2008.
8. WERNLE J. D., DAMRON T. A., ALLEN M. J., MANN K. A. Local irradiation alters bone morphology and increases bone fragility in a mouse model. *J Biomech.* v. 14, p. 2738-46, 2010.
9. WILLEY J. S., LLOYD S. A., ROBBINS M. E., BOURLAND J. D., SMITH-SIELICKI H., BOWMAN L. C., NORRDIN R. W., BATEMAN T. A. Early increase in osteoclast number in mice after whole-body irradiation with 2 Gy X rays. *Radiat Res.* v. 170, n. 3, p. 388-92, 2008.

Structure-texture relationships in bakery products

A. Cornish¹

¹Campden BRI, Station Road, Chipping Campden, Gloucestershire, GL55 6LD, UK,

Aims

The texture of food products is directly related to the structure¹. This is particularly apparent for cellular products, where attributes such as thicker cell walls and smaller cells result in firmer products, whilst thinner cell walls and larger cells produce products which are less resistant. Texture is an important factor in consumer acceptability of a product.

Well established methods exist for texture analysis and these are used routinely in the food industry. During development of new products texture analysis is used to check that the desired texture is being produced, but 3D structural measurements are not routine.

X-ray micro-CT is a fantastic tool for measuring the 3D structure of bakery products. This work shows how 3D structural measurements obtained using X-ray micro-CT methods can be used to complement data obtained from routine texture measurements.

Method

Two commercially available samples were obtained for this study: White sliced sandwich bread and sliced rye bread. Textural and structural measurements were obtained from both samples.

An X-ray micro-CT system (Bruker 1172) was used to obtain structural measurements. A pastry cutter was used to cut a 50 mm disc from the centre of a slice for each sample. The sample was then transferred into a screw top plastic pot to prevent drying (and subsequent shrinkage) during the scan. This container was stuck to a brass sample stub before being mounted inside the scan chamber.

Analysis of the micro-CT data was performed using CTAn. Firstly a circular volume of interest with a diameter of 30 mm was selected. This VOI excluded the edges of the sample. It was important to exclude this region because it was compressed during the cutting process and therefore the original structure was not intact. The data was binarised using a global threshold. Noise was minimised by removing all objects except the largest (a despeckle function). 3D object analysis was performed, including measurements of morphometry, structure separation and structure thickness.

A texture analyser (Stable Micro Systems, TA-Xt plus) fitted with a 50 kg load cell was used to obtain texture measurements. A two bite compression test was performed using a 25 mm diameter cylindrical probe. Whole, individual slices of bread were placed on a flat bed beneath the probe. The probe was driven at a speed of 5 mm s⁻¹ into the centre of each slice of bread. When the probe reached 35% strain, it was driven upwards, off the slice, then driven down again at the same speed for a second compression (again until 35% strain). 10 replicate slices were measured for each sample. Each slice was removed from the packaging immediately prior to the compression test to avoid texture changes due to drying. The replicate slices were placed on the base in the same orientation to avoid variation due to orientation related effects.

Results

Figure 1 shows texture analysis profiles for a double compression test for white sandwich bread and rye bread (note the different scales on the two plots). The rye bread required considerably more force to compress than the white sandwich bread which means that the rye bread has a firmer texture. For every replicate for both samples, the maximum force was higher for the first compression than the second. This is partly due to the fact that the sample had not fully recovered by the time of the second compression, and also due to damage to the cellular structure which occurred during the first compression.

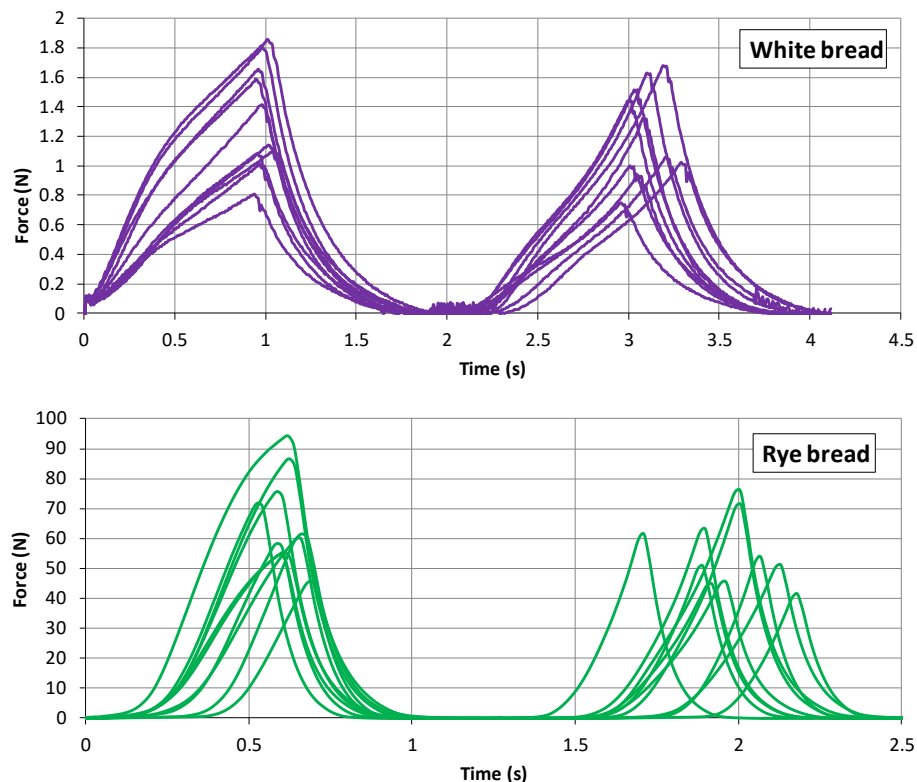


Figure 1: Texture profile tests (top) white sandwich bread (bottom) rye bread

The structure of these samples was measured using X-ray micro-CT. Figure 2 shows images of the structure, structure thickness and structure separation (calculated using CTAn and visualised using CTVox). A storyboard was saved within CTVox which allows different datasets to be orientated and imaged in the same position. For the structure images, shadows have been cast into the pores, making them appear dark. For the structure thickness and structure separation images, a rainbow transfer function was created. A program was developed (in IDL) to create transfer functions automatically without the need to use manual sliders within CTVox. Small diameters are shown in dark blue and large diameters are shown in red. This allows a visual comparison of the sizes of pores and the thickness of the cell walls.

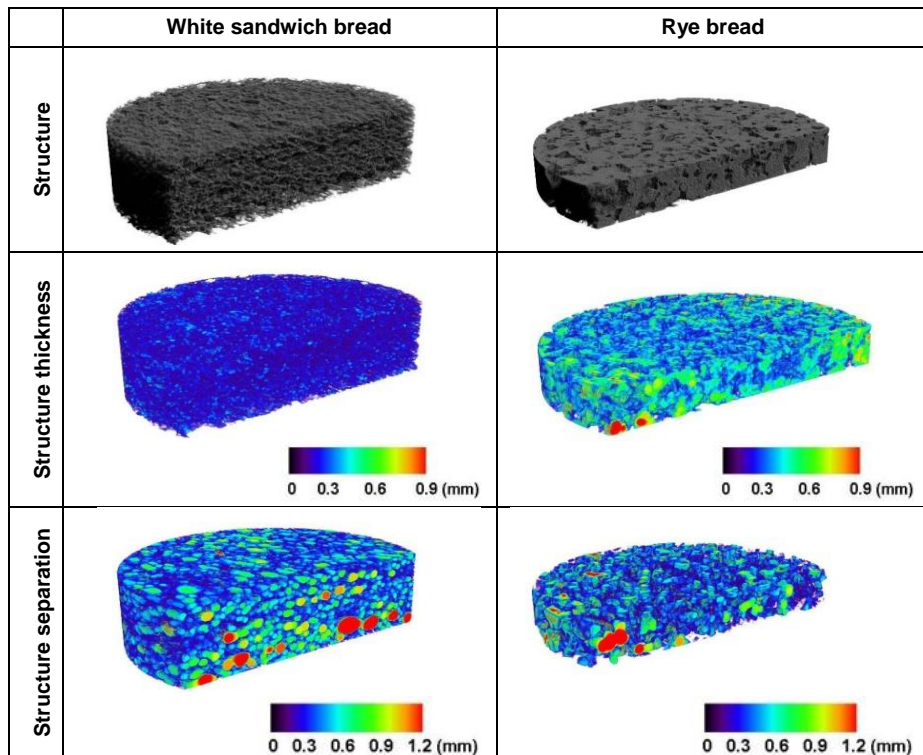


Figure 2: X-ray microCT images showing the structure, structure separation and structure thickness for samples of white sandwich bread and rye bread

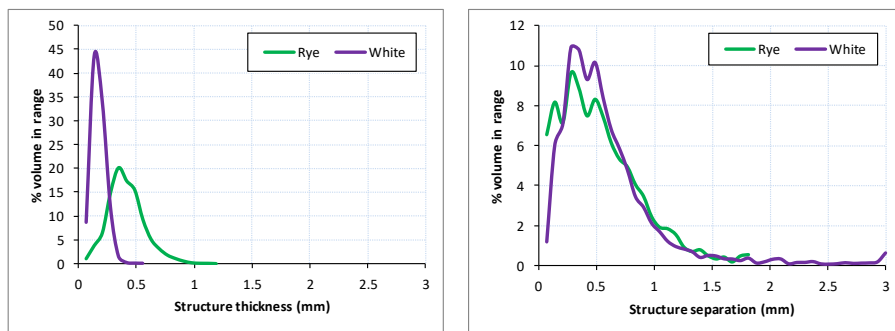


Figure 3: Plots of structure separation and structure thickness for samples of white sandwich bread and rye bread

Figure 3 shows plots of structure thickness and structure separation (the same data as shown in Figure 2). For the white sliced bread, a narrow thickness distribution with a peak at 0.14 mm was obtained whereas a broader distribution with a peak at 0.35 mm was obtained for the rye bread. This indicates that the rye bread has thicker, more irregular cell walls.

This is apparent within the images in Figure 2. The structure thickness image for white bread is predominantly blue (small diameters) but the corresponding image for rye bread shows brighter colours, revealing the positions of thick walls. Both samples show very similar structure separation distributions indicating that there is a similar distribution of pore sizes within these products. The structure separation images for these two samples are similar. Regions with large (bright) pores and smaller (dark blue) pores are visible for both samples.

The majority of pores within bakery products are interconnected due to foam to sponge conversion which occurs during the baking process (otherwise bread would collapse when taken out of the oven). Therefore, segmentation of discrete bubbles is not possible and analysis of structure separation is an appropriate method to characterise the bubble structure.

Morphometry analysis was also performed using CTAn; parameters of particular importance for bakery products are total porosity and connectivity. The white bread had a total porosity of 69.7% whereas the rye bread had a total porosity of 31.8%. Less than 1% of the total porosity was classified as closed porosity.

Conclusion

This work shows that 3D structural data can provide important information which can be used to help understand the reasons for differences in texture between different products. For the example products presented in this abstract, the rye bread was shown to have firmer texture than the white bread. 3D structural analysis revealed that this difference was due to thicker cell walls and lower porosity of the rye bread compared to the white bread. Both products were shown to have a similar cell size distribution.

This simple study is intended to illustrate the value of 3D structural characterisation data to aid understanding of texture analysis data. The example samples presented in this abstract differ in ways other than structure (they contain different ingredients) so in this case, textural differences are not solely due to structural differences.

References:

1. C Wilkinson, G.B Dijksterhuis, M Minekus, "From food structure to texture", Trends in Food Science & Technology, 442-450, 2000

Quantitative assessment of brain tumor radiation treatment reveals decrease in tumor-supporting vessels

David Haberthür¹, Ruslan Hlushchuk¹, Marine Potez¹, Audrey Bouchet¹, Valentin Djonov¹

¹Institute of Anatomy, University of Bern, Switzerland

Aims

Angiogenesis—the formation of new blood vessels—is an important factor for tumor growth [6]. Reducing tumor-supporting vessels by radiation treatment is a powerful option for treating tumors; specialized treatments that deliver high radiation doses have shown to enable *excellent* survival rate [3]. Among rodent models for brain tumors, the 9L-gliosarcoma model is a widely used one, since it mimics important features of human brain tumor growth.

Method

Brain tumors were induced in 10-week-old Fisher 344 rats (n=59) by inoculation of gliosarcoma cells into the right caudate nucleus through the skull [1].

Ten days after inoculation, tumor volume was assessed by MRI performed with a 4.7 T [Bruker Avance III](#) console [4]. Based on tumor volume, animals were split into groups with comparable tumor size ready for either microbeam radiation therapy (MRT), conventional radiation therapy (so called broad beam, BB) or no therapy (CTRL).

Irradiation was performed at the [ID17 biomedical beamline](#) at the European Synchrotron Radiation Facility. Details on the facility and the radiation treatment are described by [2].

Briefly, rats were irradiated ten days after inoculation using two 8 x 10 mm irradiation fields focused onto the tumor location in the anterior part of the right hemisphere. For the MRT-animals, the irradiation field was split into 40 microbeams (width 50 µm, 200 µm on-center spacing) using a multislit collimator. The in-microbeam entrance dose was 250 Gy, the valley dose approximately 9 Gy. For the BB-animals, the irradiation was homogeneously applied to the same area with a dose equivalent to the MRT valley dose.

On days 6, 10 and 14 after radiation treatment, rats were again imaged by MRI. Subsequently, they were infused with a contrast agent (µAngiofil, [5]) and their brains extracted. Fifty-four of those brains were imaged with a [Bruker SkyScan 1272](#). The brains were immersed in 4 % PFA in a custom-made sample holder and imaged at 5 µm voxel size.

After manually delineating the tumor regions of interest (ROIs) in CTAn we used a custom image processing pipeline in Python to assess the data sets and extract the aforementioned values. The automatic assessment pipeline analyzes the 54 data sets fully autonomous and in a reproducible way.

Due to the contrast agent, separating blood vessels from the tumor volume was as easy as using standard gray value thresholding. This makes it possible to easily extract values like tumor and vessel volume and thus the vessel volume ratio. With a distance transformation we can also extract the vessel diameter and the vessel surface.

Results

Tumor ROIs can easily be visualized. Figure 1 shows three example tumors from the whole set of scans.

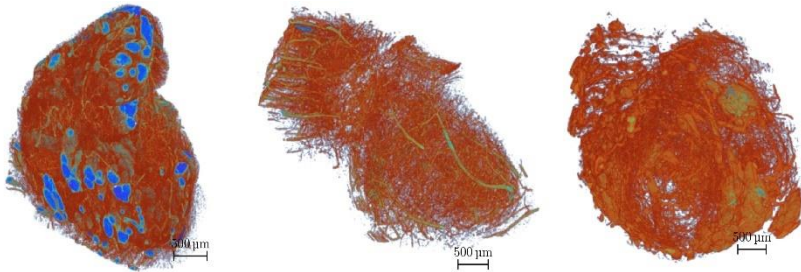


Figure 7: Visualization of three of the 54 scanned tumors. Left to right: Control, microbeam and broad beam radiation therapy.

Radiation treatment reduces the vasculature in the tumor, as can be seen in Figure 2 to the left.

Conclusion

Using the described approach, we show that radiation treatment decreases the vasculature in the tumor, i.e. less vessels are available to provide the tumor with nutrients. Our unbiased, automatic assessment shows that the performed radiation treatment is successful.

In parallel to performing the scans, we developed the analysis pipeline. The reproducible analysis made it possible to easily add more samples, i.e. preliminary results could be obtained early on in this study.

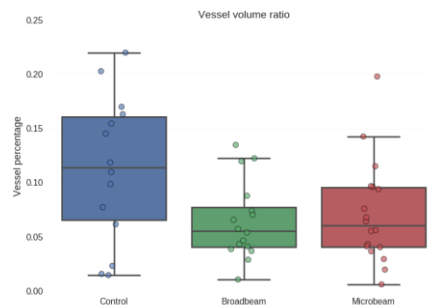


Figure 8: Box plots of the vessel volume per tumor volume.

References:

10. Bouchet, Audrey, et al., 2014, "Characterization of the 9L gliosarcoma implanted in the Fischer rat: an orthotopic model for a grade IV brain tumor.", *Tumor Biology*, doi:10.1007/s13277-014-1783-6
11. Bouchet, Audrey, et al., 2016, "Better Efficacy of Synchrotron Spatially Microfractionated Radiation Therapy Than Uniform Radiation Therapy on Glioma.", *International Journal of Radiation Oncology*Biophysics*, doi:10.1016/j.ijrobp.2016.03.040
12. Laissue, Jean A., et al. 1998., "Neuropathology of ablation of rat gliosarcomas and contiguous brain tissues using a microplanar beam of synchrotron-wiggler-generated X rays.", *International Journal of Cancer*, doi:10.1002/(SICI)1097-0215(19981123)78:5<654::AID-IJC21>3.0.CO;2-L
13. Lemasson, Benjamin, et al., 2015, "Multiparametric MRI as an early biomarker of individual therapy effects during concomitant treatment of brain tumours.", *NMR in Biomedicine*, doi:10.1002/nbm.3357
14. Schaad, Laura, et al., 2017, "Correlative Imaging of the Murine Hind Limb Vasculature and Muscle Tissue by MicroCT and Light Microscopy.", *Scientific Reports*, doi:10.1038/srep41842
15. Sherwood, Louis M., et al., 1971, "Tumor Angiogenesis: Therapeutic Implications.", *New England Journal of Medicine*, doi:10.1056/NEJM197111182852108

Investigating Zoledronate Treatment as a Preventative Strategy for Paget's Disease of Bone

R.J. van 't Hof, G. Charlesworth, A. Prior, A. Daroszewska

Institute of Ageing and Chronic Disease
University of Liverpool
The William Duncan Building
6 West Derby Street
Liverpool L7 8TX
United Kingdom

Aims

Paget's disease of bone (PDB) is a common bone disease affecting approximately 3% of the population over the age of 55. It is characterized by focally increased bone turnover caused by hyperactive osteoclasts, the bone resorbing cells. PDB leads to bone pain, bone deformation and associated complications such as osteoarthritis, deafness and rarely osteosarcoma. PDB is often not diagnosed until skeletal complications have already occurred. Treatment that inhibits the osteoclasts, using drugs called bisphosphonates, is very successful at reducing bone pain, but does not lead to repair of damaged bones and joints.

PDB is a disease with a strong genetic component, and the most common mutations leading to PDB are mutations in the SQSTM1 gene. This opens up the possibility of screening family members of current patients for the presence of these mutations, and treating carriers of the mutations with bisphosphonates before complication arise, thereby preventing the skeletal damage, pain and disability caused by the disease.

We have recently developed a mouse model of PDB, which carries the most common PDB-associated mutation in the SQSTM1 gene, the P394L mutation¹. With ageing, these mice develop lesions comparable to those observed in human patients (see Fig. 1). The aim of this study was to investigate if treatment of young adult P394L mice, that have no PDB lesions yet, with the bisphosphonate zoledronate, prevents the development of PDB.

Method

Mice homozygous for the P394L mutation were injected intraperitoneally with zoledronate at a dose of 85 ng/g body weight or vehicle control (PBS) every 2 months from the age of 4 months (N=10). The dose used is equivalent to the dose most commonly used in humans. At the age of 12 months, the mice were humanely killed, the hind limbs harvested, fixed overnight in 4% phosphate buffered formaldehyde, washed in PBS and stored in 70% ethanol. The mice were labeled with intra-peritoneal injections of calcein green (Sigma, UK) 5 days and 2 days prior to culling to enable histological analysis of bone formation.

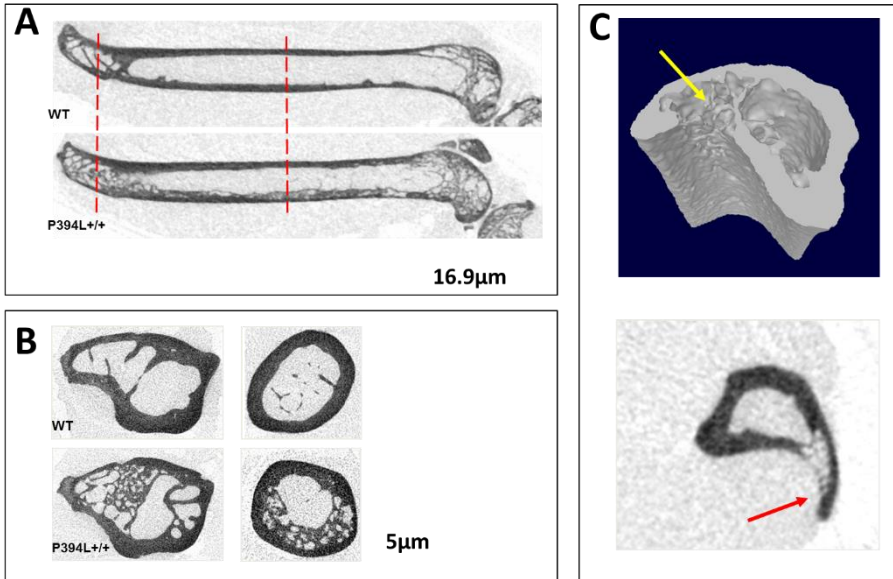


Figure 1: Development of Pagetic lesions in mice homozygous for the P394L mutation.

Panel A shows a comparison of a normal WT femur (WT) and the femur of a P394L mutant mouse at 12 months of age. Note the abnormal spongy appearance of the cortex of the mutant mouse. Panel B shows transaxial slices at higher resolution from the same bone, taken at the level indicated by the dotted red line in panel A. Note the abnormal structure of the bone. Panel C shows a 3D image created using CTVox of a Pagetic lesion in the tibia of a mutant mouse, indicated by the yellow arrow. The lower image shows the typical appearance of this lesion in Dataviewer.

Both hind limbs of each mouse were scanned using a Skyscan 1172 μ CT scanner, fitted with a robotic sample changer. The hind legs were scanned inside 1ml syringes in 70% ethanol. Initial scans were performed of the entire hind limbs at a resolution of $9\mu\text{m}$, X-ray source at 50kV and 200 μA and a 0.5 mm Al filter using the oversize scanning option. The rotation step size was 0.5° , and the camera was set to 2x2 binning. The resulting scans were reconstructed using NRecon, and analysed for the presence of pagetic-like lesions using the Dataviewer and CTVox programs. Additional scans used to analyse bone micro-architecture were performed at the distal femur at a resolution of $4.5\mu\text{m}$, without camera binning, and a rotation step size of 0.3° . Scans were reconstructed using NRecon and analysed using CTAn.

Finally, to analyse tissue mineralization, samples were equilibrated overnight in water, and the distal femur scanned inside drinking straws. The scanner settings were: resolution $4.5\mu\text{m}$, X-ray source at 50 kV and 200 μA , 0.5 mm Al filter, camera binning 2x2, rotation step size 0.3° , averaging at 3. Hydroxy-apatite standards (Skyscan, Belgium), were scanned using identical settings to calibrate mineral density.

For further histological analysis, the bones were embedded in methylmethacrylate, and sections cut at 5 μm . The sections were stained with von Kossa/van Giesson to visualize mineralized and unmineralised (osteoid) bone respectively. Goldner's trichrome stain was used for general imaging of matrix and cells. Tartrate resistant acid phosphatase (TRAP) staining was used to identify osteoclasts, and a calcein blue counterstain was used for imaging the calcein green bone labels. Sections were imaged on a Zeiss Axiolmager motorized microscope.

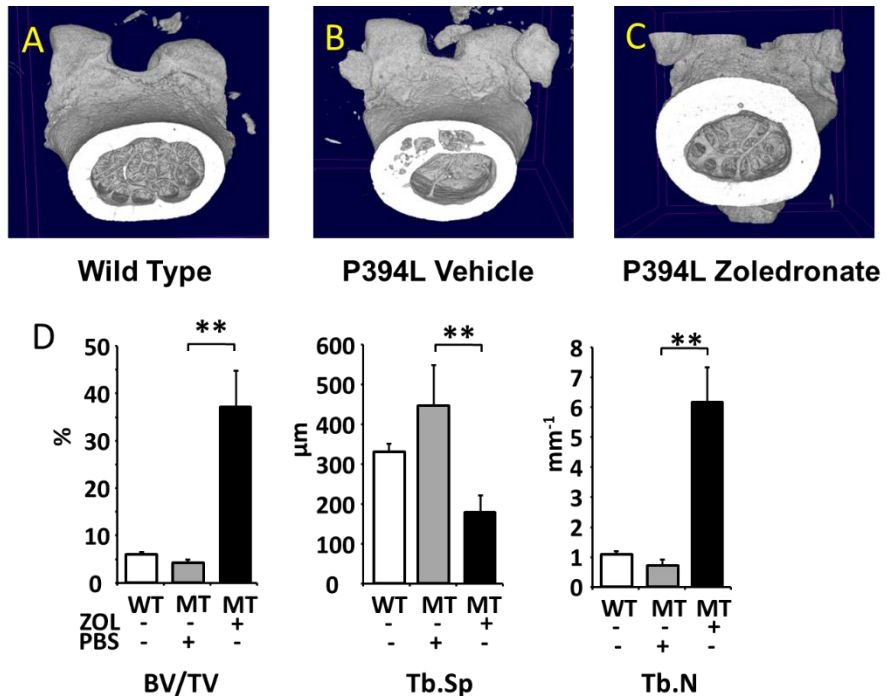


Figure 2: Zoledronate treatment prevents the development of Pagetic lesions in P394L mutant mice.

Bones were scanned at a resolution of 4.5 μm , and visualized using CTVox. Panel A shows the distal femur of a wild type mice, and pane BI a typical femur cortical lesion in a P394L mutant mouse. Panel C shows the absence of lesions in the zoledronate treated mice. However, the cortex is abnormally thick. Panel D shows the results of the trabecular bone analysis, performed using CTAn. Zoledronate treatment resulted in significant increases in trabecular bone volume (BV/TV) and trabecular number (Tb.N) and a decrease in trabecular separation (Tb.Sp). **: $p < 0.01$.

Results

At 12 months of age, all ten mutant mice treated with vehicle developed pagetic lesions in the femurs and tibias. Figure 2 shows a typical lytic lesion in the femoral cortex of a mutant mouse. None of the wild type or zoledronate treated mice developed lesions. However, the

bones of the zoledronate treated mice exhibited an abnormally high trabecular bone volume and substantially increased cortical bone thickness (Figure 2C). Analysis of the trabecular bone showed a dramatic increase of bone volume in the zoledronate treated mice, compared to both the vehicle treated and wild type mice (Figure 2D). This was accompanied by an increase in trabecular number and a reduction in trabecular separation.

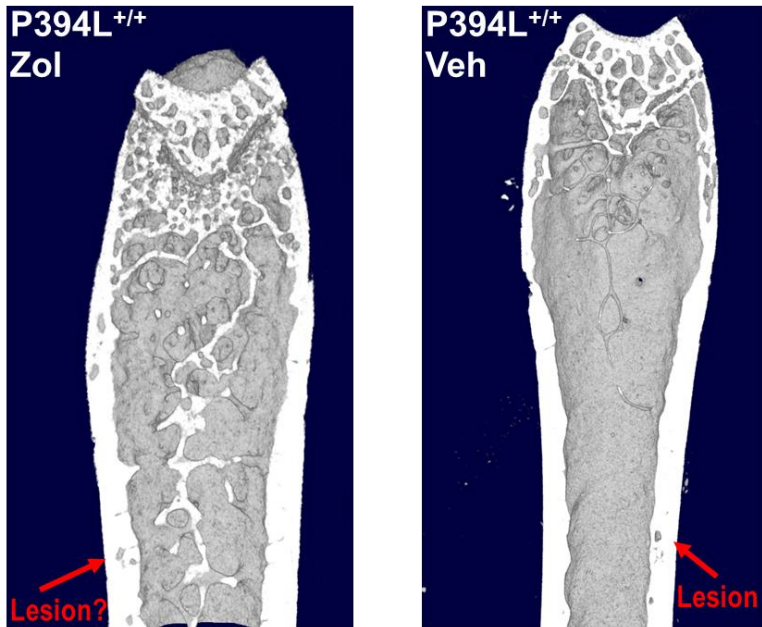


Figure 3: Abnormal cortical pores in zoledronate treated mice. Femurs were scanned at 4.5 μm resolution and visualized using CTvox. Note the numerous pores in the thickened cortical bone of the zoledronate treated mice.

Although typical pagetic lesions were not observed in the zoledronate treated mice, we did observe frequent irregularly sized pores in the cortical bone of zoledronate treated mice. Pagetic lesions are characterized by the presence of large numbers of very large osteoclasts and increased bone formation. To investigate whether the observed pores were possibly “mini” pagetic lesions we analysed sections of these samples by histology.

TRAP staining revealed many, large osteoclast in a pagetic lesions in a vehicle mouse femur (indicated by the red arrows in figure 4) and extensive calcein double labels (indicated by yellow arrow in figure 4). The pores observed by μCT in the zoledronate treated bone (indicated by green arrow in detail inset in figure 4) showed a complete absence of osteoclasts. These structures were also devoid of calcein double labels (see detail inset top right figure 4). These findings suggest that the cortical pores in the zoledronate treated mice are not pagetic lesions, and that bone turnover is significantly suppressed in these animals.

Low bone turnover tends to result in hyper mineralization of the bone matrix. During sectioning for histology, we observed that the zoledronate treated samples were extremely brittle, and caused substantial damage to the microtome knives, further suggesting hyper mineralization.

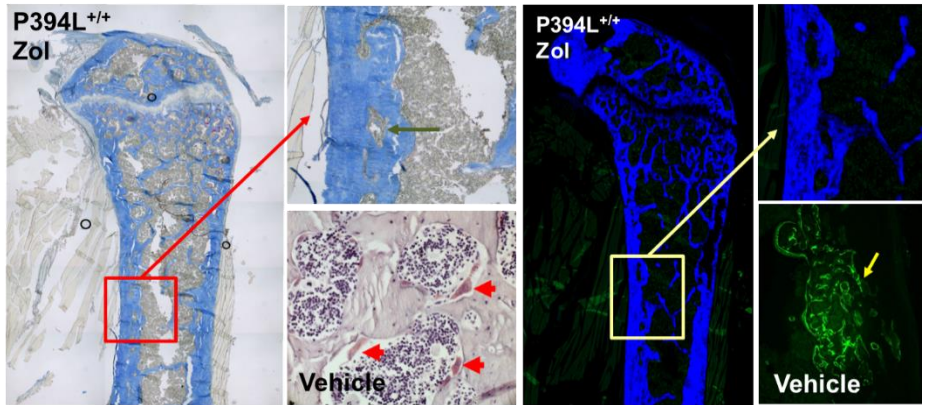


Figure 4: Cortical porosities in zoledronate treated mice do not resemble pagetic lesions. Note the absence of TRAP stained osteoclasts and calcein green double labels in the detail inset images. Sections from pagetic lesions in vehicle control mice showed numerous red stained osteoclasts (red arrows) and extensive calcein double labels (yellow arrow).

To investigate whether the zoledronate treated bones were indeed hyper mineralised, we performed additional scans of the distal femurs, with increased averaging and camera binning, to analyse the tissue mineralization in these bones. Figure 5A and B show the difference in image noise between the standard acquisition for morphology (A) and the density scan settings (B). A visual comparison of femurs from vehicle and zoledronate treated mice, already shows an increase in highly attenuating voxels in the zoledronate treated mice, as indicated by the increase in blue voxels in figure 5D versus predominantly green voxels in figure 5C. To quantify these images, we performed a calibration using 2 standards with 0.25 g/cm^3 and 0.75 g/cm^3 of hydroxyapatite respectively. Next, datasets consisting of 300 slices at the mid shaft of the femur were thresholded to identify the bone, and the resulting binary was eroded (3D space) with a sphere with a radius of 2 to remove voxels affected by partial voxel effects. This binary was then used as a mask to measure the mineral density in mineralized tissue only (the tissue mineral density or TMD). This analysis showed a TMD of $1.42 \pm 0.016 \text{ g/cm}^3$ for the vehicle treated mice, and $1.48 \pm 0.14 \text{ g/cm}^3$ for the zoledronate treated mice ($p < 0.001$), clearly demonstrating increased bone mineralization in the zoledronate group.

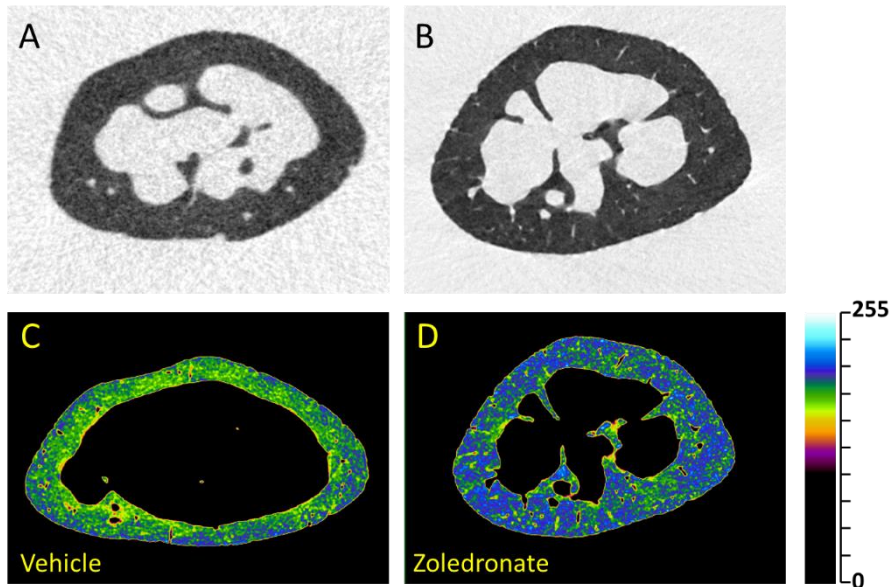


Figure 5: Analysis of tissue mineralization.

A: transaxial image of femur obtained using standard scan settings. B: transaxial image obtained using density scan settings. Note the substantial reduction in image noise in B compared to A. C and D are colour coded images of vehicle and zoledronate treated femurs respectively. The lookuo table used is shown in the scale next to D. Note the increase in blue pixels in D, indicating higher X-ray attenuation.

Conclusion

Treatment of the P394L mutant mice with zoledronate completely prevented the development of pagetic lesions. However, the treatment also resulted in a very strong suppression of normal bone turnover, and resulted in hyper-mineralised, brittle bone. The increased mineralization may make the bone more prone to fracture.

Our findings may have implications for the long term treatment of individuals carrying Paget's-associated mutations of the SQSTM1 gene. A careful evaluation of the benefits and possible drawbacks of long term zoledronate treatment of young, still unaffected SQSTM1 mutation carriers should be made before this treatment is started.

References:

1. Daroszewska A, van 't Hof RJ, Rojas JA, Layfield R, Landao-Basonga E, Rose L, Rose K, Ralston SH. A point mutation in the ubiquitin-associated domain of SQSTM1 is sufficient to cause a Paget's disease-like disorder in mice. *Hum Mol Genet* 20:2734-44, 2011

Determining the concentration of diamond powder deposited on a textile yarn: a multitechnique approach

S. Ciattini¹, L. Chelazzi¹,

¹Center of Structural Crystallography (CRIST). University of Florence. Via della Lastruccia 3, 50019 Sesto Fiorentino (Firenze), Italy

Aims

The development of an analytical method to determine the amount of diamond powder deposited on a textile yarn arises from the need to certify the concentration of diamond itself in textile fabric. Due to the fact that diamond textile yarn had to be used to produce luxury and high fashion manufactures, the certification was an absolute need in the marketing of such products that are proposed with a remarkable price to the final users.

The production line of the diamond wire was developed by a company of Prato (Tuscany, Italy) textile area. In figure 1 a very simplified scheme of production is reported. A special apparatus drives the wire through a container where a mix of viscous resin, diamond powder and glitter is present. The mixture is stirred during the whole process. The thread, once soaked in the viscous mixture and enriched with diamond powder, is dried and then rolled ready to be used.

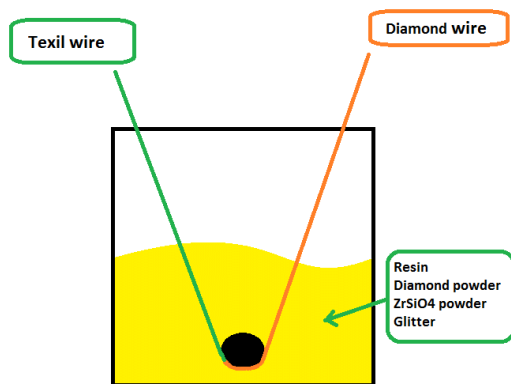


Figure1. Schematical representation of the apparatus used to produce the diamond-enriched textile yarn

The analytical issues could be pointed out as follow:

- 1) verification of the presence of the diamond powder on the final fabric and as consequence on the textile yarn,
- 2) determination of the linear concentration of diamond on the textile yarn,
- 3) verification of the homogeneity of the product sample, *i.e.* the concentration should be constant throughout the whole process production.

Diamond is pure carbon and, as a consequence, practically indistinguishable, through the normal analytical techniques, from cotton and resin that are both made up as well mostly by

carbon. The determination of the concentration of diamond in these conditions has been represented as a real challenge for all the analytical laboratories that had been involved.

Method and results

CRIST (Crystallography Center - Università di Firenze) is an academic facility with a wide range of available X-ray instrumentations, most of them dedicated to X-ray diffraction analysis. Then, the first idea was to verify the presence of diamond in the final fabric through an X-ray diffraction analysis. In fact, diamond, thanks to its crystalline structure, well diffracts X-ray. The fabric was analyzed with a Bruker D8 diffractometer, configured with Bragg-Brentano geometry, using Cu K α radiation, the diffractometer was equipped with a Euler cradle in order to allow the positioning and orientation of the specimen (*Figure 2*)

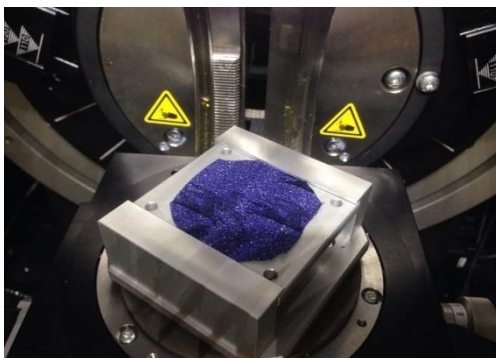


Figure 2

The XRPD (X-ray Powder Diffraction) pattern in *figure 3* shows the characteristic peaks of the diamond at 43.92° in the 2 Θ range 43-45° angle. Thus XRPD analysis¹ was useful to easily solve the first analytical question confirming the presence of diamond on the finished fabric.

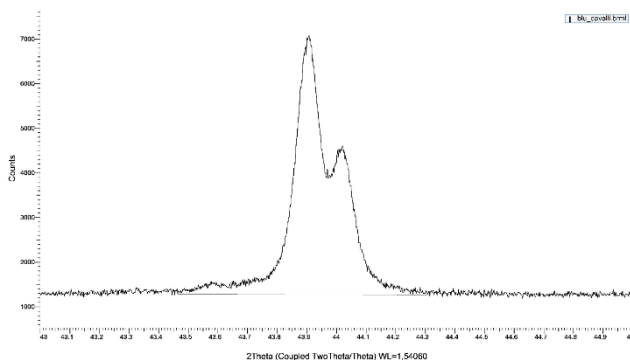


Figure 3. Fabric XRPD pattern

Unfortunately, the XRPD technique is not easily suitable for an absolute quantitative determination. Thus, to give an answer to the remaining analytical questions, it was necessary to follow a different approach.

The diamond is pure carbon so its mass attenuation coefficient (MAC) is too similar to those of resin and cotton substrate MAC, therefore, μ -Tomography (μ -CT) analysis did not seem, at first glance, helpful for our analytical purposes.

In fact, as evidenced in figure 4, where the 3D rendering of the analyzed textile yarn is reported, a first μ -CT analysis confirmed the impossibility to distinguish the diamond from the wire (the spots highlighted in green are due to the glitter grains).

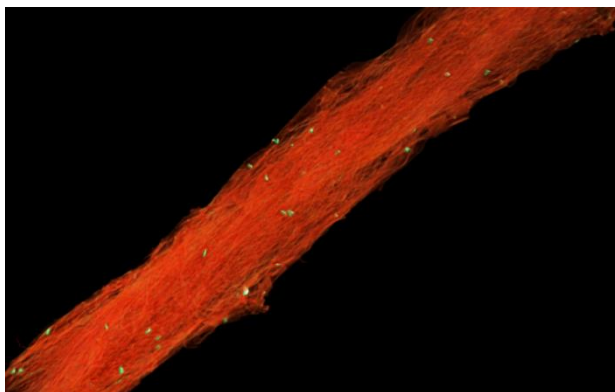


Figure 4

Then in order to solve the analytical problem we started to think in a different way, and we consider the only other component (well visible by using the μ -CT device) present in the fabric yarn, *i.e.* the glitter. The glitter describes a wide assortment of small fragments mainly consisting in the copolymers, small sheets of aluminum, titanium dioxide, iron oxide, bismuth oxychloride and other oxides and/or metals, painted with iridescent colors capable to reflect the light in the visible spectrum.

The glitter has the function to shine the light. In fact, the diamond powder is grey as it absorbs light, does not have a high optical dispersion index and, as a consequence, it has not the brilliance of the cut stone.

The XRPD pattern of the diamond powder, figure 5, shows the high peak of the diamond itself (red), the $\text{Zr}_{0.87}\text{Y}_{0.214}\text{O}_{1.7}$ Zirconium Yttrium Oxide (blue) and some other not identified impurities.

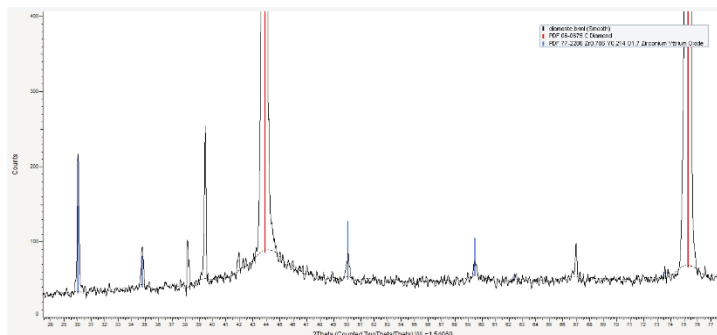


Figure 5

The analysis of the diamond powder by wavelength dispersion X-ray fluorescence spectroscopy (WDXRF) has confirmed the presence of Zr, Y and some other elements as reported in the following table:

Element/Compound	Result	Detection limit	Element Line
C	99.9%		
P2O5	0.0751%	0.00079	P-K α
CaO	0.0203%	0.00055	Ca-K α
SiO2	0.0114%	0.00095	Si-K α
ZrO2	0.0059%	0.00022	Zr-K α
Fe2O3	0.0025%	0.00050	Fe-K α
Y2O3	0.0019%	0.00021	Y-K α
MgO	0.0016%	0.00147	Mg- K α
Al2O3	0.0013%	0.00060	Al-K α
CuO	0.0004%	0.00030	Cu-K α

Table 1

These preliminary results suggested us to add a small weighted amount of an inorganic compound containing zirconium to the diamond powder to get a strong x-ray absorption contrast with the carbonaceous matrix of the diamond yarn. Zirconia was excluded due to its radioactivity, and zircon, ZrSiO_4 , was chosen as perfect candidate. The zircon sand was sieved with 120 μm first and then 80 μm mesh, this step selected grains with a known size range. The sieved sand was mixed to the diamond powder in known proportions, then the powder mixture was kneaded with the resin. Progressively the proportion of silicate was increased taking care that the standard quality level of the textile yarn was preserved. The mixture used had ZrSiO_4 / diamond ratio equal to 1: 4. Samples were withdrawn in different times during the production process and they were analyzed with a $\mu\text{-CT}$, Skyscan 1172². Four meters of yarn rolled on a plastic support was analyzed in each scan. The zircon grains are clearly visible as shown in figure 6.

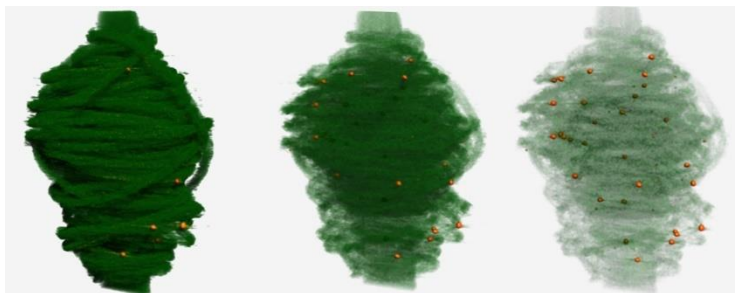


Figure 6

The measuring conditions were selected to better define the size of the zirconium silicate grains and to exclude any glitter contribution.

Filter	Cu+Al
Resolution	19,5 μm
Rotation step	0,44°
Voltage (kV)	100kV
Current (mA)	100mA
Hounsfield Unit range	0-4000Hu

The left part of figure 8 is a 3D rendering of a portion of a roll of yarn acquired in the same condition reported in table 2 but without primary filters, and the relative reconstruction carried out by selecting a proper HU range to highlight either the wire, the particles of ZrSiO_4 (cyno circle) and the glitter (red circle). The right section of figure 8 shows the same sample acquired and reconstructed with the conditions reported in the table 2, only the ZrSiO_4 grain are displayed.

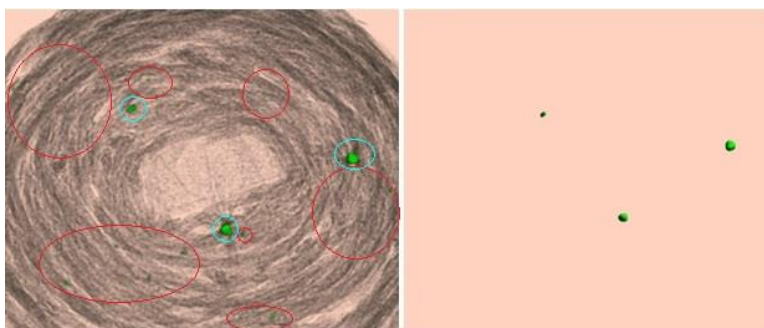


Figure 8

With the knowledge of the range grain size of the sand it was possible to adjust the correct threshold to use for the determination of the total grain volume. As it shown by the thickness

distribution, most of the identified ZrSiO_4 particles are within the range between 80 and $120\mu\text{m}$:

Structure thickness distribution			
Range (mm)	Mid-range (mm)	Volume (mm^3)	Percent volume in range (%)
0.020 - <0.060	0.040	0.00071	1.6251
0.060 - <0.100	0.080	0.01655	37.7031
0.100 - <0.140	0.120	0.02663	60.6717
Standard deviation of structure thickness: 0.02mm			

The concentration is calculated just applying the formula:

$$[(d_{\text{ZrSiO}_4} \times V_{\text{ZrSiO}_4})/M_{\text{sample}}] \times 4 = M_{\text{diamond}} \text{ gr/Kg}$$

Where:

d_{ZrSiO_4} is the density of ZrSiO_4 sand

V_{ZrSiO_4} is the total volume of the grain sand measured from $\mu\text{-CT}$ analysis

M_{sample} is the total mass of the yarn used for $\mu\text{-CT}$ analysis

M_{diamond} is the concentration expressed in gr of diamond for Kg of yarn

Analysis of the production batch 1402N1S is reported. Four samples were analyzed: Test1 from the beginning of the production process, Test2 and Test3 from two intermediate times, and Test4 at the end of the process. The expected concentration value (expressed in gr of diamond over Kg of yarn) was 7.5gr. Table 3 summarized the results from tomography analysis:

Sample	Sample weight	gr. of diamond over Kg. yarn
Test1	105mg	6.54-8.20gr.
Test2	72mg	4.65-5.50gr.
Test3	103mg	7.16-8.70gr.
Test4	103mg	6.73-8.52gr.

The concentration is reported within a minimum and a maximum value that correspond to the two limits of threshold used in the binarization step during the particle volume determination. The measurement accuracy for Test1, Test3, Test4 is acceptable for the final purpose of the analysis and the average value is almost constant throughout the process production. Test2 shows a lower concentration value respect to the other three results: it's important to notice that in this case just 72mg of yarn was used for the analysis, such smaller amount of sample was not statistical representative of the ZrSiO_4 distribution.

The residue amalgam mix (resin silicate of zirconium and diamond in the container) at the end of the production process was also analyzed via XRPD. The semi quantitative analysis calculated from the diffractogram revealed exactly a relative concentration of 20% for ZrSiO_4 (red) and 80% for diamond (blue). That is the same composition before the beginning of the process, this result confirms that the ZrSiO_4 /diamond ratio remains 1: 4 during the whole process production.

Conclusion:

The multitechniques approach was successful in all the analytical issues. In fact, XRPD easily identified the diamond powder either in the final fabric and in the textile yarn. The concentration of zircon on the textile yarn was determined by micro tomography technique. The homogeneity of the product sample was verified by micro tomography technique and supported by the XRPD analysis on the residue resin. The combination of results allowed us to evaluate the diamond concentration on the yarn.

Acknowledgement:

We thank the Product Manager **Dr. Alessia Beconcini** (Industrie Bitossi, Sovigliana, Vinci) that supplied us the zircon sand.

References:

- 1 Bruker-AXS, DIFFRACPlus TOPAS: TOPAS 4.2 Technical Reference, Bruker-AXS GmbH, Karlsruhe, Germany (2008)
- 2 Feldkamp L.A., Davis L.C., Kress J.W. Practical cone-beam algorithm. J Opt Soc Am. A1:612-619, 1984.

Survey of petrosal bone of the inner ear of Late Miocene baleen & toothed whales from Northwest Caucasus through tomography (First experience).

K.K.Tarásenko¹, E.S. Kovalenko², A.V. Pakhnevich¹, K.M. Podurets²

¹PIN RAS, 117997 Moscow, Profsoyuznaya str., 123,

²NRC "Kurchatov Institute" 123182 Moscow, Akademika Kurchatova pl., 1

Aims

Cetaceans, unlike all other terrestrial and aquatic mammals, have a number of special specialties associated with the aquatic environment, including the ability to hear underwater, which attracted the attention of many researchers¹⁻³. We know that modern odontocetes and mysticetes hear in two different ways: at high and low frequencies (respectively). It is very important to know how these two groups of whales developed hearing abilities in different ways. For Late Miocene baleen & toothed whales of the Eastern Paratetis, the morphology of the petrosal bone has been studied rather well, but the microstructure and morphology of the labyrinth of the petrosal bone has not yet been studied⁴⁻⁶. Here, we report the discovery of inner ear of Late Miocene baleen & toothed whales from Northwest Caucasus through Tomography. The goal of this work is researching petrosal bone of baleen and toothed whales from the Late Miocene, choice of methods morphological descriptions obtained reconstructed sections of petrosal bone, as well as the identification of stable and non variability informative morphological characters of the labyrinth structure in petrosal bone.

Method

Synchrotron tomography carried out in NRC "Kurchatov Institute" by using "Kurchatov synchrotron radiation source", at the station "LIGA". Filtered synchrotron radiation with a spectrum maximum about 56 keV (a filter Cu 1.5 mm) is used. A frame exposure time was 150 ms; a resolution – 130 µm; step of rotation – 0.5°. A vertical scanning step 1 mm is applied. In the morphological description of virtual sections, it is very important to choose the correct projection of the sample, taking into account the position of the cochlear ducts (the cochlear channels must be dissected by a crossing plane perpendicular to the axis of the stony part of the stony bone. We choose frontal direction with selected sections pass at a small angle (5-7 degrees) to the longitudinal axis of the bone (fig. 1) in contrasting with classical works^{1,2}. Another series of cuts made in the latero-medial direction at a slight angle to the part of the cochlea.

Another part of the sample (petrosal bone from smaller toothed whales) was investigated in the Paleontological Institute of Russian Academy of Sciences, on the X-ray micro-CT Skyscan 1172. Microtomography parameters: I=100 mA, U=103-104 kV, a filter – Al (1 mm), a pixel size was from 25 to 34.1 µm, a rotation - 180°, steps of rotation were 0.7°, random movement – 10, frame averaging – 8. TView, NRecon, CTAn programs are used.

Results

In the course of studying and comparing the 3D models for *Kurdalagonus* sp. and *Zygiocetus nartorum* Tarasenko, 2013 revealed significant differences in the structure of the semicircular canals of the labyrinth, endolymphatic and perilymphatic structure of channels, as well as in the structure of the facial nerve canal. We occurred that the number of turns of the

cochlea in the Eastern Paratethian Cetotherium like whales close to that of herpetocetinae and is about 3 turns. Representatives of the genus *Kurdalagonus* *Zygiocetus* differs from the structure of the semicircular canals. In *Kurdalagonus* lateral semicircular canal on the front side ends with well-defined membranous ampullae adjacent to neighboring ampoule front semicircular canal; and the rear end of the lateral semicircular canal lies beneath the rear base of the semicircular canal ampullae and has virtually no well-defined self-ampoules. In *Zygiocetus* lateral semicircular canal has its own well-defined vial, ampoule adjacent to the anterior semicircular canal, and 2.5 times greater than its size. The rear edge of the lateral and rear of the semicircular canals, unlike *Kurdalagonus*, have significantly smaller vial similar in size and underlying the bulge adjacent to a small hillock lying behind the front lateral channel ampoules. The representatives of the genus *Kurdalagonus*, unlike *Zygiocetus*, much longer overall membranous leg connecting the front and rear semicircular canals, their ratio is about 5: 1. In general, *Kurdalagonus* semicircular canal system is more complicated than that *Zygiocetus* (see. Fig. 2).

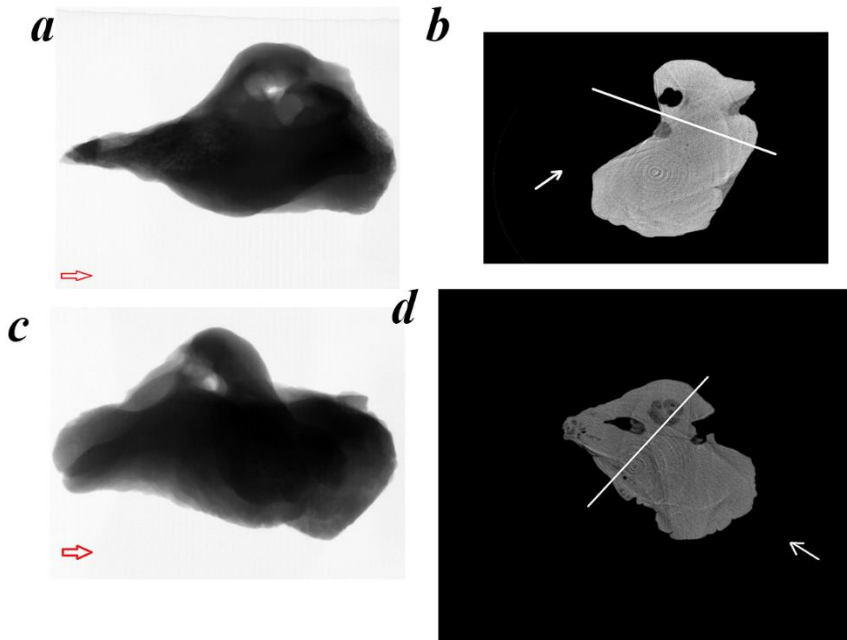


Figure 1: The direction of the oriented investigated samples: a-b *Zygiocetus nartorum* Tarasenko, 2014; c-d *Kurdalagonus* sp.

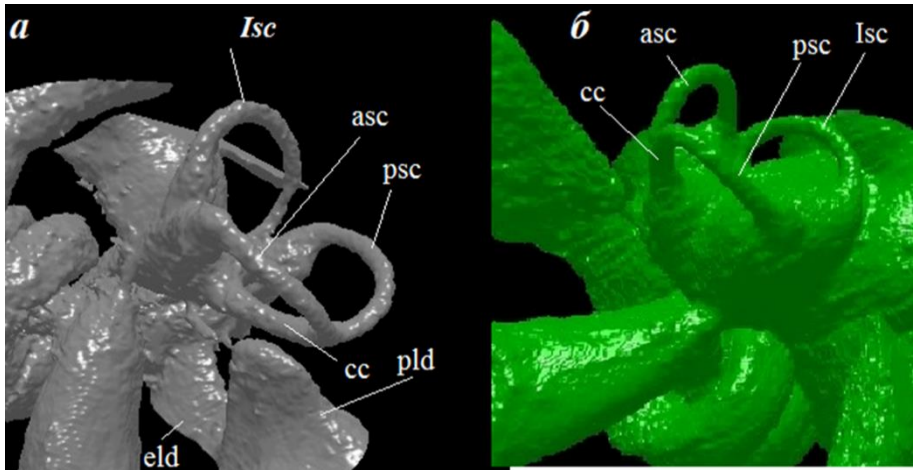


Figure 2: 3D model of the semicircular canals Kurdalagonus (a) and Zygiocetus (b): Isc - lateral semicircular canal; Asc - front semicircular canal; Psc - posterior semicircular canal; Ss - common webbed leg (crus commune); Eld - endolymphatic duct; Pld is the perilymphatic duct.

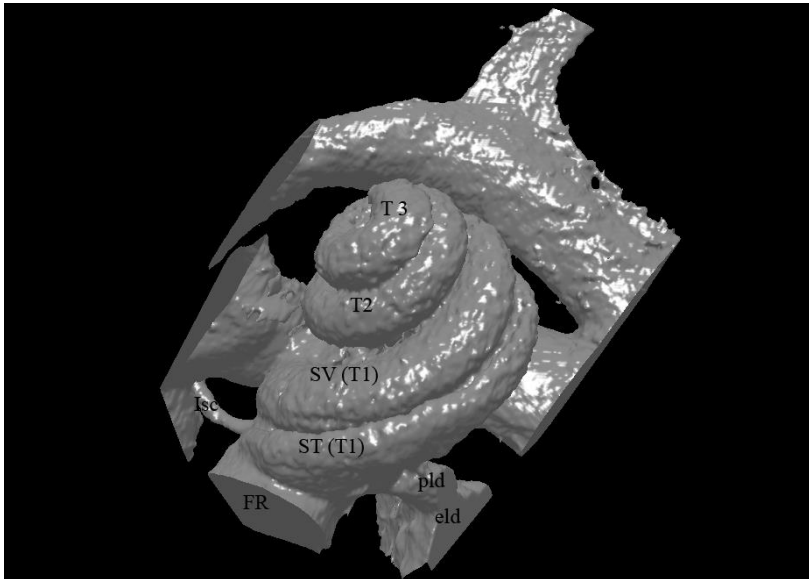


Figure 3: 3D model of the turns of the cochlear canals Kurdalagonus : Isc - lateral semicircular canal; Eld - endolymphatic duct; Pld is the perilymphatic duct; FR – fenestra rotunda; ST (T1) – scala tympani of the third cochlear turn; SV (T1) – scala vestibule (including scala cochleari) of the first cochlear turn; T2 – the second turn of the cochlear canal; T3 – the third cochlear turn.

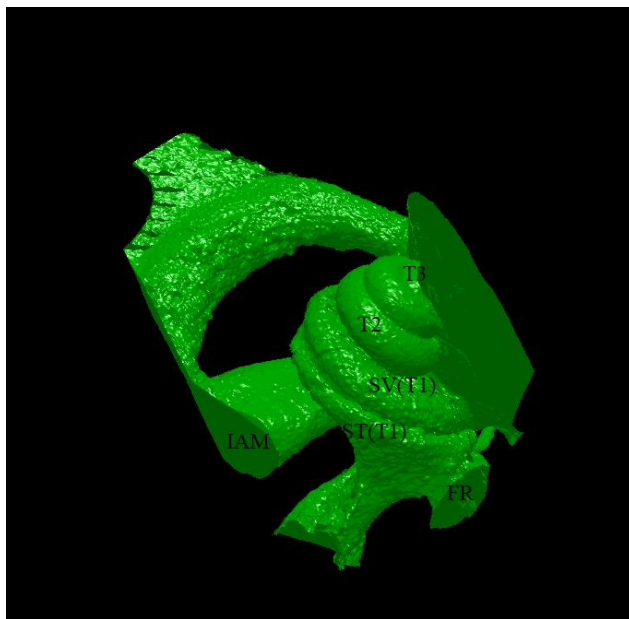


Figure 4: 3D model of the turns cochlear canals Zygiocetus : IAM - internal auditor meatus; Lsc - lateral semicircular canal; Eld - endolymphatic duct; Pld is the perilymphatic duct; FR – fenestra rotunda; ST (T1) – scala tympani of the first cochlear turn; SV (T1) – scala vestibule (including scala cochleari) of the first cochlear turn; T2 – the second turn of cochlear canal; T3 – the third cochlear turn.

Another important morphological feature distinguishing *Kurdalagonus* from *Zygiocetus* and *Cetotherium* is the structure of the round window (Fig. 3, 4). It is considerably wider and longer than *Zygiocetus* and *Cetotherium*, and has a circular shape in cross section in contrast to the more oval in *Zygiocetus*. In *Herpetocetus* threshold (spherical vestibule sensu Geisler et Luo) has a rounded shape, unlike *Kurdalagonus*, which is more flattened, with clear and distinct ampoules semicircular canals, and from *Zygiocetus* front part which, together with ampoules of the semicircular canals form a remarkable expansion. In the work it was noted that the number of cochlea turns in whales of Eastern Paratethis is close to that of herpetocetinae and is about 3 turns (fig. 3, 4). As we can notice, no cetaceans other *Herpetocetus* & *cetotherium* like whale has more over 2,5 turns of cochlear^{2,3,7,8}. However, close to this condition, perhaps, in *Parietobalaena palmeri*, *Metopocetus durinasus*⁹.

As for the third sample (*Vampalus sayasanicus* PIN № 5341-4), most of the cavities was packed with highly absorbent mineral X-rays, tomography at an energy of about 60 keV turned uninformative. Therefore, neutron tomography was performed, for which the restriction is not met, but it has a lower resolution, at the moment about 170 µm.

Also, in the course of this study, virtual sections of the stony bone of the Late Miocene toothed whale from Caucas were described (Fig.5). The cochlear channels were partially filled with a matrix, which in places lowered the image quality.

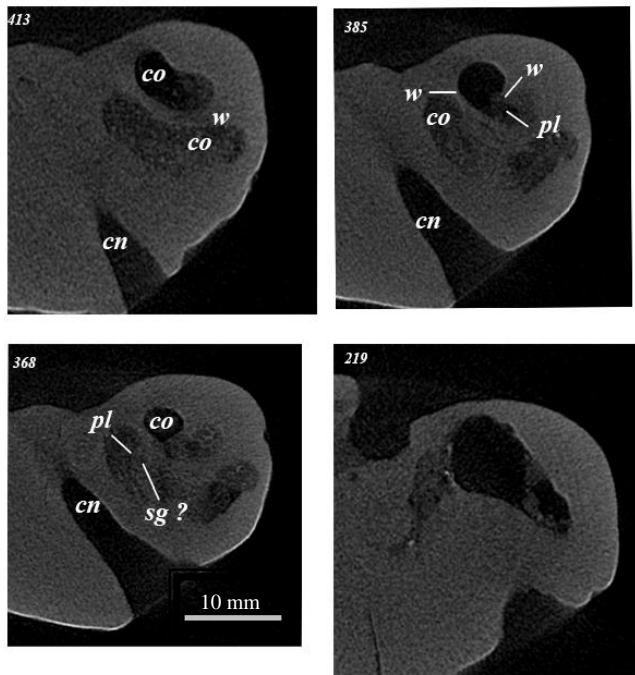


Figure 5: Original CT slices through petrosal bone Late Miocene odontoceti from Caucas (Numbers refer to specific CT slices): cn – canal for cranial nerve VIII within modiolus; co – cochlea; pl – primary bony lamina; sg – canal for spiral ganglion within primary bony lamina; w – wall separating successive turns of cochlea.

Conclusion

Thereby, In the course of the experiment 3D models petrosal bones from Late Miocene toothed & baleen whale, demonstrating some important diagnostic features that can be used in diagnosis of diagnosis genera and species taxa. However, these morphological features need to be verified by examining similar structures in a wide variety of material. This is planned to be done on a new extensive paleontological material.

This work was supported by Russian Foundation for Basic Research (project no. 17-29-04461 OFI M).

References:

1. Fraser, F. & Purves, P. "Hearing in cetaceans. Evolution of the accessory air sacs and the structures of the outer and middle ear in recent cetaceans" Bull. Brit. Mus. 7, 1-140(1960).
2. Geisler, J., Luo, Z. " The petrosal and inner ear of *Herpetocetus* sp. (Mammalia: Cetacea) and their implications for the phylogeny and hearing of archaic mysticetes " J.Paleontol. V.70. №6, 1045-1066 (1996).

3. Ekdale, E. & Racicot, R. " Anatomical evidence for low frequency sensitivity in an archaeocete whale: comparison of the inner ear of *Zygorhiza kochii* with that of crown Mysticeti "J. Anatomy. 226, 22-39 (2014).
4. Tarasenko, K. & Lopatin, A. "New baleen whale genera (Cetacea, Mammalia) from the Miocene of the Northern Caucasus and Ciscaucasia: 1. *Kurdalagonus* gen. nov. from the Middle–Late Sarmatian of Adygea"J. Paleontol. 5, 531–542 (2012).
5. Tarasenko, K. "New genera of baleen whales (Cetacea, Mammalia) from the Miocene of the northern Caucasus and Ciscaucasia: 3. *Zygiocetus* gen. nov. (Middle Sarmatian, Adygea)"J. Paleontol. 5, 99–109 (2014).
6. Tarasenko, K. " Kentriodontidae (Cetacea, Mammalia) from the Upper Miocene of the Azov Sea and the North-West Ciscaucasia" Modern paleontol.clas. and modern meth., 8, 44-45 (2011).
7. Yamada, M., Yoshizaki, F "Osseous labyrinth of Cetacea". Sci Rep Whales Res Inst 14, 291–304 (1959).
8. Luo, Z-X., Eastman, ER "Petrosal and inner ear of a squalodontoid whale: implications for evolution of hearing in odontocetes" J Vertebr Paleontol 15, 431–442 (1995).
9. Ekdale, E Morphological variation among the inner ears of extinct and extant baleen whales (Cetacea: Mysticeti) J. Morphology 277(12), 1-28 (2016)

Tracking Cells in vitro using Micro CT

David Shepherd¹, Eleonora Vriend¹, Jennifer Shepherd¹, Serena Best¹, Ruth Cameron¹

¹Cambridge Centre for Medical Materials, University of Cambridge, Cambridge, UK

Aims

The aim of this work was to develop a technique that would allow cells to be tracked *in vitro* using Micro CT. Currently the main technique to track cells is completed by staining and then sectioning the scaffolds that the cells are cultured in to visualise them under optical/fluorescent microscopes. The sectioning can lead to movement of the fixed cells, especially when the scaffold is soft, not allowing a true position of the cells to be identified. The use of Micro CT allows non-destructive visualisation of cells *in situ*. Whilst osmium-tetroxide has previously been used¹ as a contrast agent for the micro-CT imaging of cells (ref) it is extremely hazardous and thus we consider less toxic options.

Method

Lyophilised collagen scaffolds were produced in a method modified from Davidenko et al². Scaffolds were then subsequently sterilised through a process of washing in sterile 70% ethanol, sterile water and PBS. All samples were left in media for 24 hours before the experiment to allow protein adsorption onto the scaffold struts.

HT 1080 cells were cultured until 70% confluent. These cells were then passaged so that there were enough cells for the experiment. Barium Sulphate (Micropaque, Guerbet) was then added to the media at 35 μ l per ml of media (DMEM, Sigma Aldrich) in the flask, based on a method previously described³. Cells were allowed to take up the contrast agents for just over 72 hours. Another flask of cells was cultured with just media present.

The cells were left to culture for 3 days before being seeded onto a collagen scaffold at 130,000 cells per scaffold in a bead of 15 μ l. These were then left to stick to the collagen scaffold for 1 hour in a 48 well plate before being moved into a new 48 well plate and the well flooded with new plain media. Cells on the scaffolds were subsequently cultured for either 1 day, 3 days or 7 days. At each timepoint scaffolds were removed, washed in PBS before being fixed in ultrapure glutaraldehyde. These scaffolds were subsequently freeze dried.

The dry scaffolds were scanned in their entirety using a Skyscan 1172 with a pixel size of 2.93 μ m, an operating voltage of 25 kV, 0.2° stepsize with frame averaging of 2 and 180° rotation. The resulting projections were processed into 3D data sets using a full cone beam Feldkamp reconstruction algorithm with NRecon software. Images were viewed using Data Viewer.

Following Micro CT scaffolds were cut in half and one half was subsequently stained using DAPI. This stained the cell nuclei with a fluorescent (358 nm) stain. This was then viewed using a Zeiss Axio Observer Z1 phase contrast microscope fitted with a Zeiss Axio 503 mono camera using a 10X objective lens.

Results

Before trypsinising, cells were viewed under the microscope and contrast agent uptake clearly observed.

The presence of cells and their penetration through the scaffold was more evident in the presence of contrast agent. *Figure 1* shows a collagen scaffold that has had HT1080 cells containing barium sulphate cultured in it with media for 24 hours. *Figure 1A* is the coronal image of the scaffold and the cells appear to be present near the top of the scaffold as expected as they will not have yet migrated into the scaffold. The red line shows where the transaxial image of the scaffold (*Figure 1B*) was taken. This image shows how the cells are distributed.

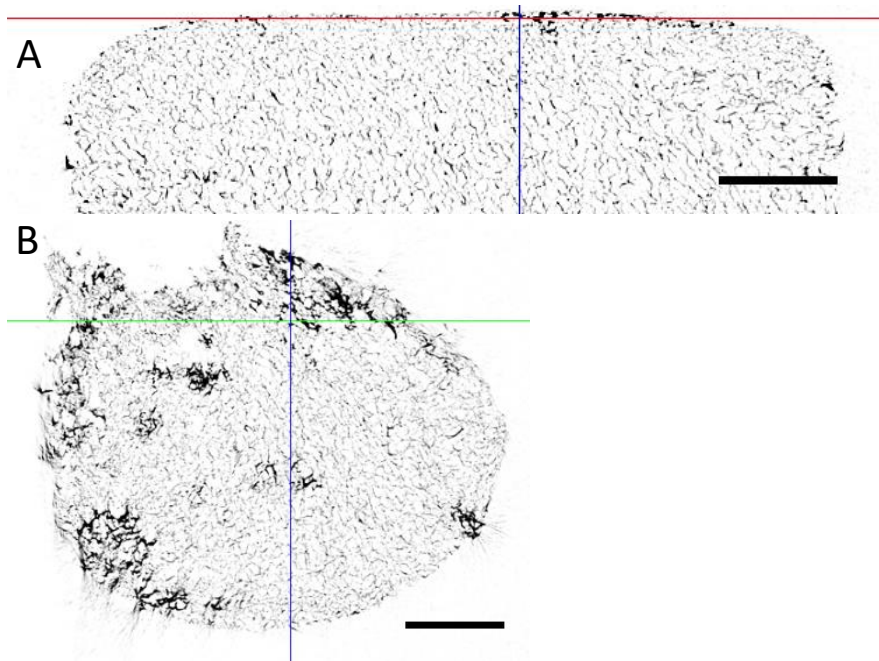


Figure 9: Micro CT images (Coronal (A) and Transaxial (B)) of a collagen scaffold seed with HT1080 cells (precultured in barium sulphate and media) and cultured for 1 day (Scale bar is 250 μ m)

Figure 2 shows a collagen scaffold that has had HT1080 cells, pre-cultured in barium sulphate, cultured on them for 3 days. By comparing *Figure 1* and *Figure 2* it is possible to determine that the cells have spread across the scaffold but have also migrated through the collagen scaffold.

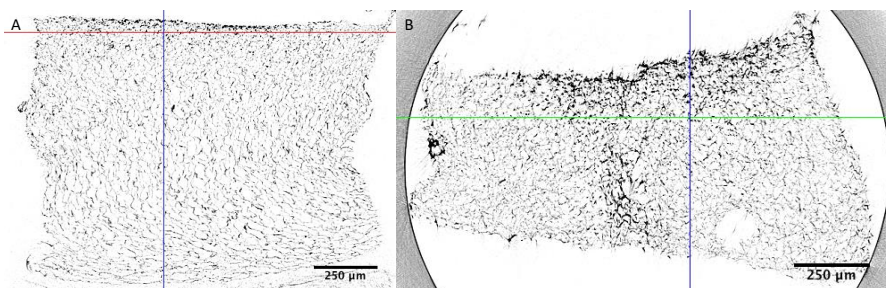


Figure 10: Micro CT image of collagen scaffold (Coronal (A) and Transaxial (B)) seeded with HT1080 cells (precultured in barium sulphate) after culture for 3 days

To check that the cells are in the position observed using Micro CT, the samples were sectioned and then half was stained with DAPI. *Figure 3* shows the HT1080 cells were located in the same place in the scaffold as they were using Micro CT.

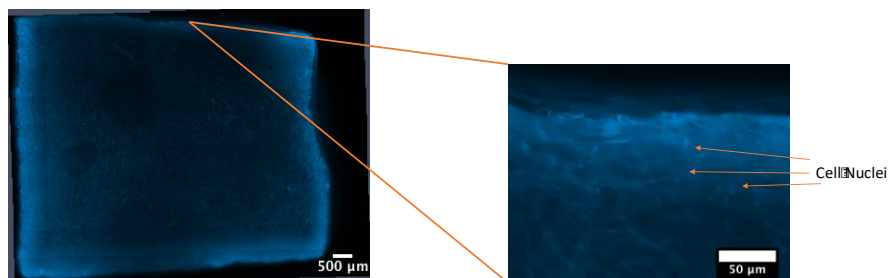


Figure 11: Same Scaffold as Figure but has been sectioned and subsequently stained with DAPI. The left image shows the entire scaffold whilst on the right is a closeup of the scaffold clearly showing the cell nuclei.

Conclusion

From the work presented in this scaffold we have found that it is possible to use desktop Micro CT to visualize cells within a collagen scaffold. With adaptations of this technique using scaffolds with varying pore structures it will be possible to track cell movement within collagen structures.

References:

1. Silva, M.M.C.G., *et al.* *Biomaterials* 27 (35) (2006): 5909–5917
2. Davidenko, N., *et al.* *Acta biomaterialia* 25 (2015): 131-142
3. Dullin, C., *et al.* *Journal of synchrotron radiation*, 22(1) (2015), 143-155

Using MicroCT Scanning Techniques to Assess the Performance of Dental Students' Tooth Cavity Preparation Skills

Barry F. Quinn¹, Phil Salmon² and Margaret J. Cox¹

¹ King's College London Dental Institute, Tower Wing, Guy's Hospital, London SE1 9RT.
United Kingdom

² Bruker MicroCT Kartuizersweg 3B, 2550 Kontich, Belgium

Aims

To use Micro-CT Scanning techniques to compare the results of undergraduate dental students' clinical cavity preparation skills; trained traditionally versus haptically using a virtual reality simulator (hapTEL).

Method

The study took place in a university healthcare undergraduate dental setting in which clinical skills are initially taught through students working on plastic or discarded natural teeth at a Phantom Head workstation. Each of the 77 workstations, shown in Figure 1 is equipped with dental instruments, teeth in a jaw, a chair and most of the equipment seen in a dental surgery.



Figure 1 – Tutors instructing students in the Phantom Head Laboratory

The Bachelor of Dental Surgery undergraduate programme to become a qualified dentist in the UK is five years. The 1-year study discussed in this paper was one of a series of studies conducted between 2008 to 2017 to investigate the impact of teaching year-1 Dental Undergraduate students clinical skills using a virtual haptic dental device (haTEL) designed to simulate the traditional Phantom Head. The students' clinical skills' progression is traditionally monitored by tutor observation and assessed by looking at the end result of the pre-clinical task, such as the removal of decayed tissue from a tooth.

The student cohort for this study was 138 Year-1 Dental Undergraduate students being taught removal of caries using plastic teeth in the traditional Phantom-Head Laboratory (n=96, Fig. 1) or virtual teeth using the hapTEL work-stations (n=42, Fig.3). The hapTEL work-station is shown in Figure 2 below.

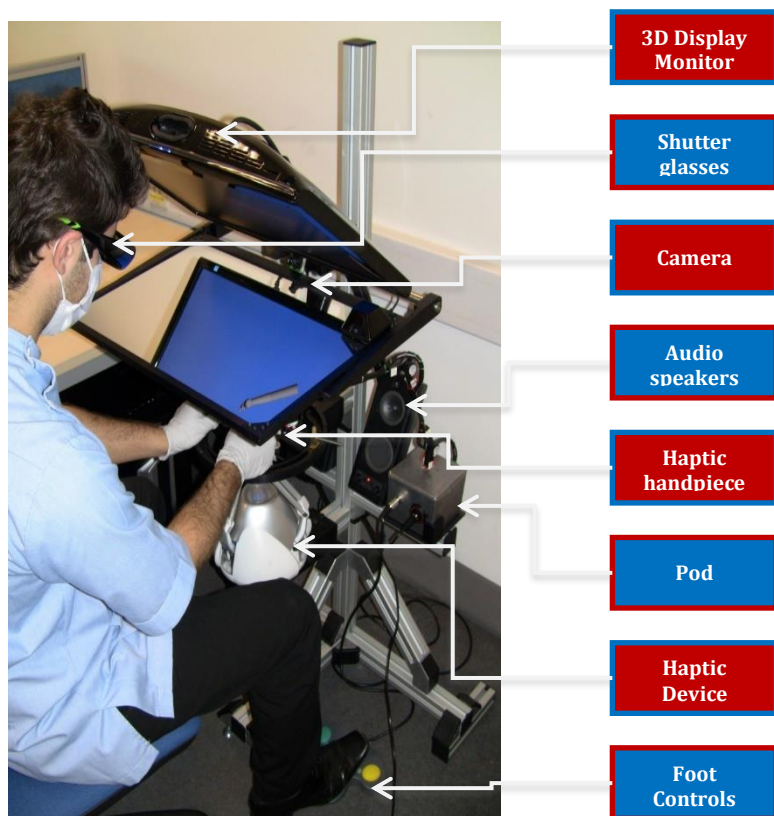


Figure 2 – The hapTEL Curriculum Version

For the traditionally trained students the task involved learning to use a dental drill to remove simulated decayed tissue from plastic teeth, designed by Frasaco to be similar to the anatomy of real human teeth with different tissue densities to represent the various layers. For the haptically trained students using the hapTEL simulator the students were required to work on a virtual tooth using the hand-piece which provides haptic feedback as with a real drill and stores all the procedures the students conduct (Shahriari-Rad, Cox & Woolford, 2017).



Figure 3 – Tutors assessing students in the Phantom Head Laboratory

Assessment of students' skills.

Traditionally, when assessing the students, the tutors are mainly only able to see discreet stages and the final outcome (prepared tooth cavity) of every student because there are too many students to observe at the same time (Shahriari-Rad, 2014). In order to assess the students' cavity preparation skills more precisely this study involved all students (traditionally and haptically trained) being required to remove simulated caries from a plastic tooth manufactured by Frasaco after the training sessions in Year 1 had been completed.

Assessment-techniques:

A range of assessment methods have been used in the series of studies to measure the effects of the simulation training on students' learning of fine and gross motor skills and clinical skills (San Diego, Newton, Quinn, Cox & Woolford, 2014). For the study reported in this paper, students in both cohorts were required to excavate carious tissue from a plastic tooth after their training sessions to determine what they had learnt. These teeth shown in Figure 4 were scanned to determine the very fine differences between individual student's performances and the accuracy of their operations. This involved the following:

1. Micro-CT Scanning of the excavated plastic teeth (n=84) to determine the volume of artificial caries removed, healthy tissue (enamel and dentine) remaining and surface roughness.
2. Micro-CT Scanning of the manufacturer produced cavities (n=10) where the artificial caries had not been removed. In order to investigate the consistency of the manufactured Frasaco teeth.

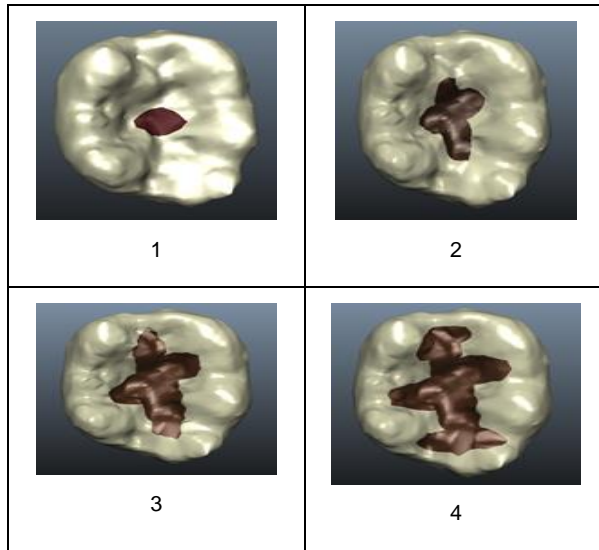


Figure 5 – Caries lesions in plastic and hapTEL teeth showing increasing caries size from 1 - 4

The teeth used for this study were for Task 3 which had a complex carious lesion extending near to the pulp. The teeth scanned were compared to find out: (a) how consistent was the manufacturing of the individual teeth; (b) how accurately the students prepared a cavity and removed the carious tissue and (c) which cohort of students (traditional or haptically) achieved the most accurate results removing the highest volume of carious tissue without drilling into the pulp or removing too much healthy tissue.

Scanning techniques

All 94 plastic teeth were scanned using the Bruker SkyScan 1275 shown in Figure 6. Each Frasaco tooth was loaded and scanned which took about 30 minutes. (Fig. 7)

The variables recorded and calculated included: lower and upper grey threshold, object volume, percentage object volume, object surface, intersection surface, object to surface volume ratio, object surface density and surface convexity index. From these data the amount of volume removed by each student and the mean for the whole cohort can be calculated, and the surface roughness of the operation by each student.



Figure 6 – Bruker SkyScan 1275

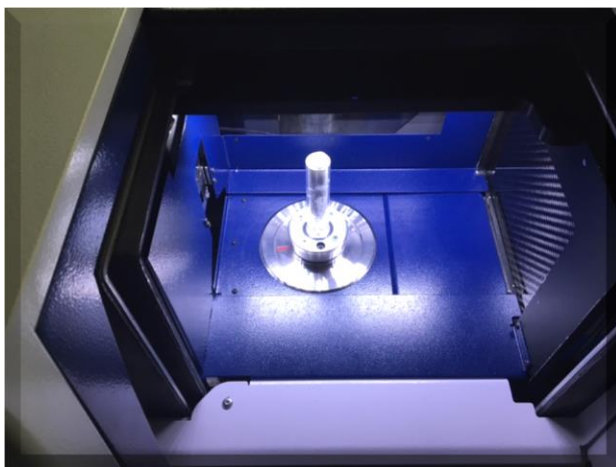


Figure 7 – Analogue Frasaco Tooth set up for scanning

Results

The scans for each tooth showed the sagittal, coronal and axial cross-sections of each tooth, an example of which is shown in Figure 8. The central rod depicted as the same colour as the surroundings is the screw in the plastic tooth which enabled it to be screwed into an artificial plastic jaw before operation.

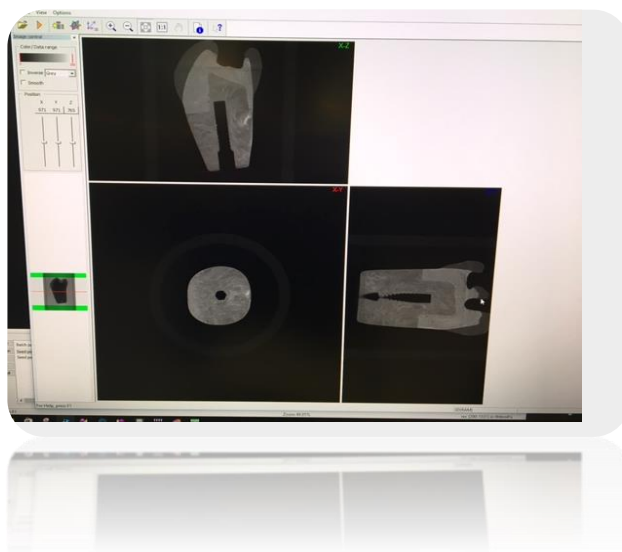


Figure 8 showing the sagittal, coronal and axial cross-sections of a tooth

The cavity cut by the student can be enhanced through colour to enable the researcher to view the tooth more accurately. (Fig. 8 below)



Figure 9 showing the colour enhanced tooth the identify the cut cavity

The results for the total teeth scanned showed the following:

- Volume (or %) of Caries removal
- Dimensions of the cavity
- Proclivity to tilt the hand-piece (dental drill) to one side or next Angle of entry into the tooth
- Morphometric differences in cavity preparation

The lower and upper grey limit chosen for the analysis was 128 and 255 respectively.

The results for all 94 teeth showed significant variations between the different teeth cut by the individual students for the all the relevant variables, a sample of which is shown in Table 1 below.

Table 1 – Range of key tooth scan variables

Variable	Range
Object volume	15.187 – 33.843
Percentage of object volume	0.42 – 0.91
Total volume of pore space	3590 - 3773

Further analysis of the scan data is still in progress but this variation shows that it can reveal accurate differences in the performance of each student and of the original Frasaco teeth enabling us to have more precise measurements of students' cavity preparation skills than can be obtained using traditional methods.

Conclusions

The conclusions to date of this study are that MicroCT affords a quantitative volumetric analysis of dental undergraduate students' cavity preparation skills and progression in their learning. Furthermore, the scans of the excavated plastic teeth can measure and provide the most permanent and accurate record of students' clinical skills. Additionally it has the advantage of both quantitatively and qualitatively (by visual analysis) measuring the surface roughness of the cut cavities which cannot be achieved through any other assessment process.

References

- de Boer, I. R., Lagerweij, M. D., Wesselink, P. R., & Vervorm. Evaluation of the appreciation of virtual teeth with and without pathology. *European Journal of Dental Education*, 19(2), 87–94. 2015
- Quinn, F., Keogh, P., McDonald, A., & Hussey, D. A study comparing the effectiveness of conventional training and virtual reality simulation in the skills acquisition of junior dental students. *European Journal of Dental Education*, 7(4), 164–169. 2003
- Quinn, B.F., Dunne, S., Wilson, N. & Cox, M.J. Micro-CT Analysis of Cavities by Students Trained Haptically or Traditionally. *Journal of Dental Research* 93(B):797 · June 2014

San Diego, J. P., Newton, T., Quinn, B. F., Cox, M. J., & Woolford, M. J. Levels of agreement between student and staff assessments of clinical skills in performing cavity preparation in artificial teeth. *European Journal of Dental Education*, 18(1), 58–64. 2014

Shahriari-Rad, A. *Enhancement of clinical skills assessment using haptic technology*. PhD Thesis, King's College London, University of London. 2014

Shariari-Rad, A., Cox, M.J. & Woolford, M. Investigating assessment methods for clinical skills using the hapTEL simulator

Shariari-Rad, A., Cox, M.J. & Woolford, M. Clinical Skills Acquisition: Rethinking Assessment Using A Virtual Haptic Simulator. *Tech Know Learn*. 1-13. 2017

Wang, D., Zhao, S., Li, T., Zhang, Y., & Wang, X. Preliminary evaluation of a virtual reality dental simulation system on drilling operation. *Journal of Biomedical Material and Engineering*, 26(1), 747–756. 2015

A 3D analysis of how oil absorption of fried dough is affected by freezing conditions using X-ray micro-CT

Teresa Molina¹, Pedro Bouchon¹

¹Pontificia Universidad Católica de Chile, Avda. Vicuña Mackenna 4860, Macul, Santiago,

Aims

Food microstructure is affected by freezing, and this could well have an impact in food on oil absorption during frying. Deep-fat frying is a unit operation where the food is immersed in an edible oil or fat at high temperatures (around 170 and 190°C) to produce fast dehydration and desirable microstructural characteristics: a dry, crispy and oily crust or outer layer, and a wet cooked core [1]. A vigorous escape of water occurs during frying, thereby preventing a large amount of oil from being absorbed during the immersion period. As a consequence, most of the oil is absorbed after removing the product from the fryer because of a competition between suction and drainage of oil that takes place in the surface of the fried product [2,3]. Therefore, superficial and microstructural parameters have been relevant to get a better understanding of oil uptake [4,5,6]. The freezing process is an important method for food preservation, but freezing rate and freezing storage produce changes in crystal morphology, size and distribution, which involve significant microstructural damages on food [7]. The aim of this work was to study the effect of freezing conditions on the oil absorption of gluten-starch dough after deep-fat frying, and its microstructure was analyzed by using X-ray micro-computed tomography.

Method

Laminated dough was made with wheat starch (88% d.b.) and gluten (12% d.b. Samples were subjected to fast or slow freezing, and to short or prolonged cold storage. Thereafter, they were defrosted and fried. Total oil content (TO) was determined gravimetrically by Soxhlet extraction using petroleum ether. The microstructure of frozen and fried dough was analyzed using X-ray microtomography (micro-CT). Samples of fried dough or frozen and fried dough were scanned using Skyscan 1272 X-ray micro-computed tomography system (version 1.1, Bruker Corp., Belgium), and the following settings were used: 50 kV and 200 μ A; exposure time = 2400 ms; rotation angle from 0° to 180°; rotation step = 0.1°; 2 frames for each exposure to reduce de noise; and, Al 0.25 mm filter. CT scanning produced between 2407 and 2657 image slices for each experiment with a voxel size of 3.75 μ m \times 3.75 μ m \times 3.75 μ m. The resolution of each image was 4032 \times 2688 pixels. With the purpose of cutting the region of interest (ROI), processing the images and quantifying the volume of matrix, air and oil, and their pore size distribution, each set of images was divided in three sections and they were analyzed using the CTAn software (version 1.15, Bruker Corp., Belgium). The 3D structure of the dough was created in CTAn and it was observed using the CTVol software (version 2.3, Bruker Corp., Belgium).

To compare the results obtained by micro-CT (volume values) and soxhlet extraction (mass values), the densities of oil and milled defatted dry fried dough were measured in a glass pycnometer.

Results

In order to understand the microstructural relationship between oil absorption and freezing conditions, a non-invasive procedure was used to observe and differentiate the components of fried dough with minimal intrusion. Cross-sectional microtomography images and 3D visualization of fried dough are presented in **Fig. 1** and **Fig. 2**. **Fig. 1** shows the main resulting images after applied the image processing. The important steps during this processing were noise removal from original image, image masking to generate ROI and the segmentation of matrix, empty pores (air) and pores filled with oil. As can be observed, the magnification used in this study allowed to successfully distinguish the gluten-starch matrix network (yellow) from the oil (purple) and the air (white). The three-dimensional internal structure of fried dough is shown in **Fig. 2**. On the one hand, **Fig. 2.A** illustrates a 3D rendering of oil-filled pores labeled with different colors which represent a broad range of sizes (expressed as voxels unit). On the other, **Fig. 2.B** shows the 3D network of pores filled with oil, the gluten-starch matrix and the structure of a fried dough. Additionally, the cross-section of a fried dough presents how the oil and air (empty pores) are distributed inside of it. This clear representation of the matrix, the air and the oil enabled us to quantify the distribution of empty and oil-filled pores, as well as the volume of each of these components.

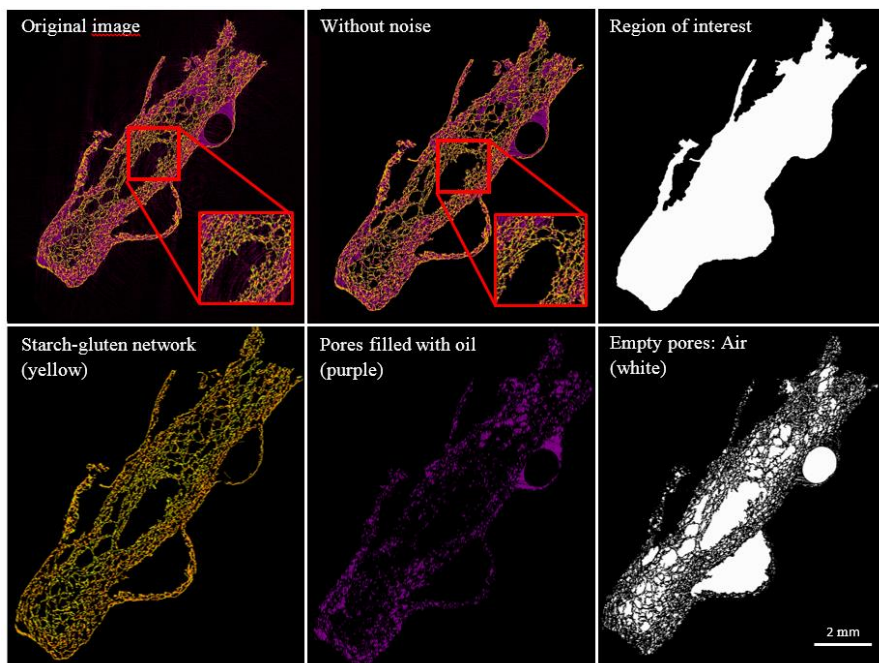


Figure 1. Reconstructed 2D cross-sectional μ CT image of directly fried starch-gluten dough showing its main components.

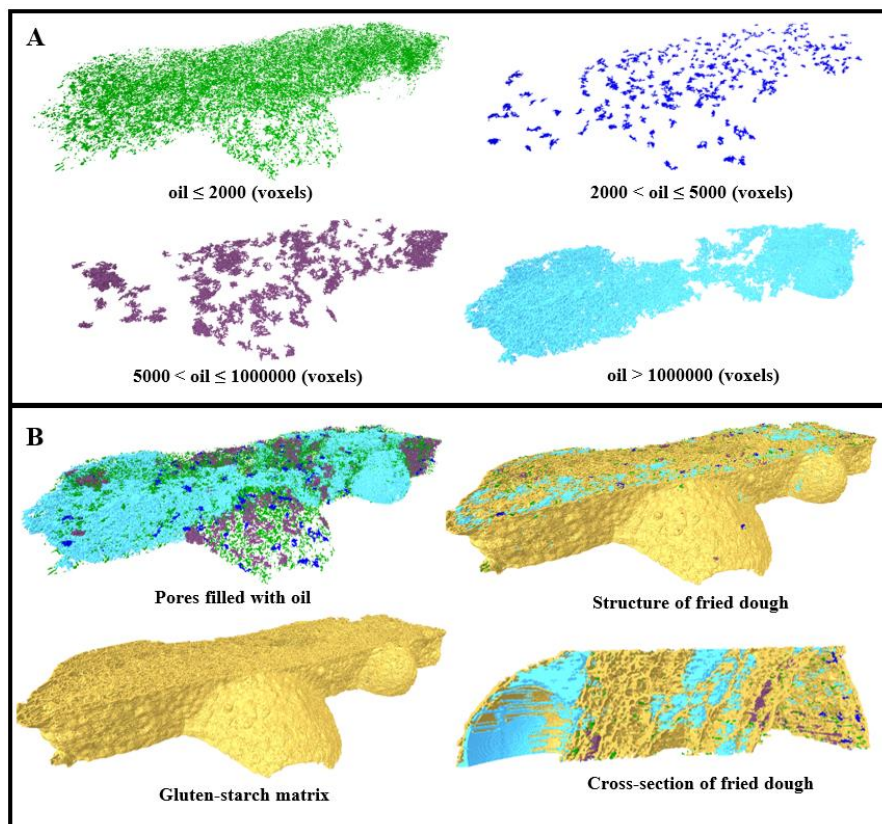


Figure 2. The three-dimensional X-ray μ CT visualization of different sizes of oil volume (A) and the structure of directly fried dough (B) showing the starch-gluten matrix and the pores filled with oil as solid network.

To test and verify the protocol for processing and analyzing images developed in this study, the results of the total oil content obtained by the soxhlet extraction test (T_{soxhlet}) and the micro-computed tomography (TO μ CT) were contrasted and presented in **Fig. 3**. A strong positive correlation was found between the mean values of total oil content measured by soxhlet and those quantified by X-ray micro-CT ($R^2 = 0.8661$), indicating that X-ray micro-computed tomography is an excellent method to provide complementary information about effect of microstructure of fried doughs on oil absorption.

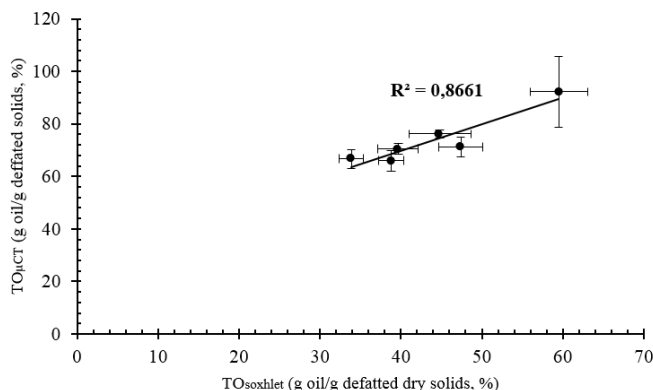


Figure 3. Total oil determined by Soxhlet (TO_{soxhlet}) v/s total oil obtained by microtomography (TO_{μCT}). Least squares regression coefficient (R^2) and mean values \pm standard error are presented.

To get a better understanding of oil and air distribution inside the structure of fried dough, pore size distribution of these components were quantified. **Fig. 4** shows the pore size distribution of oil and **Fig. 5** shows the pore size distribution of air inside the doughs, which were fried after being subjected to different freezing rates, and stored during 3 days at -18°C . As can be shown in **Fig. 4**, most of the oil is located in pores whose size is larger than $3.7\ \mu\text{m}$ and lower than $90\ \mu\text{m}$, specifically, between 88 and 99% of the oil is located in pores of that size probably due to capillary forces [8,9]. However, it was possible to observe important differences between directly fried doughs and those subjected to freezing conditions: most of the oil of directly fried dough is in the range $[3.75 - 26.25]\ \mu\text{m}$, whereas frozen and fried doughs significantly increase the oil-filled pores in the ranges $[26.25 - 86.25]$ and $[86.25 - 138.75]\ \mu\text{m}$. In pores higher than $86.25\ \mu\text{m}$ the percentage of oil is lower than in the other ones, however the frozen dough at a high rate has pores whose size is even higher than $566\ \mu\text{m}$. These results suggest that not only the smaller pores are significant to understand the oil uptake but also the higher pores could affect and promote this absorption.

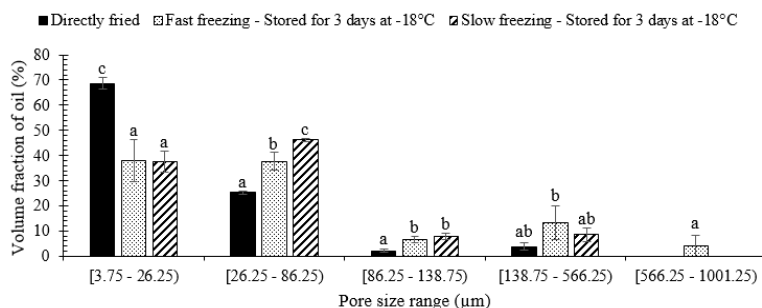


Figure 4. Pore size distribution from X-ray μCT of pores filled with oil inside the doughs that were subjected to different freezing rates and stored during 3 days at -18°C . Data are means \pm

standard error ($n = 3$). Different lowercase letters by range denote significant differences ($p < 0.05$).

As can be shown in **Fig. 5**, the pore size distribution of air has a wider range of size compared to the pore size distribution of oil, having pores even larger than $1000\ \mu\text{m}$. With the using of X-ray μCT it was possible to identify pores much larger than it is possible to detect by means of other image analysis methods, as [10] and [11] used. Moreover, it can be seen that freezing reduces air volume and increases matrix volume, which is more affected by slow freezing, and fast freezing further reduces the air volume because of the higher increment of the oil absorption.

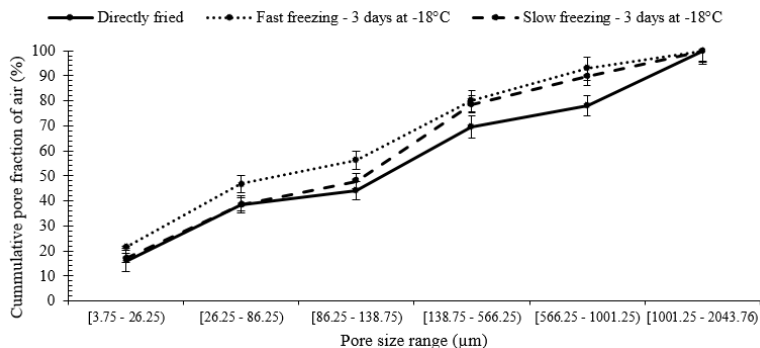


Figure 5. Pore size distribution from X-ray μCT of empty pores (air) inside the dough that were subjected to different freezing rates and stored during 3 days at -18°C . Data are means \pm standard error ($n = 3$).

Conclusion

The effect of freezing rate on oil absorption of deep-fat fried doughs were examined in this study. X-ray micro-computed tomography provided an excellent non-destructive technique to distinguish the gluten-starch matrix from the oil and the air, and to analyze the pore size distribution of those two last components. The 3D approach allowed having a general prospect of the inner structure of fried dough before performing the quantitative data analysis. From the results of total oil content, it was possible to obtain a good correlation among micro-CT imaging and soxhlet techniques. The distribution of oil was mainly located in pores whose size is between 3.7 and $90\ \mu\text{m}$, but larger pores were also important to understand the effect of freezing. Therefore, the X-ray μCT is a valuable technique for gets information about the microstructure of fried dough and complements the results of conventional lab methodologies.

References:

1. Bouchon, P., & Aguilera, J. M. "Microstructural analysis of frying potatoes". *International Journal of Food Science & Technology*, 36(6), 669-676. (2001)
2. Bouchon, P., Aguilera, J. M., & Pyle, D. L. "Structure oil-absorption relationships during deep-fat frying". *Journal of Food Science*, 68(9), 2711-2716. (2003).
3. Moreno, M. C., Brown, C. A., & Bouchon, P. "Effect of food surface roughness on oil uptake by deep-fat fried products". *Journal of Food Engineering*, 101(2), 179-186. (2010).
4. Dueik, V., Moreno, M. C., & Bouchon, P. "Microstructural approach to understand oil absorption during vacuum and atmospheric frying". *Journal of Food Engineering*, 111(3), 528-536. (2012).

5. Adedeji, A. A., Liu, L., & Ngadi, M. O. "Microstructural evaluation of deep-fat fried chicken nugget batter coating using confocal laser scanning microscopy". *Journal of Food Engineering*, 102(1), 49-57. (2011).
6. Pinthus, E. J., & Saguy, I. "Initial interfacial tension and oil uptake by deep-fat fried foods". *Journal of Food Science*, 59(4), 804-807. (1994).
7. Kiani, H., & Sun, D.-W. "Water crystallization and its importance to freezing of foods: A review". *Trends in Food Science & Technology*, 22(8), 407-426. (2011).
8. Bouchon, P., & Pyle, D. L. "Modelling oil absorption during post-frying cooling: I: model development". *Food and Bioprocesses Processing*, 83(4), 253-260. (2005).
9. Moreira, R. G., Sun, X., & Chen, Y. "Factors affecting oil uptake in tortilla chips in deep-fat frying". *Journal of Food Engineering*, 31(4), 485-498. (1997).
10. Moreno, M. C., & Bouchon, P. "Microstructural characterization of deep-fat fried formulated products using confocal scanning laser microscopy and a non-invasive double staining procedure". *Journal of Food Engineering*, 118(2), 238-246. (2013).
11. Kawas, M. L., & Moreira, R. G. "Characterization of product quality attributes of tortilla chips during the frying process". *Journal of Food Engineering*, 47(2), 97-107. (2001).

Multiscale Characterization of Heterogeneous Porous Media by Means of Micro-CT Images

I.F. Mantovani¹, A.C. Moreira¹, C.P. Fernandes¹

¹Federal University of Santa Catarina – UFSC,

Aims

Heterogeneous pore medium is often very complex with a broad range of pore size system. In natural materials, such as petroleum reservoir rocks, the morphology and connectivity of the porous system characterization contributes to improvements in hydrocarbon recovery strategies. In order to analyze the whole pore space of carbonate rocks with X-ray tomography, and due to the technique limitation of image spatial resolution, we have to carry out a set of image acquisitions. With the purpose of quantify the data from the different acquisitions as a one value we developed a multiscale composition model to determine total porosity and total pore size distribution. Consequently, our goal is used the CT technique to allow us extract the properties from the 3D images in different complementary scales so we can put all information together as a single value (such as total porosity and total pore size distribution) by means of a mathematical model. The method was applied on a carbonate rock due to its complex porous system with a multiple pore-sized, from nanometers to centimeters (Choquette and Pray, 1970).

Method

To describe the complex pore system of carbonates and illustrate the multiscale composition model were study two samples of carbonate rocks from Brazil (C1 and C2). Initially the samples were analyzed in low and medium spatial resolution with Micro-CT (sample size plug and sub-volume). We also used a stochastic method to reconstruct a 3D image based on statistics information extract from SEM (Scanning electron microscope) 2D image to reach the high resolution (Liang et al., 1998). The porous media parameters quantification (porosity and pore size distribution) are determined with digital image analysis in each scale. These parameters were used as input data to the multiscale composition model.

The multiscale model is simple and demonstrated as below. Figure 1 represents a measurement concerning three spatial scales, in which E_3 is contained in E_2 and E_2 is contained in E_1 ($E_3 \subset E_2 \subset E_1$). Their spatial resolutions are respectively r_1 , r_2 , and r_3 , where $r_1 \gg r_2 \gg r_3$, in numerical terms.

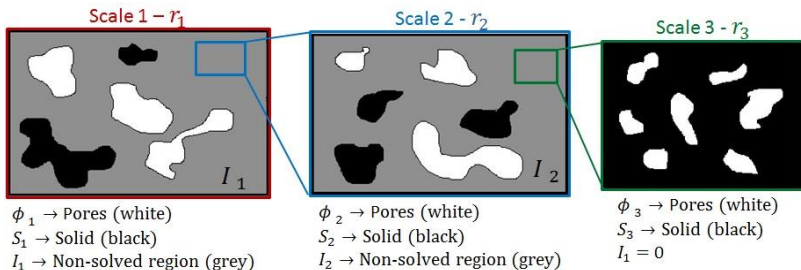


Figure 1. Diagrammatic representation of the multiscale composition model for three spatial scales. r_n denoted de spatial resolution of each scale, where $n=1, 2, 3$.

The regions denoted by ϕ_1 and S_1 are the volumetric fraction of pores and material phase (white and black), respectively. These regions can be well defined with the spatial resolution r_1 , where $\phi_1 + S_1 + I_1 = 1$. On the other hand, this resolution (r_1) is not enough to define the grey area, denoted by I_1 and called as non-solved region. In this region, pores with sizes smaller than the resolution r_1 are possible to occur. To solve this, images with better resolution (E2) have to be analyzed.

For the Scale 2, the hypothesis of a homogeneous spatial distribution of the pore and material phases is assumed. In this way, just a subvolume of this region will be analyzed and considered representative. Therefore, the new pore and material phases, as well the new non-solved region are ϕ_2 and S_2 and I_2 , where $\phi_2 + S_2 + I_2 = 1$.

For this example, a third scale is enough to characterize the pore sizes of this hypothetical porous medium. Image from Scale 3, there is not a non-solved region ($I_3=0$), only pore and material phases ($\phi_3 + S_3 = 1$).

Considering an arbitrary number of n scales, the total porosity (ϕ_T) is given taking into account the total volume at first scale (E1) as following:

$$\phi_T = \phi_1 + \left[\sum_{i=2}^n \left(\phi_i \prod_{k=1}^{i-1} I_k \right) \right] \quad (1)$$

For each i scale, there are f_{ij} volumetric fractions for each one of the j classes of pore sizes. For the whole image scales, it must to be normalized by the total pore volume in each n scale. Thus, the volume fractions f_{ij}^* is given by:

$$f_{ij}^* = \left(f_{ij} \phi_i \prod_{k=1}^{i-1} I_k \right) / \phi_T \quad (2)$$

Results

To validate the multiscale composition model we compared the results with laboratory measurements. Table 1 showed the spatial resolutions of the images (for each scale), also presented the results of total porosity determined with the multiscale model (Equation 1) and laboratory data. The heterogeneity of the carbonate rock is quite clear on the images on Figure 2 and we can observe the differences between each scales. Images of low and medium resolution (scales 1 and 2) (Figures 2a and 2b, respectively) were acquired with micro-CT while the high resolution image (scale 3) (Figures 2c) was achieved by means of SEM. Pore size distribution property was plotted in Figure 3. We can compare the results of both method: multiscale model (Equation 2) and mercury injection porosimetry (MIP).

Table 1. Spatial resolution at each scale and results of individual porosity, total porosity (by multiscale composition model) and laboratory porosity data.

Sample	Spatial resolution (μm)	Individual porosity (%)	Multiscale porosity (%)	Laboratory porosity (%)
C1	20	0.98	19.75	25.60
	1.16	12.82		
	0.13	12.31		
C2	13	2.60	13.94	27.80
	1.88	12.13		

	0.17	4.63		
--	------	------	--	--

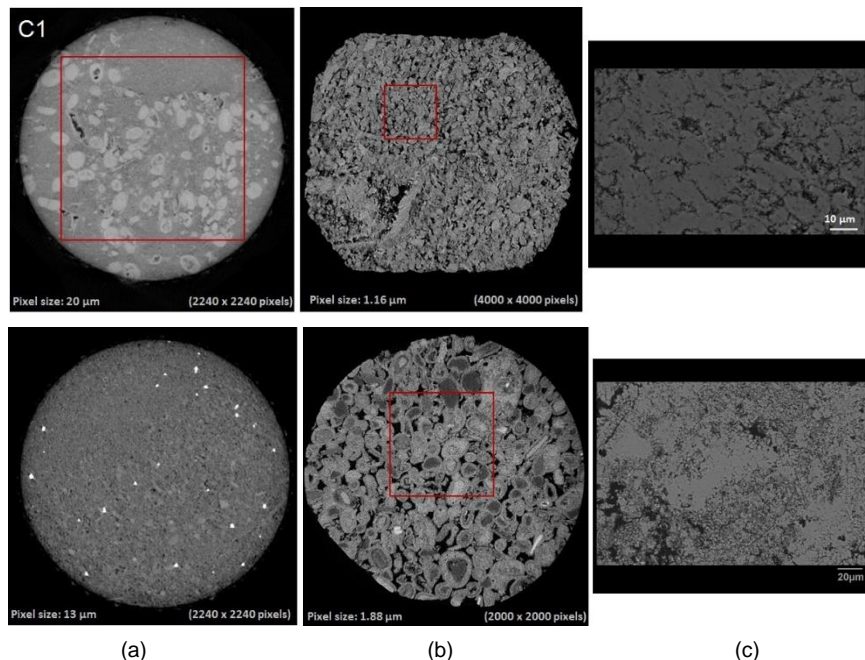


Figure 2. Figure 2 presents 2D image of each scale and sample, analysed region is highlighted in red: (a) scale 1 (micro-CT), (b) scale 2 (micro-CT) and (c) scale 3 (MEV), for sample C1 and C2, respectively. Check Table 1 for spatial resolution.

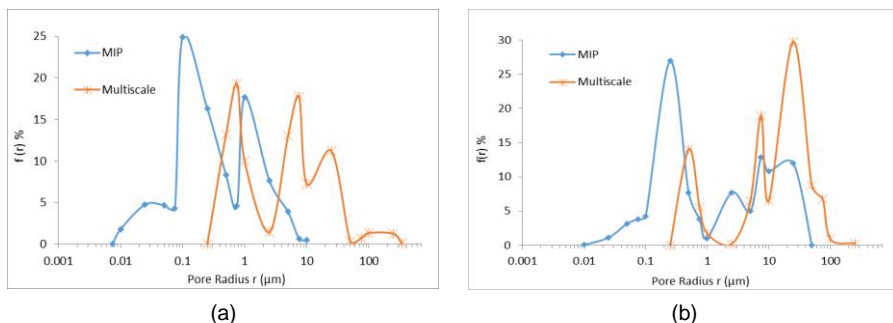


Figure 3: Pore size distribution measure by mercury injection method (blue curves), and total pore size distribution determined by multiscale composition model (red curves) for the samples (a) C1 and (b) C2.

Conclusion

The total porosity determined by means of multiscale composition model present better agreement with laboratory data than the individual values at each scale. Taking into account the uncertainties derived from laboratorial experiments and the differences between the physical principles of the two techniques (mercury injection and multiscale model), pore size distribution data also concurring. The better agreement presented by the composed porosity with laboratory data, and the pore size distribution data comparison, shows the relevance about to evaluate and compose several scales to quantify some complex porous media. Multiscale composition is an alternative method to describe more precisely heterogeneous porous media and physical parameters of reservoir rocks when image analysis is the characterization technique adopted. The model also can be apply in many kinds of materials and different situations as far as the initial conditions are preserved.

References:

1. Choquette, P.W. and Pray, L.C. "Geologic nomenclature and classification of porosity in sedimentary carbonates." AAPG Bulletin, v. 54/2, 1970.
2. Liang, Z. R., Fernandes, C. P., Magnani, F. S., Philippi, P. C. "A reconstrucion technique for three-dimensional porous media using image analysis and fourier transforms." Journal of Petroleum Science & Engineering, v. 723, 1998.

Long term quantitative evaluation of muscle and bone wasting induced by botulinum toxin in mice using microCT

Daniel Chappard¹, Hélène Libouban¹, Claude Guintard^{1,2}, Nicolas Minier¹, Eric Aguado^{1,2}

¹ GEROM Groupe Etudes Remodelage Osseux et bioMatériaux, IRIS-IBS Institut de Biologie en Santé, CHU d'Angers, Université d'Angers, 49933 ANGERS Cedex -FRANCE.

² Anatomy and bone surgery groups, ONIRIS, Ecole Nationale Vétérinaire, route de Gachet, 44307 Nantes Cedex 3 - FRANCE

Aims

Muscle and bone masses are highly correlated and muscles impose large loads on bone. Long term immobilization or prolonged exposure to microgravity induce a severe muscle wasting and bone loss. Muscle wasting that accompanied bone loss has been poorly investigated mainly due to the lack of simple analytical methods to quantify muscle loss. We have previously shown that a single injection of botulinum toxin (BTX) in the right quadriceps muscle induces a transient paralysis and a rapid bone loss due to disuse ¹⁻³. However, muscle changes have not been considered because of their radiolucency ⁴.

Method

21 female mice were spread into 7 groups. At day 0, 18 mice received a BTX injection in the quadriceps muscle to induce paralysis of the right hind limb; the left contralateral side was used as control. Mice were sacrificed at 7, 14, 21, 28, 56 and 90 days post-BTX (3 mice per group). The remaining group was not injected and sacrificed at day 0. Trabecular bone volume was determined by microCT at the proximal tibial metaphysis on both sides. Hind limbs were immersed in a contrasting solution containing HgCl₂ for muscle visualization by microCT ⁵. On the 2D sections, the surface area, circularity and aspect ratio were measured for M. quadriceps at mid-tigh and M. gastrocnemius at mid-leg. These muscles were then carefully dissected by trained anatomists and weighed (anatomical method).

Results

MicroCT and anatomical analysis of muscle evolution

In order to obtain a scan of the whole hindlimb, the multi-scan mode of the Skyscan 1172 microCT was used. The whole musculature in a complete mouse leg was easily "stained" by the HgCl₂ solution (Fig. 1). 2D sections provided a sharp contrast between the muscles and tendons and images were similar to MRI in humans. The surface area of M. gastrocnemius and M. quadriceps were significantly lower in the paralyzed limb from 7d; the decrease was maximum at resp. 21 day (-46.9%) and 28 day (-47.9%). No difference in geometric form-factor parameters were found between the paralyzed and non-paralyzed limb indicating that the global shape of the muscles was respected. Significant correlations were obtained between the surface area obtained by microCT and weight data obtained by the anatomical method.

MicroCT analysis of bone loss

Bone volume decreased in the paralyzed side at the femur and tibia. Bone loss was maximal at 56 day followed by recuperation at 90 day. Bone loss is observed in the metaphysis and the epiphysis ⁶.

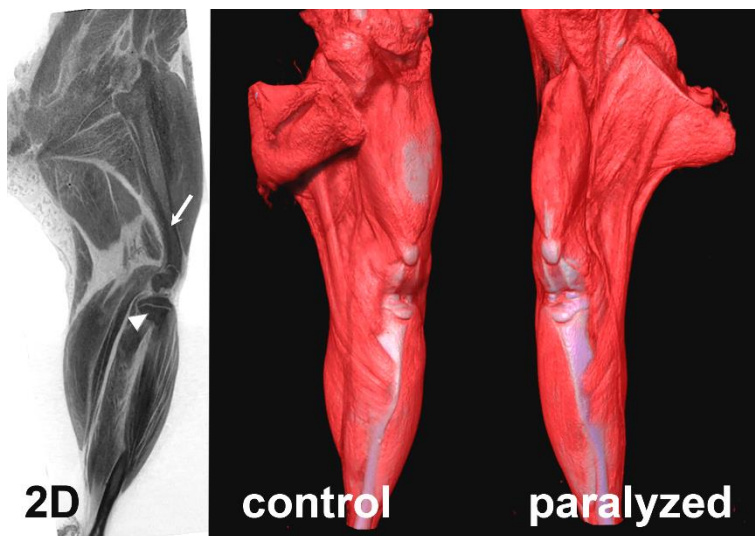


Figure 1: MicroCT analysis of the muscle anatomy of a full leg after contrast enhancement with HgCl_2 . A) 2D section of a leg showing the different muscle bodies impregnated with Hg (arrow indicates the femur, arrowhead indicates the proximal tibia extremities). To improve visualization and contrast, the image is inverted. B) 3D reconstruction image of the left (control) side of a mouse at 21 days; C) 3D reconstruction image of the right (paralyzed) side of the same animal which received a BTX injection in the right M. quadriceps. 3D images produced with CTVox with a look-up table emphasizing muscle in red and bone in white.

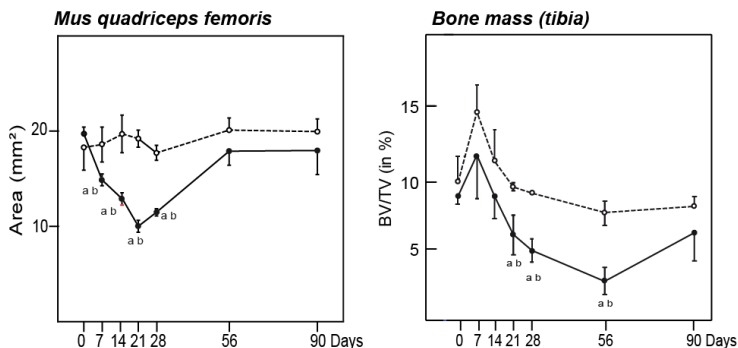


Figure 2: Left: MicroCT analysis of M. quadriceps evolution during the time course of the study in cross sections images of the tibia. Right: evolution of trabecular bone volume at the proximal tibial extremity. ○ identifies the left side and ● the paralyzed right side with BTX. Significance: ^a Same limb, different from t0 ; ^b Same time, different from opposite limb.

Conclusion

The use of a metallic contrast agent opens new perspectives to better understand the changes occurring within soft tissues ⁷. A quantitative analysis of muscle loss and muscle recovery was possible by a microCT technique in the BTX animal model. MicroCT and fine anatomical dissection were correlated. Loss of bone secondary to muscle wastage induced by BTX and recovery showed a parallel evolution for bone and muscles. This study reports for the first time a quantitative analysis of muscle loss and muscle recovery by a microCT technique. Although the number of animals is limited in each group, the sensitivity of the methods used here (microCT after Hg "staining" and fine anatomical dissection) provided similar results which are consistent with previous studies. The study also confirmed the associated loss of bone secondary to muscle wastage induced by BTX and their parallel evolution. Contrast enhancement of muscular structures can be useful to provide a quantitative approach of sarcopenia in other animal models.

References

- 1.Chappard D, Chennebault A, Moreau M, Legrand E, Audran M, Baslé MF. Texture analysis of X-ray radiographs is a more reliable descriptor of bone loss than mineral content in a rat model of localized disuse induced by the Clostridium botulinum toxin. *Bone* 2001; 28:72-79
- 2.Marchand-Libouban H, Le Drévo MA, Chappard D. Disuse induced by botulinum toxin affects the bone marrow expression profile of bone genes leading to a rapid bone loss. *J Musculoskelet Neuronal Interact* 2013; 13:27-36
- 3.Mabilleau G, Mieczkowska A, Libouban H, Simon Y, Audran M, Chappard D. Comparison between quantitative X-ray imaging, dual energy X-ray absorptiometry and microCT in the assessment of bone mineral density in disuse-induced bone loss. *J Musculoskelet Neuronal Interact* 2015; 15:42-52
- 4.Bouvard B, Mabilleau G, Legrand E, Audran M, Chappard D. Micro and macroarchitectural changes at the tibia after botulinum toxin injection in the growing rat. *Bone* 2012; 50:858-864
- 5.Pauwels E, Van Loo D, Cornillie P, Brabant L, Van Hoorebeke L. An exploratory study of contrast agents for soft tissue visualization by means of high resolution X-ray computed tomography imaging. *J Microsc* 2013; 250:21-31
- 6.Chappard D, Libouban H. Vector analysis of porosity evidences bone loss at the epiphysis in the BTX rat model of disuse osteoporosis. *J Anat Soc Ind* 2016; 65:3-8
- 7.Metscher BD. MicroCT for comparative morphology: simple staining methods allow high-contrast 3D imaging of diverse non-mineralized animal tissues. *BMC Physiol* 2009; 9:1

Independent Active Contours Segmentation

V. Ch. Korfiatis¹, S. Tassani², J. Noailly², M.A. González Ballester^{2,3}, G. K. Matsopoulos¹

1 School of Electrical and Computer Engineering of the National Technical University of Athens, 9 Iroon Polytechniou Str., 157 80, Zografou, Athens, Greece.

2 Universitat Pompeu Fabra, Department of Information and Communication Technologies, Barcelona, Spain.

3 ICREA, Barcelona, Spain.

Aims

The study of trabecular bone enables the investigation of various bone pathologies, such as osteoarthritis and osteoporosis [1-2], bone functions, such as bone remodeling [3], bone biomechanical properties [4] and response to treatment [5, 6]. The use of micro-CT imaging technology permits the three-dimensional (3D), non-destructive investigation of a bone specimen with relatively low cost and scanning efficiency, without any special specimen preparation [8]. Following the scanning, the micro-CT volume is segmented producing a binary image, where the foreground represents the bone. This is a mandatory and crucial step for the calculation of morphometrical parameters of the trabecular three-dimensional framework [9, 10]. The performance of the segmentation step is critical due to the high sensitivity of the morphometrical parameters to errors/deviations [10-11].

However, there is currently no accepted and well-established method for micro-CT segmentation [12-14]. The most widely used algorithmic segmentation methods are based on intensity histogram thresholding, either by a manual selection of a global threshold [12, 15-18] or by semi-manual selection using an initial human estimation followed by algorithmic refinement [20]. Although the above approaches are easy to implement, their need for manual intervention makes them time-consuming for the experts and subjective. Other intensity threshold-based segmentation techniques have been proposed, including Otsu Thresholding [20], Hysteresis Thresholding [22], Dual-Thresholding [23] and Adaptive Thresholding [24]. But, these methods remain sensitive to noise, provide medium accuracy (especially on high resolution images), still require some form of manual intervention and may miss some important parts of the foreground, such as small trabecular bone. In order to overcome these limitations, Active Contours [25, 26] techniques have been recently proposed as an alternative. These provide easy multiple objects' segmentation, higher accuracy and object identification ability, but are computationally heavy, sensitive to initialization and need manual determination of their optimal parameters' values. These drawbacks lead to medium robustness and slower execution times.

The aim of this paper is to enhance both the performance and the quality of the 2D micro-CT trabecular bone image segmentation process, through the proposal of a novel segmentation framework, called Independent Active Contours Segmentation (IACS), which is based on Active Contours segmentation algorithms.

Method

The proposed Independent Active Contours Segmentation (IACS) framework, illustrated in Fig. 1, is based on two autonomous modules: Automatic ROI Extraction and Independent Active Contours (IAC) Evolution. The Automatic ROI Extraction module is a pre-processing step that aims at removing the majority of image background, while maintaining all the foreground. This is accomplished in four consequent steps: Background Elimination, which is based on the iterative application of unimodal thresholding, Heuristic Thresholding, which is a novel denoising technique using iterative global thresholding, Image Patching using a user-defined patch size and ROI Extraction by connecting each patch with its neighboring patches

above, below, on the left and on the right. This module's output is a coarse pre-segmentation of the 2D micro-CT image that serves as input for IAC Evolution module, which provides the final accurate segmentation. To accomplish this, it applies one independent instance of the modified Chan-Vese Active Contour (CV-AC) segmentation algorithm in each ROI. As it is implied by its name, every instance evolves simultaneously but independently from the others, which means that IACS naturally takes into account the local ROI characteristics, resulting in more accurate segmentation images. At the same time, it represents a progress in the AC algorithms' state-of-the-art.

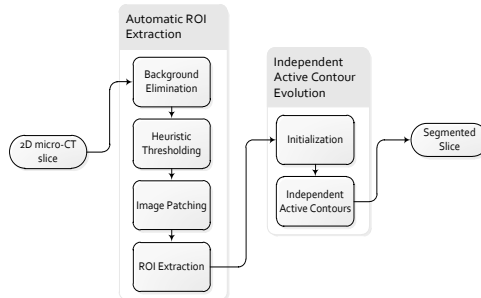


Fig. 12. Block Diagram of the proposed IACS framework

In order to evaluate the performance of the proposed IACS framework, comparisons have been made with the following two well-established algorithms:

1. **Otsu Thresholding:** Otsu is a thresholding algorithm that automatically determines the optimal threshold value of the intensity histogram. As a result, it does not have any parameters [21]. It was chosen, because it is currently the most popular automatic segmentation algorithm for micro-CT trabecular bone images.
2. **Original Chan-Vese Active Contour (CV-AC):** is one of the most popular implicit region Active Contours algorithms and is also the base for our proposed modified algorithm. It has three parameters, contour regularization r and force coefficients λ_1 and λ_2 [27]. Also, it needs an initialization mask, which determines the initial position for its evolution. It was chosen in order to illustrate the performance of a typical active contour algorithm on micro-CT trabecular bone images.

The experimental data consisted of a micro-CT Phantom, with 991 gray-level slices of 1024x1024 resolution [7] and a real trabecular bone image with the same attributes. The micro-CT Phantom contained 15 objects of various sizes and shapes, whose thickness ranged from 20 μm to 1000 μm , and has been found to provide a very good approximation of the real-case scanning environment [7]. In order to provide a reference illustration of the actual micro-CT Phantom, a gold standard (GS) segmented-image dataset for the Phantom micro-CT is introduced, called hereafter micro-CT Phantom GS. The micro-CT Phantom GS calculation was based on object's thickness and dimensions, pixel size information (pixel size= 19.47 μm) [7] and the use of "CTAnalyzer" software, Bruker [28]. Specifically, error calculation between the nominal and the calculated thickness was carried out for each object separately, instead of globally as it was done in the seminal paper, by cropping the corresponding slices and inputting them to CTAnalyzer. The intensity threshold that provides the smallest error for each object was kept, and the segmented result was placed in the Phantom GS dataset, in the same place as the original. The two smallest wires (20 μm and 50 μm) and the smallest foil (20 μm) could not be standardized using the above procedure due to their small size. The 50 μm wire and the 20 μm foil, were manually segmented using the reported pixel size and the objects' dimensions and coordinates, and were placed in the GS. The 20 μm wire was

practically invisible even by human experts, as a result it was omitted from the micro-CT Phantom GS.

Results obtained by the different segmentation procedures over the whole phantom were analyzed also in terms of final measured thickness for each objects. Spheres were excluded from this analysis due to their dimensions, not comparable to the other objects.

Results

A. Phantom Micro-CT 3D Reconstructions

The qualitative assessment of the segmentation performance using 3D reconstructions, highlights critical elements, such as the importance of small objects and the effect of noisy artifacts on the final result. The reconstructions, illustrated in Fig. 2, were produced using VTK 6.3 library [29] in Python 2.7.

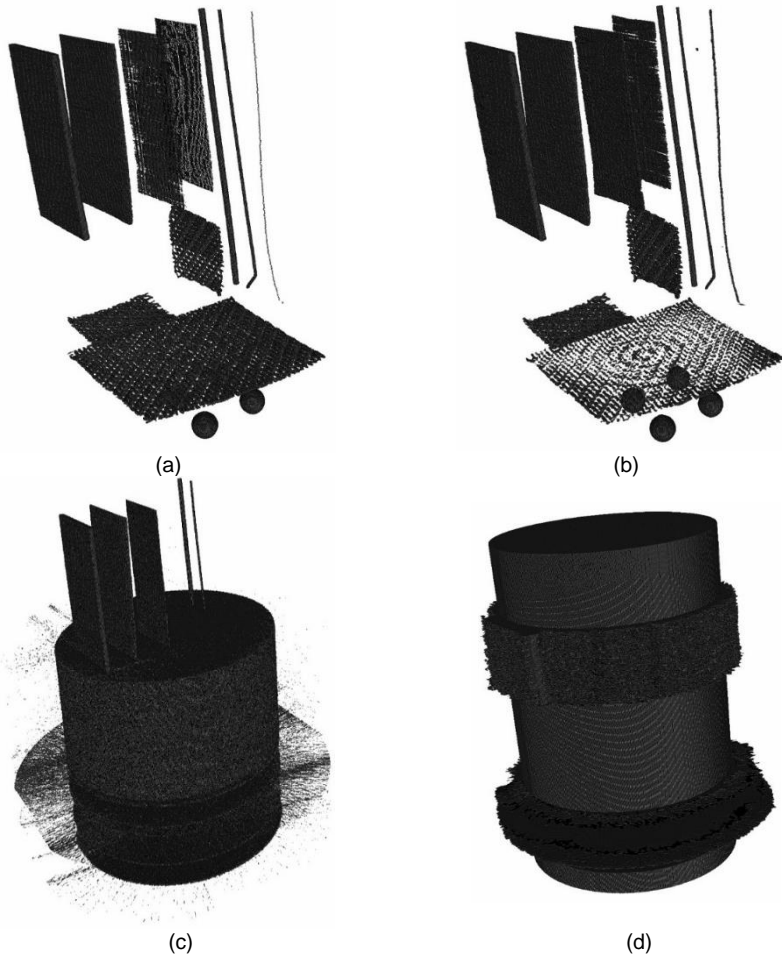


Fig. 2. 3D reconstructions of the results of each algorithm on micro-CT Phantom dataset. (a) Micro-CT Phantom GS, (b) IACS, (c) Otsu thresholding, (d) Chan-Vese AC

It is clear that the proposed IACS scheme provides superior performance compared to the other two methods and finds all the visible objects, even those that couldn't be identified during the GS creation using the aforementioned process. On the other hand, both Otsu and CV-AC provide low quality results with a lot of noise, segmenting usually most of the dark background instead of the objects inside it.

Looking at the analysis of the single objects, CV-AC was actually unable to segment any of the single objects, while OTSU identified 7 out of the 11 considered objects. Otsu also showed the worst absolute error in the remaining segmented objects. The fixed global threshold was used as reference since it is probably the most used segmentations technique in micro-CT. This segmentations showed the best absolute error but miss the segmentation of three objects. Finally IACS showed intermediate error and only one object not segmented (Table 1).

	<i>Fixed Threshold (143)</i>	<i>OTSU</i>	<i>IACS</i>
Foil (250µm)	11.64	28.86	4.81
Foil (100µm)	10.23	34.23	14.16
Foil (50µm)	10.92	26.45	26.66
Foil (20µm)			44.57
Wire (250µm)	18.46	18.53	12.15
Wire (125µm)	44.52	0.22	12.68
Wire (50µm)			20.89
Wire (20µm)			
Mesh big (100µm)	34.84	25.76	34.27
Mesh horizontal (100µm)	18.25	47.54	2.56
Mesh Vertical (100µm)	9.86		38.26
Total error (µm)	19.84	25.94	21.10

Table 1. Absolute error reported for each object of the phantom and as total error.

B. Results on Real Micro-CT Data 3D Reconstructions

In Fig. 3, 3D reconstructions of a real bone sample before (left column) and after compression (right column) are illustrated, using IACS (a)-(b) and Otsu (c)-(d). Otsu, is characterized by a big miss-segmentation around the broken area and coarser contours, most clearly visible on the bottom of the sample. On the other hand, IACS provides both clear and accurate results, with tighter areas.

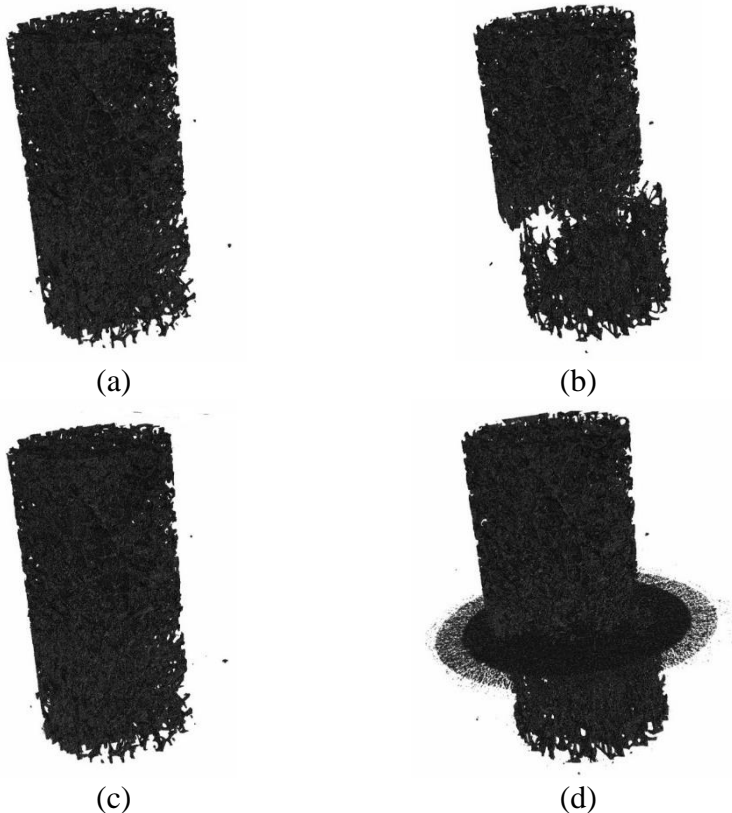


Fig. 3. 3D reconstruction of a real bone dataset. The left column contains the sample before compression and the right column the sample after compression. (a)-(b) IACS before and after compression. (c)-(d) Otsu before and after compression.

Conclusion

Trabecular bone's segmentation from 2D micro-CT images is a critical, yet understudied, procedure that constitutes the first step in any type of relevant further study and/or processing, such as biomechanical analysis and fracture zone prediction using morphometrical parameters, or bone visual assessment using 3D reconstructions. The presented IACS framework, based on the state-of-the-art segmentation techniques of Active Contours and on its aforementioned novelties provides quality segmentation performance that is characterized by high area accuracy, high object identification ability, high stability, low error and almost seamless human interaction. The absolute error showed by IACS is intermediate and comparable in magnitude to the one of the fixed threshold and OTSU. However, the algorithm illustrated the capability of identifying the smallest objects of the phantom that were impossible to segment using other techniques. These newly introduced enhancements can lead to better diagnostic procedures and treatment evaluation of several bone-related pathologies, to the

facilitation and further advancement of bone research, and to the overall increase of the popularity of micro-CT imaging technology.

References:

1. D. D. McErlain et al., "Study of subchondral bone adaptations in a rodent surgical model of OA using in vivo micro-computed tomography," *Osteoarth. and Cart.*, vol. 16, no. 4, pp. 458-469, Sep. 2007.
2. A. Laib, J. L. Kumer, S. Majumdar, and N. E. Lane, "The Temporal Changes of Trabecular Architecture in Ovariectomized Rats Assessed by MicroCT," *Osteop. Int.*, vol. 12, no. 11, pp. 936-941, Nov. 2001.
3. A. T. Cowan CM, Chou YF, Walder B, Zhang X, Soo C, "MicroCT evaluation of three-dimensional mineralization in response to BMP-2 doses in vitro and in critical sized rat calvarial defects," *Tiss. Engin.*, vol. 13, no. 3, Mar. 2007.
4. S. T. Ho and D. W. Hutmacher, "A comparison of micro CT with other techniques used in the characterization of scaffolds," *Biomat.*, vol. 27, no. 8, pp. 1362-1376, Mar. 2006.
5. D. W. Dempster et al., "Effects of Daily Treatment with Parathyroid Hormone on Bone Microarchitecture and Turnover in Patients with Osteoporosis: A Paired Biopsy Study*," *J. Bone and Miner. Res.*, vol. 16, no. 10, pp. 1846-1853, Oct. 2001.
6. D. J. Waarsing JH, Weinans H, "Longitudinal micro-CT scans to evaluate bone architecture," *J. Musculoskelet Neuronal Interact.*, vol. 5, no. 4, Oct.-Nov. 2005.
7. E. Perilli, F. Baruffaldi, M. C. Bisi, L. Cristofolini, and A. Cappello, "A physical phantom for the calibration of three-dimensional X-ray microtomography examination," *J. of Microsc.*, vol. 222, no. 2, pp. 124-134, May 2006.
8. M. L. Boussein et al., "Guidelines for assessment of bone microstructure in rodents using micro-computed tomography," *J. of Bone and Miner. Res.*, vol. 25, no. 7, pp. 1468-1486, Jul. 2010.
9. S.-W. Lee et al., "Stem cell-mediated accelerated bone healing observed with in vivo molecular and small animal imaging technologies in a model of skeletal injury," *J. Orthop. Res.*, vol. 27, no. 3, pp. 295-302, Mar. 2009.
10. M. Ding, A. Odgaard, and I. Hvid, "Accuracy of cancellous bone volume fraction measured by micro-CT scanning," *J. Biomech.*, vol. 32, no. 3, pp. 323-326, Mar. 1999.
11. T. Hara, E. Tanck, J. Homminga, R. Huiskes, "The influence of microcomputed tomography threshold variations on the assessment of structural and mechanical trabecular bone properties," *Bone*, vol. 31, no. 1, pp. 107-9, Jul. 2002.
12. D. P. Clark and C. T. Badea, "Micro-CT of rodents: State-of-the-art and future perspectives," *Phys. Med.*, vol. 30, no. 6, pp. 619-634, Sep. 2014.
13. I. Lima, M. S. Rocha, and R. T. Lopes, "Ethanol bone evaluation using 3D microtomography," *Micron*, vol. 39, no. 5, pp. 617-622, Jul. 2008.
14. J.-T. Hsu et al., "The assessment of trabecular bone parameters and cortical bone strength: A comparison of micro-CT and dental cone-beam CT," *J. Biomech.*, vol. 46, no. 15, pp. 2611-2618, Oct. 2013.
15. C. Öhman et al., "Mechanical testing of cancellous bone from the femoral head: Experimental errors due to off-axis measurements," *J. of Biomech.*, vol. 40, no. 11, pp. 2426-2433, Jan. 2007.
16. E. Perilli et al., "MicroCT examination of human bone specimens: effects of polymethylmethacrylate embedding on structural parameters," *J. of Microsc.*, vol. 225, no. 2, pp. 192-200, Feb. 2007.
17. H.-Q. Luan et al., "The application of micro-CT in monitoring bone alterations in tail-suspended rats in vivo," *Adv. in Space Res.*, vol. 53, no. 11, pp. 1567-1573, Jun. 2014.
18. G. Michel et al., "Micro-CT Analysis of Radiation-Induced Osteopenia and Bone Hypovascularization in Rat," *Calc. Tiss. Int.*, vol. 97, no. 1, pp. 62-68, Jul. 2015.
19. S. Tassani and G. K. Matsopoulos, "The micro-structure of bone trabecular fracture: An inter-site study," *Bone*, vol. 60, no. pp. 78-86, Mar. 2014.

20. L. De Schaepdrijver, P. Delille, H. Geys, C. Boehringer-Shahidi, and C. Vanhove, "In vivo longitudinal micro-CT study of bent long limb bones in rat offspring," *Repr. Tox.*, vol. 46, no. pp. 91-97, Jul. 2014.
21. Otsu, "A Threshold Selection Method from Gray-Level Histograms," *IEEE Trans. On Systems, Man and Cybern.*, vol. 9, no. 1, pp. 62-66, Jan. 1979.
22. P. Dong et al., "3D osteocyte lacunar morphometric properties and distributions in human femoral cortical bone using synchrotron radiation micro-CT images," *Bone*, vol. 60, no. pp. 172-185, Mar. 2014.
23. H. R. Buie, G. M. Campbell, R. J. Klinck, J. A. MacNeil, and S. K. Boyd, "Automatic segmentation of cortical and trabecular compartments based on a dual threshold technique for in vivo micro-CT bone analysis," *Bone*, vol. 41, no. 4, pp. 505-515, Oct. 2007.
24. A. Burghardt, T. Link, and S. Majumdar, "High-resolution Computed Tomography for Clinical Imaging of Bone Microarchitecture," *Clin. Orthop. and Rel. Res.*, vol. 469, no. 8, pp. 2179-2193, Aug. 2011.
25. A. C. Jones et al., "Analysis of 3D bone ingrowth into polymer scaffolds via micro-computed tomography imaging," *Biomat.*, vol. 25, no. 20, pp. 4947-4954, Sept. 2004.
26. S. Tassani, V. Korfiatis and G. K. Matsopoulos. "Influence of segmentation on micro-CT images of trabecular bone," *J Microsc.* vol. 256, no. 2, pp. 75-81, Nov. 2014.
27. T. F. Chan and L. A. Vese, "Active contours without edges," *IEEE Trans. On Im. Proc.*, vol. 10, no. 2, pp. 266-277, Aug. 2001.
28. Bruker microCT [Online]. Available: <http://bruker-microct.com/products/ctan.html>
29. The Visualization Toolkit [Online]. Available: <http://www.vtk.org/>

Morphological Characterisation of Solid Pharmaceutical Products using X-ray tomography

Frederik Doerr^{1,2}, Elanor Brammer^{1,2}, Sarahjane Wood^{1,2}, Gavin Halbert^{1,2}, Alastair Florence^{1,2}

¹ Strathclyde Institute of Pharmacy & Biomedical Sciences (SIPBS), Strathclyde University, Glasgow, G4 0RE, UK

² Doctoral Training Centre in Continuous Manufacturing and Crystallisation, University of Strathclyde, Glasgow, G4 0RE, UK

Aims

The measurement of morphological descriptors is widely applied in the pharmaceutical industry to evaluate (intermediate) solid forms in terms of their critical quality attributes that influence product-handling in the manufacturing process or to allow a prediction of the performance of the final dosage form. Previous publications have demonstrated the use of micro-focused tomography to analyze formulations and relate the product performance to structure and sample homogeneity¹.

The aim of this study was to assess the use of a commercial nano-focused x-ray tomography system to non-invasively investigate the three-dimensional structure of various solid pharmaceutical products. Special emphasis was given to sizing, the quantification of internal voids and the characterization of formulated samples.

Method

A Skyscanner 2211 x-ray tomograph (NanoCT, Bruker, Kontich, Belgium) was utilized to assess its capabilities for the analysis of solid pharmaceutical products. The samples were scanned in microfocus with an image pixel size of 0.8 μm – 4.2 μm , frame averaging of 4 – 8 and a rotation step size of 0.1 – 0.2. Additionally, cross-section analysis was carried out using a customized image-processing script in Matlab (MathWorks). Scanning electron microscopy was employed to visually validate the structural characteristics of selected samples using a SU6600 (Hitachi, Japan). Samples were gold coated with a ACE200 low vacuum sputter coater (Leica, Germany).

Results

Particles obtained from droplet drying experiments (sizes 0.5 mm – 2 mm) were analysed by x-ray tomography to visualize the three-dimensional structure of the solids and characterize the particles in terms of internal voids, (primary) particle sizes and particle sphericity.

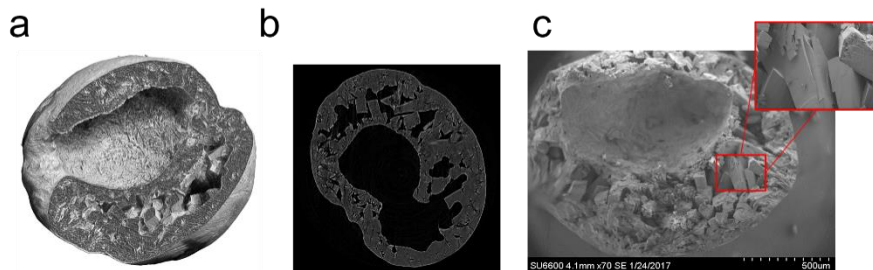


Figure 1: (a) Visualisation of a lactose particle (1.86 mm mean diameter) with a hollow solid crust. (b) Selected cross-section showing large inner void and block-shaped crystals. (c) Images from SEM analysis confirm particle structure as visualised by CT analysis.

The images in Figure 1 show a volume rendered model and a selected cross-section of a lactose particle (Figure 1, a - b) that can be initially used to qualitatively assess particle properties. Moreover, a SEM image (Figure 1, c) was acquired to validate these observations and shows a high correlation in the visual appearance of the sample morphology.

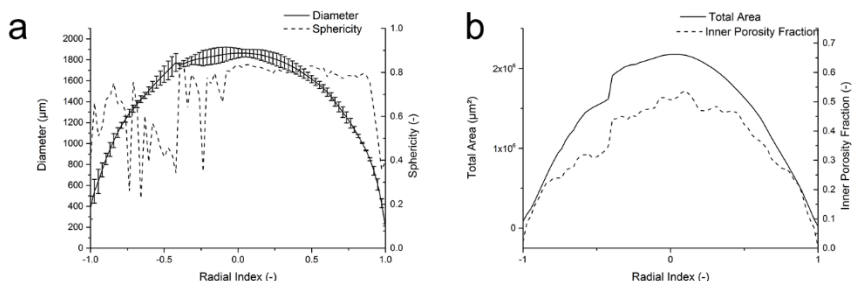


Figure 2: Results of a cross-section analysis of a lactose particle displaying (a) particle diameter and sphericity as well as (b) total cross-section area and inner porosity fraction.

The results of a cross-section analysis are displayed in Figure 2. The graphs indicate a partially anisotropic particle structure demonstrated by large fluctuations in the particle sphericity value at a negative radial index (Figure 2, a) and an increasing fraction of the inner porosity towards the particle center (Figure 2, b). These particle properties have direct implications on the particle performance in the down-stream formulation process.

Nanotomography was used to evaluate the manufacturing process of an injection moulded tablet (Figure 3, a – c) and a 3D-printed tablet (Figure 3, d), respectively. The visualizations of these formulated solid dosage forms were used for process development to improve the structural characteristics as well as the homogeneity of the final product. As visualized in Figure 3, c, the injection moulded tablet shows a high inhomogeneity in its x-ray attenuation with areas of higher apparent density. These differences in the sample homogeneity could be related to changes in its chemical composition during the manufacturing process.

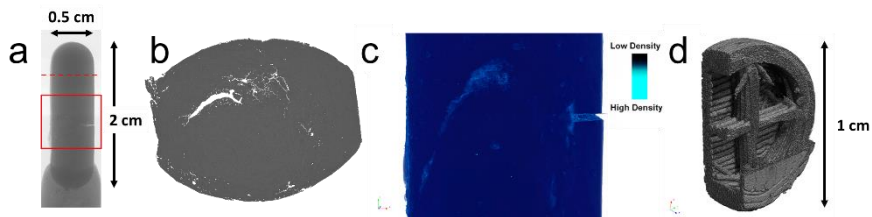


Figure 3: (a) Single scan of an injection moulded tablet, (b) cross-section identifying void areas within the injection moulded tablet and (c) volume rendered model illustrating chemically inhomogeneous regions. (d) visualization of a 3D-printed tablet.

The results of a cross-section analysis are shown in **Figure 4**. The analysis was used to quantify the internal porosity within a subset of 226 cross-sections. The results show unevenly distributed porosity fractions which could influence the final performance of this oral dosage form. The total area of each cross-section remains mostly stable, however, indicated a deformation around cross-section No. 90.

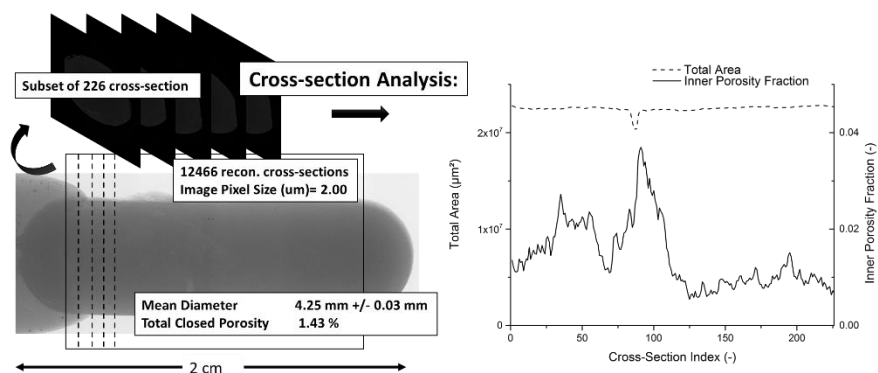


Figure 4: Cross-section analysis of a subset of 226 cross-sections to extract relevant structural data such as the 2D area fraction of detected closed porosity and the progress of the tablet size along its main axis.

Conclusion

Nano-focused x-ray tomography was successfully employed to characterize solid pharmaceutical products in terms of their structural characteristics and solid phase homogeneity. The results can be directly employed to evaluate and improve production processes and enable a prediction of the (final) solid product performance. Future work will focus on extraction of quantitative data to inform rapid product and process development.

Acknowledgements

The authors would like to thank EPSRC and the Doctoral Training Centre in Continuous Manufacturing and Crystallisation (Grant Ref: EP/K503289/1) and the Centre for Innovative Manufacturing in Continuous Manufacturing and Crystallisation (Grant Ref EP/I033459/1) for funding this work. The authors would like to acknowledge that this work was carried out in the

CMAC National Facility supported by UKRPIF (UK Research Partnership Fund) award from the Higher Education Funding Council for England (HEFCE) (Grant ref HH13054).

References:

1. Martinez-Marcos, L., Lamprou, D. A., McBurney, R. T., & Halbert, G. W., "A novel hot-melt extrusion formulation of albendazole for increasing dissolution properties", *International Journal of Pharmaceutics*, 175–185, 2016

The Youngest Tasmanian Wolf: Scanned

F. Spoutil¹, A.N. Herdina², J. Prochazka¹, R. Sedlacek¹, M. Knitlova³

¹Czech Centre for Phenogenomics, Institute of Molecular Genetics ASCR, v.v.i. (division BIOCEV), Prumyslova 595, CZ-25250 Vestec, Czech Republic

²Department of Physiology and Pharmacology, Karolinska Institutet, SE-17177 Stockholm, Sweden

³Department of Zoology, Charles University in Prague, Vinicna 7, CZ-12844 Prague, Czech Republic

Aims

Thylacinus cynocephalus (Harris, 1808) also known as Tasmanian wolf or Tasmanian tiger was the last living species of marsupial family Thylacinidae, whose last known specimen died in 1936. Since then zoologists can study only museum specimens including those interested in development of this species so similar to Canidae (wolves, jackals, foxes etc.). Recently the world youngest specimens were rediscovered and described in the collection of Department of Zoology, Faculty of Science, Charles University in Prague (Czech Republic): a jar containing four pups preserved in unknown liquid¹.

As the faculty is interested in as much detail information about the samples as possible without any disruption of the sample, non-invasive methods were looked for, and microCT seemed as the best choice. SkyScan 1176 localized at the Czech Centre for Phenogenomics (Vestec, Czech Republic), which is able to scan large, fixed samples, fitted well for this goal.

Method

Setting up the scanning procedure was the crucial part of obtaining the data. The samples bound to glass plate by a thread were supposed to be quite soft (with low level of ossification), with no contrast agent and placed in a large jar made from thick glass and with relatively huge amount of liquid. Moreover, no one could be sure, how a more then hundred years long preserevation influences suitability of the samples for microCT.

SkyScan 1176 was set up for full, 360°scanning with image pixel size of 8.67 µm and no filter. The final voltage, current and exposure time were set up for 90 kV, 265 µA, and 3,000 s. Reconstruction was provided in NRecon 1.6.9.15 (Bruker) with parameters for smoothing, ring artifacts correction, and beam hardening correction set up for 3, 19, and 4 % respectively and intensities threshold from 0.000 to 0.013.

The reconstructed digital slices undergone definition of area of interest and several operations for removing noise signal and smoothing the surface of developing bones in CTanalyzer 1.14.4.1 (Bruker). Resulting black and white bitmaps were converted in FiJi (imagej.nih.gov/ij) to be suitable for ITK-Snap 3.6 (Yushkevich & Gerig), where final segmentation of bones were provided according to their morphology and spatial situation.

Results

Although nothing from the soft tissue was visible, the morphology of developing bones was clear in all four samples enabling further data analysis. The samples show characteristics typical for marsupial mammal of this stage, e.g. well developed mouth apparatus with angular processes of mandible rotated medially, and well developed front limbs compared to the hind ones.

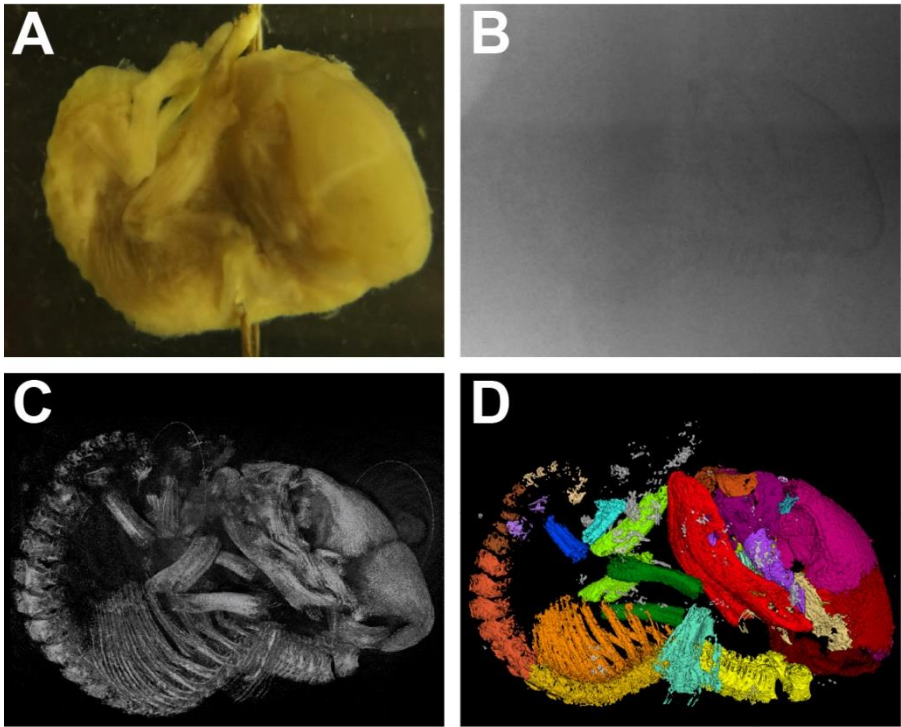


Figure 1: Pup of *Thylacinus cynocephalus*: A) original sample, B) scout-scan of the sample in A, C) bone morphology of the sample from A in CTvox 3.2 (Bruker), D) bone segmentation of the sample from A in ITK-Snap. Head of the sample on the right, abdomen to the top. See disproportion between frond and hind limbs development.

Conclusion

MicroCT is usable also for nondestructive analysis of soft and rare biological samples of old age with long preservation time, when sustaining integrity of sample is needed.

Acknowledgements

The project is supported by LM2015040 by MEYS and OP RDI CZ.1.05/1.1.00/02.0109 BIOCEV by MEYS and ERDF.

References:

1. Sleightholme SR, Robovsky J & Vohralík V, "Description of four newly discovered Thylacine pouch young and a comparison with Boardman (1945)", Australian Zoologist 36(2), pp 232-238, 2012

Insights in the spatial and temporal heterogeneity of biofilm lithification

A. Foubert¹, D. Jaramillo-Vogel¹, E. De Boever¹, S. Krause³, H. Hamaekers^{1,2}

¹Department of Geosciences, University of Fribourg, Switzerland

²Department of Earth and Environmental Sciences, K.U. Leuven, Belgium

³GEOMAR – Helmholtz Centre for Ocean Research, Kiel, Germany

Aims

The role of microbes in the precipitation of carbonate minerals has often been discussed and precipitation mechanism at multiple spatial dimensions still needs to be unravelled. This study highlights the importance of multi-scaled X-ray computed tomography and 3D visualization at micro- and meso-scale combined with field (in-situ) and lab (in-vitro) experiments to understand the precipitation mechanisms of microbial-mediated Ca-Mg carbonates in natural settings.

Method

Different case studies have been selected showing how in-situ 3D visualization at multiple scales may unveil the pathway from crystal nucleation over crystallization to lithification. Mineralogy has been further identified using XRD (X-ray diffractometry) and TEM (Transmission Electron Microscopy). Correlative microscopy combining confocal laser scanning microscopy, SEM and microCT scanning made it possible to study the tight interaction between the cell wall, the biofilm (with EPS) and the nano-crystals.

Samples have been measured with the Bruker Skyscan 2211 (multi-scale X-ray nano-CT system) using an open X-ray source (energies varying between 60 and 120 kV, <4W) with Be-window. Two types of detectors have been used (resp. the 6 Mp flatpanel detector and the 11Mp cooled CCD detector) and voxel resolution was varying between 500 nm and 10 micrometer. Filter-sets were evaluated to enhance the segmentation of different carbonate minerals (calcite, dolomite, aragonite). Defined carbonate standards have been added during the scans facilitating segmentation. Images have been reconstructed using InstaRecon. Image segmentation and visualization have been performed using resp. CT-An, CT-Vox and Avizo (FEI).

Results

The first case study presents field precipitation experiments on different substrates of continental tufa deposits in the Gotteron Valley (Fribourg, Switzerland) and of hot spring deposits in Greece and Hungary. Scanning and microscopy at different scales shows that calcite and aragonite starts precipitating within distinct layers and/or directly on the cell-wall of cyanobacterial filaments (Figure 1).

The second case study visualizes microbial-mediated precipitates in biofilms produced under aerobic and anaerobic conditions in constrained lab experiments. Results show that nucleation of nanocrystals and crystallization processes are clustered within the biofilm and that only in a second phase nanocrystals are clustering together forming spherical aggregates and/or dendritic structures.

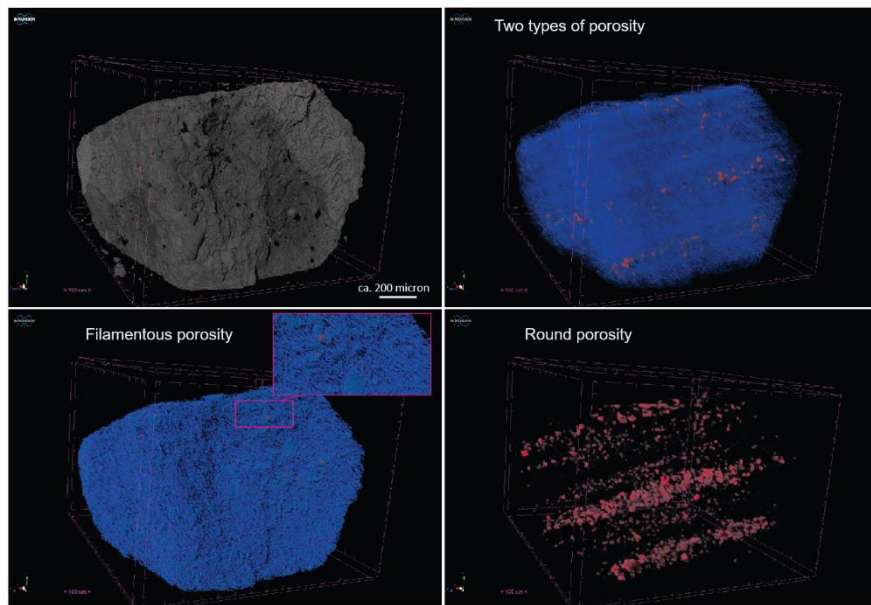


Figure 1: CT-scan image of tufa-deposits (Gotteron Valley, Fribourg). Image represents the precipitation of calcite within distinct layers and around the cell wall of cyanobacterial filaments leading to elongated, filamentous pores (blue color). Degradation of organic matter results in distinctive types of porosity along laminae (red color).

Conclusion

This study highlights the necessity of high-resolution CT-scanning in combination with other microscopy techniques to understand the mechanisms and processes involved in the precipitation of microbial-mediated carbonates.

Scaling and morphological analysis of the lizards vestibular system, using micro CT scanning

M. Vasilopoulou-Kampitsi¹, J. Goyens¹, R. Van Damme¹, S. Baeckens¹, P. Aerts^{1,2}

¹ University of Antwerp, Laboratory of Functional Morphology, Universiteitsplein 1, B-2610 Antwerp, Belgium,

² University of Ghent, Department of Movement and Sport Sciences, Watersportlaan 2, 9000 Ghent, Belgium

Aims

The detection of body motion and orientation by the vestibular system of the inner ear forms one of the basic senses shared by all vertebrates. Because the vestibular system is crucial for maintaining balance, studying its anatomical characteristics could lead to a better understanding of balance control in fast moving animals, such as lizards. Lacertid lizards

(small to medium sized lizards) use a variety of habitats, that may differ greatly in structural complexity (high or low vegetation, rocky or sandy areas, trees and bushes) (*Figure 1*). As such, we examine whether and how structural habitat complexity selects for changes in the size and shape of the vestibular system. In addition, studying its anatomical characteristics and the way they scale with the animal's size could give us information on the existence of any size constraints and as a result, on the ability of very small or large animals to maintain their balance and stability.



Figure 1. Lizard of the species *Phoenicolacerta kulzeri* (Muller&Wettstein,1932) . Photo taken by S. Baeckens

Method

Sample preparation for micro CT scanning:

24 male preserved individuals of 24 different lizard species of the family Lacertidae were obtained from the collections of the Functional Morphology laboratory at the University of Antwerp and from a private collection of dr. A. Herrel (Muséum National d'Histoire Naturelle, Paris). Because in this study, we focus on the bony labyrinth, staining of the samples was not necessary. Nevertheless, we stained the samples to enable imaging of the soft tissue (and possibly the membranous labyrinth) for future research. The samples were dehydrated in a graded ethanol series and fixated in 70% ethanol. Next, all animals were decapitated and the heads were placed in a staining solution of 5% phosphomolybdic acid (PMA; Sigma-Aldrich, St Louis, MO, USA) and 70% EtOH for a minimum time of 14 days.

Micro CT scanning:

The samples were scanned with a SkyScan 1172 high resolution micro CT scanner (Bruker micro CT, Kontich, Belgium), which is managed by the BiostruCT Hercules consortium (<https://sites.google.com/view/biostruct>). For the scanning of the specimens we used an average voltage of 80kV and a current of 124 μ A with an Aluminum-Copper filter of 1mm. The pixel size varied from 4.17 μ m to 13.45 μ m due to the size difference between species. The rotation angle of the scans was 0.40° and the exposure time 1300ms.

Segmentation:

The bony labyrinth was clearly visible on the reconstructed scans as a network of connected tunnels at the posterior end of the skull bone. We imported the reconstructed slice images in the specialized 3D image processing software Amira (Amira 5.4.3 VSG systems, Mérégnac, France). We selected the voxels belonging to the bony labyrinth, by combining automatic grey-scale thresholding and manual corrections in the three orthogonal views. The result was a 3D model of the vestibular system (*Figures 2,3,5*).

Measurements

The linear dimensions of the 3D models were measured using the built-in measurement tools of Amira. Some of them were used directly for the scaling analysis whereas others were used to calculate more complicated variables that describe the vestibular system anatomy, such as the length and width of the semi-circular canals, the ampullae surface area and the canal orientations. External head width, length and height were measured for each individual (*Figures 2&3*).

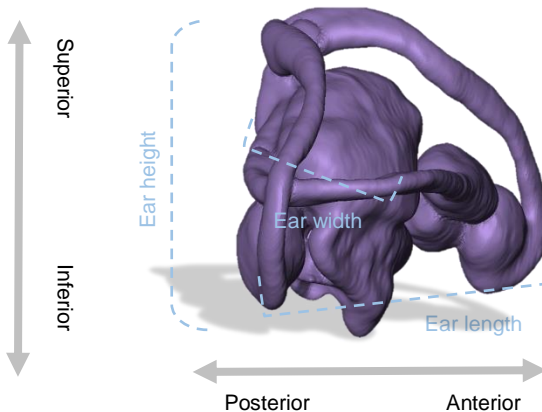


Figure 2. 3D model of the vestibular system of the lizard species *Iberolacerta monticola* and indication of the ear width, length and height.

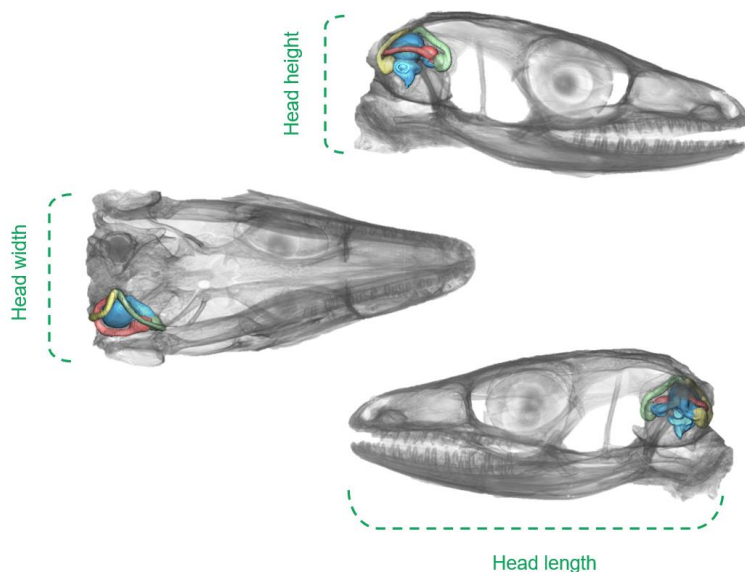


Figure 3. Shadow image of a *Takydromus sexlineatus* head from a dorsal and two lateral views and indication of the overall size measurements of the head. The 3D model of the vestibular system is illustrated in color.

Results

3D model of the vestibular system

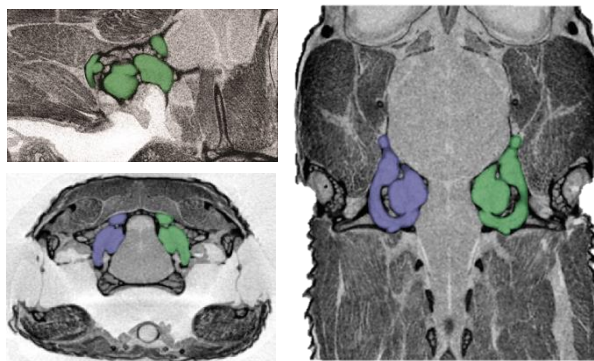


Figure 4. Sagittal (top left), transversal (bottom left) and frontal (right) slices of an *Ichnotropis capensis* head. The vestibular systems are highlighted in purple and green.

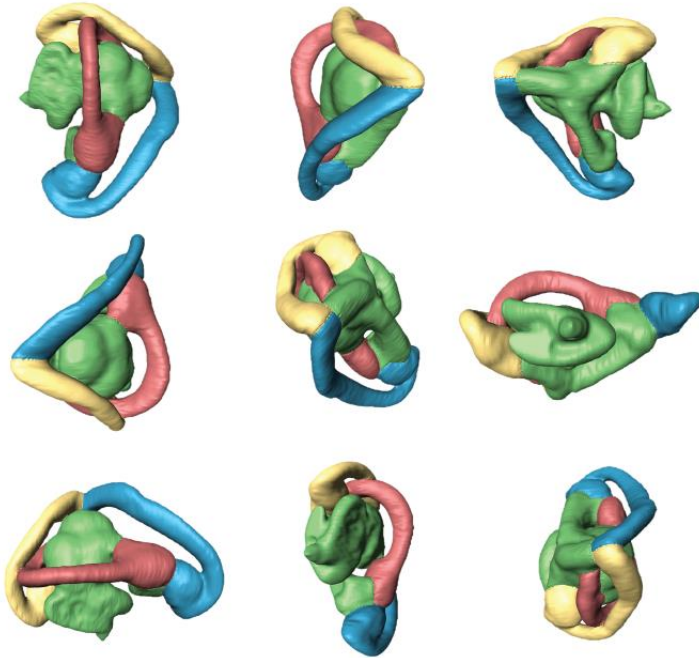


Figure 5. 3D model of the vestibular system of the species *Pediplanis lineocellata* from different views. The different colors represent the three semi-circular canals and their ampullae: anterior (blue), posterior (yellow) and lateral (pink) semi-circular canal.

Segmentation of the images acquired from the scanning procedure (*Figure 4*) gave us the 3D models of the 24 inner ears. *Figure 5* illustrates an example of those results. The bony labyrinth of the inner ear contains a series of interconnecting ducts and sacs, known as the membranous labyrinth. These ducts form three semicircular canals: the anterior, posterior and lateral canal, which can be easily distinguished when looking at the 3D models of the bony labyrinth.

Scaling:

The inter- specific scaling analysis showed a negative allometric relationship between head size of the individuals and most of the inner ear anatomical characteristics. Hence, larger species appear to have disproportionally smaller vestibular system's traits for their given size. However, some of the traits appear to change isometrically with head size.

Conclusion

Using the 3D models acquired from the micro CT scanning, we were able to compare the morphology of the inner ear between the species of our interest. The scaling analysis results suggest that there is a constraint in size for the inner ear which could lead to the assumption that bigger animals do not need an inner ear proportionally as large as their size in order to perform as well as smaller animals. Moreover we could suggest that having a non-proportionally bigger inner ear for a given size is morphogenetically less costly, leaving enough free space in the cranial cavity for the other structures.

Further research on the variability between species but also including phylogeny in our analysis could give us more information on the function of the vestibular system and its variation among species.

Finally, the 3D models and their measurements will be combined with the lizards different ecologies so that we can discover if there is a connection between habitat use, balance maintenance and inner ear morphology.

References:

1. Billet G., Hautier L., Lebrun R., "Morphological diversity of the bony labyrinth (inner ear) in extant xenathrans and its relation to phylogeny" *Journal of Mammalogy*, 658-672, 2015
2. Boistel R., Herrel A., Lebrun R., et al., "Shake rattle and roll: The bony labyrinth and aerial descent in squamates" *Integrative and Comparative Biology*, 957-968, 2011
3. Pfaff C., Martin and Ruf I., "Bony labyrinth morphometry indicates adaptations in the squirrel related clade (Rodentia, Mammalia)" *Proceedings B*, 282:20150744, 2015
4. Perier A., Lebrun R., and Marivaux L., "Different level of intraspecific variation of the bony labyrinth morphology in slow- versus fast- moving primates", *Journal of Mammalian Evolution*, 353-368, 2016
5. Spoor F., Garland T., Krovitz G., et al. "The primate semicircular canal system locomotion", 10808-10812, 2007
6. Vanhooydonck B., Van Damme R., "Evolutionary relationships between body shape and habitat use in lacertid lizards" *Evolutionary Ecology Research*, 785-805, 1999

Micro-CT application within Automotive R&D: Optimising Metal Weld joints in automotive sensors

G. Deering¹, J. Wasson²

^{1,2}Sensata Technologies, Unit 11 Technology Park, Antrim, Northern Ireland (U.K.)

Aims

Sensata Technologies is a world leader in pressure sensing technology. One of the key industries in which Sensata operates is the Automotive industry, supplying sensors to all of the household name OEMs. As sensors become more and more integral in the operation of vehicles it is the duty of suppliers like Sensata to ensure these products are designed to last the lifetime of the car and beyond.

Micro-Computed Tomography has been introduced in Sensata as an analysis method to aid research and development and to provide a method of non-destructive failure analysis. The technology is currently being used in the following applications: assessing injection moulded plastics, identifying failed electrical components; assessing adhesives and many others.

This paper discusses the use of Micro-CT to optimize a metal laser-welded joint (figure 1) between a connector and lead-frame of a sensor located in the engine of an internal combustion vehicle. The optimisation of this joint is an iterative process. Traditionally it would have been necessary to assess a number of sensors at each iteration of the weld settings by conventional metallography and microscopy techniques, requiring extensive man-hours of technicians and design engineers. The introduction of micro-CT analysis allowed the development time to be cut significantly by giving design engineers feedback on weld joints within 24 hours rather than several days or weeks. The non-destructive nature of micro-CT also means the parts are usable for testing after the weld joint has been analysed.



Figure 1. Weld joints between connectors and lead frame

Method

Laser spot welding of metal components is a topic which is covered in literature (Yilbas and Kar, 1997), (Tao et al., 2008). The literature gives a great understanding of the welding process but for the specific purpose of laser spot welding the sensor components it was necessary to perform an iterative trial-and-error development process. Initial laser weld settings for the optimization were established based upon visual inspection of several of the preliminary iterations. Criteria was set out for what would constitute an acceptable laser weld. The criteria was as follows:

- Good melt must be achieved on lead frame and connector, resulting in both components being joined.
- Over-melting resulting in a hole through the spot weld location is not acceptable
- Voids should be kept to a minimum to ensure long-term weld integrity.
- A high level of sample to sample consistency must be observed

Results

Figure 2 (previous pg): Sample from each iteration of laser spot weld optimization. A) Initial laser weld settings caused too high melt on one joint causing melt through material. B) Inconsistency of weld joints, one shows good weld with some voiding, others haven't melted enough. C) Poor melt resulting in poor joint. D) Better melt but inconsistent over four joints resulting in some poor joints. E) Good melt in all four joints, consistent but void is large and potentially problematic. F) Good consistency of melt over four joints, void is still larger than preferred. G) Good consistency of welds, good melt, voids are still present but at a more acceptable level.

Three samples were welded, scanned and analysed at each iteration of weld optimisation. The images shown in figure 2 are screenshots from one sample of each iteration of laser weld optimisation. The first iteration of welded parts showed poor weld consistency within single parts and across the three samples. The sample to sample consistency improved vastly over the optimization process and the welds within each sample also showed a significant improvement in consistency as well as weld quality.

Conclusion

The implementation of micro-CT analysis to assess laser spot weld quality meant the time to complete a weld optimisation was more than halved and the man-hours required to complete the process improvement was reduced by over 75%.

Automation of the micro- CT scanning process allowed for utilisation of down time such as evenings and weekends without the need for an operator. The use of an auto-changer carousel on the Bruker Skyscan1275 meant that for each iteration of the process optimisation, all 3 samples could be set up for scanning at once and left to complete. The use of batch reconstruction also meant that all parts could be reconstructed consecutively without the operator needing to be present.

The design engineers involved in the project were able to use the results of this optimisation to act as a base for subsequent validation. As a result of the success of this project, micro-CT scanning is being adopted by more designers as a key analysis method used during design verification and product validation.

References:

- Tao, W., Li, L., Chen, Y. and Wu, L. (2008). Joint strength and failure mechanism of laser spot weld of mild steel sheets under lap shear loading. *Science and Technology of Welding and Joining*, 13(8), pp.754-759.
- Yilbas, B. and Kar, A. (1997). Laser spot welding and efficiency consideration. *Journal of Materials Engineering and Performance*, 6(6), pp.766-770.

First steps in morphological analysis of the of the reproductive system of *Doto pinnatifida* (Montagu, 1804)

M. Candás¹, G. Díaz-Agras¹, V. Urgorri^{1,2}

¹Estación de Biología Mariña da Graña-Universidade de Santiago de Compostela, Rúa da Ribeira 1-4, E-15590 A Graña, Ferrol, Spain,

²Department of Zoology, University of Santiago de Compostela, Santiago de Compostela, Spain.

Aims

The genus *Doto* Oken, 1815 (Mollusca, Opisthobranchia) is currently composed by 90 species (Bouchet & Gofas, 2017). The differentiation between species is mainly made according to external characters (coloration, number and shape of cerata, shape of the rhinophoral sheath) (Ortea & Urgorri, 1978).

Opisthobranchia are hermafrodite, and the anatomy of its reproductive system is an important feature used to distinguish among species (Thompson, 1976). It is usually studied through techniques of classical histology, although in the last years some authors (Candás *et al.*, 2016; Moles, 2016) have already made an approach to its study through micro-computed tomography (micro-CT).

The aim of this work is to make a comparative study of the anatomy of the reproductive system of *Doto pinnatifida* (Montagu, 1804) through the use of micro-CT, in order to establish if there are any morphological features that could be considered as intraspecific differences. Moreover, morphometric parameters were calculated to determine if there is a relation between the size of the animal and the development of the reproductive system.

Method

Specimens with lengths between 0.60 and 10 mm were studied. After being collected, they were kept in 70° ethanol. Subsequently, they were dehydrated in consecutive ethanol baths (80°, 90° and 96°) and stained with 1% iodine in 96° ethanol for three days. They were then washed with 96° ethanol, dried with hexamethyldisilazane (HMDS) for 2 hours and left to dry overnight (Alba Tercedor & Tocino, 2011; Faulwetter *et al.*, 2013; Candás *et al.*, 2016).

Scannings were performed with a Skyscan 1172 system using the following parameters: 55 kv, 165 µA, and no filter was used. Samples were rotated 360°. The X-ray projection images obtained during scanning were reconstructed with the software NRecon. The sections obtained were processed with the softwares CTAn and DataViewer. 3D representations were obtained with the softwares CTVox and Amira 5.3.3. Morphometric parameters (specimen length, vas deferens length, ampulla length, ampulla maximum width, genital atrium-bursa copulatrix distance, bursa copulatrix diameter) were calculated with DataViewer and Amira 5.3.3.

Results

The reproductive system of *Doto pinnatifida* is located in the anterior part of the animal. It can be distinguished three parts: masculine, feminine, and a third part formed by the ovotestis and the ampulla. The masculine part is composed by a vas deferens (which widens forming the prostate) and a penis, which opens in the genital atrium anteriorly to the vagina (fig. 1).

The feminine part consists in an oviduct which opens into receptaculum seminis; this latter leads distally into the vagina. There is also a bursa copulatrix and several glands (responsible for adding protective and nutritive layers to the egg-masses), which end in the atrium (fig. 1).

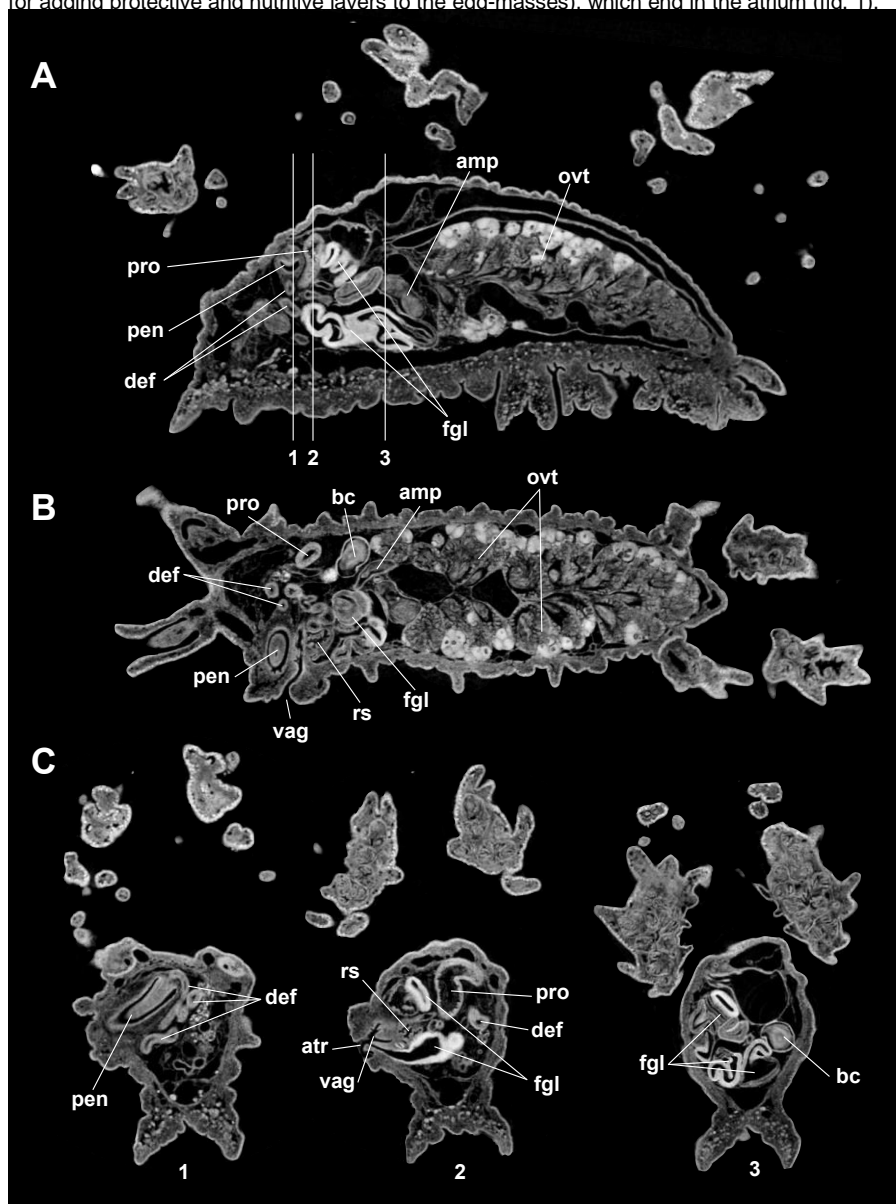


Figure 1: *Doto pinnatifida*, adult (4.08 mm length). A: 2D sagittal section; B: 2D frontal section; C: 2D transverse sections. Abbreviations: amp: ampulla; atr: genital atrium; bc: bursa copulatrix; def: vas deferens; fgl: feminine gland; ovt: ovotestis; pen: penis; pro: prostate; rs: receptaculum seminis; vag: vagina.

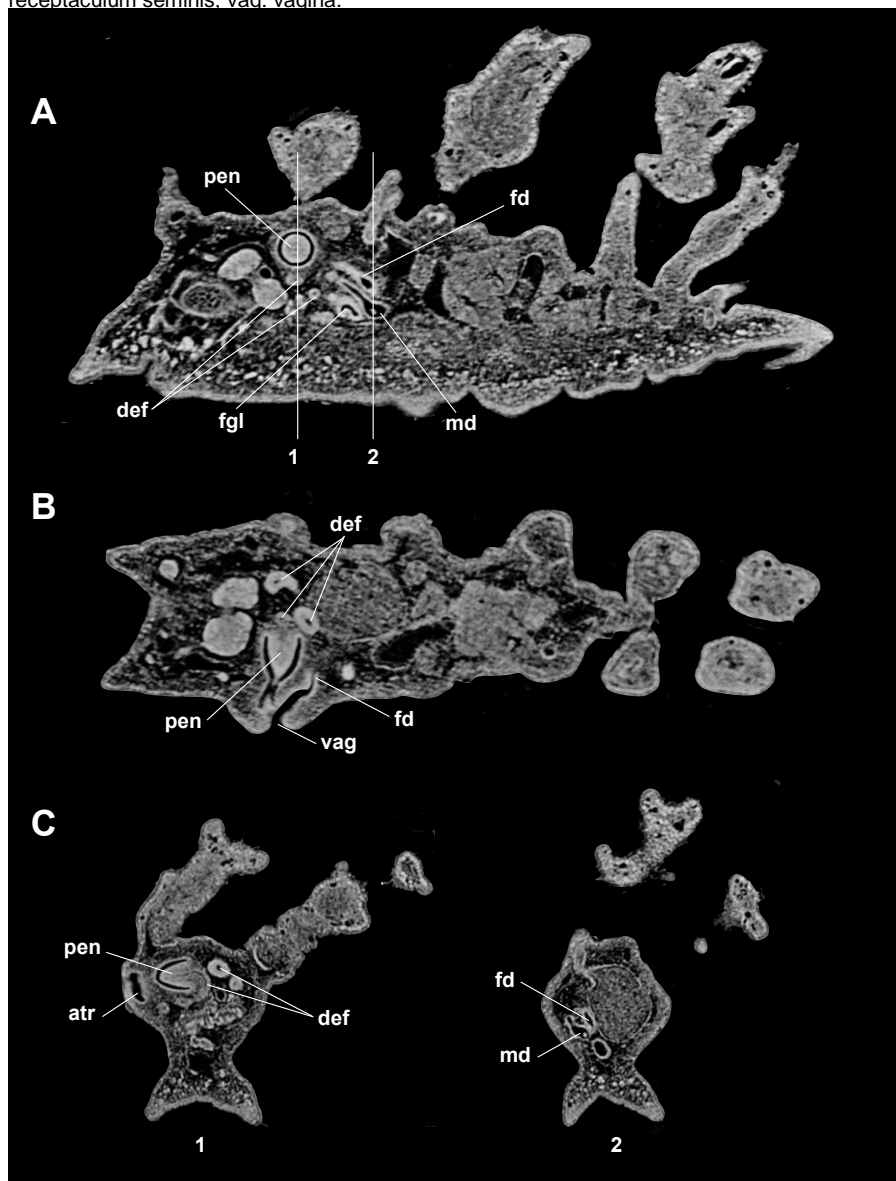


Figure 2: *Doto pinnatifida*, juvenile (1.43 mm). A: 2D sagittal section; B: 2D frontal section; C: 2D transverse sections. Abbreviations: atr: genital atrium; def: vas deferens; fgl: feminine gland; fd: feminine duct; md: masculine duct; pen: penis; vag: vagina.

The third part comprises an ampulla connected with the ovotestis. The ampulla is also connected to masculine and feminine parts through gonoduct.

The reproductive system can be readily observed in 2D and 3D images in the studied specimens. All the features are easily developed in those animals equal or larger than 1.43 mm. In the smaller ones, structures like the penis or the bursa copulatrix are not completely formed, and others like prostate are hardly seen.

The measurements of the linear structures (that is, bursa copulatrix and ampulla) are measured in 2D sections (transverse, frontal and sagittal) by DataViewer. However, it is impossible to measure the length of ducts with this software; for this purpose we use the software Amira.

It is observed that bursa copulatrix and ampulla are located in the right part of the animal in adults. However, there are not such structures in individuals equal or smaller than 1.43 mm length (fig. 2); the ends of the feminine and masculine ducts are found in the left side of the animal, next to the feminine glands (fig. 2C).

Penis is observed in specimens equal or longer than 1.12 mm length.

Feminine and hermaphrodite parts are not distinguished in animals shorter than 0.70 mm. It is only observed a short duct that opens to the outside; because of its wall thickness, this duct should be a rudimentary vas deferens.

According to the results obtained, we can conclude that *D. pinnatifida* reaches its sexual maturity from aprox. 1.4 mm individual length.

Conclusion

This study shows the development of the reproductive system of the nudibranch *D. pinnatifida* from juvenile stages to adults, by means of micro-computed tomography. We can conclude that there is a general trend, the larger the animal the larger the structures measured. Moreover, we have not observed any intraspecific differences.

All the features are easily developed in those animals equal or larger than 1.43 mm. In the smaller ones, structures like the penis or the bursa copulatrix are not completely formed, and others like prostate are hardly seen.

The images of the sections obtained are of high quality. The level of detail achieved with this technique is good, when comparing them with histological sections. The use of the micro-CT in the study of the internal anatomy of *Doto* species has been previously tested, also with great results (Candás *et al.*, 2014; Moles *et al.*, 2016).

Micro-CT results in a great tool for this kind of research. It allows us to study a big number of samples in a relatively short period of time, comparing with classical histology. Besides, we can obtain sections in three planes (transverse, frontal and sagittal) from one sample, which is impossible by histological techniques. It also allows measuring some structures quite easy.

Furthermore, we can use the obtained sections in other reconstruction softwares like Amira. Micro-CT sections have the advantage that they are already aligned (alignment must be performed manually in classical histology); this means reducing time and labour. Unfortunately, DataViewer does not allow us to measure the length of ducts; this problem is solved by measuring them in the Amira 3D reconstructions.

References:

1. Alba-Tercedor J, Sánchez-Tocino L, "The use of the SkyScan 1172 high-resolution micro-CT to elucidate if the spicules of the sea slugs (Mollusca: Nudibranchia, Opisthobranchia) have a structural or a defensive function", SkyScan Users Meeting 2011, 113- 121, 2011.

2. Bouchet P, Gofas S, “*Doto* Oken, 1815”, In: MolluscaBase (2017). Accessed through: World Register of Marine Species at <http://www.marinespecies.org/aphia.php?p=taxdetails&id=137916> on 2017-03-16, 2017.
3. Candás M, Díaz-Agras G, Urgorri V, “The use of micro-CT for the study of the internal anatomy of sea slugs (Opisthobranchia, Nudibranchia, Dotidae)”, SkyScan Users Meeting 2014, 241- 243, 2014.
4. Candás M, Díaz-Agras G, Abad M, Barrio L, Cunha X, Pedrouzo L, Señarís MP, Tato R, García-Álvarez Ó, Urgorri V, “Application of microCT in the study of the anatomy of small marine molluscs”, Microscopy and Analysis, 30(2), S8- S11, 2016.
5. Faulwetter S, Dailianis T, Vasileiadou A, Arvanitidis C, “Contrast enhancing techniques for the application of micro-CT in marine biodiversity studies”, Microscopy and Analysis, 27(2): S4-S7, 2013.
6. Moles J, Wägele H, Ballesteros M, Pujals Á, Uhl G, Ávila C, “The end of the cold loneliness: 3D comparison between *Doto antarctica* and a new sympatric species of *Doto* (Heterobranchia: Nudibranchia)”, PlosOne, 11(7): e0157941, 2016.
7. Ortea JA, Urgorri V, “El género *Doto* Oken, 1815 en el Norte y Noroeste de España”, Boletín de la Estación Central de Ecología, ICONA, 7(14): 73-92, 1978.
8. Thompson, TE, “Biology of opisthobranch molluscs. Volume 1”, The Ray Society, London, 207 pp, 1976.

Time Effective Reservoir Properties Estimation by Digital Rock Physics Protocols

C.A. Santos¹, P.R. Fernández¹, J. Bautista²

¹Repsol Technology Center, Madrid, Spain.

²EXA. CA, USA.

Aims

Reservoir rock properties estimation using digital analysis tools exhibits several advantages compared with its experimental counterpart [1, 2, 3]. Some of this technology benefits include better time to deliver solutions, better sample statistics and new properties estimations not achievable with conventional laboratory protocols. In this work a real industrial case is presented and these benefits were explored and verified by reducing time to deliver outputs more than 80%, producing a more representative dataset by increasing between 6 and 20 times the amount of reservoir properties data points and by gaining a deeper insight on rock types by the interpretation of X-Ray interactions with rock samples.

Method

To obtain an initial picture of samples quality and current state, a pre-screening process was conducted by radiographic exploration of all samples, in this case a 20 samples batch from a single well. During this very fast procedure attenuation (transmission) data was recorded and statistical cummulants were calculated in all images. Energy, exposure time, filters and source-object-camera distances were kept constant in order to isolate the effect of material attenuation for comparison analysis in the complete dataset. With the fixed acquisition parameters configuration, recorded attenuation will be mainly associated to the material properties density and atomic number [4] which are also inherently related with porosity and mineral composition. In order to exploit these relationships a cluster analysis was performed on the attenuation statistics to obtain rock types for reservoir heterogeneity understanding and for representative samples selection to apply advanced numerical simulation protocols.

Rock typing sensitivity was verified by reservoir engineers using well log data. However, an energy dispersion curve per rock type experiment was designed to establish a definitive correlation between rock types and energy transmission through the sample material. For this experiment three rock types were selected and all acquisition parameters were fixed but source energy. An attenuation statistics vs energy curve was obtained per rock type and the results showed characteristic behaviors. A more detailed analysis of these phenomena is going to be presented somewhere else.

A full tomographic campaign was conducted in the complete batch at 2um resolution in sub-plugs of 2-3mm radii. Sub-plugs were taken from sample end-trims so most of the samples could be returned to the reservoir manager for further analysis in just a few days after reception. Image reconstruction, processing and segmentation were performed to obtain a binary image for solid and porous phase. This workflow details were already presented in [5]. The segmented pore space was then subjected to a connectivity analysis to assure that all the represented pore space to use in numerical simulation was connected and contributing to effective flow inside the digitized model.

As a starting point for reservoir property estimation, percolation model from Winland [6] was applied to the structure separation output from 3D Analysis. This output is constituted by the pore size distribution in the segmented pore space. Even when this morphometric approach could lead to inaccurate final values, it will certainly be of aid in the qualitative analysis of flow zones in the area of study. After this initial Reservoir Quality Index (RQI) approximation a new cluster analysis verified the strong relationship between X-Ray transmission and rock types as the new groups obtained by porosity/permeability data strongly agreed with previous groups obtained by x-ray attenuation.

Absolute permeability and relative permeability curves were obtained using Exa DigitalROCK technology due to its extensive O&G benchmarking. The solver is based on the Lattice Boltzmann method (LBM). Single fluid phase simulations are run to obtain absolute permeability, an inherent rock property exclusively dependent on the pore space geometry. The flow simulation results provide the Darcy velocity and pressure drop through the rock sample, from which the absolute permeability is computed. The same analysis is applied to sub-domains of the overall simulation domain. For example, the full domain can be divided into octants as shown in figure 1. Individual porosity and permeability values are reported for each one of the sub-domains. This provides a porosity-permeability relation for the simulated rock type, which is very useful information for static reservoir modeling and well-log interpretation.

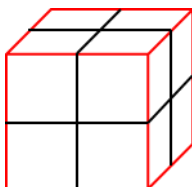


Figure 1: Initial cubic image domain (red) and octants subdomain for multipoint simulations (black lines)

The relative permeabilities of oil and water were obtained from multi-phase flow simulation. Parameters relevant to the physical system, including viscosity, interfacial tension, flowrate, wettability and, initial fluid distribution are user specified inputs to the simulation. Based on the specified wettability, each surface element is assigned a contact angle between 0° and 180° . The simulation method evolves the system from connate water to residual oil while calculating water and oil relative permeability at multiple saturations. There are many advantages of these simulations compared to traditional lab experiments. Laboratory tests can take months whereas simulations can be done in days. Precise control of the fluid-rock system parameters in simulation enables sensitivity studies that are not either cost or time effective in the laboratory. Finally, other rock sources besides whole core like sidewall cores, cuttings, etc. can be used, providing a significant amount of data not previously available for reservoir modelers.

Results

The pre-screening radiographic protocol is a very fast process to obtain X-Ray information from the samples. An area of interest was selected inside the material projection in order to exclude the air area as can be seen in figure 2. The size and characteristics of this area were kept constant in all radiographs.

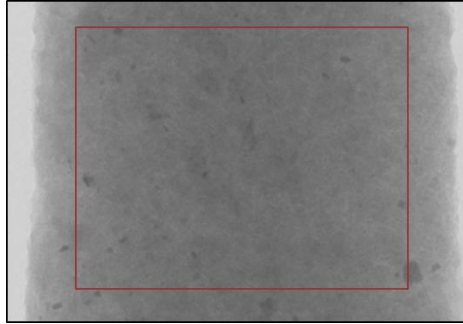


Figure 2: 3mm diameter subplug radiograph and selected area of interest (red square) for attenuation statistics calculation

As previously stated, the attenuation statistics lead to an initial rock typing for reservoir heterogeneity understanding. Figures 3 and 4 contain the performed cluster analysis and the depth correlation of the 3 main rock types found respectively.

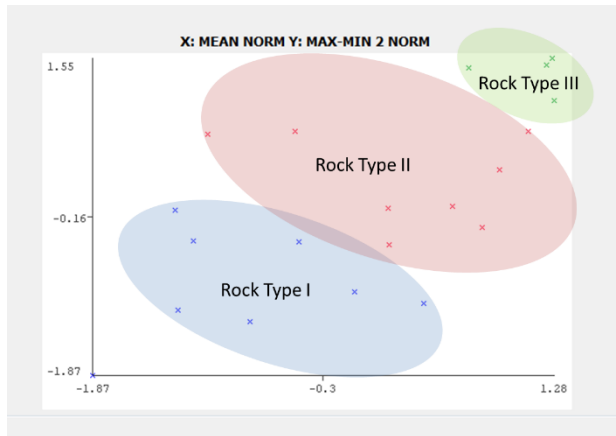


Figure 3: Cluster analysis for rock typing based on X-Ray attenuation statistics.

Vertical distribution of rock types suggested an important lithological change at depth N (see figure 4). Actual depth for the samples is not shown because data confidentiality, however usually it has values around the several thousand feet. This fact allowed characterizing two main reservoir groups the “top” and the “bottom” portion which very likely will exhibit dissimilar reservoir performance. This top and bottom limit “N” and the reservoir performance differences were later confirmed by reservoir engineers using well logs and laboratory data.

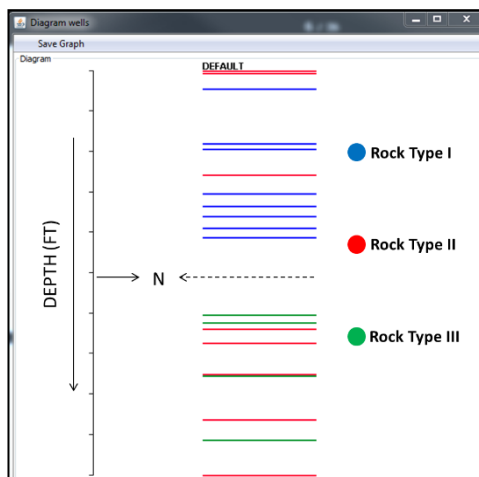


Figure 4: Depth profile for rock types distribution. An important lithological change can be expected at depth N.

This categorical discrimination using X-Ray attenuation was verified by obtaining distinctive energy dispersion curves for the 3 rock types as can be seen in figure 5. The objective for this procedure was to observe important differences in X-Ray attenuation behavior for the 3 identified rock types.

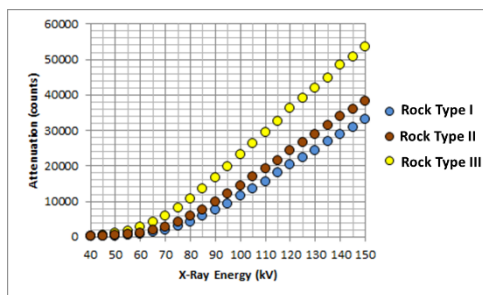


Figure 5: Attenuation vs Energy curves for 3 different rock types.

As already stated after the radiographic pre-screening a complete tomographic scanning campaign was conducted to obtain a detailed pore space 3D model. Typical scanning times were around 4-6 hours and reconstruction, image processing and 3D analysis took around 1 hour per sample. These time frames translated into a 2-3 sample rate per day which allowed the scanning of the complete batch in less than 2 weeks.

In order to obtain really fast reservoir properties estimation, the morphometric approach for permeability was performed. It is based on the cumulative pore size distribution and some critical controlling pore radii [7]. This procedure can be performed in minutes after the 3D

analysis is finished. This output even when not perfectly accurate is precise enough to obtain a first picture of relative reservoir properties distribution in the vertical profile. The initial porosity-permeability trend is showed in figure 6.

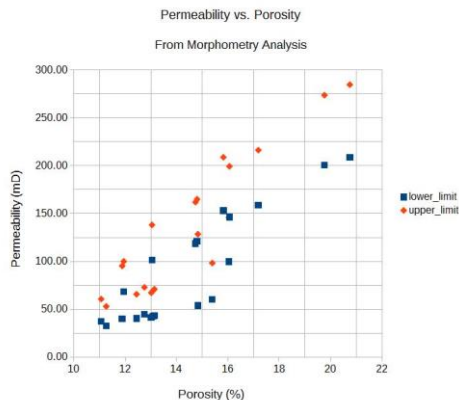


Figure 6: Morphometric permeability estimation vs. porosity trend in the studied well.

This early information can help reservoir managers to get an impression about rock quality distributions and how the “good” and the “bad” performers are scattered in the well. More accurate information either from conventional lab analysis or numerical simulation can be delivered later to fine tune specific reservoir properties values. In this study, we used the LBM tool to obtain more accurate absolute permeability information. Laboratory tests and regional data later confirmed the accuracy of the numerically obtained outputs. In figure 7 a comparison between the morphometric and LBM obtained permeability showed a very strong correlation between these two values. Due to the power law nature of the percolation model a logarithmic difference is inherited, estimated morphometric values can give an order of magnitude discrepancies. However morphometric values can be an excellent indicator of better performance levels and with a good database the values can be calibrated to specific geographical areas.

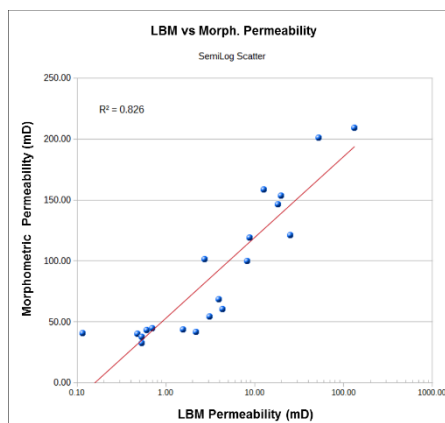


Figure 7: LBM vs. Morphometric permeability semilog scatterplot. A strong correlation ($R^2=0,826$) was observed.

In order to obtain subdomain data and relative permeability curves the segmented datasets were uploaded in HPC systems to run the EXA DigitalROCK software suite. The initial run for the complete 20 sample batch were ran in around 10 days. It comprised representative elementary volume analysis, mercury intrusion simulation and absolute permeability and porosity for the complete domain and several subdomains (25+ points per sample). One of the typical outputs from the LBM monophasic algorithm can be seen in figure 8.

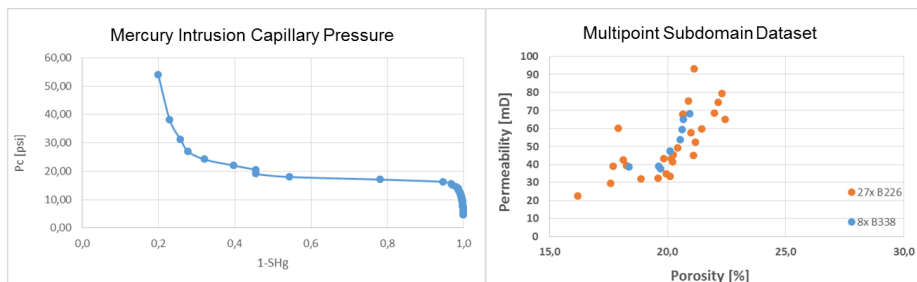


Figure 8: (Left) Simulated capillary pressure curve. (Right) Poro-Perm scatter plot for several subdomains, 8 points for 338 voxel cubes in blue and 27 for 226 voxel cubes in orange.

Based on the previous rock type categorization 5 samples were chosen for partial relative permeability curves (end-points) and 3 for full relative permeability curves. This second multiphase run took around 13 days to be completed. It is important to remember that using the same resources in our reservoir lab, the same properties calculation using our experimental facilities would take around 5 months to be finished. This early information helped to make more educated decisions for the reservoir team in certainly less time. In figure 9 the typical outputs for this second run are presented.

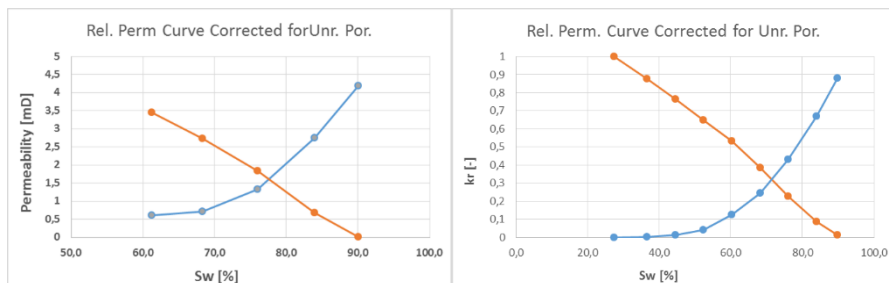


Figure 9: (Left) End points multiphase numerical simulation. (Right) Numerical simulated full relative permeability.

Conclusion

Based on X-ray radiographic attenuation data, significant rock type categorization can be made. Morphometric based permeability estimation showed promising outputs for very fast absolute permeability estimation even when not fully accurate now. LBM provided very reliable information for mercury intrusion simulated curves, poro-perm trends and relative permeability in a fraction of the time required by its experimental counterpart. By the subdomain approach the porosity-permeability trends were more populated getting more than 25 points per sample, allowing very good uncertainty description for the limited sample batch. These trends were lately matched with regional information with excellent results. Digital rock analysis was successfully applied in this project and promises important improvements in time, cost and representativeness in reservoir characterization efforts.

References:

1. Andra et al, "Digital rock physics benchmarks—part II: Computing effective properties" *Computers & Geosciences*, 33-43, 2003.
2. Dvorkin et al., "Relevance of computational rock physics", *Geophysics*, 76, pp. E141–E153, 2011.
3. Ravlo, et al, "Using digital rock technology for multiscale reservoir characterization" *Gulf Coast Association of Geological Societies Transactions*, v. 66, p. 859–863, 2016.
4. Als-Nielsen & McMorrow, "Elements of Modern X-ray Physics", 2nd Edition, Wiley, 2011.
5. Santos et al, "Reservoir Performance Evaluation by Cost Effective Digital Petrophysics Workflows", *Bruker Micro CT memoirs*, 2016
6. Kolodzie, S., "Analysis of Pore Throat Size and Use of the Waxman-Smits Equation to Determine OOIP in Spindle Field, Colorado", *SPE Paper 9382*. 1980.
7. Pittman, E.D., "Relationship of Porosity and Permeability to Various Parameters Derived from Mercury Injection-Capillary Pressure Curves for Sandstone" *Bull. American Association of Petroleum Geologists*, 76, 191-198. 1992.

Longitudinal *in vivo* analysis of nanostructured hydroxyapatite-functionalized gelatins osteoinductive properties in relation to endogenous or human mesenchymal stromal cells

A. Parrilli¹, E. Della Bella^{2,3}, A. Bigi⁴, S. Panzavolta⁴, S. Amadori⁴, M.Fini².

¹BITTA Laboratory, Rizzoli RIT Department, Rizzoli Orthopaedic Institute, via di Barbiano 1/10, 40136, Bologna, Italy,

²Laboratory of Preclinical and Surgical Studies, Rizzoli Orthopaedic Institute, via di Barbiano 1/10, 40136, Bologna, Italy

³Department of Medical and Surgical Sciences, University of Bologna, via G. Massarenti 9, 40138, Bologna, Italy

⁴Department of Chemistry "G. Ciamician", University of Bologna, via Selmi 2, 40126, Bologna, Italy

Aims

Despite the high ability of bone tissue to regenerate itself, there are clinical situations in which using scaffolds becomes necessary (e.g. in cases of large defects caused by trauma, tumors or infection, but also in cases of spinal fusions or implant osteolysis).

Among scaffolds, relevant attention is addressed to gelatin, which is less antigenic than collagen¹ and susceptible to degradation by proteases². To improve the biological and mechanical properties of gelatin we have previously developed biomimetic porous gelatin-nanocrystalline hydroxyapatite (HA) scaffolds with tailored properties³. In the present study, we investigated the osteoinductive properties of these scaffolds (GEL-HA10), compared to scaffolds containing just gelatin (GEL) without the inorganic phase. The osteoinductive ability was studied in a heterotopic model (subcutaneous implant in nude mice). The influence of human mesenchymal stromal cells (hMSCs) within implants was examined as well.

Method

The materials used for scaffolds preparation were Type A gelatin (280 Bloom, Italgelatine SpA, Cuneo, Italy) from pig skin, and hydroxyapatite nanocrystals synthesized in aqueous medium as reported in Panzavolta et.al³. Samples were 5 mm in diameter and 2 mm in thickness (volume ~40 mm³), as shown in Fig.1.

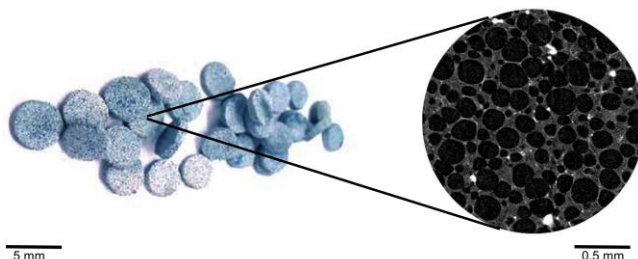


Figure 1: GEL and GEL-HA10 scaffolds and a detail of the porosity of GEL-HA10.

In vivo experimentation was conducted in accordance with the European and Italian Law on animal experimentation. The protocol was approved by the Ethical Committee of the Rizzoli Orthopaedic Institute and authorized by the Italian Ministry of Health.

Twenty-five athymic male mice (Harlan Laboratories Srl, Udine, Italy, aged 6 weeks, 25±5g b.w.) were used for the study. Commercial hMSCs were seeded on materials 24 hours before implantation at a density of 10⁶ cells/implant.

Non-seeded or hMSC-seeded GEL or GEL-HA10 samples were implanted into subcutaneous left and right side pockets formed in the dorsal surface of the mice. Experimental groups included: (1) GEL; (2) GEL + hMSCs; (3) GEL-HA10; (4) GEL-HA10 + hMSCs.

Surgery was performed under general anesthesia and mice were maintained in single cages in a confined room in the postoperative period until complete recovery. Animals were checked daily for evaluation of general clinical conditions. No complications or reactions in the implant sites were registered. At the end of experimental times (8 weeks), mice were euthanized under general anesthesia with i.c. injection of 0.5 ml Tanax (Hoechst Roussel Vet GmbH, Wiesbaden, Germany).

At 0 and 8 weeks the process of ectopic bone formation was monitored by *in vivo* microtomography (Skyscan 1176, Bruker microCT, Kontich, Belgium) applying a source voltage of 50 kV and a source current of 500 uA. The nominal resolution used for images was set at 9 µm (pixel size). The images (2672x4000 pixels) were then reconstructed with NRecon program (version 1.6.8.0, Bruker) to obtain the micro-CT sections (4000x4000 pixels, maintaining the relative pixel size). In addition to the specific alignment, beam hardening and a reduction of ring artifact were used as correction factors in the reconstruction process. The presence of mineralized tissue in the micro-CT sections was analyzed and expressed qualitatively and quantitatively using CTAn (Bruker microCT, Kontich Belgium) after applying a global threshold determined by the differences in pixel grey level between soft and hard tissues. The threshold of the rat vertebrae bone was taken as reference (Fig.2).

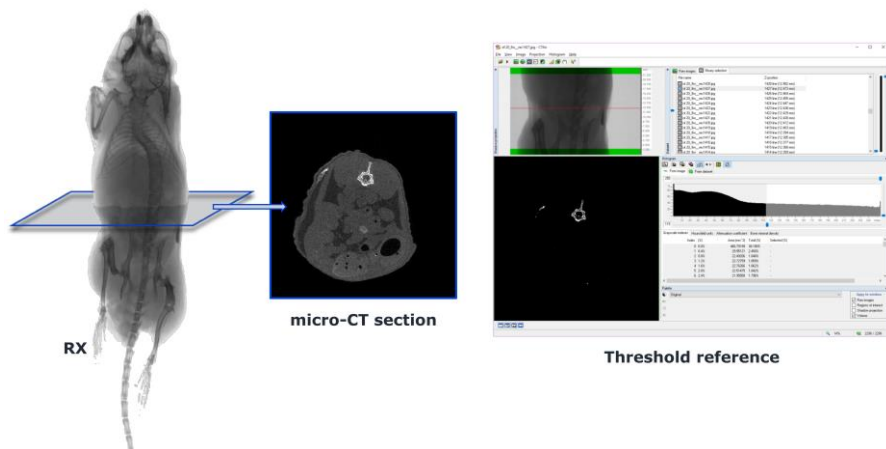


Figure 2: *In-vivo* micro-CT scan, reconstruction and a CTAn screenshot showing the threshold selected according to mouse vertebrae.

After euthanasia, the implants were retrieved and cut into halves. One half of the retrieved implants were fixed in 10% neutral buffered formalin for 24 hours and then decalcified and paraffin embedded. Five micrometer-thick sections were cut transversally and stained with hematoxylin and eosin for histological analysis. The other half of each implant was processed for gene expression analysis.

Relative expression was assessed differentially for the following human or mouse genes: *COL1A1*, *BGLAP*, and *ALPL*, with *GAPDH* as reference.

Statistical analysis was performed using the GraphPad Prism software. A two-way ANOVA with Holm-Sidak multiple comparisons was used to test the differences among samples and conditions. Unpaired t-tests were used to compare the expression of human genes between GEL and GEL-HA10 samples.

Results

The osteoinductive capability of the scaffolds was evaluated by the presence of mineralized tissue in the micro-CT sections. The mineralized areas in the correspondence of the implants presented lighter grey colored pixels (Fig.3). This ectopic bone formation was analyzed and expressed both as proportion (positive cases in total cases) and as volume in mm^3 (Fig.4). At 8 weeks, the results showed that both cell-free GEL and GEL-HA10 samples mineralized. On the other hand, with the presence of hMSC, the mineralized tissue was detected in only one in 10 cases (10%) in GEL samples, while GEL-HA10 continues to have a high percentage of samples with an ectopic bone formation (90%), even though the quantified volume of mineralized tissue was significantly lower than cell-free scaffolds (Fig.4).

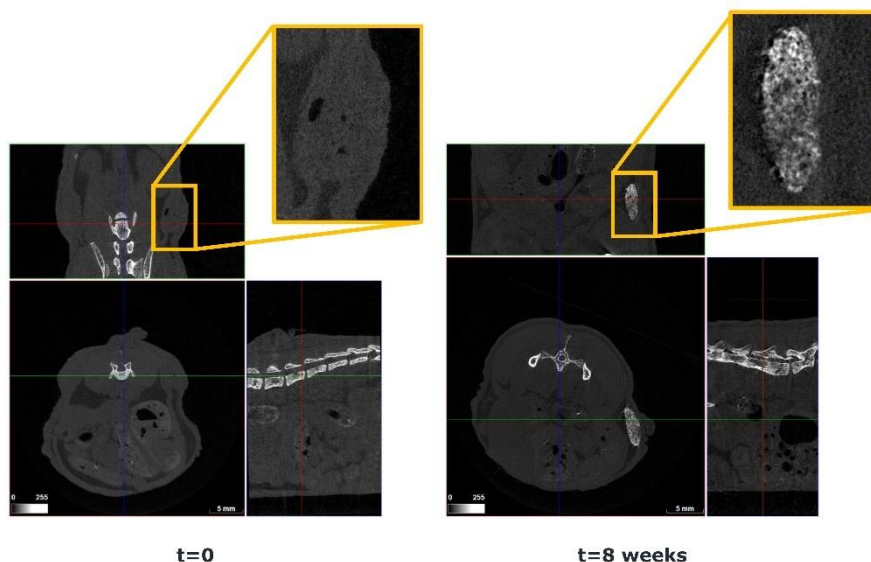


Figure 3: *In-vivo* micro-CT sections of samples with subcutaneous GEL implantation just after the surgery ($t=0$) and after 8 weeks ($t=8$ weeks). In the top yellow panels, detailed pictures corresponding to the implanted scaffolds are shown. At $t=0$ the implants are not yet mineralized while at $t=8$ a lighter grey pixels are detectable.

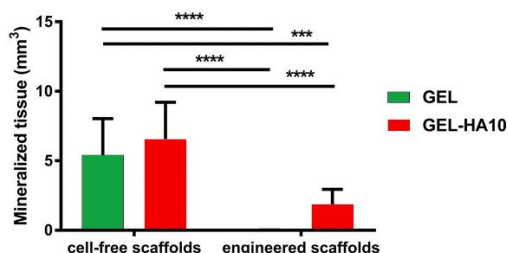


Figure 4: Histogram of the detected mineralized tissue in mm³ (***:p<0.001; ****:p<0.0001)

In positive samples, qPCR analysis showed that the expression of murine bone-specific genes was unvaried between scaffolds, with an upregulation of murine *Col1a1* and *Alp* enhanced by the presence of hMSCs. On the contrary, the different composition of scaffolds resulted in a different pattern of expression of human genes, revealing that the presence of nanocrystalline HA induced the upregulation of bone-specific genes.

In addition, results of Fig.4 showed that in GEL+hMSC samples nearly no mature mineralized tissue was found at 8 weeks, whereas mineralized areas were found in all other groups. The combination of those results (micro-CT and *in vivo* gene expression) suggests that the presence of mineralized tissue in GEL-HA10 could be entirely due to the osteogenic activity of hMSC and the presence of HA.

Conclusion

Both GEL and GEL-HA10 scaffolds mineralized when implanted without hMSCs. On the contrary, the presence of preimplanted hMSC abolished or reduced mineralization of GEL and GEL-HA10 scaffolds. However, we could observe a species-specific response to the presence of HA, which stimulated the osteogenic differentiation of human cells only.

References:

1. Su K, Wang C. Recent advances in the use of gelatin in biomedical research, *Biotechnol Lett*, 37: 2139-2145, 2015
2. Cole B. Gelatin, In *Wiley Encyclopedia of Food Science and Technology* 2nd ed. Francis, F.J, John Wiley & Sons, New York, NY, USA; 1183-1188, 1999
3. Panzavolta S, Torricelli P, Amadori S, Parrilli A, Rubini K, Della Bella E, Fini M, Bigi A. 3D interconnected porous biomimetic scaffolds: In vitro cell response, *J Biomed Mater Res A*, 101: 3560-3570, 2013

Application of X-Ray Computed Tomography Imaging in the Evaluation of Aging Effects of Batteries and Fuel Cell Components

Barbara Satola¹, Maren Rastedt¹, Lidiya Komsiyiska¹, F. Javier Pinar¹, Peter Wagner¹, Alexander Dyck¹

¹NEXT ENERGY · EWE Research Centre for Energy Technology at the University of Oldenburg, Carl-von-Ossietzky-Str. 15, 26129 Oldenburg, Germany,

Aims

The increasing amount of electricity from fluctuating renewable energies in the grid requires the implementation of electrochemical energy storage like batteries and conversion devices like fuel cells in order to enable balance between energy supply and demand. There is a variety of systems available which are differing in composition, application and characteristics. An important property is the requested lifetime from applications which are dependent on aging of single necessary components due to harsh environments and operation conditions. In order to optimize the systems and prolong their lifetimes it is necessary to obtain indications about post-operation defects and corrosion within these units. Bearing in mind that many of the single components of these devices are complex porous materials, consisting of various compartments, knowledge not only about the surface topography but also about the bulk morphology is crucial. Therefore, high resolution computed tomography (CT) can be used to image three-dimensional (3D) structures at the micro- and nanoscale, offering also qualitative information on the material's composition and aging effects. The aim of the present paper is to demonstrate the application of CT in the research field of the electrochemical energy storages and conversion devices by investigation and evaluation of three components and giving valuable information regarding their internal alterations and characteristics.

The membrane electrolyte assembly (**MEA**) is the core component of the fuel cell (FC) that converts chemical into electrical energy and heat. In this work the degradation process of a high temperature polymer electrolyte membrane (HT-PEM) FC is demonstrated by analyzing the influence of contact pressure cycling applied to MEAs. The mechanical changes of the MEA due to different operation strategies between beginning of life and end of test can be detected and visualized by means of microCT investigations [1][2].

The bipolar plate (**BPP**) is an important component for vanadium redox flow batteries (VRFB) as it serves as physical separator and electrical conductor of adjacent cells in a stack. These components are usually carbon based composite materials with complex structure. In the VRFB the BPP can be exposed to acidic media and harsh operational conditions [3]. Thus during battery operation the BPP can undergo significant aging. In order to study the aging propagation within the BPP bulk, pristine and aged graphite-polypropylene composite BPP samples were investigated using microCT.

High resolution nanoCT is also a suitable method for characterization of aging phenomena in cathodes for Li-ion batteries. In general the **cathodes** for the Li-ion battery technologies consist of active materials such as LiCoO_2 , LiFePO_4 , $\text{LiNi}_x\text{Mn}_y\text{Co}_z\text{O}_2$, conductive additives and polymer binders [4]. Due to the difference in the X-ray absorption coefficients of the active materials and the binder-conductive additive matrix it is possible to perform separate analysis of both components with the nanoCT.

Method

1. **MEA:** Two studies on contact pressure cycling of HT-PEM MEA consisting of 5 layers with a nominal active area of 25 cm² were carried out. The first test was performed in-situ within a test station under real FC operation conditions (H₂ and air supply, current density of 0.2 A/cm²). The second test was done in a small ex-situ compression unit that was specially developed to fit into the microCT device and that was used without FC operation mode [1][2]. Three repetitive cycles of compression variations using 0.2, 0.5, 1 and 1.5 MPa have been applied in both systems.

2. **BPP:** Overload charging conditions were executed on a BPP with an active surface area of 1 cm² in an ex-situ electrochemical cell using a current density of 100 mA/cm² for 3 h in the positive VRFB electrolyte consisting of 1.6 M vanadium in 2 M sulfuric acid and a state of charge of 90%.

3. **Cathode:** Commercially available 2 Ah Li-ion batteries in pouch cell format were continuously charged and discharged in climatic chambers at 25 °C within the voltage range 2.8 to 4.0 V at a C-rate of 1 until reaching different states of health (SOH). After the cell disassembly the different cathodes were characterized using high resolution nanoCT.

CT scanning was performed in order to analyze the inner microstructures of the mentioned single components in energy storage and conversion devices. For the investigations high resolution Skyscan 2011 nanoCT and Skyscan 1172 microCT were applied. 3D reconstruction, image processing, visualization and data analysis were performed by means of included software of the micro and nanoCT equipment (NRecon, DataViewer, CTVOX, CTAn, Bruker, Belgium). The scanning parameters are shown in Table 1.

Table 1: Overview of scanning parameters.

Parameter	MEA	BPP	Cathode
Device	microCT	microCT	nanoCT
Source voltage [kV]	78-82	80	80
Optical resolution [μm]	2.50-3.00	1.44	1.00
Rotation step [°]	0.15	0.20	0.18
Averaging frames	4	5	6
Diameter sample size [mm]	6	16	0.75

Results

1. MEA: A cross-sectional image of a MEA compressed with 0.2 MPa serves as ante-mortem reference sample (Figure 13a). After completing three compression cycles in the ex-situ compression device, the mechanical changes can be clearly recognized by many defects and gaps within the catalyst layers (Figure 13b). In comparison, the post-mortem imaging analysis of the MEA, which was treated in-situ in the FC test station, is shown in Figure 13c. Apparently, the result is quite similar to that one gained via ex-situ compression tool. However, here the defect catalyst layers are going through the membrane resulting in short-circuit formation. By comparing these in- and ex-situ post-mortem microCT analyses, it is obvious that the influence of compression cycling is immense while the additional effect of FC conditions is only minor to the mechanical degradation of the MEA [1][2].

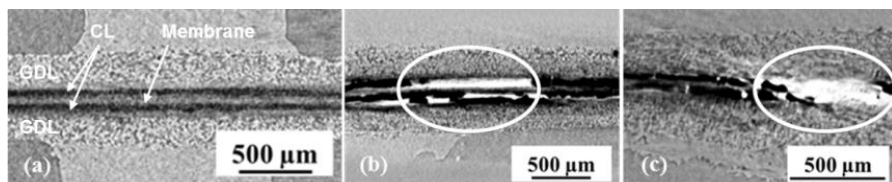


Figure 13: 2D microCT images of MEAs (DataViewer), (a) ex-situ ante-mortem, (b) ex-situ post-mortem and (c) in-situ post-mortem [1]. CL, catalyst layer; GDL, gas diffusion layer.

2. BPP: The 3D image of a pristine BPP shows characteristic features of the composite material. It consists of a homogeneously ordered bulk material with integrated segments of local higher density matter and a rough surface texture (Figure 14a). The overload charging conditions led to a damaged surface with increased open porosity, cracks and material loss drawn through the bulk material due to surface oxidation and subsequent CO_2 evolution [5] (Figure 14b). By means of microCT it is possible to visualize the depth of aging effects and the appearance and formation of corrosion events.

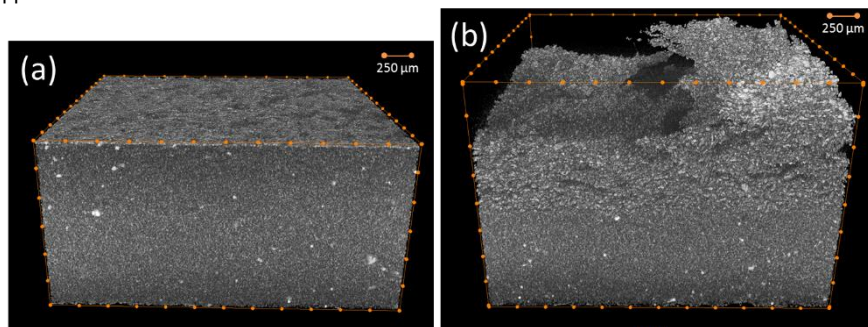


Figure 14: Graphite-polypropylene composite BPP (DataViewer) (a) before and (b) after aging.

3. Cathode: The quantitative evaluation of the nanoCT images shows a decrease in the average particle size and an increase in number of particles of LiCoO_2 with decreasing SOH of the battery (Figure 15). By means of nanoCT technique the active material particle breaking upon aging was suggested as aging mechanism [6].

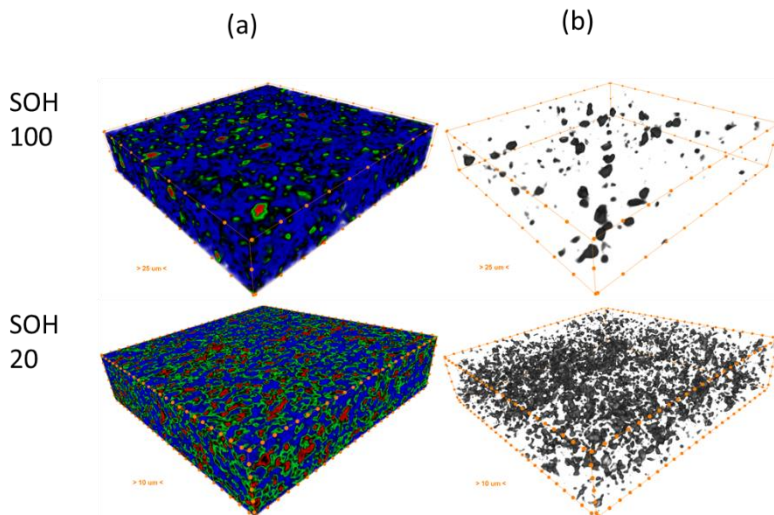


Figure 15: CT images (DataViewer) of (a) LiCoO₂ cathodes with different SOH; (b) Objects with highest densities in the LiCoO₂ cathodes are pointed out [6].

Conclusion

The lifetime of fuel cells and energy storage systems is determined by alteration and corrosion of single system components. In order to investigate such critical influences on integral components one assessment criteria is the comparison of interior morphological structures between ante- and post-mortem specimens. Therefore X-ray micro and nanoCT are powerful and essential tools to analyze their inner texture, characteristics and aging effects. It was shown that CT is applicable to investigate components such as MEAs, BPPs and electrodes from fuel cells and energy storage systems and to give evidence for their aging mechanisms.

References:

- [1] F.J. Pinar, M. Rastedt, N. Pilinski, P. Wagner, "Effect of Compression Cycling on Polybenzimidazole-based High-Temperature Polymer Electrolyte Membrane Fuel Cells", *Fuel Cells*, 140-149, 2015
- [2] M. Rastedt, D. Schonvogel, P. Wagner, "Impact of Load Cycling at High Current Densities on the Degradation Behavior of Membrane-Electrode-Assemblies", *ECS Transactions*, 741-753, 2014
- [3] S. Rudolph, U. Schröder, I. M. Bayanov, G. Pfeiffer, "Corrosion Prevention of Graphite Collector in Vanadium Redox Flow Battery" *Journal of Electroanalytical Chemistry*, 93-98, 2013
- [4] B. Lestriez, "Functions of Polymers in Composite Electrodes of Lithium Ion Batteries", *Comptes Rendus Chimie*, 1341-1350, 2010
- [5] H. Liu, L. Yang, Q. Xu, C. Yan, "Corrosion Behavior of a Bipolar Plate of Carbon-Polythene Composite in a Vanadium Redox Flow Battery", *RSC Advances*, 5928-5932, 2015
- [6] L. Komsijska, S. A. Garnica Barragan, M. Lewerenz, D. Ledwoch, O. Ostera, "Detecting Aging Phenomena in Commercial Cathodes for Li-ion Batteries using High Resolution Computed Tomography", *Advances in Science and Technology*, 158-163, 2014

Acknowledgements

The authors thank the European Commission for supporting this work by the FCH-JU through the project CISTEM (Grant Agreement Number 325262) and the companies Danish Power Systems and Eisenhuth for providing MEAs and BPPs. The main author also kindly acknowledges the Heinrich Böll Stiftung for providing a PhD scholarship.

The use of microcomputed tomography to evaluate the cervical barrier in internal tooth bleaching

Y.T.C. Silva-Sousa¹, M. C. A. Amaral¹, G.B. Leoni¹, I. C. M. Moris¹, D. C. F. Messias¹, J. F. Mazzi-Chaves², M.D.Sousa-Neto²

¹ Faculty of Dentistry, University of Ribeirão Preto UNAERP, Ribeirão Preto - São Paulo, Brazil,

² Department of Restorative Dentistry, Dental School of Ribeirão Preto, University of São Paulo, Brazil

Aims

Nowadays, with the advances of aesthetic dentistry, the demand for patients has been increased in search of treatments that offer a satisfactory smile. The tooth discoloration has been one of the main complaints of patients, especially when it is related to the anterior teeth, because it compromises the aesthetics. Internal or external dental bleaching has been proposed as a first alternative of aesthetic treatment to recover cases of color change (1). For bleaching of endodontically treated teeth, whitening agent is applied inside the pulp chamber over a cervical barrier. The procedure can be performed in up to 4 sessions according to the degree of dental color alteration. The function of the cervical barrier is to promote adequate sealing to minimize and even prevent the diffusion of the bleaching agent through dentinal tubules to the outer root surface, causing an inflammatory reaction, resulting in root and bone resorption (2). Therefore, the materials used for cervical barriers and their position are important factors to avoid these adverse effects and to achieve success. Different methodologies have been used to study intracoronal bleaching, such as: evaluation of optical density and quantification of hydrogen penetration (H₂O₂) by spectrophotometry (3, 4, 5) and evaluation of fracture resistance (6), which are destructive methods and allow only bidimensional analysis. To the best of the authors' knowledge, there is no study of cervical barrier using micro-CT. Thus, the aim of this study was to evaluate, quantitatively and qualitatively, the marginal misfit and porosity of cervical barrier made of different materials after application of the bleaching gel, using microcomputed tomography analysis.

Method

Forty 6 mm-length root sections of bovine maxillary incisors were obtained and each section was apical sealed with gutta-percha. Thus, the samples were distributed into 4 groups (n=10), according to the material used for cervical barrier: Group GI (conventional glass of ionomer cement), Group GIR (glass of ionomer cement reinforced by resin), Group FR (flow resin) and Group MTA (mineral trioxide aggregate). The barriers were placed 2 mm height and the samples were subjected to four applications of 35% hydrogen peroxide for 15 min each. The samples were scanned before and after each bleaching procedure, by using a micro-CT device (SkyScan1176; Bruker-microCT, Kontich, Belgium). The scanner parameters were set at 90 kV, 278 μ A, isotropic resolution of 8.6 μ m, averaging frames of 2, 180° rotation and rotation step of 0.5°, using a 0.1 mm-thick copper filter.

The acquired projection images were reconstructed and co-registered by pairs (preoperative scan and each scan after bleaching agent application) using DataViewer v.1.5.1.2 software. Then, CTAn v.1.14.4.1+ software (Bruker-microCT) was used for the bidimensional (marginal misfit) and three-dimensional (porosity) evaluation of the cervical barrier materials. To bidimensional analysis of the marginal misfit, initially the coronal cross-sections of each sample was salvaged as dataset using DataViewer v.1.5.1.2 software. After that, in the CTAn

v.1.14.4.1+ software, it was selected the middle coronal cross-section and, the lateral and apical misfit was evaluated (μm) by six and three measurements, respectively (Figure 1).

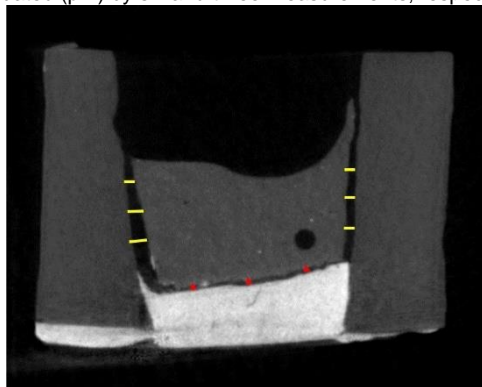


Figure 1. Evaluation of lateral (yellow marks) and apical (red marks) marginal misfit (μm) in CTAn software.

To porosity analysis (three dimensional evaluation), the ROI defined was a round with 2.5 mm of the diameter and 0,5 mm height. The same ROI was used in the analysis of each bleaching session (Figure 2). The threshold was adjusted to each material and then, the 3D porosity analysis (volume and percentage) were done.

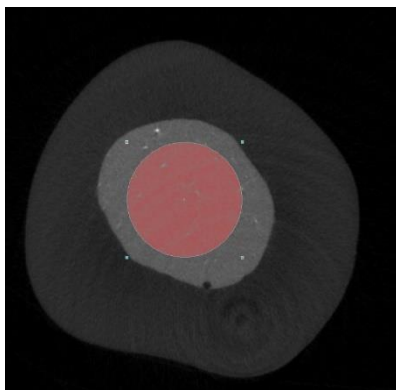


Figure 2. Region of interesting defined to analysis the porosity in CTAn software.

Results

The results of this study for marginal misfit of the cervical barrier showed statistically significant differences among the groups ($p < 0.05$). RF and GI groups presented, respectively, the lowest and the highest values of lateral and apical marginal misfit (Figure 3).

In the intra-group comparison (evaluation of the influence of the bleaching session) of lateral marginal misfit, it was observed that RF and MTA groups did not present statistically significant differences, while, the second session of GIR group was statistically different from initial session. The third and fourth session of GI group were greater than others ($p < 0.05$). For apical marginal misfit, no statistically difference was observed for any group ($p > 0.05$).

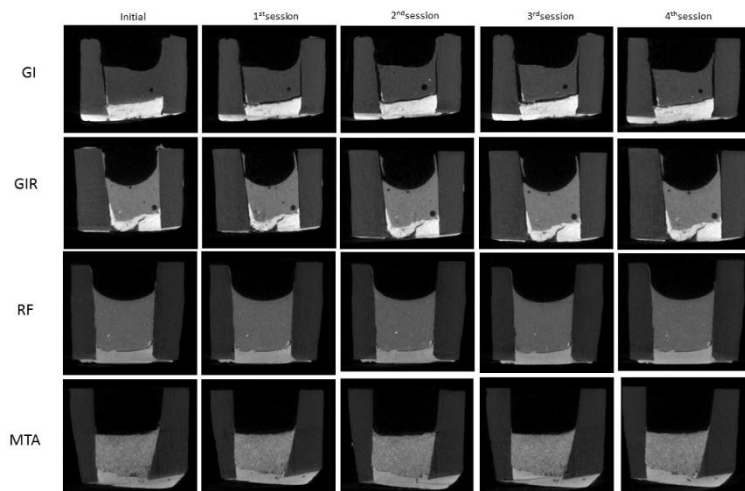


Figure 3. Marginal misfit (μm) in different materials used as cervical barrier.

Regarding the percentage and volume of pores in the different materials used for cervical barrier, statistical difference was observed among groups ($p < 0.05$). RF group presented lowest values to percentage and volume of pores and GIR presented the highest values. When the intra-group comparison was made, there was no statistically significant difference of percentage and volume of pores in any of the groups ($p > 0.05$) (Figure 4).

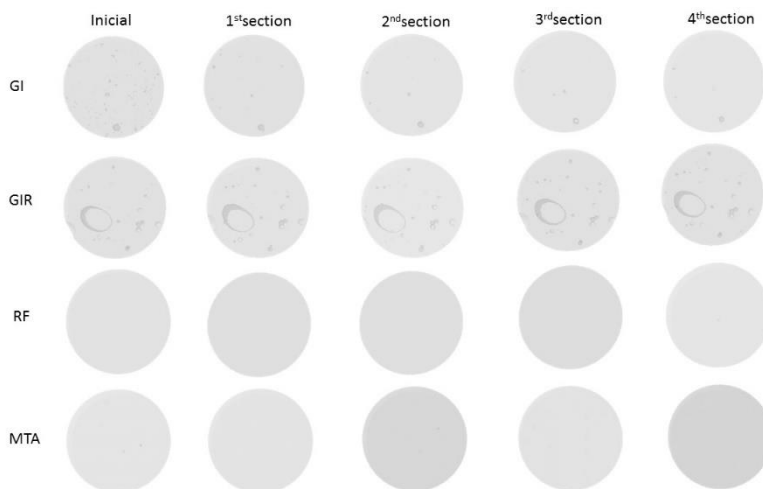


Figure 4. Porosity in different materials used as cervical barrier.

Conclusion

The microcomputed tomography was adequate to characterization and evaluation of the different materials used as cervical barrier, being that the flow resin (RF group) showed the greater marginal misfit and porosity results.

References:

1. Kwon SR, Wertz PW. Review of the mechanism of tooth whitening. *J Esthet Restor Dent.* 240-257, 2015.
2. Vosoughhosseini S, Lotfi M, Shahmoradi K, Saghiri MA, Zand V, Mehdipour M, Ranjesh, Mokhtari H, Salemmilani A, Doosti S. Microleakage comparison of glass-ionomer and white mineral aggregate used as a coronal barrier in nonvital bleaching. *Med Oral Patol Oral Cir Bucal.* 1017-1021, 2011.
3. Briso AL, Gonçalves RS, Costa FB, Gallinari Mde O, Cintra LT, Santos PH. Demineralization and hydrogen peroxide penetration in teeth with incipient lesions. *Braz Dent J.* 135-140, 2015.
4. Mena-Serrano AP, Parreiras SO, do Nascimento EM, Borges CP, Berger SB, Loguercio AD, Reis A. Effects of the concentration and composition of in-office bleaching gels on hydrogen peroxide penetration into the pulp chamber. *Oper Dent.* 76-82. 2015.
5. Cintra LT, Benetti F, Ferreira LL, Gomes-Filho JE, Ervolino E, Gallinari Mde O, Rahal V, Briso AL. Penetration capacity, color alteration and biological response of two in-office bleaching protocols. *Braz Dent J.* 169-175, 2016.
6. Azevedo RA, Silva-Sousa YT, Sousa-Gabriel AE, Messias DC, Alfredo E, Silva RG. Fracture resistance of teeth subjected to internal bleaching and restored with different procedures. *Braz Dent J.* 117-121, 2011.

Comparison of conventional and synchrotron X-ray microCT scanning of thin membranes in the inner ear

J. Goyens¹, L. Mancini², V. Van Nieuwenhove³, J. Sijbers³, P. Aerts^{1,4}

¹ Lab of Functional Morphology, university of Antwerp, Universiteitsplein 1, Antwerp, Belgium,

² Elettra - Sincrotrone Trieste S.C.p.A., Basovizza (Trieste), Italy

³ imec Vision Lab, University of Antwerp, Universiteitsplein 1, Antwerp, Belgium

⁴ Department of Movement and Sport Sciences, University of Ghent, Watersportlaan 2, Ghent, Belgium

Aims

Sensing head movements is essential for balance during locomotion. Angular accelerations of the head are sensed by the membranous labyrinth in the inner ear^{1,2}. Little is known, however, about the anatomy of the membranous labyrinth. This lacuna is caused by the difficulty to visualize the membranes by conventional microCT: a) the membranes are very thin (about 10-15 μm ^{3,4}), b) contrast is limited because the X-ray density difference of the membranes and the fluid surrounding them is very small and c) the surrounding dense bone obliges using a high voltage X-ray beam. Other visualization methods, such as histological sections and serial grinding, are not appropriate because of the artefacts they inevitably incur.

Method

Sample preparation We acquired *Takydromus sexlineatus* lizards from a commercial dealer (Fantasia Reptiles, Antwerp, Belgium), and *Lacerta agilis* and *Phoenicolacerta laevis* specimens from the FunMorph collection. We fixated the heads in 4% formaldehyde. Next, they were stained with Phosphotungstic acid for 3 weeks.

Conventional microCT scanning We performed 2 microCT scans with the Skyscan 1172 microCT scanner (Bruker, Kontich, Belgium) that is managed by the bioSTR μ CT Hercules consortium (<https://sites.google.com/view/biostruct>). For the first one, we used a source voltage and current of resp. 100 kV and 100 μA and a 1 mm Aluminum-Copper filter. Further, we used an exposure time of 1700 ms, a frame averaging of 4 and a rotation step of 0.17° over 180°. This resulted in an image pixel size of 2.49 μm , and the scan took 3h20m to be finished. For the second scan, we adapted the scan parameters to resemble those of David et. al⁵, who already succeeded in visualizing the membranes with conventional microCT. We reduced the rotation step to 0.15°, we increased the frame averaging to 6 images and made a 360° scan which took 10h27m.

Synchrotron microCT scanning We performed a phase-contrast synchrotron X-ray microCT scan at the SYRMEP beamline of the Elettra facility in Basovizza (Trieste, Italy). We used a filtered (1.5 mm Silicon filter + 1 mm Aluminum filter) polychromatic beam, with a medium energy of 22 keV. A 16bit sCMOS detector was used, setting the pixel size to 2.02 μm and the sample-to-detector distance to 150 mm. We recorded 1800 projections over 360°, with an exposure time of 2s. The scan duration was 1h.

Dynamic flat field correction Before a microCT scan is started, a projection image is recorded without a sample in the field of view. In a perfect world, such flat fields (also called "white fields") would be homogeneous. However, in reality, grey-scale fluctuations do occur

because of non-uniform sensitivity of the camera, non-uniform response of the scintillator screen and instability of the X-ray beam⁶. To correct for these fluctuations, the projection images that are acquired during a scan are normalized using the flat fields. This is usually done by dividing the projection image, pixel by pixel, by the flat field. This elegant and easy technique is generally satisfying, but it assumes that the camera, scintillator and beam are stationary. In other words, it requires that the flat fields do not change over time. If this is not the case, dynamic flat field correction may yield better results because it takes fluctuations of the flat fields into account. We tested the effect of dynamic flat field correction on both our conventional and synchrotron microCT scans, using the method with eigen flat fields of Van Nieuwenhove et al.⁶.

Results

180° versus 360° conventional microCT scan In the shorter scan of 3h20m (over 180°), the membranes are not visible (see Fig. 1A). In the longer scan over 360°, discerning the membranes is possible (see Fig. 1B). However, the contrast is limited and substantial noise hampers easy (let alone automatic) segmentation of the voxels that belong to the membranes.

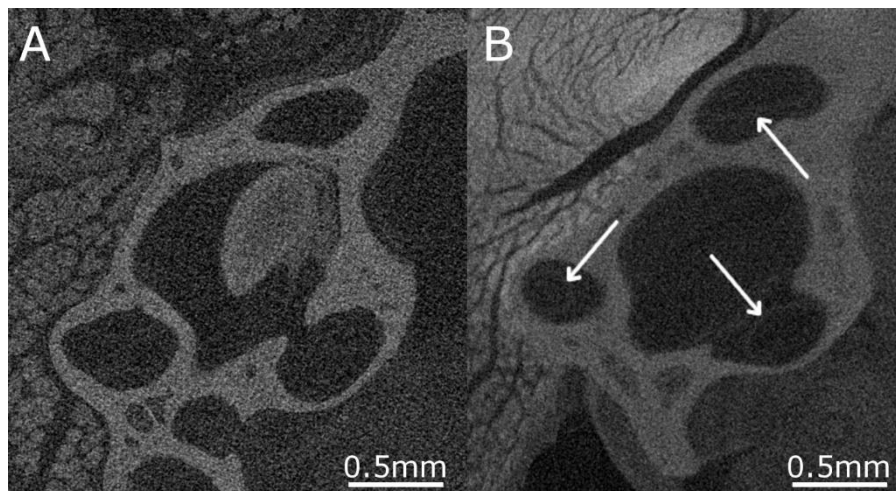


Figure 1: Reconstructed slices of conventional microCT scans of 180° (A) and 360° (B). The membranes are only visible in the long scan (white arrows).

Synchrotron microCT scan A lot less noise is present in the synchrotron-based microCT scan (see Fig. 2A). The membranes are clearly visible, but the contrast is still low. This can be improved by phase retrieval (see Fig. 2B), however, this comes at the cost of some blurring.

Dynamic flat field correction Very little variation was present in the flat fields that were acquired for the conventional microCT scans. Hence, the dynamic flat field procedure selected only a single flat field based on a principle component analysis (see Fig. 3). Hence, dynamic flat field correction won't improve our conventional microCT scan. For the synchrotron microCT scan, on the other hand, 3 eigen flat fields were selected by the dynamic flat field procedure (see Fig. 4). Also, there is clearly more structure (a less random pattern) in these flat fields compared to the conventional microCT scanner. Both observations suggest that the synchrotron scans can be further improved by applying dynamic flat field correction.

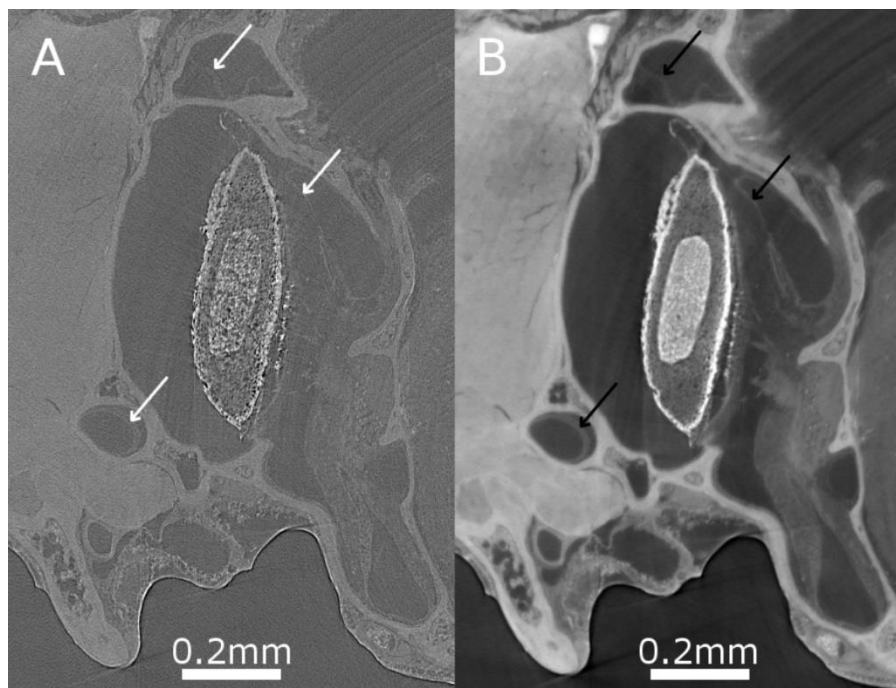


Figure 2: Reconstructed slices of phase-contrast synchrotron X-ray microCT scans without (A) and with (B) phase retrieval. The membranes are indicated with arrows.

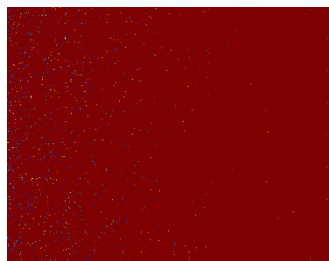


Figure 3: The single eigen flat field that was selected for the conventional microCT scan.

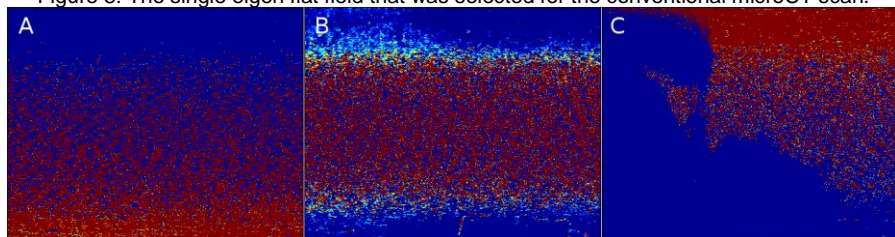


Figure 4: The three eigen flat fields selected for the synchrotron X-ray microCT scan.

Conclusion

Both conventional and synchrotron radiation microCT scanning showed to be able to visualize the membranes in the inner ear. For conventional microCT scanning, a small rotation step, high frame averaging and 360° scanning were necessary. This results in a very long scan (>10h). In a relatively short time span (1h), better contrast and less noise are achieved using synchrotron-based microCT scanning, especially after phase retrieval. This enables semi-automatic detection of the membranes in Amira (VSG systems, Mérignac, France) (see Fig. 5). However, the difficult access to synchrotron facilities and its cost, prevent synchrotron microCT scanning from being applied routinely.

We also found that the quality of the synchrotron microCT scans may be further improved using dynamic flat field correction. This was not the case for the conventional microCT scans. This difference is caused by additional fluctuations that can be present in the synchrotron setup, such as instabilities in the bending magnets of the synchrotron or vibrations of other beamline components⁶.

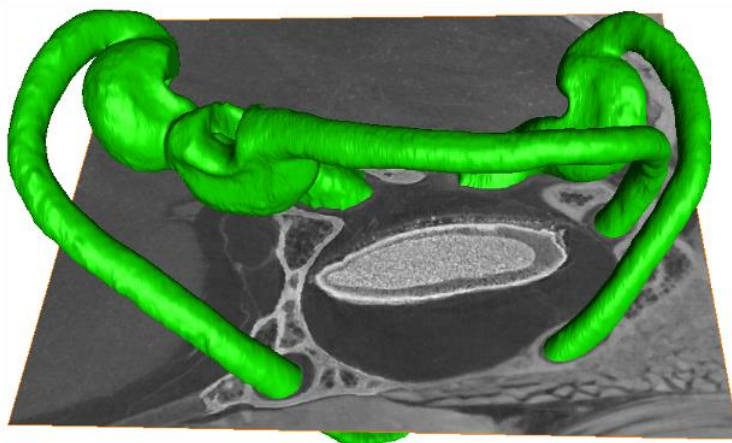


Figure 5: 3D model of the membranous labyrinth in the inner ear.

References:

1. Rabbitt, R. D., Damiano, E. R. & Grant, W. J. in *The vestibular system* (eds. Highstein, S. M. & Fay, R. R.) 153–201 (Springer New York, 2004).
2. Cullen, K. E. The vestibular system: Multimodal integration and encoding of self-motion for motor control. *Trends Neurosci.* **35**, 185–196 (2012).
3. Curthoys, I. S., Blanks, R. H. & Markham, C. H. Semicircular canal radii of curvature (R) in cat, guinea pig and man. *J. Morphol.* **151**, 1–15 (1977).
4. Wu, C. & Wang, K. Three-dimensional Models of the Membranous Vestibular Labyrinth in the Guinea Pig Inner Ear. in *4th International Conference on Biomedical Engineering and Informatics* 544–547 (2011).
5. David, R., Stoessel, A., Berthoz, A., Spoor, F. & Bennequin, D. Assessing morphology and function of the semicircular duct system: introducing new in-situ visualization and software toolbox. *Sci. Rep.* **6**, 32772 (2016).
6. Van Nieuwenhove, V. *et al.* Dynamic intensity normalization using eigen flat fields in X-ray imaging. *Opt. Express* **23**, 27975–27989 (2015).

X-ray micro-CT as a base for Discrete Element Method modelling of fracture phenomenon in various materials

Ł. Skarżyński¹, J. Suchorzewski¹, J. Tejchman¹

¹Gdansk University of Technology, Narutowicza 11/12, 80-233 Gdańsk, Poland

Aims

The main objective of this study is to experimentally investigate fracture in various materials like concrete or pills. These materials have a very complicated heterogeneous structure, changing from few nanometers to millimeters. Therefore, fracture which is a main phenomenon in these materials is an extremely complex process because it consists of main macro-cracks with various branches, complementary cracks and micro-cracks [1-4]. Fracture greatly affects strength of materials and therefore its understanding is vital for a reliable engineering design and production.

The experiments and numerical simulations evidently show that macroscopic concrete behaviour strongly depends on properties of its meso-components (aggregate volume, aggregate size, aggregate roughness, aggregate stiffness, particle size distribution, mortar volume and macro-porosity). Thus, in order to realistically describe the concrete behaviour, its microstructure should be taken into account, at least at the meso-scale. We used the discrete element method (DEM). The outstanding advantages of DEM include its ability to explicitly handle the modelling of particle-scale properties including size and shape which play an important role in the concrete fracture behaviour [5]. DEM allows for a direct simulation of microstructure and can be used to comprehensively study local phenomena at the meso-level such as mechanism of the initiation, growth and formation of cracks [6].

Investigations of concrete

The main goal is to check the capability of DEM for simulating a complex quasi-static multi-cracking in concrete specimens under uniaxial compression. The geometry of concrete microstructure at the meso-scale level was incorporated into DEM from real concrete specimens using a high resolution and non-destructive technique in the form of the 3D X-ray micro-computed tomography using extended Skyscan 1173. In addition, a 2D scanning electron microscope (SEM) Hitachi TM3030 and manual 2D digital microscope Scalar were used.

In order to measure the width of ITZs in non-damaged concrete specimen on the front surface, the SEM with the maximum magnification factor 1000 was used. ITZs were characterised by an extremely thin and porous structure. Due to a very smooth aggregate surface, their width was merely 5-10 μm . ITZs appeared mainly around aggregate but they were also visible around some large cement particles (Figure 1). Figure 2 demonstrates the 3D micro-CT images of the two cracked cubical concrete specimens in the region of the peak load ($\varepsilon=0,12\%$ and $\varepsilon=0,08\%$). All cracks were strongly curved mainly due to a random presence of aggregate grains. The first crack occurred at the bottom right edge of the specimen on the front side. It propagated through a weak aggregate and then along the left edge of the large aggregate particle. Next it branched into two cracks surrounding two aggregate particles above. Later a central crack was created on the front side which was not visible on micro-CT scans as it is closed due to unloading. However, it was observed during deformation with the aid of the manual digital microscope. All cracks mainly propagated through ITZs along

aggregate particles since they were the weakest phase in concrete. Distribution of macro voids and crack is depicted in Figure 3.

The x-ray source voltage of the micro-CT scanner was set to 130 keV, the current was 61 μ A and exposure time was equal 2400 ms. The 0.25 mm brass filter was used. The pixel size was 31.35 μ m. The x-ray projections were recorded with the rotation increment of 0.2° within 360° . In order to reduce the noise in the X-ray projections, the frame averaging option was 10 and random movement option was 50. The FF interval was 100 and the scanning time was approximately 14 hours. The Bruker-Skyscan software (NRecon, CTan, DataViewer and CTvox) were used to reconstruct and process images.

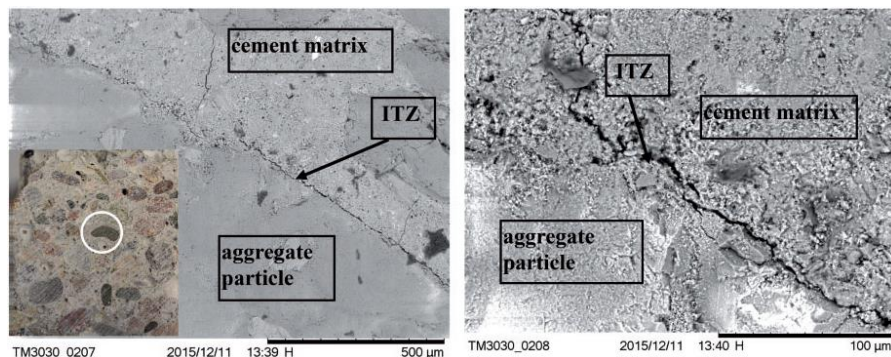


Figure 1: Images of ITZs between aggregate and cement matrix in concrete specimen using scanning electron microscope (SEM): left with the magnification factor 200 and right with the magnification factor 1000

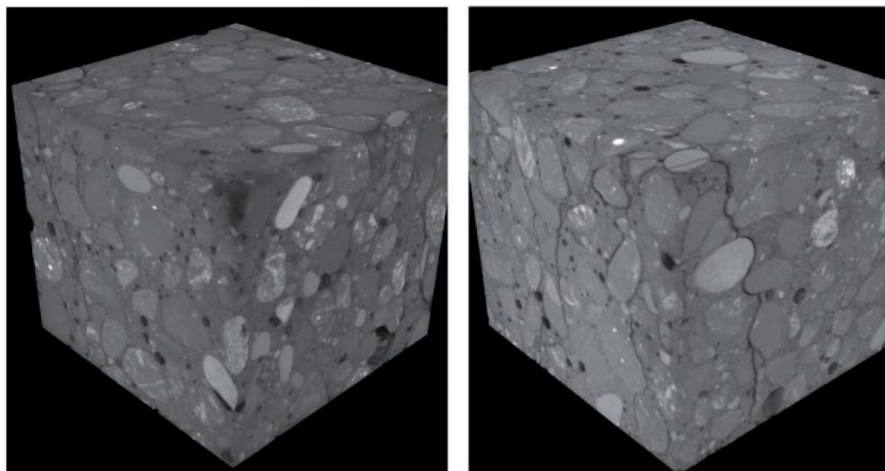


Figure 2: Three-dimensional micro-CT scans of two cracked cubic concrete specimens close to peak stress for $\epsilon=0,12\%$ and $\epsilon=0,08\%$

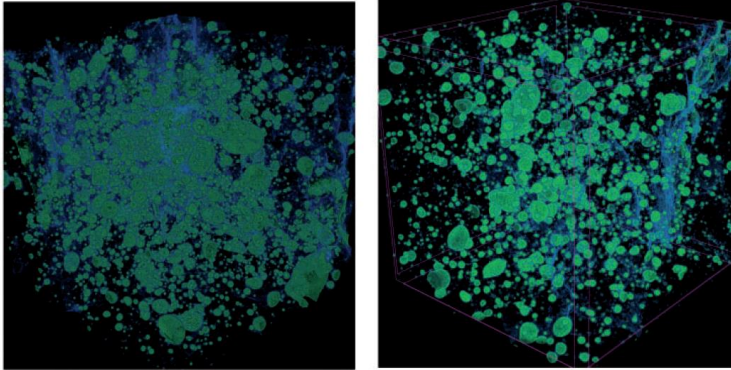


Figure 3: Three-dimensional micro-CT scans with distinguished macro voids (in green) and cracks (blue) in cracked cubic concrete specimens close to peak stress

Numerical simulations were carried out with the real aggregate distribution modelled either by clusters of spheres and by spheres with the equivalent area based on 3D micro-CT images scans (Figure 4a). The calculated curves were in satisfactory agreement with the experimental ones with respect to modulus of elasticity and strength. The calculated crack pattern with clusters composed of spheres on the specimen front surface was approximately similar as in the experiment (Figure 4b). In DEM both main cracks appeared in the same regions (right and central part). The calculated crack at the right edge side did not obviously propagate through a small aggregate grain. However, a further crack shape was realistically reproduced including branching around two grains at the specimen. The calculated central crack also occurred at the same position. The width of the calculated main crack on the right side of the specimen was $w_c=0.22$ mm (clusters of spheres) and $w_c=0.20$ mm (spheres) whereas in the experiments the width was $w_c=0.18$ mm. The calculated crack pattern with spheres (Figure 4c) was different than this with clusters of spheres. The cracks were more straight and their number was higher.

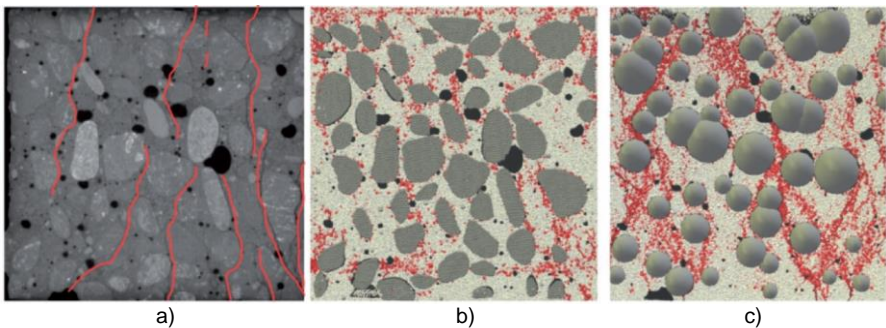


Figure 4: Two-dimensional cracked specimen ($\epsilon=0,12\%$): a) micro-CT image of the specimen, b) DEM for real aggregate (clusters of spheres) and c) DEM for real aggregate (spheres) (red colour - cracks, black colour - voids, grey colour - aggregate and cement matrix)

Investigations of pills

To investigate the quality of the pills micro-CT was used to investigate interior structure of each pill. The main goal of the pharmacy company was to prepare a mix and the compression technique that can result in no cracks and limited volume of air voids in pills. Samples were scanned with the x-ray source voltage of the micro-CT scanner was set to 60 keV, the current was 133 μA and exposure time was equal 2500 ms. The 1.0 mm aluminum filter was used. The pixel size was 5.16 and 9.92 μm . The x-ray projections were recorded with the rotation increment of 0.2° within 360° . In order to reduce the noise in the X-ray projections, the frame averaging option was 6 and random movement option was 10. The FF interval was 200 and the scanning time was approximately 9 hours. The Bruker-Skyscan software (NRecon, CTan, DataViewer and CTvox) were used to reconstruct and process images.

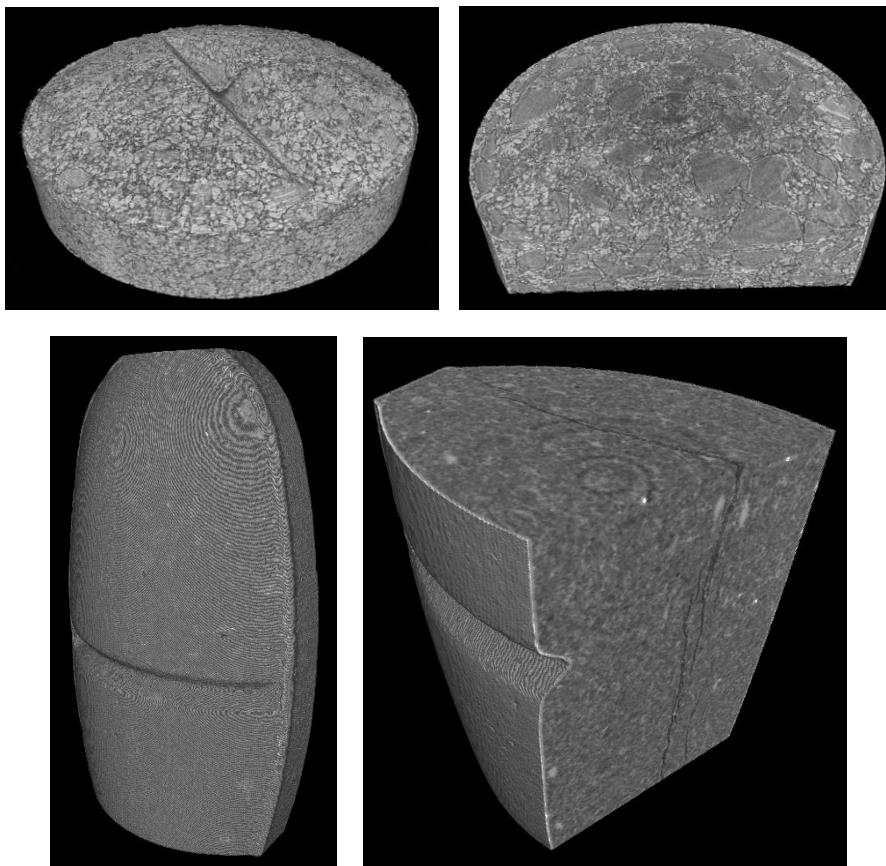


Figure 5: Images of different pills by 3D micro-CT: top view show the heterogeneous structure of analysed pill, bottom view presents initial crack inside pill due to inappropriate compression

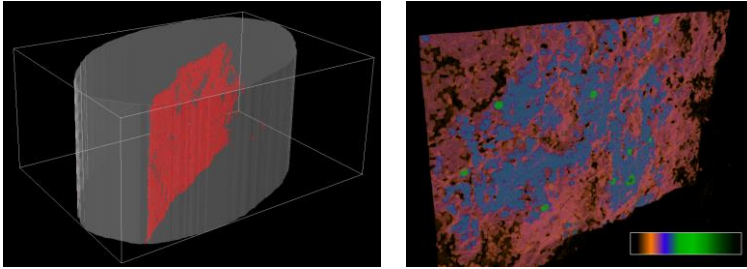


Figure 6: 3D crack in a pill and crack width distribution in pill measured using structure thickness by micro-CT

Real-time micro-CT imaging of fracture - rotating frame

To analyse behaviour of the materials during compression or bending a prototype micro-CT Skyscan 1173 was mounted on Instron 5569 static machine. Sample can be compressed or bended with the maximum force up to 50 kN. The problem was how to rotate sample, under mechanical loading, to make a 3D image. To this end a rotation frame was designed with an incremental encoder (Figure 7). Furthermore a rotating frame was synchronised with micro-CT. Scanning procedure is typical as for the standard scanner. One can choose source voltage and current, exposure time, filter, pixel size, and rotation step. The imaging process consists of three main steps:

- micro-CT makes an initial image then sends signal to rotation frame that the image is done;
- rotation frame rotates sample with the assumed angle (the lower limit is 0.1°);
- after the sample is rotated, micro-CT makes a second image.

Micro-CT rotating frame was installed in December 2016 and up to date only a preliminary experiments were carried out. During the user meeting 2017 results of concrete specimen under compression will be presented.

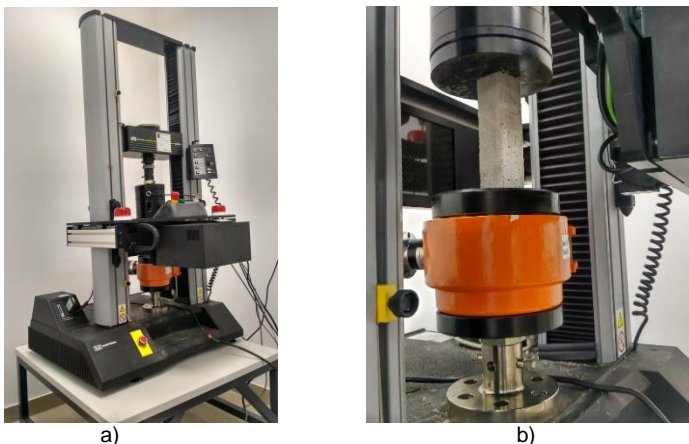


Figure 7: Micro-CT station for imaging of fracture under mechanical loading: a) Skyscan 1173 mounted on Instron 5569 and b) rotating frame with encoder and compressed sample

Conclusion

The following conclusions can be drawn from quasi-static experiments on notched concrete beams under three-point bending:

- X-ray micro-CT is a powerful tool for the visualization of any material micro-structure and crack propagation.
- X-ray micro-CT allows to analyse crack and crack surface width distribution in 3D.
- The concrete micro-structure in calculations was directly taken from real concrete specimens based on 3D X-ray micro-CT images.
- The DEM model demonstrated its accuracy and applicability for concrete in terms of its elasticity and fracture properties. It realistically followed fracture including the occurrence of micro-cracks during their onset, formation and propagation (including phenomena of crack bridging, crack branching and interlocking).
- The real-time micro-CT 3D imaging under mechanical loading with the maximum force up to 50 kN is now possible with synchronisation of the Skyscan 1173 mounted on Instron 5569 with the rotation frame.

Acknowledgements

We would like to express our sincere gratitude to Alexander Sasov for his inexpressible and unconditional support to the rotating frame installation. Furthermore, We would like to express our acknowledgements to Kjell Lappere for his patience and willingness to help in image analyses.

References:

1. Bažant, Z. and Planas, J. Fracture and size effect in concrete and other quasi-brittle materials. CRC Press LLC, Boca Raton, 1998.
2. Ren, W., Yang, Z. and Sharma, R. Two-dimensional X-ray CT image based meso-scale fracture modelling of concrete. *International Journal of Damage Mechanics* **133**, 24-39, 2015.
3. Skarżyński, Ł., Nitka, M. and Teichman, J. Modelling of concrete fracture at aggregate level using FEM and DEM based on X-ray μ CT images of internal structure, *Engineering Fracture Mechanics* **147**, 13-35, 2015.
4. Skarżyński, Ł. and Teichman, J. Experimental Investigations of fracture process in plain and reinforced concrete beams under bending, *Strain* **49**, 521-543, 2013.
5. Donze, F. V., Magnier, S. A. and Daudeville, L. Numerical study of compressive behaviour of concrete at high strain rates. *Journal for Engineering Mechanics* **122(80)**, 1154-1163, 1999.
6. Nitka, M. and J. Teichman, J. Modelling of concrete behaviour in uniaxial compression and tension with DEM. *Granular Matter* **17**, 145-164, 2015.

Comparing micro-CT results of insects with classical anatomical studies: The European honey bee (*Apis mellifera* Linnaeus, 1758) as a benchmark (Insecta: Hymenoptera, Apidae)

Javier Alba-Tercedor & Ignacio Alba-Alejandre

Department of Zoology. Faculty of Sciences. University of Granada. Campus de Fuentenueva, 18071-Granada. Spain

Introduction

In many papers are mentioned the advantages of the micro-CT because it does not damage the samples, and because the images are comparable with others we can get with scanning

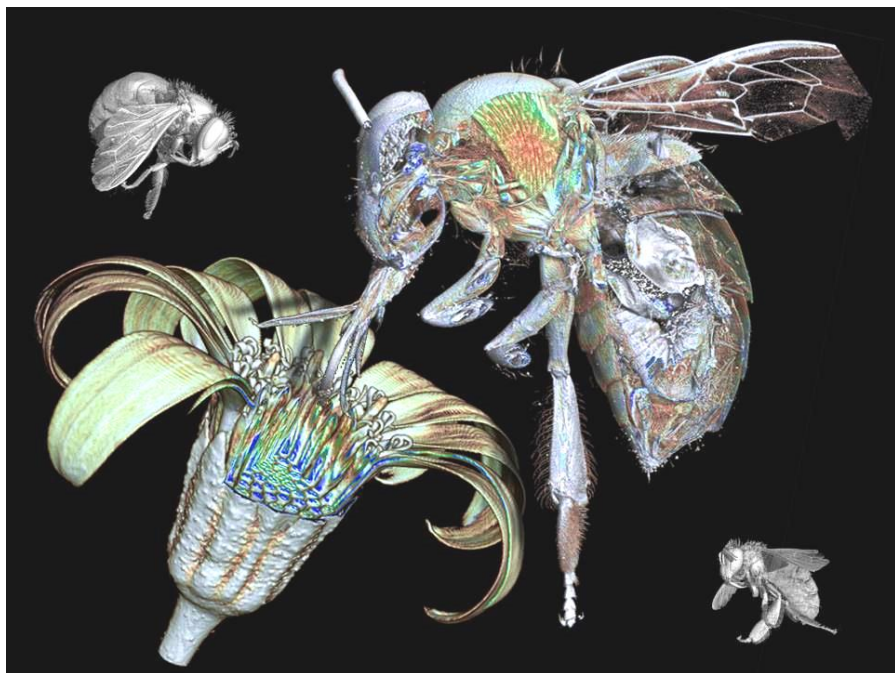


Figure 1. Picture composition of volume rendering reconstructions of honey bee workers in their daily activities: foraging and sipping nectar on a daisy flower (*Aster* sp.). To point out the internal structures the insect and the flower have been “virtually” cut by using the free Skyscan’s software CTVox. Colors were obtained varying the color transfer function curves, conjunction with the lighting and shadowing options within CTVox’s software, as described by [1].

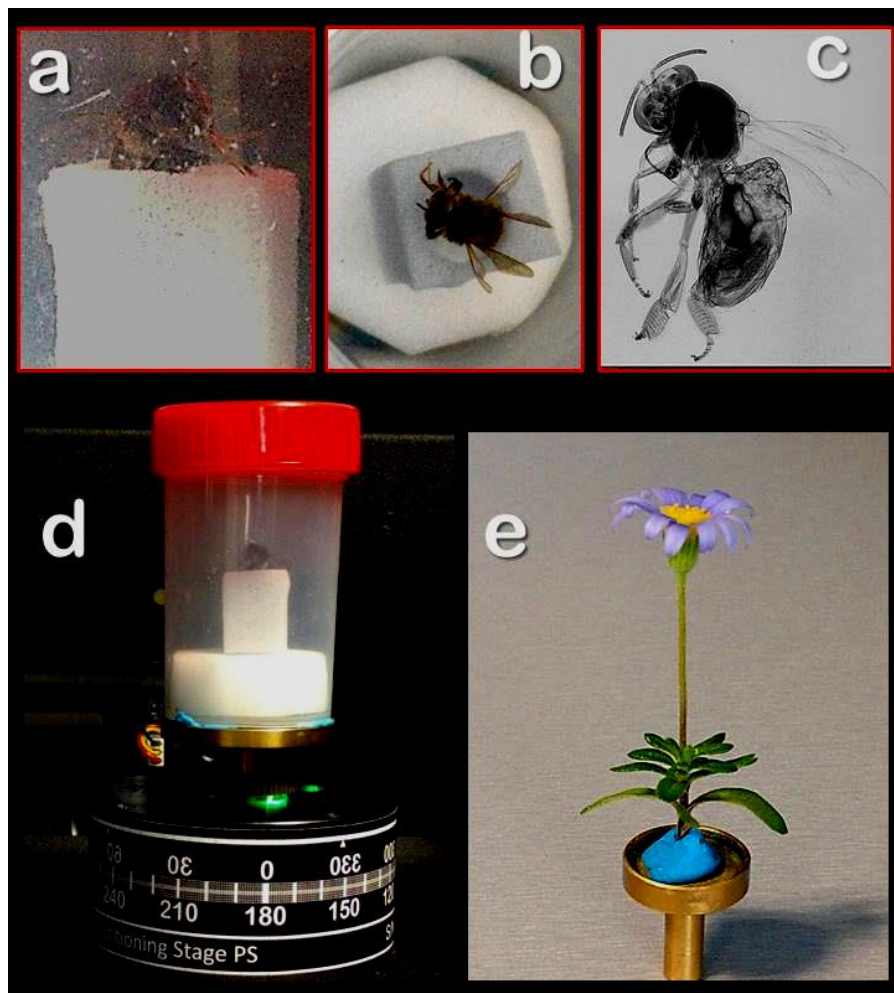


Figure 2. Mounting and fixation of samples to the sample holder for the scanning process. A prepared honey worker bee, on an excavated piece of Basotect®, inside a plastic container (**a**, **b**, **d**); **e**: garden daisy flower (*Aster* sp.), fresh-fixed with plasticine; **c**: detail of a NRecon's view of a specimen to show how transparent is the Basotect® material to x-ray.

electron microscopy (SEM). There is no discussion about it, and there is a general consensus on this respect [2]–[5]. In many of them obtained rendering images are of high quality, permitting to defend that micro-CT is more than a complementary technique [4], [6], [7]. Previously we have been publishing different studies of small animals anatomy pointing out the incredible results that can be obtained not only in the field of the anatomy [5], [8]–[18], but

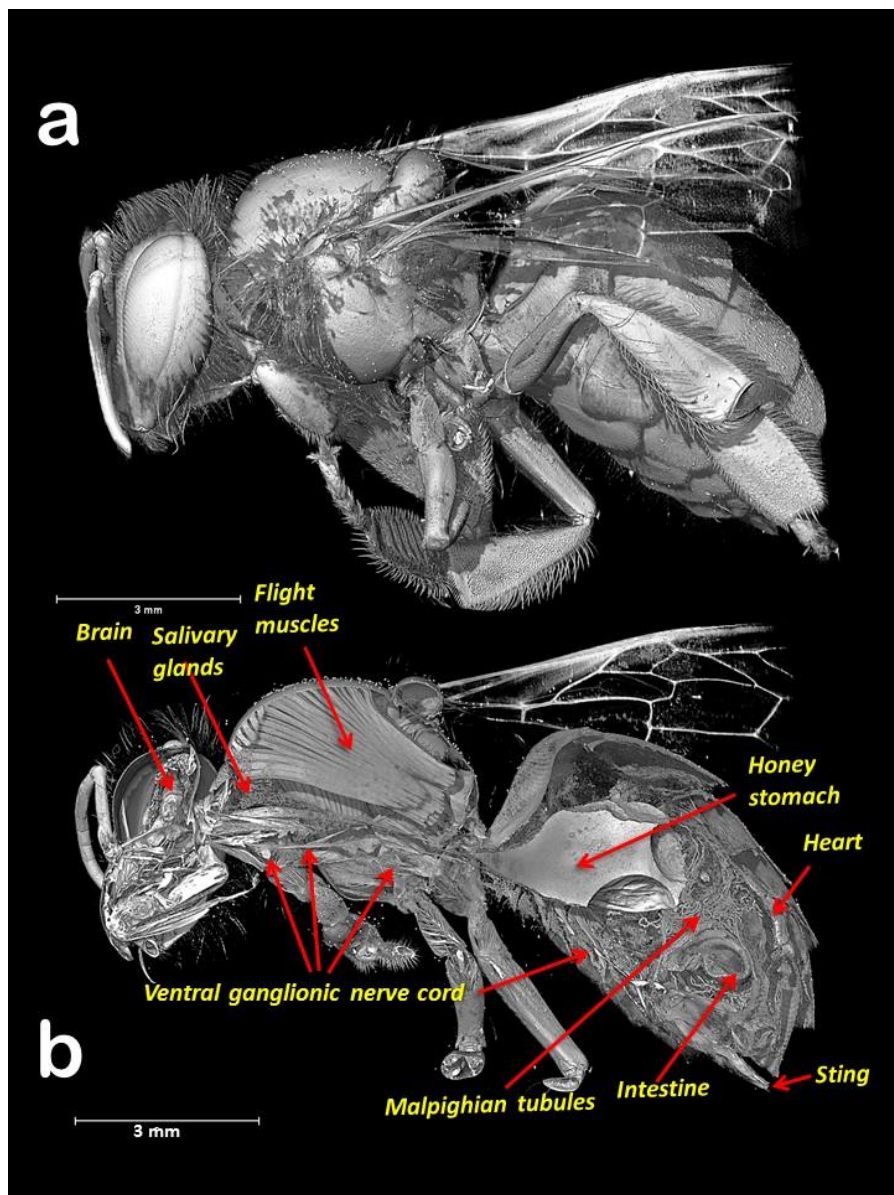


Figure 3. Volume rendering of a honey worker bee. External anatomy in lateral view (a); sagittal cut showing the internal structures and organs (b).

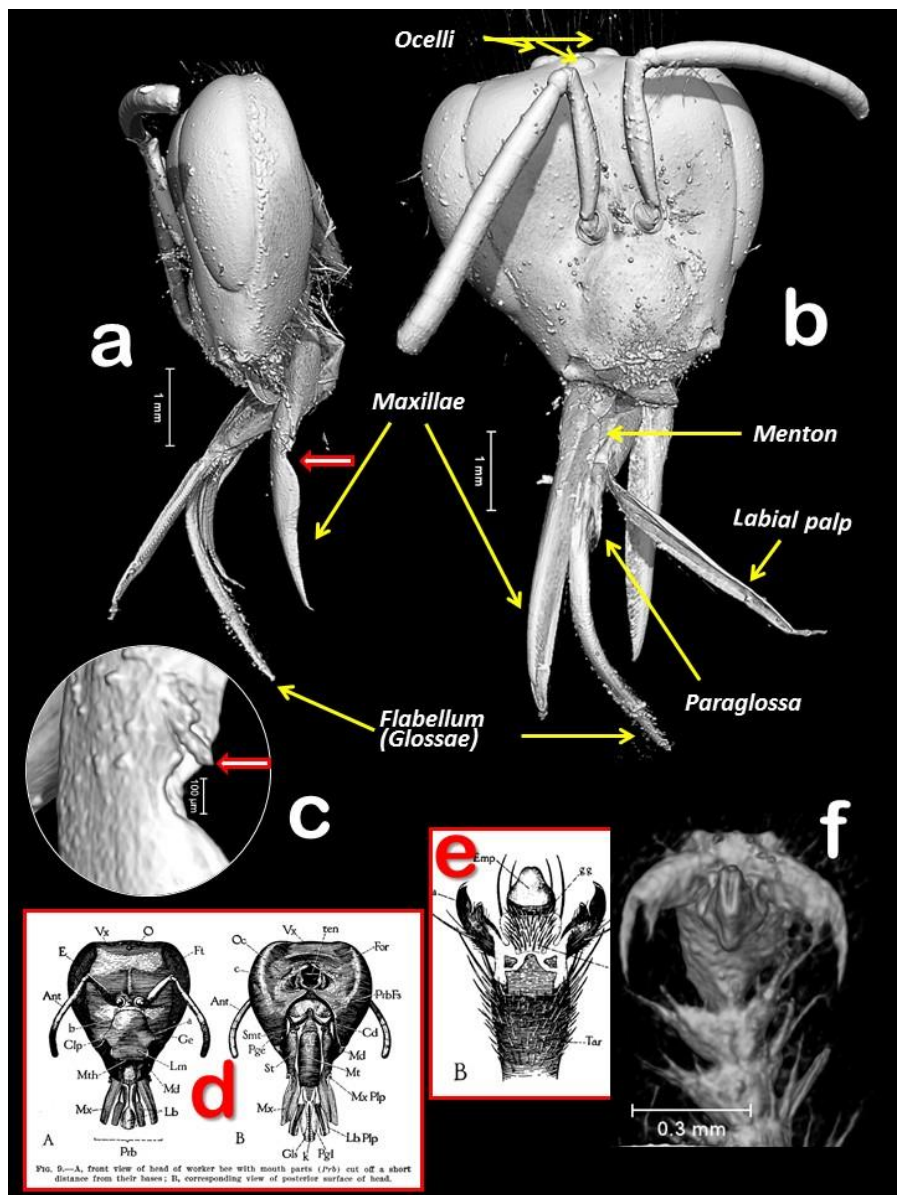


Figure 4. Volume rendering of a honey worker bee showing the external anatomy of the head in a lateral (**a**) and a frontal view (**b**), with mouth parts composing the sucking proboscis, and details of the very reduced maxillary pal (see red arrow in **a**, and **c**). Ventral view of the tip of the tarsus of first leg (**f**). Original figures (**d**, **e**), from Snodgrass (1910)'s are included to be able to compare.

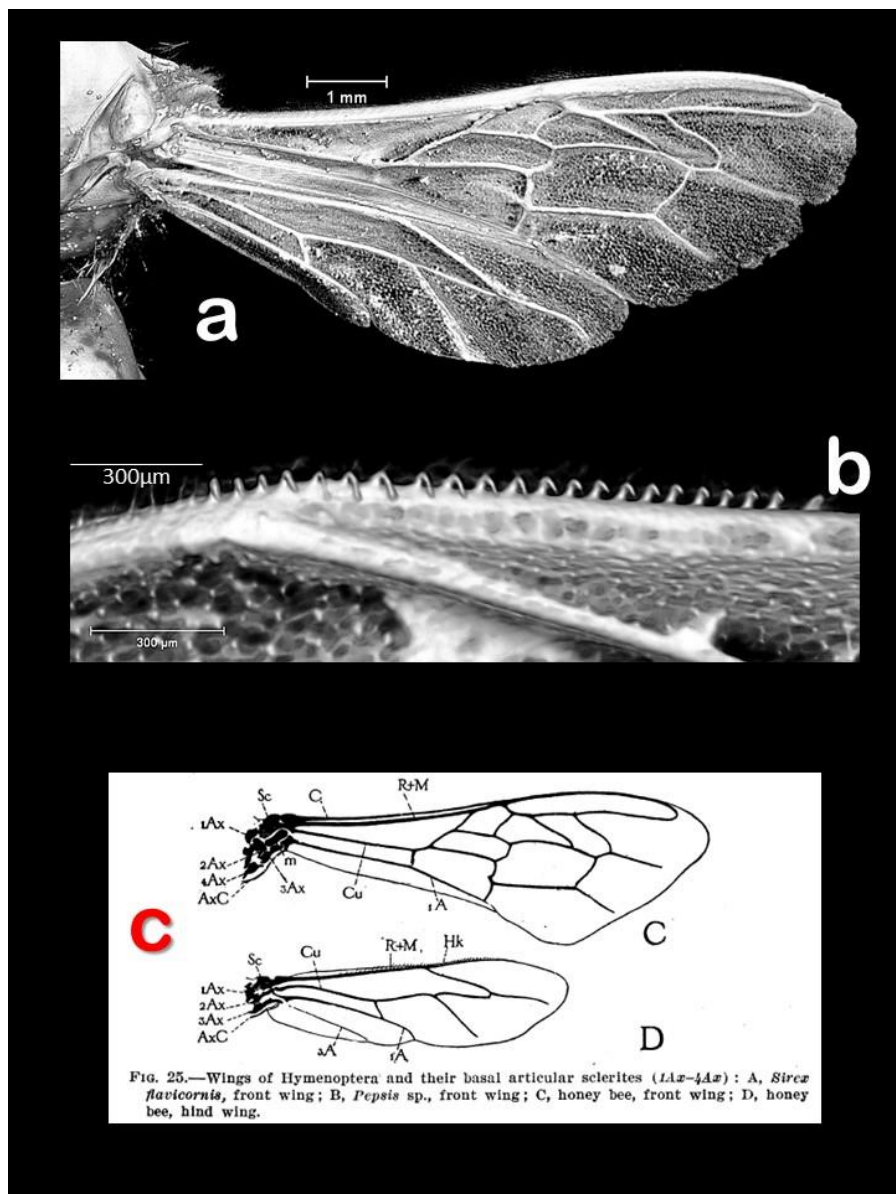


Figure 5. Volume renderings of the wings (a) of a honey worker bee showing in b details of the *hamuli* (a row of hook on the fore margin of the hind wing. These fix and attach it to the fore wing, permitting to synchronize the flight movements). Original figure by Snodgrass (1910) it is included to be able to compare (c).

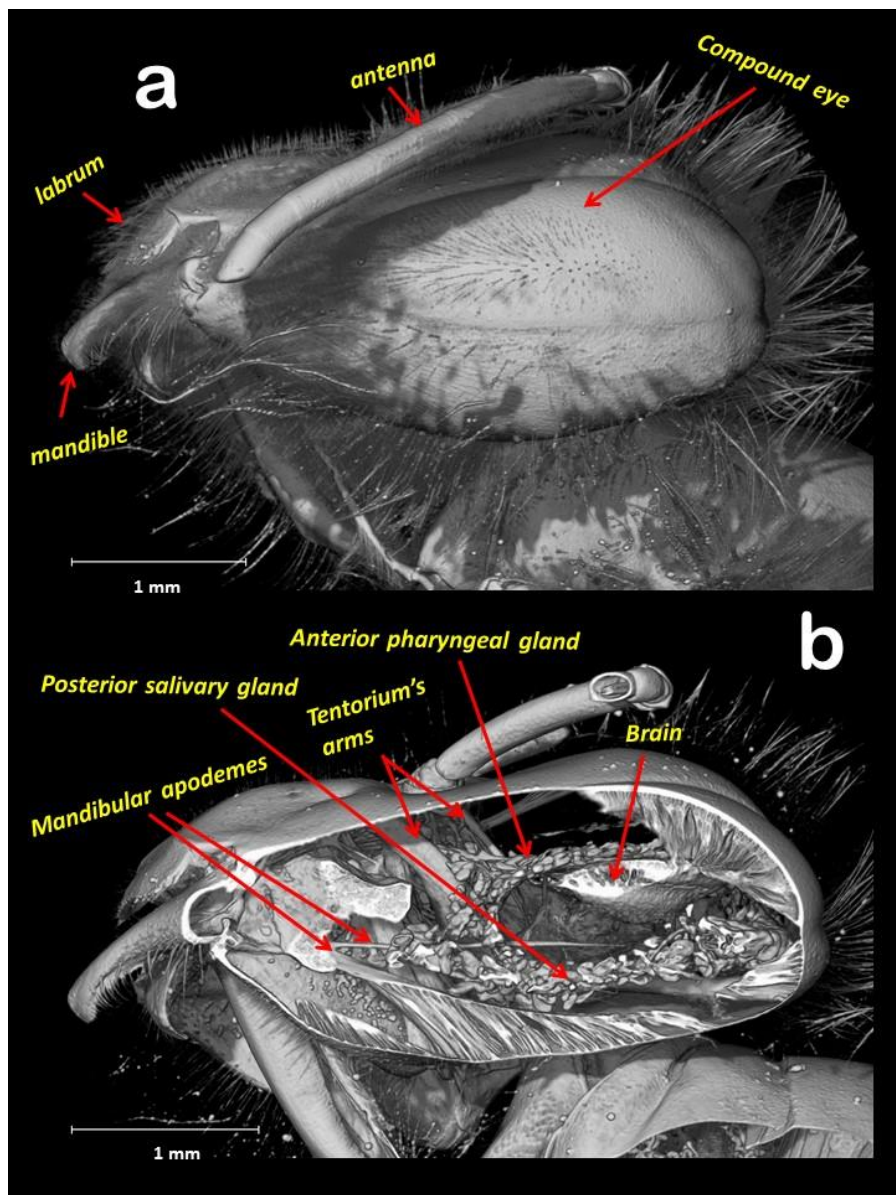


Figure 6. Volume renderings of the head in a lateral view, showing the external (a) and internal (b) anatomical structures.

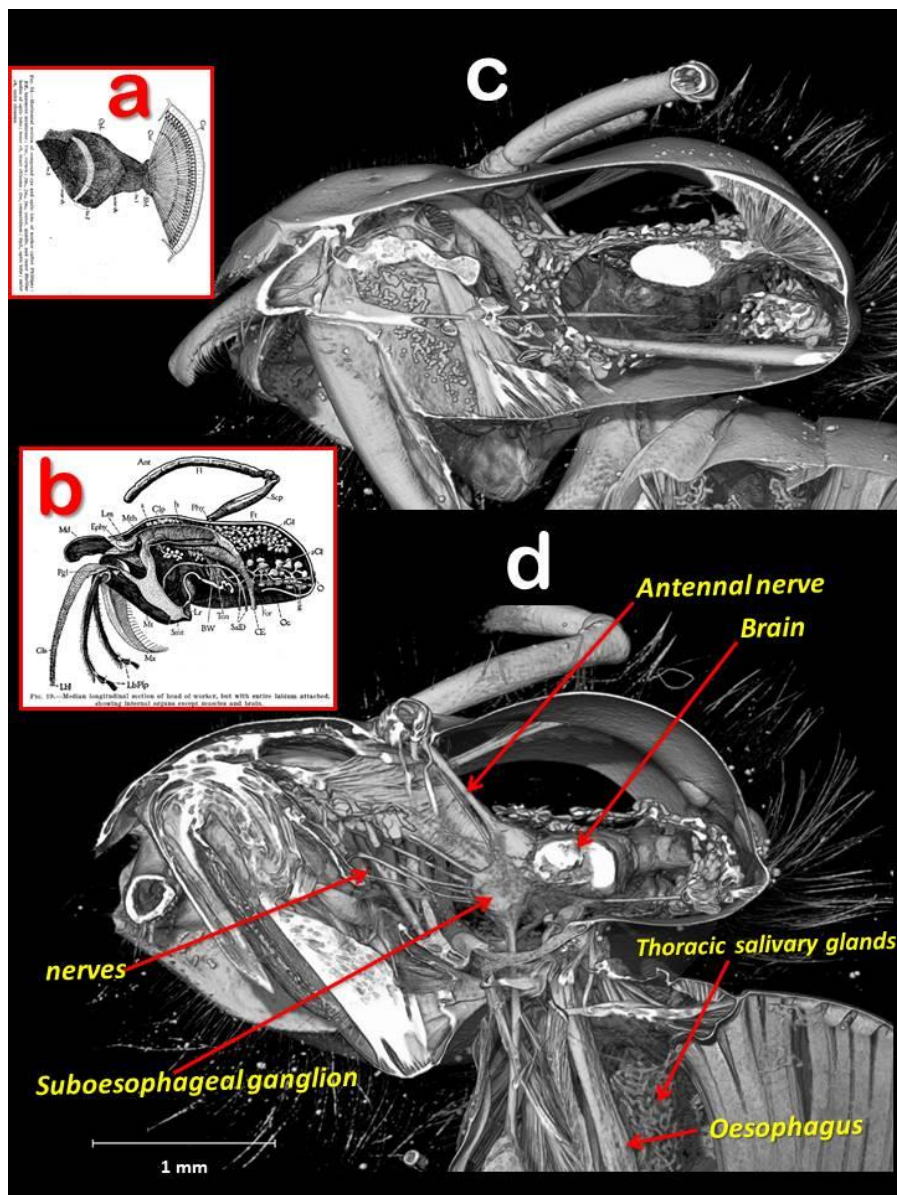


Figure 7. Volume renderings of internal anatomy of the head in a lateral view, progressive cuts (c, d) show the internal anatomical structures with a high definition. Observe the correspondence with the original Snodgrass (1910)'s figures (a, b).

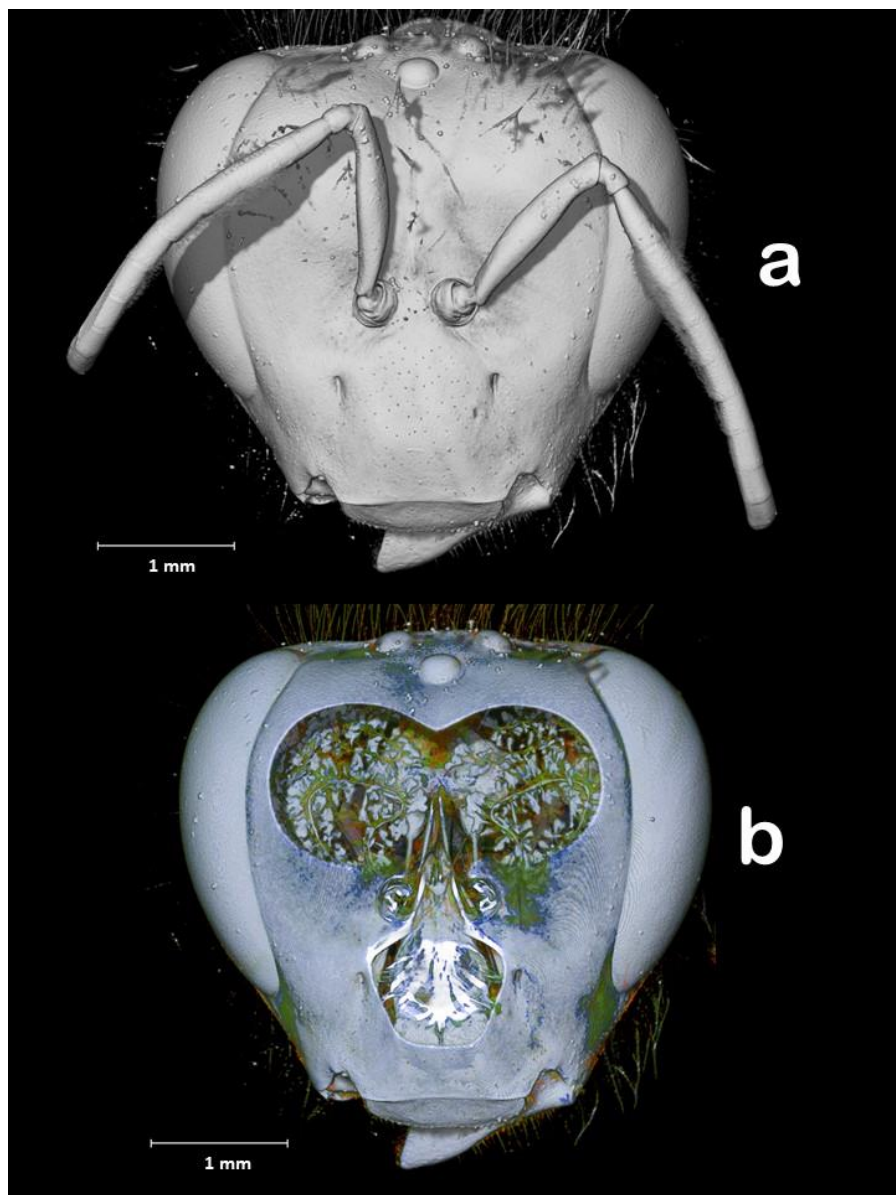


Figure 8. Volume renderings of head in a frontal view. In the colored lower picture the external surface has been slightly cut permitting to evidence the fore glandular complex.

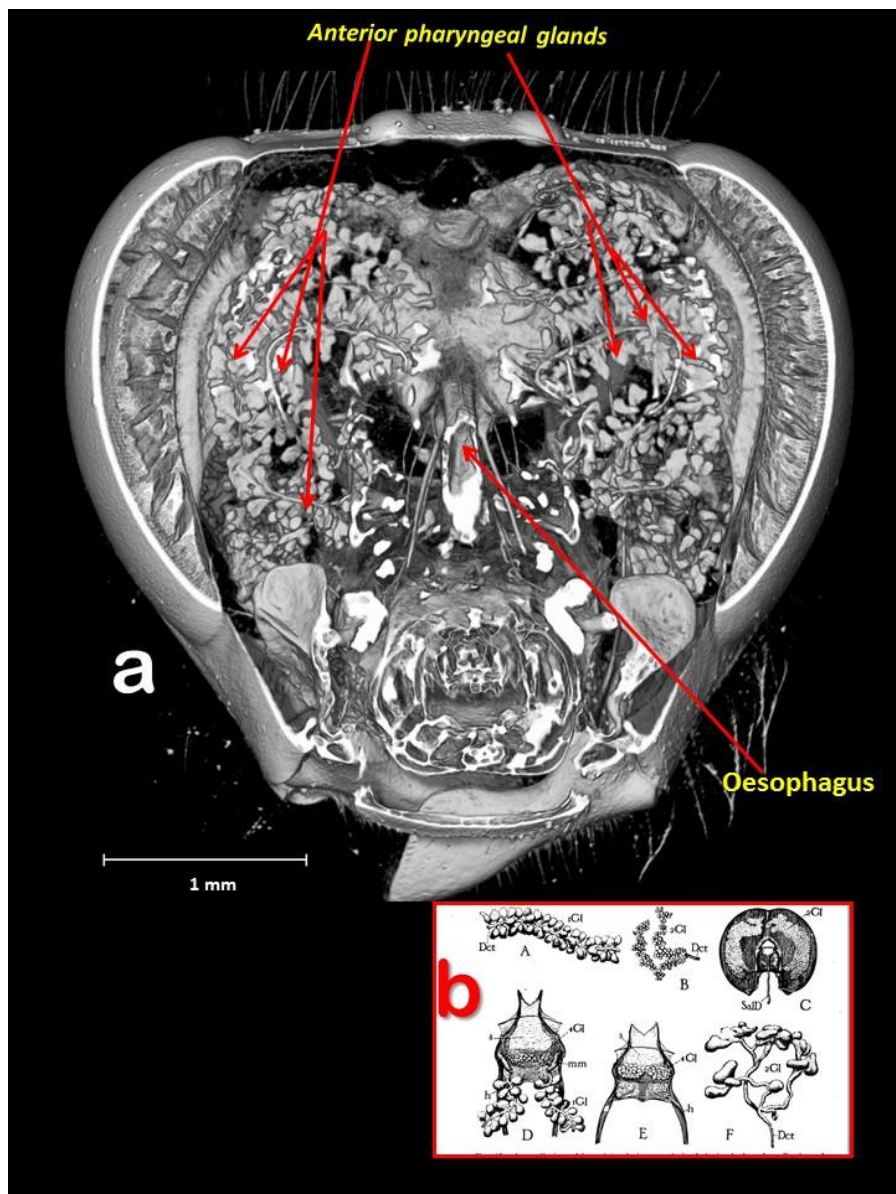


Figure 9. Volume rendering superficial section of head in a frontal view permitting to see the internal structures, and especially the anterior pharyngeal glands. Original Snodgrass (1910)'s figure (b), is included to be able to compare.

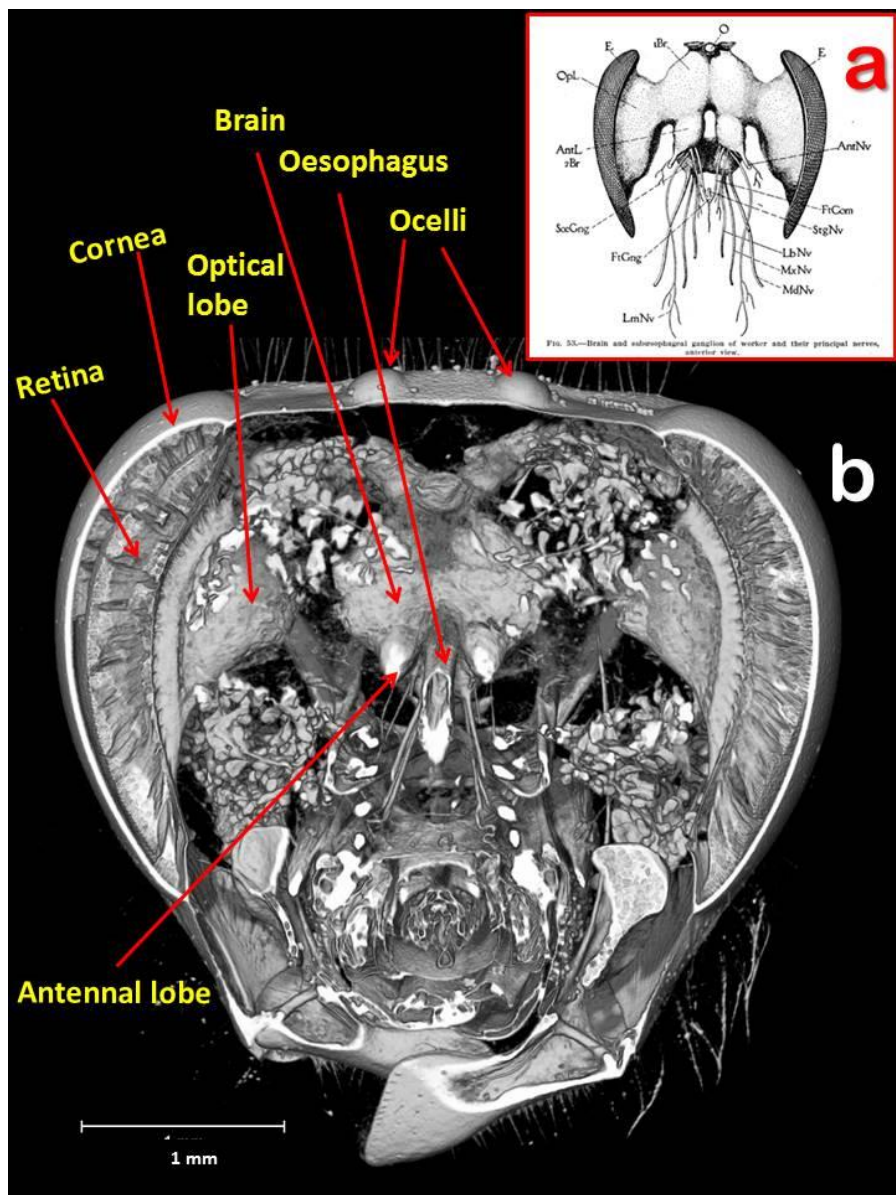


Figure10. Volume rendering section of the head in an anterior view, evidencing the brain and its main nerves, as well as the eyes structure.

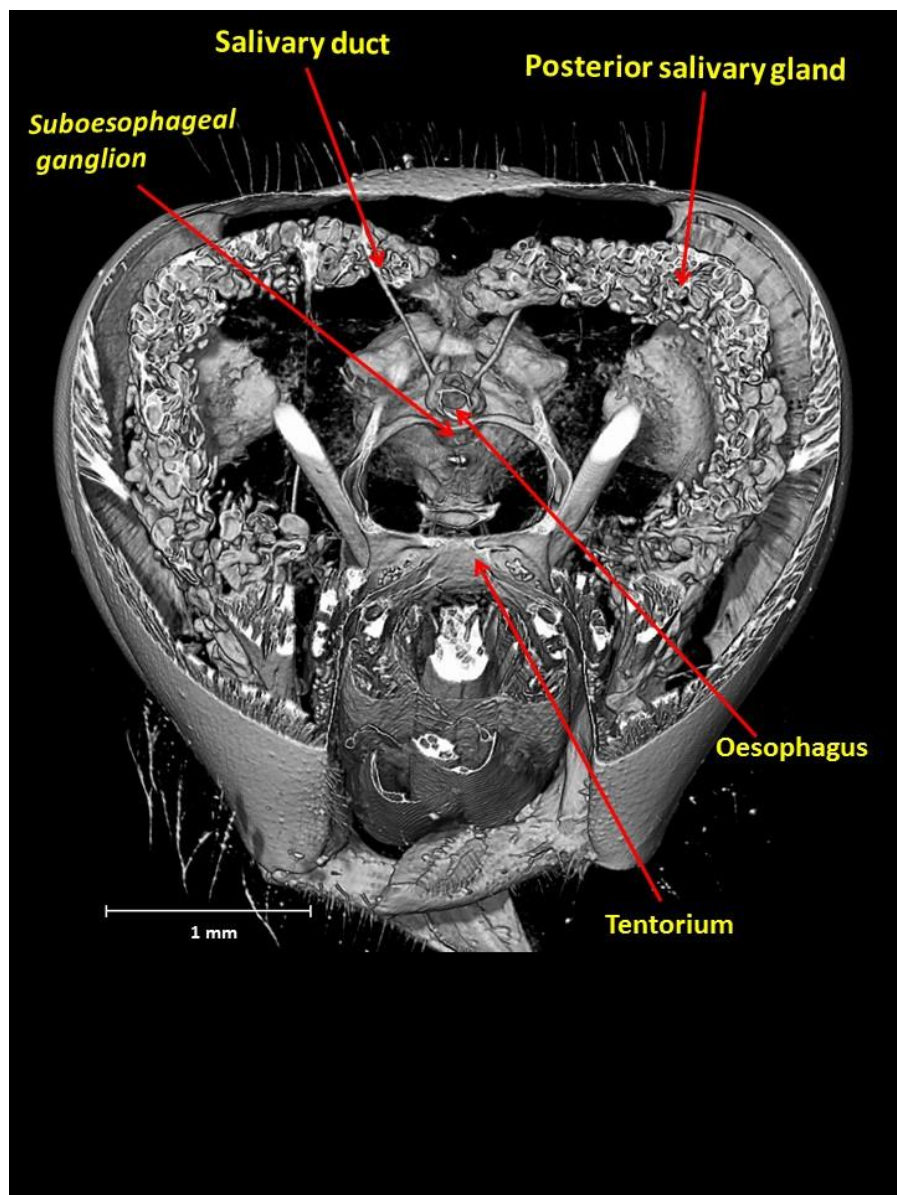


Figure11. Volume rendering section of the head in a posterior view showing the internal structures.

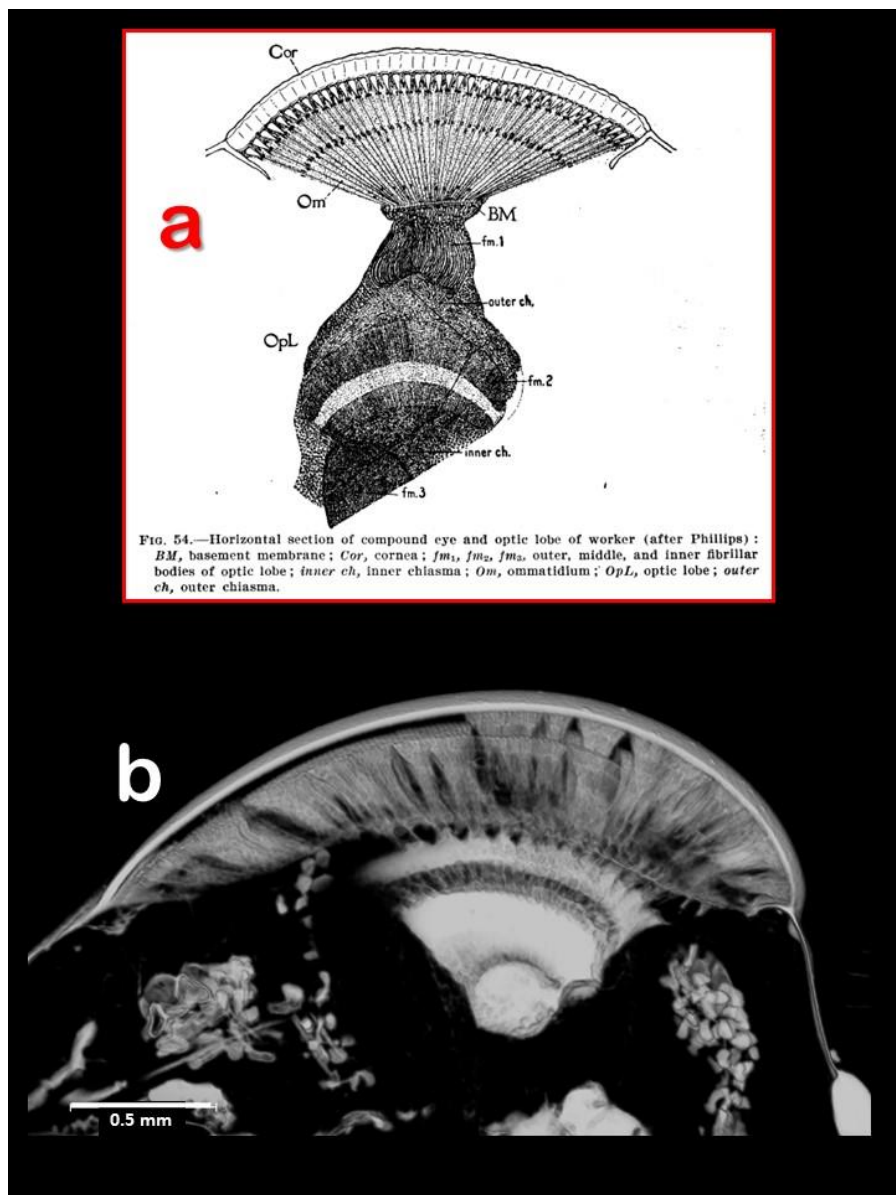


Figure12. Volume rendering of a front-posterior section of the head showing the detailed structure of the compound eye (**b**), permitting to compare it with the Philip's original figure reproduced the classic study by Snodgrass (1910) (**a**). For details about the use of micro-CT to study the insect's eye structure see [8].

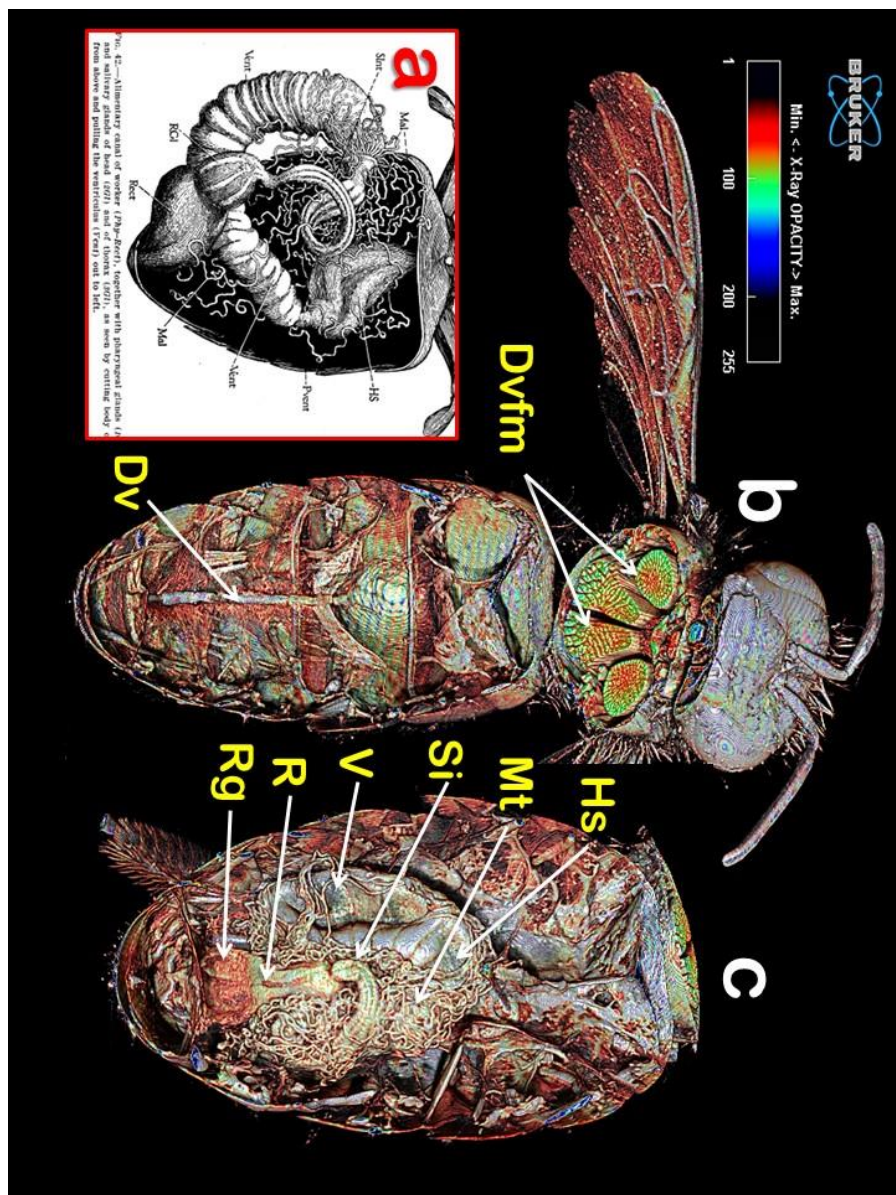


Figure13. Volume renderings of the internal organs of a honey worker bee in ventro-dorsal (**b**) and dorso-ventral (**c**) views, respectively and the comparison with the original figure by Snodgrass (1910). To be able to get these images it was used the sphere cutting in the cutting/clipping option within CTvox's menu. Colors are artificial and represent the opacity of structures to x-Ray, according with the scale.

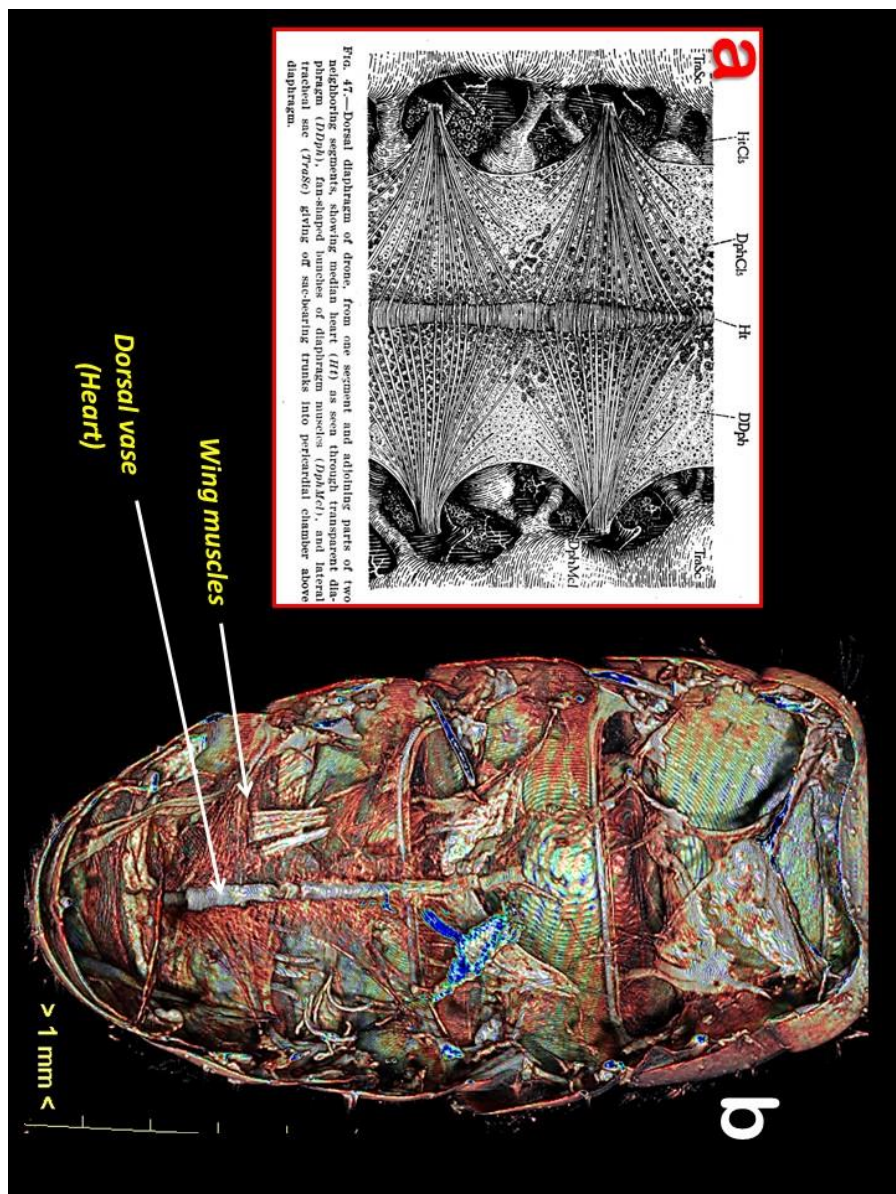


Figure14. Volume rendering of an internal view of the dorsal abdominal region of the honey bee's worker showing the dorsal vase (heart) and winged shaped muscles, as well other structures (**b**). It is included an original figure by Snodgrass (1910) to compare. To be able to get this image it was used the sphere cutting options in the cutting/clipping option within CTVox's menu. Colors are artificial and represent the opacity of structures to x-Ray, according with the scale in figure 13.

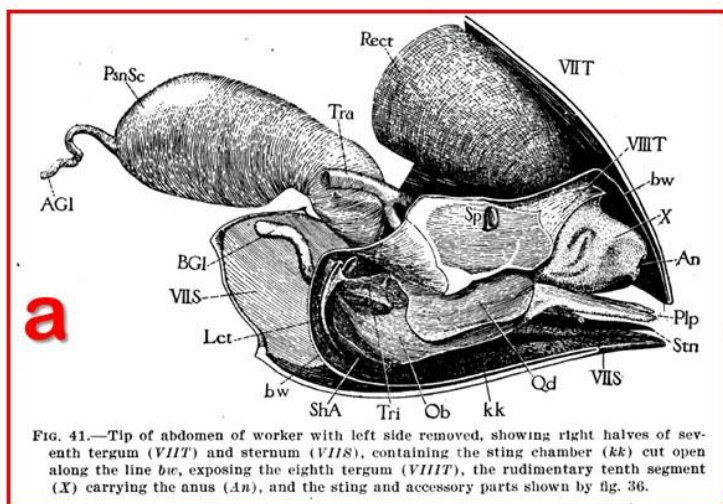


Figure15. Volume rendering of a mid-section of the hind abdominal part of the honey worker bee (**b**) and its comparison with the original figure by Snodgrass (1910) (**a**)

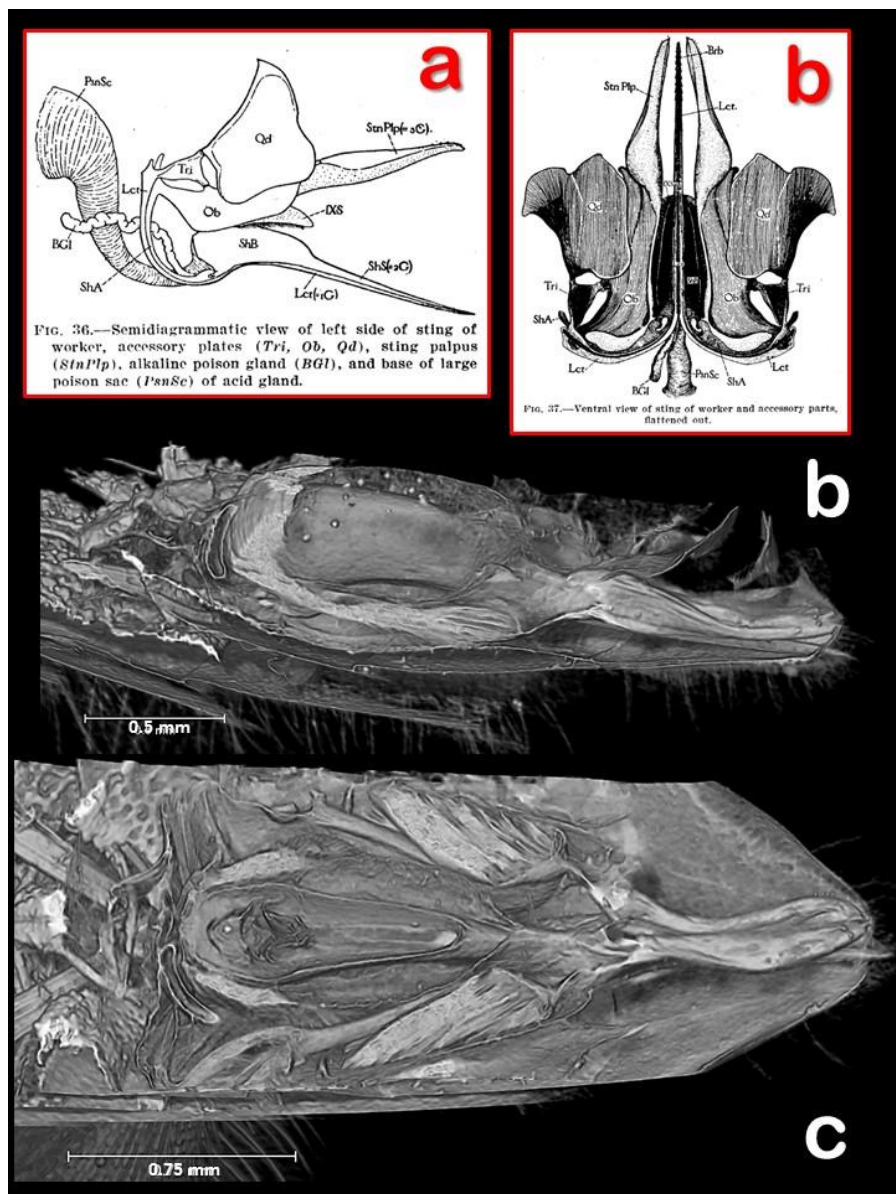


Figure 16. Volume renderings of sections of the hind abdominal part of the honey worker bee, in a lateral (b) and a dorso-ventral view (c), showing the detailed anatomy of the sting and its accessory structures. For comparison the original figures by Snodgrass (1910)- in a lateral (a) and a dorso-ventral (b) views- have been included.

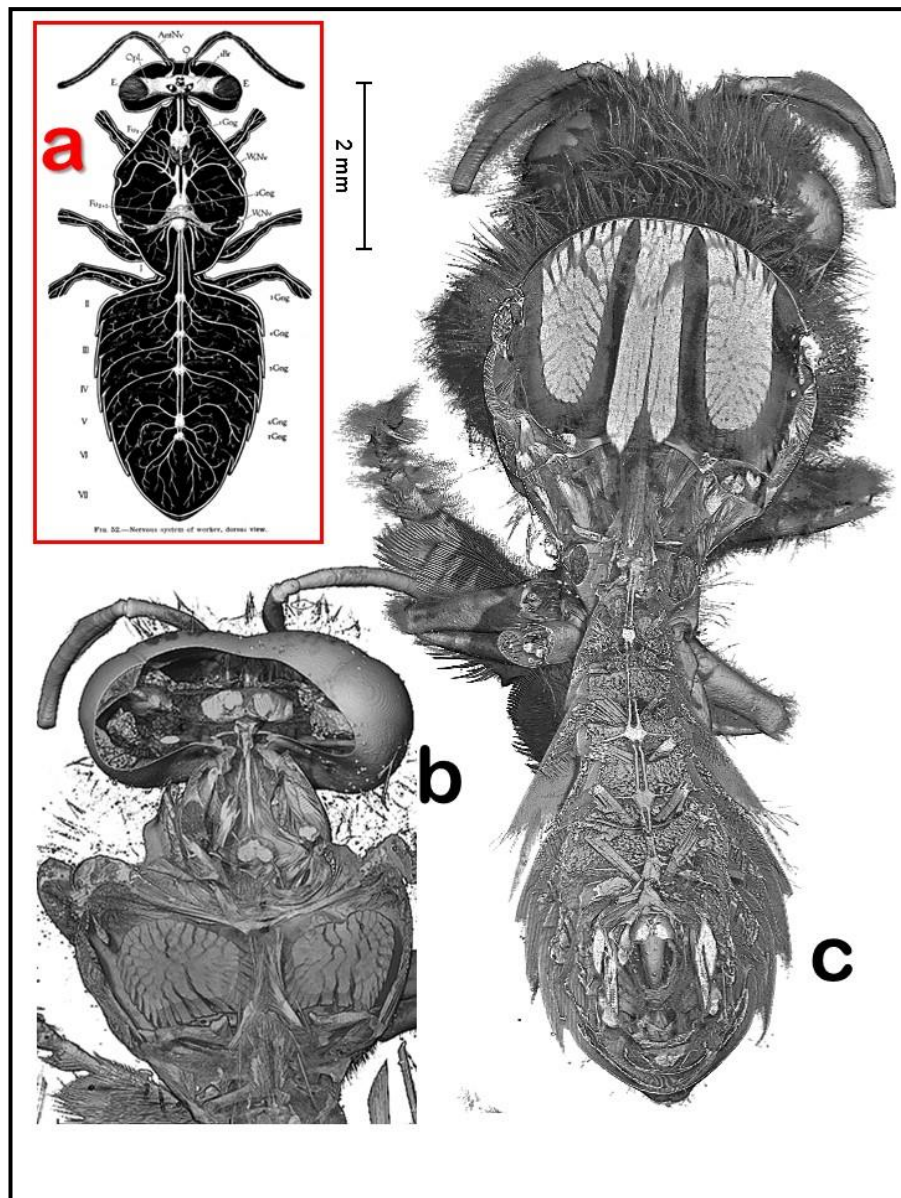


Figure17. Volume renderings of section, in dorso-ventral views, of the internal anatomy of the honey worker bee. Most of the internal structures have been removed with software to be able to see the nervous system: the brain in the head, and the thoracic (b), and abdominal (c) ventral ganglionic nerve cord, permitting to compare it with a similar view drawn by Snodgrass (1910) (a)

also resulted of relevant importance to elucidate adaptive survival strategies of insects [19], [20].

Aims

We already tested the quality of the images obtained with micro-CT [12]–[14], [17], [18], [21]–[25], with the advantage that the images dataset can be visualized as many times as needed with the possibility to change the observation perspective and the original sample can be returned to the collections or museum where it is deposited. Now that it seems that there are no doubts about the importance of micro-CT as a modern research tool, as it is demonstrated in the increasing of papers using it. Because we are involved in a project studying bees, recently we published a general micro-CT study of a mason bee (*Osmia rufa*) [9], and we decided to undertake a detailed micro-CT study of the European honey bee (*Apis mellifera* Linnaeus, 1758), species well known for the general public and from which has been published much literature. However, a classical anatomical study was published in the beginning of the twentieth century [26], still it is the more complete compendium about the anatomy of the honey bee and in general it represents some sort of bible about the knowledge of the insect anatomy. Recently have been published different papers in which using modern microscopic techniques, or even micro-CT, are studied different body structures, but mainly the brain (i.e. [27]–[34]). We decided in this paper to show details of the external and internal anatomy of the whole body of worker bees, comparing the micro-CT volume renderings images with the Snodgrass' drawings as the most classic representative study.

Method

Workers of the the European honey bee (*Apis mellifera* Linnaeus, 1758) were collected alive when foraging in the Sierra Nevada mountains, southern Spain (11-12-2016, 2-1-2017, Pinos Genil, Granada 980 m. a.s.l.). Specimens were killed and preserved in 70% ethanol for 5 days and then transferred to a 1% solution of Iodine in 100% ethanol during 24 hours, after that they were submerged in Hexamethyldisilazane for 9-24 hours and overnight air dried. The sample was mounted in a piece of BASOTECT® (melamine resin foam, created by the Chemical Company BASF), inside a plastic container to avoid any movement provoked by the air refrigerating current or forced air during the scan process (see fig. 2). The Basotect's material results of very low density, and thereafter very transparent to X-Ray (see fig. 2c), and therefore it can be easily eliminated during the segmentation procedure.

A SkyScan 1172 high resolution microtomograph, upgraded to have a Hamamatsu 100/250 source and a SHT 11Mp camera was used. The scanning parameters were setup as it follows: Isotropic voxel size = 4.45 μm per pixel; Source Voltage=53-55KV, Source Current=124-127 μA , and image. Rotation step=0.5°, 360° of rotation scan. The daisy flower (*Aster* sp.) used for the artistic composition of fig.18, was cut from the garden of the faculty campus, immediately fixed with plasticine to the sample holder, and fresh scanned the following setting parameters: Isotropic voxel size = 23.5 μm per pixel; Source Voltage=54KV, Source Current=43 μA , and image. Rotation step=0.5°, 180° of rotation scan.

For primary reconstructions and the "cleaning" process to obtain the datasets of cross-section images ("slices") it was used the up-to-date last versions of the free Bruker micro-CT's Skyscan (www.skyscan.be) software (NRecon, DataViewer, CTAnalyser.). Volume renderings images were obtained with FEI's Amira software v.6.2 [35]. The free Skyscan's software CTVox was used to get color volume rendering images in figures: 1, 13 and 14. Colors were obtained varying the color transfer function curves, conjunction with the lighting and shadowing options. For more detailed explanation of the process see the previous paper [1]. It is important to point out that Amira's volume renderings were obtained directly by loading image datasets obtained with the Bruker-microCT Skyscan's, resulting mirrored inverted images.

Results and discussion

In figures 3 to 17 are illustrated the results obtained of this study on the anatomy of the honey bee and the respective comparison of the structures as were drawn by Snodgrass in his classic paper of the first decade of the twentieth century [26]. These demonstrate the high precision with which the old authors did the anatomical studies, because after a thorough comparison can be observed only small differences in shapes. In general Snodgrass drawings are somewhat more elongated than real, but even when looking at very delicate small structures as the brain and its nerves agree with what we could enhance by using the modern technique of micro-tomography.

Conclusion

As other authors found and we observed in previous papers, micro-CT is not only valid but incredibly reliable for anatomical studies, permitting to study the animals or structures scanned as many times as desired, virtually moving the sample and exploring it from any angle/perspective. Making this extremely valuable not only for actual, but for future new studies based on the same stored images dataset. Thereafter, we consider very important to start to organize an international depository where to upload images datasets that could help the researchers in a similar way as genetic database depositories already are being used by researchers around the world to share their discoverings.

Acknowledgements

To Bruker-Skyscan staff for fast and effective support, their patience and effectiveness, and for their constant improvements to the software and in implementing new options we requested. Also for their kindness in providing the senior author fast and effective suggestions and answers to queries. In this respect, we are especially indebted to: Alexander Sasov, Stephan Boons, Xuan Liu, Phil Salmon, Jeroen Hostens, and Vladimir Kharitonov

To Dr. Nikolaus Nestle from BASF, SE, Ludwigshafen am Rhein in Germany who let we know about the utility for micro-CT of the Basotec® material, providing us with the first sample of it, and to Luisa Kari and Stephanie Thum from the BASF company who kindly sent us additional material.

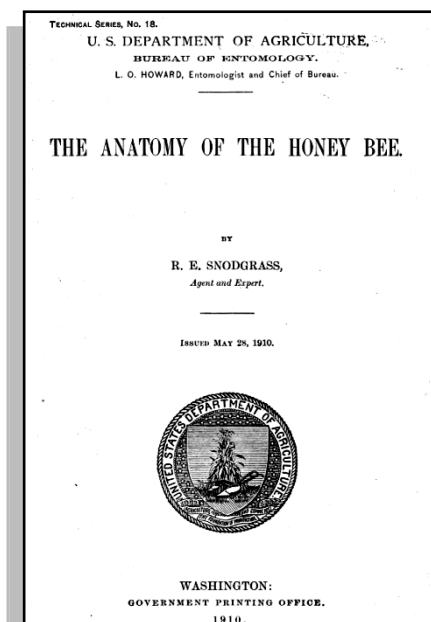
This paper benefited of the project: "Developing an Infrastructure and Product Test Pipeline to Deliver Novel Therapies for Citrus Greening Disease", 2015 (extended in 2017), lead by Dr. S.Brown, Kansas State University and funded by the USDA's National Institute of Food and Agriculture through the Specialty Crops Research Initiative/Citrus Disease Research & Extension.USDA NIFA Award No.2015-70016-23028. As well of the project granted by the Spanish government MIMECO: "Life history strategies to cope with human-induced rapid environmental changes"(CGL2013-47448-P), lead by Dr. Daniel Sol.

References:

- [1] J. Alba-Tercedor, "From the sample preparation to the volume rendering images of small animals : A step by step example of a procedure to carry out the micro-CT study of the leafhopper insect *Homalodisca vitripennis* (Hemiptera: Cicadellidae)," *Bruker Micro-CT Users Meet. 2014*, pp. 260–288, 2014.
- [2] B. D. Metscher, "MicroCT for comparative morphology: simple staining methods allow high-contrast 3D imaging of diverse non-mineralized animal tissues.," *BMC Physiol.*, vol. 9, no. 1, p. 11, Jan. 2009.
- [3] S. J. Schambach, S. Bag, L. Schilling, C. Groden, and M. A. Brockmann, "Application of micro-CT in small animal imaging.," *Methods*, vol. 50, no. 1, pp. 2–13, Jan. 2010.
- [4] G. L. J. Paterson, D. Sykes, S. Faulwetter, R. Merk, F. Ahmed, L. E. Hawkins, J. Dinley, A. D. Ball, and C. Arvanitidis, "The pros and cons of using micro-computed tomography in gross and micro-anatomical assessments of polychaetous annelids," *Mem. Museum Victoria*, vol. 71, no. December, pp. 237–246, 2014.

- [5] J. Alba-Tercedor, "Microtomografías de invertebrados," *Investig. Cienc.*, vol. Mayo, pp. 42–43, 2014.
- [6] W. Ribi, T. J. Senden, A. Sakellariou, A. Limaye, and S. Zhang, "Imaging honey bee brain anatomy with micro-X-ray-computed tomography," *J. Neurosci. Methods*, vol. 171, no. 1, pp. 93–97, Jun. 2008.
- [7] C.-P. Richter, X. Tan, H. Young, S. Stock, A. Robinson, O. Byskosh, J. Zheng, C. Soriano, X. Xiao, and D. Whitlon, "A comparison of classical histology to anatomy revealed by hard x-rays," 2016, p. 996711.
- [8] J. Alba-Tercedor, "Microtomographic study on the anatomy of adult male eyes of two mayfly species," *Zoosymposia*, vol. 11, pp. 101–120, 2016.
- [9] J. Alba-Tercedor and I. Bartomeus, "Micro-CT as a tool straddling scientist research, art and education. Study of *Osmia* sp., a mason bee (Insecta, Hymenoptera: Megachilidae)," in *Bruker Micro-CT Users Meeting 2016*, 2016, pp. 74–91.
- [10] M. G. Paoletti, R. J. Blakemore, C. Csuzdi, L. Dorigo, A. L. Dreon, F. Gavinelli, F. Lazzarini, N. Manno, E. Moretto, D. Porco, E. Ruzzier, V. Toniello, A. Squartini, G. Concheri, M. Zanardo, J. Alba-Tercedor, M. Paoletti, R. Blakemore, C. Csuzdi, L. Dorigo, A. Dreon, and F. Gavinelli, "Correction: Barcoding *Eophila crodabepis* sp. nov. (Annelida, Oligochaeta, Lumbricidae), a Large Stripy Earthworm from Alpine Foothills of Northeastern Italy Similar to *Eophila tellinii* (Rosa, 1888)," *PLoS One*, vol. 11, no. 8, pp. 1–2, Aug. 2016.
- [11] M. G. Paoletti, R. J. Blakemore, C. Csuzdi, L. Dorigo, A. L. Dreon, F. Gavinelli, F. Lazzarini, N. Manno, E. Moretto, D. Porco, E. Ruzzier, V. Toniello, A. Squartini, G. Concheri, M. Zanardo, and J. Alba-Tercedor, "Barcoding *Eophila crodabepis* sp. nov. (Annelida, Oligochaeta, Lumbricidae), a Large Stripy Earthworm from Alpine Foothills of Northeastern Italy Similar to *Eophila tellinii* (Rosa, 1888)," *PLoS One*, vol. 11, no. 3, p. e0151799, 2016.
- [12] J. Alba-Tercedor and I. Sánchez Almazo, "The use of micro-CT for the study of eggs and development in insects : a comparison of two microtomographs," *Microsc. Anal.*, no. March, pp. 7–10, 2014.
- [13] J. Alba-Tercedor, "Study of the anatomy of the common housefly *Musca domestica* Linnaeus, 1758 (Insecta: Diptera, Muscidae) scanned with the Skyscan 1172 high resolution micro-CT," *Bruker Micro-CT Users Meet. 2013*, pp. 275–289, 2013.
- [14] J. Alba-Tercedor and I. Sánchez Almazo, "Looking beyond the small: micro-CT study of eggs and development in insects: comparison of the results obtained with the Skyscan 1172 and the attachment for SEM microtomographs," in *Bruker Micro-CT Users Meeting 2013*, 2013, pp. 102–110.
- [15] J. Alba-Tercedor and L. Sánchez-Tocino, "High-Resolution Micro-CT of the Anatomy of the Sea Slug *Polycera quadrilineata*," *Microscopy and Analysis*, vol. 26, no. 1, pp. 17–19, 2012.
- [16] J. Alba-Tercedor, "Studying the anatomy of wet specimens of mayflies of the genus *Baetis* (Insecta : Ephemeroptera) by scanning them into a liquid with the Skyscan 1172 high resolution micro-CT," *SkyScan Micro-CT Users Meet. 2012*, pp. 192–195, 2012.
- [17] J. Alba-Tercedor and C. E. Sáinz-Cantero Caparrós, "Volume rendering reconstructions of the anatomy of small aquatic beetles (Insecta : Coleoptera) scanned with the Skyscan 1172 high resolution micro-CT," in *SkyScan Micro-CT Users Meeting 2012*, 2012, pp. 75–84.
- [18] J. Alba-Tercedor and L. Sánchez-Tocino, "High-Resolution Micro-CT of the Anatomy of the Sea Slug *Polycera quadrilineata*," *Microsc. Anal.*, vol. 26, no. 1, pp. 17–18, 2012.
- [19] J. R. Verdú, J. Alba-Tercedor, and M. Jiménez-Manrique, "Evidence of different thermoregulatory mechanisms between two sympatric *Scarabaeus* species using infrared thermography and micro-computer tomography.," *PLoS One*, vol. 7, no. 3, p. e33914, Jan. 2012.
- [20] J. Alba-Tercedor, M. Sáinz-Bariáin, and C. Zamora-Muñoz, "Using micro-CT to elucidate the pupal case architecture as a survival strategy of a caddisfly," in *Bruker Micro-CT Users Meeting 2015*, 2015, pp. 163–172.
- [21] J. Alba-Tercedor, *Micro-CT study of the anatomy of the nymph of the mayfly species Prosopistoma pennigerum*. <http://www.youtube.com/watch?v=-rGBsC5iNDw>, 2012.
- [22] J. Alba-Tercedor, *3D micro-CT study of the anatomy of the nymph of the mayfly Baetis alpinus*. <http://www.youtube.com/watch?v=TfSAhrDnt5E>, 2012.
- [23] J. Alba-Tercedor, M. Comas, S. Reguera, F. J. Zamora-Camacho, and J. M. Pleguezuelos, "How micro-CT can help zoologists to determine the age of reptiles," in *Bruker Micro-CT Users Meeting 2013*, 2013, pp. 219–223.

- [24] J. Alba-Tercedor and C. E. Sáinz-Cantero Caparrós, "Studying Aquatic Insects Anatomy with the SkyScan 1172 high-resolution micro-CT," in *SkyScan User Meeting 2010*, 2010, p. 2: 8-11.
- [25] J. Alba-Tercedor and L. Sánchez-Tocino, "The use of the SkyScan 1172 high-resolution micro-CT to elucidate if the spicules of the ' sea slugs ' (Mollusca : Nudibranchia , Opisthobranchia) have a structural or a defensive function," in *SkyScan Micro-CT User Meeting 2011*, 2011, pp. 113–121.
- [26] R. E. Snodgrass, *Anatomy of the Honeybee*, vol. 18. Washington: Government Printing Office, 1910.
- [27] D. Flanagan and A. R. Mercer, "AN ATLAS AND 3-D RECONSTRUCTION OF THE ANTENNAL LOBES IN THE WORKER HONEY BEE, APIS MELLIFERA L. (HYMENOPTERA @BULLET APIDAE)," *Int. J. InsectMorphol. Embryol*, vol. 183, no. 2, pp. 145–159, 1989.
- [28] M. K. Greco, J. Tong, M. Soleimani, D. Bell, and M. O. Schäfer, "Imaging live bee brains using minimally-invasive diagnostic radioentomology.," *J. Insect Sci.*, vol. 12, p. 89, Jan. 2012.
- [29] D. S. Porto, G. A. R. de Melo, and E. A. B. de Almeida, *Clearing and dissecting insects for internal skeletal morphological research with particular reference to bees*. 2015.
- [30] W. Ribi, T. J. Senden, A. Sakellariou, A. Limaye, and S. Zhang, "Imaging honey bee brain anatomy with micro-X-ray-computed tomography," *J. Neurosci. Methods*, vol. 171, no. 1, pp. 93–97, 2008.
- [31] J. Rybak and R. Menzel, "Anatomy of the Mushroom Bodies in the Honey Bee Brain: The Neuronal Connections of the Alpha-lobe," *J. Comp. Neurol.*, vol. 334, pp. 444–465, 1993.
- [32] J. Rybak, A. Kuß, H. Lamecker, S. Zachow, H.-C. Hege, M. Lienhard, J. Singer, K. Neubert, and R. Menzel, "The Digital Bee Brain: Integrating and Managing Neurons in a Common 3D Reference System," *Front. Syst. Neurosci.*, vol. 4, article, no. July, pp. 1–15, 2010.
- [33] D. B. Smith, G. Bernhardt, N. E. Raine, R. L. Abel, D. Sykes, F. Ahmed, I. Pedroso, and R. J. Gill, "SUPPLEMENTARY INFORMATION Exploring miniature insect brains using micro-CT scanning techniques," *Sci. Rep.*, vol. 6, p. 21768, 2016.
- [34] D. B. Smith, G. Bernhardt, N. E. Raine, R. L. Abel, D. Sykes, F. Ahmed, I. Pedroso, and R. J. Gill, "Exploring miniature insect brains using micro-CT scanning techniques," *Sci. Rep.*, vol. 6, p. 21768, Feb. 2016.
- [35] Amira, "3D Visualization and Analysis Software." v. 6.2. FEI, Hillsboro, Oregon, USA, 2016.



Experimental analyses by X-ray μ -CT for the study of the effects of firing temperature on the ceramic body morphology

G. Ricci¹, A.M. Kulkov², M.A. Kulkova³, E. Zendri¹,

¹ Ca' Foscari University of Venice, Department of DAIS, Via Torino 155, 30174 Venezia-Mestre, Italy

² SPbSU, Uljanovskaja st.1, SPb, Russia

³ Herzen State Pedagogical University, Moika emb. 48, SPb, Russia

Aims

This work proposes a new analysis procedure by the use of X-ray Micro Computed Tomography (μ -CT) aiming to study the effects of firing conditions on the final features of ceramic materials in order to distinguish the influences of the production techniques.

Recent results on archaeological and art materials by the innovative and non-destructive X-ray μ -CT show promising results in Cultural Heritage field. This technique offers the advantages to provide information by images of the inner part of the object preserving its integrity [1]–[3].

Ceramics are complex objects, rich source of information and constitute a large part of the staple memory of past and present human activities. The study of this material is essential in order to thoroughly understand the materiality of historical events and their echo in the present. Archaeometric research on potteries are focused on studying their production techniques, provenance, age, usage and conservation state. In order to contribute in these issues, scientific analyses on ceramic materials, able to provide the characterisation of the chemical and morphological features of the artefacts which are connected to production aspects, are forcefully involved. Chemical and mineralogical composition, particle packing, porosity, microstructure, as well as morphology of ceramic matrix are correlated to native material composition and firing temperature [4], [5].

This research work presents the innovative results obtained investigating the physical properties, such as the total porosity (close and open porosity) of the ceramic materials by X-ray μ -CT. The investigation by means of μ -CT of micro-structural characteristics of ancient ceramics is of particular interest in archaeometry and a few works were found in literature aiming at determining production technology and use of pottery by studying the present inclusions [1], [6].

Laboratory-made raw ceramic materials and Early Medieval potteries coming from the archaeological site of Torcello, in the Venetian Lagoon, have been considered and analysed. The research was performed at first by studying the relationship between raw material composition, firing temperatures and the final chemical-physical features of raw ceramic samples *ad hoc* made in laboratory, following traditional methods and using three kinds of raw clay materials and different firing temperatures (between 400° and 1000°C). Subsequently, archaeological potteries from Torcello, one of the first settled islands on the northern Venetian lagoon, were selected as interesting case studies.

These samples were investigated by chemical, mineralogical and morphological points of view, with particular regard to the porosity of ceramic mixture, which was proved to have a key role to understand its structural parameters, material composition and firing temperature [7], [8].

Method

The lab-made ceramic samples and those coming from the archaeological site in Torcello island were scanned using the nano-CT scanner SkyScan 2011 device of the “Geomodel”

Research Centrum of Saint-Petersburg University with a beam energy of 50 kV, a current of 200 μ A and performing a 180° rotation with a step size of 0.25°.

Elaboration and visualization of images were performed by CTvox and CTan programs, and the percentage of the voids as a function of pore size in the range between 1 to 100 μ m of the analysed samples was calculated.

The chemical-mineralogical composition of ceramics was determined by Scanning Electron Microscope (SEM-EDX), X-ray Diffraction (XRD) and Fourier-Transform Infrared Spectroscopy (FT-IR) analyses. Furthermore, μ -CT investigation and results were compared and integrated with those obtained by traditional methods such as Mercury Intrusion Porosimetry (MIP), which provides information regarding the open porosity of meso and macro pores (pore size range between 0.003–20 μ m), and SEM images for morphological and microstructural considerations.

Results

Archaeological potteries (1154_10, 1159_2, 1210_1 and 1151_5 samples) and the lab-made raw ceramics of three pastes (LS, S and G) at room-temperature (unfired, T0) and those fired at 400°C (T1), 700°C (T4), 900°C (T6) and 1000°C (T7), were analysed. Morphological and microstructural changes were quantified carrying on porosity studies by means of MIP and μ -CT.

Total porosity measured by μ -CT (Fig.1-2) of LS and G pastes, fired at different temperatures, increases at 700°C and decreases at 900°-1000°C. The reduction of total porosity at higher temperatures may be in accordance to the morphological observations made on the basis of SEM images (Fig.3), where the samples fired at high temperature (900° and 1000°C) have a more compact aspect than that one related to samples fired at lower temperature (400° and 700°C).

In the case of S samples, μ -CT results emphasizes the variations which occur in the matrix at 700°C and 1000°C, suggesting that the reactions of dehydroxilation of clay minerals and the beginning of silicate melting strongly affect the microstructure of the raw ceramic samples.

Archaeological samples as 1154_10 and 1159_2 exhibit lower total porosity than 1210_1 and 1151_5 sherds. These last two sherds with higher total porosity are those including secondary calcite, while the first two with lower total porosity include primary calcite, both detected by FT-IR investigations. As it is shown in Fig.4, MIP and μ -CT results seems to have opposite trends for the 1154_10, 1159_2, 1210_1 and 1151_5 samples. Probably the secondary calcite has been formed by precipitation process after burial period, suggesting that secondary calcite tends to reform in smaller pores. These consideration may explain the low open porosity calculated by MIP, which analyses meso and macro open pores, and the high total porosity obtained by μ -CT, which allows to investigate total porosity between 1 to 100 μ m. The lower total porosity measured by tomographic analyses of 1154_10 and 1159_2 sherds are in agreement with the morphological observations which suggested higher densification stage and firing temperature (800-850°C).

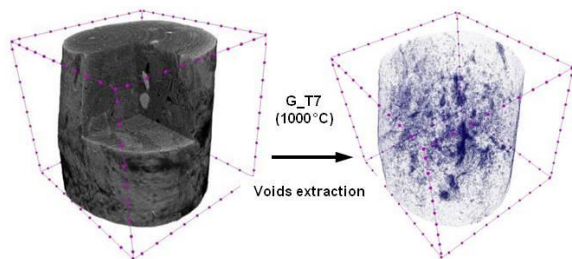


Figure 1: μ -CT viewings of a raw ceramic sample (G_T7, fired at 1000°C).

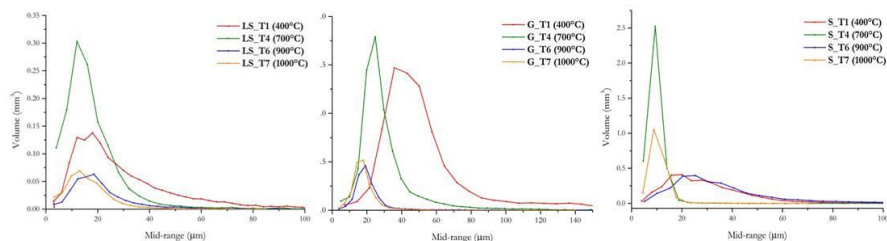


Figure 2: Pore volume vs pore radius calculated by μ -CT of lab-made raw ceramic specimens.

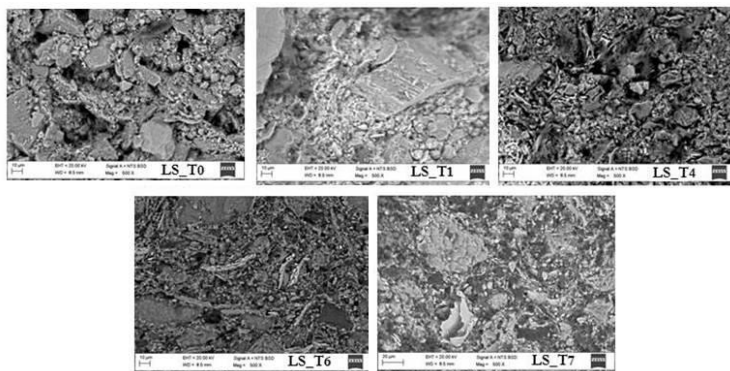


Figure 3: SEM micrographs of polished cross-sections of raw ceramic samples (LS) unfired and fired at different temperatures. SEM images show a more densification stage at higher temperatures.

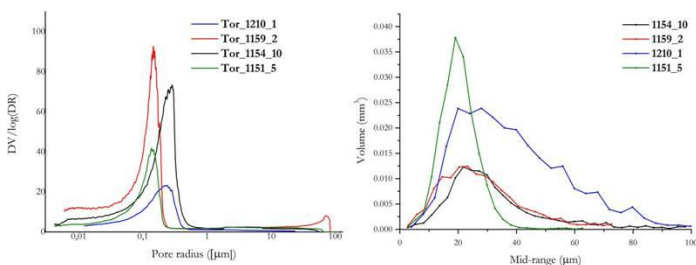


Figure 4: On the left: pore size distribution curves of open pores of the analysed sherds from Torcello measured by MIP. On the right: total pore volume vs pore radius calculated by μ -CT of selected Torcello samples.

Conclusion

The interesting and promising porosimetry results obtained by μ -CT are connected to both firing temperature and mineralogical composition of the potteries. Tomographic results brought out the different behaviour of the porosity considering both open and closed pores and greater

pore radius, opening new insights in considering the influence of the closed porosity that needs to be studied for a complete awareness of the ceramic material features.

The results obtained encourage the application of X-ray μ -CT allowing the implementation of the data obtained by MIP and SEM in a non-destructive way, offering the possibility of obtaining imaging of the microstructure and pore distribution and more specifically to investigate the role of close porosity on the material microstructure and the porosity behaviour during the firing processes.

References:

- [1] M. A. Kulkova and A. M. Kulkov, "Investigations of Early Neolithic ceramics from Eastern Europe by X-Ray microtomography and petrography," in *Bruker Micro-CT User Meeting 2014*, 2014, pp. 30–37.
- [2] M. P. Morigi, F. Casali, M. Bettuzzi, D. Bianconi, R. Brancaccio, S. Cornacchia, a. Pasini, a. Rossi, a. Aldrovandi, and D. Cauzzi, "CT investigation of two paintings on wood tables by Gentile da Fabriano," *Nucl. Instruments Methods Phys. Res. Sect. A Accel. Spectrometers, Detect. Assoc. Equip.*, vol. 580, no. 1, pp. 735–738, Sep. 2007.
- [3] F. Casali, "X-Ray digital radiography and computed tomography for cultural heritage," *Archeometriai Műhely*, vol. 1, pp. 24–28, 2006.
- [4] M. Riccardi, B. Messiga, and P. Duminuco, "An approach to the dynamics of clay firing," *Appl. Clay Sci.*, vol. 15, pp. 393–409, 1999.
- [5] G. Dal Sasso, L. Maritan, S. Salvatori, C. Mazzoli, and G. Artioli, "Discriminating pottery production by image analysis: a case study of Mesolithic and Neolithic pottery from Al Khiday (Khartoum, Sudan)," *J. Archaeol. Sci.*, vol. 46, pp. 125–143, Jun. 2014.
- [6] L. Jacobson, F. C. de Beer, and R. Nshimirimana, "Tomography imaging of South African archaeological and heritage stone and pottery objects," *Nucl. Instruments Methods Phys. Res. Sect. A Accel. Spectrometers, Detect. Assoc. Equip.*, vol. 651, no. 1, pp. 240–243, Sep. 2011.
- [7] G. Cultrone, E. Sebastián, K. Elert, M. J. de la Torre, O. Cazalla, and C. Rodriguez–Navarro, "Influence of mineralogy and firing temperature on the porosity of bricks," *J. Eur. Ceram. Soc.*, vol. 24, no. 3, pp. 547–564, Mar. 2004.
- [8] M. M. Jordan, M. A. Montero, S. Meseguer, and T. Sanfeliu, "Influence of firing temperature and mineralogical composition on bending strength and porosity of ceramic tile bodies," *Appl. Clay Sci.*, vol. 42, no. 1–2, pp. 266–271, Dec. 2008.

Solving the Challenges of Submicron MicroCT (NanoCT) for Delicate samples.

Dane Gerneke¹, Candace Lang², Nazanin Ebrahimi¹ Alexander Dixon¹.

¹Auckland Bioengineering Institute, 70 Symonds Street, Auckland 1010, New Zealand

² Engineering, Macquarie University, Balaclava Road, North Ryde NSW 2109, Australia.

Aims

Current bench top microCT instrumentation (CT) is able to image samples at sub-micron pixel resolution. This allows ever-finer 3D details to be acquired in a non-destructive manner from both dry and fully hydrated samples. Realizing sub-micron pixel resolution in soft tissues, however, brings added challenges for accurate 3D reconstruction. The hours required to collect the large number of individual x-ray projections for reconstruction requires great stability of both the source and sample, particularly at high magnifications. To achieve the 350 nm pixel resolution in the case of a SkyScan 1272, the sample is placed 12 mm from the source. The total energy dose, to which samples are exposed when close to the source, is however often neglected. A simple method to assist in successful imaging at sub-micron pixel resolution is proposed.

Method

In CT, magnification is the geometrical relationship of source to sample and source to camera. Positioning the sample very close to the source and the camera far away gives the greatest magnification and thus the smallest pixel resolution.

INSTRUMENT	PIXEL RESOLUTION - μm				
	0.35	0.4	0.5	1.0	5.0
1272	12 mm	15mm	18mm	37mm	*45 to 150mm
1172	-	-	21mm	39mm	121mm

* Camera position: close to far.

Table 1. Source to sample distances.

Small biological tissues samples are extremely delicate and dry out very quickly. Mounting in a dissimilar amorphous supporting medium (fat) was found to be an advantageous method to support this type of sample without damage when imaging. Nevertheless a stained rat embryo mounted in palm fat (MP 27 °C) in a 2 mm diameter straw was not stable as the mounting medium had softened considerably by the end of a 2.5 hour scan at 1.0 μm pixel resolution. Tempered cocoa butter (MP 37 °C) was then tested as a mounting medium which improved the sample stability but still partly softened when scanning at 0.5 μm pixel resolution. The visual difference of heat on mounting media is illustrated in fig 1. Cocoa butter tube on the right and palm fat on the left, which becomes more translucent when heated.

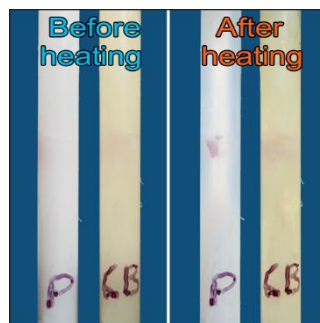


Fig 1. Softening of mounting medium

Calculating, or determining, heating caused by x-ray ionizing interaction would be difficult and complex and would have to be on a specimen to specimen basis. It is felt the ionization effect of x-rays is not a substantial factor in heating tiny samples¹ although beam damage in the form of bond breaking is known to occur in synchrotron imaging². It is more likely heating comes from the generation of x-rays in the source as 1% of the input energy generates x-rays whereas 99% is lost to heat³ even if microfocus sources have the advantage of radial heat transfer⁴. Moving from a pixel resolution of 1 μm to 0.5 μm requires halving the source-sample distance but this quadruples any radiant heat load on the sample from the x-ray source. Heating causes drying and dimensional changes in delicate samples. Furthermore, small volumes and low mass samples have limited capacity to absorb radiated energy without a rise of temperature.

To better understand radiant heating effects on samples from a heat source, bench experiments were carried out using a 10 W halogen lamp at 7.5 V. This source is not intended to be equivalent to heat output from the x-ray microfocus source. Changes of temperature were measured in an air-filled 2 mm diameter straw at 1 minute intervals from 37 mm to 12 mm (Fig 2). There is relatively minimal temperature change until 17 mm from the heat source is reached where a distinct increase is noted. At 12 mm from the source, a sharp increase occurred. In the Bruker Skyscan 1272 a 37 mm distance corresponds to 1 μm pixel resolution and 12 mm to 0.35 μm pixel resolution. Samples which have a greater thermal heat capacity will take longer to reach a stable temperature than if measured in air.

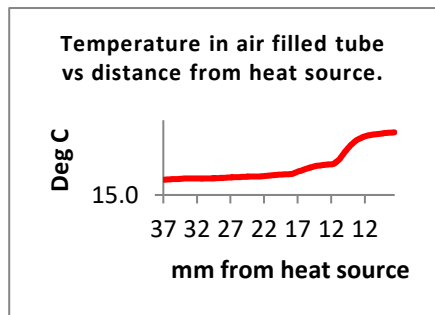


Fig 2. Temperature vs. distance.

Furthermore the percentage of the 39 degree incident x-ray beam the sample is exposed to increases as the sample moves closer to the source. To illustrate this, taking the area that filled the field of view at 1 μm pixel resolution (4.9 x 3.2 mm), and calculating the percentage of the beam irradiating this same area at smaller pixel resolutions the following numbers were obtained. At 1 μm = 3.0%, 0.5 μm = 12.1 % and 0.35 μm = 24.6% of the beam (Fig 3a). There is a substantial increase in area of the beam impinging on the sample as the source to sample distance decreases. The graph (Fig 3b) clearly shows how significant this factor becomes below 1 μm pixel resolution.

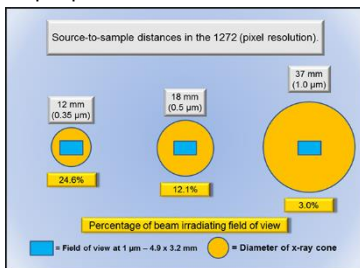


Fig 3a. Percentage of the x-ray cone a unit area is exposed to for 1272.

■ = Unit area. ● = Diameter cone.

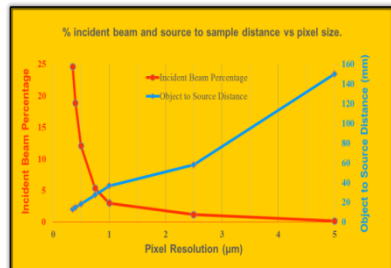


Fig 3b. Incident beam vs. source-sample distance vs. pixel size for 1272.

Cooling the sample by means of a cold stage, or modifying the instrument to provide cooling air, are costly and could limit the sample distance to the source thus becoming problematic for work at sub-micron pixel resolutions. Mounting the sample in a medium that has greater heat capacity is certainly an option as has been shown. Nevertheless this proved not to work consistently as the heat flux could still be too great when working below 1.0 μm pixel resolution.

Self-adhesive Mylar tape reflects light & heat⁵ and is transparent to low energy x-rays. Wrapping tape around the sample tube and repeating the temperature vs. distance experiment limited the rate of temperature rise & peak temperature observed (Fig 4). The rate of cooling when removed from the heat source suggests the 20 μm aluminum layer of the Mylar tape is also acting as a heat sink as it has high thermal diffusivity thus dissipating heat away from the zone being heated by the source.

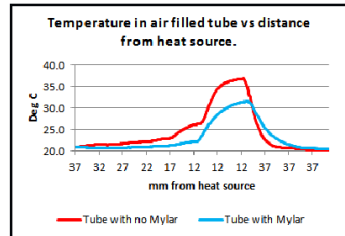


Fig 4. Heating in a tube – No Mylar® vs. Mylar® covered.

Results

As an example a 10.5 day old rat embryo, fixed in 4 % PFA in PBS for 30 hours and stained with 0.3% PTA in 70 % ethanol for 43 hours, was mounted using tempered cocoa butter in a 2 mm diameter straw. It was initially imaged with two layers of Mylar® tape around the outside of the straw in a Bruker SkyScan 1272 at 0.45 μm pixel resolution (Plate 1).

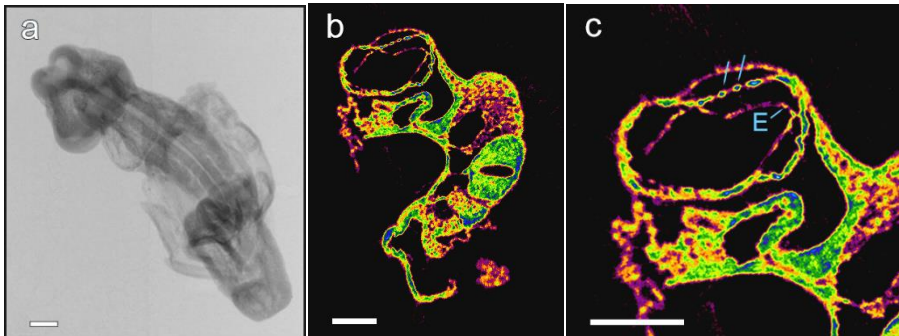
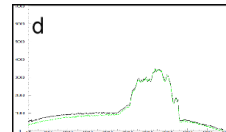


Plate 1.

Projection image (embryo length = 1.5 mm). (b) Trans-axial reconstruction in heart area. (c) Heart area enlarged. Excellent resolving of fine structures (arrowed), in particular, the single cell layer of forming endocardium. (E). (d) Good alignment profile.

Scale bar = 100 μm .



The Mylar® tape was then removed and the sample imaged again using the same parameters. A 4 layer Aluminum foil filter was placed in front of the camera to approximate the filtration by the Mylar tape. Images were recorded at the beginning and end of the scan to

monitor sample movement. Initially the reconstructed trans-axial plane appears to be acceptable however on detailed inspection there is reduced resolution and quality (Plate 2).

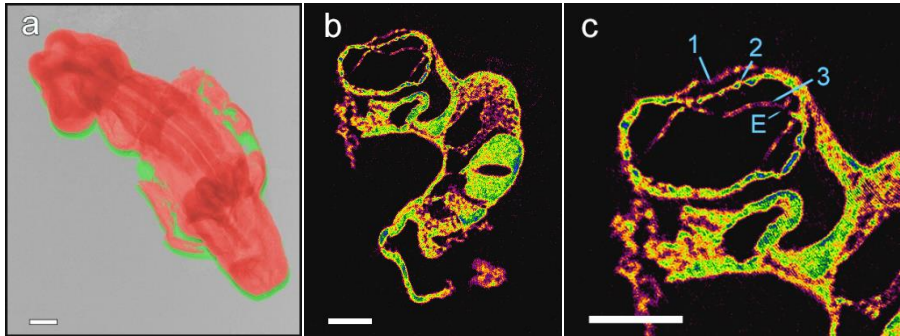
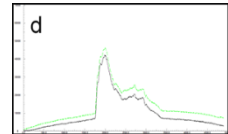


Plate 2.

(a) Overlay of start and finish projection images to show 27 μm sample movement during the 2.5 hour scan. Green = start. Red = end. (b) Trans-axial reconstruction. (c) Enlarged area: 1. Collapsed amniotic sac. 2. Reduce sharpness. 3. Forming endocardium layer appears thicker. (d) Poor alignment profile. There is a distinct loss of fine structural detail. Scale bar = 100 μm .



Visualizing in 3D the dataset obtained with the sample in a Mylar covered straw illustrates the structural elements of an embryo.

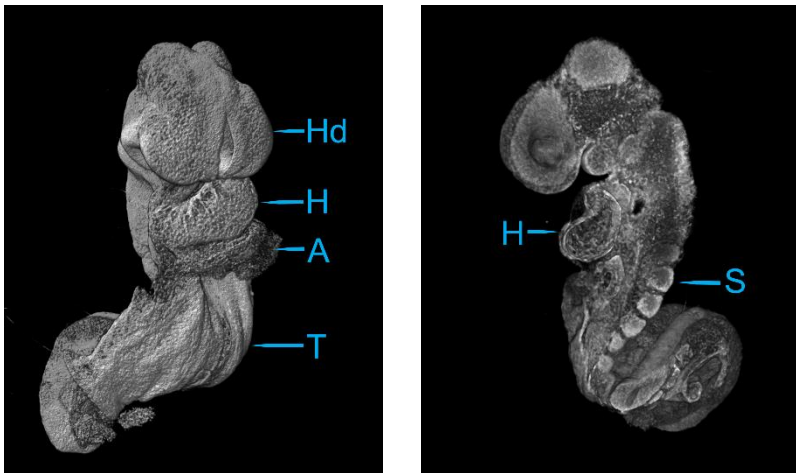


Plate 3.

3D visualization. (a) Anatomy: Hd-Head, H-heart, A-amniotic sac, T-tail, (b) Planar cutaway to show internal structure. S-somite. Length of embryo = 1.5 mm.

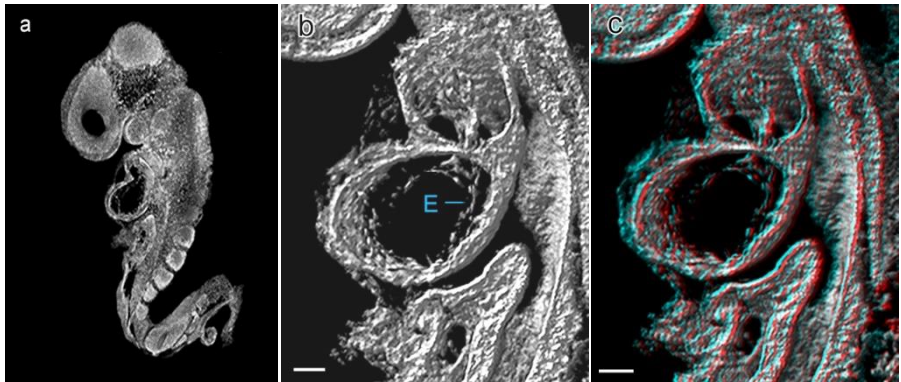


Plate 4.

(a) An effective 3D thin slice in the area of heart. (b) Enlargement showing single cell layer of forming endocardium- E. (c) To fully appreciate the fine level of detail achieved, viewing the stereo image using red – green stereo glasses is required. Scale = 25 µm.

Conclusion

In this study, we show that the temperature rise in a sample will be dependent on the heat capacity of the sample plus mounting medium, as well as the specific heat capacity, heat load and ionization cross-section from impinging x-rays. The heat capacity of an object is more or less proportional to its size, or mass, and a characteristic of the material known as the specific heat. Simply stated, the heat load on the sample is the sum of the fraction of the beam impinging on the sample, the distance from the source and the power of the source to which is added the exposure time. Work in progress is to develop continuous recording of sample temperatures in the MicroCT instruments.

We have shown that a simple, inexpensive and effective method to reduce the sample heating effects in order to obtain higher quality results at sub-micron pixel resolution of delicate samples in microCT is to wrap the outside of the sample tube with layers of Mylar tape. This reduces the unwanted radiated heat from the x-ray source which otherwise results in sample movement or change in sample shape. To successfully image at sub-micron pixel resolutions, it is not only necessary to optimize the imaging parameters: kV, mA & ms but also to select the source-to-sample distance to manage heat load. Finally, it is important to mount in a manner which increases heat dissipation, thereby increasing the stability of the sample.

References:

1. *Pers comm.* Professor Leslie Allen, Melbourne University, Melbourne, Australia.
2. Ravelli and McSweeney, "The 'fingerprint' that X-rays can leave on structures" *Structure*, 8:315-328, 2000.
3. Delfaure et al., "Nanofocus diamond x-ray windows: Thermal modeling of nano-sized heat source systems". *Diamond & related Materials* 59:104-115, 2015.
4. Flynn et al. "Microfocus X-ray sources for 3D microtomography". *Nuclear Instruments and Methods in Physics research*. 312-315. 1994.
5. Heaney. "Efficiency of aluminized mylar insulation at cryogenic temperatures". *Proc. SPIE3435, Cryogenic Optical Systems and Instruments VIII*, 150. 1998.

3D morphological characterization of polymeric microcarriers for stem cell expansion

S. de Bournonville^{1,2}, L. Geris^{1,2}, G. Kerckhofs¹

¹Prometheus, Division of Skeletal Tissue Engineering, O&N1 Herestraat 49, KU Leuven, Leuven, Belgium.

²Biomechanics Research Unit, Université de Liège, Chemin des Chevreuils, Liège, Belgium

Aims

Tissue Engineering (TE) is an interdisciplinary field aiming to provide solutions for the regeneration of organs and tissues. Many typical TE processes make use of stem cells due to their pluripotent behavior and their self-renewal capacities. The latter allows scientists to minimize the number of stem cells harvested from a donor and expand them at large scale to reach a desired amount of cells for a given therapy. In the field of large scale stem cell expansion, micro-carriers are commonly used. These are typically degradable porous or non-porous beads on which cells are seeded and expanded during culture in a spinner flask. However, one of the remaining challenges related to the use of micro-carriers for cell expansion is the limited information on their morphological characteristics provided by the manufacturers. This information is, however, crucial to improve process parameters for cell expansion, such as the cell seeding density, culture time, etc. For instance, the available surface area, on which the cells can attach, is an important property influencing the initial cell seeding density, and is highly dependent on the micro-carriers morphology (porosity, pore size, roughness, etc.), but it is rarely provided by the manufacturers. Therefore, it has been highlighted how useful a database of 3D morphological characteristics of different micro-carriers could be¹. X-ray microfocus computed tomography (microCT) could provide a solution, as it allows for non-invasive analysis of the 3D morphology of porous materials. However, most of the micro-carriers we currently use are polymeric and they should be characterized in wet state to obtain the proper morphometric characteristics. Since there is no or negligible image contrast difference between the micro-carriers and the surrounding liquid when they are in wet state, in this study we propose the use of contrast-enhanced X-ray computed tomography (CE-CT), combined with detailed image processing and analysis, for 3D morphological characterization of polymeric micro-carriers. We will present the results for one specific type of porous micro-carrier, namely CultiSpher S, by which we highlight the added value of CE-CT combined with morphological quantification for in-depth characterization of polymeric micro-carriers.

Methods

Micro-carriers

CultiSpher STM (HyCloneTM) micro-carriers were used. These micro-carriers are based on gelatin derived from collagen to enhance cell attachment and proliferation. From the manufacturer and providers websites, the particles are claimed to be in the 130 – 380 µm diameter range (255 µm on average) in wet state. By assuming spheres with diameters in this range and taking into account the average porosity of the micro-carriers found in the current study, this information can be extrapolated to get an approximation of the average volume of the particles of around 0.068 mm³. The micro-carriers have macro-pores to increase the attachment surface of the cells, yet no information on the pore size or porosity is provided by the manufacturers.

Contrast-enhanced CT

In order to enhance the contrast of the micro-carriers, two different contrast agents were used. The commonly used and commercially available phosphotungstic acid (PTA) was compared to an in-house developed hafnium-substituted polyoxometalate compound (referred to as Hf-POM). For PTA, a concentration of 2.5% in phosphate buffered saline (PBS) was used, while for the Hf-POM a concentration of 3.5% in PBS was applied. Two staining times (30 minutes and 7 days) were compared to get a better understanding of the diffusion dynamics of these compounds through the micro-carriers.

The samples were scanned, in wet state, on a Nanotom S [GE] at 2 μ m voxel size, 75 kV, 0.1mm Al filter, 500ms exposure time, 2400 images, fast scan mode (20 min. scan time).

Morphological assessment

A global threshold using Otsu's automatic thresholding was applied to binarize the full dataset. In order to separate the micro-carriers from each other, regions of interest (ROIs) were drawn manually around each individual micro-carrier using CTAn (Bruker MicroCT). From these ROIs, each micro-carrier was represented as an individual binary dataset. On each of these datasets, a convex envelope around the micro-carrier was calculated using a 2D+ approach, written in Matlab. More specific, convex envelopes were computed along the three axes for all the slices covering the micro-carrier, and they were combined with a Boolean inclusive 'OR' operation.

Using the 3D convex envelope and with CTAn (Bruker MicroCT), 3D analysis of the micro-carrier volume, the open pore volume (pores in the micro-carrier, accessible from the outside), the closed pore volume (pores trapped inside the micro-carriers) and the porosity were calculated. From the envelope volume of each micro-carrier, the particle size was computed assuming a sphere with the same volume. This parameter is useful for comparison with the information provided by the manufacturer.

Using the ROI shrink-wrap function in CTAn with increasing stretch over holes (from 0 to 20 voxels), the throat size of the pores was calculated, which is an important parameter to determine the percentage of open internal pores that is accessible to the cells to expand. 3D renderings of the micro-carriers were done using CTVox (Bruker MicroCT).

Finally, by convoluting a 1 pixel wide cubic structural element over the micro-carrier datasets from which the closed pores were removed, the pixels that were part of the inner surface of the micro-carrier were identified (i.e. the pixels in contact with the outside void in their direct neighborhood). This way, a 1 pixel thick layer can be generated for each micro-carrier, corresponding to the surface area of the micro-carrier.

Results

Contrast agent staining

Figure 1 shows typical reconstructed cross-sections of the CultiSpher S micro-carriers, stained with the different contrast agents, and for different staining times. It is clear that there is a difference in diffusion dynamics between the two contrast agents. Indeed, the grayscale profile through PTA-stained micro-carriers showed that after 30 minutes of staining time, only the outer surface of the micro-carriers was stained. Even after 7 days of staining, PTA did not fully penetrate the micro-carriers. In contrary, Hf-POM showed much faster diffusion throughout the micro-carriers, as only 30 minutes of staining was enough to have a homogeneous staining throughout the micro-carriers.

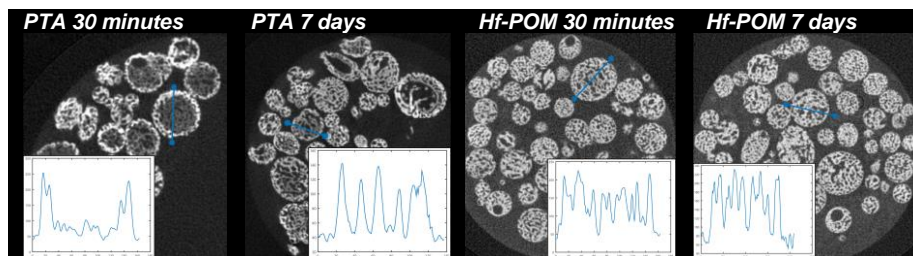


Figure 1: Typical reconstructed cross-sections of Cultispher S micro-carriers after staining using the two contrast agents (PTA and Hf-POM) and two staining times (30 minutes and 7 days). The plot in each image corresponds to the grayscale profile along the blue line across a typically stained micro-carrier, generated using DataViewer (Bruker MicroCT).

Morphometrical characterizations

Figure 2 shows 3D renderings of a CE-CT dataset of 128 micro-carriers stained for 7 days with Hf-POM. Different grey-scales were assigned for each individual micro-carrier.

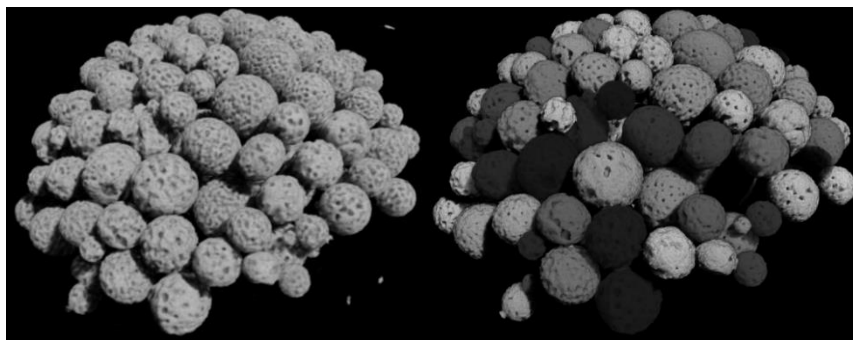


Figure 2: 3D visualization of Cultispher-S (Sigma Aldrich ©) micro-carriers from CE-CT scans (7 days Hf-POM staining). The micro-carriers (left) were manually segmented and assigned random grayscale values (right).

The different structures of interest, computed as explained above, are shown on Figure 3, on one typical micro-carrier that was stained for 7 days with the Hf-POM. This figure qualitatively highlights the added value of 3D visualization of the micro-carriers, as their core structure can be deeply understood.

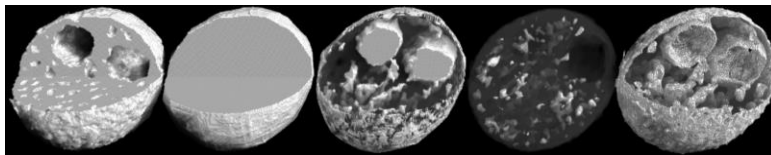


Figure 3: 3D visualization of one typical Cultispher-S and the different structures of interest. From left to right: the micro-carrier, the convex envelope of the micro-carrier, the open pores inside the micro-carrier (in dark transparent shade), the open pore network inside the micro-carrier and the opened surface area.

Figure 4 presents the CE-CT based morphometric properties of 128 Hf-POM stained micro-carriers, along with the information provided by the manufacturer. The morphometric characteristics were highly variable amongst one dataset, indicating that one micro-carrier is not the other in terms of shape, size and pore structure. However, the porosity ratio and the estimated particle size seemed to be less variable than the other parameters; the lower variation of the latter being inherently due to its estimation method with a cubic root smoothing the variation from the computed volumes. The micro-carrier volume and convex envelope volume showed a strong correlation, indicating a certain amount of consistency amongst the micro-carriers in terms of porosity, which was confirmed by the effective calculations.

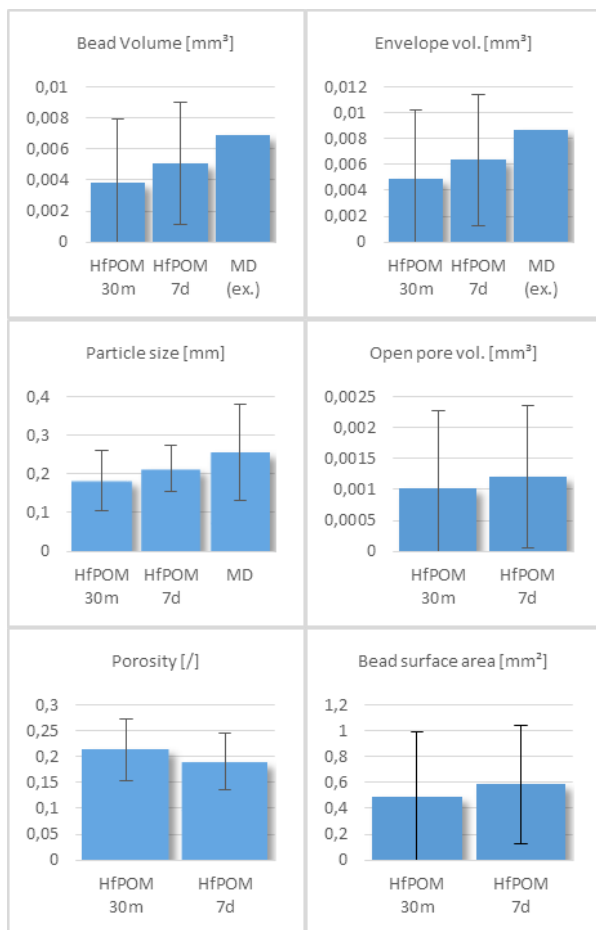


Figure 4: Average volume (top left), convex envelope volume (top middle), particle size (top right), open pore volume (bottom right), porosity (bottom middle) and surface area (bottom right) of the micro-carriers (Hf-POM stained samples, 30 min and 7 days staining), along with the provided manufacturer data (MD) or

extrapolated data (ex.). The error bars show the standard deviations among all the micro-carriers ($n = 128$) of one dataset.

The statistical distribution of each morphological property can be analyzed based on histograms. These are shown in Figure 5. The histogram distributions give a deeper understanding on the homogeneity of those properties amongst the micro-carriers. Briefly, we can see that the porosity and the particle size showed normal distributions, whereas the other properties presented more skewed distributions.

The results of the throat size analysis are shown in Figure 6 for one micro-carrier of the Hf POM, 7 days staining sample. Around 2.1% of the pores had a throat size between 0 and 4 μm , 7.3% had a throat size between 4 and 8 μm , 10.4% had a throat size between 8 and 12 μm and around 80% had a throat size about 12 μm . Therefore, given the size of the cells that are expanded with these micro-carriers, one can estimate on average which percentage of the pores is effectively accessible by the cells.

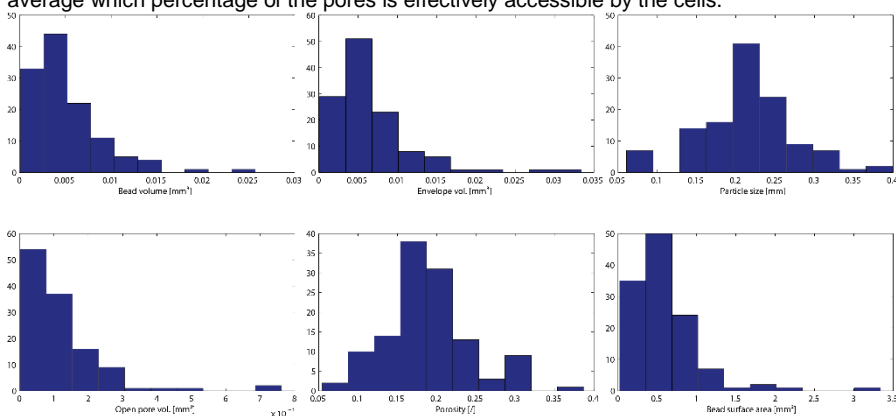


Figure 5: Histogram distributions of the volume (top left), convex envelope volume (top middle), particle size (top right), open pore volume (bottom left), porosity (bottom middle) and surface area (bottom right) of the micro-carriers (Hf-POM stained sample, 7 days staining).

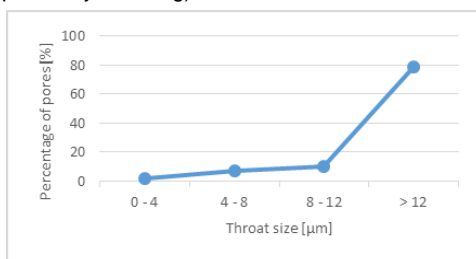


Figure 6: Throat size analysis showing the percentage of pores with a throat size below 4 μm , between 4 and 8 μm , between 8 and 12 μm and above 12 μm .

Conclusion

Using CE-CT combined with 3D image processing and analysis to characterize the morphometric properties of CultiSpher-S micro-carriers, we were able to highlight the added value of this technique for full morphological screening of polymeric micro-carriers to be used for stem cell expansion. Our novel approach allowed to generate much more information on

the 3D morphometric properties of micro-carriers than is currently available. This information is important to improve the cell expansion process using micro-carriers. We would like to highlight that the detailed morphological quantification method developed in this study can be applied to any type of polymeric micro-carrier, and is not limited to the microCT device we used. Future steps consist of developing an automatic micro-carrier separation algorithm and validating it against the manually separated data presented in this study. Moreover, other types of micro-carriers will be screened and characterized to further update the morphometric database of available micro-carriers.

References:

1. Sart, S. and Agathos, S.N., "Large-Scale Expansion and Differentiation of Mesenchymal Stem Cells in Microcarrier-Based Stirred Bioreactors.", *Methods Mol. Biol.* 1502:87-102, 2016

Micro-CT for the visualization of the mouse brain

Christos Bikis¹, Philipp Janz², Georg Schulz¹, Gabriel Schweighauser³, Jürgen Hench³, Carola A. Haas², and Bert Müller¹

¹Biomaterials Science Center, Department of Biomedical Engineering, University of Basel, Gewerbestrasse 14, 4123 Allschwil, Switzerland

²Experimental Epilepsy Research, Department of Neurosurgery, University Medical Center Freiburg, Breisacher Strasse 64, D-79106 Freiburg i. Brsg., Germany

³Institute of Pathology, Department of Neuropathology, University Hospital Basel, Schönbeinstrasse 40, 4001 Basel, Switzerland

Aims

Micro computed tomography using synchrotron radiation is a powerful method for the non-destructive visualization of biological tissue, down to true micrometer resolution, even revealing subcellular detail¹. Nevertheless, the access to synchrotron radiation facilities is limited and costly. We have thus proposed the use of a laboratory-based microCT system with an operation voltage of 40 to 60 kV for the visualization of paraffin-embedded human brain samples². In the present communication, we show that the desktop system Skyscan 1275, that can operate reliably at an accelerating voltage of 20 kV, provides an improved contrast. This allows for a time-efficient visualization of the entire mouse brain and soft tissues of other model animals of similar size.

Method

Following extraction, the mouse brain was fixed in 4 % histological-grade buffered paraformaldehyde, dehydrated in ethanol, transferred to xylene and finally embedded in a paraffin/plastic polymer mixture. Out of the obtained paraffin block, a cylindrical sample with a diameter of 8 mm was extracted, by means of a robotic drill.

For the measurements, we have used the laboratory micro-CT system Bruker Skyscan 1275. An acceleration voltage of 20 kV and a beam current of 175 μ A were selected. The effective pixel size was set to 5.5 μ m. Over a range of 360°, 1200 projections were acquired equi-angularly. At each angular position, nine images with an exposure time of 0.6 s were acquired. This resulted in a total scanning time of two hours for an entire mouse brain hemisphere. After reconstruction with the dedicated manufacturer software, the resulting dataset was imported in the VGStudio MAX 2.1 software, for visualization and 3D rendering. This software was also used for the semi-automatic segmentation of brain structures of interest (e.g. hippocampus) by means of a region-growing approach.

Results

The beneficiary effect of μ CT using photon energies below 20 keV for the visualization of nervous tissue embedded in paraffin is reflected in the quality of the acquired tomograms. Several anatomical structures of the mouse brain can be easily identified, such as the cerebral cortex, caudate putamen, corpus callosum, hippocampus, hypothalamus and thalamus. The ventricular system, as well as several vessels are also unequivocally localized (see selected images in Figure 1).

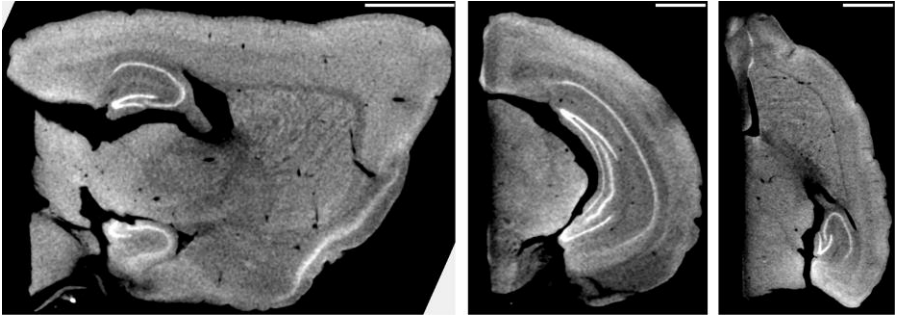


Figure 1: Sagittal, frontal, and horizontal slices of mouse brain. Scale bar: 1 mm.

The contrast of the acquired tomograms allows for the semi-automatic segmentation of specific structures, such as the ventricles, vessels, caudate putamen, and hippocampus. For the latter, see Figure 2 for the results of a region-growing segmentation approach.

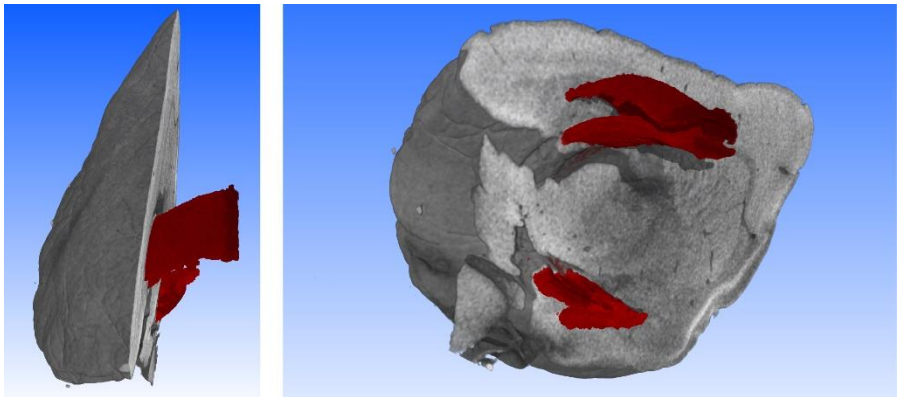


Figure 2: Three-dimensional visualization of mouse brain and segmented hippocampus (red)

Conclusion

We have previously reported the use of synchrotron-radiation double-grating interferometry for the investigation of the mouse brain³. The Bruker 1275 micro-CT desktop system yields comparable image quality for the case of paraffin-embedded brain tissue, mainly owing to photon energies below 20 keV and the paraffin embedding itself. Thanks to their ease of use, desktop size and reasonable costs, such systems are a prime candidate for complementing histology in several laboratory and clinical applications.

References:

1. S. E. Hieber et al. "Tomographic brain imaging with nucleolar detail and automatic cell counting", *Scientific Reports* 6, 32156 (2016)
2. A. Khimchenko et al. "*Extending two-dimensional histology into the third dimension through conventional micro computed tomography*", *NeuroImage* 139, 2636 (2016)
3. C. Bikis et al. "High-resolution synchrotron radiation-based phase tomography of the healthy and epileptic brain", *Proceedings of SPIE* 9967, 996706 (2016)

Swelling and drying of non-treated and treated spruce wood during and after exposure to liquid water

N. Nestle¹, A. Šandor¹, M. Žlahtič Zupanc², M. Humar², I. Serša³, U. Mikac³

¹BASF SE Advanced Materials and Systems, D-67056 Ludwigshafen, Germany,

²University of Ljubljana, Biotechnical Faculty, Dept. of Wood Science and Technology
Jamnikarjeva 101, 1000 Ljubljana, Slovenia

³Jožef Stefan Institute, Jamova 39, 1000 Ljubljana, Slovenia

Aims

Non treated wood is known to exhibit pronounced anisotropic swelling upon exposure to moisture. Furthermore, moist wood is much more susceptible to degradation by various pests such as fungi. Moisture uptake into wood can occur both from the gas phase and from liquid water. Liquid water transport into wood is especially problematic as capillary flow can effectively lead large quantities of water deep into the wood, and can results in much higher values that achieved with water vapor adsorption. This, in turn, leads to long drying times and like that long times during which the wood is susceptible to biodegradation. Furthermore, fast local water uptake may lead to macroscopic deformation of the wood and in the worst case to mechanical damage to the wooden structures.

Protection of wooden surfaces occasionally exposed to liquid water is therefore an important technical challenge. In the past, waterproof coatings were used in this context. Such coatings are effective as long as they are intact. However, any moisture ingress through even small damages will have difficulties to escape again from the wood leading to longer moisture exposure than without the protective cover. More recently, hydrophobic treatments of the wood have become more popular which aim at excluding liquid water from the wood while keeping the vapour phase transport properties for wood almost unchanged. In such a structure, liquid water won't be transported by capillary suction any more while moisture exchange via gas phase diffusion is still possible. Various hydrophobic treatments to wood are available such as impregnation with liquid oil or with wax dispersions. The aim of the present study was to visualize dimensional changes and the distribution of liquid water inside the wooden structures both during immersion into liquid water and during subsequent drying. Samples were prepared according to a protocol similar to that used in a recently conducted MRI study [2].

Method

All studies were conducted on a Bruker-Skyscan 1172 equipped with a 10 W X-ray generator with a maximum acceleration voltage of 100 kV (Hamamatsu, Hamamatsu Japan) and an 11 MPixel X-ray camera (Ximea, Münster, Germany). For all experiments, unfiltered 40 keV radiation was used. Series of usually 30 scans were conducted with a 1K data matrix. Typical scan times were in the range of 15 min for images with a voxel size of 23.8 µm. Single mages with higher resolution were performed with larger data matrices before and after the serial measurements.

The samples were cubes with 1 cm side length cut with one side aligned with tree growth rings (and thus with the axial and tangential directions of the wood, see figure 1). In order to study both water uptake and drying without changing the position of the sample, the samples (equilibrated with lab air of 50% RH at 23 °C) were glued to the bottom of a 2.2 cm diameter cylindrical PE vial by means of a cone of modelling wax. A first scan was conducted for the cube inside the empty tube. Then the cylindrical vial was filled with water until the cube was

fully immersed into the water and a first series of images was recorded to study water intrusion into the cube.

After several hours of water uptake, the water was removed as good as possible by suction into rolled pieces of paper towel. After that, the vials were left open and drying of the wood into the ventilated scanning chamber (29°C) was observed by means of another series of scans.

The recorded μ CT data sets were rotated in the Data Viewer software (Bruker Skyscan, Antwerp) to align the axes of the cube with the axes of the data set.

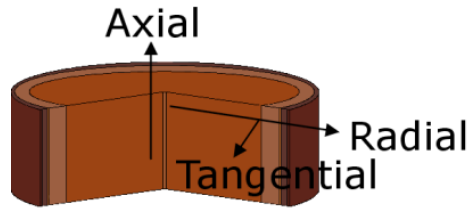


Figure 1 Terminology of the different directions in wood. Figure from [1]

Results

In figure 2, a crosshair views from the beginning and the end of the immersion series for native wood are given.

Several observations can be made from the images presented in figure 2:

- Water uptake occurs mainly along the axial direction of the wood which is oriented parallel to the y-direction in the sagittal sections given in the lower right field of the crosshair views. When comparing the coronal sections from the centre of the cube (upper left field in the crosshair views), a substantial increase in X-ray absorption can be even seen in this innermost slice of the wooden cube. The water uptake occurs mainly by capillary suction in some but not all of the wood fibers oriented along this axis.
- Almost no dimensional change occurs in the wood along this direction. By contrast, the strongest dimensional change can be seen along the tangential axis (which is positioned parallel to the x-direction in the coronal sections). Some swelling occurs also along the radial direction (parallel to y-axis in the coronal section).

The macroscopic findings are in accordance to the expectations from experience with moisture uptake in wood. The fact that not all fibers contribute to water transport in the same way is macroscopically not as easy to observe but rather obvious from the images.

In figure 3, a comparison of the crosshair views directly after removal of the water and about 8 hours later is given. The strongly X-ray absorbing structure at the bottom of the images in figure 3 A is liquid water which was not fully removed in the suction process for water removal. This water is removed due to drying after about 2,5 h. Nevertheless, drying of the wood is not yet complete after 8 h. This can be seen from the incomplete shrinkage to the cube's original dimension as well as from the presence of remaining moisture inside the wood structure.

As the intrusion of moisture is dominated by fast long-range transport by capillary processes while drying occurs mainly via diffusion of moisture in vapour state, it is not really surprising that drying is considerably slower than moisture uptake during immersion.

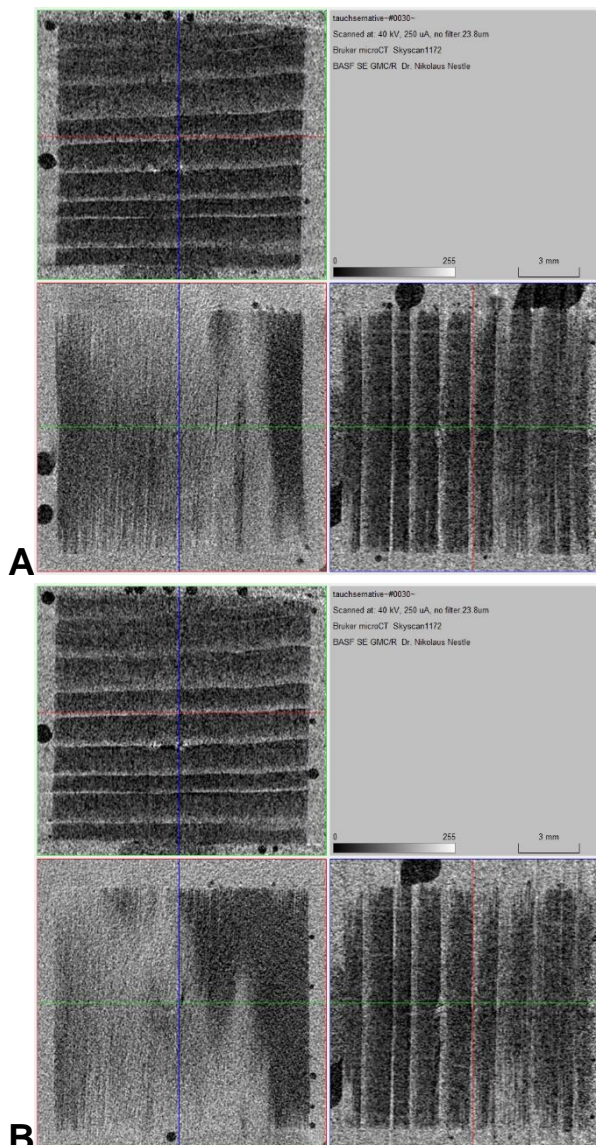


Figure 2 Crosshair views for native spruce wood (A) directly after immersion and (B) 8 h later

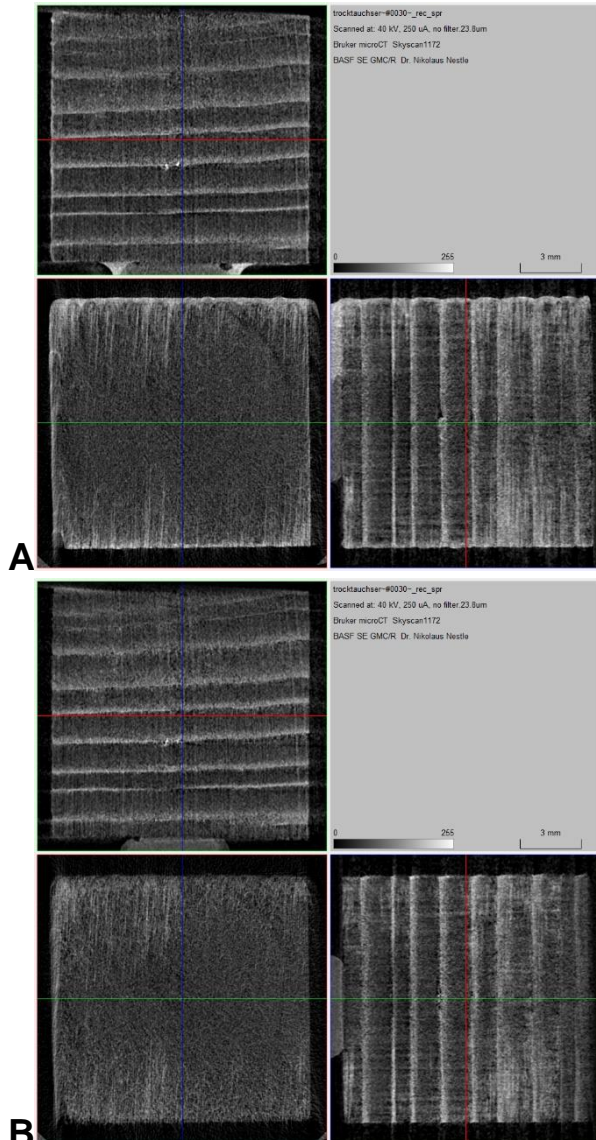


Figure 3 Crosshair views for native spruce wood (A) directly after removal of the water and (B) 8 h later

In figure 4, a wood specimen treated with a wax dispersion is shown right after immersion into water and 8 h later. In contrast to the experiments with native spruce wood, almost not water uptake and also no significant dimensional change are observed for this specimen.

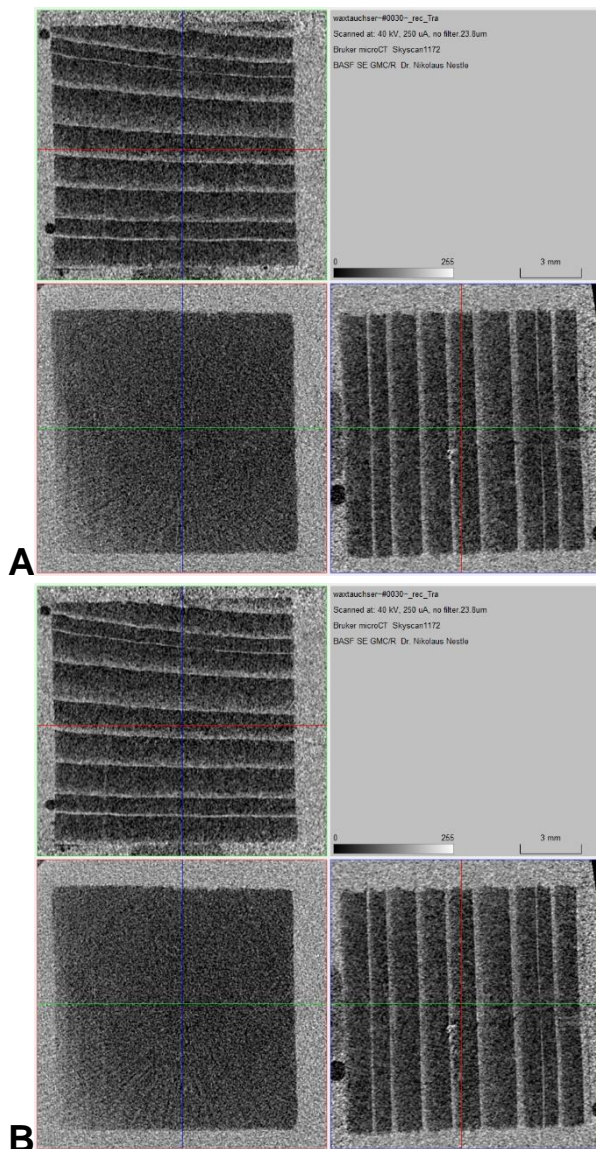


Figure 4 Crosshair views for spruce wood treated with wax dispersion (A) directly after immersion and (B) 8 h later

In figure 5, the corresponding images obtained after water removal in the drying phase are given. Again, no dimensional changes are visible. Furthermore, the presence of a mainly

superficial moisture layer with a few individual wood fibers where some moisture saturation extends partially into the sample can be seen directly after water removal. After 8 hours of drying, this superficial moisture is completely gone. As expected, no dimensional changes are observed during drying either.

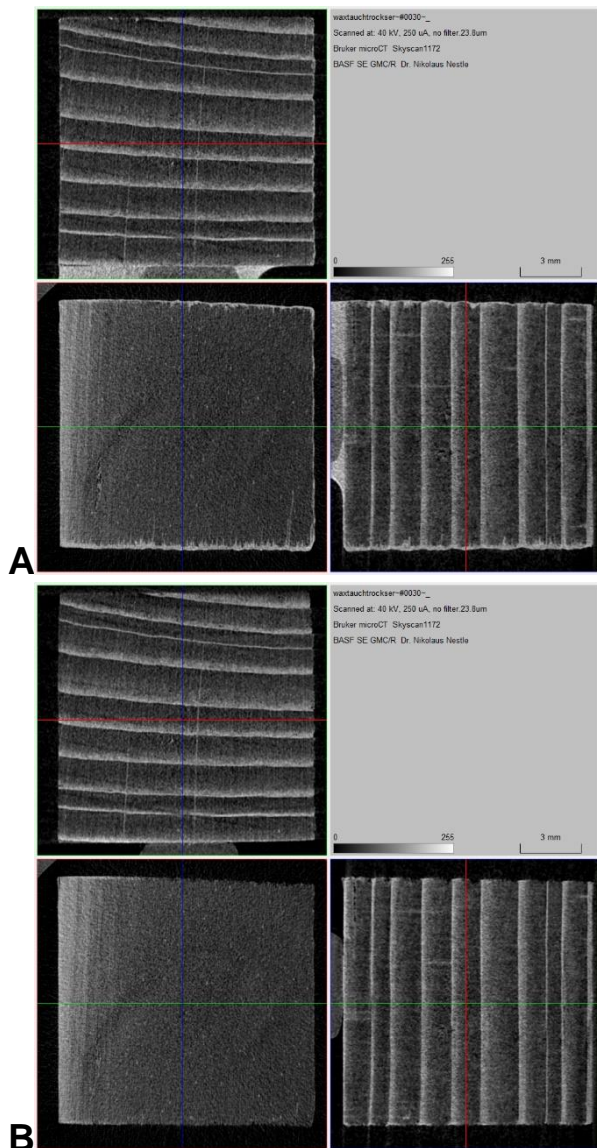


Figure 5 Crosshair views for spruce wood treated with wax dispersion (A) directly after water removal and (B) 8 h later

Conclusion

X-ray micro-CT is an excellent tool to follow the distribution of moisture in wood specimens during water immersion and subsequent drying. The spatial resolution achievable in time series of μ CT scans is sufficiently good to gain insights into processes at the level of individual wood fibres.

For untreated wood, considerable water uptake along the fibre direction is observed while almost no water transport along other directions could be seen. By contrast, considerable moisture-induced dimensional changes are observed especially in tangential direction. Drying into air of about 30% RH at 29°C occurs much slower than water ingress.

References:

1. From section "wood structure 2" on <http://www.materials.unsw.edu.au/tutorials>
U. Mikac, I. Serša, M. Žlahtič Zupanc, M. Humar, M. Merela, P. Oven "Application of MR microscopy for research in wood science" submitted to Microporous and Mesoporous Materials

POSTER PRESENTATIONS

The effect of nicotine and / or bisphosphonates on alveolar bone repair in irradiated and non-irradiated ovariectomized rats

Gina D. Roque-Torres¹; Amaro I Vespasiano Silva²; Yuri Nejaim³; Danieli Moura Brasil³, Solange Maria de Almeida Bóscolo³; Francisco Haiter Neto³, Frab Norberto Bóscolo³, Francisco Carlos Groppo³, Mario Jefferson Quirino Louzada⁵

¹Center of Dental research, Loma Linda University, USA

²Department of Oral Radiology, Pontifical Catholic University of Minas Gerais, MG, Brazil

³Department of Oral Diagnosis, State University of Campinas, SP, Brazil.

⁴. State University Paulista Júlio de Mesquita Filho, SP, Brazil

Aims

This study aimed to evaluate the effect of nicotine and / or bisphosphonates on alveolar bone repair in irradiated and non-irradiated ovariectomized rats..

Method

We selected sixty rats, aged 70 days. The animals were randomly divided into twelve groups: control, six irradiated and six non-irradiated (control of both groups and with administration of sodium alendronate, zoledronic acid, nicotine, nicotine/sodium alendronate, nicotine/zoledronic acid and nicotine/zoledronic acid. Initially, was administrated for 6 times a week Nicotine in the corresponded groups, throughout the last 15 weeks of the research, and then, at 90 days of age all being subjected to ovariectomy. Five days after this procedure were administrated in the corresponded groups, sodium alendronate and zoledronic acid, during the last 10 weeks of the research. Fifty six days after ovariectomy was performed the extraction of the mandible right first molar in all groups. Three days later, proceeded to the irradiation of the head and neck with 15 Gy in the groups intended to irradiation. The animals were sacrificed 21 days after the dental extraction. Alveolar bone repair was examined by radiographic density expressed in millimeters of aluminum and bone microarchitecture analyzed by three-dimensional parameters for evaluation of bone trabecular by microcomputed tomography. The analyzes used were two-way ANOVA and Kruskal-Wallis test.



Figures 1. Ovariectomy procedure.



Fig 2. Extraction of the mandible right first molar



Fig 3. Irradiation procedure

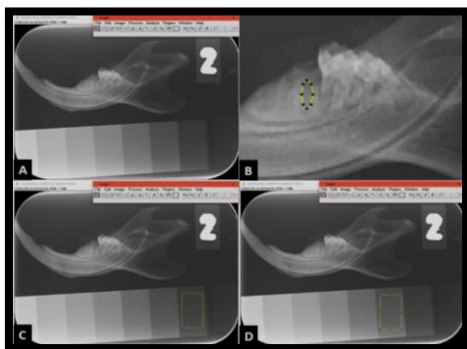


Fig 4. Radiographic bone density measured

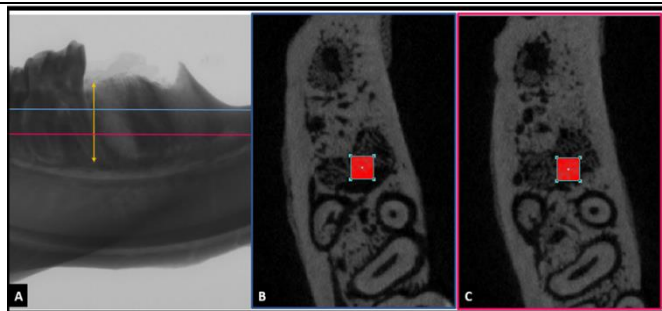
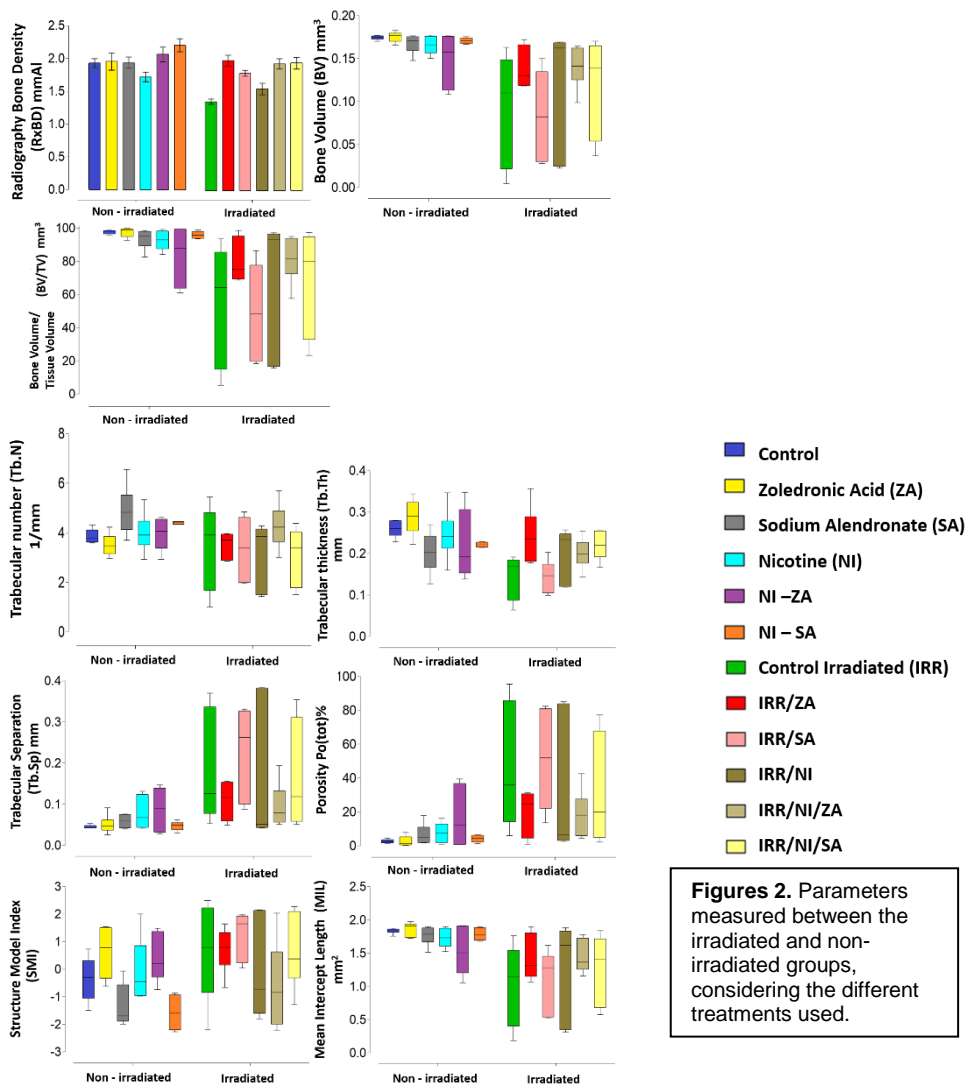
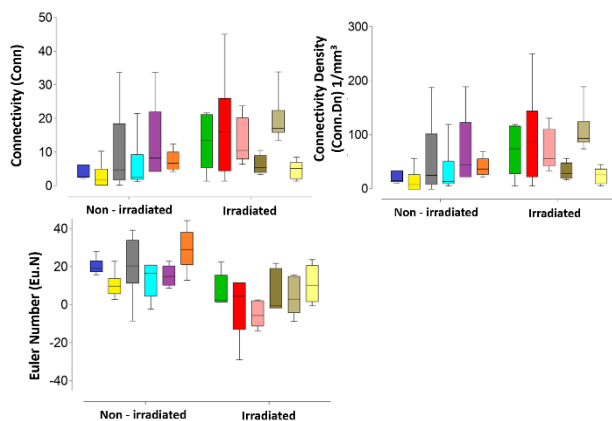


Fig 5. Microtomography measured of the distal alveolar of the mandible.

Results

Regarding the radiographic density the nicotine group and irradiated/nicotine were those that showed less density, as well as sodium alendronate and zoledronic acid significantly improved the density in the presence of nicotine and irradiation ($p < 0.05$). As for the bone microarchitecture, nicotine and irradiation affect the bone microarchitecture in all parameters ($p < 0.05$) showing deleterious effects. In the group non-irradiated/nicotine, with administration of zoledronic acid increasing parameters like bone volume, bone volume/tissue volume, connectivity and connectivity density; while with sodium alendronate increased trabecular number and both kept stable the structure model index, increased trabecular thickness and decreased trabecular separation and porosity ($p < 0.05$).





Conclusion

In these experimental conditions, it is concluded that radiation X and nicotine had a deleterious effect by the radiographic density and bone microarchitecture, and bisphosphonates have shown significant potential in the alveolar bone healing even when it were present the nicotine and radiation X.

References:

1. Parfitt A, Drezner M, Glorieux F, Kanis J, Malluche H, Meunier P, Ott S, Recker R (1987) Bone Histomorphometry : Standardization of Nomenclature, Symbols, and Units. *Journal of Bone and Mineral Research*, 2: 595-610
2. Bouxsein ML1, Boyd SK, Christiansen BA, Guldberg RE, Jepsen KJ, Müller R. Guidelines for assessment of bone microstructure in rodents using micro-computed tomography. *J Bone Miner Res*. 2010 Jul;25(7):1468-86.

Correlative imaging of the skeletal muscle vasculature by microangioCT and light microscopy

R. Hlushchuk¹, L. Schaad¹, S. Barré¹, R. Gianni-Barrera², D. Haberthür¹, A. Banfi², V. Djonov¹

¹ Institute of Anatomy, University of Bern, Bern, Switzerland

² Department of Biomedicine, University Hospital Basel, Basel, Switzerland

Background/Rationale:

The cardiovascular diseases are the leading cause of death globally. Billions of cardiovascular patients would benefit from the effective angiomodulating treatments.

The murine hind limb is a widely used model to study pro-angiogenic treatment strategies. Traditionally, the vasculature is evaluated based on histological sections, which lacks essential 3D information. A detailed vascular visualization and adequate quantification is essential for the proper assessment of novel angiomodulating strategies.

Aims

To develop an ex vivo microangioCT-based imaging approach for the 3D visualization of the entire vasculature down to the capillary level and rapid estimation of the vascular volume and vessel size distribution. Moreover, it should be suitable for the successive morphological analysis using light or transmission electron microscopy.

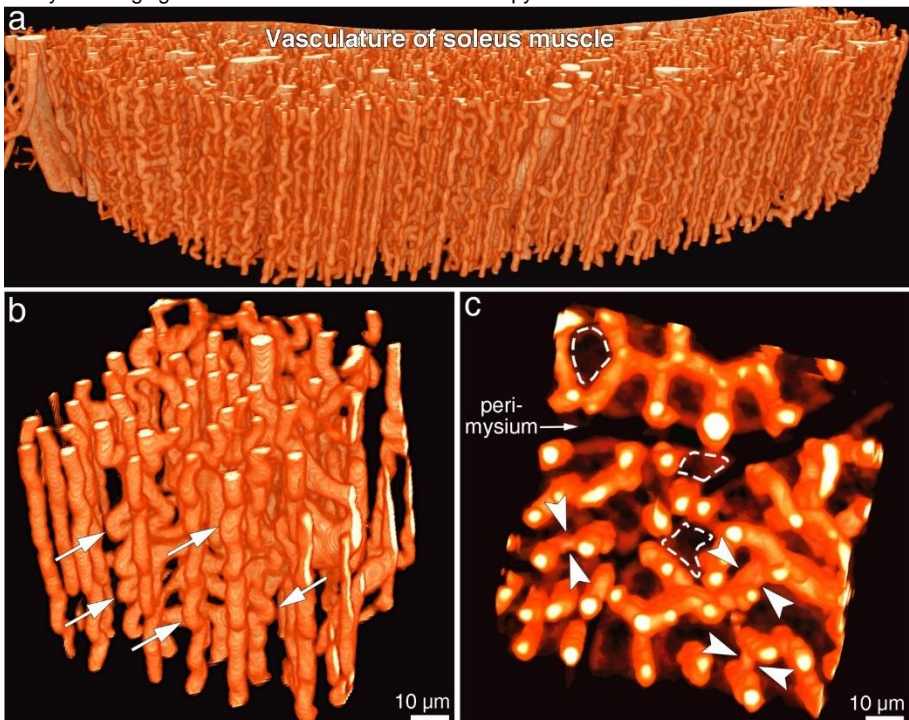


Fig. 1 Microangio-CT of the vasculature of the skeletal muscle. Panel a: overview of the 500µm-thick slice of the murine soleus muscle. Panel b and c represent a subvolume of the volume in a: the capillaries

with their connections and tortuosity are clearly and unambiguously visualized (arrows, panel **b**). In panel **c** the perimysium as well as borders of the single muscle fiber cells can be easily recognized (*dashed line*).

Method/Results

A correlative imaging approach comprising two microCT scanning modalities followed by histology was introduced. After the perfusion with μ Angiofil®, a novel polymerizing contrast agent, low- and high-resolution scans (Skyscan 1272; voxel side length: 2.58-0.66 μ m) of the entire vasculature were acquired. In a second step, samples were dehydrated and rescanned to delineate the muscle fiber architecture. Based on the microCT data, sites of interest were defined and samples further processed for correlative morphology (Fig. 2). The solidified μ Angiofil® remained in the vasculature and its autofluorescence allowed co-registering the histological sections with the corresponding microCT-stacks.

The perfusion efficiency of μ Angiofil® was validated based on lectin-stained histological sections: $98\pm0.5\%$ of the total blood vessels were μ Angiofil®-positive, whereas $93\pm2.6\%$ were lectin-positive.

By applying this approach we analyzed the angiogenesis induced by cell-based delivery of a controlled VEGF dose. VEGF increased vascular density by 426% predominantly by increasing the proportion of medium-sized vessels (20-40 μ m).

Conclusion

The introduced correlative and quantitative imaging approach is highly reproducible and allows a detailed 3D characterization of the vasculature and muscle tissue. Combined with histology, a broad range of complementary structural information can be generated.

References:

1. Schaad L, Hluschuk R, Barré S, Gianni-Barrera R, Haberthür D, Banfi A, Djonov V. "Correlative Imaging of the Murine Hind Limb Vasculature and Muscle Tissue by MicroCT and Light Microscopy." *Scientific Reports*.7:41842. (2017).

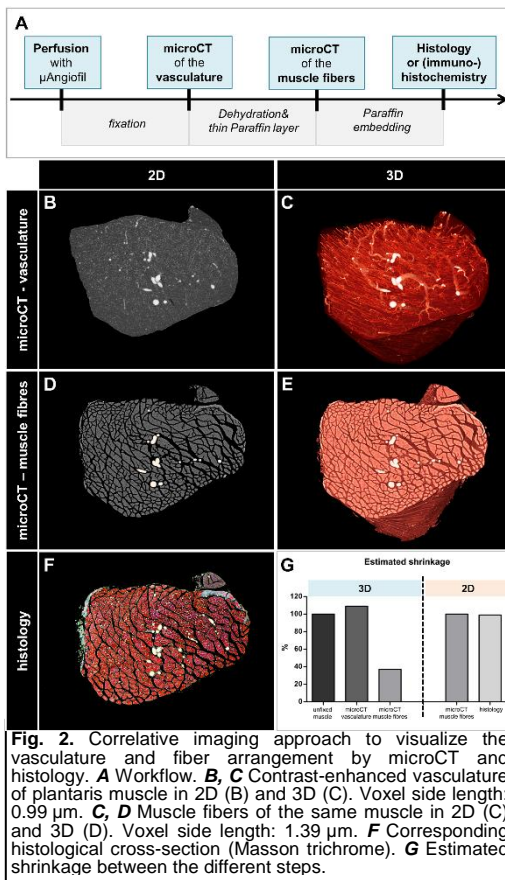


Fig. 2. Correlative imaging approach to visualize the vasculature and fiber arrangement by microCT and histology. **A** Workflow. **B, C** Contrast-enhanced vasculature of plantaris muscle in 2D (**B**) and 3D (**C**). Voxel side length: 0.99 μ m. **C, D** Muscle fibers of the same muscle in 2D (**C**) and 3D (**D**). Voxel side length: 1.39 μ m. **F** Corresponding histological cross-section (Masson trichrome). **G** Estimated shrinkage between the different steps.

Local androgen/bisphosphonate combination treatment to enhance bone healing: Proof of principle in human and porcine bone explants

Nicole Bakker, Cindy van de Ven, Jan Gossen¹

Osteo-Pharma, Kloosterstraat 9, 5349 AB Oss

Aims

Bone healing, especially in elderly patients is a complex process with limited therapeutic options. In recent years a wealth of information has been obtained on the use of BMP2 for fracture healing. However, for many applications superficial amounts of BMP2 were required for efficacy due to the absence of local sustained release carriers. Several severe side effects have been reported limiting the use of BMP2 in a clinical setting. Here we present an alternative method based on the use of a combination of low molecular weight compounds, Stanolone and Alendronate, with established safety profiles in men. Moreover, in contrast to BMP2 which activates both osteoblast and osteoclasts, this combination of drugs enhances osteoblast activity but simultaneously inhibits osteoclast activity resulting in a net effect of bone growth

Method

In these experiments 5 x 8 mm porcine or human bone biopsies (n=6) were cultured for 4 weeks in the presence of various concentrations Stanolone (3-375 nM) with and without 2 uM Alendronate. Medium was changed every 3-4 days and used to determine alkaline phosphatase activity (ALP). ALP is an early biomarker for osteoblast activity. At the end of the study biopsies were scanned in a MicroCT (Bruker Skyscan 1076). CTan was used to analyze bone parameters. Bone strength was measured using Hounsfield (H10KT) test equipment

Results

A significant increase in ALP response was measured in porcine biopsies after 7 and 10 days of culturing, indicating more active osteoblasts present when the biopsies were stimulated with Stanolone (S) in combination with Alendronate (A) compared to the control (Figure 1). MicroCT analysis of the porcine biopsies revealed a ~40% increase in bone volume (trabecular and cortical bone) when the biopsies were stimulated with a combination of Stanolone and Alendronate after 28 days (Figure 2). In addition, a significant increase in bone strength was measured (Fig 3) indicating the formation of high quality bone tissue. In the human bone biopsies an increase up to 150% in bone volume was measured when the human biopsies were stimulated with the combination of Alendronate and Stanolone.

Conclusion

Treatment of human or bovine bone biopsies with a combination of an androgen (Stanolone) and a bisphosphonate (Alendronate) significantly enhance bone growth. Moreover, bone strength was increased indicating the formation of high quality bone tissue.

Significance: The current data are the basis for developing sustained release materials to be applied locally at the bone fracture site. By encapsulating Stanolone and Alendronate in a biodegradable polymer coating, release up to 5 weeks of the pharmaceuticals can be achieved. Due to the local application low amounts of the drugs are required and thus will not

result in systemic exposure. Such a coating can be applied in combination with collagen membranes to be administered near a fracture to improve bone healing or as a coating onto implants to improve osseointegration.

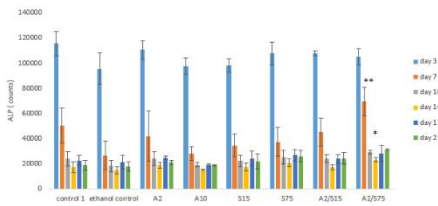


Figure 1: Alkaline Phosphatase activity in porcine biopsies on different time points

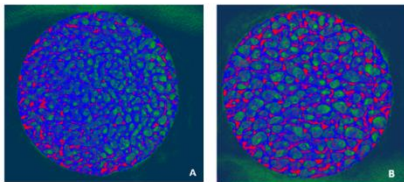


Figure 2b: 3D microCT analysis, Porcine biopsies stimulated for 28 days with only ethanol(A) or with 2 μ M Alendronate in combination with 75 nM DHT (B).

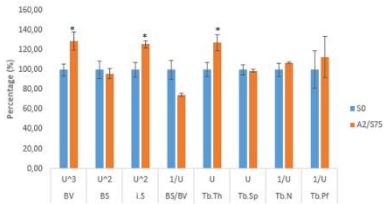


Figure 2a: 3D microCT analysis of porcine biopsies

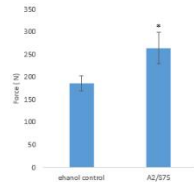


Figure 3: Bone strength measurements of porcine biopsies

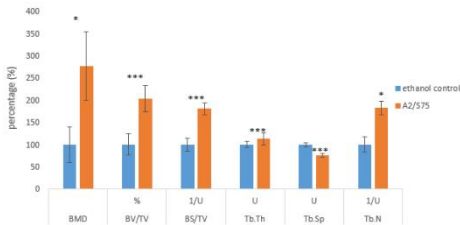


Figure 4: 3D microCT analysis of human biopsies

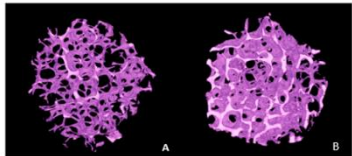


Figure 5: 3D microCT analysis, Human biopsies stimulated for 28 days with only ethanol or with 2 μ M Alendronate in combination with 75 nM DHT.

Micro-CT of biomineralized gelatin scaffold for bone regeneration

S.G.Pastore¹, D. Altamura¹, M.G. Raucci², I. Fasolino², D. Mele³, F. Intranuovo⁴, E. Altamura⁴, F. Mavelli⁴, C. Giannini¹

¹Institute of Crystallography (IC), National Research Council, Bari 70126, Italy

²Institute of Polymers, Composites, and Biomaterials (IPCB), National Research Council, Naples, Italy

³Department of Geology, University of Bari, 70126 Bari, Italy

⁴Department of Chemistry, University of Bari, 70126 Bari, Italy

Aims

Regenerative medicine is a multidisciplinary field aiming to regenerate tissues by combining biological factors and engineering fundamentals [1]. Recently, the use of stem cells is a rapidly emerging field in the treatment of bone defects thanks to their capacity to differentiate into multiple lineages. Human mesenchymal stem cells (hMSCs) can be expanded to high number of cells and their addition to an appropriate scaffold material facilitates the healing of bone defects [2]. The structure of the scaffold has a very real effect on how cells express signalling process. The scaffold porosity —i.e. the % of empty space in the structure created by pores— and the size and the shape of pores can impact cell attachment, alter the permeability of media and nutrients, and facilitate cell migration. It is known that 100–400 µm pores are suitable for bone regeneration, depending on the porosity and the scaffold materials used [3]. The goal of the present study is to assert the micro structural parameters of the scaffold during the fabrication process, in order to understand how the chemical and biological factors added to the material can affect the structure and the cellular response. Micro-CT is a non destructive technique that is suitable for our purposes. Moreover, results are supported by X-ray diffraction measurements [4] to assert the mineralized phase inside the scaffold and laser scanning confocal microscopy (LSCM) to confirm cell differentiation.

Method

Scaffold made of type B gelatin (Sigma-Aldrich) matrix from bovine skin was synthesized from a 5% wt/V aqueous gelatin solution, prepared in distilled water at 40 °C with constant adjustments of the pH (10–10.5) and stirred for 2 hours. After that, the gel system was poured into the Teflon molds (5×10 mm), quenched to –80 °C, and freeze-dried for 48 hrs to obtain a random porous structure [5]. Then, treatment 1, consisting of simulated body fluid (SBF) and bone morphogenic protein factor (BMP2) addition, was performed in order to promote further biomineralization. As last step, treatment 2, consisting of hMSCs seeding (passage 3, for 28 days in Eagle's alpha minimum essential medium α -MEM supplemented with 10% fetal bovine serum, antibiotic solution-streptomycin 100 µg/mL- and penicillin 100 U/ml, Sigma Chem. Co, with 2 mM L glutamine incubated at 37 °C in a humidified atmosphere) was carried out. The scaffold was subjected to micro-CT analysis before the treatment and after treatments 1 and 2. Samples were scanned using a high-resolution micro-CT system SkyScan 1172 (Bruker, Kontich, Belgium) for a quantitative three dimensional (3D) analysis of the material porosity. The source voltage and current were set at 25 KV and 140 µA respectively, with a nominal resolution of 4 µm (pixel size), 1x1 camera binning, frame averaging of 4, 0.3° rotation step, and the use of 180° rotation. The duration of each scan was nearly 3 hours. Dataset were then reconstructed with the software NRecon (Bruker) to obtain the microtomographic sections using the specific alignment correction depending on the scan, smoothing and ring artifacts reduction. Then, quantitative 2D and 3D analysis were carried out using the software CTAn (version 1.16, Bruker) on the correspondent volume of interest (VOI). The visualization of the

scaffold structure was achieved using CTVol (version 2.3, Bruker). For the hydroxyapatite phase identification inside the scaffold, wide angle X-ray diffraction was performed on several selected points. Laser scanning confocal microscopy was also carried out on selected slices of the scaffold using fluorescent dyes in order to label the osteocalcin protein, which is a marker of the ongoing osteogenic differentiation.

Results

Scaffold before treatment presents open and connected pores as analyzed in 3D by means of micro-CT. After the first treatment consisting of calcium-phosphate precursor solution and a growth factor addition, a reduction of 2% in terms of open porosity has been detected. The third treatment (cells seeding), which induced hydroxyapatite formation as consequence of cellular differentiation, produced a reduction of original porosity of 4%. The volume rendering of bare gelatin scaffold, hydroxyapatite phase, and scaffold with hydroxyapatite are shown in Figure 1. All the related parameters are summarized in Figure 2.

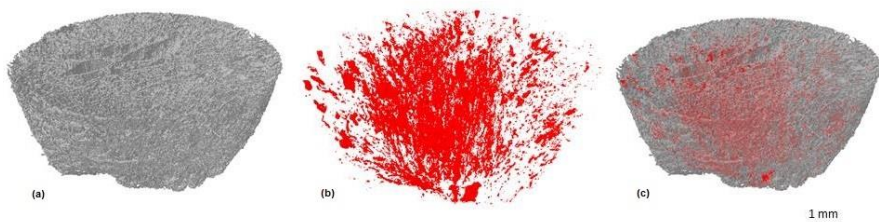


Figure 1: Visualization of bare gelatin scaffold (a), hydroxyapatite phase (b) and scaffold with hydroxyapatite as last step of treatment (c) in CTVol

Structure separation and thickness distribution of open pores are shown in Figure 3. Treatment 2 resulted in a wider structure thickness distribution of the scaffold matrix.

		Before Treatment Gel	Treatment 1 Gel+SBF+BMP2	Treatment 2 Gel+SBF+BMP2+Cells
Total VOI volume	mm ³	27.4	27.4	27.4
Object Volume	mm ³	3.81	4.38	4.84
Percent object volume	%	13.9	16	17.6
Volume of closed pores	mm ³	1.93E-07	4.07E-08	6.14E-03
Closed porosity (percent)	%	5.07E-06	9.29E-07	1.27E-01
Volume of open pores space	mm ³	23.6	23	22.6
Open porosity (percent)	%	86.1	84	82.3
Total volume of pore space	mm ³	23.6	23	22.6
Total Porosity	%	86.1	84	82.4

Figure 2: Porosity parameters from 3D analysis

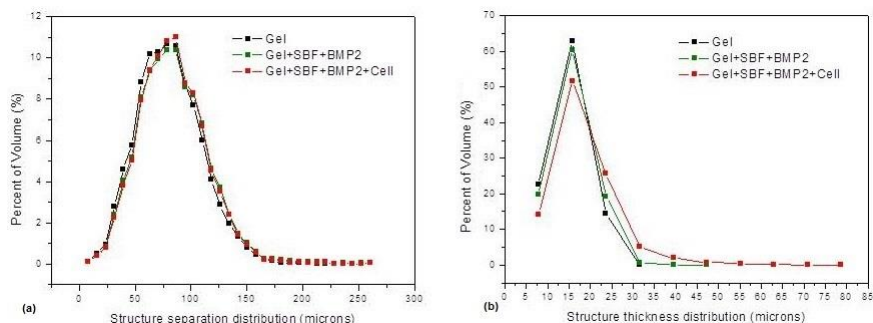


Figure 3: Structure separation (a) and thickness (b) distributions of open pores

Conclusion

Micro-CT represents a powerful non destructive technique for a step by step characterization of porous bone scaffolds which undergo different treatments in different times before the application. Since scaffold fabrication process influences the inner microstructure of the material, a monitoring approach after each treatment can definitely improve the scaffold performance.

Acknowledgements

We are grateful to Prof. P. Favia for access to micro-CT laboratory at Department of Chemistry, University of Bari, Italy. The projects "PON Ricerca e Competitività 2007-2013" (Avviso n.254/Ric del 18 maggio 2011) and SISTEMA (PONa3_00369 MIUR, Laboratorio per lo sviluppo Integrato delle Scienze e delle Tecnologie dei Materiali Avanzati e per dispositivi innovativi) are gratefully acknowledged for having partially funded this research.

References:

1. S. Lin, N. Sangaj, T. Razafiarison, C. Zhang, S. Varghese, "Influence of Physical Properties of Biomaterials on Cellular Behavior" *Pharm Res*, 28, 1422–1430, 2011
2. P. Kasten, I. Beyen, P. Niemeyer, R. Luginbu, M. Bohner, W. Richter, "Porosity and pore size of β -tricalcium phosphate scaffold can influence protein production and osteogenic differentiation of human mesenchymal stem cells: An in vitro and in vivo study", *Acta Biomaterialia*, 4, 1904–1915, 2008
3. F.J. O'Brien, BA Harley, IV. Yannas, L.J. Gibson, "The effect of pore size on cell adhesion in collagen–GAG scaffolds", *Biomaterials*, 26, 433–441, 2005
4. D. Altamura, SG. Pastore, MG. Raucci, D. Siliqi, F. De Pascalis, M. Nacucchi, L. Ambrosio, C. Giannini, "Scanning Small- and Wide-Angle X-ray Scattering Microscopy Selectively Probes HA Content in Gelatin/Hydroxyapatite Scaffolds for Osteochondral Defect Repair", *ACS Appl. Mater. Interfaces*, 8, 8728–8736, 2016
5. MG. Raucci, V. D'Antò, V. Guarino, E. Sardella, S. Zepetelli, P. Favia, L. Ambrosio, "Biomaterialized Porous Composite Scaffolds Prepared by Chemical Synthesis for Bone Tissue Regeneration", *Acta Biomaterialia*, 6, 4090–4099, 2010

3D imaging and quantitative analysis of vasculature networks: light-sheet microscope vs. micro computed tomography

C. Schürmann¹, J. Epah¹, K. Pálfi¹, K. Schröder¹, R. P. Brandes¹

¹ Institut für Kardiovaskuläre Physiologie, Goethe Universität Frankfurt a.M.

Aims

New imaging technologies and software-based analysis will increase our knowledge on vascular networks and its remodeling in vivo. Here we analyzed the ability of light-sheet microscopy (LSM) and micro computed tomography (μCT) to investigate vessel networks.

Method

Vascular networks of kidney, heart or arteriosclerotic carotid arteries and lesions were analyzed in vivo or ex vivo. Mice were injected with in vivo blood pool contrast agent AuroVist 15 nm or perfused post mortem with polymerizing contrast agent MicroFil. Whole animals or dissected organs were analyzed via μCT. Moreover mice were injected with Alexa647-labeled IsolectinB4 to stain all vessels. Specimens of interest were subjected to classic analysis such as immunohistochemistry or to whole mount staining and LSM.

Results

We observed that visualization and quantification of big vessels (d:>100μm) like kidney, carotid arteries or coronary arteries is more practicable by the use of blood pool or polymerizing contrast agents. Immunological staining of the vessel wall does not easily allow 3D analysis of big vessels due to missing contrast of the lumen. On the other hand, in vivo staining of the vasculature via fluorescent-labeled IsolectinB4 leads to a homogenous staining of all vessels and enables quantitative analysis of capillary structures (d:~10μm) at high resolution. Interestingly capillarization of arteriosclerotic lesions can be visualized by this technique.

Conclusion

Micro-CT scanners enable the assessment of the vasculature or vascular complications in vivo and ex vivo. Thereby, this technique gives new insights into disease progression and works well in longitudinal studies. Light sheet microscopy provides aesthetic visualisation of vascular networks and appears to be a reliable tool to analyse vascular remodelling and capillary growth.

A Micro-Computed Tomographic Study of Band-shaped Root Canal Isthmuses in the Apical Third

Ali KELES¹, Cangül KESKİN¹

¹ Ondokuz Mayıs University, Faculty of Dentistry, Department of Endodontics, Samsun, Turkey

Aims

This study aimed to conduct a quantitative analysis of the band-shaped isthmus area, the floor of which was in the apical third in the mesial roots of mandibular first molars using micro-computed tomography (micro-CT).

A clinical knowledge of root-canal anatomy and possible anatomical variations certainly reduces the challenges associated with each phase of root canal treatment, from access cavity design to the three-dimensional obturation of the root-canal system¹. Root-canal anatomy has been extensively investigated in previous studies using a number of different techniques^{2,3}, and micro-CT has emerged as the most accurate of these with regard to revealing the morphology and complexity of the root canal system, and redefined morphological classification systems as a result of the discovery of new variations²⁻⁴.

It has been observed that the mesial root canals of mandibular molar teeth have a highly complex internal anatomy, showing isthmuses, branching, fins, and rejoining root canals at different levels⁵, and the isthmuses have been described and classified based on variable standards^{6,7}. A recent study evaluated the morphological features of isthmuses in the root canals showing Vertucci type II root canal configuration. The results of this study reported that ovality of apical foramen increased as the length of the isthmus was shortened². Despite the oval cross-sectional shapes from isthmus roof to the apical foramen, it might be advantageous to have a single apical foramen in root canals with Vertucci type II root canal configuration. Whereas, isthmuses located at the apical third and presenting with 2 or more apical foramina might present challenges for root canal treatment. These isthmuses might be described as band-shaped isthmus due to their band-shaped appearance between the isthmus roof and the isthmus floor. The aim of the present study was to make a quantitative analysis of the isthmus area in the apical root canals of the mesial roots of mandibular first molars with a band-shaped isthmus using micro-CT

Method

Micro-CT images of 269 specimens were evaluated, and 40 specimens showing a band-shaped isthmus, with a floor in the apical third, were selected. The major diameter, minor diameter, and roundness values for the most coronal and apical slices where the isthmus was visible were measured. The distances between these slices were measured as the isthmus height, and the total volume of the isthmus was measured. The distances between the isthmus floor and two apical foramina and the number of root canal orifices were calculated. The dimensions of the isthmus roof and the floor were compared, and the data were analyzed using descriptive statistics and one-way analysis of variance tests with a significance threshold set at 5%.

Results

The percentage of roots showing a band-shaped isthmus in their apical third was 14.86% of the total 269 specimens. Of these, 75% had two root canal orifices, while 15% and 10% had three orifices and one orifice respectively. Table 1 presents the major, minor, and

roundness diameters of the slices corresponding to the isthmus roof and floor. Table 2 details the distance between each apical foramen and isthmus floor, isthmus height, and volume.

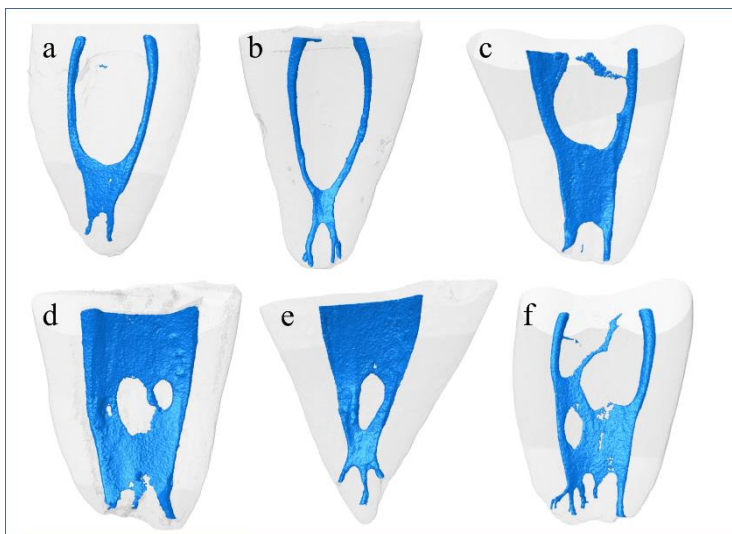


Figure 1: Three-dimensional models of the specimens showing band-shaped isthmus at the apical third provides insight regarding the difficulties of root canal treatment procedures. Instrument might cross diagonally through the isthmus and reach the apical part of the adjacent root canals according to the buccolingual direction of root canals (a- c). The difficulty of three-dimensional obturation of apical root canals that redivide from the isthmus floor is displayed (d-f).

Table 1: Mean \pm standard deviation values of quantitative anatomical features of horizontal cross sections of all specimens

	Isthmus roof	Isthmus floor
Roundness	0.12 ± 0.05^a	0.14 ± 0.10^a
Major diameter (mm)	2.67 ± 0.73^a	1.65 ± 0.55^b
Minor diameter (mm)	0.36 ± 0.09^a	0.30 ± 0.14^b

Different superscript letters in the same line mean statistically significant difference ($P < 0.05$)

Table 2: Mean \pm standard deviation values of height and volume of the band shaped isthmus and distance between apical foramen and isthmus floor

		Mean \pm standard deviation	Minimum - maximum	Median
Distance to apical foramens (mm)	1	1.05 ± 0.61	0.53 – 3.18	0.99
	2	1.51 ± 0.65	0.20 – 2.72	1.45
Length (mm)		2.47 ± 1.65	0.13 – 6.95	2.26
Volume (mm³)		0.98 ± 0.82	0.04 – 3.46	0.77

Conclusion

The present study propounds the quantitative and qualitative features of band-shaped isthmuses in the apical third of mesial roots of mandibular first molars. These features might complicate three-dimensional root canal preparation and obturation. Further studies are warranted to evaluate the efficacy of root canal preparation and obturation procedures on roots with band-shaped isthmuses.

Acknowledgements

This study was supported by the Scientific and Technological Research Council of Turkey-TÜBİTAK (grant no. 114S002). Authors deny any conflicts of interest.

References:

1. Cleghorn BM, Christie WH, Dong CC, "Root and root canal morphology of the human permanent maxillary first molar: a literature review" J Endod,32:813-21, 2006.
2. Keleş A, Keskin C, "Apical Root Canal Morphology of Mesial Roots of Mandibular First Molar Teeth with Vertucci Type II Configuration by Means of Micro-Computed Tomography" J Endod, 43:481-5, 2017.
3. Gao X, Tay FR, Gutmann JL, et al. "Micro-CT evaluation of apical delta morphologies in human teeth" Sci Rep, 6:36501, 2016.
4. Ahmed H, Versiani M, De-Deus G, Dummer P, "A new system for classifying root and root canal morphology" Int Endod J, 2016.
5. Villas-Bôas MH, Bernardineli N, Cavenago BC, et al. "Micro-computed tomography study of the internal anatomy of mesial root canals of mandibular molars" J Endod, 37:1682-6, 2011.
6. Teixeira F, Sano C, Gomes B, et al. "A preliminary in vitro study of the incidence and position of the root canal isthmus in maxillary and mandibular first molars" Int Endod J, 36:276-80, 2003.
7. Hsu Y-Y, Kim S, "The resected root surface. The issue of canal isthmuses" Dent Clin North Am, 41:529-40, 1997.

Spinal cord injury impairs bone healing and deteriorates bone microstructure as evidenced by μ CT assessment.

M.M.Butezloff¹, K. Astolpho¹, M.D. Sousa-Neto², J.B. Volpon¹, A. Zamarioli¹

¹Department of Biomechanics, Medicine and Rehabilitation, School of Medicine of Ribeirao Preto of University of Sao Paulo, Brazil

²Department of Restorative Dentistry, Dental School of Ribeirao Preto, University of Sao Paulo, Brazil.

Aims

The objective of this study was to investigate the microstructural changes in the bone tissue and in the bone callus in rats with spinal cord injury.

Method

All the experimental procedures used in this study were approved by the Animal Care and Use Committee of our University.

Ten male Wistar rats with six weeks were divided into 2 experimental groups: (1) CON+FRAC: control rats with bone fracture; (2) SCI+FRAC: rats with spinal cord injury with bone fracture. SCI was performed in the same manner as previous studies⁽¹⁾. Ten days after spinal cord injury a fracture was created in the femoral diaphysis by closed method and immediately fixed by an intramedullary nail. The right distal femur was shaved and then disinfected with 70% alcohol. Subsequently, bone was placed in a device especially manufactured to perform a closed fracture in the mid-femur (Figure 1). Immediately after fracturing bone, an incision was made parallel in the proximal extremity of the femur. A 1-mm-diameter Kirschner wire was introduced into the medullary canal in order to stabilize the bone fragments. The wound was closed with resorbable sutures. The status of the fracture was radiographically confirmed immediately after surgery and followed every week (Figure 2). Any fractures not consistent with standardized placement criteria (mid-diaphyseal) or grossly comminuted were excluded. The bone healing was observed for fourteen days post-fracture. At the end of the experiment, animals were killed, femurs and tibias were harvested and submitted to tridimensional microstructure analysis of both the trabecular and cortical bone, as well as the bone callus. Prior to μ CT scanning the k-wire nail was removed while taking great care to not disrupt the fracture site and callus.

A high-resolution, desktop micro-CT system (SkyScan 1174v2; Bruker-microCT, Kontich, Belgium) was used to quantify the BMD and the three-dimensional microarchitecture parameters in the femur and tibia. The specimens were scanned using 40 kV and 800 mA, with the aid of a 0.5-mm-thick aluminum filter to optimize the contrast, a rotation step of 1°, three-frame averaging and an isotropic resolution of 26.7 μ m. Images of each specimen were reconstructed with dedicated software (NRecon version 1.6.3; Bruker-microCT), providing axial cross-sections of the inner structures of the samples.

In the tibia, two regions of interest were made, one at the tibial proximal metaphysis, which mainly contains trabecular bone and, another at the mid-diaphysis, which mainly contains cortical bone. The reconstruction of the metaphysis was selected manually starting just proximally of the growth plate for an extension of 3 mm. The reconstruction of the diaphysis was defined by a 2-mm region starting 8 mm proximally from the growth plate. Cortical and trabecular bone were isolated using manually drawn contouring. CTAn software (Bruker-microCT), version 2.2.1, was used for the determination of the optimal threshold from the image histograms and was set to exclude soft tissue but to include poorly mineralized bone.

The same threshold was used in all of the samples, but differed between trabecular, callus and cortical bone. The thresholded image was used as a mask to measure the BMD of the bone structures (trabecular). For the accurate calculation of BMD, appropriate calibration of the Skyscan CT analyzer was performed with known density calcium hydroxyapatite phantoms (0.25 and 0.75 g/cm³). Once the phantoms' BMDs were calibrated in the CTAn software, a VOI of 3 mm was selected in the bone. Trabecular architecture of the proximal metaphysis was characterized by determining trabecular bone volume (BV), trabecular bone volume fraction (BV/TV), specific bone surface (BS/BV), trabecular number (Tb.N), trabecular thickness (Tb.Th), trabecular separation (Tb.Sp) and connectivity density (Conn.D) (Figure 5). Cortical architecture was assessed in the diaphysis and was characterized by cortical volume (Ct.V and Ct.BV/TV), cortical thickness (Ct.Th) and cortical porosity (Ct.Po).

In the femur, the region of interest was made the bone callus, the reconstruction was selected manually for all extension of the callus. Bone callus architecture was characterized by determining bone callus volume (BV), bone callus volume fraction (BV/TV). All bone morphometric measurements and nomenclature are in accordance with recommendations of the ASBMR⁽²⁾.

Results

The spinal cord injured rats exhibited a substantial loss of bone tissue and uncoupled bone remodelling, whence resorption was up-regulated and formation was down-regulated, when compared to the control animals. These changes occurred in both the trabecular (Figures 4 and 5) and the cortical bone (Figures 6 and 7).

Figures 4 and 5 show that within 14 days post fracture, the SCI rats exhibited a marked deterioration in the trabecular architecture in the tibial proximal metaphysis (reduction of -85% in BV, -79% in BV/TV, -78% in Tb.N, -4% in Tb.Th, -65% in Conn.D and +6% in Tb.Sp).

Figures 6 and 7 show that within 14 days of fracture in the SCI rats decreases were also found in the cortical bone (-33% in Ct.V, -4% in Ct.BV/TV, -11% in Ct.Th and +2% in Ct.Po).

Figure 8, 9 and 10 show that within 14 days post fracture, the SCI rats exhibited a marked decrease in bone healing of the bone callus (-30% in BV and -11% in BV/TV).

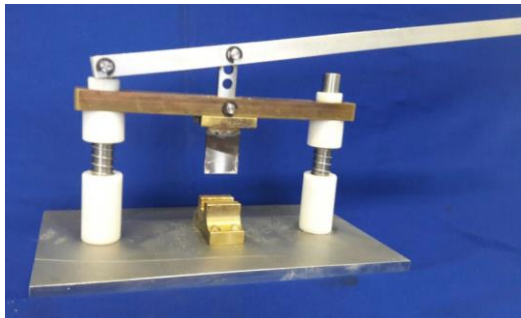


Figure 1: Device used to cause closed fracture in mid-femur.

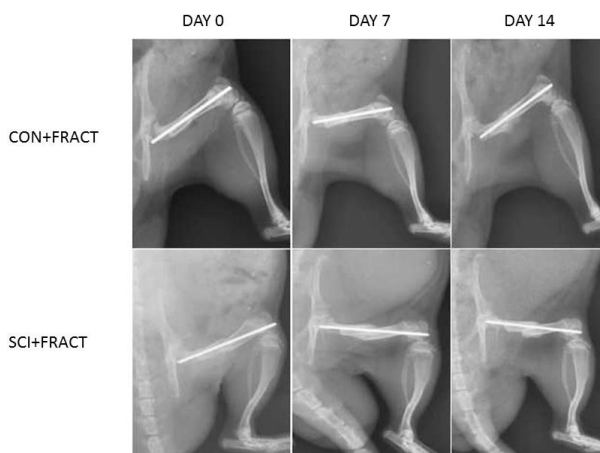


Figure 2: X-ray images to confirm the fracture and alignment immediately following surgery (PO 0, PO 7 and PO 14).

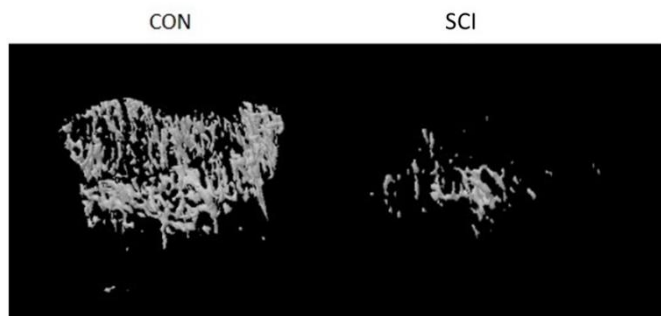


Figure 4: Trabecular bone microstructures of tibial metaphysis showing a dramatic reduction of trabecular bone in the spinal cord injured rats (SCI).

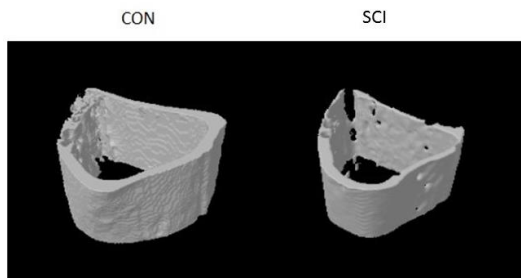


Figure 6: Cortical bone microstructures of tibial diaphysis.

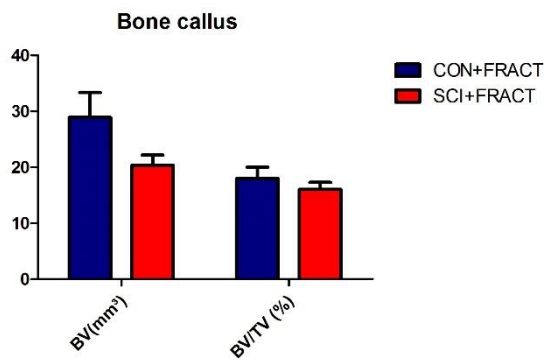


Figure 7: Quantitative analysis of bone callus microstructure.

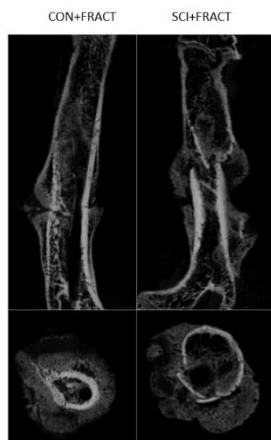


Figure 8: μ CT images of bone callus, both in sagittal and axial planes. SCI induced decreased bone healing, where bone callus is smaller than in the control rats.

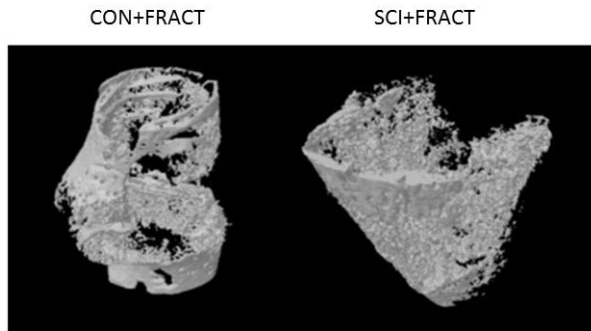


Figure 9: Bone callus microstructures of femur.

Conclusion

We concluded the spinal cord injury negatively affected the bone microarchitecture in rats, where changes occurred in both the trabecular and the cortical tissue. Furthermore, bone healing was also affected by the spinal cord injury, where the volume of bone callus was smaller than in the controls.

References:

1. Zamarioli A, Battaglini R, Morse L, Okubo R, Maranhão D, Shimano AC. Passive Standing and Functional Electrical Stimulation Preserves Bone Strength in Paraplegic Rats Following Acute Spinal Cord Injury. *Osteoporosis Int. Mar*;23:S415-S6, 2012.
2. Bouxsein ML, Boyd SK, Christiansen BA, Guldberg RE, Jepsen KJ, Muller R. "Guidelines for assessment of bone microstructure in rodents using micro-computed tomography". *J Bone Miner Res*, 1468-1486, 2010.

Micro-computed tomography as a tool for finding new taxonomic characters in polychaetes

M. Candás¹, X. Cunha-Veira¹, J. Moreira², J. Parapar³

¹Estación de Bioloxía Mariña da Graña-Universidade de Santiago de Compostela, Rúa da Ribeira 1-4, E-15590 A Graña, Ferrol, Spain.

²Departamento de Biología (Zoología), Facultad de Ciencias, Universidad Autónoma de Madrid, Calle Darwin 2, E-28049, Cantoblanco, Spain.

³Departamento de Bioloxía Animal, Bioloxía Vexetal e Ecoloxía, Universidade da Coruña, Rúa da Fraga 10, E-15008 A Coruña, Spain.

Aims

In this work, we present a comparative anatomical study of three species of marine polychaetes, *Syllis garciai* (Campoy, 1982), *Euclymene oerstedii* (Claparède, 1863) and *Sphaerodoropsis* sp. by means of micro-computed tomography. This was done to assess the strength of this technique when studying the internal and external polychaete anatomy. We also aim to find anatomical structures with potential taxonomic and phylogenetic value that may be studied easily with micro-CT.

Method

Specimens of *S. garciai* and *E. oerstedii* were collected at the Santa Lucía Bay, located in the Ría de Ferrol (Galicia, NW Iberian Peninsula). Specimens of *Sphaerodoropsis* sp. were collected off Icelandic waters in the frame of the BIOICE project. Specimens were initially fixed in 4% formalin and then transferred to 70% ethanol for preservation. Subsequently, the specimens were gradually dehydrated in consecutive ethanol baths and eventually kept in 96° ethanol. Before scanning, animals were dehydrated for 2 hours with hexamethyldisilazane (HMDS) and left to dry overnight (Alba Tercedor & Sánchez-Tocino, 2011; Faulwetter *et al.*, 2013; Candás *et al.*, 2016).

Scanning was carried out with a microtomograph Skyscan 1172 by applying these parameters: voltage of 55 kv, current of 165 µA, no filter was used and samples were rotated 360°; pixel size was 0.95 µm in *S. garciai* and 2.98 µm in *E. oerstedii*.

A second specimen of *E. oerstedii* and two specimens of *Sphaerodoropsis* sp. were stained with 1% iodine in 96° ethanol for three days, dehydrated for 2 hours with HMDS and left to dry overnight. The parameters used during the scanning were: 40 kv, current of 250 µA, no filter was used, and sample was rotated 360°. Pixel size was 2.98 µm in *E. oerstedii*; pixel size was 1.49 µm and 1.15 µm in each specimen of *Sphaerodoropsis* sp.

The X-ray projection images obtained during scanning were reconstructed with the software NRecon. The sections obtained were processed with CTAn and DataViewer, and 3D representations with CTVox.

Results

Syllis garciai (Campoy, 1982)

All external body macroscopic characters are well observed in 3D reconstructions. However, several characters of high taxonomic relevance in polychaetes, such as chaetal structures, could not be properly observed.

The body wall musculature can be readily observed in 2D and 3D images. Dorsal and ventral longitudinal muscle layers are the most evident; likewise, muscles associated with parapodial and chaetal movement were also seen (fig. 1A).

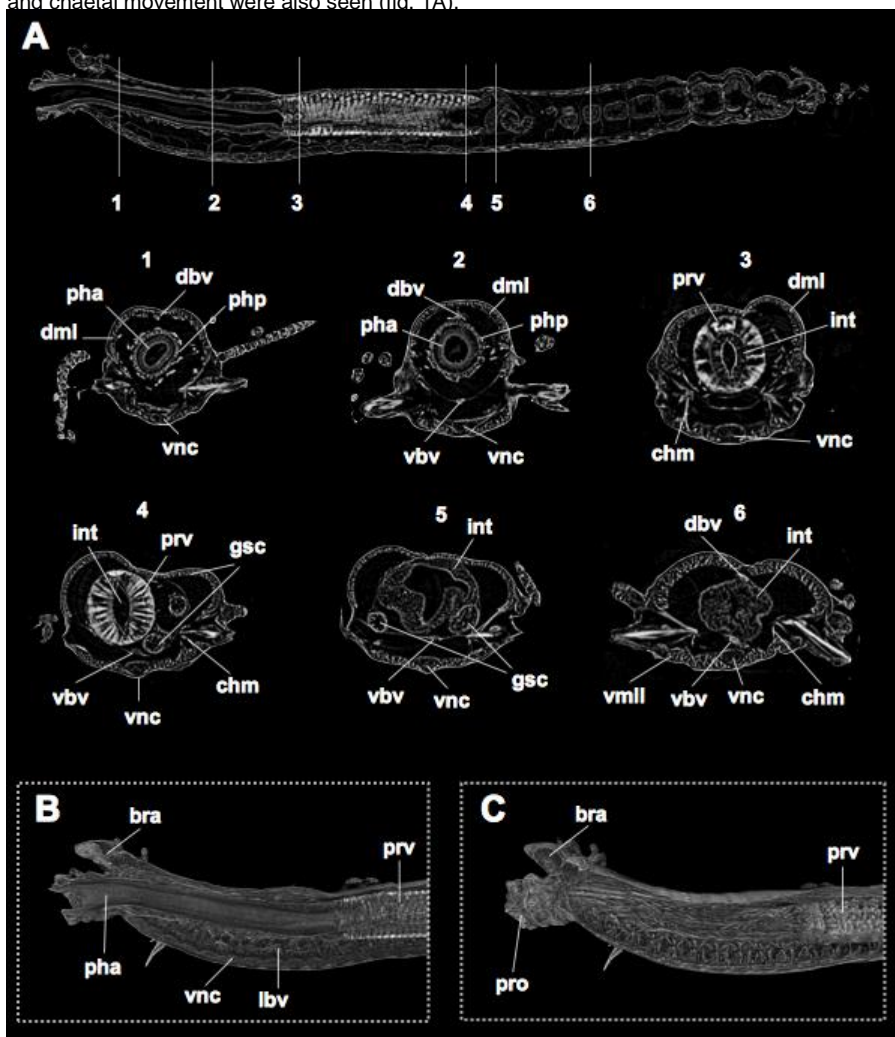


Figure 1: *Syllis garciai* (Campoy, 1932). A: 2D sagittal section and 2D transverse sections; B, C: 3D sagittal sections (anterior body). Abbreviations: bra: brain; chm: chaetal muscle; dbv: dorsal blood vessel; dml: dorsal muscle layer; gsc: gastric caeca; int: intestine; lbv: lateral blood vessel; pha: pharynx; php: pharyngeal plexus; pro: proboscis; prv: proventricle; vbv: ventral blood vessel; vml: ventral longitudinal muscle layer; vnc: ventral nerv cord.

The circulatory system is evident both in 2D and 3D images (fig. 1). Due to their low diameter, blood vessels are easier to detect in 2D than in 3D transversal sections. The plexus surrounding the pharynx is quite well observed.

The digestive system is composed by a pharynx (divided into a pharyngeal proboscis and a proventricle), an esophagus (or ventricle, provided with well-developed gastric caeca) and an intestine (fig. 1). All the structures are well observed both in 2D and 3D. In the studied specimen, the distal part of the pharyngeal proboscis is projected. The proventricle is clearly visible, even in the X-ray projections, because of the presence of microcrystalline inclusions of hydroxyapatite in the radial muscle fibers.

Regarding the nervous system, the ventral nerve cord is well seen (fig. 1). However, the cerebral ganglion, located in the prostomium, is hardly detected (figs. 1B,C), and its connection with the nerve cord through the circumpharyngeal nerves was not observed.

Euclymene oerstedii (Claparède, 1863)

While external anatomy was better observed in stained specimen, the internal anatomy was more properly seen in the unstained one.

The most relevant macroscopic external body characters (e.g. the shape of prostomium, cephalic plaque and cephalic rim, shape and relative length of body segments, dorsal notopodia and ventral neuropodia) are well seen in the 3D reconstructions. However, microstructure of notochaetae and ventral uncini are again hardly to detect with low definition. A pair of supposedly holes located ventrally in body surface at the seventh segment corresponds probably to gonopores.

Similarly to *S. garciai*, all main internal body structures are clearly seen (fig. 2). Circular and longitudinal muscular layers are well seen (fig. 2), as well as the muscles associated with the pharynx (figs. 2A,E).

The circulatory system is also visible both in 2D and 3D images; the following structures can be identified: internuchal vessels in the cephalic plaque; ventral, dorsal and lateral blood vessels (fig. 2); a pharyngeal plexus (fig. 2A,E); and a pair of longitudinal neural vessels running closely associated with the ventral nerve cord (fig. 2A).

The digestive system is also well observed and is composed by a proboscis, a voluminous pharynx, an esophagus, a stomach, and an intestine (the latter was not studied in these specimens). A pair of nephridia is present latero-ventrally to the stomach (fig. 2E).

The nervous system is hardly detected in this specimen, although traces of the cerebral ganglion associated to the cephalic keel and the ventral nerve cord (fig. 2E) could be discerned.

Sphaerodoropsis sp.

Some macroscopic external characters, such as the prostomium, peristomium and body surface macrotubercles and papillae, are properly seen in the 3D reconstructions (figs. 3A,C). However, smaller structures associated with the anterior end (e.g. antennae and palps) and the microstructure of chaetae are badly seen.

Musculature is visible both in 2D and 3D images. Pharyngeal muscle is very conspicuous (fig. 3). Dorsal and lateroventral longitudinal body wall muscular layers are clearly present, as well as transverse muscles and those associated with parapodial and chaetal movement (fig. 3C).

The circulatory system is hardly seen apart from the ventral longitudinal blood vessel.

A highly muscularized pharynx and an voluminous stomach are observed, both in 2D and in 3D images (fig. 3).

The brain and circumoesophageal nerve ring is very well seen in the anterior body end (figs. 3B,C), as well as the segmental nerve ganglia along the ventral part of the animal (fig. 3C).

Conclusion

2D images obtained from the studied polychaete specimens are of high quality, but showing obviously less detail than ones obtained by traditional histological sectioning (e.g. Pilgrim,

1965). Nevertheless, the level of anatomical detail achieved with micro-CT has proven to be adequate enough to identify main body systems and organs, some of them with relatively good detail.

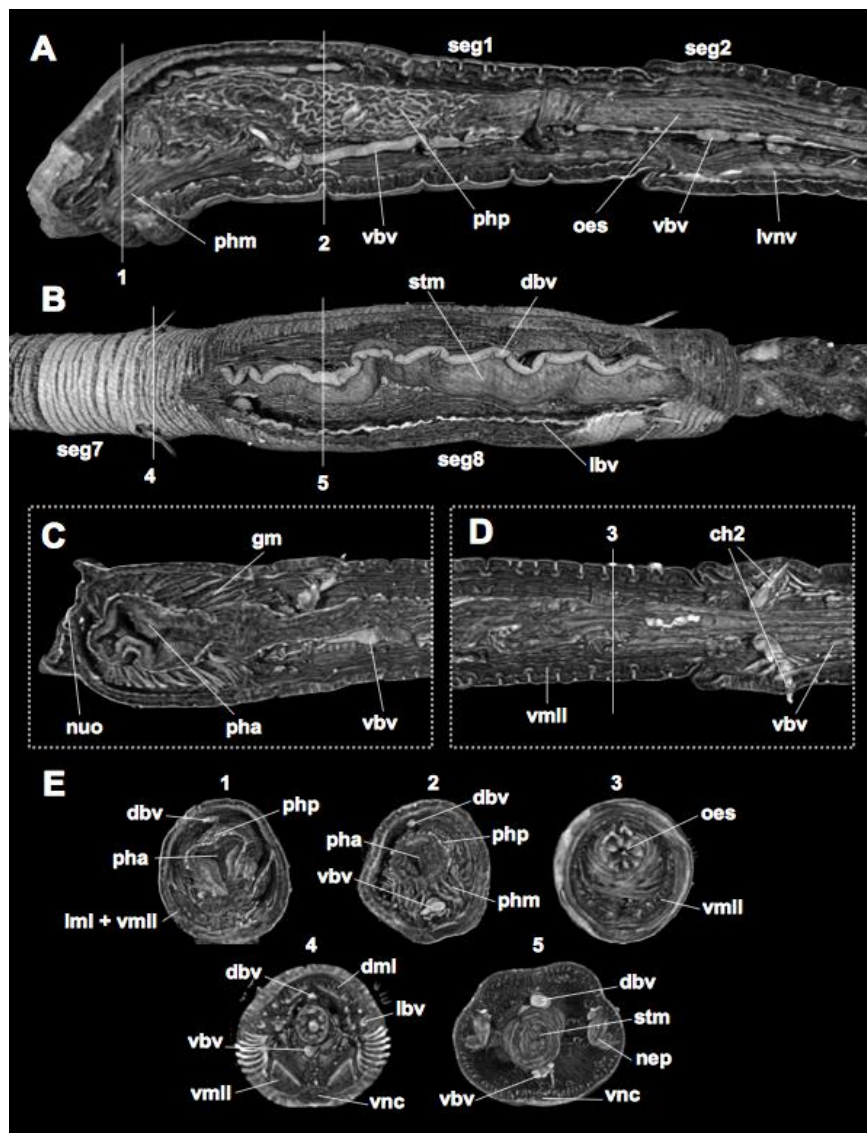


Figure 2: *Euclymene oerstedii* (Claparède, 1863). A: 3D sagittal section; B: 3D frontal section; C: 3D frontal section (anterior body); D: 3D frontal section (middle region); E: 3D

transverse sections. Abbreviations: ch: chaetiger; dbv: dorsal blood vessel; dml: dorsal muscle layer; gm: gular membrane; lbv: lateral blood vessel; lml: lateral muscle layer; lvnv: left ventroneural vessel; nep: nephridium; nuo: nuchal organ; oes: oesophagus; pha: pharynx; phm; pharyngeal muscles; php: pharyngeal plexus; stm: stomach; vbv: ventral blood vessel; vmll: ventral longitudinal muscle layer; vnc: ventral nerv cord.

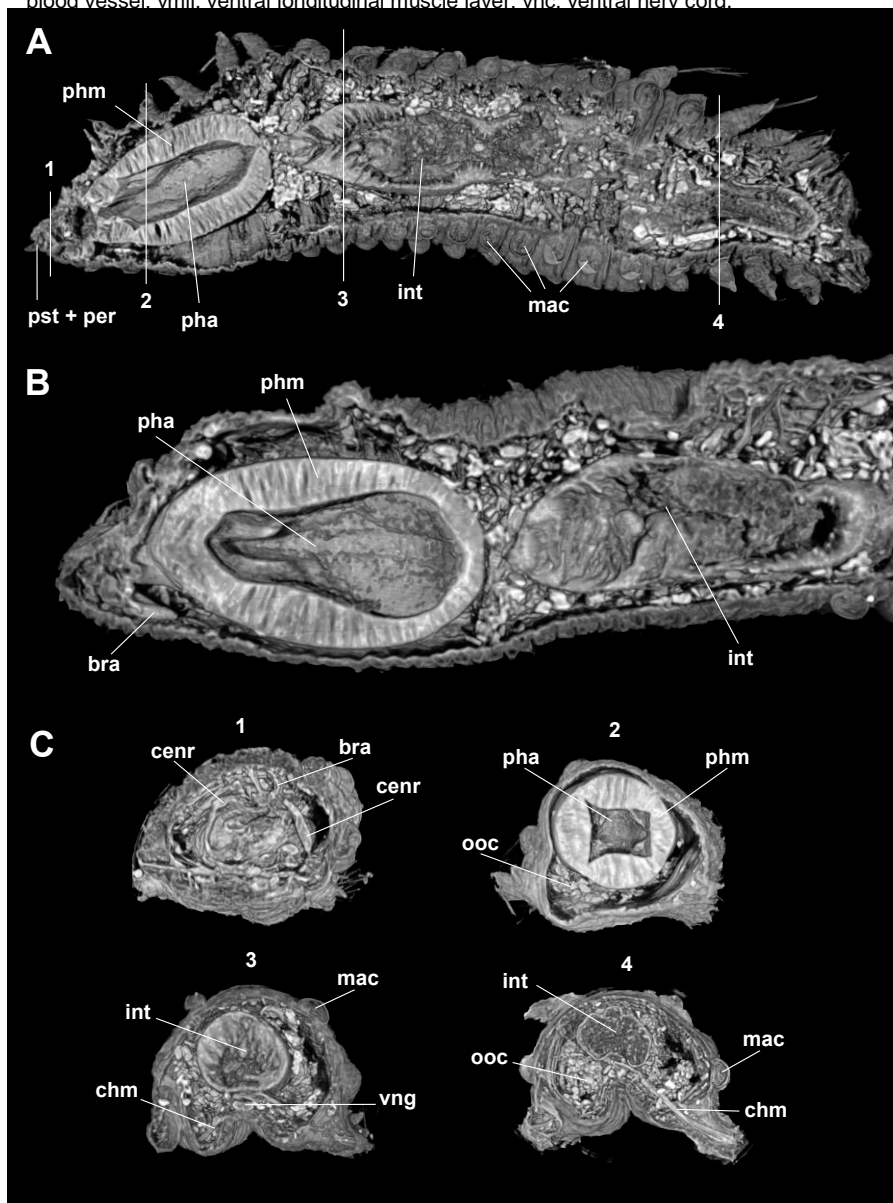


Figure 3: *Sphaerodoropsis* sp. A: 3D frontal section; B: 3D sagittal section; C: 3D transverse sections. Abbreviations: bra: brain; chm: chaetal muscles; cenr: circum-oesophagic nerve ring; int: intestine; mac: macrotubercules; ooc: oocytes; pha: pharynx; phm; pharyngeal muscles; per: peristomium; pst: prostomium; vng: ventral nerv ganglia.

3D images of external anatomy show good definition for all species, but only of macroscopic characters. However, as was previously noticed by Faulwetter et al. (2013), the images definition of highly relevant taxonomic (e.g. chaetal shape) is still poor. In this sense, the level of detail is noticeably lower to that obtained with other image techniques such as the Scanning Electron Microscopy (SEM) (e.g. Darbyshire, 2013).

Previous works have also used micro-computed tomography in the study of marine polychaetes (e.g. Faulwetter *et al.*, 2013, Parapar *et al.*, 2015a, b). It was also achieved good results with and without different stains (iodine, PTA). Our work demonstrates that the use of HMDS without stain allows to achieve enough contrast of soft tissues to be used in comparative polychaete anatomy research, at least for the studied species. Anyway, our preliminary work suggests that results differ depending on the species and the applied technique.

References:

1. Alba-Tercedor J, Sánchez-Tocino L, "The use of the SkyScan 1172 high-resolution micro-CT to elucidate if the spicules of the sea slugs (Mollusca: Nudibranchia, Opisthobranchia) have a structural or a defensive function", SkyScan Users Meeting 2011, 113- 121, 2011.
2. Candás M, Díaz-Agras G, Abad M, Barrio L, Cunha X, Pedrouzo L, Señarís MP, Tato R, García-Álvarez Ó, Urgorri V, "Application of microCT in the study of the anatomy of small marine molluscs", Microscopy and Analysis, 30(2): S8- S11, 2016.
3. Darbyshire T, "A new species of *Micromaldane* (Polychaeta: Maldanidae) from the Falkland Islands, southwestern Atlantic, with notes on reproduction", Zootaxa, 3683: 439-446, 2013.
4. Faulwetter S, Vasileiadou A, Kouratoras M, Dailianis T, Arvanitidis C, "Micro-computed tomography: introducing new dimensions to taxonomy", Zookeys, 263: 1-45, 2013.
5. Parapar J, Moreira J, Helgason GV, "First record of genus *Orbiniella* Day, 1954 (Polychaeta: Orbiniidae) in North Atlantic Ocean with the description of a new species", Zootaxa, 4006(2): 330-346, 2015a.
6. Parapar J, Moreira J, O'Reilly M, "A new species of *Terebellides* (Polychaeta: Trichobranchidae) from Scottish waters with an insight into branchial morphology", Marine Biodiversity, 46: 211-225, 2015b.
7. Pilgrim M, "The functional anatomy and histology of the alimentary canal of the maldanid polychaetes *Clymenella torquata* and *Euclymene oersted*", Journal of Zoology, 147: 387-405, 1965.

Mechanical stimuli upregulate IGF-1 levels and restore bone mass and microarchitecture on both non-fractured and fractured femurs in diabetic rats

A. Zamarioli¹, M.S. Campos¹, J.P.B. Ximenez², M. Butezloff¹,
M.D. Sousa-Neto², J.B. Volpon¹

¹ School of Medicine of Ribeirao Preto of University of Sao Paulo, Brazil

² School of Pharmaceutical Sciences of Ribeirão Preto - University of São Paulo, Brazil.

² Dental School of Ribeirao Preto, University of Sao Paulo, Brazil.

Aims

The aim of this study was to assess the effects of mechanical stimuli on the bone quality and fracture healing in diabetic and non-diabetic rats.

Method

The experimental protocol was approved by the Institutional Animal Care and Use Committee of the School of Medicine of Ribeirão Preto, University of São Paulo (protocol 201/2014).

112 female Wistar rats (200±10g) were assigned to four groups: (1) SHAM, (2) sham with vibration therapy (SHAM+VT), (3) diabetes mellitus (DM), and (4) DM+VT. Diabetes was induced with a single intravenous injection of streptozotocin (60 µg/g body weight in 0.1 M citrate buffer; Sigma, St. Louis, MO)⁽¹⁾. Non-diabetic rats (SHAM) were injected with buffer alone. Blood glucose levels were examined 7 days after the streptozotocin injection by obtaining blood from the tail vein and measuring glucose concentration with a glucometer (Abbott, IL, USA). Diabetes in rats was diagnosed on the basis of blood glucose concentrations of ≥250 mg/dL on two consecutive days. Animals were monitored three times per week for body weight and blood-glucose concentration.

Thirty days after diabetes induction (or citrate buffer injection), animals underwent closed bone fracture at the right mid-femur, followed by surgical stabilization of bone fragments⁽²⁾. The right distal femur was shaved and then disinfected with 70% alcohol. Subsequently, bone was placed in a device especially manufactured to perform a closed fracture in the mid-femur (Figure 1).

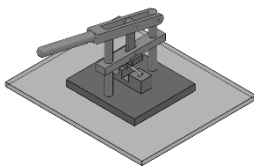


Figure 1: Device used to cause closed fracture in mid-femur.

Immediately after fracturing bone, an incision was made parallel in the proximal extremity of the femur. A 1-mm-diameter Kirschner wire was introduced into the medullary canal in order to stabilize the bone fragments. The wound was closed with resorbable sutures. The status of the fracture was radiographically confirmed immediately after surgery and then followed-up weekly (Figure 2). Any fractures not consistent with standardized placement criteria (mid-diaphyseal) or grossly comminuted were excluded.

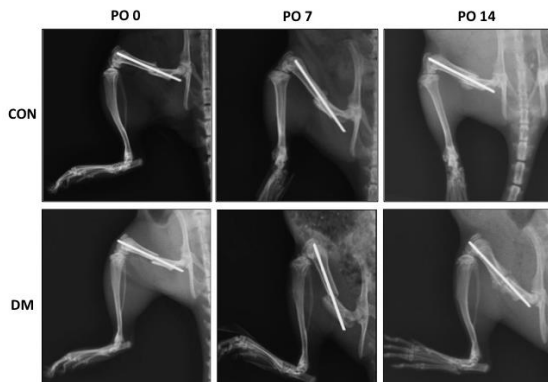


Figure 2: X-ray images to confirm the fracture and alignment immediately following surgery (PO 0) and post-surgery; on the 7th (PO7) and on the 14th (PO14) days post-fracture.

Three days after bone fracture, DM+VT rats and their age-matched controls (SHAM+VT) were subjected to whole-body vibration therapy. For this therapy, rats were placed in a single, special cage on a vibrating platform with a peak-to-peak vertical displacement of 1 mm at a frequency of 50 Hz. Therapy was performed three days per week for 20 minutes for 14 and 28 days, depending on the experimental follow-up period.

On days 14 and 28 post-fracture (representing two distinct phases of normal bone healing: soft and hard bone callus formation, respectively), the rats were euthanized, blood was collected for serum bone marker analysis, and both femurs were collected for micro-computed tomography and histological analysis in order to assess bone quality (left femur) and fracture healing (right femur). Serum samples stored at -80°C were used for the determination of insulin-like growth factor I (IGF-1), RANK and CTX-I levels by ELISA as indicated by the manufacturer (Boster Immuno Leader and MyBioSource, USA).

A high-resolution, desktop micro-CT system (SkyScan 1174v2; Bruker-microCT, Kontich, Belgium) was used to quantify the three-dimensional microarchitecture parameters in the femur. The specimens were scanned using 50 kV and 800 mA, with the aid of a 0.5-mm-thick aluminum filter to optimize the contrast, a rotation step of 1°, three-frame averaging and an isotropic resolution of 26.7 μm . Images of each specimen were reconstructed with dedicated software (NRecon version 1.6.3; Bruker-microCT), providing axial cross-sections of the inner structures of the samples. In the non-fractured bone, two regions of interest were made, one at the femoral distal metaphysis, which mainly contains trabecular bone and, another at the mid-diaphysis, which mainly contains cortical bone. The reconstruction of the metaphysis was by manual selection starting just proximally from the growth plate for an extension of 3 mm. The reconstruction of the diaphysis was defined by a 2-mm region starting 8 mm proximally from the growth plate. Cortical and trabecular bone were isolated using manually drawn contouring. CTAn software (Bruker-microCT), version 2.2.1, was used for the determination of the optimal threshold from the image histograms and was set to exclude soft tissue but to include poorly mineralized bone. The same threshold was used in all of the samples, but differed between trabecular and cortical bone. The thresholded image was used as a mask to measure the BMD of the bone structures (trabecular). For the accurate calculation of BMD, appropriate calibration of the Skyscan CT analyzer was performed with known density calcium hydroxyapatite phantoms (0.25 and 0.75 g/cm^3). Once the phantoms' BMDs were calibrated in the CTAn software, a VOI of 3 mm was selected in the bone. Trabecular architecture of the distal metaphysis was characterized by determining trabecular bone volume (BV), trabecular bone volume fraction (BV/TV), specific bone surface (BS/BV), trabecular number (Tb.N),

trabecular thickness (Tb.Th), trabecular separation (Tb.Sp) and connectivity density (Conn.D) (Figure 5). Cortical architecture was assessed in the diaphysis and was characterized by cortical volume (Ct.V and Ct.BV/TV), cortical thickness (Ct.Th) and cortical porosity (Ct.Po). All bone morphometric measurements and nomenclature are in accordance with recommendations of the ASBMR⁽³⁾. The volume of callus was analyzed by using the CTAn software, where the entire callus was selected as the ROI. Seven femurs from each group were casually selected for histological analysis.

The entire fractured femur with a small quantity of adherent soft tissue was fixed in cold 4% paraformaldehyde, decalcified in cold 10% EDTA, embedded in paraffin, sectioned at 5 μ m, and placed on charged slides (Manco Inc., USA). Coronal sections were stained with hematoxylin and eosin (HE). Sections were analyzed under bright field microscopy (Axiovert; Carl Zeiss, Germany), and images were captured with a CCD camera (AxioCam MRc; Carl Zeiss, Germany) in the region of the bone callus, with magnifications of 12.5, 50, and 200x.

Continuous variables were expressed as the means and standard deviations (SD). The results obtained in the four groups were compared using Kruskal-Wallis one-way analysis of variance, followed by Dunn's post hoc test, and the results are shown as the geometric mean and 95% confidence interval. p values less than 0.05 were considered statistically significant. All statistical analyses were performed with RStudio 0.99.902 (RStudio, Inc., USA).

Results

Upon study entry (day 0), the body mass was similar among all groups ($p>0.05$). All rats gained weight during the observation period. However, diabetic rats gained less weight than sham rats. Thus, the final body weight of the diabetic rats was significantly lower than sham rats ($p<0.05$). Vibration seemed to influence body mass gain in diabetic trained rats, but not in sham animals; the final body masses of the diabetic trained rats were 7% and 16% higher than in non-trained diabetic rats at 14 or 28 days after fracture, respectively ($p<0.05$) (Figure 3).

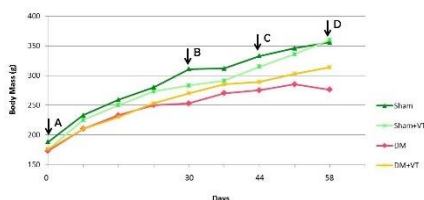


Figure 3. Comparison of body mass (in grams) among groups. A: Upon study entry (day 0, diabetes/sham induction), body mass was similar among all groups ($p>0.05$). B: Closed femoral fracture procedure. C: Final observation period of 14 days post-fracture. Body mass was lower in diabetic rats than in sham rats ($p<0.05$). D: Final observation period of 28 days post-fracture.

Diabetes led to a dramatic impairment of both bone quality and fracture healing in both end-points assessment (with a time-dependent feature). The level of circulating IGF-1 was significantly reduced in diabetic rats (-93%, $p<0.05$). However, vibration therapy significantly increased the IGF-1 level by 839% ($p<0.05$). The CTX-I level was increased by 1385% in diabetic rats. Vibration therapy significantly decreased the RANK-L level by 19% in diabetic rats. Vibration therapy also decreased the RANK-L level by 20% in the sham rats, but without statistical significance (Table 1).

Table 1. The levels of circulating IGF-1, RANK, and CTX-I. IGF-1 was significantly decreased in diabetic rats and was increased by vibration therapy. CTX-I levels were significantly increased by diabetes. Letters indicate significant differences ($p<0.05$).

Circulating levels of IGF-1, RANK and CTX-I (pg/ml) mean \pm SD			
SHAM	SHAM+VT	DM	DM+VT

IGF-1	3014.35±826.48	1822.56±962.34	246.04±181.38 ^a	1889.54±652.13 ^b
RANK	445.35±126.89	346.46±48.86 ^a	453.01±98.37	366.43±79.73 ^b
CTX-I	149.19±49.12	419.56±91.49 ^a	623.29±170.71 ^a	692.89±158.73

^ap<0.0001 vs SHAM

^bp<0.03 vs DM

In intact bone, diabetes caused detrimental changes in bone microarchitecture (reduced BV by 90%, BV/TV by 87%, TbN by 85% and Conn.D by 77%). VT was effective at ameliorating trabecular microarchitecture (augmented BV by 494%, BV/TV by 386%, TbN by 394% and Conn.D by 233%) (Figure 4).

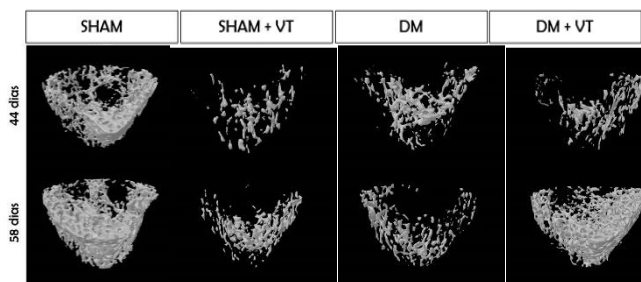


Figure 4: Trabecular bone microstructures of femoral metaphysis.

In bone healing, diabetes caused a delay in cell proliferation; 81% in callus volume and 69% in callus mineralization. VT was effective at improving fracture healing by accelerating osteogenic and chondrogenic cell proliferation at the fracture callus (Figure 5), thus increasing callus volume by 52% (Figure 6).

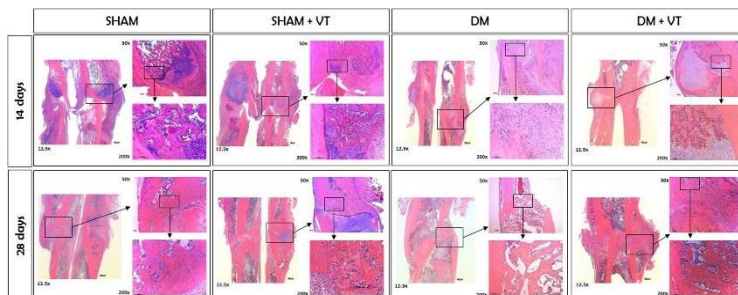


Figure 5: Histological slides of fractured femurs stained with HE at magnifications of 12.5, 50, and 200x.

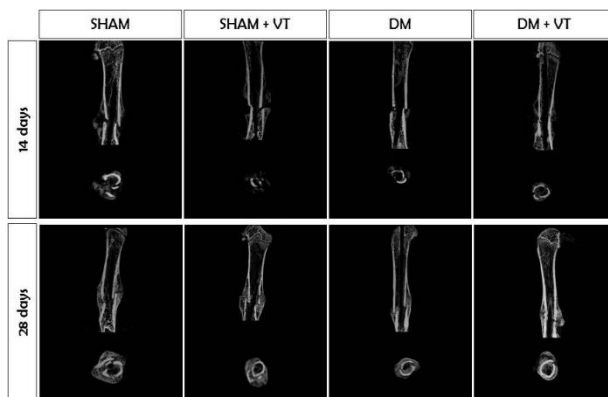


Figure 6. Coronal and axial tridimensional μ CT images of fractured femurs. Diabetes impaired bone healing, and bone calluses were smaller and less mineralized than in sham rats during both follow-up periods. Vibration therapy significantly increased bone callus volume and mineralization on both follow-ups, but only in diabetic rats.

Conclusion

We concluded that diabetes had detrimental effects on both non-fractured bone quality and fracture healing. Vibration therapy was very effective at counteracting the significant disruption in bone metabolism, mass and microarchitecture on both non-fractured and fractured femurs of diabetic rats.

References:

- 1- Follak N, Kloting I, Wolf E & Merk H. Improving metabolic control reverses the histomorphometric and biomechanical abnormalities of an experimentally induced bone defect in spontaneously diabetic rats. *Calcif Tissue Int* 2004 74 551-560.
- 2- Santiago HA, Zamarioli A, Sousa Neto MD, Volpon JB. Exposure to secondhand smoke impairs fracture healing in rats. *Clin Orthop Relat Res* 2016.
- 3- Bouxsein ML, Boyd SK, Christiansen BA, Guldberg RE, Jepsen KJ, Muller R. "Guidelines for assessment of bone microstructure in rodents using micro-computed tomography". *J Bone Miner Res*, 1468-1486, 2010.

Dissolution pattern of injectable ceramics in large animal model

Patrina S.P. Poh¹, Michael Diefenbeck², Eva Liden³, Martijn van Griensven¹

¹ Experimental Trauma Surgery, Klinikum rechts der Isar, Technical University of Munich, Ismaninger Str. 22, 81675 Munich, Germany.

² Scientific Consulting in Orthopaedic Surgery, Hamburg, Germany.

³ BoneSupport AB, Lund, Sweden.

Aims

In this study, micro-computed tomography (μ CT) was utilized for the investigation of cascade of event, from biomaterials' dissolution to bone formation for an injectable bioceramic using an ovine model with critical-sized bone defect.

Method

At time-points, samples were retrieved, fixed in 4% paraformaldehyde (PFA), transferred into 70% ethanol and stored at 4°C until ready to scan. Samples were kept in 70% ethanol and scanning was performed at 35 μ m resolution using 0.11mm Cu filter at 90 kV and 260 μ A. Scan data were reconstructed using 3DRecon and analyzed using CTAn.

Results

Through thresholding, we could follow the progression of biomaterials' dissolution and reformation towards formation of new bone over the course of 6 months as shown in Figure 1.

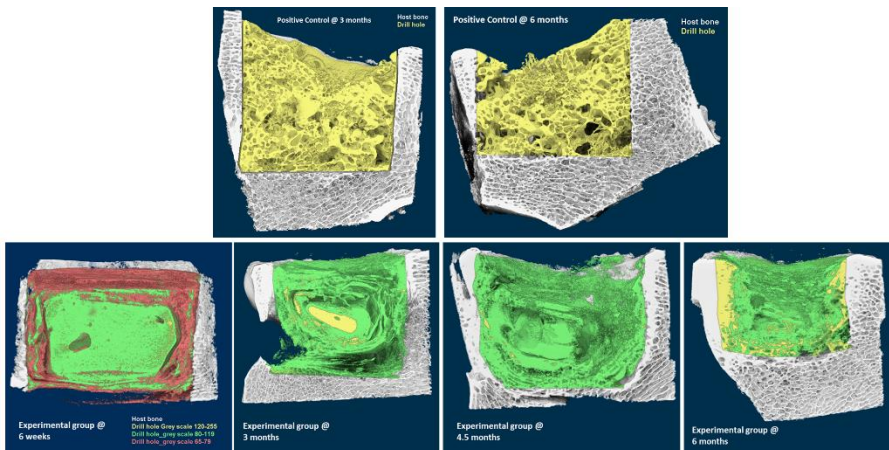


Figure 16 3D reconstruction images generated using CTVox. (top row) showing positive control group at 3 and 6 months' time-point and (bottom row) showing experimental group at 6 weeks, 3, 4.5 and 6 months' time-point.

By custom analysis, the BV/TV were calculated and illustrated in Table 1. The bioceramics implanted have very similar threshold to host bone. Hence, for the analyses, volume of interest (VOI) was set with a cylindrical-shaped measuring 2.5 (diameter) x 2 cm (length) to recapitulate the drill hole defect and threshold was standardised at 65-255 greyscale value.

Table 1 Samples with the corresponding TV, BV and BV/TV values.

Biomaterial	Duration	Total drill hole volume (TV)	Biomaterial/ Bone volume (BV)	BV/TV
Experimental	6 weeks	10.852 cm ³	8.532cm ³	78.62468 %
	3 mths	14.714 cm ³	6.018 cm ³	40.90276%
	4.5 mths	9.411 cm ³	2.886 cm ³	30.66785 %
	6 mths	9.193cm ³	5.548cm ³	60.35383%
Positive control	3 mths	11.48 cm ³	4.86 cm ³	42.31366%
	6 mths	10.322 cm ³	3.229 cm ³	31.28726%

Results indicated that the biomaterial undergoes dissolution upon implantation, thereby altering the microenvironment (i.e. ions content) at the defect site triggering a cascade of events towards the formation of new bone.

Conclusion

This study show that μ CT is a viable way to follow the progression of biomaterials' dissolution and reformation towards formation of new bone.

Acknowledgement

This study was sponsored by BoneSupport AB.

Micro-CT investigation of the eye tumor

B. Leszczczyński¹, M. Śniegocka², M. Elas², A. Wróbel¹, P. Sojka-Leszczczyńska³, R. Pędrys¹

¹ M. Smoluchowski Institute of Physics, Jagiellonian University, Krakow, Poland

² Faculty of Biochemistry, Biophysics, and Biotechnology, Jagiellonian University, Krakow, Poland

³ Regional Ophthalmology Hospital, Krakow, Poland

Aims

The Bomirski Hamster Melanoma (BHM) (Bomirski et al., 1988) is a spontaneous skin melanoma cell line. This neoplasm has been successfully used as an eye tumor animal model in the studies on tumor vascular network, metastasis and radiation treatment (Romanowska-Dixon et al., 2001; Romanowska-Dixon et al., 2013).

Uveal melanoma is the most common eye tumor in humans. The lack of lymphatic vessels in the eye results in hematogenous spread as the main route of metastasis of uveal melanoma.

BHM melanoma implanted in the hamster eye is characterized by a rapid tumor growth, metastatic expansion and intensive development of pathological vasculature. In this work we have optimized micro-CT scanning and analysis for simultaneous visualization of normal ocular tissues, the melanoma, and its vasculature.

Method

This pilot study included visualization and image analysis of two hamster eyeballs: one from experimental group with implanted melanoma cells to the anterior chamber of the globe, and the second eyeball from the non-tumor control group. After enucleation both eyeballs were fixed in 4% formaldehyde. For X-ray contrast enhancement we used iodine staining technique (Leszczczyński, 2016). Samples were stained in the pure Lugol solution for 96h at 4°C. After that, samples were scanned using the Bruker SkyScan 1272 micro-CT system. The scanning parameters were set as follows: voltage of 60 kV, current of 166 µA, rotation step of 0.4°, pixel size of 6 µm. The 0.25 mm Al filter was used. The final projection images were averaged from 8 frames each, for signal to noise ratio enhancement.

Quantitative and qualitative analysis was done based on micro-CT reconstruction images histograms using CTAnalyser software. 3D volume rendering models of investigated samples were performed using CTvox software.

Results

The non-tumor sample provided high quality, well contrasted images presenting normal anatomy of the hamster eyeball as shown in Fig. 1a. A great number of anatomical structures such as cornea, lens and layers of the globe walls can be appreciated in fine details. Advanced malignancy, with the tumor occupying the entire anterior chamber and the pathological disorganized irregular tumor vascular network was visualized in the experimental group eyeball, presented in Fig. 1b.

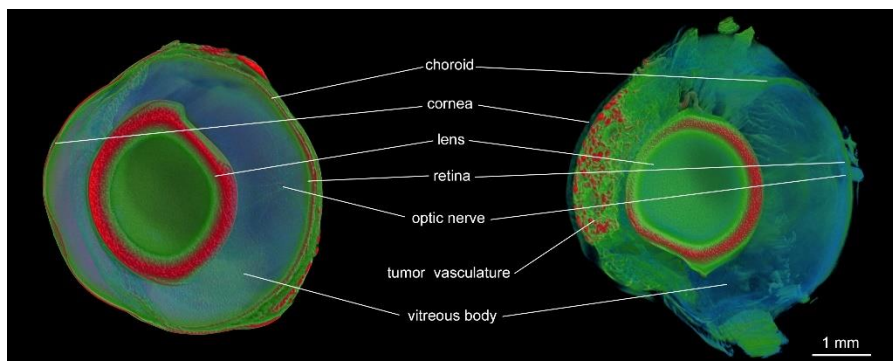


Fig. 1. Volume rendering models of hamster eyeballs stained in Lugol solution for 96h: non-tumor control group (a), Bomirski melanoma implanted experimental group (b).

Analysis of the grey level histograms for both samples has shown significant difference between the grey level distributions. Transfer function manipulation allowed to distinguish grey level range corresponding to the particular eye and tumor structures, as presented in Fig. 2.

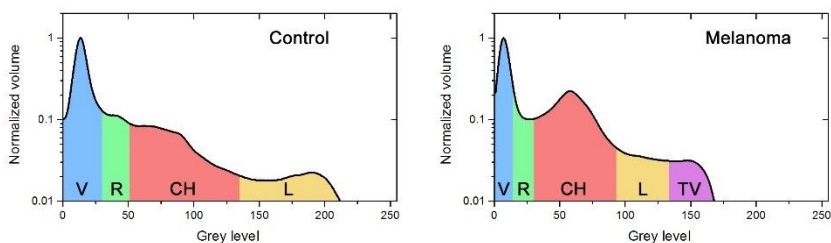


Fig. 2. Grey level histograms for control and melanoma sample. Ranges corresponding to particular eye and tumor structures are highlighted with different colors: blue (V) - vitreous body; green (R) - retina; red (CH) - choroid; yellow (L) - lens; magenta (TV) - tumor vessels.

Conclusion

Micro-CT visualization enhanced with Lugol solution staining provides high resolution images of the animal eye globes, much more detailed in comparison to previously used techniques such as ultrasonography or vascular endocasting. Therefore this method has a great potential in preclinical eye cancer research using small animal models. Micro-CT quantitative analysis tools can be successfully applied to investigate cancer vascularization.

References

1. Bomirski A., Słominski A., Bigda J. (1988) The natural history of a family of transplantable melanomas in hamsters. *Cancer Metastasis Rev* 7: 95–118
2. Romanowska-Dixon B., Urbanska, K., Elas, M., Pajak, S., Zygulska-Mach, H., Miodonski, A. (2001) Angiomorphology of the pigmented bomirski melanoma

- growing in hamster eye. *Annals Of Anatomy - Anatomischer Anzeiger*, 183(6), 559-565.
3. Romanowska-Dixon B., Elas M., Swakoń J., Sowa U., Ptaszkiewicz M., Szczygieł M., Krzykawska M., Olko P., Urbańska K. (2013) Metastasis inhibition after proton beam, β - and γ -irradiation of melanoma growing in the hamster eye.
 4. Leszczyński B. (2016) Optimization of research procedures in medical applications of X-ray microtomography, PhD thesis, Jagiellonian University, Krakow, Poland

Revision of Root Canal fillings with machine processing – a μ -CT analysis

S. Reimann¹, J. Pöhlmann², A. Weber¹, C. Bourauel¹, M. Frentzen²

¹ Oral Technology, University of Bonn, Germany

² Department of Operative and Preventive Dentistry, Dental Faculty, University of Bonn, Germany

Aims

This study analyzes the efficacy and efficiency of the M_{two}[®] basic sequence and the M_{two}[®] retreatment files (VDW, Munich, Germany) compared to the conventional manual processing (Hedström and K files) for the revision of root fillings.

Method

For these ex vivo, in vitro experiments, 33 human lower molar roots were collected and separated into individual roots. The canals of the individual roots were manually prepared up to ISO 40 and were filled with gutta-percha cones and sealer according to the technique of lateral condensation and stored for one week at 37° C in sodium azide solution. The roots were randomly divided into three groups (Group 1: Hedström and Kerr files, Group 2: M_{two}[®] base sequence, Group 3: M_{two}[®] retreatment system). All characteristics (Schneider angle (angle of curvature of the tooth root), canal length, mesial / distal and canal configuration) were represented in the equal numbers in each group.

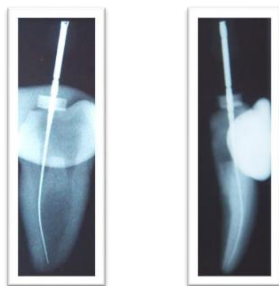


Figure 1: X-ray measurement image, taken in two directions. The file is approximately 1 mm in front of the radiographic apex.

After one week the root fillings up to ISO 40 were revised. The time, material breaks, and material residues were documented. The material residues were recorded semi quantitatively radio graphically (X-ray, 60 kV, 125 ms), semi quantitative-computer tomography and digital micro-computed tomography (SkyScan 1174v2, 50kV).

The data were analyzed statistically using SPSS, Kruskal-Wallis test and Chi-square test.

Results

The M_{two}[®] revision system was able to perform root filling revision significantly faster ($p = 0$). In the group of the M_{two}[®] basic sequence, the most frequent file fractures ($p = 0.1$) occurred. All

three systems left material residues. In the manual revision form, the least amount of material residues could be measured ($p = 0$).

There are no major differences in the material residues between the M_{two}° base sequence and the M_{two}° revision system; but the revision system was significantly more time-saving and had no instrument fractures. The remaining material residues could be well represented in the in vitro μ -CT analysis and this method of investigation also provided further information on channel configuration and revision behavior of the files.

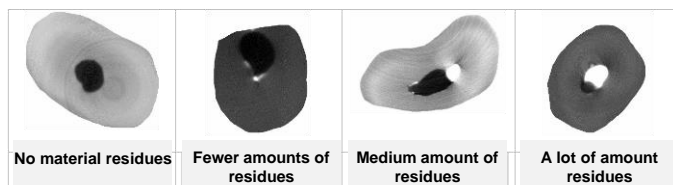


Figure 2: Examples of the classification of the gutta-percha residues in the ROI (the white regions).

Conclusion

The μ -CT scan was effective with a low scan time, particularly when compared to a histological preparation [1]. The samples can be re-used in this non-destructive process; all data are reproducible and stored in digital form.

References:

1. Wolf M, Küpper K, Reimann S, Bourauel C, Frentzen M, "3D analyses of interface voids in root canals filled with different sealer materials in combination with warm gutta-percha technique." *Clinical Oral Investigations*, 155–161, 2014

Micro-CT based analysis of porous cryogel scaffolds for bone formation analysis in critical size defect and other tissue engineering applications

A.K. Teotia¹, Anamika¹, D.B. Raina², A. Kumar¹

¹Department of Biological Sciences and Bioengineering, Indian Institute of Technology Kanpur, Kanpur, Uttar Pradesh, India. 208016

²Department of Orthopedics, Lund University, Lund 22185, Sweden

Aims

During the past century improvements in biomaterials and tissue engineering have made important contributions in field of regenerative medicine. New improved techniques, approached and therapies are devised to treat critical size defects which were once thought impossible to treat. Tissue engineering employs combination of biomaterials, growth factors and cells to generate functional tissue which can substitute or complement the host tissue functionality. Cryogels are macroporous hydrogel scaffolds with highly interconnected pore architecture generated using cryogelation technology. Cryogels are highly tunable for their properties and can be synthesized using different natural and synthetic polymers. We have synthesized cryogels in different forms, architecture and composition for tissue engineering applications in area of neural and bone tissue engineering. Micro-CT analysis was performed on the cryogel scaffolds and conduits to check scaffold porosity, pore architecture, uniformity and integrity. Further micro-CT based bone formation analysis performed 8 weeks post implantation of bone substitutes and porous bioactive molecule enriched hydroxyapatite-polymer composite scaffold in critical size defect showed 4 times more bone formation in comparison to empty defect site.

Method

Porous Composite Bilayered Scaffold for Bone Regeneration:

Porous bilayered polymer composite scaffolds (BS) consisting lower polymer layer composed of bioactive glass, hydroxyapatite and silk fibroin was synthesized using cryogelation technology [1]. Briefly polymer solution containing bioactive glass and hydroxyapatite in dispersed phase was frozen at -15 °C in presence of 0.2 % v/v glutaraldehyde as crosslinker for a period of 12 hrs. Upon thawing after incubation period melting of ice crystals lead to formation of highly interconnected porous architecture. For generation of bilayered scaffold the porous composite scaffold was integrated with nano-hydroxyapatite-calcium sulphate bone substitute (NC) [2] [3]. The NC was functionalized by incorporating zoledronic acid (ZA) and recombinant bone morphogenetic protein-2 (rhBMP-2) in NC. Incorporation of anabolic rhBMP-2 and anticatabolic ZA was done to enhance bone formation and inhibit bone resorption overall getting rapid defect healing. The NC alone or bilayered scaffold (BS) was implanted in 8.5 mm critical defect in rat calvarial bone defect model for a period of 12 weeks. The animals were implanted with BS functionalized with either ZA/rhBMP-2 or both, in control group no treatment was given and defect was left empty. Highly mineralized tissue formation was analysed using micro-CT analysis *in-vivo* 8 weeks post implantation and *in-vitro* 12 weeks post implantation. Further histology based bone formation analysis was performed 12 weeks post implantation using Masson's trichrome and alizarin red staining on decalcified and undecalcified sections respectively.

Aligned Porous Cryogel Scaffold Conduits for Nerve Regeneration:

Porous cryogel based nerve conduits having aligned pore architecture were synthesized using cryogelation and electrospinning technology. Firstly, the hollow polyurethane conduit was fabricated by electrospinning technique. Secondly, chitosan-gelatin aligned cryogel filler using glutaraldehyde (1.5% v/v) as crosslinker was fabricated by directional freezing using liquid nitrogen vapors in the lumen of the conduit [4]. The formed scaffolds were then kept at -20 °C for gelation for 12 hrs. After thawing the ice crystals melted resulting into highly aligned and interconnected porous architecture which was analyzed using SEM and micro-CT facility for pore architecture and porosity.

Results

Micro-CT based Porosity and Pore Architecture Analysis

Micro-CT analysis of the synthesized composite and polymer scaffolds was performed to analyze porosity, pore interconnectivity and architecture analysis (Figure-1). Micro-CT provides a non-destructive technique for physicochemical characterization of soft materials and composite scaffolds. The porosity and pore architecture analysis was also carried out using other more conventional techniques such as porosity and pore size distribution using liquid extrusion porosimeter (LEP®, Porous Materials Incorporated, USA) and using Archimedes principle. The scaffolds were having 70-75% porosity.

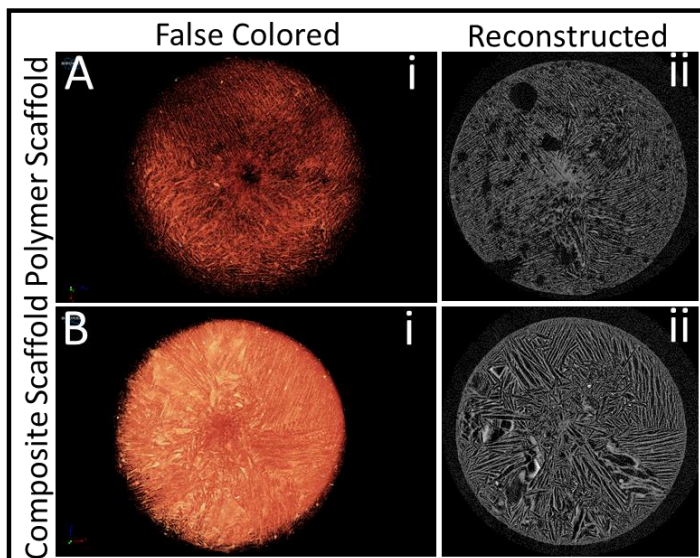


Figure 1: Micro-CT analysis of porous scaffolds. A(i) and B(i), False colored image A(ii), B(ii) Regenerated micro-CT image of polymer (A) and hydroxyapatite-polymer (B) composite scaffolds showing porous architecture pore alignment.

The pore architecture and pore alignment was evaluated out using scanning electron microscopy (SEM). It was observed both from micro-CT as well as SEM analysis (Figure-2) that the directional freezing performed in neural conduits leads to generation of porous scaffolds with highly aligned pore organization. The presence of highly aligned pores (Figure-2) is very important for providing directional growth of the regenerating nerve fibers which in absence of such directional cues fail to form interconnection between the proximal and distal ends of the damaged nerve fibers.

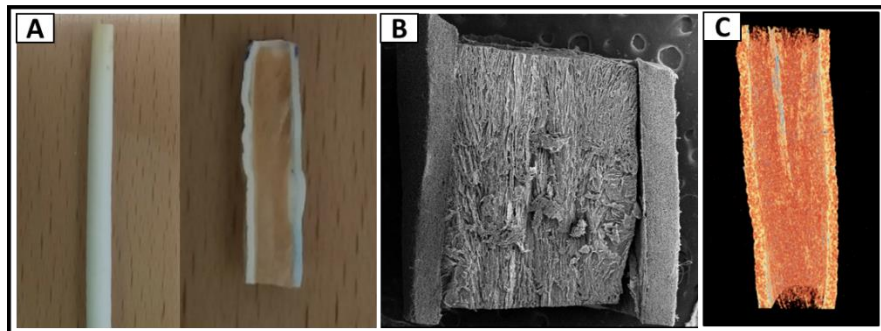


Figure-2: Images of the nerve conduit for peripheral nerve regeneration (A) Digital images of the polyurethane nerve guide filled with aligned chitosan-gelatin cryogel. (B, C) SEM and Micro-CT image showing the aligned porous architecture respectively.

A high level of correlation was observed between the results obtained using micro-CT and other conventional methods for performing physicochemical characterizations.

Micro-CT based Histomorphometry and Tissue Mineralization analysis

Micro-CT analysis of the defect site 8 and 12 week post implantation of NC (Figure-3) and bilayered scaffold (BS) (Figure-4) (Figure-5) showed difference in amount of ossification and BS present in the defect site among the groups.

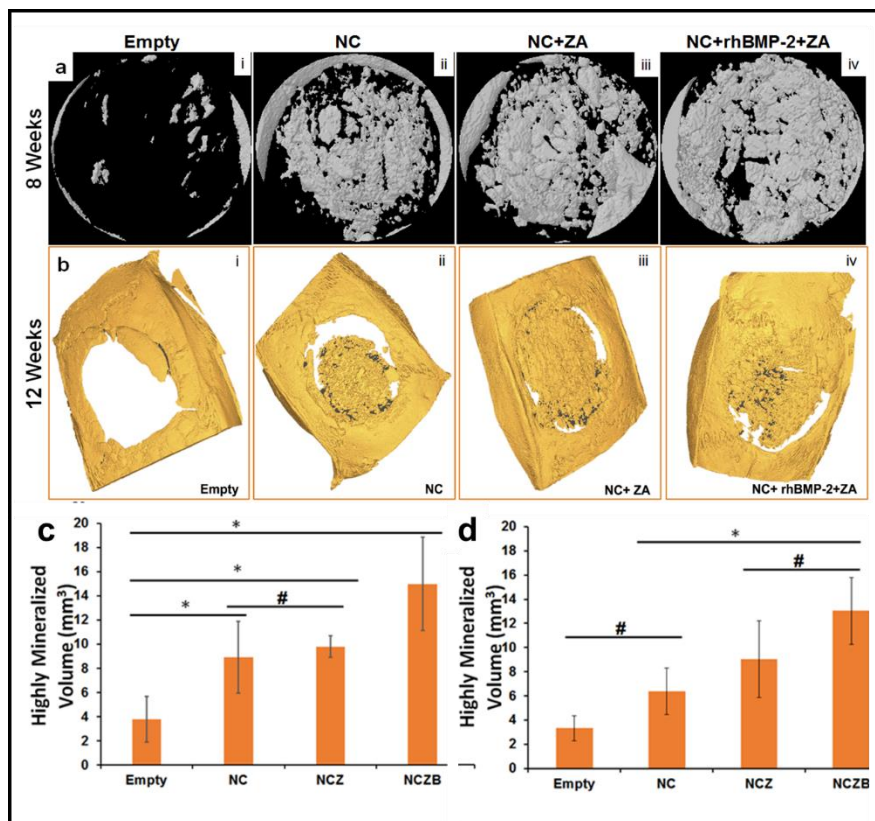


Figure 3: Micro-CT analysis of the defect site post nano-cement (NC) implantation cranial defect model. (a) 8-Weeks post implantation, (b) 12-Weeks post implantation, (c and d) micro-CT based histomorphometry analysis of tissue mineralization of defect site post implantation.³

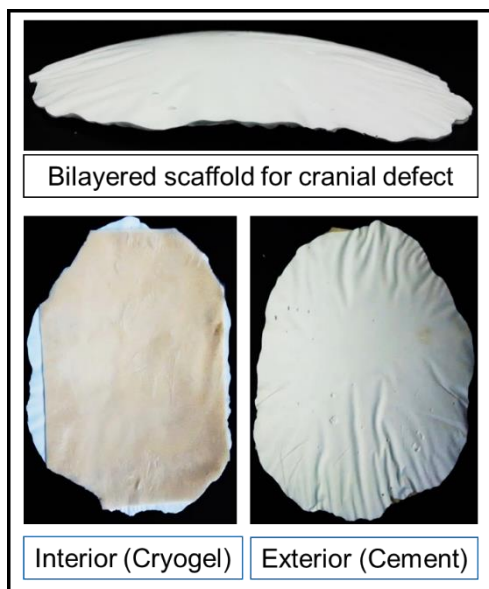


Figure 4: Nano-cement-composite bilayered scaffold for cranial defect regeneration.

In all the groups the NC got resorbed to give rise to porous architectures inside the defect. The dissolving NC has also integrated well with the underlying composite porous scaffold layer. These structures will provide the osteoconductive surfaces for cell infiltration and proliferation. In control group least amount of mineralized tissue was present at the defect site, with highest amount present in NC+rhBMP-2+ZA group, followed by NC+ZA group, this can be due to inhibition of resorption due to presence of ZA in the latter and induction of ossification in addition of inhibition of resorption due to presence of both ZA and rhBMP-2 in former. The degree of mineralized tissue present was highest in NC+rhBMP-2+ZA group (15.0 mm^3) ($p < 0.05$) followed by NC+ZA group (9.81 mm^3), then NC alone group (8.93 mm^3) followed by empty (3.4 mm^3) (Figure-3). Observations were similar after 12 weeks also both in radiological and micro-CT analysis (Figure-3). The NC-alone group showed prominent loss of implant NC from defect site at earlier time points also, this might have lead to decreased cell infiltration and differentiation due to lack of osteoinductive factors at defect site leading to formation of fibrous tissue only at defect site. Excessive ossification observed at early time points in NC+rhBMP-2+ZA group may be due to combined effects of BMP and ZA and slowly leaching calcium sulphate, which at later time points became lower due to bone remodeling activity and resorption of excessive mineralization from defect site (Figure-3). In BS alone or BS functionalized with ZA/rhBMP-2 groups implanted at the defect site (Figure-5) highest amount of mineralized tissue was present in the BS+rhBMP-2+ZA group (0.8 mm^3), followed by BS+ZA (0.4 mm^3) group, then by BS alone group (0.5 mm^3). The BS alone and BS+ZA group showed no significant difference in amount of tissue mineralization at the defect site. BS+ZA group also showed least amount of material resorption from the defect site. The empty group showed least amount of the tissue mineralization at the defect site and defect healing as was confirmed by histomorphometric analysis (Figure-6).

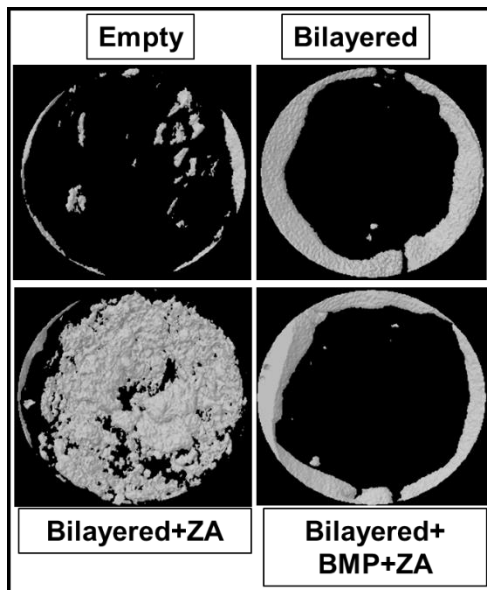


Figure 5: Micro-CT analysis of mineralization at the defect site 8-weeks post implantation of nano-cement-composite bilayered scaffold (BS) implanted in 8.5 mm critical rat cranial defect model.

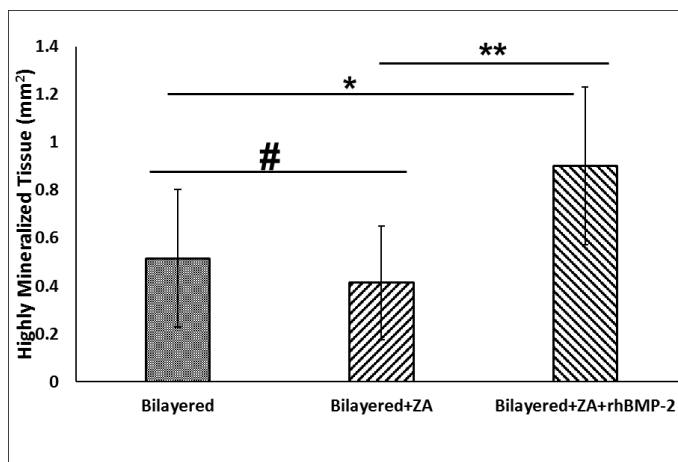


Figure 6: Histomorphometric analysis of tissue mineralization at the defect site 8-weeks post implantation of nano-cement-composite bilayered scaffold (BS) implanted in 8.5 mm critical rat cranial defect model.

Conclusion

A high level of correlation was observed between the results obtained using micro-CT and other conventional methods. Micro-CT provided advantage that several of the physicochemical and physical characterizations such as architecture, composition analysis, sample uniformity, particle distributions, porosity, pore architecture and interconnectivity etc. can be performed on a single platform in a non-destructive manner on a single sample specimen leading to time, sample and cost savings.

References:

- [1] D. B. Raina, H. Isaksson, A. K. Teotia, L. Lidgren, M. Tägil, and A. Kumar, "Biocomposite macroporous cryogels as potential carrier scaffolds for bone active agents augmenting bone regeneration," *J. Control. Release*, vol. 235, pp. 365–378, 2016.
- [2] A. K. Teotia, A. Gupta, D. B. Raina, L. Lidgren, and A. Kumar, "Gelatin-Modified Bone Substitute with Bioactive Molecules Enhance Cellular Interactions and Bone Regeneration.," *ACS Appl. Mater. Interfaces*, vol. 8, no. 17, pp. 10775–87, May 2016.
- [3] A. K. Teotia, D. B. Raina, C. Singh, N. Sinha, H. Isaksson, M. Tägil, L. Lidgren, and A. Kumar, "Nano-Hydroxyapatite Bone Substitute Functionalized with Bone Active Molecules for Enhanced Cranial Bone Regeneration," *ACS Appl. Mater. Interfaces*, vol. 9, no. 8, pp. 6816–6828, Mar. 2017.
- [4] Wu, X., Y. Liu, X. Li, P. Wen, Y. Zhang, Y. Long, X. Wang, Y. Guo, F. Xing, and J. Gao. "Preparation of aligned porous gelatin scaffolds by unidirectional freeze-drying method," *Acta biomaterialia* 6, no. 3 pp. 1167-1177, Mar. 2010.

Optimization of Endodontic Irrigation Procedure using Computational Fluid Dynamics: Preliminary Results

Andy L. Olivares¹, Víctor Carmona¹, Guillem García¹, Arnau Manasanch¹, Roger Domingo¹, Oscar Camara¹, Jerome Noailly¹, M.A. González Ballester^{1,3}, M.D. Sousa-Neto², M.A. Versiani², Simone Tassani¹

¹ Universitat Pompeu Fabra, C/ Roc Boronat, 138 08018 Barcelona, SPAIN

² Department of Restorative Dentistry, Dental School of Ribeirão Preto, University of São Paulo, Brazil

³ ICREA, Barcelona, Spain.

Aims

Root canal treatment is necessary when the pulp, the soft tissue inside the root canal, becomes inflamed or infected. The inflammation or infection can have a variety of causes such as deep decay, repeated dental procedures on the tooth, and cracks caused by trauma. If pulp inflammation or infection is left untreated, it can cause pain or lead to an abscess.¹⁻³ Therefore, the purpose of endodontic therapy is the removal of all vital or necrotic tissue, microorganisms, and microbial by-products from the root canal space.⁴⁻⁶ Several procedure steps are necessary aiming to achieve this goal, including diagnosis, access opening, shaping and cleaning procedures,¹⁻¹⁴ obturation,¹⁵⁻¹⁷ and restauration of the compromised tooth. Among the treatment steps, shaping and cleaning procedures play a pivotal role in eliminating or reducing bacterial populations from the main root canal,^{4,12} but the disinfecting effects of instruments (shaping) and irrigants (cleaning) may be somewhat hampered in cases with complex anatomy^{3,10,11,14,18-32} and the resistance of microbial biofilms.^{4-6,8,9,12,15,33,34} Cutting-edge advances with micro-computed tomography (micro-CT) analysis brought new perspectives on the overall mechanical preparation quality of the root canal space confirming the inability of shaping tools in acting within the anatomical complexity of the root canal.^{6,7,22,27} overall, the amount of mechanically prepared root canal surface is frequently below 60%.^{5-7,10,13,14,30} These mechanical substandard results certainly compromise intracanal disinfection since pulp tissue or biofilm may remain untouched over non-instrumented dentine areas, offering the possibility for microorganisms to re-colonize the canal system, leading to treatment failure.⁴⁻⁶ Thus, the use of an efficient irrigating protocol grabs the major role to optimize the final quality of the intracanal disinfection.^{5,12,13} In this way, considerable scientific efforts have been made to improve the overall efficiency of irrigating solutions, as well as its delivering methods, aiming to push chemicals to the hard-to-reach areas of the root canal.²⁶ In order to understand the intracanal effect of irrigants by different irrigation protocols, several experimental models have been used.³¹ The close-to-ideal experimental model should overcome these limitations, allowing reliable *in situ* volumetric quantitative evaluation of irrigation efficacy.¹³ It would also be able to track three-dimensionally whether irrigants are able to reach defiant areas of the root canal space, mainly the ones untouched by the instruments, offering a deeper and comprehensive understanding on capabilities and limitations of different irrigation protocols. Ultimately, it would drive research towards the seeking requisite of a full microcirculation by irrigants into the anatomical complexities of the root canal system.^{4-6,9,12,13,15,31,34,35}

The aim of this study was to develop a methodology using a Computational Fluid Dynamic approach over a micro-CT model of a real tooth to trace irrigant distribution within curved canals enlarged by different instruments.

Method

Image Processing

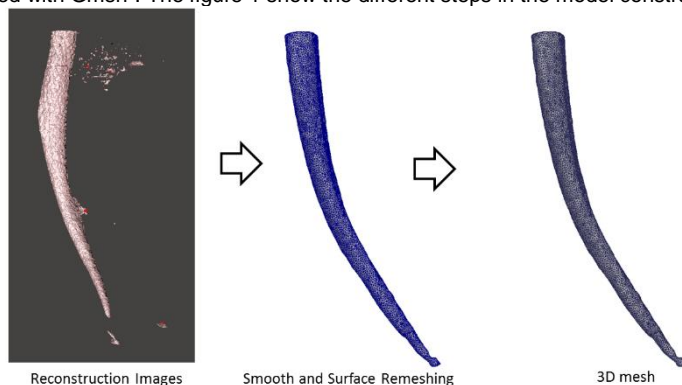
One mesial root of a human mandibular first molar with 2 independent and curved root canals was selected and scanned in a micro-CT device (SkyScan 1174v2; Bruker-microCT, Kontich, Belgium) at 50 kV, 800 μ A, and isotropic pixel size of 19.7 μ m. Scanning was performed by 180° rotation around the vertical axis, camera exposure time of 7000 ms, rotation step of 1°, frame averaging of 2, using a 0.5-mm-thick aluminum filter. The canals were negotiated to length with a size 10 K-file and the coronal thirds were flared with a size 2 LA Axxess bur. Flaring was followed by irrigation with 5 mL of 2.5% NaOCl delivered in a syringe with a 30-gauge needle. Patency was confirmed by inserting a size 10 K-file through the apical foramen before and after completion of root canal preparation. Working length (WL) was established at 0.5 mm from canal length. After canal preparation with Reciproc R25 instrument, a new scan was done following the initial parameters. Then, canals were sequentially enlarged with Reciproc R40 instrument and a final scan was performed. Images were reconstructed (NRecon v.1.6.10.4; Bruker-microCT) and a 3D model of the root canal before and after the enlargement with R25 and R40, in .STL format, was created using CTAn 1.16 software (Bruker-microCT).

Experimental Design

The experiment was designed to analyze the effect of 3 main factors (needle type, needle depth and root canal gauge) over the velocity and the shear stress of the irrigation solution over the dentin. For each factor 2 levels were tested: 2 types of needle (open-ended and lateral-opening), 2 depths of the needle from the root tip (1 mm and 5 mm), and 2 canal enlargements (R25: ISO 25 tip and 0.08 taper; and R40: ISO tip size 40 and 0.06 taper). The number of factors and levels lead to 8 modeling combinations. Measures of average velocity and shear-stress were obtained from the developed models at 0.5, 2.5 and 5 mm from the root tip. The measurement plan was handled as a fourth feature with three levels, obtaining a total number of 24 measurements.

Computational Irrigation Fluid Model

Models of root canal were made from the images segmentation. Subsequently, the needle was designed and added to the root surface model using MeshMixer¹. Location and physical dimensions of needle were controlled. From the triangulated surface, the tetrahedral mesh was created with Gmsh². The figure 1 show the different steps in the model construction.



¹ <http://www.meshmixer.com/>

² <http://gmsh.info/>

Figure 1. Smoothing process and surface remeshing were applied to the micro-CT reconstruction of the root canal to create a 3D mesh of the root.

The models of the needles were added to the geometry of the root in order to create all the different configurations described above (Figure 2).

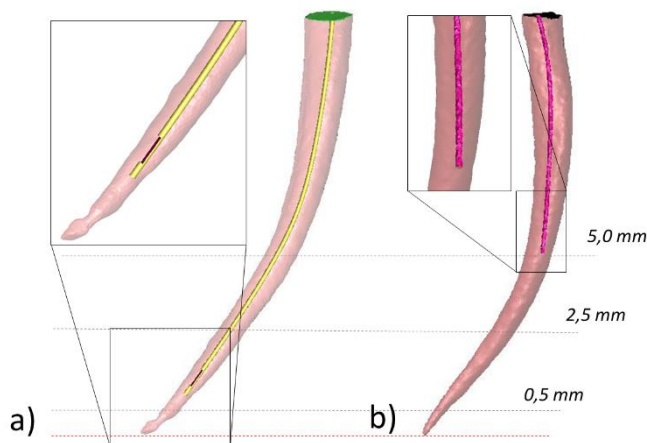


Figure 2. The figure shows the geometry of the two needles, (lateral-opened – a, and open-ended - b), the preparation of the canal (R25 – a, R40 – b), the positioning of the needle (1mm – a, 5mm – b) and the three measurement plane.

A second order implicit unsteady formulation was used for the solution of the momentum equations in the Computational Fluid Dynamic simulations, in conjunction with a standard partial discretization for the pressure (under-relaxation factors of 0.3 and 0.7 for the pressure and momentum, respectively). Irrigation flow was modelled with the incompressible Navier–Stokes and continuity equations. Residuals of mass and momentum conservation equations lower than 0.001 were considered as absolute convergence criteria. The irrigant was modelled as an incompressible Newtonian fluid like water with density $\rho = 1000 \text{ kg/m}^3$ and dynamic viscosity $\mu = 0.001 \text{ Pa}\cdot\text{s}$. Simulations were run using a laminar flow hypothesis under isothermal and non-gravitational effects. All root walls were simulated rigid (like bone) and with no-slip conditions. The conditions applied mimic the injection of cleaner liquid with a maximum inlet flux of 0.25 mL/s . Atmospheric pressure at the top of the root canal was applied. Velocities and wall shear stress were computed and analyzed in three different zones and related with the force to remove the content from the root canal space.

Statistical Analysis

Multi-factorial ANOVA was performed and the analysis focused on the study of the main factors and 2-way Interactions, and a regression analysis was performed to verify the significance of each factor and interaction. The absence of multiple root canal morphologies forced the use of an experimental design in which higher level interactions were not analyzed and their degrees of freedom were used to estimate the error. All the differences were deemed to be statistically significant at a probability of $p < 0.05$.

Results

Data of average wall shear stress and velocity were extracted from all the eight simulations (Figure 3) and analyzed.

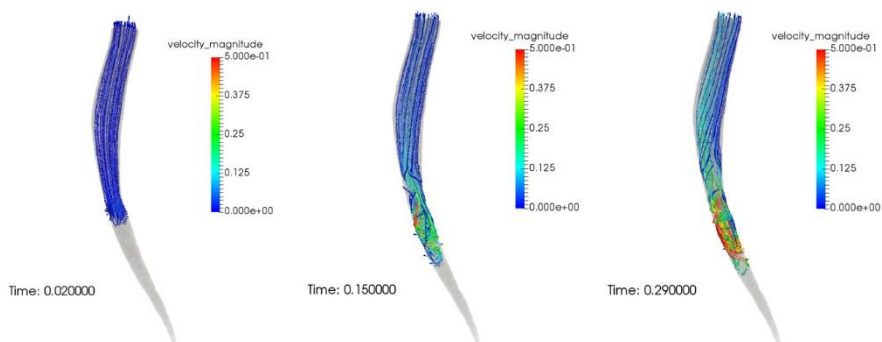


Figure 3. The velocity of the irrigation fluid is showed at three different time points during the injection.

The ANOVA analysis showed no significant differences in wall shear stress for main effects nor 2-ways interactions. On the other hand, significant differences were found in main velocity in 3 main factors and in two interactions (Figure 4).

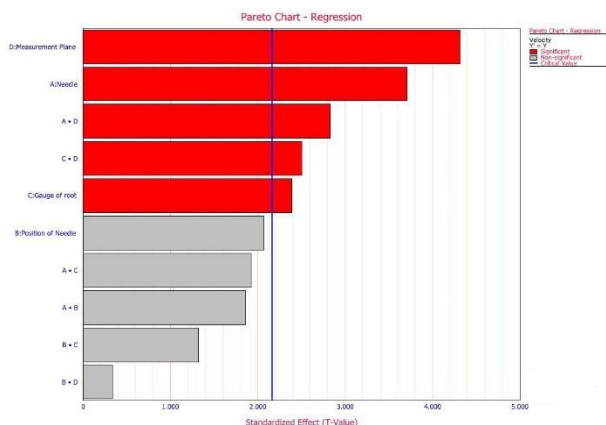


Figure 4 Regression results for each tested combination. Regressions showing a T-value bigger than 2.16 (p -value 0.05) were deemed statistically significant.

In any of the tested combinations, the velocity at 0.5 mm from the root tip showed to be close to zero. The measurements of the velocity taken in 3 different planes showed significant differences ($p < 0.05$). The highest mean velocity were observed at 5 mm from the root tip. However, the analysis of interactions suggests that the needle type and canal enlargement may have different effects over the speed of the irrigation fluid (Figure 5). In fact, the highest irrigation speed was observed with the Lateral opened needle and at the canal enlarged with R25 instrument.

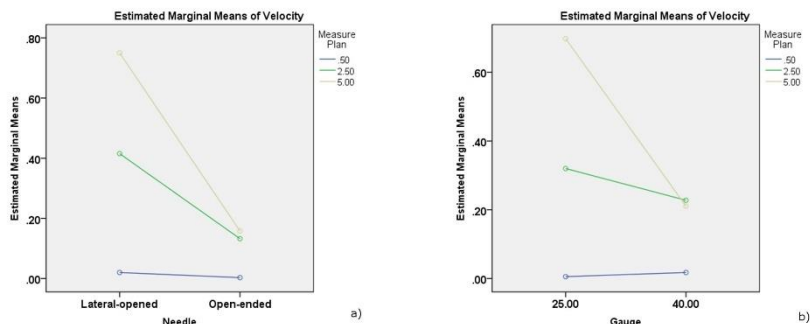


Figure 5. Interactions between the plan of measurement and the needle type (a) and canal enlargement (b).

Conclusion

Results from this preliminary analysis suggest that the tested irrigation protocols were unable to allow irrigant solution to efficiently reach the deepest areas of the root canal space. Independently from the combination analyzed, results always report velocity of the irrigation fluid around 0.01 mL/s in the deeper part of the root, which may be insufficient to mechanically remove bacterial biofilm from the dentinal wall surface. However, there were some improvements in the irrigation efficiency specially when using lateral opened needle and enlargement of the root canal with Reciproc R25 instrument.

References

1. De-Deus G, Belladonna FG, Silva EJ, Souza EM, Carvalho JC, Perez R, Lopes RT, **Versiani** MA. Micro-CT assessment of dentinal micro-cracks after root canal filling procedures. *Int Endod J*. 2016. Epub ahead of print [doi: 10.1111/iej.12706].
2. De-Deus G, Belladonna FG, Souza EM, Silva EJ, Neves Ade A, Alves H, Lopes RT, **Versiani** MA. Micro-computed tomographic assessment on the effect of protaper next and twisted file adaptive systems on dentinal cracks. *J Endod*. 2015; 41:1116-9.
3. De-Deus G, Silva EJ, Marins J, Souza E, Neves Ade A, Gonçalves Belladonna F, Alves H, Lopes RT, **Versiani** MA. Lack of causal relationship between dentinal microcracks and root canal preparation with reciprocation systems. *J Endod*. 2014; 40:1447-50.
4. Alves FR, Andrade-Junior CV, Marceliano-Alves MF, Perez AR, Rocas IN, **Versiani** MA, Sousa-Neto MD, Provenzano JC, Siqueira JF, Jr. Adjunctive steps for disinfection of the mandibular molar root canal system: a correlative bacteriologic, micro-computed tomography, and cryopulverization approach. *J Endod*. 2016; 42:1667-72.
5. Siqueira JF, Jr., Alves FR, **Versiani** MA, Rocas IN, Almeida BM, Neves MA, Sousa-Neto MD. Correlative bacteriologic and micro-computed tomographic analysis of mandibular molar mesial canals prepared by self-adjusting file, reciproc, and twisted file systems. *J Endod*. 2013; 39:1044-50.
6. **Versiani** MA, Alves FR, Andrade-Junior CV, Marceliano-Alves MF, Provenzano JC, Rocas IN, Sousa-Neto MD, Siqueira JF, Jr. Micro-CT evaluation of the efficacy of hard-tissue removal from the root canal and isthmus area by positive and negative pressure irrigation systems. *Int Endod J*. 2016; 49:1079-87.

7. De-Deus G, Belladonna FG, Silva EJ, Marins JR, Souza EM, Perez R, Lopes RT, **Versiani** MA, Paciornik S, Neves Ade A. Micro-CT evaluation of non-instrumented canal areas with different enlargements performed by NiTi systems. *Braz Dent J.* 2015; 26:624-9.
8. De-Deus G, Marins J, Silva EJ, Souza E, Belladonna FG, Reis C, Machado AS, Lopes RT, **Versiani** MA, Paciornik S, Neves AA. Accumulated hard-tissue debris produced during reciprocating and rotary nickel-titanium canal preparation. *J Endod.* 2015; 41:676-81.
9. Keles A, Alcin H, Sousa-Neto MD, **Versiani** MA. Supplementary Steps for Removing Hard Tissue Debris from Isthmus-containing Canal Systems. *J Endod.* 2016; 42:1677-82.
10. Marceliano-Alves MF, Sousa-Neto MD, Fidel SR, Steier L, Robinson JP, Pecora JD, **Versiani** MA. Shaping ability of single-file reciprocating and heat-treated multifile rotary systems: a micro-CT study. *Int Endod J.* 2015; 48:1129-36.
11. Ordinola-Zapata R, Bramante CM, Duarte MA, Cavenago BC, Jaramillo D, **Versiani** MA. Shaping ability of reciproc and TF adaptive systems in severely curved canals of rapid microCT-based prototyping molar replicas. *Journal of applied oral science : revista FOB.* 2014; 22:509-15.
12. Perez R, Neves AA, Belladonna FG, Silva EJ, Souza EM, Fidel S, **Versiani** MA, Lima I, Carvalho C, De-Deus G. Impact of the needle insertion depth on the removal of hard-tissue debris. *Int Endod J.* 2016.
13. **Versiani** MA, De-Deus G, Vera J, Souza E, Steier L, Pecora JD, Sousa-Neto MD. 3D mapping of the irrigated areas of the root canal space using micro-computed tomography. *Clin Oral Investig.* 2015; 19:859-66.
14. **Versiani** MA, Pecora JD, de Sousa-Neto MD. Flat-oval root canal preparation with self-adjusting file instrument: a micro-computed tomography study. *J Endod.* 2011; 37:1002-7.
15. Keles A, Alcin H, Kamalak A, **Versiani** MA. Oval-shaped canal retreatment with self-adjusting file: a micro-computed tomography study. *Clinical Oral Investigations.* 2014; 18:1147-53.
16. Keles A, Alcin H, Kamalak A, **Versiani** MA. Micro-CT evaluation of root filling quality in oval-shaped canals. *International Endodontic Journal.* 2014; 47:1177-84.
17. Keles A, Arslan H, Kamalak A, Akcay M, Sousa-Neto MD, **Versiani** MA. Removal of filling materials from oval-shaped canals using laser irradiation: a micro-computed tomographic study. *Journal of Endodontics.* 2015; 41:219-24.
18. Ahmed HM, **Versiani** MA, De-Deus G, Dummer PM. A new system for classifying root and root canal morphology. *Int Endod J.* 2016. doi: 10.1111/iej.12685.
19. Filipo-Perez C, Bramante CM, Villas-Boas MH, Hungaro Duarte MA, **Versiani** MA, Ordinola-Zapata R. Micro-computed tomographic analysis of the root canal morphology of the distal root of mandibular first molar. *J Endod.* 2015; 41:231-6.
20. Fumes AC, Sousa-Neto MD, Leoni GB, **Versiani** MA, da Silva LA, da Silva RA, Consolaro A. Root canal morphology of primary molars: a micro-computed tomography study. *European archives of paediatric dentistry : official journal of the European Academy of Paediatric Dentistry.* 2014; 15:317-26.
21. Leoni GB, **Versiani** MA, Pécora JD, Sousa-Neto MD. Micro-computed tomographic analysis of the root canal morphology of mandibular incisors. *Journal of Endodontics.* 2014; 40:710-6.
22. Ordinola-Zapata R, Bramante CM, **Versiani** MA, Moldauer BI, Topham G, Gutmann JL, Nunez A, Duarte MA, Abella F. Comparative accuracy of the Clearing Technique, CBCT and Micro-CT methods in studying the mesial root canal configuration of mandibular first molars. *Int Endod J.* 2017; 50:90-6.
23. Ordinola-Zapata R, Bramante CM, Villas-Boas MH, Cavenago BC, Duarte MH, **Versiani** MA. Morphologic micro-computed tomography analysis of mandibular premolars with three root canals. *J Endod.* 2013; 39:1130-5.

24. Ordinola-Zapata R, Monteiro Bramante C, Gagliardi Minotti P, Cavalini Cavenago B, Gutmann JL, Moldauer BI, **Versiani** MA, Hungaro Duarte MA. Micro-CT evaluation of C-shaped mandibular first premolars in a Brazilian subpopulation. *Int Endod J*. 2015; 48:807-13.
25. Souza-Flamini LE, Leoni GB, Chaves JF, **Versiani** MA, Cruz-Filho AM, Pecora JD, Sousa-Neto MD. The radix entomolaris and paramolaris: a micro-computed tomographic study of 3-rooted mandibular first molars. *J Endod*. 2014; 40:1616-21.
26. **Versiani** MA, Ordinola-Zapata R. Root canal anatomy: implications in biofilm disinfection. In: Chavez de Paz L, Sedgley C, Kishen A, editors. *Root canal biofilms*. 1 ed. Toronto: Springer International Publishing AG; 2015. p. 23–52.
27. **Versiani** MA, Ordinola-Zapata R, Keles A, Alcin H, Bramante CM, Pecora JD, Sousa-Neto MD. Middle mesial canals in mandibular first molars: A micro-CT study in different populations. *Archives of oral biology*. 2016; 61:130-7.
28. **Versiani** MA, Pecora JD, de Sousa-Neto MD. Root and root canal morphology of four-rooted maxillary second molars: a micro-computed tomography study. *J Endod*. 2012; 38:977-82.
29. **Versiani** MA, Pecora JD, Sousa-Neto MD. The anatomy of two-rooted mandibular canines determined using micro-computed tomography. *Int Endod J*. 2011; 44:682-7.
30. **Versiani** MA, Pecora JD, Sousa-Neto MD. Microcomputed tomography analysis of the root canal morphology of single-rooted mandibular canines. *Int Endod J*. 2013; 46:800-7.
31. **Versiani** MA, Pécora JD, Sousa-Neto MD. Update in root canal anatomy of permanent teeth using microcomputed tomography. In: Basrani B, editor. *Endodontic irrigation: chemical disinfection of the root canal system*. 1 ed. Switzerland: Springer International Publishing AG; 2015. p. 15-44.
32. **Versiani** MA, Sousa-Neto MD, Pécora JD. Pulp pathosis in inlayed teeth of the ancient Mayas: a microcomputed tomography study. *Int Endod J*. 2011; 44:1000-4.
33. De-Deus G, Roter J, Reis C, Fidel S, **Versiani** MA, Alves H, Lopes RT, Paciornik S. Assessing accumulated hard-tissue debris using micro-computed tomography and free software for image processing and analysis. *J Endod*. 2014; 40:271-6.
34. Leoni GB, **Versiani** MA, Silva Sousa YT, Bruniera JF, Pécora JD, Sousa Neto MD. Ex vivo evaluation of four final irrigation protocols on the removal of hard-tissue debris from the mesial root canal system of mandibular first molars. *Int Endod J*. 2016 doi: 10.1111/iej.12630.
35. **Versiani** MA, Santana BP, Caram CM, Pascon EA, de Souza CJ, Biffi JC. Ex vivo comparison of the accuracy of Root ZX II in detecting apical constriction using different meter's reading. *Oral Surg Oral Med Oral Pathol Oral Radiol Endod*. 2009; 108:e41-5.

Lung μ CT imaging and analysis of chronic diseases and animal models of lung diseases.

M-J.Beaulieu¹, C-A Huppé¹, C Racine¹, D Marsolais^{1,2}, M.C. Morissette^{1,2}

¹Quebec Heart and Lung Institute – Université Laval, Quebec City, Canada

²Department of Medicine, Université Laval, Quebec City, Canada

Aims

Chronic lung diseases affect millions of individuals worldwide and are some of the most prevalent medical conditions. Pollution, smoking, chronic infections and genetic mutations are some of the origins of lung pathologies such as emphysema, chronic obstructive pulmonary disease, pulmonary arterial hypertension, asthma, hypersensitivity pneumonitis, and idiopathic pulmonary fibrosis. These pathologies are defined by structural changes with features such as fibrosis, alveolar destruction, airway/artery remodeling, or significant lymphoid cell infiltration. All these human diseases can be modeled in mice, giving to researchers the opportunity to investigate the pathophysiological mechanisms and assess diverse pharmacological treatments.

Ex vivo micro-computed tomography (μ CT), allows 3D analysis and characterization of lung tissue from both humans and small animals. At the Quebec Heart and Lung Institute, we have access to fresh human lung tissues obtained from surgical lung resections as well as a myriad of mouse models of chronic lung diseases. μ CT evaluation of structural changes caused by diverse human lung pathology will allow us to compare the pulmonary features between humans and mice and develop quantification techniques to measure specific structural parameters.

Method

Human lung samples:

Human lung tissues were obtained from patients undergoing resection for lung cancer or emphysema. All specimens were provided after written informed consent in accordance with an Internal Review Board-approved protocol.

Mouse model of hypersensitivity pneumonitis:

Methanospaera stadmanae (total extract; 50 μ l of a 2mg/ml) or vehicle was delivered intranasally in C57Bl/6 mice three days a week, for three consecutive weeks¹. Animal studies were carried out in strict accordance with the recommendations for the Care and Use of Laboratory Animals of the Canadian Council on Animal Care (CCAC).

Preparation of lung tissues and μ CT scan parameters and analysis:

Lung tissues were fixed in 4% formaldehyde, dehydrated for 2 hour each in 50%, 70%, 90% and 100% ethanol, then immerse in hexamethyldisilazane and passively air-dried overnight in a fumehood². Tissues were scanned in a SkyScan 1174 micro-CT scanner (Bruker MicroCT, Kontich, Belgium) at 40kV and 400 μ A or 50kV and 800 μ A for human and mouse specimen respectively, using four-frame averaging and 0.5 angular rotation step with pixel sizes ranging from 9.3 μ m to 11.4 μ m. Reconstruction and analyses were carried out with SkyScan NRecon and CTan software (Bruker MicroCT).

Results

Micro-CT analysis of healthy and emphysematous human lung tissues:

μ CT scan of human healthy lung samples shows that most of the tissue is composed of well-structured alveoli and bronchioles or arterioles (Figure 1A). The fine lace structure of alveoli is partially destroyed or enlarged in severe emphysema (Figure 1B). Areas of fibrosis can also be observed in the parenchyma. Moreover, fine particles trapped in the lungs as a result of cigarette smoking are also present (Figure 1C). Analysis of structure thickness and separation distribution supports the pathophysiological observations and is characteristic of emphysema (Figure 2).

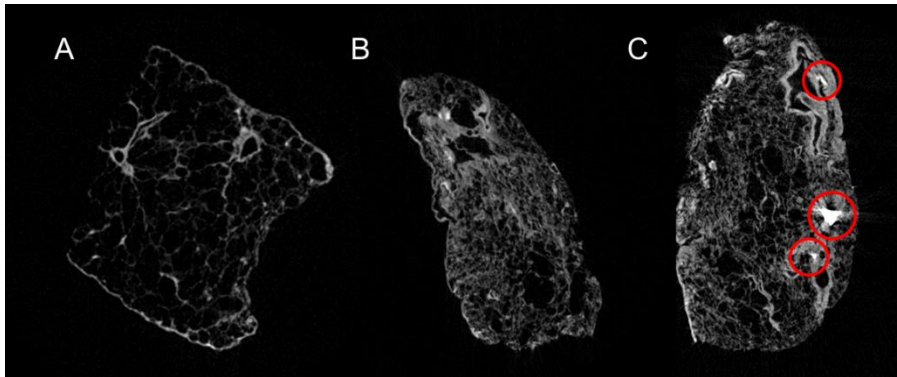


Figure 1: *Ex vivo* μ CT scan of human lung tissue. Representative sections of A) healthy, B) emphysematous and C) emphysematous tissue with trapped particles identified by red circles.

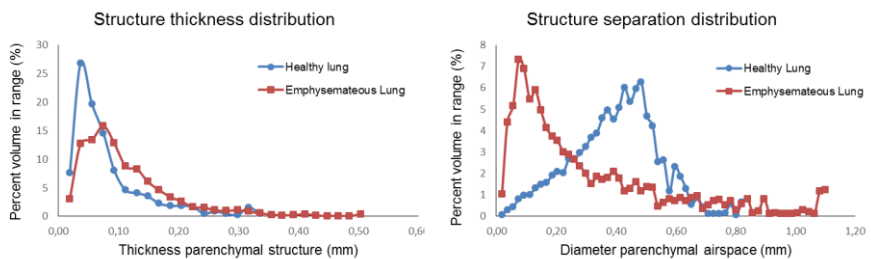


Figure 2: Representative results of structure thickness and structure separation distributions for healthy and emphysematous human lung tissue.

μ CT evaluation of pulmonary lymphoid cell infiltration in a mouse model of hypersensitivity pneumonitis:

An important feature of *Methanospaera stadtmanae* chronic exposure is the development of tertiary lymphoid tissue (TLTs), a structure formed of B and T lymphocytes in the lungs. These lymphoid tissues can be visualized by μ CT scan (Figure 3). TLTs are dense structures around upper airways and more disparate in lower airways. Intranasal delivery preferably reached the upper lung, likely explaining the distribution of the TLTs.

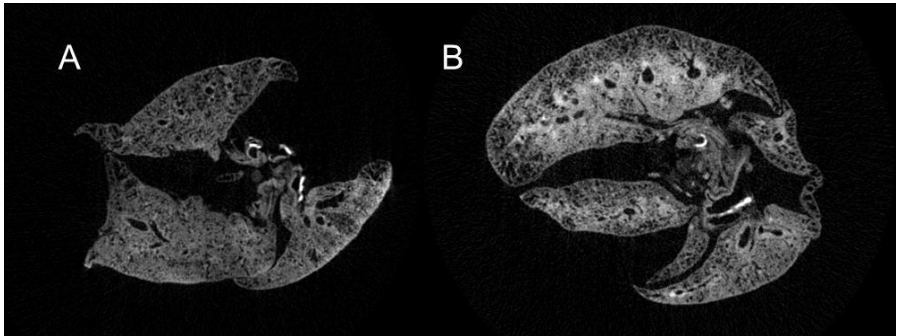


Figure 3: Representative scans of A) C57Bl/6 mouse lung exposed to vehicle (saline) and B) tertiary lymphoid tissue accumulation around upper airways in the lung of mouse exposed to *Methanosphaera stadtmanae*.

Conclusion

Micro-CT scan of human lung tissue allows a better and refine characterization of pathophysiology of lung disease. Combine to analysis of lung function, inflammation and histology, micro-CT scan of an entire mouse lung give us a better overview of the model.

References:

1. P. Blais-Lecours, C. Duchaine, M. Taillefer, C. Tremblay, M. Veillette, Y. Cormier, D. Marsolais, "Immunogenic Properties of Archaeal Species Found in Bioaerosols PLOS One, 2011.
2. Adaptated from Bruker-MicroCT method note: Enhancing the contrast in specimens by chemical drying.

Excellent definition can be obtained between the gray and white matter of the mouse brain using a modified staining technique and X-ray micro-CT.

Aida Halilagic Rajic¹, Duncan Bell¹, Nick Corps², David Mortimore³, Silvia Atanasio¹, Christopher Cobb¹, Margarita Pitsiani⁵, Leigh Wilson⁴, Cathy Fernandes⁵, Richard Wingate⁴

¹ Faculty of Health, Science and Technology, University of Suffolk, Waterfront building, Neptune Quay, Ipswich, IP4 1QJ, UK;

² Bruker, Banner Lane, Coventry, CV4 9GH, UK

³ Newbourn Solutions Ltd, Newbourn, IP12 4NR, Suffolk, UK

⁴ MRC Centre for Neurodevelopmental Disorders, New Hunt's House, King's College, London, SE1 1UL, UK and

⁵ SGDP Research Centre, Kings College, De Crespigny Park, Denmark Hill, London, SE5 8AF, UK

Aims

It has generally been agreed that it is very difficult, if not impossible, to get satisfactory differential radiological definition between the gray and white matter of the brain or spinal cord using X-ray computerised tomography (CT) in either hospital-sized or with micro-CT scanners because of similarities in the X-ray attenuation values of the two neural tissues. In contrast, micro MRI scanners are being increasingly used especially in mouse brain studies as good separation between white and gray matter is relatively easy with this technique (Dorr et al 2008). However, micro MRI scanning is not without its problems as a) the cost of the scanners is considerably higher than that of an X-ray micro-CT scanner b) they are much larger in size c) more difficult to use than X-ray micro-CT scanners and therefore d) there are few of them in use. Furthermore, even the most up to date micro MRI scanners cannot go below a resolution of about 35 microns (Metscher, 2009). Therefore, the aim of this study was to test whether the differential attenuation between the gray and white matter of stained mouse brains using a X-ray micro-CT can be improved with the use of various radio-opaque dyes (Metscher, 2009; Martin et al., 2015; Anderson and Maga, 2015; Smith et al., 2016)

A number of dyes that had previously been reported as staining soft tissues had initially been used, such as PTA and Potassium Iodide (I_2/KI) (Martin et al., 2015; Anderson and Maga, 2015; Smith et al., 2016) but in each case the staining was non-specific and thus unsatisfactory for our purposes. Following these initial studies, Iohexol, a water-soluble non-ionic stain, was chosen due to the superior differential attenuation values obtained between the white and gray brain matter (Salto and Murase, 2012). Here we report our encouraging preliminary results.

Method

As part of a collaborative study between King's College, London and The University of Suffolk, we are currently studying a cohort of 50 adult mouse brains (equal number of male and female) comprising experimental and control samples from a larger study of neuroendocrine function. Mice were sacrificed at 3 months-old, their brains were removed and stored in 70% ethanol. The water-soluble non-ionic iodinated contrast agent used was Iohexol (Omnipaque, GE Healthcare AS) as the contrast agent used by Salto and Murase (2012) is not available in the UK. The concentration of the dye supplied by the manufacturer was 300mg of Iohexol per mL. This was diluted with 4% Paraformaldehyde to the required concentration of 150-200 mg/mL. After rehydration, the brains were immersed in the diluted Iohexol solutions and left for

periods of between 3 days and up to several weeks before being micro-CT scanned. The majority of the brains were scanned using a Skyscan 1027 scanner at a setting of 124 μ A and 80kV using a 1mm aluminium filter. The brains were all scanned at 15 times magnification which corresponded to an isotropic interpixel distance of 19.3 μ m. The scans were reconstructed in the Skyscan NRecon software (version 1.5.1.4), viewed in Disect software and qualitative analysis carried out using TomoMask software as previously described (Greco et al, 2014). Three of the brains were also scanned at isotropic interpixel distance of 9.0 μ m on a Skyscan 1272 scanner and the results compared with those obtained using isotropic interpixel distance of 19.3 μ m. Histological confirmation of the structures identified radiologically was carried out using Haematoxylin and Eosin (H&E) staining, and myelin-specific Luxol Fast Blue (LFB) stain.

Results

Unexpectedly clear visualisation of large white matter tracts, such as the corpus callosum, was obtained even after immersion of the mouse brains in the various concentrations of Iohexol solutions for as little as three days. Optimum results were obtained with immersing the brains in a concentration of 150-200 mg/mL of Iohexol for about 14 days by which time most of the larger white matter structures were clearly visible. Structural demarcation of the corpus callosum, cingulum, the external capsule, the anterior commissure, *Arbor vitae* of the cerebellum, the three cerebellar peduncles, and the cerebral peduncle were all clearly visible (Figure 1 A and B). The structural detail seen at resolution of 9.0 μ m was greater than that seen using resolution of 19.3 μ m. This is in contrast to images obtained with brains that were immersed in I2/KI where no clear demarcations of specific brain structures can be seen (Figure 2).

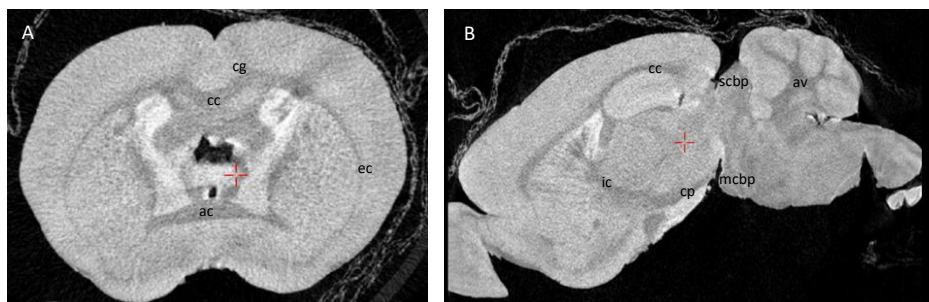


Figure 1: A - Coronal view of mouse brain, B – sagittal view of mouse brain. Major white matter tracts including corpus callosum (cc), cingulum (cg), the external capsule (ec), the anterior commissure (ac), *Arbor vitae* of the cerebellum (av), the medial cerebellar peduncle (mcbp), superior cerebellar peduncle (scbp) and the cerebral peduncle (cp) are clearly distinguishable. The brains were immersed in 150 mg/mL Iohexol for 14 days and scanned at a resolution of 9 μ m.

Histological analysis of the samples using H&E and LFB stains confirmed findings of our radiological study.

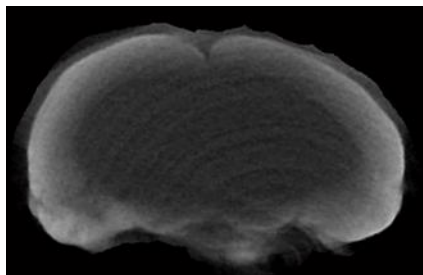


Figure 2: Coronal view of mouse brain. The brain were immersed in 10% I₂/KI for 7 days. Specific brain structures cannot be seen.

Conclusion

We have shown that, contrary to common belief, it is possible to obtain high-resolution images of the mouse brain with clear differences between white and grey matter. The anatomical detail that can be obtained with X-ray micro-CT scanning is fast approaching that of the much more expensive and not so readily-available micro-MRI scanners which at the moment can only go down to a resolution of about 35 microns. We have shown good visualisation with X-ray micro-CT to 9 microns and intend to now try even higher resolutions.

References:

1. Anderson R. and Maga A.M. (2015), A novel procedure for rapid imaging of adult mouse brains with micro-CT using iodine-based contrast, PLOS ONE/ DOI:10.1371/journal.pone.0142974.
2. Dorr A.E., Lerch J.P., Spring S. *et al.* (2008), High resolution three-dimensional brain atlas using an average magnetic resonance image of 40 adult C57Bl/6J mice, *Neuroimage*, 42, pp. 60-69.
3. Greko M.K., Bell G.D., Woolnough L. *et al.* (2014), 3-D visualization, printing, and volume determination of the tracheal respiratory system in the adult desert locust, *Schistocerca gregaria*, *Entomologia Experimentalis et Applicata*, 152, pp: 42-51.
4. Martin de S. E. Silva J, Zanette I, Noel PB *et al.* (2015), Three-dimensional non-destructive soft-tissue visualization with X-ray staining micro-tomography, *Scientific Reports*, 5:14088/DOI:10.1038/srep14088, pp. 1-7.
5. Metscher BD. (2009), MicroCT for comparative morphology: simple staining methods allow high-contrast 3D imaging of diverse non-mineralized animal tissues, *BMC Physiology*, 9:11.doi: 10.1186/1472-6793-9-11 PMID: 19545439
6. Saito S., and Murase K. (2012), *Ex vivo* imaging of mouse brain using micro-CT with non-ionic iodinated contrast agent: a comparison for myelin staining, *The British Journal of Radiology*, 85: e973-978.doi: 10.1259/bjr/13040401 PMID: 226747125.
7. Smith D.B., Bernhardt G., Raine N.E. *et al.* (2016), Exploring miniature insect brains using micro-CT scanning techniques, *Scientific Reports*, 6:21768/DOI:10.1038/srep21768

Influence of the composition on the composite structure and properties of current collectors for vanadium redox flow batteries

Gaurav Gupta¹, Rouven Henkel², Lidiya.Komsiyska¹, Corinna Harms¹

¹NEXT ENERGY · EWE Research Centre for Energy Technology, Carl-von-Ossietzky-Str. 15, 26129 Oldenburg, Lower Saxony, Germany

²Eisenhuth GmbH & Co. KG, Friedrich-Ebert-Str. 203, 37520 Osterode am Harz, Lower Saxony, Germany.

Aims

The Vanadium redox flow battery (VRFB) is an electrochemical storage technology based on vanadium species in different oxidation states. The vanadium species are dissolved in sulphuric acid electrolyte and stored in tanks. The catholyte (positive electrolyte) and anolyte (negative electrolyte) tanks contain $\text{VO}^{2+}/\text{VO}_2^+$ and $\text{V}^{2+}/\text{V}^{3+}$ species, respectively. Both electrolytes are pumped into the corresponding half cells during operation, where the redox reactions occur on porous graphite electrodes. As shown in Figure 1 the ionic coupling between the positive and negative half cells is realized via ion conducting membrane separator.

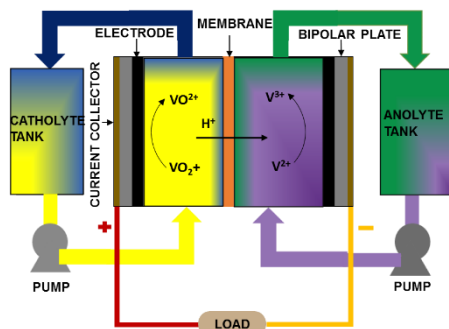


Figure 1: Schematic of VRFB cell

Bipolar plates (BPPs) are vital components of the VRFB and act as current conductors, physical half-cell separators and provide mechanical support to the battery stacks [1,2]. In general the BPP for VRFB are carbon/polymer composites that are sufficiently stable in the highly acidic medium and corrosive environment [1, 2]. The polymer matrix acts as binder and is electrically insulating whereas the electrical conductivity is provided by conductive fillers, such as graphite particles, carbon black and fibers [2]. An efficient dispersion and distribution of filler material into polymer matrix is crucial for desired electrical and mechanical properties [2]. However, the properties and the interaction of the components such as polymer, filler and additives influence significantly the 3D structure of the composite materials and thus the performance of the BPPs. In the present contribution, the high-resolution micro CT is employed to elucidate the influence of the single components on the structural composite parameters of new polypropylene-graphite (PP-G) research composites that have the potential to be used for the production of BPPs for VRFB.

Method

Studied samples are tabulated (Table 1) according to their polymer and filler material:

Table 1 Composition of research composites

Sample	Polymer	Filler
A	PP- homopolymer	μ-sized graphite 1
B	PP- homopolymer + copolymer	μ-sized graphite 1
C	PP-copolymer	μ-sized graphite 2

Skyscan 1172 micro CT was used to analyze the different PP-G samples using the measurement parameters presented in table 2:

Table 2 Measurement parameters

Sample size	5 mm x 5 mm x 5 mm
Resolution	2 μm/pixel
Average framing	6
Rotation step	0.180

The reconstruction of raw data for the measured samples, volume-of-interest (VOI) rendering and 3D visualization were obtained on the NRECON, CTVOX application and region of interest (ROI) defined on the CTAN application was used to derive quantitative analysis for comparison.

The electrical conductivity was measured in the through plan direction on a pressure device, samples were placed between gold plated copper electrodes and GDL sheets were used to reduce the contact resistance between the samples and electrodes [2,3]. A constant load of 1 N/mm² was applied during the measurement and a multi-meter was used to determine resistances.

Conductivity values were determined by the following formula:

$$\sigma = L / R * A$$

where,

σ is the electrical conductivity, S/cm.

L is the sample thickness, cm.

R is the resistance of the sample, Ω.

A is the surface area of the plate, cm².

Results

Presented in Figure 2, are the 3D images of the VOI for each research composite and a graphical representation of their total porosity percentage.

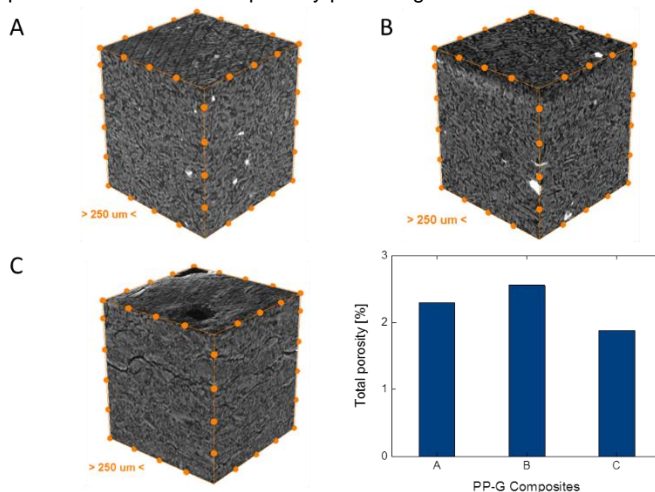


Figure 2: 3D images and percentage of total porosity of the studied composites

Table 3 Sample properties from micro CT, mercury porosimetry and electrical conductivity

Sample	Object surface density, [1/ μm]	Open porosity, [%]	Closed porosity, [%]	Total porosity derived from mercury intrusion [%]	Through-plane electrical conductivity, [S/cm]
A	0.009	1.64	0.67	4.58	30
B	0.010	1.68	0.89	3.21	29
C	0.006	1.76	0.12	3.88	15

The CTAN application helps to determine the total porosity for each sample and further distinguishes between pores that are surrounded completely with the solid object i.e. composite material (volume of closed pores) and pores that had access to space outside the solid object (volume of open pores). The volume of open and closed pores as percentage of the total VOI volume is noted in Table 3. The object surface density defines the ratio of the object surface area to the total volume of the VOI; the determined values indicate that unlike sample C samples A and B have comparable values. The total VOI defined for all samples was the same, sample C has a lower surface area (determined on CTAN) resulting in a lower object surface density value. Thus the structures of sample A and B were similar to each other compared to sample C.

As it can be seen in Figure 2, the samples A and B show a homogeneous and slightly porous structure. The quantitative analysis of the CT images show, that both samples exhibited

similar morphometric properties. It could also be derived from Figure 2 and 3 that both composites show comparable macro-porosity values and pore size distributions. As a result, the bulk conductivity values are also comparable, indicating that the used PP binders displayed similar interaction with the graphite filler.

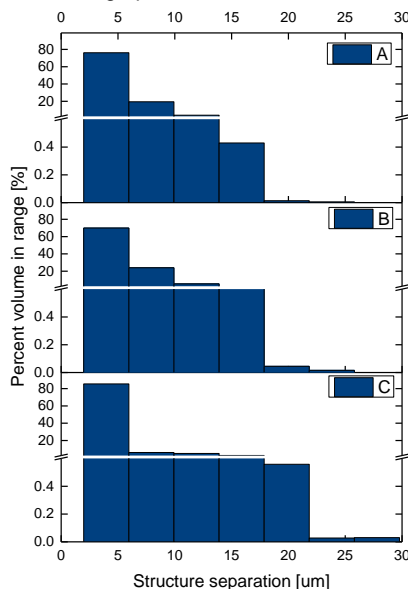


Figure 3: Structure separation distribution for samples A, B, C

In contrast the bulk of sample C was more compact and demonstrated lower porosity values in comparison to sample A. This observation was also verified by mercury porosimetry measurements (Table 3). However the measured conductivity values were much lower. A close observation of the CT-images (Figure 3) revealed that the sample C had micro cracks and inhomogeneities within the 3D structure. The reduced electrical conductivity in this case can be assigned to the brittle and inhomogeneous bulk structure of the composite, which can arise due to the lower polymer crystallinity and difference in the binder-filler interaction.

Conclusion

The performed study demonstrates the significance of the high resolution micro CT as an imperative tool for characterization of composite materials such as bipolar plates for VRFB. The CT measurements performed on research composites based on polypropylene binder and graphite fillers reveal that the properties and the interaction of the polymer and the graphite have a significant influence on the composite structure, governing also the electric conductivity of the materials.

Acknowledgments

The authors express their gratitude to the German Federal Ministry of Economic Affairs and Energy, for granting the funding for this project "Top Level Redox Flow" under the framework of the central innovation program for SMEs (FKZ ZF4090701ZG5).

References:

- [1] K. H. Kim, B. G. Kim, D. G. Lee, "Development of carbon composite bipolar plate (BP) for vanadium redox flow battery (VRFB)" *Compos. Struct.*, 253-259, 2014.
- [2] B.Caglar, P. Fischer, P. Kauranen, M. Karttunen, P. Elsner, "Development of carbon nanotube and graphite filled polypropylene sulfide based bipolar plates all-vanadium redox flow batteries" *J. Power Sources*, 88-95, 2014.
- [3] B. Caglar, J. Richards, P. Fischer, J. Tuebke, "Conductive polymer composites and coated metals as alternative bipolar plate materials for all-vanadium redox-flow batteries" *Adv. Mat. Lett.* 2014, 299-308, 2014.

Added value of Micro-CT in tooth resorption assessment

Mavridou AM¹, Kerckhofs G², Wevers M³, Lambrechts P¹

¹Department of Oral Health Sciences. BIOMAT Research Cluster., KU Leuven & University Hospital Leuven, ²Skeletal Biology and Engineering Center, Department of Development and Regeneration, KU Leuven, Leuven, Belgium, ³Department of Materials Engineering (MTM), KU Leuven, Leuven, Belgium

Aim:

To highlight the added value of non-destructive, high resolution techniques to efficiently investigate complex phenomena in dentistry, such as tooth resorption.

Methodology:

In this study three characteristic types of tooth resorption, namely external cervical (ECR), internal and external replacement, were included. After extraction, the teeth were assessed with a high performance NanoTom S scanner (GE Measurement and Control Solutions, Wunstorf, Germany), which provided accurate images with a resolution of 7 µm. Internal and external structural analysis of the tooth and 3D visualization was done by using the CTAn, CTvol, CTvox and DataViewer softwares (Bruker micro-CT, Kontich, Belgium)¹⁻⁴.

Results For the selected experimental settings, an accurate observation of the resorption tissues was possible. This allows for the analysis of the morphological characteristics and pattern of the resorption. Thus it is possible to clearly distinguish the different types of resorption. In particular, the high spatial resolution and image quality make it possible to assess the following parameters: initiation point of the resorption (portal(s) of entry), resorption extent, Heithersay resorption channels inside dentin and enamel, pulp reaction through calcification, the Pericanalar Resorption Resistant Sheet (PRRS) which surrounds the root canal, extent of reparative bonelike tissue formation inside the tooth and interconnections with the external root surface (PDL interconnections) (Fig.1). Furthermore, representative 3D models for each resorption condition can be used to get a better insight on the evolving phenomena and can significantly help dental researchers and clinicians to better understand and differentiate between the different types of tooth resorption.

Conclusions Micro-CT is an efficient and non-invasive technique for *in vitro* analysis, that can be successfully applied in dentistry for tooth resorption. In particular the different types of resorption can be accurately assessed, whereas their pattern is clearly observed. It is believed that this will help clinicians to obtain a better understanding of complex dental phenomena.

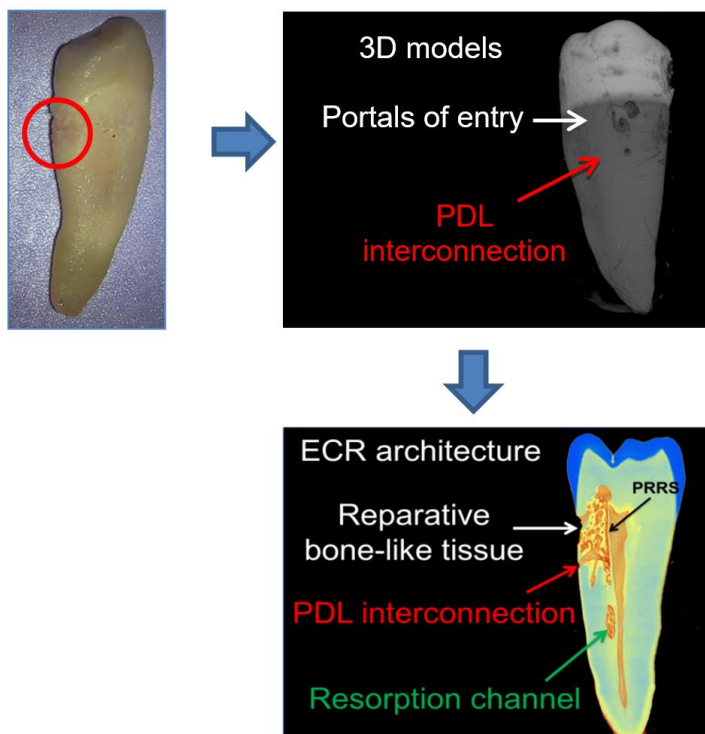


Figure 1: Tooth with external cervical resorption (ECR): a schematic representation of the use of microCT for tooth resorption screening.

References

1. Mavridou AM, Pyka G, Kerckhofs G, Wevers M, Bergmans L, Gunst V, Huybrechts B, Schepers E, Hauben E, Lambrechts P (2016) A novel multimodal methodology to investigate external cervical tooth resorption. *International Endodontic Journal*, 49(3):287-300.
2. Mavridou AM, Pyka G, Wevers M, Lambrechts P (2016) Applying Nano-CT technology in Endodontology: understanding external cervical root resorption. Paper presented in European Society of Endodontics conference, Barcelona 16-19 September 2015. *International Endodontic Journal*, 49 (1):41.
3. Mavridou AM, E. Hauben, Wevers M, Schepers E, Bergmans L, Lambrechts P (2016) Understanding external cervical resorption in vital teeth. *Journal of Endodontics*, 42(12): 1737-51.
4. Mavridou AM, E. Hauben, Wevers M, Schepers E, Bergmans L, Lambrechts P (2017) Understanding external cervical resorption in endodontically treated teeth. *International Endodontic Journal*, in press.

Mechanoadaptive increases in bone mass accretion via regionally-coupled formation and resorption: a 4D MicroCT longitudinal study

Behzad Javaheri, Sebastian Wylie, Andrew A Pitsillides

Comparative Biomedical Sciences, Royal Veterinary College, London, United Kingdom

Aims

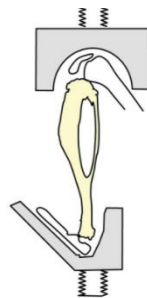
Bones' primary function is to maintain sufficient mass and architecture to bear functional loads without unsustainable damage. To achieve this function, bone size, architecture, and strength must be modified according to the mechanical forces experienced. The duration for which the beneficial bone effects of mechanical loading are maintained after its cessation and how the corresponding bone formation and resorption are spatially regulated at the bone organ level post loading remain, however, unclear. Herein, we have assessed using *in vivo* micro-CT and 3D registration, the bone formation/resorption that occurs along the length of tibia in response both to 2 week-long loading period and the subsequent 12 week-long post loading period.

Method

The right hindlimb of eighteen 12-week old female C57Bl/6J mice was subjected to *in vivo* tibial dynamic loading at 12N, 2Hz, with 10sec rest periods between cycles, 40 cycles/day through the knee joint three times a week for 2 weeks. Right hindlimbs of 6 separate mice served as an additional non-loaded control.

Scanning of the tibia was achieved using the 1176 Skyscan (Skyscan, Kontich, Belgium) *in vivo* scanner, under anaesthetic, at 40kV, 600µA, 9µm voxel size with an exposure of 2000ms and a rotation step of 0.800 degrees. The mice were scanned at 6 time points; 3 days prior to the start of loading, as well as after week 1 and 2 of loading. A repeat scan was also performed 3 days after the completion of the loading regime. Thereafter, 6 mice from the loaded group were sacrificed. Six and 12 weeks after the end of loading (at 20 and 26 weeks of age, respectively), the mice were re-scanned and a further 6 sacrificed at each of these time points. The control group had the same number of scans within the same timeframe.

The slices were then reconstructed using NRecon 1.1.7.1 (Skyscan, Kontich, Belgium) and 3D registration was performed using DataViewer. Data relating to formation and resorption were obtained using CT Analyzer 1.16.9. Whole bone analysis was performed and finally, CTvox was used for 3D visualization.



Loading apparatus

Tibia is placed between two cups with both the knee and ankle in flexed positions. Load is passed axially along the tibia.

Results

Our data indicate that a return to habitual use prompts enhanced bone resorption that is regionally-mapped and a diminished bone formation that is not mapped to the net bone accretion induced in response to the prior loading period. Intriguingly, our analysis reveals that the latter occurs at an alternative location along the tibial length.

In addition, we found that that osteogenic effects of bone loading are not lost after the cessation of loading but are instead regionally-controlled, suggesting that a short-term exposure to loading activates long-term consequences to bone mass and architecture that is retained with ageing.

Conclusion

In conclusion, using *in-vivo* micro-CT we found a loading induced coupling of formation and resorption in the proximal tibia which has not been shown before. This is perhaps due to the difficulty in discerning the location of resorption without micro-CT. The spatial uncoupling of formation and resorption in the post-loading period has never previously been described; this has been made possible by the use of *in-vivo* micro-CT. Our data indicate that loaded tibiae exhibit regionally-controlled remodelling after the cessation of loading; a suppressed bone formation close to the midshaft, upon a return to solely habitual use, that is not matched to the region of the tibia exhibiting early load-related formation.

Contrast-enhanced microCT to visualize and quantify the 3D vasculature in biological tissues without the need for perfusion

G. Kerckhofs^{1,2}, S. Stegen^{1,3}, J. Cornillie⁴, A. Wozniak⁴, J. Wellens⁴, FP. Luyten^{1,2}, L. Geris^{1,5,6}, G. Carmeliet^{1,3}, TN. Parac-Vogt⁷

¹Prometheus, Division of Skeletal Tissue Engineering, KU Leuven, O&N 1, Herestraat 49 - PB813, B-3000 Leuven, Belgium;

²Dept. Development and Regeneration - Skeletal Biology and Engineering Research Center, KU Leuven, O&N 1, Herestraat 49 - PB813, B-3000 Leuven, Belgium

³Dept. Clinical and Experimental Medicine - Clinical and Experimental Endocrinology, KU Leuven, O&N 1, Herestraat 49 - PB902, B-3000 Leuven, Belgium

⁴Dept. Oncology - Laboratory of Experimental Oncology, KU Leuven, O&N 1, Herestraat 49 - PB815, B-3000 Leuven, Belgium

⁵Biomechanics Research Unit, Université de Liege, Chemin des Chevreuils 1 - BAT 52/3, B-4000 Liège, Belgium

⁶Dept. Mechanical Engineering - Biomechanics Section, KU Leuven, Celestijnenlaan 300C - PB 2419, B-3001 Heverlee, Belgium.

⁷Dept. Chemistry - Molecular Design and Synthesis, KU Leuven, Celestijnenlaan 200f - PB2404, B-3001 Leuven, Belgium

Introduction and aim:

Blood supplies oxygen, nutrients and minerals to the different tissues in the human body. This supply is critical to support normal tissue homeostasis and repair [1]. In most tissues, the blood supply is via the arteries, whereas special venous structures, sinusoids, exist to carry off blood [2]. A well-structured organization of these different types of vascular structures is necessary to avoid hypoxic environments within the vascularized tissue; this could lead to impaired tissue homeostasis. However, both the functional 3D organization and the blood flow dynamics of the vascular network in several tissue types still remain poorly understood [3]. A detailed 3D visualization of the entire vascular network could provide a solution for thorough quantification of the vascular structure, and for a better understanding of the vascular organization and of the blood flow.

Standard histological sectioning is routinely used for evaluating biological tissues, but it only provides 2D information and is thus not suitable for quantifying the 3D structure of the vascular network. Intravital two-photon imaging has been recently applied to determine the flow dynamics in the bone marrow vasculature of flat bones [3]. However, this technique only allows evaluating a thickness of about 300 µm and is thus not applicable to long bones or thick tissues.

X-ray micro- and nanofocus computed tomography (micro- & nanoCT) have conventionally been used for 3D quantitative imaging of mineralized skeletal tissues [4, 5] and can also visualize the 3D vascular network when combined with perfusion and casting of a radiopaque contrast agent [6-8]. Shortcomings of this technique are (i) the potential need for dual energy scanning or bone decalcification after perfusion when bone is concerned [9] and (ii) limited perfusion of the sinusoids, where the flow velocity is assumed to be low, and capillaries [6].

To visualize and quantify spatially all the different vascular structures, we propose to use a novel contrast agent for contrast-enhanced computed tomography (CE-CT) that allows visualizing the 3D vasculature with sufficient distinct contrast compared to the surrounding tissues, and this without the need for perfusion of the contrast agent. Recently, we have

validated this novel contrast agent, a polyoxometalate (POM), and we have shown the added value of the 3D quantification of the vascular structure, compared to histology (2D), for different pathologies in mouse models (i.e. ageing and high-fat diet induced Type 2 diabetes – T2DM) [10]. In this study, we will show that this novel technology provides a detailed 3D representation of the entire structure of the bone marrow vasculature, including all the different blood vessel types (= case study 1). As a second case study, we will show the potential of our novel approach to visualize the vasculature in patient-derived tumor xenografts.

Methods & results:

Case study 1: Bone marrow vascularization

The novel contrast agent is a metal-substituted polyoxotungstate, and is further referred to as Hf-POT (Hf-substituted). For the first case study, we used tibias of 8 weeks and 30 weeks old mice. After harvest and fixation in paraformaldehyde, the samples were stained with Hf-POT (3.5% Hf-POT/PBS solution) and scanned on a NanoTom S [GE] system (2 μm voxel size, 60 kV, 0.3mm Al filter, 500ms exposure time, 2400 images, fast scan mode – 20 min. scan time). For the staining, the distal metaphysis was removed, and the samples were immersed in the staining solution in an Eppendorf tube, and were put on a shaker plate during 48 hours.

Figure 1 shows a typical 3D representation (CTVox, Bruker MicroCT) of the vasculature in the tibial diaphysis of an 8 weeks old mouse. The different colors represent the different blood vessel types, which are classified based on their thickness. The red vessels are the arterioles, which drain into the arteries (green) that supply blood to the bone marrow compartment. The sinusoids, visualized in blue, carry off the blood. The skeletonization of the full vascular network (indicated in white) allows to assess the connections between the different blood vessel types. We are currently evaluating the effect of ageing on these connections, and hence on the functional organization of the blood vessels in bone marrow compartment.

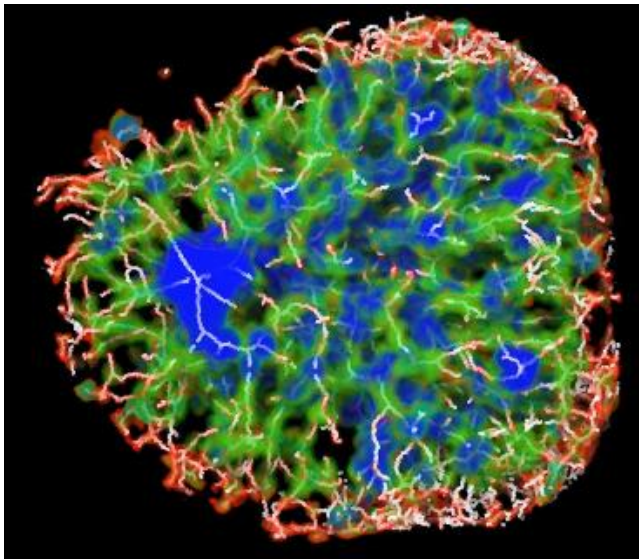


Fig. 1: 3D rendering of the different blood vessel types in the diaphysis of an 8 weeks old mouse, depending on their thickness: red = $<10\mu\text{m}$; green = $10\text{--}20\mu\text{m}$; blue = $>20\mu\text{m}$. The skeleton of the full vascular network is indicated in white.

Case study 2: Vascularization in patient-derived tumor xenografts

For the second case study, we used patient-derived tumor xenografts. These were created by transplanting fresh tumor tissue samples from patients with soft tissue sarcoma onto both flanks of an immunodeficient mouse. After harvest and fixation in paraformaldehyde, the samples were stained with Hf-POT (3.5% Hf-POT/PBS solution) and scanned on a NanoTom S [GE] system (5 μm voxel size, 60 kV, 0.3mm Al filter, 500ms exposure time, 2400 images, fast scan mode – 20 min. scan time). The samples were immersed in the staining solution in a falcon tube, and were put on a shaker plate during 2 weeks. After CE-CT scanning, the samples were embedded in paraffin and processed for histology (H&E) and CD31 immunohistochemistry (for blood vessel visualization).

The Hf-POT stained not only the fibrous tissue in the tumor xenograft (Fig. 2C) similar to histology, but it also intensively stained the blood that was still captured in the blood vessels and capillaries (Fig. 2C). This was confirmed by direct comparison to the corresponding CD31 stained histological section (Fig. 2B). The bright staining of the blood in the vessels allowed straightforward segmentation, resulting in a clear 3D rendering of the full vasculature throughout the tumor xenograft (fig. 2A). We are currently assessing different sarcoma subtypes, as well as the effect of an anti-angiogenic drug on the vasculature in these different tumors.

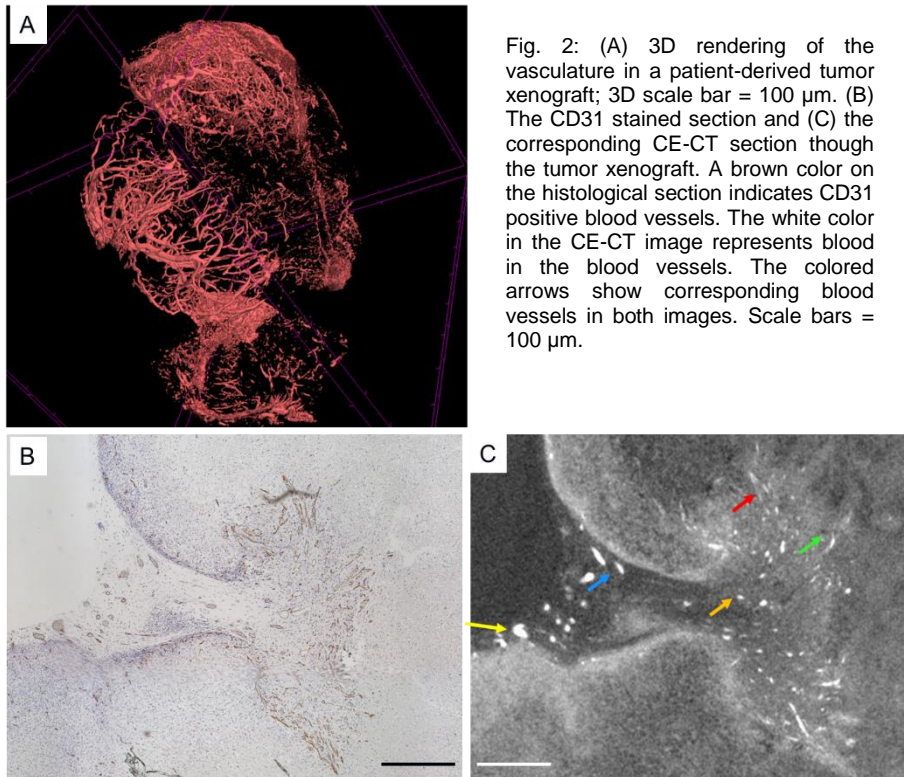


Fig. 2: (A) 3D rendering of the vasculature in a patient-derived tumor xenograft; 3D scale bar = 100 μm . (B) The CD31 stained section and (C) the corresponding CE-CT section through the tumor xenograft. A brown color on the histological section indicates CD31 positive blood vessels. The white color in the CE-CT image represents blood in the blood vessels. The colored arrows show corresponding blood vessels in both images. Scale bars = 100 μm .

Conclusion:

We have presented a novel non-invasive contrast agent for the visualization and quantification of the vasculature in different tissue types, without the need for perfusion. It allows to visualize and separate all the different blood vessel types, i.e. arteries, sinusoids and arterioles, and to evaluate their connections and organization. Since it is promising for providing additional information to standard histomorphometry, with a spatial dimension, CE-CT might bring novel insights in the importance of the vascular organization for tissue homeostasis, and in the effect of anti-angiogenic drugs on the vascular network and structure.

References:

- [1] Prisby, R.D., *Bone marrow blood vessel ossification and "microvascular dead space" in rat and human long bone*. Bone, 2014. **64**: p. 195-203.
- [2] Marenzana, M. and T. Arnett, *The Key Role of the Blood Supply to Bone*. Bone Research, 2013. **1**: p. 203-215.
- [3] Bixel, M.G., et al., *Flow Dynamics and HSPC Homing in Bone Marrow Microvessels*. Cell Rep, 2017. **18**(7): p. 1804-1816.
- [4] Kallai, I., et al., *Microcomputed tomography-based structural analysis of various bone tissue regeneration models*. Nat Protoc, 2011. **6**(1): p. 105-10.
- [5] Bouxsein, M.L., et al., *Guidelines for assessment of bone microstructure in rodents using micro-computed tomography*. J Bone Miner Res, 2010. **25**(7): p. 1468-86.
- [6] Lafage-Proust, M.H., et al., *Assessment of bone vascularization and its role in bone remodeling*. Bonekey Rep, 2015. **4**: p. 662.
- [7] Nyangoga, H., et al., *Three-dimensional characterization of the vascular bed in bone metastasis of the rat by microcomputed tomography (MicroCT)*. PLoS One, 2011. **6**(3): p. e17336.
- [8] Duvall, C.L., et al., *Quantitative microcomputed tomography analysis of collateral vessel development after ischemic injury*. Am J Physiol Heart Circ Physiol, 2004. **287**(1): p. H302-10.
- [9] Boerckel, J.D., et al., *Microcomputed tomography: approaches and applications in bioengineering*. Stem Cell Res Ther, 2014. **5**(6): p. 144.
- [10] Kerckhofs, G., et al., *Simultaneous 3D visualization and quantification of the bone marrow adiposity and vascularity using novel contrast agents for contrast-enhanced computed tomography*, in *IBMS2016*. March, 2016: Brugge, Belgium.

Osteolytica: an automated image analysis software package that rapidly measures cancer-induced osteolytic lesions in *in vivo* models with greater reproducibility compared to other commonly used method

H. R. Evans^{a, b}, T. Karmakharm^c, M. A. Lawson^{a, b}, R. E. Walker^{a, b}, W. Harris^{a, b}, C. Fellows^{a, b}, I. D. Huggins^b, P. Richmond^{c, e*} and A.D. Chantry^{a, b, d, e*}

^aSheffield Myeloma Research Team, Department of Oncology, Medical School, University of Sheffield, Beech Hill Road, Sheffield, S10 2RX, UK.

^bMellanby Centre for Bone Research, Medical School, University of Sheffield, Beech Hill Road, Sheffield, S10 2RX, UK.

^cDepartment of Computer Science, University of Sheffield, Mappin Street, Sheffield, S1 4DP, UK.

^dDepartment of Haematology, Sheffield Teaching Hospitals NHS Foundation Trust, Royal Hallamshire Hospital, Glossop Road, Sheffield, S10 2JF, UK.

^eInsigneo Institute for *in silico* Medicine, The Pam Liversidge Building, Sir Frederick Mappin Building, University of Sheffield, Mappin Street, Sheffield, S1 3JD, UK.

*Joint last authors

Aims

Methods currently used to analyse osteolytic lesions caused by malignancies such as multiple myeloma and metastatic breast cancer vary from basic 2-D X-ray analysis to 2-D images of micro-CT datasets analysed with non-specialised image software such as ImageJ. However, these methods have significant limitations. They do not capture 3-D data, they are time-consuming and they often suffer from inter-user variability. We therefore sought to develop a rapid and reproducible method to analyse 3-D osteolytic lesions in mice with cancer-induced bone disease. To this end, we have developed Osteolytica, an image analysis software method featuring an easy to use, step-by-step interface to measure lytic bone lesions.

Method

Osteolytica utilises novel graphics card acceleration (parallel computing) and 3-D rendering to provide rapid reconstruction and analysis of osteolytic lesions. To evaluate the use of Osteolytica we analysed tibial micro-CT datasets from murine models of cancer-induced bone disease (multiple myeloma and breast cancer) and compared the results to those obtained using a standard ImageJ analysis method. Secondly, to assess inter-user variability we deployed four independent researchers to analyse tibial datasets from the murine model of myeloma using both methods of analysis.

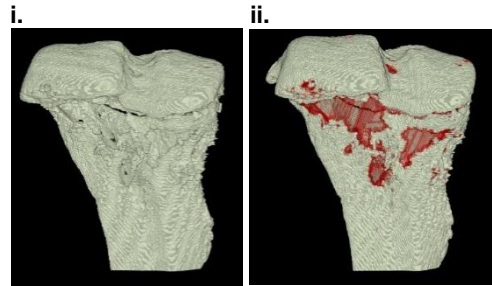


Figure 1. Micro-CT dataset of a mouse with multiple myeloma volumetrically rendered (i.) and successfully analysed with Osteolytica with bone lesions detected in red (ii.).

Results

Datasets from mice injected with myeloma cells were assessed and compared to non-tumour controls. For both methods, analysis of bone destruction was measured as total lesion area as a proportion of the region of interest. The tumour group had a significantly larger total lesion percentage compared to the non-tumour group when using both the ImageJ 2-D method and Osteolytica. Using ImageJ, there was a significant difference of $p < 0.05$ between the tumour group and the non-tumour group ($0.56 \pm 0.36\%$ vs $0.070 \pm 0.058\%$). Similarly using Osteolytica, there was a significant difference of $p < 0.05$ for the tumour group versus the non-tumour group ($6.9 \pm 1.9\%$ vs $3.7 \pm 0.5\%$). Tibial micro-CT datasets from mice injected with breast cancer cells were assessed compared to non-tumour mice using the same method. The tumour group had a significantly larger total lesion percentage compared to the non-tumour group when using both analysis methods. Using ImageJ, there was a significant difference of $p < 0.01$ for the tumour group versus the non-tumour group ($1.25 \pm 0.36\%$ vs $0.089 \pm 0.064\%$). Similarly using Osteolytica, there was a significant difference of $p < 0.01$ between the tumour group and the non-tumour group ($4.6 \pm 1.0\%$ vs $2.8 \pm 0.4\%$).

When examining inter-user variability, 4 independent researchers analysed the same 5 datasets of murine multiple myeloma using both methods. When using ImageJ, average variability was found to be 19.6%. When using Osteolytica, average inter-user variability was found to be 0.53%, substantially lower than when using the 2-D ImageJ method.

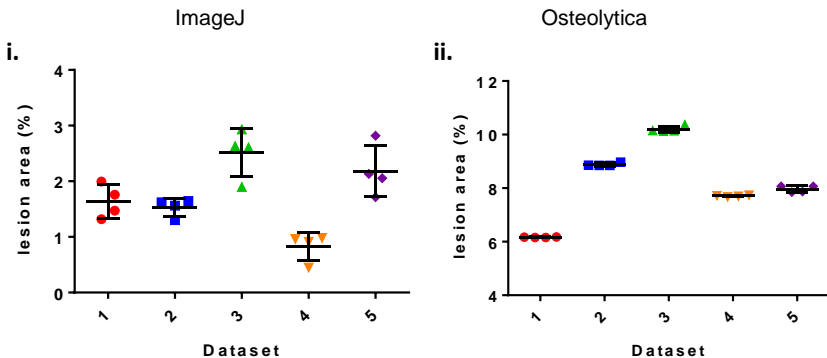


Figure 2. Inter-user variability of (i.) ImageJ method and (ii.) Osteolytica when analysing the same 5 micro-CT datasets.

Conclusion

Osteolytica can be used to successfully measure osteolytic lesions in both multiple myeloma and breast cancer mouse models, giving comparable results to the standard 2-D ImageJ method of analysis. Its usage is much quicker than the 2-D ImageJ method, and it also results in substantially lower inter-user variability, resulting in a much more robust analysis of micro-CT datasets and much better reproducibility.

Use of micro-CT to elucidate details of the anatomy and feeding of the Asian Citrus Psyllid *Diaphorina citri* Kuwayama, 1908 (Insecta: Hemiptera, Liviidae)

Javier Alba-Tercedor⁽¹⁾, Wayne B. Hunter⁽²⁾, Joseph M. Cicero⁽³⁾, Marta Sáinz-Bariáin⁽¹⁾ and Susan J. Brown⁽⁴⁾

⁽¹⁾Department of Zoology, Faculty of Sciences, University of Granada, 18071-Granada, Spain.

⁽²⁾U.S. Dept. Agriculture, Agricultural Research Service, Fort Pierce, FL 34945, USA.

⁽³⁾University of Florida, Department of Entomology and Nematology, Gainesville, FL 32611, USA.

⁽⁴⁾Ackert Hall, Kansas State University, KS, 66506, USA.

Introduction

Huanglongbing (HLB), also known as *citrus greening disease*, is caused by plant-infecting bacteria. The most prominent pathogen within the Americas: USA, Mexico, and Brazil, is *Candidatus Liberibacter asiaticus*, which affects plants of the Family: Rutaceae, in particularly citrus fruit crops of economic importance: lemons, limes, oranges, grapefruit, tangerines, and kumquats. HLB represents the most important threat to citrus sustainability worldwide. Bacterial infection causes loss of yield, bad tasting fruit, and eventually tree death. Currently no adequate control strategies are available. In Florida, an estimated 70-90% of all citrus trees are infected. Infected citrus trees showing HLB symptoms decline rapidly in yield (20-40% per year).

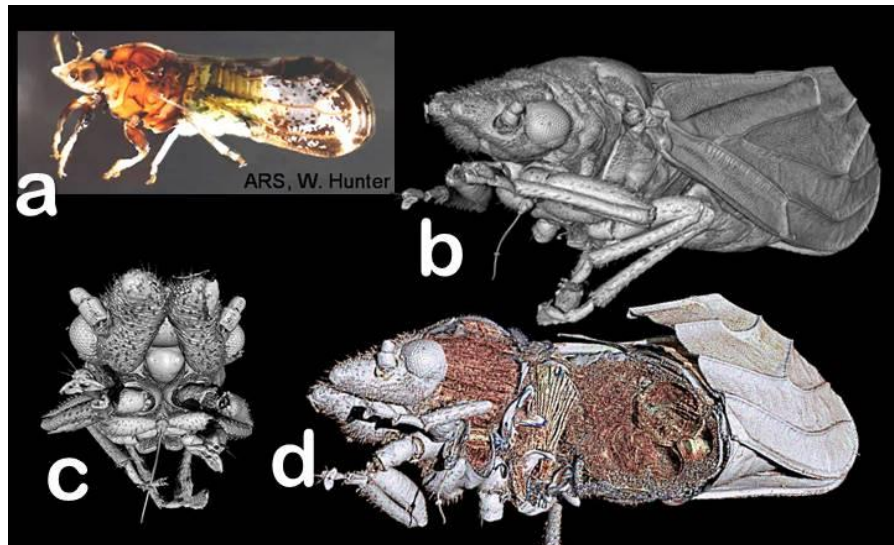


Figure 1. Light micrograph and volume rendered images of the Asian citrus psyllid. (a) Light micrograph of a living ACP. (b)-(d) Volume rendered images of a specimen that was frozen after being fed for 3 full days on an orange sprig submerged in Iomeron® contrast agent- see Fig. 2; note the extended Stylets the

insects' feeding apparatus. (b)-(c) Visualization using Amira software. (d) Visualization by reconstruction using CTvox software and colored as previously described [1].

Management of psyllid populations using insecticides has greatly increased production costs, and decreased profits. Accordingly the US Department of Agriculture, reports that citrus greening disease "has the potential to eliminate the citrus industry in the United States". Common symptoms of the disease are leaf yellowing, leaf mottling which is followed by premature defoliation, and eventually tree death. The causal agents are bacteria "*Candidatus Liberibacter asiaticus*", and "*C.L. americanus*" which are transmitted by insects known as psyllids. Psyllids are in the Order: Hemiptera: and the most common psyllid on citrus in the America's being in the Family: Liviidae. These are plant feeding insects, which use piercing-sucking mouthparts, to feed directly from the phloem of citrus trees. Two psyllid species have been identified as vectors of the disease: the African citrus psyllid, *Trioza erytreae* Del Guercio, 1918 (mainly distributed in the African regions, and already detected in Europe, in NW Spain), and the Asian citrus psyllid (ACP) *Diaphorina citri* Kuwayama, 1908 (mainly distributed in the Asian regions, has been present in Brazil, and spread to other South and Central American countries, the Caribbean, in the USA: Florida, Louisiana and Texas; and also spread into Timor-Leste and Papua New Guinea. The ACP can transmit both bacteria species (*C.L. asiaticus*, and *C.L. africanus*) (for more details see i.e:[1]–[15]).



Figure 2. Orange sprigs submerged in Iomeron® (Iomeprol) contrast agent. (a) Observation that when diluted to as low as 1%, it caused wilting when absorbed into citrus cuttings. (b) Dilution at 0.1%.

Aims

Due to the urgency for developing new methods of pest management, a research consortium of international multidisciplinary coordinated researchers, where funded to address many of these critical issues. The research grant project, lead by S. Brown from the Kansas State University, *Citrus Greening Solutions (Developing an Infrastructure and Product Test Pipeline to Deliver Novel Therapies for Citrus Greening)*, was funded by The National Institute of Food and Agriculture (NIFA). The aims of the project are focused on using a Biological Systems Approach: to build an interactive research database that will enable more rapid development and screening of potential solutions to HLB. One part of the project was focused on the establishment of an interactive Digital Video Library as a Systems Biology Approach to study psyllid anatomy and interactions with bacteria transmission by the Asian citrus psyllid. Advances in digital computed tomography (CT) allow X-ray scanning to make detailed, volume rendered images of structures inside the body of very small insects with great detail [16]–[21]. Micro-CT imaging permits digital sectioning of an insect. Combining this power with Digital Video Library (DVL) systems then enables the expansion of applications of micro-CT imaging by linking information from other databases, such as genomics, epidemiology, vector entomology, microbiology and others to enable an innovative interface using visualization and rapid data sorting interactions by the viewer. 'Interactive Information' systems are changing the way researchers and the public search for and use complex information.

Visualization of the psyllid, *Diaphorina citri*, which spreads the plant-infecting bacterium, in a 3D, rotational platform, that permits rapid dissections, analyses, and study of the internal and external anatomy of this psyllid has changed the way we 'look' at insect structure and functions. Thus the high resolution scans produced combined with computer software can also produce new ways to link and associate information. Computer systems permit the images to be colorized, cross linked to other insects, genes, and proteins in other databases (see video example: (<http://www.youtube.com/watch?v=LLz5QWYnM98>)). Furthermore, this approach provides a more pleasant, interaction for non-scientists to explore insect anatomy (video example at: <https://www.youtube.com/watch?v=RcPeotDsBK8>).

The applications of micro-CT studies are not only limited to the anatomy of the insect, but can also capture the interactions of feeding between the psyllids with their host plant. Presented herein are some of these results.

Methods

Two different methodologies were evaluated: 1) Study of the general anatomy: Live psyllids were prepared by overnight fixation in 4% glutaraldehyde with 2.5% paraformaldehyde made with sodium cacodylate buffer pH 6.5. Samples were rinsed three times, 10 min each, with 30% ethanol, and dehydrated in an ethanol series, 30 min per step, 50%, 70, 80, 90, 95, three times at 100%. Samples were chemically dried by placing in 2 ml of 100% Hexamethyldisilazane (HMDS) for 2 hours, drying overnight at 35°C. The second method: 2) Specimens in the act of feeding. Psyllids were fed for three full days on an orange sprig submerged in Iomeron® (Iomeprol) contrast agent. This is a tri-iodinated non-ionic contrast media with high concentration of iodine (400 mg/ml).

It was observed that was significantly absorbed into plant cuttings, and that even when diluted at 1% it caused plant wilting, so it was necessary to dilute it to 0.1%. The animals were flash frozen while feeding on citrus leaves using liquid nitrogen, and then processed as described. Finally, a small drop of fingernail polish on the posterior end of the psyllid and leaf, was used to hold them in place after they were processed and dried. To maintain the animals on the sample holder, different methods have been tried. For tiny samples such as psyllids, the best method developed was to glue the insect to the tip of a nylon filament line, of 200 µm diameter, fishing line by using cyanocrylate (Fig. 3).

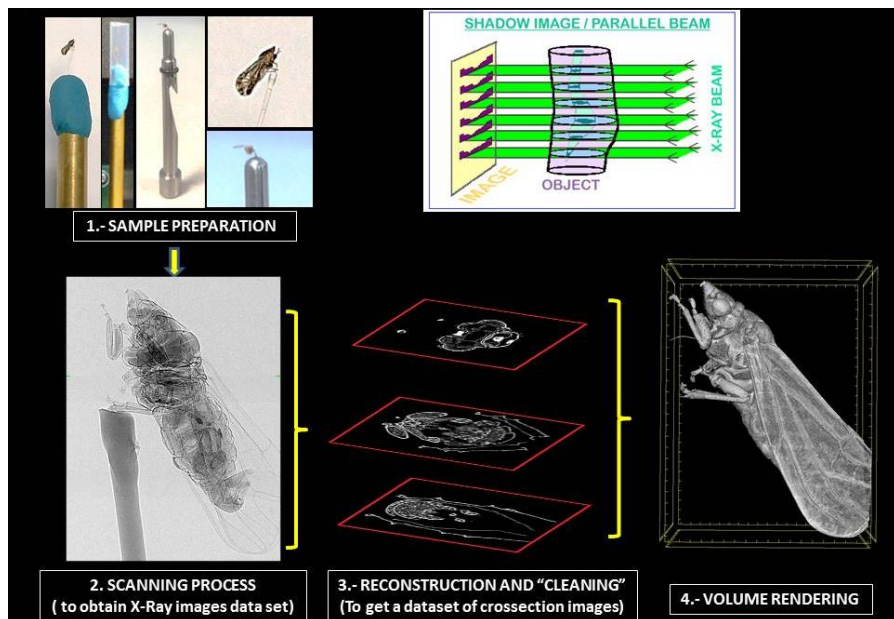


Figure 3. Schematic explanation of the process of scanning and subsequent processing until obtaining the final volume rendering images (See [21] for details).

A SkyScan 1172 high resolution microtomographer, upgraded to have a Hamamatsu 100/250 source and a SHT 11Mp camera was used. Thus, for the previous anatomical study, the scanning parameters were setup as it follows: Isotropic voxel size = $0.52 \mu\text{m}$ per pixel; Source Voltage=47KV, Source Current=51 μA , and image. Rotation step=0.2°, and 360° of rotation scan. The contrast fed animals were scanned with the following setting parameters: Isotropic voxel size = $1.02 \mu\text{m}$ per pixel; Source Voltage=55KV, Source Current=39 μA , and image. Rotation step=0.43°, and 360° of rotation scan.

For primary reconstructions and the "cleaning" process to obtain the datasets of cross-sectional images ('slices'), we used the latest versions of the free Bruker micro-CT Skyscan (www.skyscan.be) software (NRecon, DataViewer, CTAnalyser). Volume renderings images were obtained with the free Skyscan's software CTVox (color volume rendering images were obtained varying the color transfer function curves, conjunction with the lighting and shadowing options). Renderings of Figures 3, 10, 12-15 were obtained with FEI's Amira software v.6.2 [22]. For a more detailed explanation of the process see the previous paper [21].

Results and discussions

In Figures 1, and 4-11, the results show the external and internal anatomical details, similar to samples prepared for light microscopy, paraffin embedding and sections using stains, and samples from scanning electron microscopy, SEM, techniques. Images shown in Figures 11 & 12, illustrate the psyllids feeding. Stylet penetrations into the orange leaf tissues and the pathway they traveled prior to reaching the vascular tissues of the leaf (Fig.:12).

Moreover, using CTVox's volume rendering visualization with a wide angle, permitted zooming in and virtually travelling inside the lumina, hollows and passageways of the leaf structures (ie. Phloem and xylem). Thus it was possible to penetrate and visualize the inside the leaf, then to navigate through the parenchyma to locate and visualize not only abandoned salivary sheaths, but also those inserted into the phloem and xylem vessels. The sheaths being evidence of the psyllid's feeding activities (Fig. 13).

Our results confirmed existing anatomical studies of the species[23]–[27], and characteristics of the salivary sheaths studied by microscopy [28]–[30], and extended into previously unknown aspects of the species.

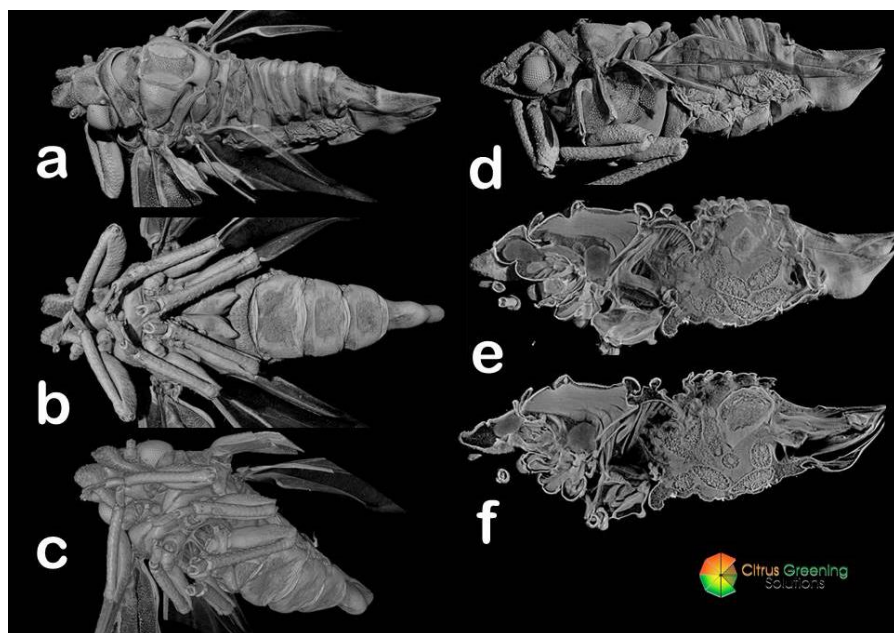


Figure 4. Volume rendering images of the external (a-d) and internal anatomy (e, f) of a female at different perspectives: dorso-lateral (a), ventral (b), ventro-lateral, and lateral (d-f). Images are shown in gray scale, similar to scanning electron microscopy, SEM.

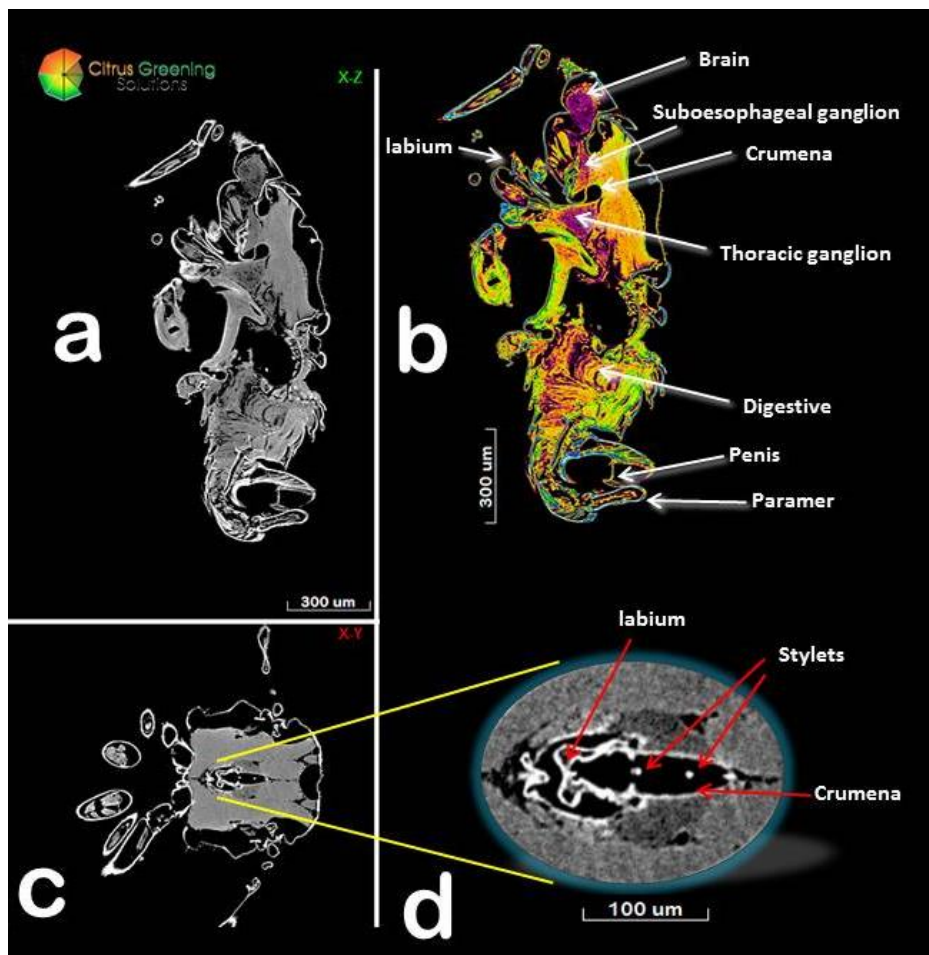


Figure 5. DataViewer's sections of an adult female psyllid showing internal details of the anatomy (a, b: sagittal, c: thoracic-transversal, d: detail showing the labium inside the thorax and stylets kept in the Crumena). Images similar to those obtained from paraffin thick sections commonly used in other insects.

Conclusion

Micro-CT, is extremely useful to enhance micro-anatomical structures of insects, and in this case to visualize the stylets and salivary sheaths of plant-feeding Hemiptera. The feeding mechanism of these "pierce-sucking feeding" insects is invisible to the eye, and normally would require hundreds of hours to prepare for standard Transmission electron microscopy analyses. The continued expansion of micro-CT, nano-CT, and fluorescent labeling techniques, will continue to produce images with greater resolution, and no doubt with new applications in biological studies and research.

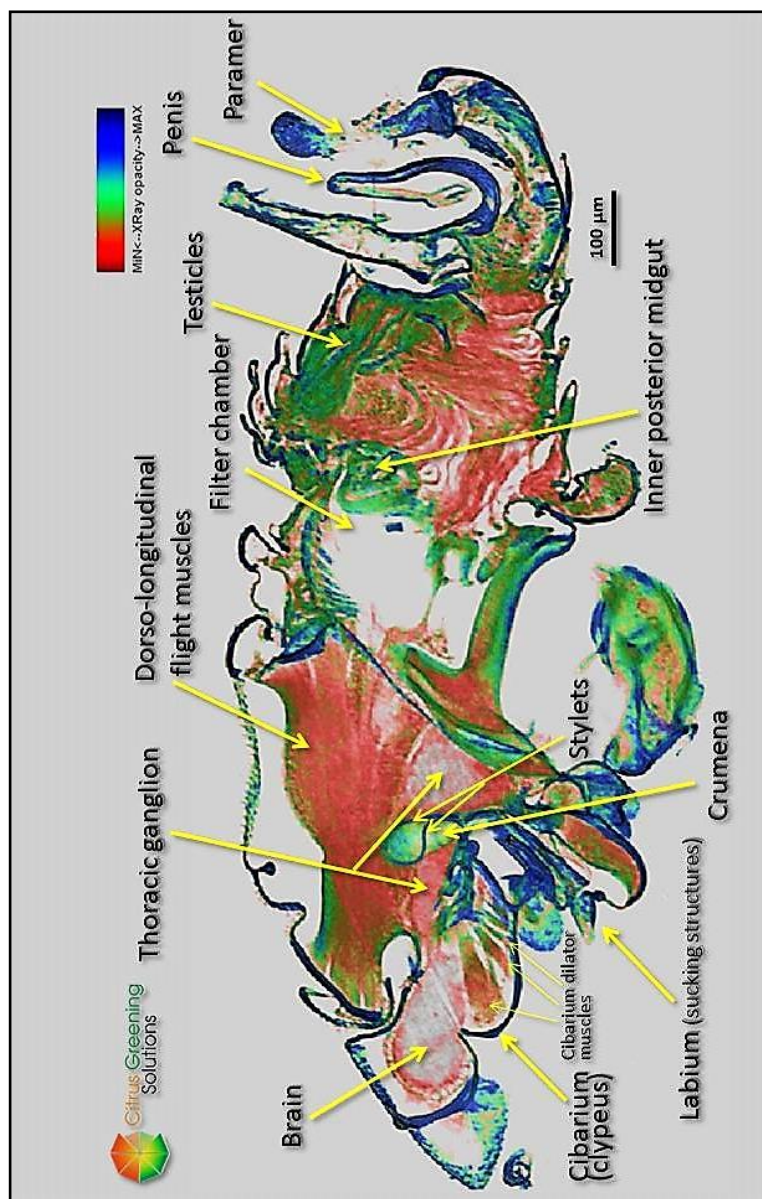


Figure 6. CTVox's volume rendering slice of a sagittal section view of the adult female psyllid showing the anatomical structures. This is similar to producing thick sections in Parafilm techniques, and then staining them. Colorization using software highlights and represent the structures opacity to x-Ray according with the scale.

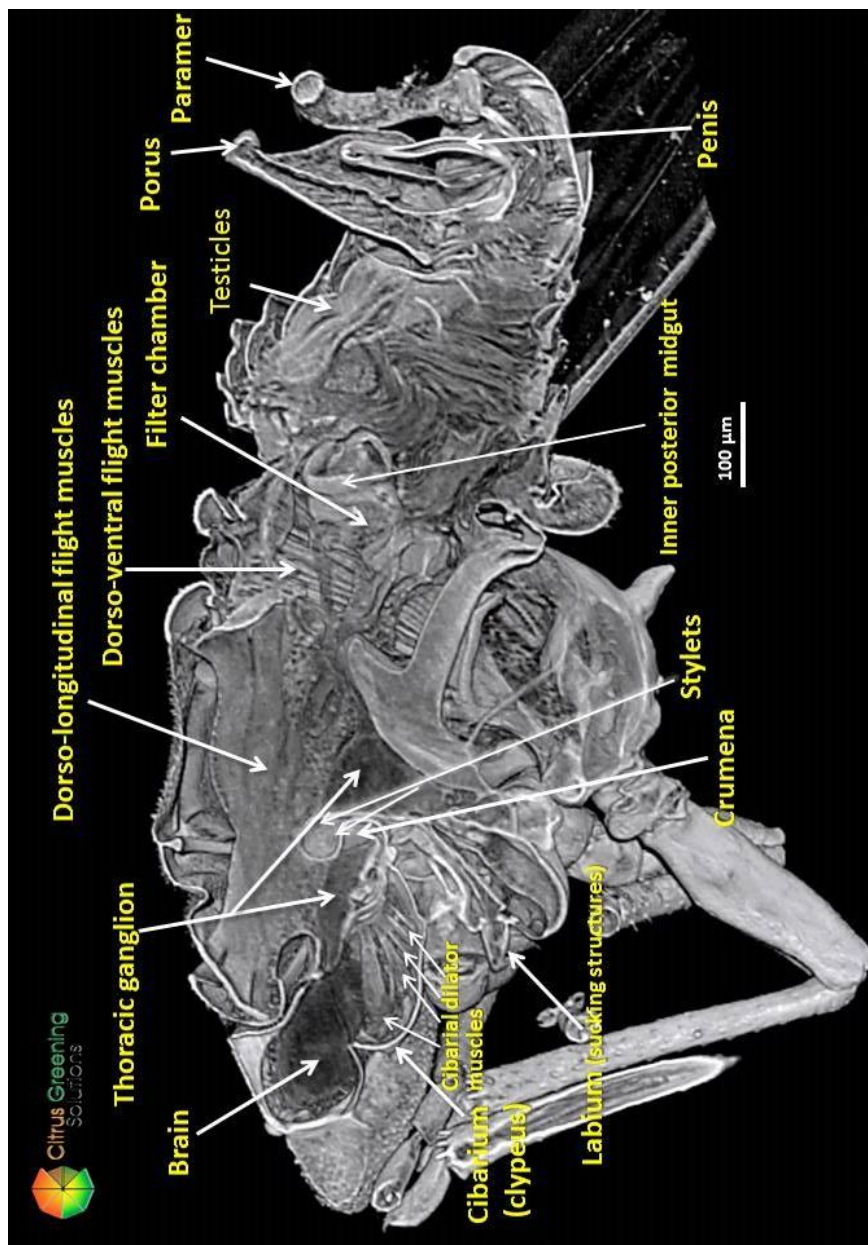


Figure 7. CTvox's volume rendering in a sagittal section of the adult female psyllid showing the anatomical structures, in scanning electron microscopy, SEM, simulated gray scale.

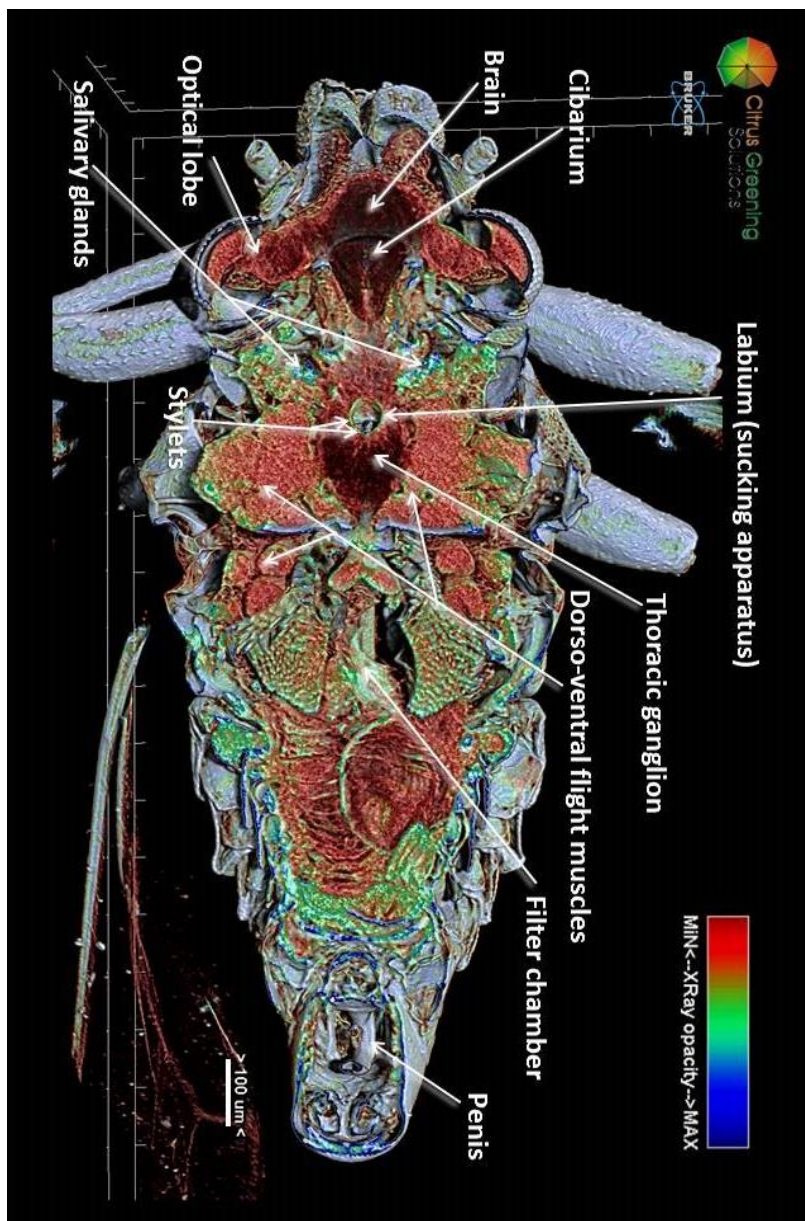


Figure 8. CTvox's volume rendering of a dorso-ventral I section view of the adult male psyllid. Shows the anatomical structures. Colors represent the structures opacity to x-Ray according to the scale.

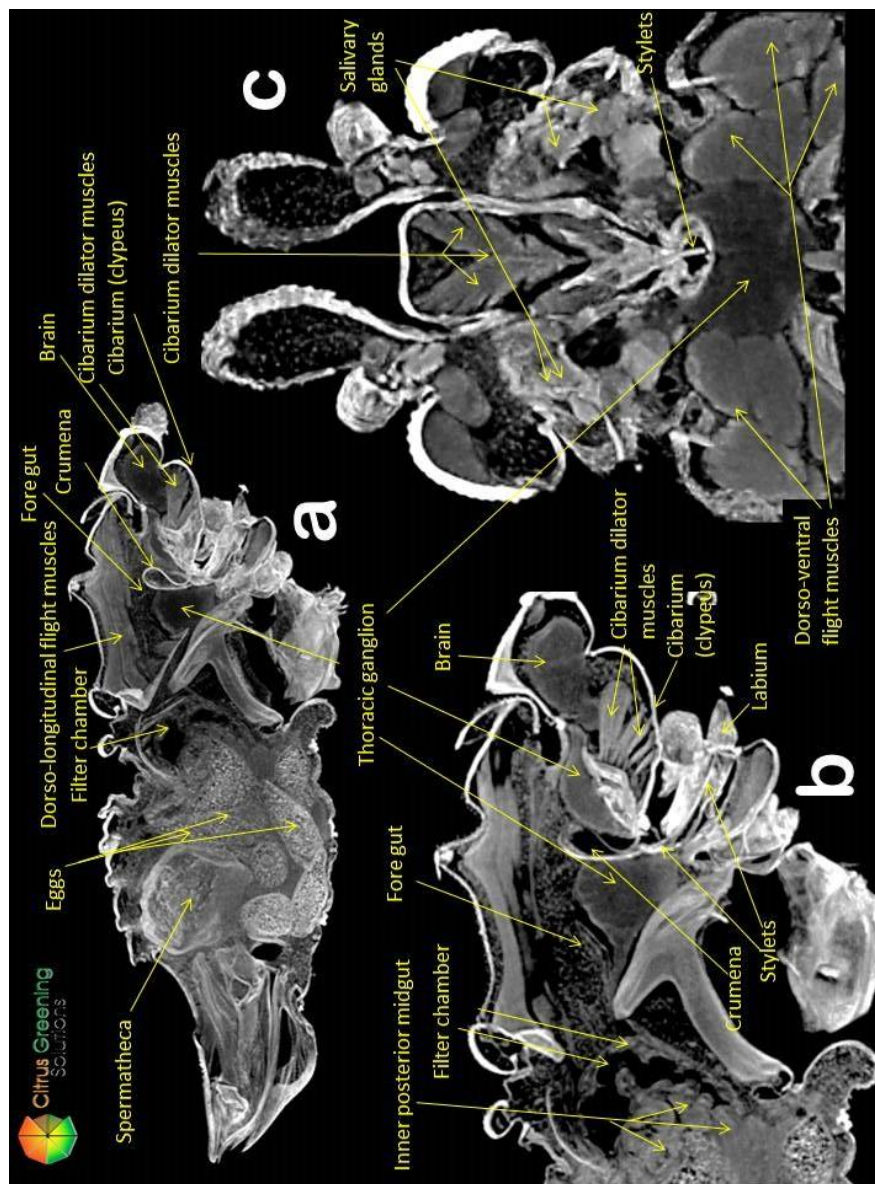


Figure 9. Amira's "maximal intensity projection" (MIP) slices of an adult female psyllid showing the anatomical structures. (a: middle sagittal view; b: detail of the middle-fore region in a middle sagittal view; c: middle dorso-ventral slice of the fore region) .

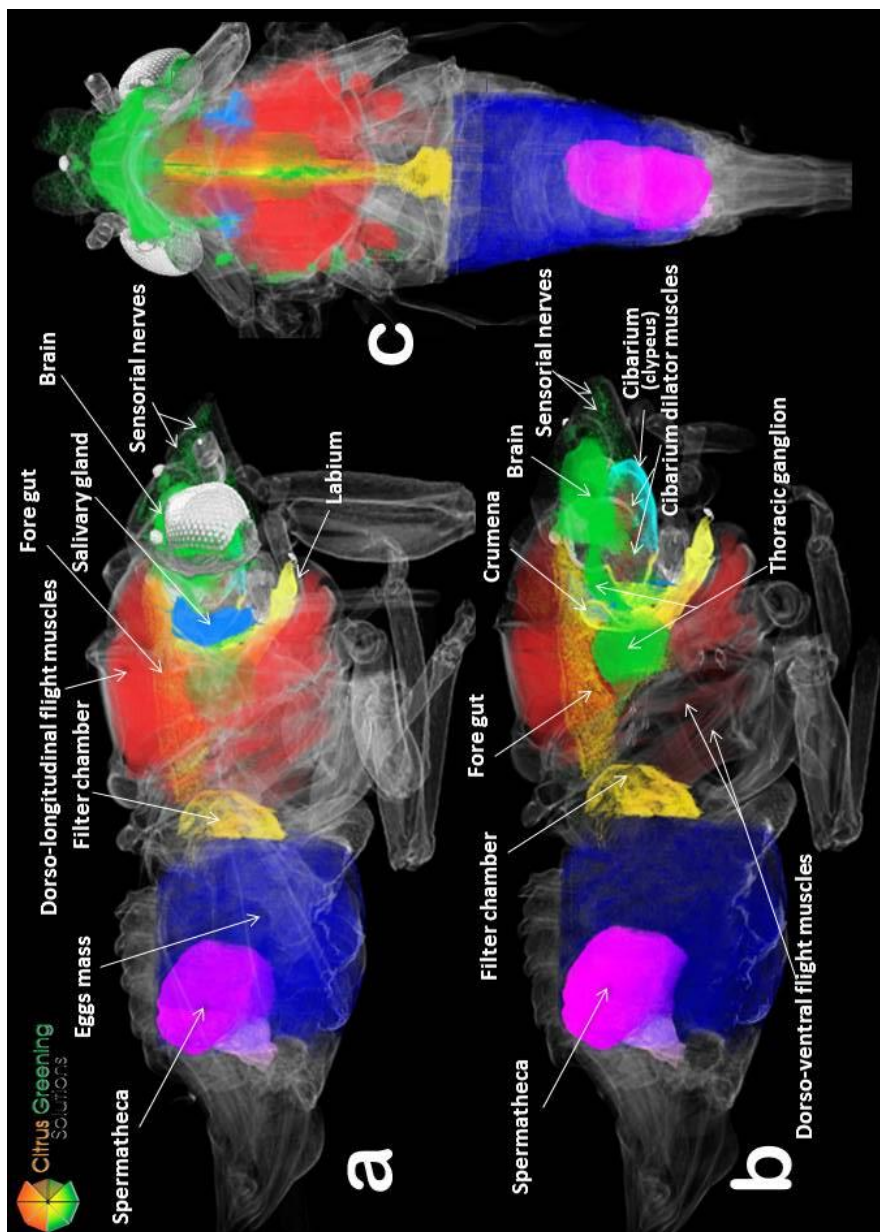


Figure 10. Amira's volume renderings of a female psyllid adult. The main internal anatomical structures have been segmented with different colors (a, b: lateral views; c: dorso-ventral view; of b with external sagittal half of part of the thorax and abdomen removed to enhance the view of the internal structures).

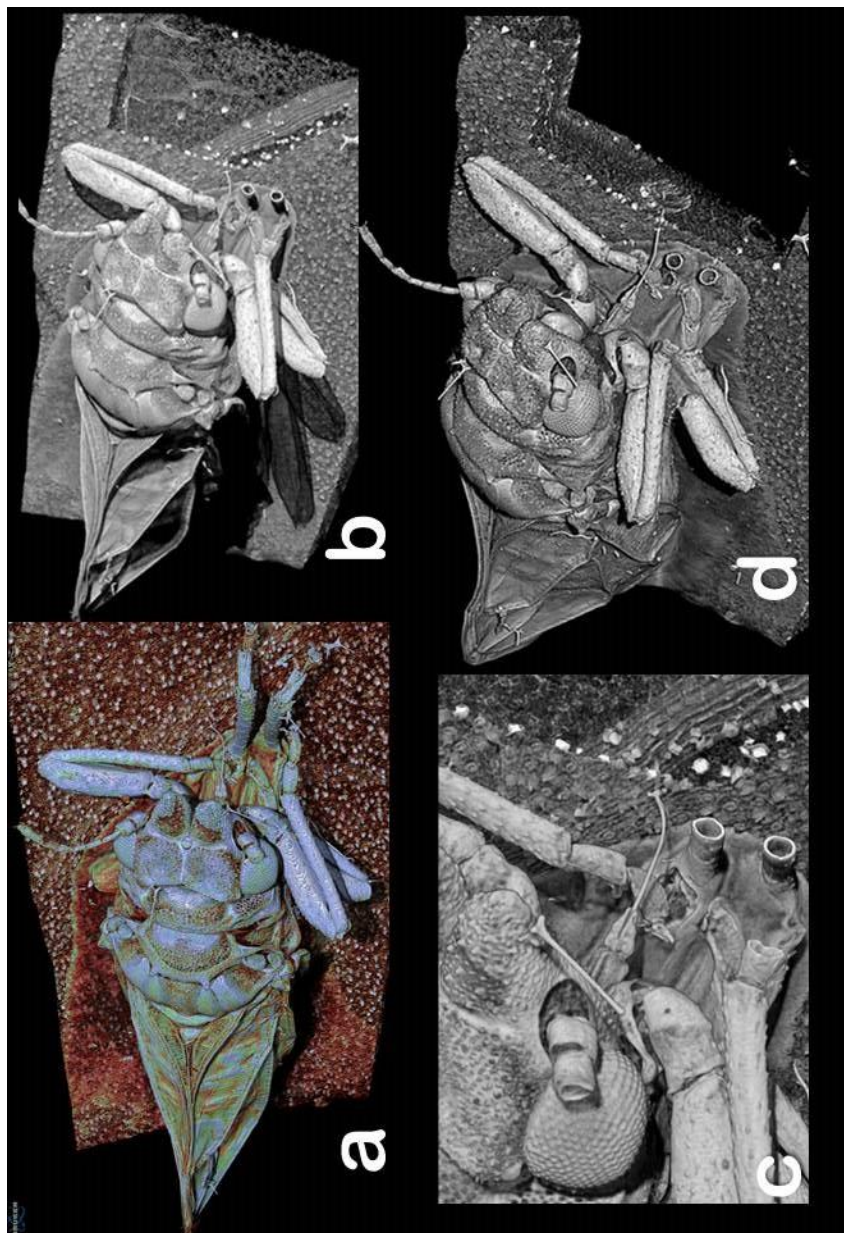


Figure 11. CTVox's volume renderings of the Asian psyllid feeding on a leaf from an orange seedling. From **a** to **d** by using the "box" cutting in the cutting/clipping option within CTVox's, the leaf's surface has been progressively eroded to visualize the vein where the insect is feeding.

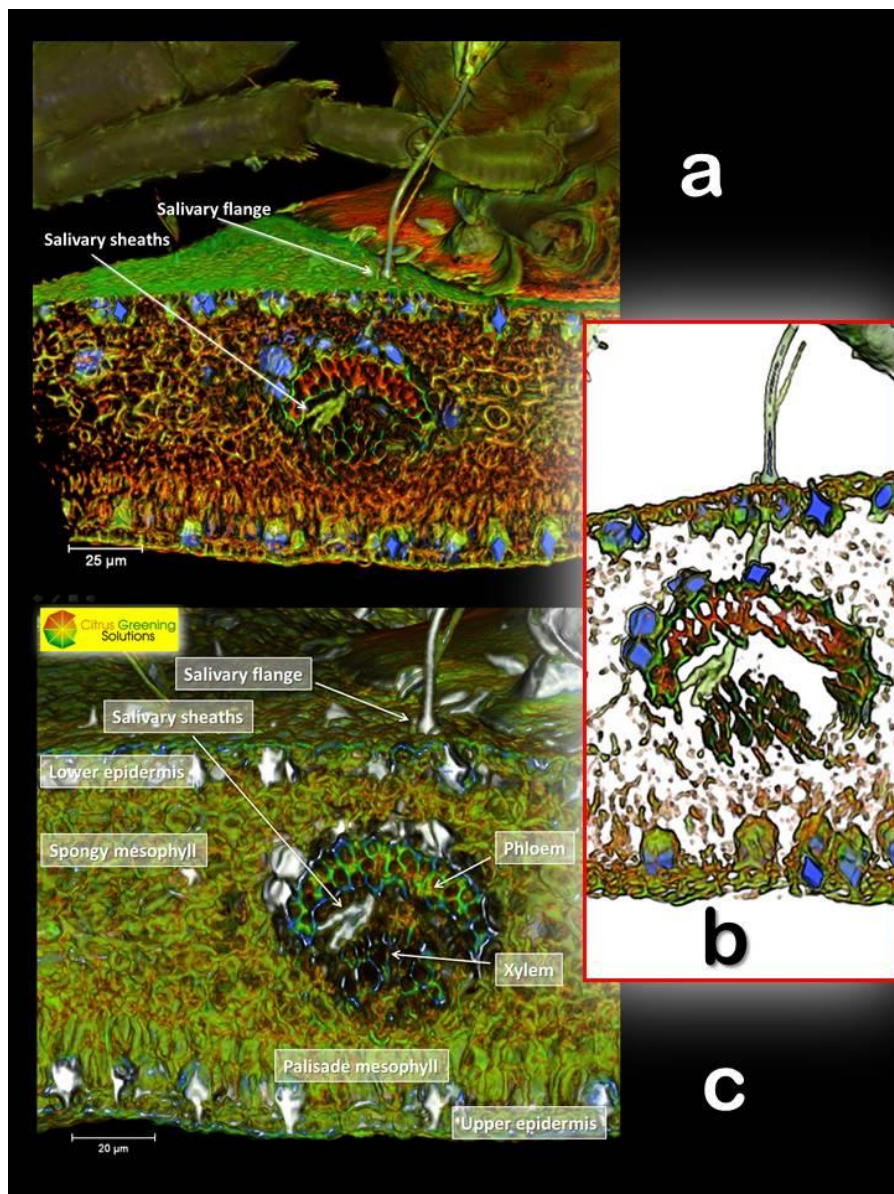


Figure 12. Amira's "volume rendering slice sections of the details of the feeding structures piercing the lower surface of the orange leaf and penetrating into sap vessels.

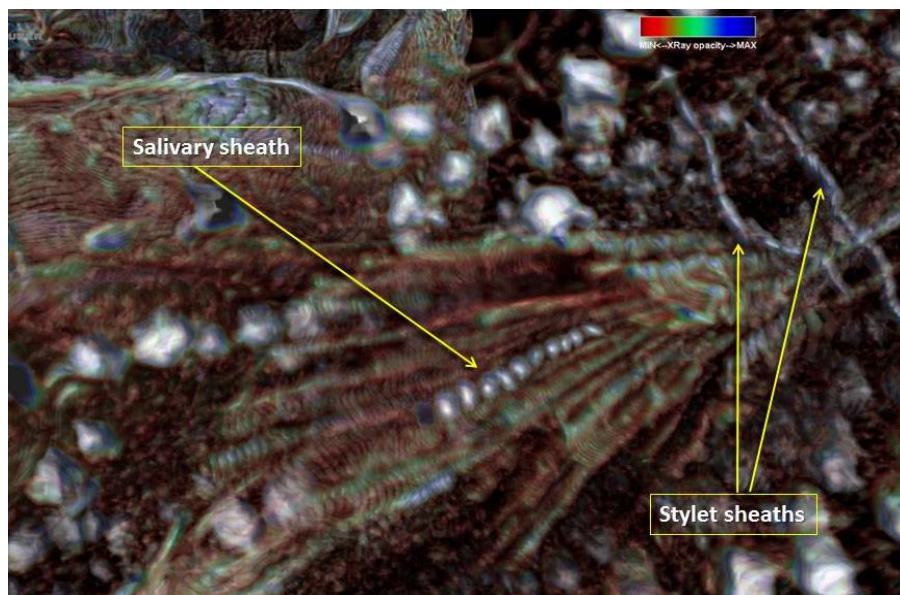


Figure 13. Using CTvox's volume rendering visualization with a wide angle, permitted zooming in and virtually travelling inside the lumina, hollows and passageways of structures. Thus it was possible to penetrate inside the leaf structure and navigate through the parenchyma to locate and visualize not only abandoned salivary sheaths (right)), but also those inserted into the phloem and xylem vessels (left), leaving tracks of the psyllid's feeding activities

Conclusion

Micro-CT, is extremely useful to enhance micro-anatomical structures of insects, and in this case to visualize the stylets and salivary sheaths of plant-feeding Hemiptera. The feeding mechanism of these "pierce-sucking feeding" insects is invisible to the eye, and normally would require hundreds of hours to prepare for standard Transmission electron microscopy analyses. The continued expansion of micro-CT, nano-CT, and fluorescent labeling techniques, will continue to produce images with greater resolution, and no doubt with new applications in biological studies and research.

Acknowledgments

To Bruker-Skyscan staff for fast and effective support, their patience and effectiveness, and for their constant improvements to the software and in implementing new options we requested. Also for their kindness in providing the senior author fast and effective suggestions and answers to queries. In this respect, we are especially indebted to: Alexander Sasov, Stephan Boons, Xuan Liu, Phil Salmon, Jeroen Hostens, and Vladimir Kharitonov.

This work is part of the project: "Developing an Infrastructure and Product Test Pipeline to Deliver Novel Therapies for Citrus Greening Disease", 2015-2017, lead by Dr. S. J. Brown, Kansas State University and funded by the USDA's National Institute of Food and Agriculture

through the Specialty Crops Research Initiative/Citrus Disease Research & Extension. USDA NIFA Award No.2015-70016-23028.

References

- [1] T. Gottwald, "Current Epidemiological Understanding of Citrus Huanglongbing*," *Annu. Rev. Phytopathol.*, 2010.
- [2] H. Su, "Citrus greening disease," *Publ. by Food Fertil. Technol.* ..., 1996.
- [3] S. Halbert and K. Manjunath, "Asian citrus psyllids (Sternorrhyncha: Psyllidae) and greening disease of citrus: a literature review and assessment of risk in Florida," *Florida Entomol.*, 2004.
- [4] S. Halbert and C. Núñez, "Distribution of the Asian citrus psyllid, *Diaphorina citri* Kuwayama (Rhynchota: Psyllidae) in the Caribbean basin," *Florida Entomol.*, 2004.
- [5] E. Grafton-Cardwell, "Asian citrus psyllid," 2005.
- [6] S. Halbert, "Citrus greening/Huanglongbing," ... at(<http://www.doacs.state.fl.us/pi/chrp/greening/> ...), 2005.
- [7] J. Bové, "Huanglongbing: a destructive, newly-emerging, century-old disease of citrus," *J. plant Pathol.*, 2006.
- [8] A. Hodges and T. Spreen, "Economic impacts of citrus greening (HLB) in Florida," 2006.
- [9] A. Batool, Y. Iftikhar, and S. Mughal, "Citrus Greening Disease—A major cause of citrus decline in the world—A Review," *Hort. Sci.*(...), 2007.
- [10] T. Gottwald, J. da Graça, and R. Bassanezi, "Citrus huanglongbing: the pathogen and its impact," *Plant Heal. Prog.*, 2007.
- [11] M. Polek, "Citrus bacterial canker disease and Huanglongbing (citrus greening)," 2007.
- [12] D. Hall, "Biology, history and world status of *Diaphorina citri*," ... spp.) y el psílido asiático los cítricos (*Diaphorina citri* ...), 2008.
- [13] K. Chung and R. Bransky, "Citrus diseases exotic to Florida: Huanglongbing (citrus greening)," 2009.
- [14] J. Qureshi and M. Rogers, "Incidence of invasive *Diaphorina citri* (Hemiptera: Psyllidae) and its introduced parasitoid *Tamarixia radiata* (Hymenoptera: Eulophidae) in Florida citrus," *J. Econ.* ..., 2009.
- [15] N. Hummel and D. Ferrin, "Asian citrus psyllid (Hemiptera: Psyllidae) and citrus greening disease in Louisiana," *Southwest. Entomol.*, 2010.
- [16] J. Alba-Tercedor and C. E. Sáinz-Cantero Caparrós, "Volume rendering reconstructions of the anatomy of small aquatic beetles (Insecta: Coleoptera) scanned with the Skyscan 1172 high resolution micro-CT," in *SkyScan Micro-CT Users Meeting 2012*, 2012, pp. 75–84.
- [17] J. Alba-Tercedor and I. Sánchez Almazo, "Looking beyond the small: micro-CT study of eggs and development in insects: comparison of the results obtained with the Skyscan 1172 and the attachment for SEM microtomographs," in *Bruker Micro-CT Users Meeting 2013*, 2013, pp. 102–110.
- [18] J. Alba-Tercedor, "Study of the anatomy of the common housefly *Musca domestica*

- Linnaeus, 1758 (Insecta: Diptera, Muscidae) scanned with the Skyscan 1172 high resolution micro-CT," *Bruker Micro-CT Users Meet. 2013*, pp. 275–289, 2013.
- [19] T. Salge, S. Boehm, B. Pauwels, A. Sasov, and J. Alba-Tercedor, "Advances in X-ray Microtomography in SEM with submicron Spatial Resolution: Applications in Life , Earth and Material Sciences," *Microsc. Microanal.*, vol. 19, no. Suppl 2, pp. 622–623, 2013.
- [20] J. Alba-Tercedor and I. Sánchez Almazo, "The use of micro-CT for the study of eggs and development in insects : a comparison of two microtomographs," *Microsc. Anal.*, no. March, pp. 7–10, 2014.
- [21] J. Alba-Tercedor, "From the sample preparation to the volume rendering images of small animals : A step by step example of a procedure to carry out the micro-CT study of the leafhopper insect *Homalodisca vitripennis* (Hemiptera: Cicadellidae)," *Bruker Micro-CT Users Meet. 2014*, pp. 260–288, 2014.
- [22] Amira, "3D Visualization and Analysis Software." FEI, Hillsboro, Oregon, USA, 2016.
- [23] E.-D. Ammar, R. G. Shatters, C. Lynch, and D. G. Hall, "Detection and Relative Titer of *Candidatus Liberibacter asiaticus* in the Salivary Glands and Alimentary Canal of *Diaphorina citri* (Hemiptera: Psyllidae) Vector of Citrus Huanglongbing Disease," *Ann. Entomol. Soc. Am.*, vol. 104, no. 3, pp. 526–533, May 2011.
- [24] F. Dossi and F. Cônsoli, "Gross morphology and ultrastructure of the female reproductive system of *Diaphorina citri* (Hemiptera: Liviidae)," *Zool.*, vol. 31, no. 2, pp. 162–169, 2014.
- [25] E. Garzo, J. P. Bonani, J. R. S. Lopes, and a Fereres, "Morphological description of the mouthparts of the Asian citrus psyllid, *Diaphorina citri* Kuwayama (Hemiptera: Psyllidae).," *Arthropod Struct. Dev.*, vol. 41, no. 1, pp. 79–86, Jan. 2012.
- [26] J. Cicero and J. Brown, "The digestive system of *Diaphorina citri* and *Bactericera cockerelli* (Hemiptera: Psyllidae)," *Ann. Entomol. Soc. Am.*, 2009. 102(4):650-665
- [27] E.-D. Ammar and D. G. Hall, "Retracted Stylets in Nymphs of the Asian Citrus Psyllid are Held Externally Against the Clypeus by a Special Paired Organ Not Found in the Adults," *Source Florida Entomol.*, vol. 96, no. 1, pp. 264–267, 2013.
- [28] J. K. Morgan, G. A. Luzio, E. D. Ammar, W. B. Hunter, D. G. Hall, and R. G. Shatters, "Formation of Stylet Sheaths in ãere (in air) from Eight Species of Phytophagous Hemipterans from Six Families (Suborders: Auchenorrhyncha and Sternorrhyncha)," *PLoS One*, vol. 8, no. 4, 2013.
- [29] T. Will, K. Steckbauer, M. Hardt, and A. J. E. van Bel, "Aphid Gel Saliva: Sheath Structure, Protein Composition and Secretory Dependence on Stylet-Tip Milieu," *PLoS One*, vol. 7, no. 10, p. e46903, Oct. 2012.
- [30] E.-D. Ammar, M. L. Richardson, Z. Abdo, D. G. Hall, and R. G. Shatters, "Differences in Stylet Sheath Occurrence and the Fibrous Ring (Sclerenchyma) between xCitroncirus Plants Relatively Resistant or Susceptible to Adults of the Asian Citrus Psyllid *Diaphorina citri* (Hemiptera: Liviidae)," *PLoS One*, 2014.

Video Refs:

- Cicero, J., Alba-Tercedor, J., Hunter, W.B. 2014. Micro CT scanned anatomical gateway to insect pest bioinformatics. <http://www.youtube.com/watch?v=LLz5QWvNM98>
- Alba-Tercedor, J., Hunter, W.B. 2014. Micro CT study of the Anatomy (Head) of the Glassy Winged Sharpshooter *Homalodisca vitripennis*. <https://www.youtube.com/watch?v=RcPeotDsBK8>

Challenges in micro-CT of fresh samples: diversity among tissue density and thickness in *Punica granatum*

Fabiana Kühne¹, Cláudio Zoppi², Livia Cordi³

¹UNICAMP, IB-DBEF, Laboratório Multiusuário, Campinas/SP, Brazil

²UNICAMP, IB-DBEF, Lapemib, Campinas/SP, Brazil,

³UNICAMP, IB-Herbarium UEC, Campinas/SP, Brazil

Aims

Our focus is setting the best tomography and reconstruction conditions to represent fruit development of pomegranate, *P. granatum*, from flower bud to fruit, despite its diversity in tissues and structures. The challenge was determine time exposure, rotation step, frame average and reconstruction parameters in a fixed and low voltage and current, without losing details among different tissues, whose vary in thickness and density.

Method

Bud flowers, flowers and fruits in different maturation stages were visualized in a Skyscan 1178 in different voltage and current in order to find the best in minimum transmission despite differences in density among samples, for example between petals and fruit peel. After set the current and the goal was to find the best relation between rotation step and frame average to get the details in structures as much as possible. Following image acquisition, samples were reconstructed in two different thresholds levels and then edited in CTVox for luminosity and opacity. The final result was a time course movie showing the evolution from bud flower to fruit.

Results

A previous visualization of all samples (fig. 1), from bud to mature fruit, in low voltage (29kV) and current (338uA) was proceed in order to access the diversity in transmission among samples – fig 2. The fruit was the denier sample, and then it was the sample of choice to set a suitable voltage and current.

The minimum transmission was determined based on the mature fruit, and then the voltage for all the subsequent tests was adjusted to 65kV and 615uA – fig 3.

The subsequent step was to choose between rotation step and frame average, at a fixed time exposure (720ms) and camera binning (80um pixel size), to find the best resolution in final image, despite the time in scanning and the file size. The filter is fixed in Skyscan 1178 (0,5mm Al filter). The first comparison was between frame average for the lowest rotation step (0,18 degree): 2 and 5. The time for scanning increased from 53min (2 frames) to 2h13 (5 frames). Despite the time, the 5 frames was the choice, because the gain in resolution was the best condition to visualize internal and small structures – fig 4.

The last thing to consider was change the threshold level from 0 to something above, in order to dismiss the mounting media effect over petals. The luminosity and opacity was determined to highlight small structures (data not shown).

All the samples was scanned and reconstructed in order to produce a time course move showing the evolution from bud flower to fruit.

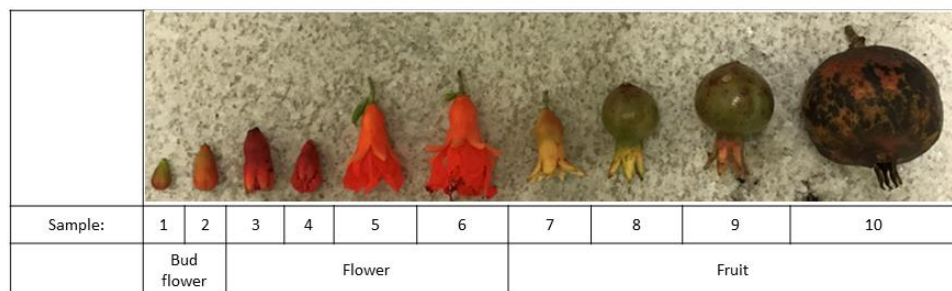


Figure 1 - Range of samples in different maturation steps, from bud flower to mature fruit.

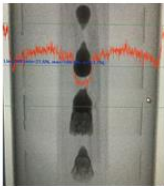
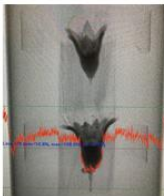
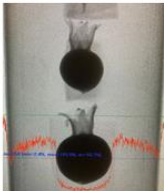
Sample	Minimum transmission	
2 - Bud flower	21,60%	
6 - Flower	18,80%	
9 - Fruit	2,40%	

Figure 2 - Range of minimum transmission in densier parts of samples in pre-visualization mode, at 29kV and 338uA.

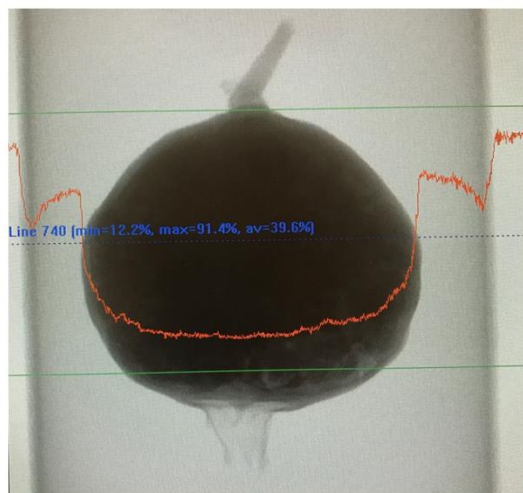


Figure 3 - Pre-visualization of fruit at voltage and current (65kV, 650uA) adjusted to 12,2% in minimum transmission.

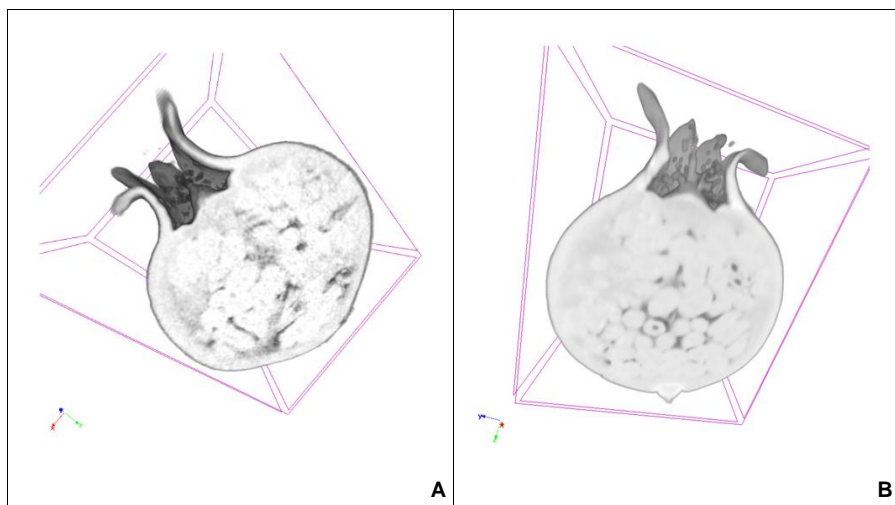


Figure 4 – A fruit cross section with frame average 2 (A) and 5 (B) scanned at 0,18 degree and 720ms, under the same reconstruction protocol.

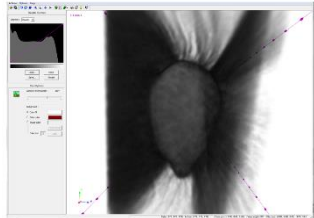
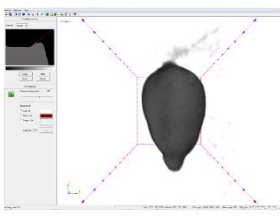
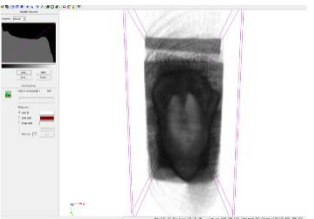
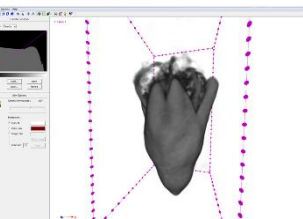
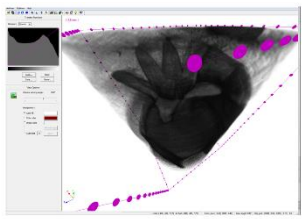
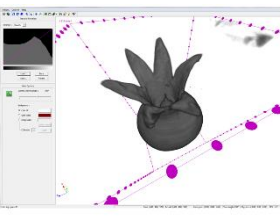
Sample	A	B
Bud flower 1		
Flower 4		
Fruit 9		
Threshold	0,000000	0.001798

Figure 5 – A fruit cross section with frame average 2 (A) and 5 (B) scanned at 0,18 degree and 720ms, under the same reconstruction protocol.

Conclusion

A lot of work in testing different parameters for scanning diverse samples is very important to determine the suitable settings to represent the variety among tissues. This generalization in parameters, at the limited resolution from 1178 (80um pixel size) makes the images not suitable for detailed morphometric analysis, but very attractive for educational purposes in visualization anatomic details in classroom, saving real samples from extraction and facilitating observation of inner structures without laboratory manipulations.

Further options in scanning with different mounting media and different voltage or time of exposure are necessary in order to change the minimum transmission of petals and preserve its representation on reconstructed images.

Enhancing micro-CT methods: Studying different contrast agents to quantify oil content and porosity in starch-gluten matrices

Contardo, I. and Bouchon, P.¹

¹Department of Chemical and Bioprocess Engineering, Pontificia Universidad Católica de Chile, Avenida Vicuña Mackenna 4869, Macul, Santiago, Chile

Aims

The porous network of starch-gluten matrices can influence physical, sensory, and nutritional properties of the final product. Processing of starchy food at high temperature induces starch gelatinization. These transformations, together with steam generation, lead to the generation of open and closed pores, having a direct influence on its complex and irregular three-dimensional geometry. The detailed understanding of the microstructure can be relevant to obtain information related to parameters such as oil content, porosity, and starch digestibility. Traditional methods to quantify oil content or assess porosity involve sample destruction. X-ray microcomputed tomography (micro-CT) has been introduced as an innovative and advantageous non-destructive method to study the internal structure based on the differences in density (atomic number) (Barigou, Douaire, Morris, & Groves (2013); Qiu et al. (2015)). In food matrices, the discrimination or contrast of certain components with low X-ray attenuation such as carbohydrates, proteins, or oil becomes a challenge when using micro-CT. The objective of this study was to explore the potential application of different contrast agents to modify the attenuation of components using micro-CT to analyze 3D microstructures of fried dough, to define a non-invasive methodology to quantify the oil content and the porosity in food matrices.

Method

Sample preparation and contrast agents

Laminated doughs were used as model matrices. These were prepared using starch (88% d.b.), gluten (12% d.b.), and distilled water (40 % moisture content). Different contrast agents were used during sample preparation (see Table 1). Doughs were fried under atmospheric conditions up to bubble-end point (~2.5 % moisture content). To incorporate and dissolve Nile Red the frying oil was previously stained with it (0.05 g/L). Nile red was used due to its successful application in other techniques of microstructural characterization as Confocal microscopy. The contrast agent concentrations were set under preliminary experiments.

Table 1: Different samples stained with contrast agents. Nile red was dissolved in frying oil at 0.05 g/L oil.

Sample	Abbreviation	Concentration
Dough	D-Control	-
Dough + Lugol	D-L0.1	Lugol solution 0.1% (w/w)
Dough + Barium	D-Ba0.5	Barium solution 0.5% (w/w) (BaCl ₂)
Dough + Nile Red	D-NR	Nile Red in frying oil 0.05g/L
Dough + Lugol + Nile Red	D-L0.1NR	Lugol solution 0.1% (w/w) + Nile Red in frying oil 0.05g/L

Image processing and analysis

The samples were scanned using a SkyScan 1272, high resolution micro-CT (Bruker, Kontich, Belgium), operating at 35 kV of source voltage and a constant source current of 231 μ A. Experimental conditions during images acquisition were optimized to allow high quality tomography projection images, considering sample size ($20 \times 20 \times 2 \text{ mm}^3$), resolution, and low scanning times (about 70 min per sample). The samples were scanned over an interval of 0-360° with a rotation step of 0.2°. An image pixel size of 11.5 μm was obtained and no filter was used for the scanning. And each sample was scanned in triplicate.

The projection images were reconstructed using *NRecon* software to produce a series of cross-sectional images (1344 x 2016 pixels). The critical parameters related to the reconstruction process were post-alignment, beam-hardening correction, ring artifacts correction level, and smoothing level. The reconstructed images were processed and analysed using *CTAn* software (CTAn, Skyscan, Belgium) to render the fried dough structure both as two-dimensional and three-dimensional images.

A volume of interest (VOI) was selected from the reconstructed images to be located from top up to more than half of the original fried dough, in order to eliminate any edge effects or artifacts. A total of 1101 slices were considered for each sample. An index intensity histogram was reconstructed from the set of images of each sample.

Thereafter, the binarized images from the VOI were processed to eliminate rings and residuary artifacts using custom processing routines, such as despeckle and ROI shrink-wrap. The reconstructed images were converted into binary images and using Global thresholding were displayed as a grey scale value calibrated between 0 and 255. A threshold level was chosen as the minimum between two distinct peak in the image histogram, and in combination with CTAn custom processing and inverse binarization the “total pores” (pores filled with air and oil phase) from total matrix for each voxel in the image was distinguished, as well the “oil pores” (pores filled only with oil phase) and the “solid matrix” (solids of the matrix phase) (as shown in Figure 1) was obtained.

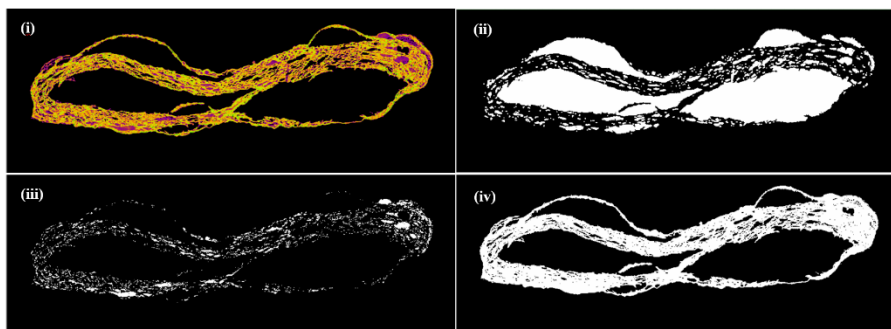


Figure 1: Example of the image segmentation procedure performed in a cross-section image (z plane) of an unstained fried dough sample (D): (i) Original image, (ii) “total pores” (pores fill with air and oil) after segmentation using Global thresholding, CTAn custom processing, and inverse binarization, (iii) “oil pores” (pores filled with oil), and (iv) “solid matrix” (solids of the matrix phase).

The following parameters were determined from 3D measurements:

Oil Content (OC) = corresponds to the volume of voxel segmented as “oil pores” multiplied by its true density over the total volume of voxels (including air, oil, and solid matrix inside of VOI) multiplied by its true density, to transform the digital data into mass units (g oil/ g de-fatted dry solids).

Total Porosity (ϵ) = corresponds the volume of voxel segmented as “total pores” (pores fill with air and oil) over the total volume of voxels (including air, oil, and solid matrix inside of VOI)

The following analytical methods were performed to compare results with those obtained by image analysis using the micro-CT approach:

Total oil content of dry samples was determined gravimetrically by Soxhlet extraction using petroleum ether (official method 920.39; AOAC International 1995).

True density (ρ_t) (kg/m^3) was determined as the ratio between the weight of the grinded sample ('defatted solids') and its volume, which was measured using a gas pycnometer (Ultrapyc 1200e, Quantachrome Instruments, FL, USA) operated with nitrogen at 19 psi. Around 1 to 1.3 g of fried dough was used and the test was performed in triplicate at room temperature.

Bulk density (ρ_b) (kg/m^3) was determined as the ratio between the weight of the sample over its bulk volume. This was measured using the volume displacement technique with ethanol/water (10%) as described by Nunes & Moreira (2009). Around 0.9 to 1.1 g of fried dough was used and the test was performed in triplicate at room temperature.

Total porosity (ϵ_p) of fried samples was obtained from the ratio between bulk density and true density as expressed in [equation 1](#):

$$\epsilon_p = 1 - \frac{\rho_b}{\rho_t} \times 100 \quad (1)$$

The results are expressed as mean \pm standard deviation (SD) of triplicate sections. Experimental data were tested by Shapiro-Wilk test to assess for normality. Analysis of one-way variance (ANOVA) was undertaken for the normally distributed datasets at a level of significance of $P < 0.05$ and any non-normally distributed dataset was analysed using Kruskal-Wallis. The differences were resolved by the LSD method at 95% confidence, using Statgraphics plus 5.1 (Manugistics, Inc., Rockville, MD, USA).

Results

[Figure 2](#) shows the histogram of the intensity index (grey level units), which gives a general information of the contrast between the different phases (attenuation) and image quality obtained by microCT methods. Three phases can be identified: air, oil, and solid matrix (which includes starch-gluten); where the minimum greyscale value (0) corresponds to the “air phase” or background, the third peak value is associated with the “solid matrix phase”, and an intermediate peak between both structures is related to the “oil phase”. Peak values depend on each sample.

All the samples stained with contrast agents, except from the one stained with barium (D-Ba0.5), showed an enhancement in the attenuation, allowing for a clear differentiation between the oil and the solid matrix phases. Specifically, fried matrices stained with Lugol solution 0.1 % (D-L0.1) showed a clear contrast between the air, the oil, and the solid matrix, as well as a high and clear define peak associated to the solid matrix. This value was around 9.4% higher than the one obtained in unstained dough (D-Control). Further, the increase in the attenuation of the solid matrix phase may be associated to an adequate fixation of the ionic dye to the starch-gluten network. In addition, the narrower base of the peak ([Figure 2](#)) reflects a decrease in the noise of the image, allowing better segmentation. Samples stained with Nile Red showed similar results with respect to phase differentiation. However, the decrease in intensity could be indicating wronger X-rays absorption with a consequent incorporation of noise. This last behaviour was even more evident in samples treated with Barium (D-Ba0.5), perhaps due to the low concentration that was used, mainly to avoid effects on the rheology of the dough, which could generate a weak effect on both the increase of attenuation in the fried matrix and the image quality.

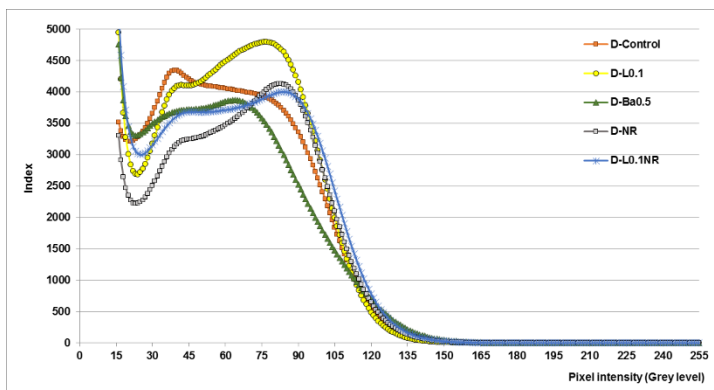


Figure 2: Histogram of intensity index of the different samples (mean of 1101 images) of starch-gluten matrices determined using CTan (n=3).

In order to test the ability of the image analysis methodology to quantify the oil content and the total porosity of the different samples, the values were compared with those obtained using traditional invasive techniques (soxhlet and pycnometry). Table 2 shows the oil content (OC) of unstained and stained fried samples, using soxhlet (OC_s) and image analysis methods (OC_{ia}).

Table 2: Values of oil content by analytical (soxhlet) and microCT (image analysis) methods. Different letters show significant differences ($p < 0.05$).

Samples	Oil content (OC _s)		Oil content (OC _{ia})	
	(g oil/ g de-fatted dry solids)			
D-Control	0.1866 ^{ab} ±	0.002	0.1665 ^a ±	0.031
D-L0.1	0.2036 ^{abc} ±	0.008	0.2192 ^{bc} ±	0.042
D-Ba0.5	0.1811 ^{ab} ±	0.005	0.1884 ^{ab} ±	0.035
D-NR	0.1759 ^a ±	0.006	0.1888 ^{ab} ±	0.029
D-L0.1NR	0.2028 ^{abc} ±	0.005	0.1827 ^{ab} ±	0.021

No significant differences in oil content were obtained using Soxhlet ($p < 0.05$), confirming that sample preparation did not interfere in oil uptake kinetics.

That is, the image analysis procedure that was established seems to be an effective technique for oil quantification.

With respect to the different staining procedures it was determined that Lugol addition (0.1% w/w solution) increased the intensity value of the solid phase improving segmentation. Under these conditions the discrimination between the air, the oil and the solid phase within the matrix could be better achieved.

Table 3 shows the total porosity (ϵ) of unstained and stained fried samples, using pycnometry (ϵ_p), and image analysis methods (ϵ_{ia}).

Table 3: Total porosity obtained by analytical (pycnometry) and microCT (image analysis) methods. Different letters show significant differences ($p < 0.05$).

Samples	Porosity (ϵ_p)		Porosity (ϵ_{ia})	
			(%)	
D-Control	56.72 ^{cd} \pm	0.34	60.45 ^d \pm	7.28
D-L0.1	50.46 ^{ab} \pm	0.06	52.57 ^{abc} \pm	3.86
D-Ba0.5	51.22 ^{abc} \pm	0.04	55.81 ^{bcd} \pm	5.08
D-NR	54.05 ^{bc} \pm	0.02	56.60 ^{cd} \pm	1.01
D-L0.1NR	47.70 ^a \pm	0.01	51.26 ^{abc} \pm	4.94

Regarding results of total porosity (including air and oil), the differences obtained between the samples could be due to the irregularity of the porous network as a result of the different formulations. These differences could be linked to changes in the gluten network and dough elasticity, due to the addition of the different agents. More evidence is needed to confirm or discard this behaviour.

In D-Control samples, total porosity increased from 56.72 \pm 0.34 % to 60.45 \pm 7.28 % (analytical and microCT methods, respectively). Although these differences are not significant, these results show the highest standard deviation, indicating that the differentiation between the pore (air or oil) and the solid phases may be difficult by image analysis, when working using unstained samples. Again, samples stained with Lugol showed the closest analytics and microCT values.

In addition, no significant differences in total porosity were obtained using pycnometry and image analysis ($p < 0.05$) for a sample treated under the same conditions, confirming that microCT can be a good alternative to further examine the porous microstructure.

Conclusion

Micro-CT and associated image analysis show to have a great potential to quantify the oil content and the total porosity of fried starchy-gluten matrices non-invasively. Further, this technique has the potential to provide additional information of the 3D-microstructural network, without intrusion, including pore size distribution and stratification, to better understand the effect of formulation and/or processing conditions on oil content or textural properties of interest.

Specifically, Lugol seems to be a promising agent to enhance the attenuation and consequent intensity the starch-gluten matrix improving the image quality, facilitating image segmentation. On the other hand, Nile Red, even though it decreased the intensity of the starch-gluten matrix, it allowed better contrast between oil and solid phase of food matrix. In addition, Nile Red stained samples may be further examined using confocal laser scanning microscopy, due to its fluorescence nature, a complementary technique that may use to better understand the inner microstructure.

References:

1. AOAC, "Official methods of analysis". 16th edition. Washington: Association of Official Analytical Chemists, 1995
2. Barigou, M., Douaire, M., Morris, V., & Groves, K. "X-ray micro-computed tomography for resolving food microstructures. Food microstructures: microscopy, measurement and modelling". Woodhead, Cambridge, 246-272, 2013.
3. Nunes, Y., & Moreira, R. G., "Effect of osmotic dehydration and vacuum-frying parameters to produce high-quality mango chips". Journal of Food Science, 74(7), 2009
4. Qiu, J., Khalloufi, S., Martynenko, A., Van Dalen, G., Schutyser, M., and Almeida-Rivera, C., "Porosity, bulk density, and volume reduction during drying: Review of measurement methods and coefficient determinations," Dry. Technol. An Int. J., vol. 33, no. 14, pp. 1681–1699, 2015.

Whole Skeleton Survey of Osteoclast Activity in a Paget's Disease of Bone Mouse Model

K. Verdelis¹, J.J. Windle², D.L. Galson³

¹Center for Craniofacial Regeneration, University of Pittsburgh, PA

²Human and Molecular Genetics, Virginia Commonwealth University, VA

³Hematology-Oncology, Dpt of Medicine, University of Pittsburgh, PA

Aims

The aim of this study was to use microCT imaging to determine the frequency and severity of bone abnormalities indicative of focal areas of increased bone remodeling (abnormal osteoclastic activity) in genotypic variants of a model for Paget's Disease of Bone (PDB) mice. The relative effect of kinase TBK1, which has been implicated in PDB¹, was examined in this part of the study.

Method

Preparation/Image Acquisition: Transgenic mice expressing N-terminal FLAG-tagged human TBK1 cDNA driven by the mouse TRAP promoter in cells of the OCL lineage (TG-TBK1 mice) and wild type (WT) mice were analyzed. Dissected spines, all bones in hind and front limbs and skulls from male and female TG-TBK1 and WT 10 and 16month-old (10month-old, n total=22; 16month-old, n total=18) mice were imaged using a Skyscan 1172 scanner and the following conditions: 60KVp energy, 10mm voxel resolution, 2x2 detector binning mode in a offset function (double field of view), 400ms exposure, 8 frames per view. Spines (T8-S4 vertebrae) from six or limb/skull sets from three animals were imaged in 70% ethanol in every scan that lasted 12 hours and covered 60mm on the z-axis.

Analysis-Scoring: The reconstructed (NRecon) volumes of every spine or limbs/skull were digitally truncated from the rest of the bones they were scanned together with by CTAn and viewed in a 3 plane-mode on DataViewer for visual evaluation and measurement of PDB-like lesions after digital downsampling to 20µm for ease of operation. For vertebrae, hyperostotic lesions were characterized smaller (A) or extensive (B) when smaller or greater, respectively, than .2mm in diameter. Asymmetric thickening of the cortical bone (C) greater than 100% of the contralateral side thickness was also recorded and results were reported as frequency of mice with at least one vertebral lesion and an average A, B or C score in the genotype group, broken down by sex and age group.

Results

Bone abnormalities in our specimens in general were categorized as hyperostotic (trabecular or cortical), osteolytic (trabecular or cortical), abnormal trabecular structure or a combination of features (examples from our analysis on Fig. 1A-B). We found that a 10µm voxel size was a good compromise between high sensitivity and efficient imaging of the whole skeleton from a large number of animals. We also corroborated representative lesions as identified by microCT with histology, as this had not been performed before. The analysis included animals from both sexes and a range of older ages (10 and 16months), since the impact of TBK1 or other genetic factors also implicated in PDB on a possible sex dimorphism and the disease onset is not well known for the relevant mouse models.

Data so far have only been analyzed and results are shown for the vertebrae. TRAP-staining confirmed the macroscopically (on microCT images) appearing on the images PDB lesions, both smaller and extensive, to have a pagetic nature (Fig.1B-D). The location of the vertebrae in which a lesion was present appeared to be random.

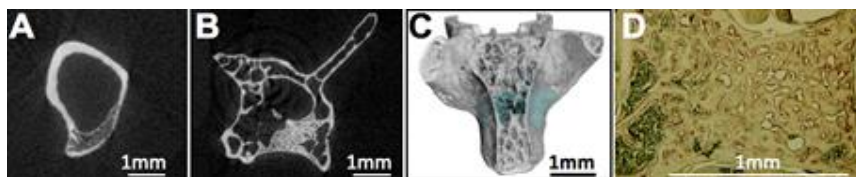


Figure 1: Transverse views of osteosclerotic lesions in (A) humerus and (B) L6 vertebra of 16month TG-TBK1 mice. (C) 3D rendering of same vertebral lesion in blue-green color and (D) histology section vertebra - substantially osteosclerotic cancellous marrow compartment with many trap-stained OCL (in red).

The frequency of animals with PDB lesions present in vertebrae within the 10 and 16month-cohorts, as well as the distribution of smaller (A) and extensive (B) hyperostotic, and asymmetric cortical bone thickening (C) lesions are presented on Table 1. It appears that at 10months the vertebral lesion frequency is four times as high and lesions are more severe in female animals that overexpress TBK1. By 16months lesions are present in both backgrounds with approximately the same severity. In the limited number of male animals in the cohort overexpression of TBK1 did not show any association with PDB type- abnormal bone formation.

10month-	Animals with vertebral lesions	Average lesions per affected animal
<i>M/TG-TBK1</i>	0/2	
<i>M/WT</i>	1/2	A=0.5
<i>F/TG-TBK1</i>	4/10	A=0.3, B=0.5
<i>F/WT</i>	1/8	A=0.125
16month-		
<i>M/TG-TBK1</i>	1/2	C=1
<i>M/WT</i>	1/2	A=0.5, B=0.5, C=1
<i>F/TG-TBK1</i>	5/7	A=3.3, B=2.3, C=0.15
<i>F/WT</i>	7/7	A=2.3, B=2.9, C=0.15

Table 1: M=male, F=female, TG-TBK1=TBK1 overexpression, WT=wild type. Lesion types (A-C) explained in Methods.

Conclusion

The possibility for a skeletal survey of mice for PDB pathology presence and severity by microCT is very important for related studies, especially there is no lesion location (for vertebrae at least) preference and only a few vertebrae can be used for evaluation by histology. 10months is a preferred age for evaluation of PDB incidence in mice, as by 16 months the chances for a PDB-type lesion presence is very high in normal animals. At 10 months of age the incidence of PDB in female animals is almost fourfold under overexpression of TBK1. Analysis of the rest of the skeleton of our specimens will allow to better understand the association of PDB with TBK1 overexpression.

Supported by U.S. National Institutes of Health R01 AR057310-06, Galson (PI)

References:

1. A Galson DL, Roodman GD. "Pathobiology of Paget's Disease of Bone" J Bone Metab. 21(2):85-98, 2014

Hydration of composite scaffolds: micro-CT study

Bartos M.¹, Spanko M.¹, Vrbova R.¹, Suchy T.²

¹ 1 Department of Stomatology, First Faculty of Medicine, Charles University in Prague, Katerinska 32, Praha 2, 128 08, Czech Republic,

² Department of Composites and Carbon Materials, Institute of Rock Structure and Mechanics, Academy of Sciences of the Czech Republic, V Holesovickach 41, Prague 8, 182 09, Czech Republic

Aims:

Composite scaffolds seeded with mesenchymal stem cells are extensively studied as a promising method for treatment of bone defects (especially critical-size bone defects). Their role is to provide temporary template for new tissue formation and promote bone regeneration while offering safe and predictable results. Scaffolds are usually porous biodegradable materials based on natural or synthetic polymer (e.g. collagen or polylactide). Scaffolds can be cell-seeded prior to implantation at the site of bone defect.

Scaffold characteristics (chemical, mechanical, biological and structural properties) influence scaffold-tissue interaction. Among structural parameters open porosity with high degree of interconnectivity is considered to be one of the key factors allowing cells to migrate into the scaffold from surrounding tissue.

Micro-CT offers non-destructive approach in structure visualization and analysis. Conventional methods (e.g. light microscopy, scanning electron microscopy) are destructive and provide limited information about 3D structure.

Scaffold structure is usually studied in dry-state. However, implantation inevitably results in hydration which can lead to structural changes, therefore influences expected outcome. Structure analysis of hydrated scaffolds is difficult to achieve. Micro-CT is promising method. However, 2 main issues have to be overcome: low X-ray density of scaffold in solution and motion artifacts.

Motion artifacts can be reduced by appropriate positioning of scaffold in plastic tube, "setting time" (without any motion) before scanning and reducing scanning time (using smaller specimen, lower resolution, higher camera binning and lower frame averaging). Scaffolds X-ray density can be enhanced by contrast solution (e.g. PTA - **phosphotungstic acid**), very often used in "soft tissue" micro-CT scanning. Contrast agent must be then sufficiently removed in order to enhance X-ray contrast between scaffold matrix and pores.

Process of scaffold hydration revealed unexpected consequence in this pilot study which had to be solved before further analysis.

Method:

Scaffolds based on a collagen matrix (30 wt%, type I isolated from calf skin), poly(DL-lactide) (PURASORB PDL 05, Corbion, NL) electrospun sub-micron fibres (47 wt%, 275-300nm, Nanospider NS LAB 500, Elmarco, CZ), 22.5 wt% of calcium phosphate nanoparticles isolated from chemically- and thermally-treated bovine bone and 0.5 wt% of sodium hyaluronate powder (HySilk, Contipro, CZ) were prepared from a collagen dispersion (5 wt%) in deionized water. The resulting homogenized dispersion was frozen at -70°C for 3 hours and lyophilized. All specimens were cylindrical in shape (diameter 5 mm, height 5 mm). Only 2 specimens were used in this pilot study.

First scaffold was immersed for 30 minutes into PTA (1%, 10 ml) and then immersed in saline infusion (10 ml) for 30 minutes to wash PTA from open pore spaces (saline was changed

three times). Second specimen was hydrated without using contrast agent. Specimen was placed on micro-stage in plastic tube filled with saline, micro-positioning and flat-field correction was performed. Specimen was left 1 hour to stabilize its position. Micro-CT scans were taken in dry-state and after 2 hours, 8 hours, 24 hours and 7 days after initial hydration. Micro-CT scans were acquired using SkyScan 1272 (Bruker, Belgium). All the specimens ($n=2$) were scanned with the following scanning parameters: $4\text{ }\mu\text{m}$ pixel size, camera binning 2×2 , source voltage = 60 kV, source current = 166 μA , a 0.25 mm Al filter, frame averaging of 2 and the use of 180° rotation. Scanning time was approximately 1 hour. The flat-field correction was updated before each acquisition.

Projection images were reconstructed with NRecon (Bruker) with the adequate setting of correction parameters (misalignment, smoothing, ring-artifact correction and beam hardening). Cross-sectional images of the scaffolds were provided by DataViewer (Bruker). In order to perform analysis, datasets were loaded into CTAn (Bruker). The visualizations of the scaffolds structure were achieved by means of DataViewer and CTVox (Bruker). Open porosity was also visualized in color-coded mode (color related to structure thickness). Analysis was performed using CTAn.

Results:

Specimens were micro-CT scanned in dry state. One specimen was hydrated without contrast agent. The second specimen was contrasted in PTA solution prior to scanning as mentioned above. Scans were acquired in dry-state and in different time intervals (2h, 8h, 24h and 7 days) after initial hydration.

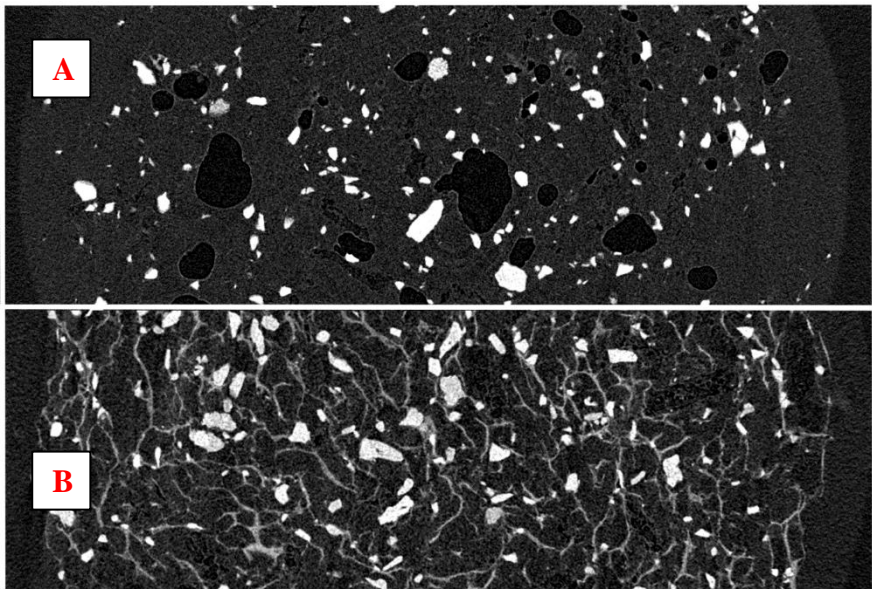


Fig.1: 2D section of hydrated scaffold (of different composition and structure than used in this study) without contrast agent (A) and after using PTA X-ray contrast agent (B)

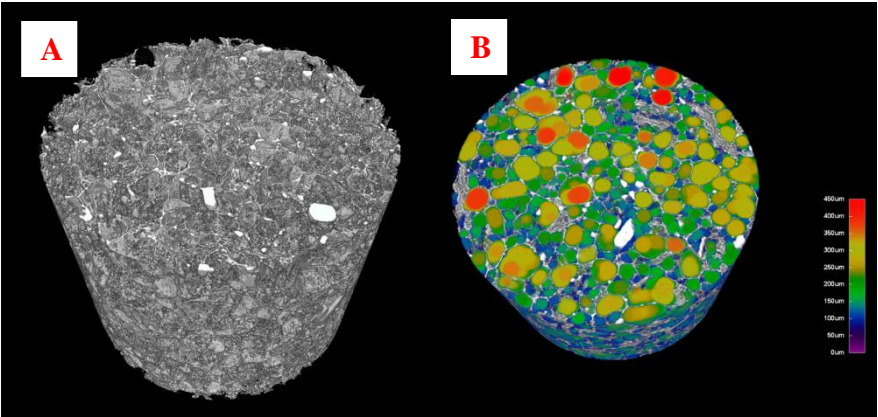
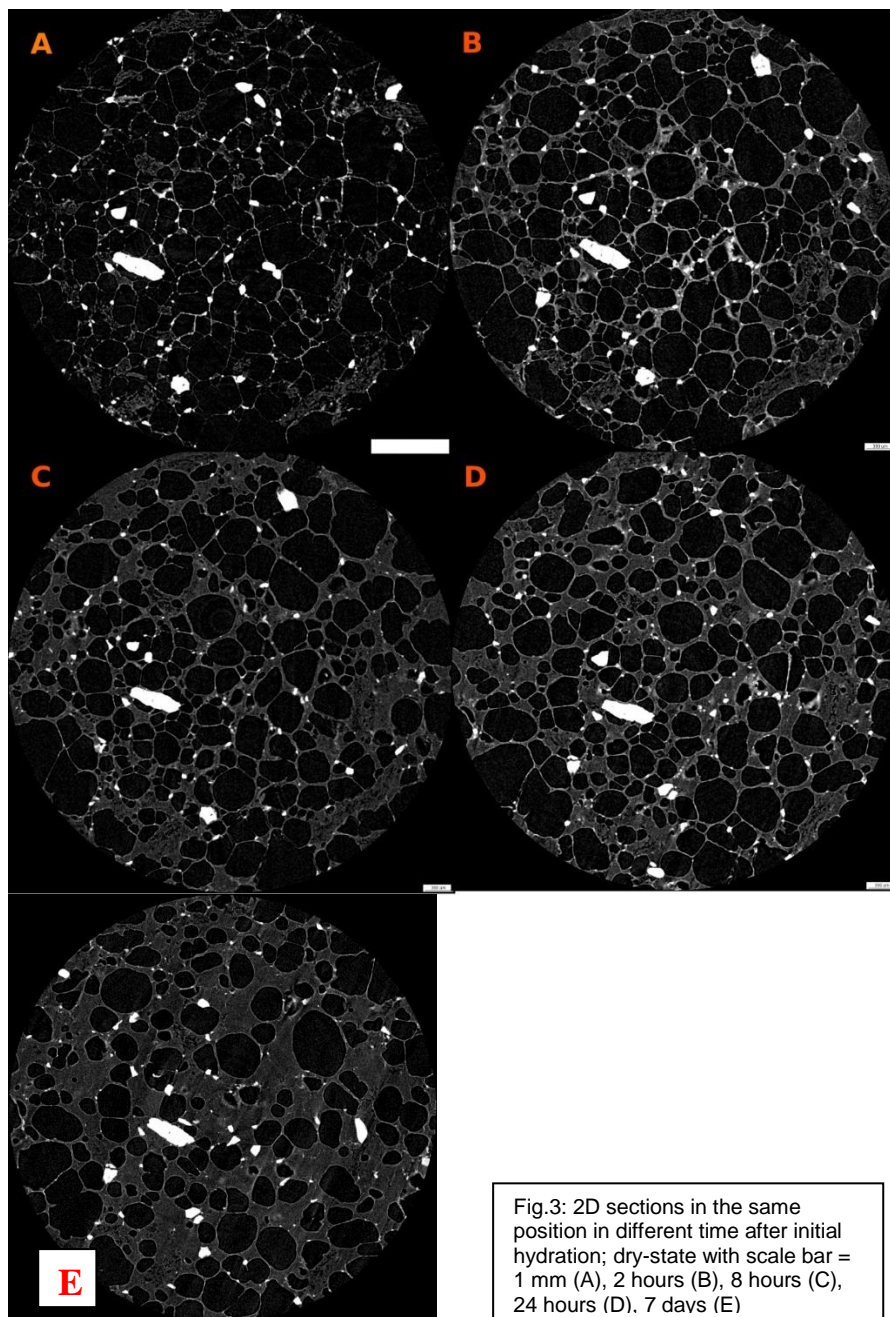


Fig.2: A) 3D visualization of dry-state scaffold (A), color-coded open pore size distribution, scale bar on the right side (B)

Table 1: Basic morphometric parameters in dry-state			
Total VOI volume	TV	98.8	mm ³
Object volume	Obj.V	13.0	mm ³
Percent object volume	Obj.V/TV	13.3	%
Structure model index	SMI	1.24	
Structure thickness	St.Th	27,83	um
Structure separation	St.Sp	174,36	um
Volume of closed pores	Po.V(cl)	0.01	mm ³
Closed porosity (percent)	Po(cl)	0.06	%
Volume of open pore space	Po.V(op)	85.7	mm ³
Open porosity (percent)	Po(op)	86.7	%
Total volume of pore space	Po.V(tot)	85.7	mm ³
Total porosity (percent)	Po(tot)	86.7	%



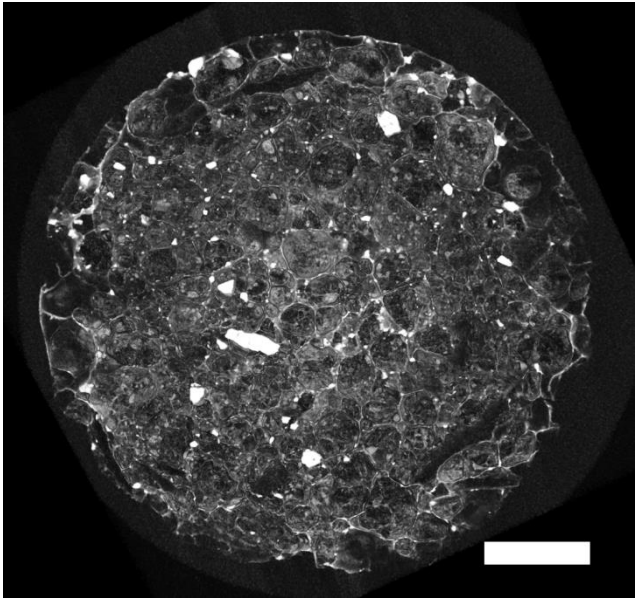


Fig. 4: 3D visualization after 8 hours of hydration, scale bar = 1 mm

Process of hydration of collagen based scaffold revealed unexpected consequence – large amount of air inside pores persisting for the whole time of this pilot study. Instead of analysis of porosity changes, we decided to quantify residual air content prior to further analysis. Air spaces were considered as pores during analysis, while scaffold matrix and hydrated pores were considered as an object.

		0h	2h	8h	24h	7d
Percent object volume	Obj.V/TV	13.3	15.4	29.5	34.4	42.9
Total porosity (percent)	Po(tot)	86.7	84.6	70.5	65.6	57.0

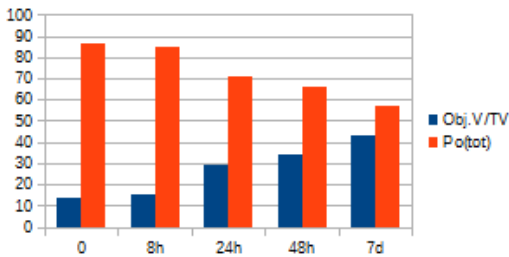


Table 2: Residual air content in scaffold in time

Conclusion

Micro-CT enables to study hydrated scaffold structure with certain limitations. Main issues to overcome are motion artifact and low X-ray density of scaffold immersed in solution. Reducing scanning time and usage of X-ray contrast agent can overcome these. While performing this pilot study, we revealed important air trapping inside scaffold structure. These scaffolds are intended to be used for bone regeneration, so they have to secure adequate micro-environment promoting tissue regeneration. Since the scaffolds will be hydrated after implantation, excessive air content can limit its function. Method of hydration has to be adjusted to secure complete scaffold hydration before implantation.

Acknowledgements

This publication is a result of the project implementation: „Technological development of post-doc programs“, registration number CZ.1.05/41.00/16.0346, supported by Research and Development for Innovations Operational Programme (RDOP) co-financed by European regional development fund and the state budget of the Czech Republic.

This project was supported by Progres Q29 Ministry of Education, Youth and Sports and by Ministry of Health of the Czech Republic, grant nr. 15-25813A.

References:

- Billström G.H. et al., Application of scaffolds for bone regeneration strategies: Current trends and future directions, *Injury, Int. J. Care Injured* 44 (2013) S28–S33.
- Landis E.N., Keane D.T., X-ray microtomography, *Material characterization* 61 (2010) 1305–1316.
- F. Peyrin, Evaluation of bone scaffolds by micro-CT, *Osteoporos Int* (2011) 22:2043–2048.
- Bose S., Roy M., Bandyopadhyay A., Recent advances in bone tissue engineering scaffolds, *Trends Biotechnol.* 2012 October ; 30(10): 546–554. doi:10.1016/j.tibtech.2012.07.005.
- Cleynenbreugel T.V. et al., Micro-CT-based screening of biomechanical and structural properties of bone tissue engineering scaffolds, *Medical and Biological Engineering and Computing*, July 2006, Volume 44, Issue 7, pp 517–525.
- Jones A.C. et al., Assessment of bone ingrowth into porous biomaterials using MICRO-CT, *Biomaterials* 28 (2007) 2491–2504.
- Karageorgiou V., Kaplan D. , Porosity of 3D biomaterial scaffolds and osteogenesis, *Biomaterials* 26 (2005) 5474–5491.
- Offendu et al. Structural determinants of hydration, mechanics and fluid flow in freeze-dried collagen scaffolds., *Acta Biomater.* 2016 Sep 1;41:193-203

X-ray microtomography analysis of porosity in batter systems

A.K.Voong¹, A.B.Norton¹, T.B.Mills¹, I.T.Norton¹

¹Univeristy of Birmingham, Department of Chemical Engineering, Edgbaston, Birmingham, B15 2TT

Aims

Batter is essentially a water and flour mixture with additional ingredients, including leavening agents, salts, gums, protein and seasoning. Structure formation in batter begins when a food product (vegetable, meat, seafood, cheese) is submerged in raw batter and then into hot oil. As the surface temperature of the batter rises, evaporation of moisture occurs causing surface drying, shrinkage and roughness (this can be seen as steam bubbling during frying). The temperature of the surrounding oil will decrease but this is compensated for by convection. Explosive evaporation occurs within the batter due to high temperature and pressure, it is this event that leads to a porous structure; voids are created to allow oil to be absorbed. It has been suggested that oil uptake is largely determined by moisture content in the food.



Fig.1 standard battered and breaded prawn product

In fried battered and breaded foods, the microstructure of the batter determines its mechanical properties, which in turn influences its sensory properties. Crispness is a sensory attribute used to assess the quality and acceptance of a product. Microstructure and porosity of batter is of interest in order to gain an understanding of crispness development. The objective of this work is to investigate porosity and pore size distribution of batter systems.

Method

Sample preparation

Samples were prepared and fried according to standard operating procedure. Following preliminary studies to investigate how breadcrumb size affected porosity, breadcrumbs were separated using a molecular sieve with the following apertures: 4.0mm, 2.8mm, 2.0mm, 1.4mm, 1.0mm, 710 μ m. The largest breadcrumb size (sieved using 4.0mm sieve) was investigated and compared to a standard batter and a batter without additional breadcrumbs. Polypropylene straws were used as sample holders and covered with parafilm to prevent moisture loss.

X-ray microtomography

Upon scanning, images were reconstructed using a global thresholding to obtain binary images, this was then analysed to obtain total porosity and size of pores. Total porosity was determined from the pixel ratio in the 2D image analysis (the void surface within the area of interest). This could then be used to determine voxel ratio (void volume in the volume of interest) for 3D image analysis. Reconstruction of scanned images were then processed using NRecon to obtain cross-sectional images, quantitative analysis was conducted using CTAn.

Table 1. Microtomography parameters for acquisition

Acquisition parameters	Value
Image size (pixel)	2000x1332
Exposure time (ms)	490
Pixel size (μm)	9.60
Rotation step ($^{\circ}$)	0.40
Frame averaging	4

Results

Table.2 Summary of total porosity and pore size distribution

Sample	Total porosity
Standard batter and breadcrumb coating	40.0% \pm 17.9
Control (batter only)	18% \pm 1.9
Batter with large breadcrumb coating (4.0mm)	67.2% \pm 5.1

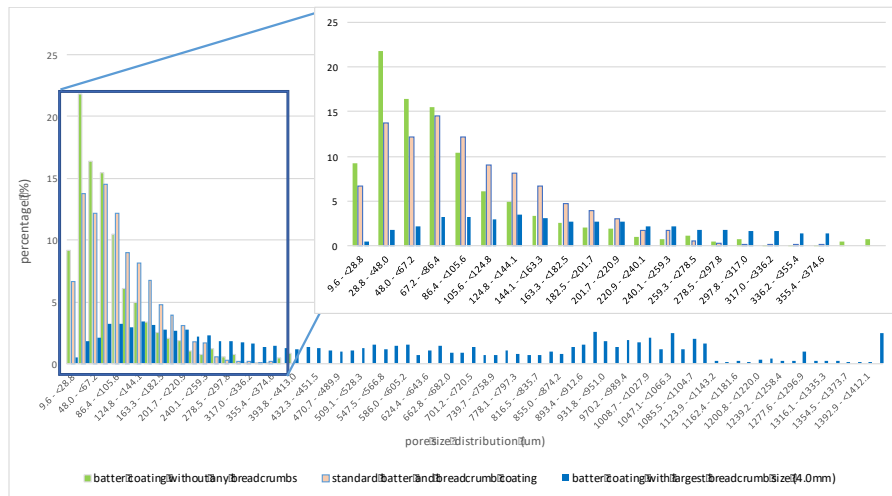


Fig.2 Pore size distribution of batter coatings. Graph zoomed in to for closer view of distribution at smaller size range

X-ray microCT was successfully used to study the size distribution of a standard batter and showed consistent total porosity. Differences in total porosity were noted in samples that were taken.

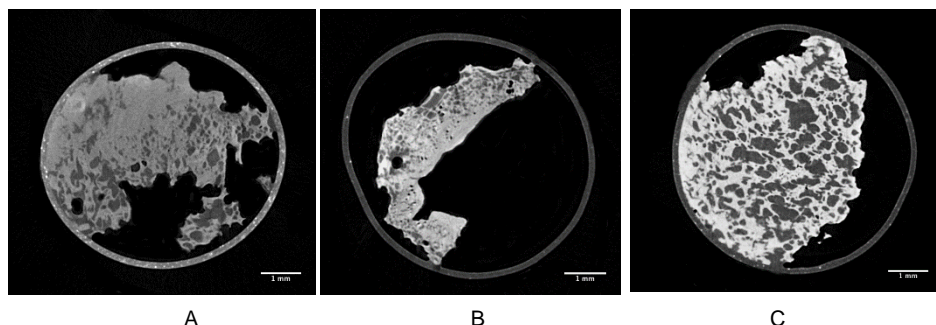


Figure 3. Reconstructed cross-sectional images of A) standard batter and breadcrumb coating B) Batter coating without any breadcrumbs C) Batter coating with largest size breadcrumbs from 4.0mm sieve

As oil penetration occurs where temperature is sufficiently high (crust), there is little oil penetration towards the core hence the microstructure of the crust primarily determines oil uptake. When comparing Fig.3A and B, a porous structure is much more visible towards the top surface of the batter coating, whereas a moist spongy coating is closer to the core, this relates to a softer texture during mastication. As shown in Fig.2 and Fig.3C the addition of coating with large breadcrumbs increases the pore size distribution and porosity, the entire cross-section is porous, suggesting low moisture, a drier surface and a harder texture during mastication.

Conclusion

MicroCT has proven a powerful tool to gain morphological information about batter structure. It is able to give access to the 3D structure, which allows analysis of porosity, pore size distribution and the interconnectivity to describe the structure. Being able to visualise the microstructure and quantify its structural properties, such as porosity, enables further work to relate microstructure to sensory and mechanical properties. Potential future work will continue to use microCT to study how porosity changes with smaller size breadcrumbs and batter formulation.

References:

1. Adediji, A. A. and M. Ngadi "Porosity determination of deep-fat-fried coatings using pycnometer (Fried batter porosity determination by pycnometer)." *International Journal of Food Science & Technology*. 1266-1275. (2011).
2. Adediji, A. A., L. Liu and M. Ngadi "Microstructural evaluation of deep-fat fried chicken nugget batter coating using confocal laser scanning microscopy." *Journal of Food Engineering* 49-57. (2011).
3. Llorca, E., Hernando, I., Pérez-Munuera, I and Fiszman, S. M "Effect of frying on the microstructure of frozen battered squid rings." *European Food Research and Technology* 448-455. (2001).

A X-ray microtomography study on faecal collection devices used for quantitative analysis of haemoglobin in faeces.

L. Chelazzi¹, S. Ciattini¹, S. Rapi², M. Berardi², F. Cellai², A. Ognibene², T. Rubeca³

¹Center of Structural Crystallography (CRIST). University of Florence. Via della Lastruccia 3, 50019 Sesto Fiorentino (Firenze), Italy

²Central Laboratory, Laboratory Department, Careggi Hospital, Florence, Italy

³Cancer Prevention and Research Institute (ISPO), Florence, Italy

Aims

In clinical laboratory setting, the standardization and harmonization of methods and the use of correct metrics parameters and reference units, are crucial to allow the comparison of analytical data and to transfer the data acquired in clinical trials to the single patient management. Many critical points were observed to obtain comparable results from quantitative methods used in faecal samples analysis. The morphological characteristic of the sample collection devices (SCDs) critically affect both pre-analytical and analytical phases of quantitative measurements on faecal tests. In the absence of guidelines or recommendations, manufacturers have developed different sample collection devices and buffers, which make the analytical results dependent on the specific analytical system^{1,2} which, in turn, could make the clinical interpretation difficult to perform. Only theoretic amount, of collected faeces and buffer volume, in sampling collection devices, are provided by manufacturers. These information result in an about twenty-fold difference in faecal concentration (mass/volume) analyzed by different methods^{3,4,5,6}. Our aims was to calculate the sampling region with a lack of precision using μ -Computed Tomography (μ -CT) and compared our results with the analysis of faeces collected, in order to identify the best device shape for a future standardization.

Method

In this study, four SCDs available in Italy for quantitative measurements of haemoglobin in faeces were included: OC-Sensor (Eiken Chemical Co. Ltd, Japan), NS-Plus (Alfred Pharma Co, Japan), HM-JackArc (Kyowa Medex Co., Ltd, Japan) and FOB-GOLD (Sentinel CH SpA, Italy). The volume of that part of the sample collection probe used for the collection of faeces was obtained from the probe diameter and its geometry (Figure 1).

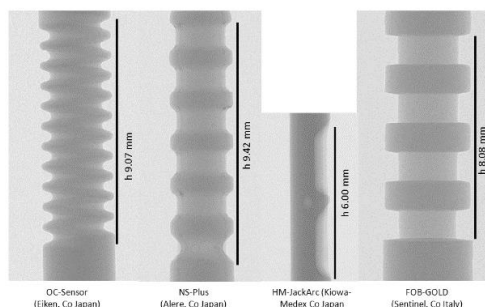


Figure 1: Four sample collection devices analyzed

We collected a μ -Computed Tomography (μ -CT) data set using a Skyscan 1172 high resolution microCT. This system has a sealed, microfocus tungsten X-ray tube with a 5 μm focal spot size. The X-ray were produced by exposing the anode to an electron beam at 71 kV and 122mA. The tip of the probe was cut off to enable it to be placed in a pedestal between the X-ray tube source and the Charge-Coupled Device (CCD) detector. The 2D X-ray images were captured over 180 rotating sample with a slice-to-slice rotation angle of 0.3° , each 2D image represents one slice. The total acquisition time was approximately 15 min. Spatial resolution of the images was kept in a range of $9.6\div 9.9$ micron in terms of pixel size.

The 3D image of the objects internal structure has been reconstructed using modified Feldkamp algorithm⁷ for cone-beam acquisition geometry realized in Nrecon v.1.6.3.10 software (Bruker-MicroCT software). The alignment, beam hardening and ring artifacts corrections were made before starting reconstruction process. CTan software (Bruker-MicroCT software) was used for the image clean up e for the measurements. The standard deviations has been evaluated considering the measured pixel size ($\pm 0.01\mu\text{m}$). In order to determine the Geometric Figure Volume (GFV), for each devices, was calculated the volume of a cylinder that inscribes the probe (Figure 2).



Figure 2: Geometric Figure Volume (GFV) obtained calculating the volume of the cylinder that inscribes the probe.

The volume of the part of the sample collection probe used for the collection of faeces, called Volume Of Interest (VOI), was calculated subtracting the probe volume (PV) evaluated from μ -CT reconstruction, to the GFV.

The collection and analysis of faeces were performed in the Laboratory of Careggi Hospital and reported here for comparison.

Results

In table 1 are reported data on: volumes obtained for the geometric figure and the sampling region through geometric estimation; amount of faeces recovered (mean and sd), in and out of the VOI (materials collected on the top of the dipsticks); amount of material collected in the sampling volumes (Recovery); the ratio between recovered materials and sampling volumes (mg/mm³); the amount of faeces targeted by manufacturer and the ratio (%) between collected and targeted amount of faeces for tested SCDs. Ratio between VOI and collected materials range from 100÷130%. Coefficient of variations obtained for tested SCDs in recovery tests ranges between 9.7÷13.3 for OC-Sensor; 11.7÷ 30.4 for NS-Plus; 14.4÷31.1 for FOB Gold and 8.6÷21.3 for HM-JackArc. Ratio between the mean collected material and the VOI results 99% for OC-Sensor; 100% for NSPlus and 129% for both HM-JackArc FOB-Gold SCDs.

	GFV*	PV**	VOI***	Collected	out VOI	Recovered	Target	C/T
	mm ³	mm ³	mm ³	mg	mg	mg/mm ³	mg	%
OC-Sensor	32.64	24.42	8.22	8.3±0.97	0.43±0.17	0.99	10	83.5
NS-Plus	31.89	24.48	7.10	7.08±1.48	0.62±0.36	1.0	10	70.8
HM-JackArc	18.24	15.16	3.08	2.38±0.35	0.28±0.21	1.29	2	119
FOB-Gold	32.3	22.86	9.44	8.36±1.93	0.53±0.29	1.13	10	83.6

* Geometric Figure Volume

** Probe Volume

*** Volume of Interest

Table 1: Volumes estimated by geometric calculation of commercial sample collection devices. Amount of faeces recovered (mean and SD), in (Collected mg) and out of the VOI (out of VOI mg) (out of the VOI were considered the materials collected on the top of the dipsticks); Ratio between Collected materials VOI (mg/mm³); Target declared by manufacturers (Target mg) and ratio in percentage between the target and the collected sample (C/T%).

As reported in table 1 the texture of samples affect the overall amounts of collected material and different amounts of faeces gives to different analytical results that may result in different clinical recommendations

Conclusion

The harmonization of faecal sampling could be obtained using devices that are similar in design and volumes of faeces collected. Considering the ratios, between the mean amount of faeces collected and the sampling volumes (Recovered in table 1) obtained, it seems that no specific attention was paid by manufacturers to address correctly the amount of collected materials. Our results could be considered as a providing support for the thesis that manufacturers should design their devices in order to collect the same mass of materials.

References:

- 1 Allison JE, Fraser CG, Halloran SP, Young GP. Comparing fecal immunochemical tests: improved standardization is needed. *Gastroenterol.*;142:422-424, 2012
- 2 Fraser CG, Allison JE, Young GP, Halloran SP, Seaman H. A standard for Faecal Immunochemical Tests for haemoglobin evaluation reporting (FITTER). *Ann Clin Biochem.*;51:301-302, 2014.
- 3 Carroll MRR, Piggott C, Pearson S, Halloran SP. Evaluation of quantitative faecal immunochemical tests for haemoglobin. *Guildford Medical Device Evaluation Centre (GMEC)*,

Guildford, UK, 2013. <http://www.worldendo.org/about-us/committees/colorectal-cancerscreening/ccs-testpage2-level4/fit-for-screening/fit-publications/>. Last access May, 10, 2016.

4 Guittet L, Elodie Guillaume E, Levillain R, et al. Analytical comparison of three quantitative immunochemical fecal occult blood tests for colorectal cancer screening. *Cancer Epidemiol Biomarkers Prev.* 20:1492-1501, 2011

5 Rubeca T, Cellai F, Confortini M, Fraser CG, Rapi S. Impact of preanalytical factors on fecal immunochemical tests: need for new strategies in comparison of methods. *Int J Biol Markers.* 30:269-274, 2015.

6 Rapi S, Fraser,CG, Cellai F, Berardi M, Rubeca T. Valutazioni preliminari per la proposta di un unico dispositivo di campionamento per la ricerca dell'emoglobina su materiale fecale. *Biochimica Clinica.* 39:559-562, 2015.

7 Feldkamp L.A., Davis L.C., Kress J.W. Practical cone-beam algorithm. *J Opt Soc Am.* A1:612-619, 1984.

Structural analysis of collagen scaffolds using X-ray microCT and effect on permeability

L.Mohee¹, A. Husmann¹, S.M. Best¹, R.E. Cameron¹

¹University of Cambridge, 27 Charles Babbage Rd, Cambridge CB3 0FS

Aims

Collagen scaffolds and polyurethane (PU) foams are porous structures that have applications in medicine, particularly employed as dressings for wound repair. In this work, we characterise and analyse the structural parameters of these materials and relate them to their permeability.

Method

Collagen scaffolds with two types of architecture (isotropic and aligned) were produced using freeze-drying methods¹ and a company called KCI supplied the PU foams.

The samples were characterised by X-ray microtomography (Micro-CT), scanning electron microscope (SEM) and confocal microscopy. The structures were analysed (average pore size, porosity and percolation² diameters) using software ImageJ and CTAnalyser. Aligned structures were studied in the direction of the aligned pores.

Permeability values were obtained by using a constant pressure set-up with a regime of 100 Pa and 1200 Pa. Fluid flow was in the direction of alignment in anisotropic structures.

Results

The porous materials are shown as 3D models in Figs. 1-3. The scale is the same for all three figures (1 mm cube).

Materials	Collagen scaffolds		PU foam
Structure	Isotropic	Aligned	Reticulated open-cell network
Avg. pore size (µm)	120	187	781
Porosity (%)	96	96	97
Percolation diameter (µm)	71	139	670
Permeability (m²)	4.6×10^{-12}	1.4×10^{-10}	6.5×10^{-9}

Table 1: Comparing collagen scaffolds and PU foam

Table 1 shows that the PU foam, Fig. 1, has an average pore size of 780 µm which is bigger than the collagen scaffolds. The aligned structure, Fig. 2, has a bigger pore size than the isotropic one, Fig. 3. All three have similar porosities. Since percolation diameter is dependent on average pore size, it is expected that the PU foam has the highest value followed by the aligned and the isotropic scaffolds. Consequently, the permeability values were highest for the foam by 1-3 orders of magnitude.

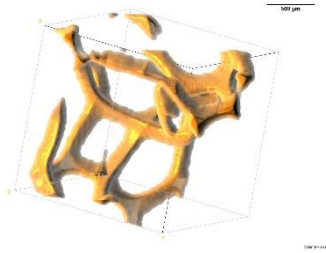


Fig. 1: PU foam

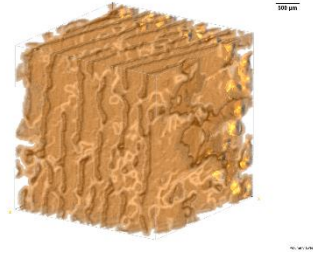


Fig. 2: Aligned scaffold

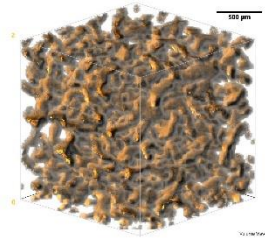


Fig. 3: Isotropic scaffold

Conclusion

Micro-CT analysis has been very useful to understand the structural parameters in terms of average pore size, porosity and percolation diameter of both the collagen scaffolds and the PU foam. Combining this study with the permeability experiments enabled to understand the fluid dynamics in these porous structures. It was found that the alignment of the pores influenced the fluid flow value. The next stage will be to investigate how these structures deform under compressed state and the consequent effect on their permeability.

References:

1. Pawelec KM et al. Appli. Phys. Rev. 1:0-13, 2014.
2. Ashworth JC et al. Mater. Tech.-Adv. Perf. Mat. 29:281-295, 2014.

Micro-CT visualization of absorbable suture material degradation

Spanko M.¹, Bartos M.¹

¹ Department of Stomatology, First Faculty of Medicine, Charles University and General University Hospital in Prague

Aims

Sutures have been used for many centuries. The synthetic absorbable polymer – polyglycolic acid – was developed in 1970s. These are the goals of wound closure: obliteration of dead space, even distribution of tension along deep suture lines and maintenance of tensile strength across the wound until tissue tensile strength is adequate. An absorbable material is a commonly used in orofacial surgery. This type of suture is preferred by some physicians because it saves their time and decreases patient's anxiety and discomfort. There are specific requirements on physical characteristics and properties, e.g. good tensile strength, dimensional stability, lack of memory, knot security, and sufficient flexibility to avoid damage to the oral mucosa. We wondered what the material looks like in a microscopic scale. Our curiosity was focused on its structural changes in a simulated oral environment. We decided to perform a short-time pilot experiment that would help answer our questions. The material disintegration was monitored for five weeks using Skyscan 1272 micro-CT.

Method

A specimen of the absorbable suture material (polyglycolic acid) was stored in a small plastic test tube filled with saline infusion. Only a short length of material was needed (ca. 3mm) to perform high resolution scans. These were made in one-week interval using parameters mentioned below.

- Micro-CT type: Bruker Skyscan 1272 (equipped with 16Mpx CCD camera)
- Scanning resolution: 4928 x 3264 px.
- Pixel size: 1µm
- Rotation step: 0,100
- Rotation: 180 degrees
- Averaging: 3

The data reconstruction was performed with an appropriate application of "Fine tuning" options (Misalignment compensation, Ring artifacts reduction, Beam-hardening correction) and with a careful histogram adjustment.

Afterwards, an analysis in CTAn program was done. Firstly, a suitable region of interest (ROI) was chosen. Then, a custom processing algorithm was designed. This appeared to be the most difficult part of the whole process. We wanted to eliminate the image noise as much as possible. On the other hand, the relevant image data had to be preserved.

The custom processing scheme included these steps:

- Filtering (conditional mean, round, radius 2, threshold 30)
- Threshold (global, *values varied*)

- Despeckle (white spots less than 4px, 2D)
- 3D analysis (basic + advanced + structure thickness-coded images)
- Save bitmaps

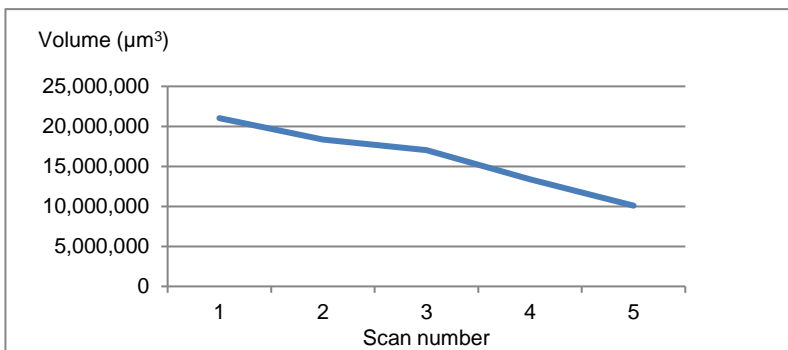
The next step was a visualization (CTvox). The histogram of structure thickness-coded images had to be stretched. This helped to set the colour curves correctly. Eventually, the analysis results were put into diagrams.

Results

We were able to watch the material structure and its disintegration in great detail. The diagrams and CTvox pictures represent our findings.

		#1	#2	#3	#4	#5
Total VOI volume	mm ³	0,121	0,121	0,121	0,121	0,121
Object volume	mm ³	0,021	0,018	0,017	0,013	0,010
Percent object volume	%	17,324	15,106	14,047	11,032	8,314

Table 1: Object volume changes



Plot 1: Object volume

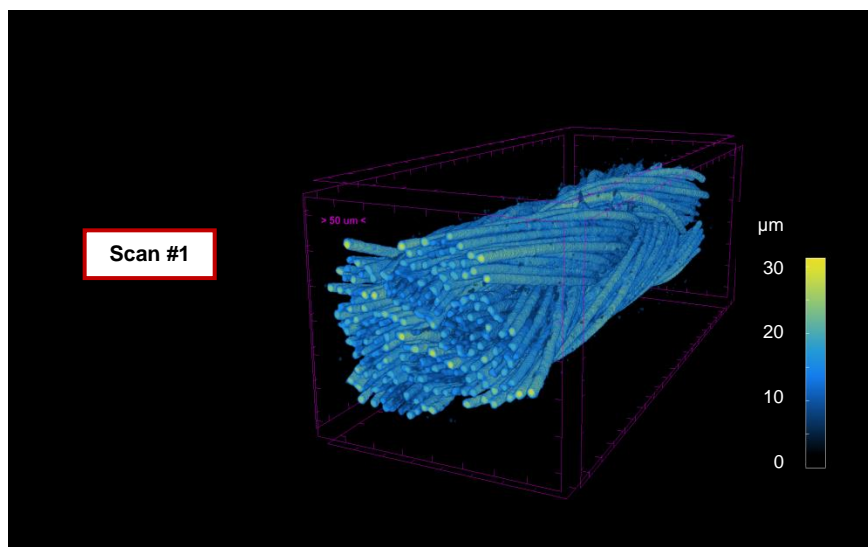
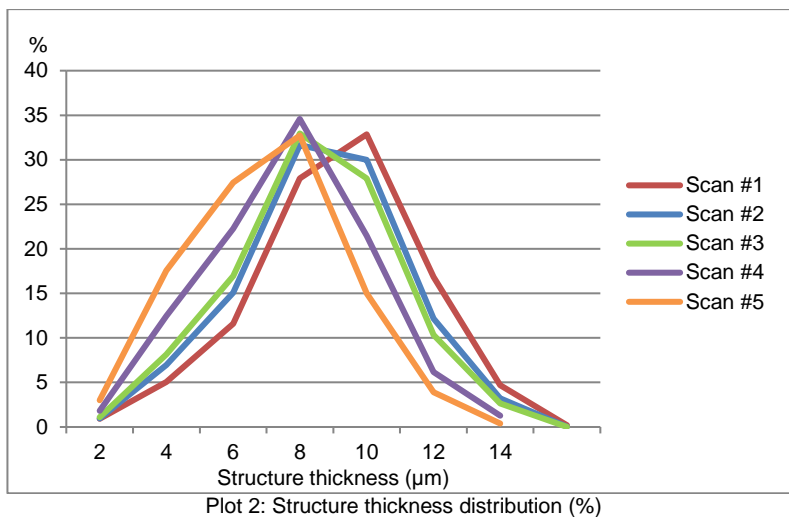


Fig.1: Material visualization in CTvox

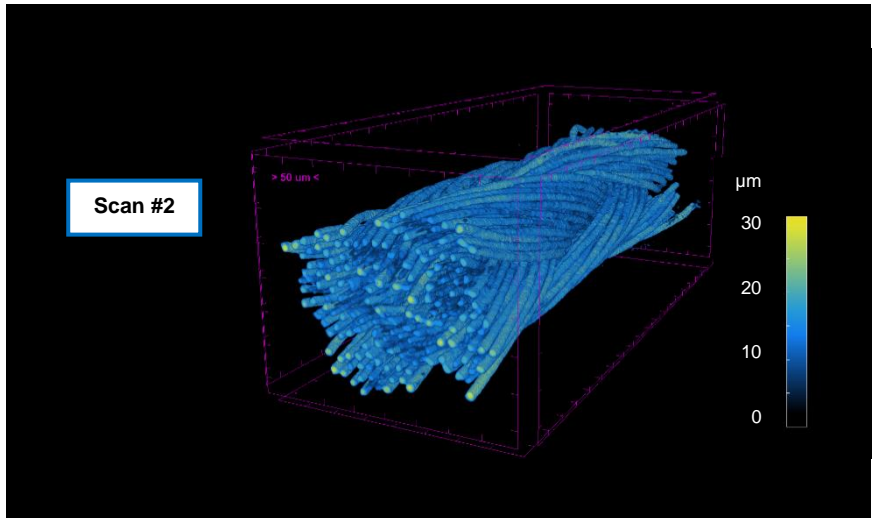


Fig. 2: Material visualization in CTvox

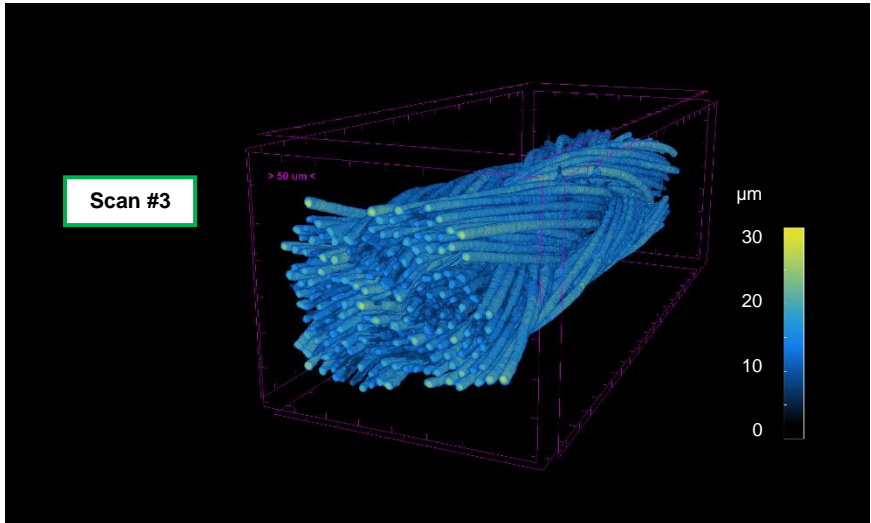


Fig. 3: Material visualization in CTvox

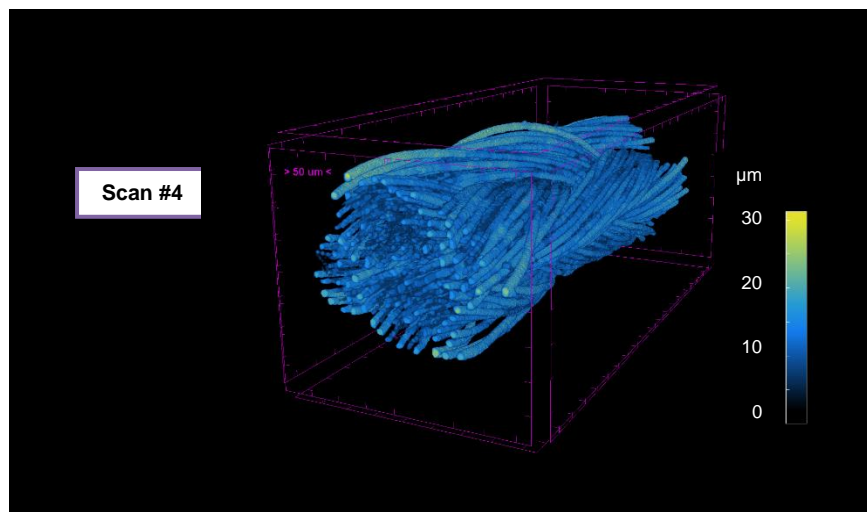


Fig. 4: Material visualization in CTvox

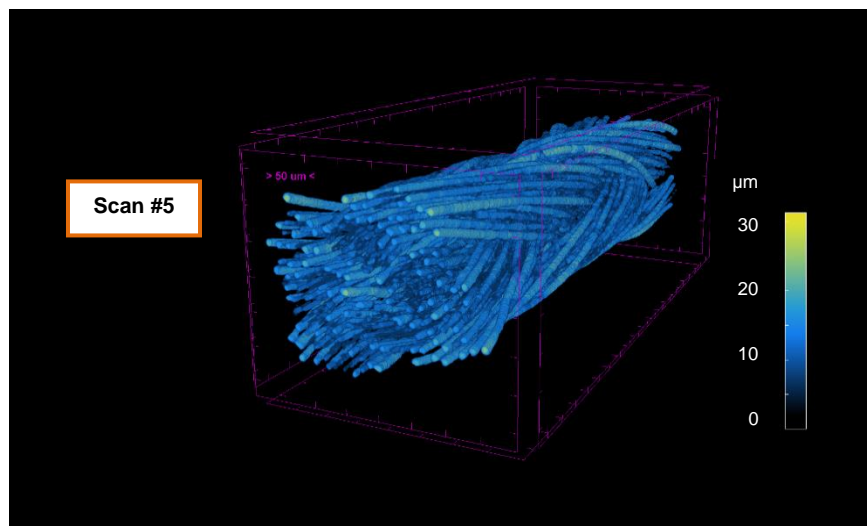


Fig. 5: Material visualization in CTvox

Conclusion

The aim of our pilot experiment was a visualization and analysis of absorbable suture material disintegration. A lot of effort was put into the procedures in CTAn software. We wanted to eliminate noise and various artifacts, yet preserving the highest possible amount of "real" image data. There is a great challenge that must be faced. A lot of parameters require a manual adjustment. Thus, even a small mistake in the data-processing can make the results inaccurate.

Acknowledgements:

This publication is a result of the project implementation: „Technological development of post-doc programs“, registration number CZ.1.05/41.00/16.0346, supported by Research and Development for Innovations Operational Programme (RDIOP) co-financed by European regional development fund and the state budget of the Czech Republic.

References:

1. S. C. Pillai CK, Review Paper: Absorbable Polymeric Surgical Sutures: Chemistry, Production, Properties, Biodegradability, and Performance, Biomater Appl., 2010
2. M. G. Joseph Parell a M. Gary D. Becker, Comparison of Absorbable With Nonabsorbable Sutures in Closure of Facial Skin Wounds, Arch Facial Plast Surg., 2003
3. Vasanthan A, Comparing suture strengths for clinical applications: a novel in vitro study., J Periodontol., 2009
4. Salmon. P., Bruker microCT method note: Color-coded structure thickness in CTVox, Bruker, 2013

Quartz: reconstruction of nature crystallogenic processes

N. N. Piskunova¹, L.Y. Kruychkova², N. V. Sokerina¹

¹Institute of Geology Komi SC UB of RAS, 54, Pervomaiskaya str., 167982, Syktyvkar, Russia,

²Saint-Petersburg State University, Per. Decembristov, 16, St. Petersburg, 199155

Aims

The study of fluid inclusions in crystals, the main method of thermobarogeochemistry, for a long time was the main way for obtaining the data about the natural mineral-forming environment. With the advent of new high-resolution non-destructive methods, it became clear that not only the solution from the inclusion, but also the data on the shape of the inclusions in the crystal volume, their orientation, and the nanorelief of the inclusion walls, can carry information about the processes that once occurred. Reconstruction of the crystallogenic processes that have taken place, beginning with a certain intermediate stage of crystal growth, is the main aim of this work.

Method

To study the nanorelief of the inclusions walls, the Ntegra Prima atomic-force microscope (NT-MDT, Russia) and standard silicon cantilevers with a tip radius of 5 nm were used.

To characterize the distribution of inclusions in the volume of the crystal and to calculate the square of their inner surface, the X-ray microtomograph Skyscan Bruker1172 was used.

Results

With the help of AFM, it was shown that the crystal (Zhelannoe depozit, Subpolar Ural, Russia), after the formation of some fluid inclusions, was first subjected to higher temperatures and pressures, and then to slow cooling during a long period of time, as evidenced by the form of dislocation hills and specificity of deposition of matter on the inclusion surface.

High-resolution images of dislocation channel outputs were obtained. Due to *in-situ* AFM experiments it became possible to establish that the accumulations of the dislocation channels are one of the main reasons for the appearance of these inclusions themselves. Also, numerous flattened top hills were found on the inner walls (Figure 1). We have shown that these hills are classical dislocation growth hills, which grow according to a well-known Frank mechanism. A mathematical analysis and comparison of profile sections of these hillocks with hillocks of growth and dissolution from model crystals *in-situ* AFM experiments were carried out, proving that the internal surfaces of the cavity of inclusions of quartz are growth surfaces. Previously, the hypothesis about the fluid substance depositing on the inclusion walls during slow crystal cooling was possible to verify only by indirect methods.

Having microtomographic data about the volume and square of the inner surface of the inclusion, accurate calculations of the volume of matter deposited on the mounds, as well as the most detailed AFM scanning of the entire surface of the open inclusions (volume of matter in the hill on graph, Figure 1) we can obtain silica in the solution at the moment of capture of the inclusion.

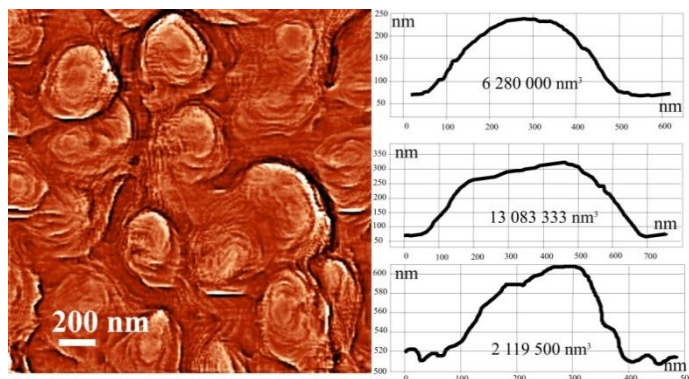


Figure 1: AFM-data: dislocation hills on the inner surface of the inclusion in quartz, their profile cuts and volume of precipitated matter.

Thus, in a plate cut from the middle of the crystal for study on a microtomograph, there were 312 fluid inclusions, from small ones volumed 25 mkm^3 to large ones volumed more than $95,000 \text{ }\mu\text{m}^3$ (Figure 2). Their surface square was from 50 to 9050 mkm^2 . We obtained a concentration of SiO_2 in the mother solution equal to 4.8 g/l. This is still a rough estimate, and, currently, the work to detail the use of nanotomography (SkyScan 2011) "ceiling" and the "bottom" of inclusions and the resolution of dislocation channels coming out of them is being underway.

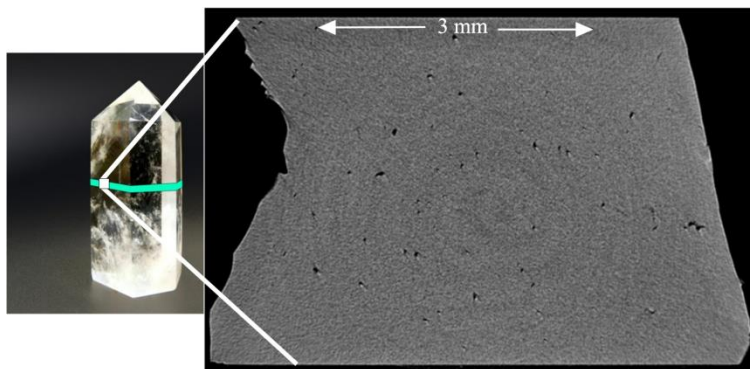


Figure 2: Microtomographic image of fluid inclusions (quartz crystal, Zhelannoe deposit, Subpolar Ural, Russia).

Conclusion

The combination of methods of microtomography with *in situ*-study of model crystals and *ex situ*-scanning of natural crystals makes it possible to carry out a partial reconstruction of natural crystallogenes processes. With the use of these methods, the concentration of silica in the mother solution at the time of capture of inclusions was estimated for the first time.

3D Images Assessment; What Could be done Without X Ray Microtomography

A.C. Moreira¹, L.R. Medeiros¹, C.P. Fernandes¹, M.V. Oliveira², I.F. Mantovani¹, K.K. Mattila³

¹Universidade Federal de Santa Catarina-LMPT/EMC, Florianópolis-Brazil,

²Instituto Nacional de Tecnologia, Laboratório de Tecnologia de Pós, Rio de Janeiro-Brazil.

³University of Jyväskylä, Jyväskylä-Finland

Aims

Currently, X Ray Microtomography (micro-CT) is a well known and widely used technique by researchers around the world. It has being an important tool with applications in several areas, from engineering to biology, from paleontology to petroleum research and so on. Micro-CT has supported researchers making possible to reach a high level of understanding of materials. However, the reality of image analysis a few years ago was completely different. With micro-CT quite restricted to medical devices, researchers had to be mostly satisfied with 2D image analysis.

So, what could be done without micro-CT for a 3D image assessment? Was that possible? This work intends to show that the answer is partly yes. For specific sorts of porous media a modeling technique based on 2D information is able to generate a 3D image. This “3D model” presents microstructural features very similar to those from the “real” porous structure. The main aim of this work is to compare microstructural characterization of 3D models with 3D images acquired with X Ray Microtomography and show that modeling techniques are still important in research of porous media like reservoir rocks.

Method

The method is called *Truncated Gaussian Modeling Method*. The model is generated based on statistics data determined from 2D images. Further details about the method can be found in literature^{1,2,3,4}. It is applicable for structures who present good degree of spatial organization, i.e. when the porous media is statistically homogeneous and isotropic, such as some kind of reservoir rocks, ceramic filters and sintered foams, for instance.

The samples analyzed are sintered titanium biomaterials. Also called as Titanium Scaffolds, this sort of sample is used as coatings for fixation of dental and orthopaedic implants (Figure 1).

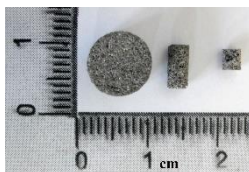


Figure 1. Titanium scaffold samples.

Four cylindrical samples (called as Ti-A to Ti-D), with different sizes, were analyzed with a Bruker-Skyscan 1172. Its 2D slices were used to apply the modeling method. This method could be applied to 2D slices from different acquisition sources, such as SEM and Optical Microscopy. However, for comparison purposes, the models were generated from 2D micro-CT images.

Porosity, pore size distribution and permeability data were determined from 3D images and 3D models in order to compare and evaluate the performance of the method. CTAn and Imago Software, as well Lattice Boltzmann⁵ simulations were used on data determinations.

Results

Regions of interest were randomly chosen and 2D micro-CT images were then cropped. The ROI's were turned into binary images and the method was applied for each sample. Cropped 2D binary images can be seen in Figure 2, as well 2D slices taken from the 3D models.

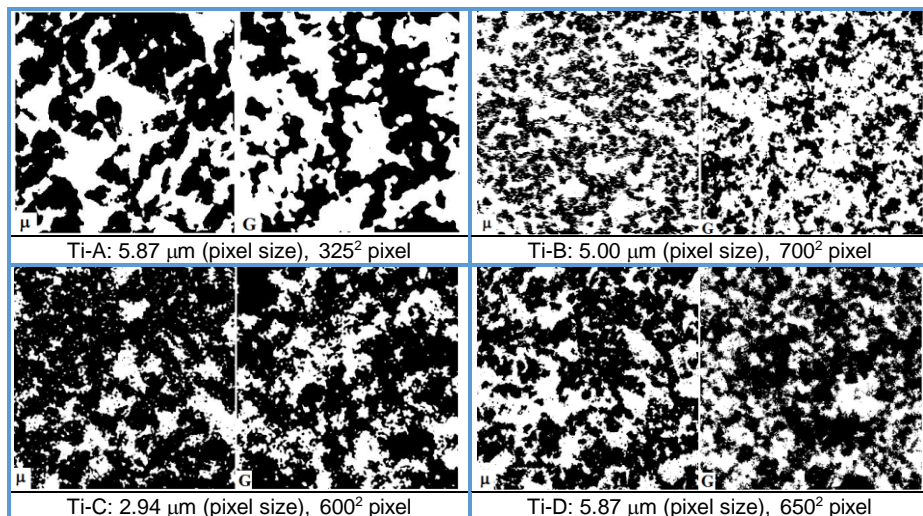


Figure 2. Binary 2D slices taken from Micro-CT (μ) images and Gaussian (G) models.

With pore phase in white and material in black, the similarity of images between Micro-CT (μ) and Gaussian Model (G) is remarkable.

The same level of similarity between micro-CT and model images is also reached in 3D, as can be seen in Figure 3. Besides visual similarity, the main intention of the Gaussian method is to reproduce a 3D model faithful to that one represented by a single 2D image, with similar physical parameters. Table 1 summarizes values of porosity and permeability determined for each set.

Sample	Porosity (%)		Permeability (10^{-11} m^2)	
	Micro-CT	Gaussian Model	Micro-CT	Gaussian Model
Ti-A	51.64	51.78	11.25	11.49
Ti-B	58.93	58.97	12.12	9.59
Ti-C	29.07	28.96	0.18	0.17
Ti-D	44.02	44.11	4.48	2.58

Table 1. Porosity and Permeability data.

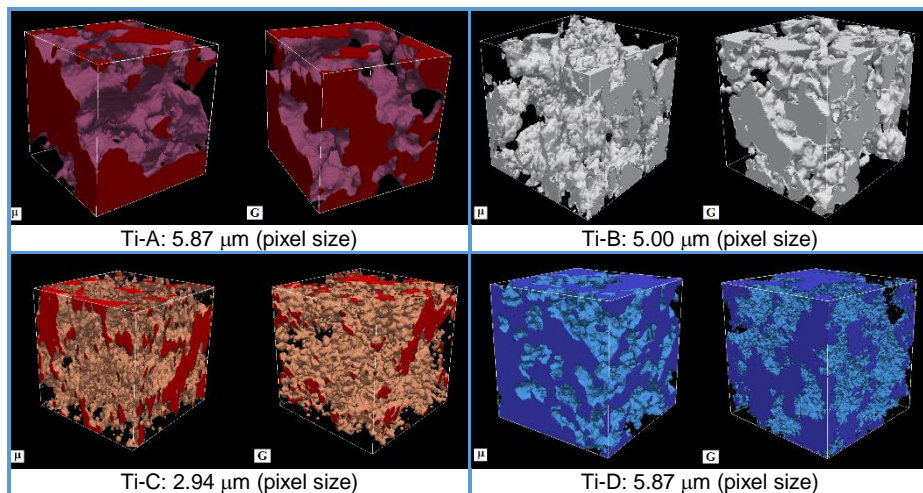


Figure 3. 3D (μ) microtomography images and (G) models (small volumes for visualization about 100^3 voxel)

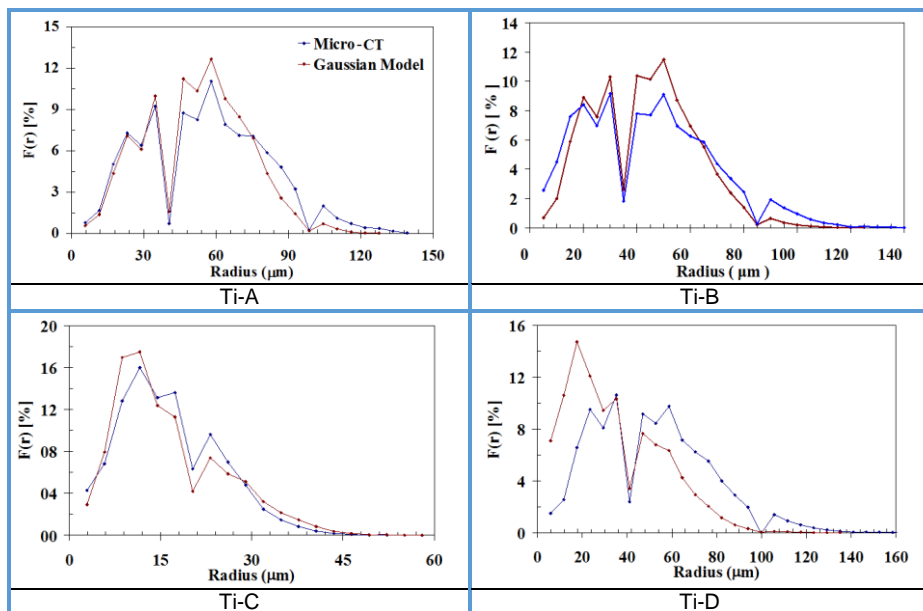


Figure 4. Comparison of the pore size distributions of the samples.

Gaussian models present porosity and permeability values quite similar from those of 3D micro-CT images. The most impressive capability of the model is to reproduce, besides porosity, pores with sizes quite similar to original. The size of pores were determined as

graphics of pore size distribution (Figure 4). These graphics gives the information of the pore sizes [radius (μm)] per occurrence frequency $[F(r)]$.

The behavior of the pore size distribution curves are quite similar for each sample, presenting equivalent trends. Even the most prominent peaks from both curves are the same and the valleys as well.

Even considering the good results obtained with 3D models in comparison from those of micro-CT images, the modeling method is highly restricted. It is just useful when the object of study is a "well behaved" porous structure. Nevertheless, this application can be very suitable in specific cases such as multi-scale analysis of reservoir rocks. It can be also convenient on research of microstructures, when a scale below that one reached by a micro-CT scanner is required. Nano-CT is a contemporaneous technique available for use, but it is still not so reachable for the most of the researchers. In these cases, Gaussian modeling process can be an alternative to estimate 3D physical parameters based on 2D image analisys.

Conclusion

The Gaussian modeling process can be applied to a single 2D image in order to generate a 3D model of a pore structure. The method just can be applied for structures statistically homogeneous and isotropic. Even though, the technique is very restricted to specific sorts of porous media, it is able to generate 3D models very faithful to the real microstructure.

Modeling process is still important currently when scale issues are concerned. When a nano-CT device is not available, a 3D assessment of a microstructure is still possible to be reached supported by modeling process.

References:

1. Joshi M.Y., in: A class of stochastic models for porous media., PhD thesis, University of Kansas, Lawrence, USA, 1974.
2. Quiblier J.A., A new three-dimensional modeling technique for studying porous media, J. Colloid Interface Science, v. 98, p. 84-102, 1984.
3. Ioannidis M.A., Kwiecien M., Chatzis I. Computer Generation and Application of 3D Model Porous Media: From Pore-Level Geostatistics to the Estimation of Formation Factor, Paper SPE 30201 presented at the Petroleum Computer Conference, Houston, TX, 1995.
4. Liang Z.R., Fernandes C.P., Magnani F.S., Philippi P.C. A Reconstruction Technique of 3D Porous Media by using Image Analysis and Using Fourier Transform, Journal of Petroleum Science and Engineering, v. 21, n. 3-4, p. 273-283, 1998.
5. Cancelliere A, Chang C. Foti E. Rothman D. and Succi, S. The permeability of a random medium: Comparison of simulation with theory, Physics of Fluids, 12, 2085, 1990.

Determination of volume colonisable by cells on β -tricalcium phosphate biomaterial for bone regeneration

M. Oger¹, L. Bégot¹, X. Holy¹ and A.L. Favier¹.

¹Institut de Recherche Biomédical des Armées (IRBA), Division Expertise et Ingénierie, Département des Services, Unité Imagerie. Centre Médecin Major Ernest Duchesne, 1 place du Général Valérie André, 91220 Brétigny sur Orge, France.

Aims

In the context of French military injuries by bullet or antipersonnel land mine, cellular proliferation on industrial TriCalcium Phosphate (TCP) biomaterials can be a useful solution to repair critical size bone defects. TCP biomaterial had proven efficacy in numerous clinical applications (1, 2). Moreover, the triple combination of scaffold, mesenchymal stem cells (MSCs) and growth factors enhances the potential of large bone defect regeneration (3). Evaluation of MSCs volume colonisation around and inside the biomaterial is very important for its biodegradation and then bone regeneration efficiency. This cellular colonisation is directly dependent on the external and internal specific porosity of the TCP (4). In this context, we have evaluated colonisable cellular volume of one structural type of these biomaterials supplied by CERAVER's industry, named Calciresorb bone like[®].

Method

The β -TCP biomaterial, 4 mm square in size was scanned with an 1174 microtomograph from Brucker (Figure 1).

The acquisition conditions were the following: Al filter = 0.5 mm; image pixel size = 9.79 μ m; voltage = 50 Kv; rotation step = 0.3°; partial width = 63%; frame averaging = 5; sharpening = 40%.

The reconstruction conditions were: smoothing = 2; smoothing Kernel = 2 (Gaussian); object bigger than FOV = ON; Ring artifact correction = 20; beam hardening correction = 20%; Min/Max CS image correction = 0.0186/0.199.



Figure 1.
Biomaterial from Ceraver,
Calciresorb bone like[®]

Image analyses were performed with both CTAn and Fiji softwares and all presentations in 3D were obtained with CTvox program.

To obtain the total colonisable cellular volume, several volumes must be quantified:

- + the volume of the biomaterial (BM),
- + the volume of internal structures that can be dissociated in 2 types of pores:
 - closed pores (CP) cannot communicate with the external part of the biomaterial and then cannot be colonised by cells.
 - opened pores (OP) communicate with the external part of the biomaterial, and then can be colonised by cells.

- + The external cellular volume (EC) included between the external surface of the biomaterial and an external wrap (WR) delimiting the total 3D volume of interest (ie 100%).

To improve the 3D imaging, the "Surface Lighting" (= texture option) was used in CTVox. As with this option, only one set of images can be used, we generated 2 different "multi-image sets" in order to visualise them in one time. These 2 sets consisting in the repartition of 3 different compressed set of images dividing in 3 the 256 levels of greys. From each "multi-image set", it was possible to apply the texture option using CTVox program.

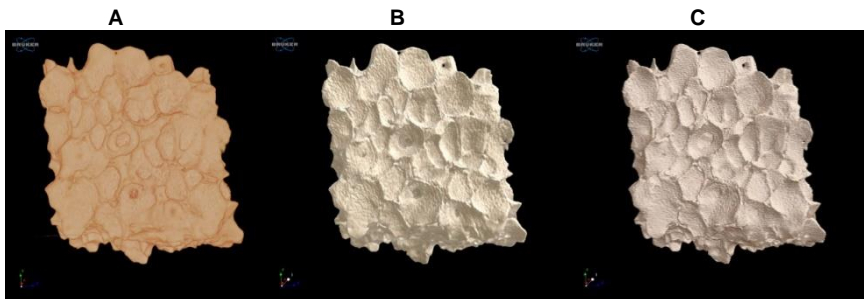
Results

The scanning, reconstruction (NRecon) and generation of digital masks (via CTAn and Fiji) of the biomaterial data image set had allowed the conception of 2 "multi-image" sets for 3D display.

The CTVox software was used with the texture option offering a real improvement of the fine details and a better depth of field (Figure 2 A-B). These sets of "multi-image" have been generated in order to apply this option with CTVox (Figure 2 B-C).

Figure 2. Different representations of Calcioreorb bone like[®] biomaterial obtained with CTVox.

- A) image without texture option applied on a standard set of images (biomaterial).
- B) image with texture option applied on the multi image set 1 (biomaterial + closed pores + opened pores)
- C) image with texture option applied to the multi image set 2 (biomaterial + biomaterial surface + wrap)



Application of the texture option had permit to highlight the complex details of the biomaterial surface relief. Nevertheless, the composition itself of a multi image set repartition seems to be interpreted differently by CTVox, generating visual variations.

Using the digital masks, the Calsiresorb bone like[®] biomaterial can be decomposed into 3 distinct elements by image processing (Figure 3 A-D): two types of pores (CP and OP), located inside the biomaterial and the biomaterial structure itself. CP have for the most part spherical geometry whereas OP can be either spherical or take more complex geometric shape.

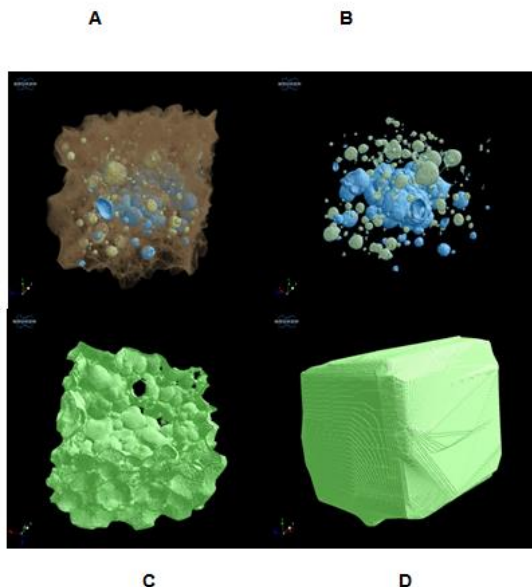
To determine the total volume colonisable by cells, a wrap volume was generated all over the external biomaterial surface from all the concave extremities.

The volume of each compartment is presented in percentage for a better understanding.

The volume of the hard structure of the biomaterial represents 57.86% of WR, the closed pore volume only 1.61%, the open pore volume 5.60% and the external fraction 34.93%. Therefore, the total volume colonisable by cells on and in the biomaterial represents 40.53% of the total 3D structures (Figure 3 E).

Figure 3. The various compartments of the Calsiresorb bone like[®] biomaterial calculated from CTAn and Fiji softwares.

- A) Presence of substructures (Closed pores and Opened pores) revealed by the transparency of the biomaterial.
- B) Isolated Closed pores (CP in grey) and Opened pores (OP in blue).
- C) Superficial surface of the biomaterial.
- D) wrapped biomaterial.



Volume of several compartments :
(in %)

Wrap	WR	100
Biomaterial	BM	57.86
Opened pores	OP	5.60
Closed pores	CP	1.61
External fraction (WR-[BM+OP+CP])	EF	34.93
Cellular colonisable (OP+EC)	CC	40.53

Conclusion

To analyse complex structures like biomaterial containing different types of pores, the generation of several data sets of images is essential. The optimization of the “texture function” in CTVOx by generating 2 “multi image sets” had improved the 3D view of the different compartment volumes inside and outside the biomaterial.

Therefore, by microtomography and image analysis, the volume of these several scaffold compartments was measured, allowing obtaining the total volume colonisable by cells on and in the biomaterial (i.e. the BM porosity available). This information is very important to found the best compromise between biomaterial and cell volume ratio to obtain an optimal biodegradable phase in the complex bone defect regeneration process.

With the emergence of three-dimensional (3D) printing, new promising opportunities are coming up in the field of bone reconstructive, with the advantage to generate patient-specific geometries from medical images fitting perfectly to the bone defect (5). Moreover, this type of structures have demonstrated the ability to serve as bone substitute scaffolds as cellular differentiation and resorption activity have been already demonstrated (6,7). Analysis of the cellular colonized volume of these 3D synthetic TCPs will help us to better understand the complex process of bone defect regeneration by using our method in routine.

References

1. D.Y. Cho *et al.*, "Cage containing a biphasic calcium phosphate ceramic (Trisite) for the treatment of cervical spondylosis", *Surg.Neurol.* , 63 (6), 497–503, discussion 503-4, 2005.
2. C. Lindgren *et al.*, "A 3-year clinical follow-up of implants placed in two different biomaterials used for sinus augmentation", *Int. J. Oral Maxillofac*, 1151–1162, *Implants* 27 (5), 2012.
3. S. Hosseinpour *et al.*, "Application of selected scaffolds for bone tissue engineering: a systematic review", *Oral Maxillofac Surg.*, Feb 13, 10.1007/s10006-017-0608-3, 2017.
4. Bajpai I. *et al.*, "Response of human bone marrow-derived MSCs on triphasic Ca-P substrate with various HA/TCP ratio", *J Biomed Mater Res B Appl Biomater.*, 105(1):72-80, 2017.
5. C.F. Marques *et al.*, "Biphasic calcium phosphate scaffolds fabricated by direct write assembly: mechanical, anti-microbial and osteoblastic properties", *J. Eur. Ceram. Soc.* 37,359–368, 2017.
6. R. Detsch, *et al.* "In vitro:osteoclastic activity studies on surface of 3D printed calcium phosphate scaffolds", *J. Biomater. Appl.*, 26 (3), 359–380, 2011.
7. C. Bergemann *et al.*, "Continuous cellularization of calcium phosphate hybrid scaffolds induced by plasma polymer activation", *Mater Sci Eng C Mater Biol Appl.*, 59:514-23, 2016.

Micro-CT imaging and analysis of low concentrated gelatin and fibrin based scaffolds

S. Schneider¹, D. Maniglio², W. Bonani², M. van Griensven¹, E. Rosado Balmayor¹, S.P.P¹. Poh¹

¹ Experimental Trauma Surgery, Klinikum rechts der Isar, Technical University of Munich, Ismaninger Str. 22, 81675 Munich, Germany

² Department of Industrial Engineering, BIOTech Research Center, Via delle Regole 101, 38123 Trento, Italy

Aims

This study aim to characterise and compare the physical properties of four types of scaffolds with different molar concentration of gelatin, fibrin and hydroxyapatite intended for bone regeneration. The difficulty here was that the scaffold component has a very low X-ray opacity. So a suitable scanning configuration needs to be found for this kind of scaffolds.

Method

The major challenge encountered was the low X-ray opacity of the scaffolds' biomaterial impeding the use of micro-computed tomography (μ -CT) for the visualization of the internal architecture. To circumvent this, scaffolds were immersed in 0.2 % Lugol's iodide solution for 30 min at room temperature prior to scanning.

After that all scaffolds were fixed on polystyrene tube and scanned in air using a Skyscan 1176 *in vivo* μ CT with the following scanning parameters 9 μ m resolution, 40 kV, 600 uA, no filter and 0.3 ° rotation step size. Subsequently, 3D reconstructions was performed using NRecon, with the following image processing parameters: smoothing of 2, ring artifact reduction of 5 and 5 % beam hardening correction.

The characterization analysis was performed by using CTAn. Because of the different sizes of the scaffolds the ROI form was standardized across all scanned samples and three ROIs were chosen, due to the two-phase- characteristic of scaffold 3 and 4, to compare the scaffolds' physical characteristic across the length.

For the 3D visualization of the whole scanned scaffolds CTVox was used.

Results

The four scaffolds (without iodine treatment) were first scanned directly in air and fixated with polystyrene tubes (SP-3200, Bruker) with 40 kV, 600 uA and no filter. Only the scaffold with hydroxyapatite inside was visible (Figure 1A). Because of the very low X-Ray opacity of most of the scaffolds, we used a Lugol's iodide solution to create a higher X-Ray opacity and scanned them again with the recently mentioned conditions. For comparison, optical microscope images (VHX, Keyence, Japan) and SEM images (JSM-6390, Jeol, USA) were performed (Figure 1). Scaffold 1 and 2 have a homogenous micro-structure. In contrast, scaffold 3 and 4 have a two-phase micro-structure, one more compact and one more sponge-like.

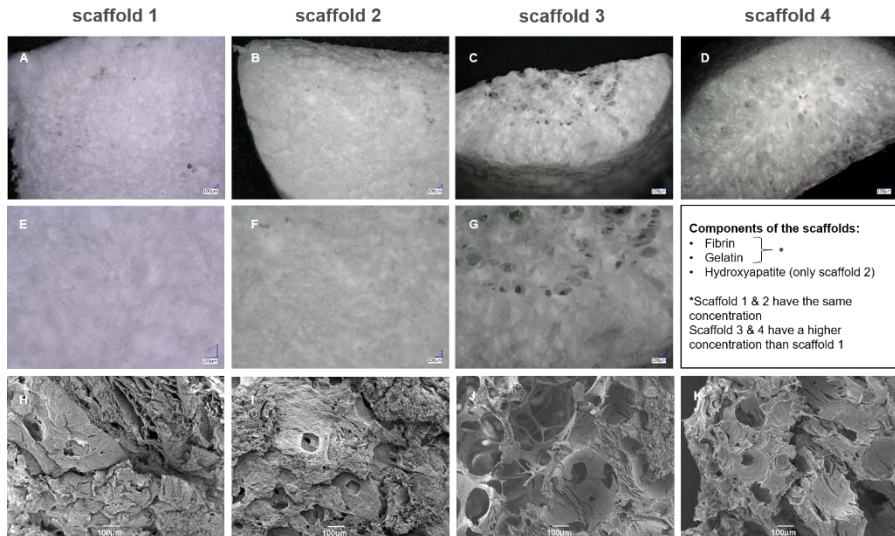


Figure 17 Images of optical microscopy (A-D: 50 x magnification; E: 200 x magnification; F-G: 100 x magnification) and SEM (H-K: 100x magnification) from the several gelatin-fibrin scaffolds.

The scaffolds are visible with the iodide treatment (Figure 2A). As the scaffolds did not have the same size, the ROI was defined smaller than the whole scaffolds. For the scaffolds 3 and 4 the ROIs are separated in three parts, one in the crossing of the two phases (a), one in the sponge-like part (b) and one in the compacter part (c).

Scaffold 1 is more anisotropic than scaffold 2. The connectivity density is for scaffold 1 two-times higher than scaffold 2, but the porosity is only 9 % lower. In opposite to that show the SEM pictures (Figure 1 H-I) a similar structure of those scaffolds. The scaffold 3 and 4 have the same connectivity density in the compact phase and nearly the same degree of anisotropy, but the total porosity is 7-times lower in scaffold 4 than in scaffold 3. Suchlike is also reflected by the ROI in the sponge part of those scaffolds, but here the porosity is only 2.5-times lower in scaffold 4 compared to scaffold 3. At the crossing part of those scaffolds the porosity is similar but there is only a connectivity density measurable in scaffold 3. Scaffold 4 looks like being completely enclosed in this ROI. The degree of anisotropy is more anisotropic in scaffold 4 than in scaffold 3, with values equal to 0.87 and 0.56 respectively.

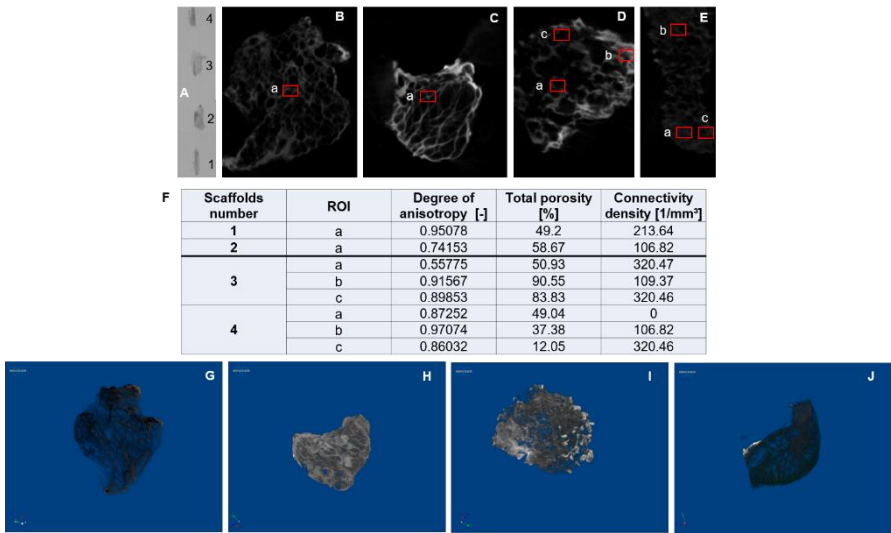


Figure 18 Different images of the reconstruction and analysis process. A: Scan of scaffolds 1-4; B- E: CTAn images of ROIs; F: Table of chosen parameters; G-J: 3D visualization in CTVox of scaffold 1-4.

Conclusion

X-ray microtomography analysis can be enhanced with iodine treatment for scaffolds with low concentration of gelatin and fibrin. This methods leads to a very fine structure mapping and a non-destructive evaluation of these scaffolds. Furthermore μ CT, beside the structure reconstruction capability, can also be an effective and quantitative image analysis method.

Acknowledgments

Sandra Schneider thanks the International Graduate School of Science and Engineering – IGSSE at the Technical University of Munich for providing her with a PhD Fellowship under the project “PreDiQure” (10.07).

Application of X-ray MicroCT for the study of unconsolidated bottom sediments of different lakes and seas

A.Khomyak¹, D.Korost¹, D.Gafurova¹

¹ Moscow State University, Moscow, Russia

Aims

In modern marine geology there is a rather wide set of methods for studying non-lithified sediments. These are a macroscopic description of the columns, thin sections, granulometric, immersion and chemical analyzes, atomic absorption, X-ray fluorescence method, electronic scanning microscopy, etc. However, the most important stage in the study of columns is their careful macroscopic description and sampling [1]. Modern researchers note that there are certain difficulties in describing the texture-structural features and revealing sediments genesis. Despite the numerous scattered evidence, there is no generalized atlas of unconsolidated bottom sediments textures and structures, also there is no single approach in the genetic interpretation of the data complex.

Method

The demonstrated results were obtained with two computer tomography (CT) systems: microCT SkyScan 1172 [2] (Bruker MicroCT, Belgium) and RCT-180 (Geologika, Russia). The SkyScan system was set with the following parameters: X-ray tube mode – 100 kV and 100 μ A, reconstructed datasets size – 4000 \times 4000 \times 2000, and pixel size – 2.2 μ m. The RCT-180 system was applied X-ray tube mode 160 kV and 5 μ A, image size – 1000 \times 1000 with pixel size – 220 μ m.

Japanese and White Sea samples, as well as sediments from Onega Lake and Lake Baikal were studied during research. All sediments were scanned, being wet, which is very important, because when samples dry out, the texture-structural features are becoming disturbed. It is important to hermetically pack sediments and prevent them from dehydration at all stages of the study.

At the first stage, was used RCT-180 tomography. The plastic pipes filled with sediment were scanned, the pipe size was 120 \times 120 \times 1000 cm. At the second stage, a more detailed survey was performed on the SkyScan 1172 CT.

Results

As a result of scanning at the first stage, the following tasks were solved:

1. Macro description detalization of the columns carried out on board, revealing textures which were not marked in the primary description (Figure 19).
2. Control of fluid discharge zones along the gas paths (Figure 19).
3. Identify violations of stratification, cracks, faults, landslides.
4. Determination of species of fauna remains (Figure 20).
5. Determination of areas of mud volcanic activity (Figure 21).
6. Creating databases of information tablets (Figure 22).

At the second stage, surveys were made on the SkyScan 1172 microtomograph to clarify the zones of mud volcanic activity.

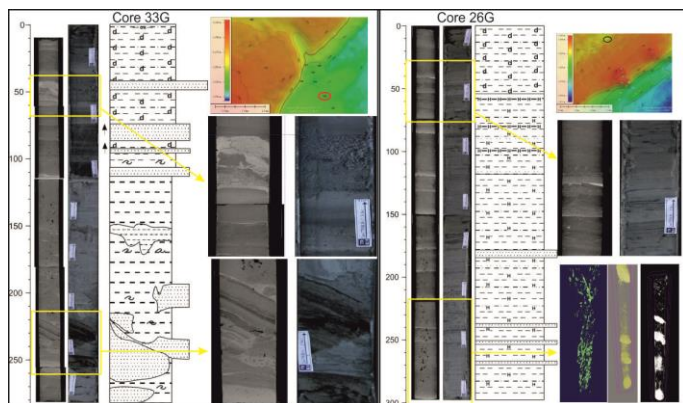


Figure 19 Correlation of the column cuts. Monitoring of fluid discharge zones following the traces of gas outlets. Lake Baikal.

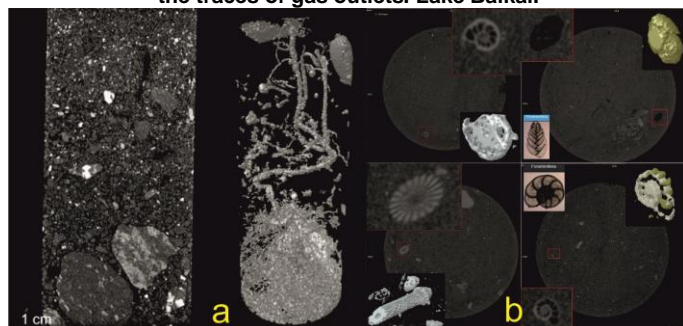


Figure 20 Determination of species of fauna remains: a) bioturbation, b) fossils. Lake Baikal.

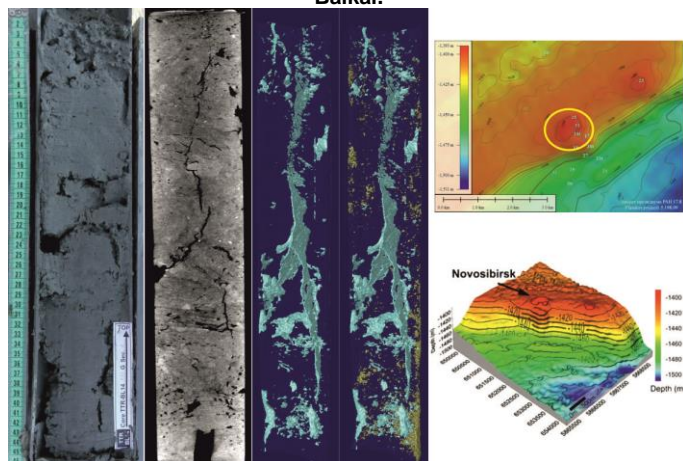


Figure 21 Determination of areas of mud volcanic activity.

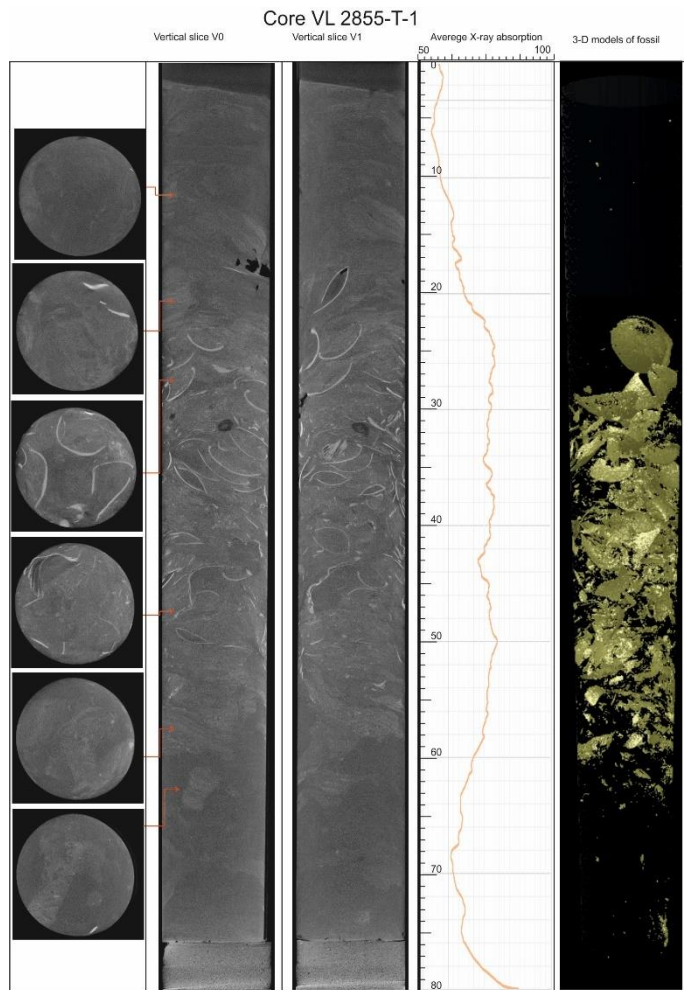


Figure 22 Information tablet on the column. Japanese Sea.

Conclusion

The main advantage of using CT for studying bottom sediments is the possibility of creating an electronic base, since the samples eventually lose moisture, and breakdown structure and texture occurs. Another important advantage is the possibility of revealing hidden features of sediments that are not fixed in the macro description.

References:

1. Свальнов В.Н. «Микроструктуры и текстуры глубоководных осадков.» М.:ГЕОС, -192с, 2001г.

X-ray microtomography of debris and aerosols from Chernobyl nuclear accident

A.V. Pakhnevich¹, A. A. Shiryayev^{2,3}, I.E. Vlasova³, R.A. Senin⁴, B.E. Burakov⁵, B.I. Ogorodnikov⁶

¹ Borissiak Paleontological Institute of the Russian Academy of Sciences, Profsoyuznaya st. 123, Moscow, 117647 Russia

² Institute of Physical Chemistry and Electrochemistry RAS, Moscow, Russia

³ Chemistry Department, Moscow State University, Moscow, Russia

⁴ National Research Centre "Kurchatov Institute", Academician Kurchatov sq. 1, Moscow, 123182 Russia

⁵ Khlopin Radium Institute, St. Petersburg, Russia

⁶ Karpov Physical Chemistry Institute, Moscow, Russia

Aims

The accident at the 4th Unit of Chernobyl Nuclear Power Plant (ChNPP) on 26 April 1986 led to destruction of the reactor core and release of an enormous amount of solid and gaseous radioactive products to the environment due to explosion and subsequent fire. Till now this remains the worst nuclear accident in history, though, unfortunately, not the last one.

In the first days after the initial explosion hot ($>1500\text{ }^{\circ}\text{C}$) fragments of fuel rods (UO_2 in Zr encasing) interacted with concrete, serpentinite, steel and other construction materials leading to the formation of so-called lava-like fuel-containing materials (LFCM) or Chernobyl "lava". Several days after the accident considerable fraction of the initial lava pool spread into other rooms of the reactor building, forming vertical and horizontal flows which solidified into a highly radioactive glassy material (fig. 1) with inclusions of high-uranium zircon crystals ($\text{Zr}_{1-x}\text{U}_x\text{SiO}_4$, particles of molten stainless steel, uranium oxide dendrites and grains, and particles of Zr-U-O phases (figs 2 – 6). Although the microstructure and other properties of the Chernobyl "lava" were extensively studied in 90-ies, many important features relevant for prediction of their long-term behavior remains poorly studied. The main obstacle is high radioactivity of the samples.

Despite creation of a new engineering cover ("The Arch") in 2016 over the building of the former ChNPP, the problem of handling thousands of tons of radioactive substances remains unsolved. Investigation of the lava and of generated aerosol particles is of great importance for prediction of future behavior of this site. Moreover, such studies are highly relevant for decommissioning of the Fukushima nuclear power plant in Japan, where formation of lava-like material, though on a smaller scale, is very plausible.

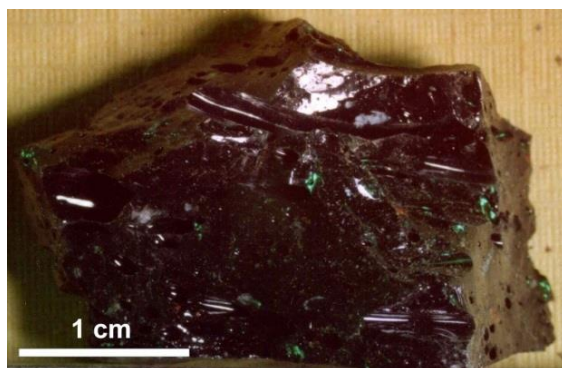


Figure 1: Black ceramics (lava)

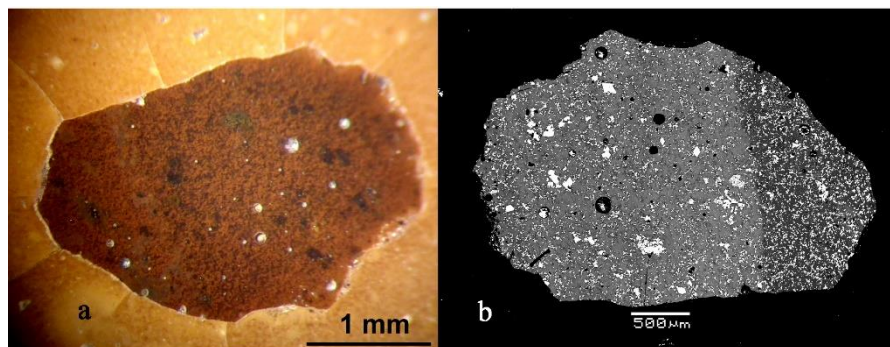


Figure 2: Brown lava with U-rich inclusions in epoxy. a – light microscope, b – SEM, white spots – inclusions.

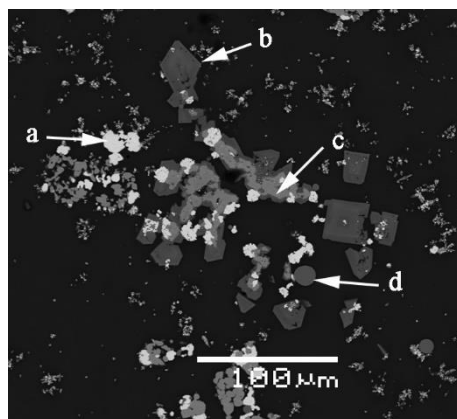


Figure 3: Different inclusions in lava. a – UO_x , b – $(\text{Zr}_{0.85-0.95}, \text{U}_{0.15-0.05})\text{SiO}_4$, c – $(\text{Zr}, \text{U})\text{O}_2$, d – Fe-Cr-Ni.

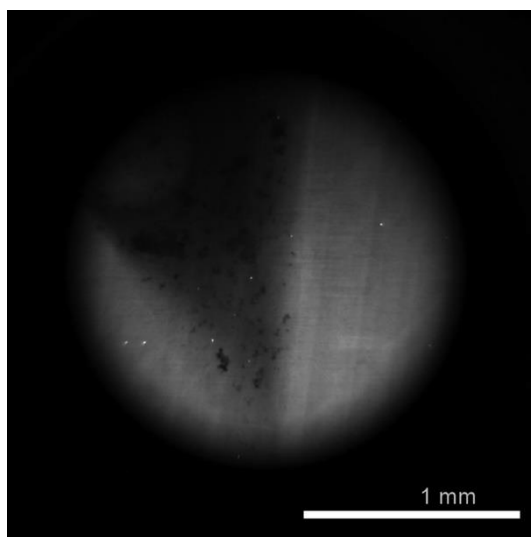


Figure 4: Lava fragment in X-ray.

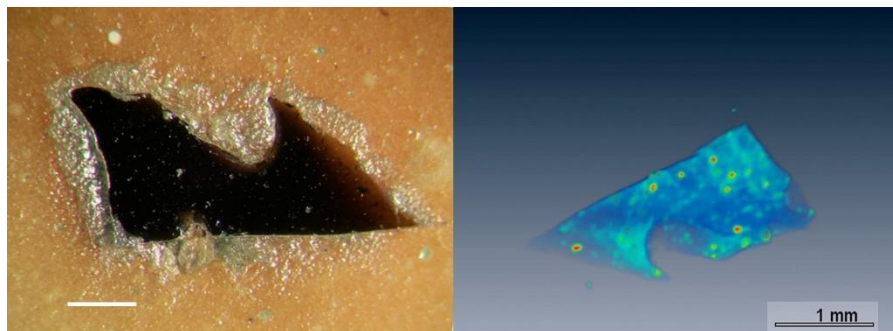


Figure 5: Brown lava with U-rich inclusions in epoxy (left – optical photo) and 3D-model of this fragment.

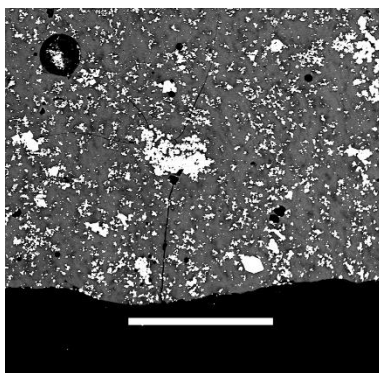


Figure 6: Cracks – manifestations of the lava destruction process. Scale bar – 500 μm .

We report here results of X-ray tomography investigation of several types of Chernobyl samples. This work represents part of larger scale study of present (as of 2014-2016) state of lava samples and aerosols collected inside the “Shelter” building (see Shiryayev et al., 2016 for details).

Method

Several types of the samples were investigated: 1) aerosol filters with “hot” particles exposed in the “Shelter” building; 2) small (100-200 microns) pieces spontaneously detached from the lava accumulations; 3) individual minerals extracted from the lava by acid dissolution.

X-ray microtomography of aerosol filters and small particles was done in Borissiak Paleontological Institute of RAS by using microtomograph Skyscan 1172 with parameters: $I=100$ mA, $U=104$ kV, with and Al (1 mm) filter, a pixel size was 1 – 2 μm , a rotation - 180°, steps of rotation were 0.4, random movement – 10, frame averaging – 8. TView, different versions NRecon and CTAn programs are used. X-ray microtomography of lava fragments was performed at National Research Centre “Kurchatov Institute” at Kurchatov synchrotron radiation source and X-ray Topography and Microtomography (XRT-MT) station (Senin et al.,

2013). Pixel size is 2.5–10 μm . Programs by A.V. Buzmakov (Chukalina et al., 2008) and Amira (FEI) were used.

Results

X-ray tomography allowed to solve several important questions and to select the most plausible options in interpretation of results obtained by other analytical methods.

Tomography was employed to investigate size of “hot” particles trapped in the aerosol filters and their location inside the filter body (fig. 7). Whereas localization of the particles in the filter plane is easily achieved using digital autoradiography, this method is unsuitable for size determination. The tomographic reconstruction (fig. 8) permitted to establish that the “hot” particles are electrostatically attached to the filter strands and are not trapped in the pores. This fact is important for understanding of the particle-filter interaction and reveals that the particles are electrically charged.

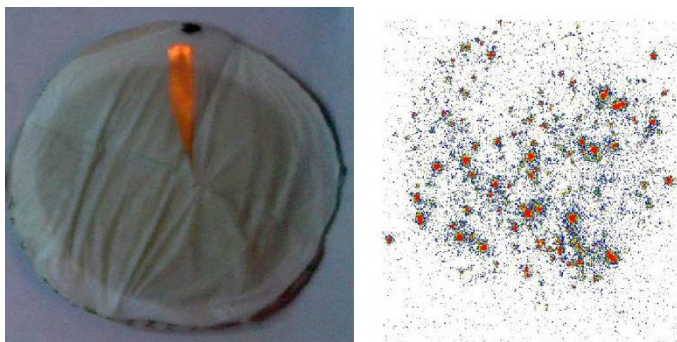


Figure 7: Aerosol filter (exposition time – 24.5 hours) with “hot” particles containing ^{137}Cs and ^{241}Am .

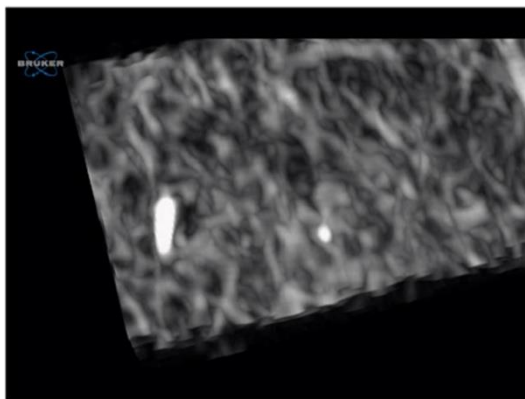


Figure 8: Tomographic reconstruction of the aerosol filter with “hot” particles.

One of the most remarkable applications of X-ray tomography in the current context is the examination of internal structure of the spontaneously detached lava particles. Their relatively

small size (<200 microns) and irregular shape prevented quantitative investigation using other methods. In particular, considerable doubts about the origin of these particles existed, since their size was surprisingly large for being transported by weak air flows. Detailed investigation of particles' morphology using Micro-CT and impressive observations of UO_2 dendrites with sizes 1-5 microns inside them provided extremely useful data about long-term stability of the lava accumulations (fig. 9).

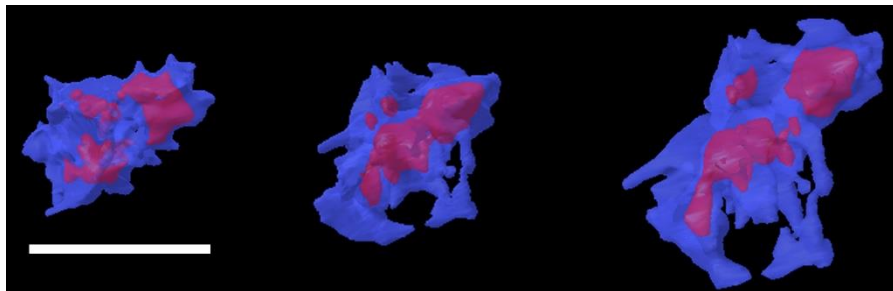


Figure 9: Different views of a spontaneously detached particle with UO_2 -inclusion (vinous color). Scale bar – 60 μm .

The last part of the presented work concerns in-depth investigation of individual mineral phases extracted from the lava by acid treatment. We know from previous electron microscopy investigation that U-rich zircon and Zr-U-O phase possess extremely complex morphology with highly irregular growth zoning (fig. 10), complicated by abundant inclusions and embayments. Results of micro-CT study of these minerals will be shown and discussed.

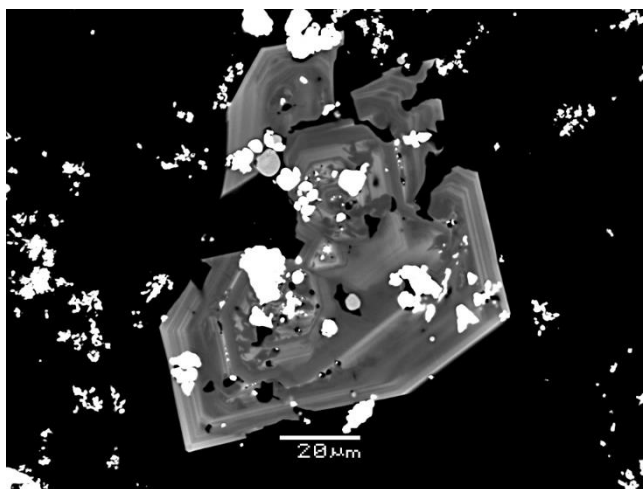


Figure 10: Inclusion of high-U zircon (chernobylite).

Conclusion

Microparticles formed as a result of chemical and mechanical destruction of the lava represent significant radioecological danger near the Chernobyl Nuclear Power Plant. X-ray micro-CT is an efficient technique for the study of their structure.

References:

1. Chukalina M., Buzmakov A., Nikolaev D., Chulichkov A., Karimov M., Rasulov G., Senin R., Asadchikov V. "X-ray microtomography using a laboratory source: Measurement technique and comparison of reconstruction algorithms" *Measurement Techniques*. V. 51. No 2. P. 136 – 145, 2008.
2. Senin R.A., Khlebnikov A.S., Vyazovetskova A.E., . Blinov I.A, Golubitskii A.O., Kazakov I.V., Vorob'ev A.A., Buzmakov A.V., Asadchikov V.E., Shishkov V.A., Mukhamedzhanov E.Kh. and Kovalchuk M.V. "Upgraded X-Ray Topography and Microtomography Beamline at the Kurchatov Synchrotron Radiation Source" *Crystallography Reports*. V. 58. No 3. P. 517 – 522, 2013.
3. Shiryayev A.A., Vlasova I.E., Burakov B.E., Ogorodnikov B.I., Yapaskurt V.O., Averin A.A., Pakhnevich A.V., Zubavichus Y.V. "Physico-chemical properties of Chernobyl lava and their destruction products" *Progress in Nuclear Energy*. V. 92, P. 104 – 118, 2016.

Up, up in the sky: the role of tomography in studying early planetary formation

Benita Putlitz¹, Lukas Baumgartner¹, Sandrine Peron² & Antoine Roth³

¹ Institute of Earth Science, University of Lausanne, Switzerland

² Institut de Physique du Globe de Paris, France

³ Institute of Physics, University of Bern Switzerland

Aims

In Lausanne, we use a Skyscan 1173 for a wide variety of research questions. Here we present two case studies, to illustrate the potential of μ XCT for the research on noble gases and planetary formation.

Results

The isotopic compositions of noble gases (He, Ne) constitute a powerful tool to study the origin of volatiles during the early stages of planetary formation, provided primitive - e.g. non-disturbed contaminated noble gas can be found. The earth mantle is a huge reservoir of such primitive noble gases. Basaltic melts from the deep mantle occur in only a few areas, the so called "hotspots" (Hawaii, Galápagos and Iceland), which are suitable. For analysis to be useful, any such noble gas has to be isolated from the atmosphere, to avoid contamination with present day noble gases and their isotope ratio. In Peron et al. (2017) we analyzed the noble gas isotopic compositions of single vesicles in samples from the Galápagos hotspot with laser ablation. Vesicles were selected based on μ XCT work in order to understand and remove this atmospheric component, as well as discriminate between different models for the noble gas origin on Earth. The samples were imaged via X-ray microtomography to locate the vesicles and to ensure that the vesicles are still intact and not connected with each other or to the outside – and thus contaminated by air.

A second application is centered around meteorites. Meteorites are believed to be the early witnesses of our planetary system, and hence they hold a key to better understand the initial history of our solar system. An original approach by Roth et al. (2016) connects meteorites, noble gas analyses and tomography. Meteorites acquired most - if not all - of their cosmogenic noble gas composition during transit to Earth. If chondrules (a chondrule is a small, rounded particle of a few 10's of μ m size - they make up parts of stony meteorite called chondrites) were exposed to cosmic rays prior to meteorite compaction, they retain an excess of cosmogenic noble gases. Such excesses can be detected, but is strongly dependent on the chemical composition of each individual chondrule. However, usually studies are limited to a few samples of meteorites, as they need to be painstakingly isolated, and subsequently irradiated in a nuclear reactor for instrumental neutron activation analysis. Roth et al. (2016) developed a novel analytical protocol that combines the measurements of He and Ne isotopic concentrations with a fast method to correct for differences in chemical composition using micro X-ray computed tomography. The basic assumption is that X-ray attenuation of chondrules, can serve as a proxy for the production rates of cosmogenic noble gases; thus chondrules and reference materials were imaged prior to noble gas analyses and the attenuation of each individual chondrule was calculated. The consistency of the data and comparisons with reference material shows that using μ XCT to correct for differences in chemical composition is accurate.

The advantage of tomographic imaging is that a large number of chondrules can be analyzed and screened prior to noble gas analysis. Moreover, tomographic images bring important additional information (e.g. on textures) to properly correct and interpret noble gas data.

Conclusion

The presented studies illustrate that tomography is a versatile method, which should be an integral part of modern analytical techniques in Earth and Planetary Sciences.

References:

Peron et al. (2017): Solar wind implantation supplied light volatiles during the first stage of Earth accretion *Geochem. Persp. Let.* (2017) 3, 151-159 | doi: 10.7185/geochemlet.1718

Roth A. et al. (2016) Cosmic-ray exposure ages of chondrules; *Meteoritics & Planetary Science* 51, Nr 7, 1256–1267 (2016) doi: 10.1111/maps.12658

XCT as a screening tool for quick characterization of silica nodules from a hydrothermal spring

M.L. Vladimir¹, I.P. José Enrique², K. Thomas^{1,2}

¹Mexican Center of Innovation in Geothermal Energy (CeMIE-Geo); Rinconada del Pedregal 95, Pedregal Playitas 22860, Ensenada, Baja California, Mexico

²Ensenada's Center for Scientific Research and Higher Education (CICESE); Carretera Ensenada-Tijuana 3918, Zona Playitas 22860, Ensenada, Baja California, Mexico.

Aims

Development of a simple qualitative methodology for a quick characterization of silica nodules (case of study for the time being but not limited to), combining the results of reconstruction and 3D visualization provided by x-ray computed tomography (XCT), 2D elemental distribution via micro x-ray fluorescence (μ -XRF), and mineral composition with micro x-ray diffraction (μ -XRD; results not included in this work).

The concept is to use XCT as the starting point for further characterization of spherical nodules found in El Tatio, a hot spring located in northern Chile. The 3D visualization provides a powerful tool to decide where to make a cuts to get slices of interest for further μ -XRF analysis of major elements distribution and mineralogy with μ -XRD.

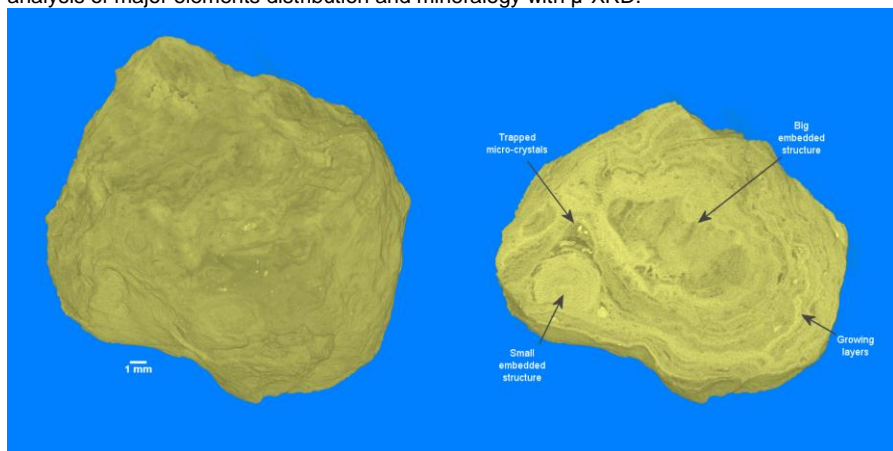


Figure 1. Left: Full 3D render of a single nodule. Right: layer of choice given the features of the sample.

Method

The region of El Tatio, among other hot springs, has become a zone of interest for researching groups aiming at finding potential biosignatures that could lead to environmental conditions for life development in other planets¹, particularly Mars being the closest to Earth and the most popular target for recent space exploration funding.

In this hot spring different formations can be found in a variety of shapes including crusts, outcrops, regoliths and nodules, and reminiscence of biotic and abiotic processes are sometimes very well captured and preserved as biosignatures, hence the interest for this minerals.

In this work we used XCT as the starting point for a characterization workflow of silica-based nodules as follows:

Step 1, sample mounting and tomography set-up: A SkyScan 2211 nano-XCT was used with fixed voltage and current of 110 kV and 90 μ A, respectively, with a 0.5 mm Ti filter; 12 μ m per pixel was the scanning resolution achieved for the micro-focus configuration in order to fit the FOV without the need of any further connection in the reconstruction stage; the scan was done for 180° with a rotation step of 0.200° and a frame averaging of 4. Total scanning time of 00:16:01 (hh:mm:ss).

Step 2, reconstruction of sinograms: NRecon v1.7.0.4 in combination with the InstaRecon v2.0.3.7 reconstruction engine was used to get the set of slices (1161).

Step 3, 3D visualization: With the use of CTvox the full volume was rendered and cropped to define a ROI subject to μ -XRF and μ -XRD in the best interest of the researcher owner of the samples.

Step 4, isolating porosity. A suitable task list was set-up to obtain the porosity from the nodule with the use of CTAn.

Results

A slice showing two-nucleus embedded in the nodule and trapped micro-crystals (figure 1) was the ROI of choice because these features can give information to elucidate about the path followed during the spherical formation of layers under the stressful environmental conditions of the zone. Also, the embedded crystals can serve as proxies of the mineralogical features of the proximity that prevailed at a particular growing stage of the nodules.

With the previous information, the nodule was cut at a specific position. This is important because these can be considered high-end samples due to the cost of geological campaigns and the time it takes for the nodules to grow this size under natural conditions.

The grey scale index of the slices can be visually coupled with the elemental distribution maps obtained with a tabletop μ -XRF spectrometer (Bruker's M4 Tornado), giving meaning to the features (growing layers) of the 3D imaging

The growing layers surrounding the biggest spherical feature show a coupling between As and Ca, except for the inner one which has a defined Ga fence. This also happens with the other main features as well (figure 2).

The brightest spots from reconstructed slices can be associated with trapped micro-crystals; location is visually plausible via XCT whilst chemical characterization is done with μ -XRF with well-defined element maps. For reference, the X-Ray spot from the μ -XRF spectrometer is 25 μ m wide, which is on par with the XCT in terms of order of magnitude. The highlighted crystals from XCT slices (white spots) can be associated mainly with Fe, K and Ti, contrasting with the matrix (which consist of Si) and the previous growing structures (figure 3). The 3D abundance and distribution can be achieved adjusting the transfer function in CTvox, and it gives insight of the transport of microcrystals toward outer layers (figure 4), a process that can be related to microbial activity.

Working with porosity (figure 5) was rather easy as the contrast from the grayscale was good enough for an easy elaboration of a tasklist for the CTAn software. A minimum despeckle was done just to get rid of small volumes neglected as noise, and a 2D analysis was carried out with particular interest in three main features (figure 6): a) the angular orientation because it can be hypothesized that the shape of the porous will be aligned with the growing layers; b) the form of the pores, which are expected to suffer elongation as they get closer to the border of the original seeding minerals; c) the size of the pores. Pores size tend to increment towards

the inner section of the nodule. The shape of the pores tends to be more irregular toward the inner sections and around the spherical features within the sample.

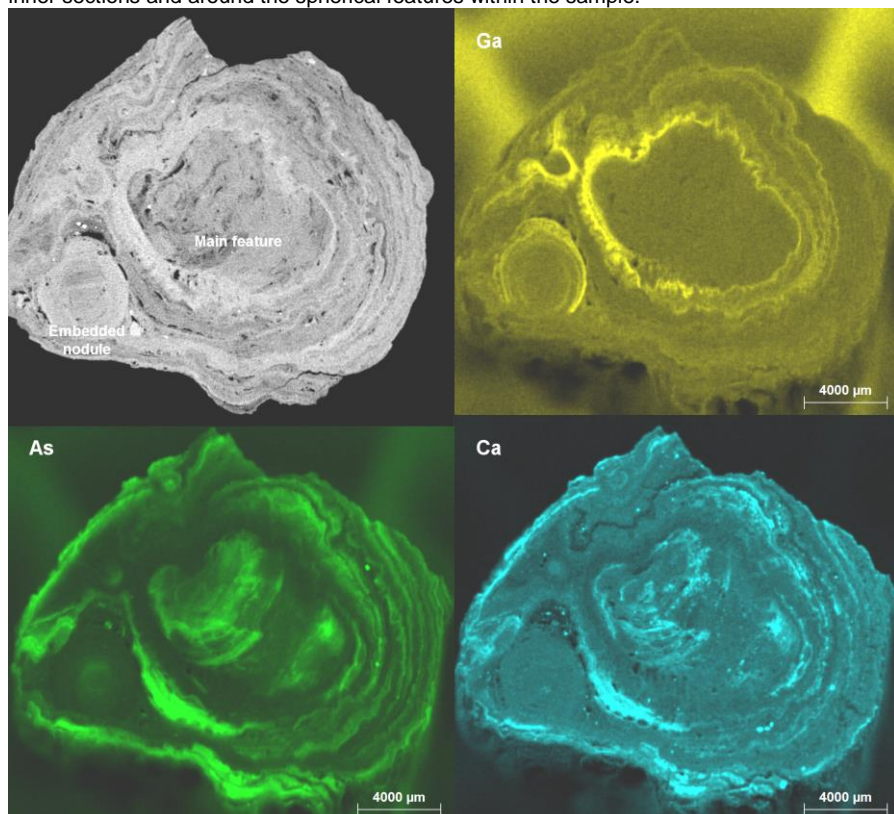


Figure 2. Single ROI slice for visual comparison between raw reconstructed XCT images and elemental distribution maps from μ -XRF. The color scales were enhanced for displaying purposes, *i.e.* the zone of more intensity reflects the highest concentration measured.

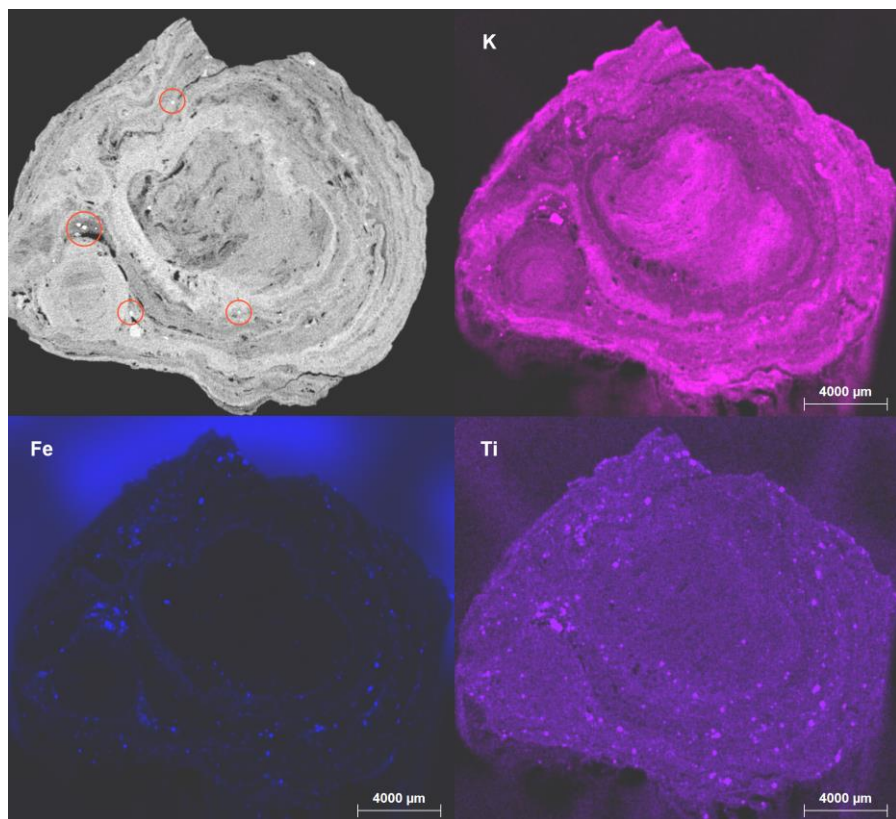


Figure 3. Trapped micro-crystals from the ROI slice from XCT compared with elemental distribution maps from μ -XRF.

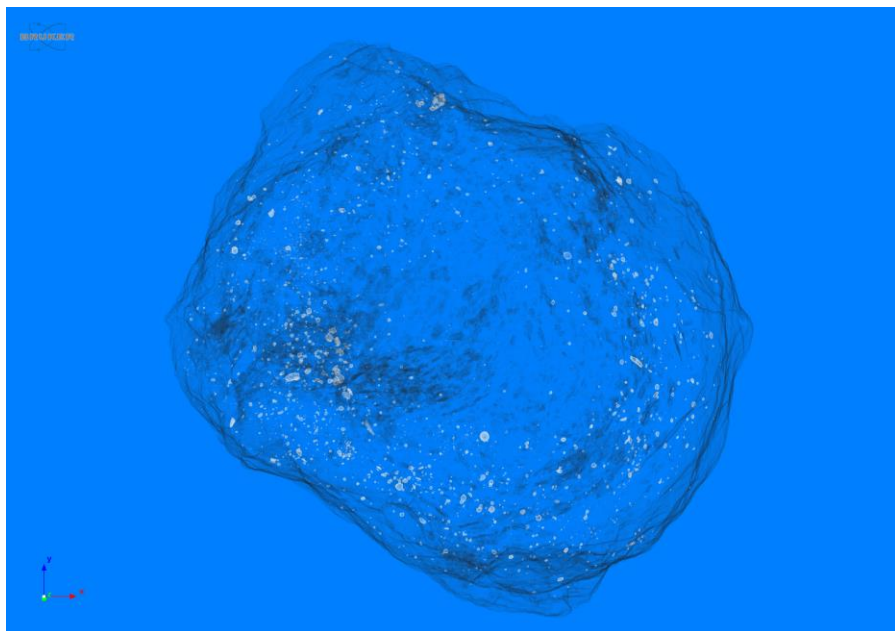


Figure 4. Top-view of the 3D distribution of micro-crystals within the nodule.

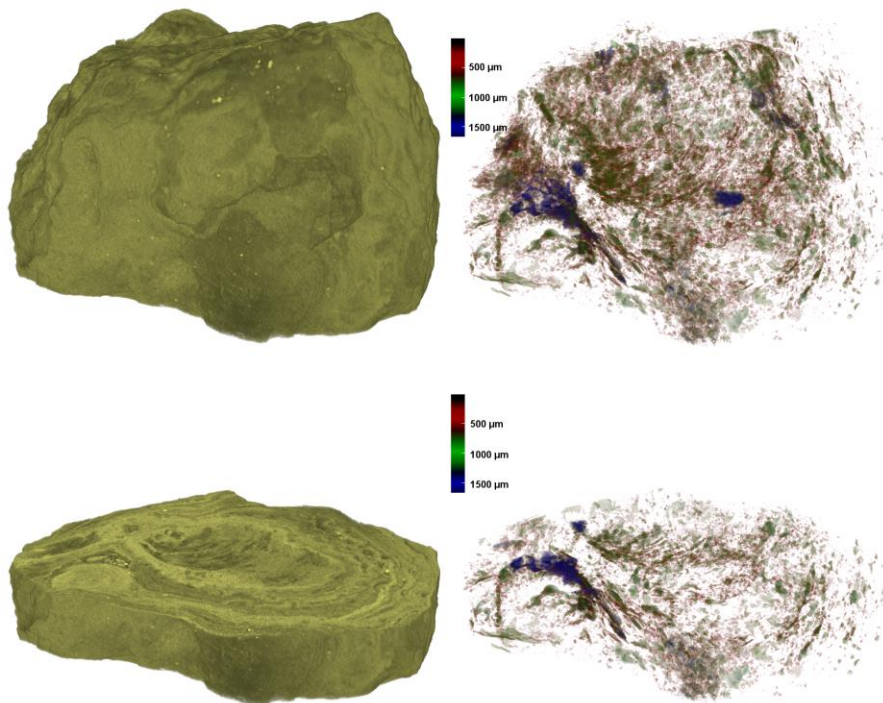


Figure 5. 3D imaging of porosity.

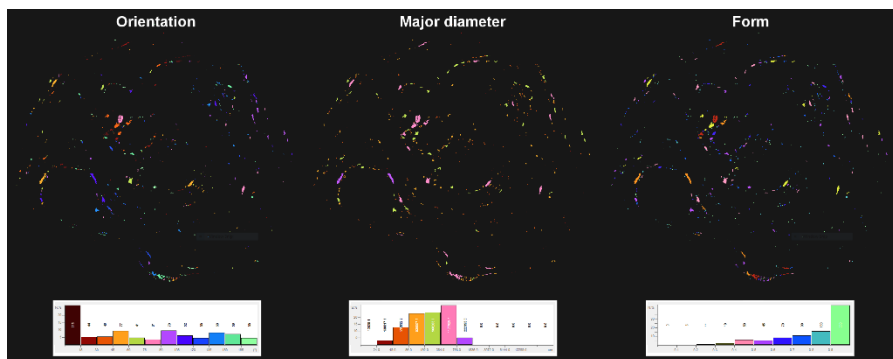


Figure 6. Example of the 2D analysis of the porosity.

Conclusion

XCT is a powerful tool not only because of the 3D visualization per se, but because it helps to avoid going blindly to sub-sample minerals that require further analysis with complimentary techniques/spectroscopies. From a geochemical/mineralogical point of view, when mineral sample show interesting features on the 3D renders, it makes it subject to XRD and suitable chemical characterization, but if you don't know where to cut or dissemble you can ruin

valuable samples. Other interesting concept for laboratories with the advantage of having a variety of instruments with the capability of making non-destructive analysis, is to linkage all of them after the XCT results, that way you won't need to create a big set of slices (for the case of geological samples); the tools (software) provided the SkyScan 2211 are good enough for a qualitative characterization with minimal information from μ -XRD and μ -XRF (down to one slice!).

References:

1. Ruff, S.W., Farmer, J.D. "Silica deposits on Mars with features resembling hot spring biosignatures at El Tatio in Chile" Nature Communications (7)13554: 1-10, 2016.

X-ray microtomography in paleontology: the perspective scientific directions

A.V. Pakhnevich

¹ Borissiak Paleontological Institute of the Russian Academy of Sciences, Profsoyuznaya st. 123, Moscow, 117647 Russia

Aims

X-ray tomography as a non-destructive technique is used in paleontology more often. The paleontological objects for tomography are very perspective. They have a high density and are mineralized. On the other side a contrast between sediment minerals and minerals of fossils can be low. First pioneer tomography study in Paleontological Institute of Russian Academy of Sciences was done by T.A. Tumanova with colleagues from USA (Gallagher et al., 1998). They have studied the skulls of dinosaur *Tarchia* by using a medical tomograph. Beginning 2006 in Paleontological Institute we are doing the studies by using X-ray micro-CT Skyscan 1172. First publications were dedicated to the investigations of a shell internal structure of recent and fossil brachiopods (Pakhnevich, 2006) and Early Paleozoic echinoderms (Bryantseva and Rozhnov, 2007). In collaboration with the National Research Centre "Kurchatov Institute" (Moscow) and the Joint Institute for Nuclear Research (Dubna) the investigations by using synchrotron and neutron tomography are carrying out (Kaloyan et al., 2014; Kozlenko et al., 2015). As a result of studies of the paleontological and geological objects an abundant experience is accumulated. In this connection there are some generalizations which could be useful for paleontologists and geologists. An aim of this report is to identify the perspective directions of paleontological objects study by using different tomography techniques.

Method

The study are carried out by using X-ray micro-CT Skyscan 1172. Microtomography parameters: I=100 mA, U= 50 – 104 kV, without a filter and with Al (1 mm), a pixel size was from 1 to 34.1 μm , a rotation - 180° – 360°, steps of rotation were 0.4 – 0.7°, random movement – 10, frame averaging – 8. TView, 3DCreator, different versions NRecon and CTAn programs are used. A material is from Paleontological Institute and author collections.

Results

There are a number of traditional tomography objects, for example, bones and teeth of vertebrate animals (fig. 1). They are dense, fine mineralized, often good contrasting with hosting rock. Inside they have some structures (spongiose tissue, channels) which are good visualized. However some more difficult, but no less interesting objects are in paleontology. It seems a progress of these fossils studies is actually.



Figure 1: A fragment of fish bone (Upper Devonian, Orel region, Gornostaevka quarry). Scale bar – 10 mm.

Paleontological objects visualization

The most important visualization condition of studied object is a difference of a contrast between the object and the hosting rock. First of all, the visualization depends on an elemental compound of a fossil and the hosting rock. The minerals calcite, aragonite, quartz, apatite, pyrite, siderite, goethite were a part of shells, bones, plant remains or replaced the original minerals as a result of a fossilization. The impurities are often in minerals. As a rule, fossils are not in monomineral rock. The impurities and a compound of rock influence on the contrast. For example, apatite and calcite are well contrasted (at $U=103-104$ kV, $I=100\mu A$), but calcite and a phosphorite, rock contained apatite, are almost not contrasted (fig. 2).

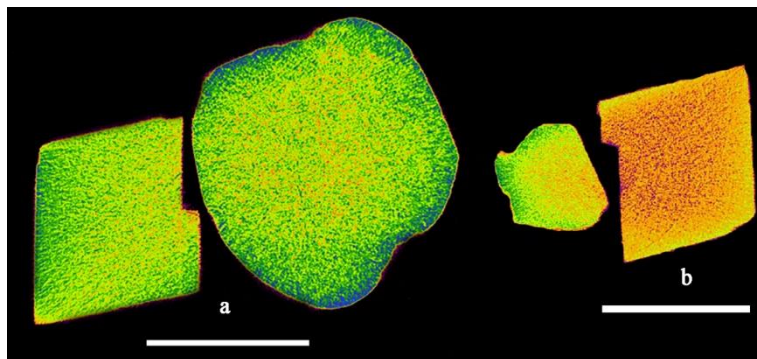


Figure 2: A contrast of minerals and rock. a – calcite (left) and phosphorite, b – apatite and calcite (right). Scale bar – 10 mm.

This scientific direction is very important for a development of the microtomography investigations, for a valuation of the research effectiveness.

Objects studied by cross-sections

Some paleontological objects are studied by using cross-sections. This process is labour-intensive and longer. Grinded fossil is completely or partially destroyed. Some sections or acetate films, or images of sections are preserved. X-ray microtomography can replace this technique. A lot of brachiopods (Pakhnevich, 2010), bryozoans (Koromyslova, Pakhnevich, 2016), corals (fig. 3), which studied by traditional cross-sections, were investigated by using micro-CT. However, sometimes the hosting rock and skeleton structures have same mineral compound and this debases results. Nevertheless, microtomography can partially replace traditional labor-intensive destructive technique.

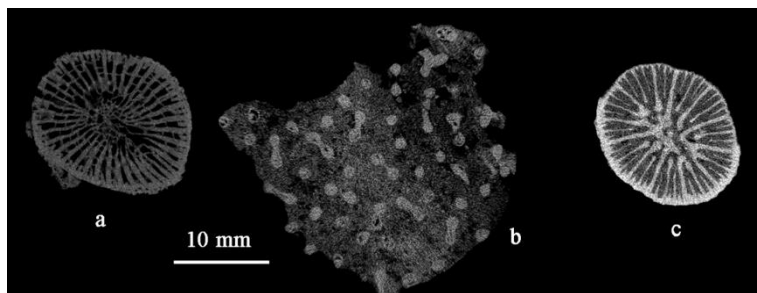


Figure 3: Virtual sections of some corals: a – rugose (Middle Carboniferous, Moscow region, Domodedovo quarry), b – tabulate (Lower Carboniferous, Tula region, Barsukovskiy quarry), c – hexaradiate (Upper Cretaceous, Saratov region).

Amber and perspectives of micro-CT investigations

Numerous microtomographic studies of arthropods in ambers are well known to paleontologists. The contrast between fossilized chitin cover and the amber due to the difference in the density is very high. But inside the arthropods internal tissue are almost not preserved (fig. 4). Another perspective objects in ambers are bacteria, including large

cyanobacteria, infusorians, testate amoebas, algae, spores and pollen, hyphae of fungi, nematodes, rotifers, small mites. A perspective is the study by micro-CT of these objects.

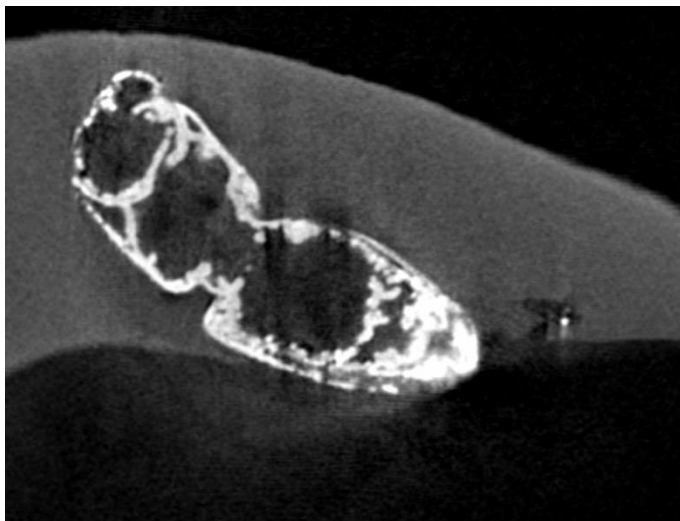


Figure 4: A beetle in Baltic amber (Eocene).

Type specimens and valuable museum exhibits

X-ray tomography are repeatedly used for study of type specimens of recent and fossil invertebrate and vertebrate animals. Type specimens of the species must be thoroughly studied and they must be completely preserved. There is a contradiction. Microtomography helps to resolve this contradiction (see Pakhnevich, 2014). No less important an investigation of valuable museum exhibit, for example, having a historical value or are particularly fragile.

Study of trace fossils

Some trace fossils are voids (borings, burrows) and they are very successful objects for the microtomography. We can investigate trace fossil form, localization, reconstruct an appearance. Some borings in subfossil shells of mussels *Mytilus trossulus* from island Adak (USA) were studied.

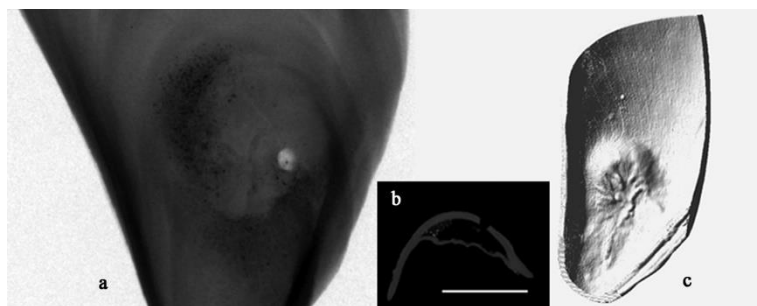


Figure 5: A boring in a shell *Mytilus trossulus* (subfossil, isl. Adak, USA). a – shell in X-ray, b – a virtual section of the shell with boring, c – 3D-model of an internal shell surface. Scale bar – 10mm.

Some borings in Jurassic belemnites are studied. Some of them were spirally twisted (fig. 6). Microtomography are used for coprolite investigation. Coprolites are fossil animal excrements. It is possible to reconstruct a structure of coprolite and some animal and plant remains (fig. 7).



Figure 6: 3D-model of the spiral borings from a belemnite rostrum (Upper Jurassic, Moscow).

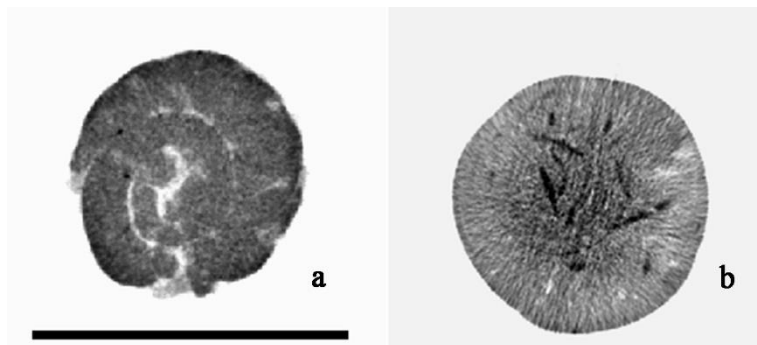


Figure 7: Coprolites: a – spiral fish coprolite (Devonian, Russian platform, material by O.A. Lebedev), b – reptile coprolite with food remains (Permian, Russian platform, material by A.A. Kurkin). Scale bar – 10 mm.

Microfossils study

A resolution of microtomographs allows to investigate a structure of different microobjects. Foraminifers, radiolarians, conodonts, diatoms, spores, pollen are still actually for a stratigraphy. There are some articles where published the data of microfossil microtomography (Görög et al., 2012; Zhuravlev, Vevel', 2012 etc). But microtomography of the single microfossils is not difficult. A problem is in the ability to identify microfossils in sedimentary rocks (fig. 8). It is especially important for mining operations.

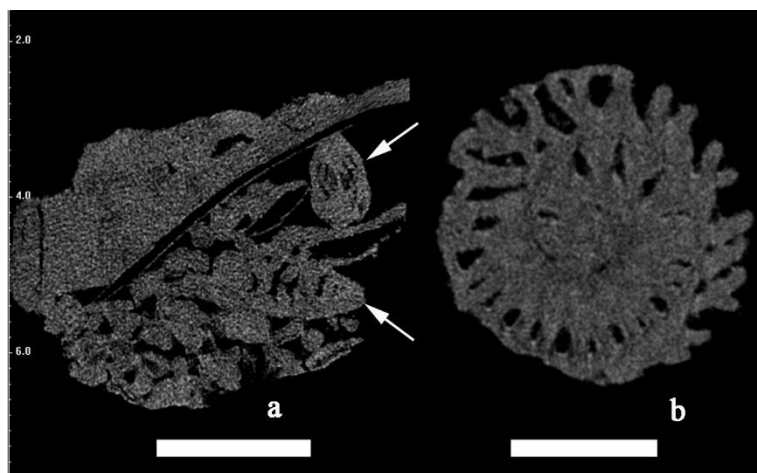


Figure 8: Foraminifers – single shell (b), in sediment (a) (Middle Carboniferous, Domodedovo quarry). Scale bar: a – 2 mm, b – 0.5 mm.

Bacterial paleontology objects

They are most difficult objects for X-ray micro-CT. Nevertheless, some recent bacteria, for example, *Beggiatoa*, *Metallogenium*, *Thiothrix* amount large sizes in hundreds of microns or

form large colonies. The granules of sulfur, iron and manganese compounds are accumulated on a surface of bacterial cells or inside them. It is important for the contrast. Cyanobacteria are no less large. Cells and covers of threads are silicified. In addition, microtomography can be an auxiliary technique for studying the rocks formed or transformed by bacterial communities, for example, stromatolites, fossilized bacterial films, iron-manganese marine and soil nodules (fig. 9).

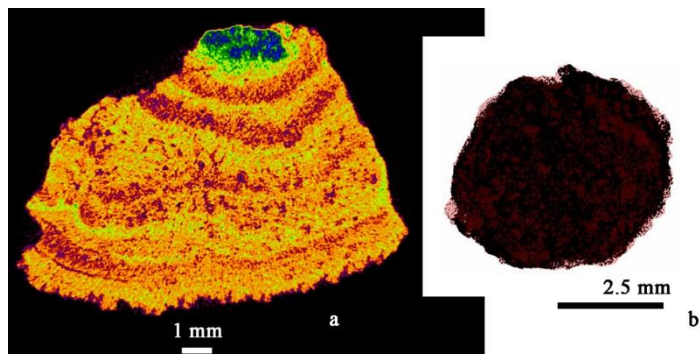


Figure 9: Marine (a) and soil (b) nodules. a – Pacific Ocean, b – Moscow region.

Investigation of microstructure and microsculpture

An investigation of a microstructure of the dense carbonate objects, for example, shell wall, by micro-CT is very difficult. However, a punctuation of shells is well object for micro-CT. This technique allows to identify the location of punctae in different layers of the shell, the punctae frequency, their branching (Pérez-Huerta et al., 2009; Pakhnevich, 2010). It can research a microsculpture by using 3D-models of shell surface and without SEM.

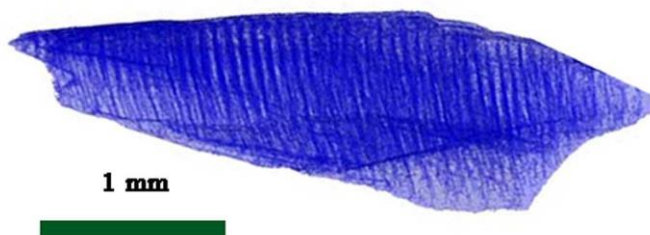


Figure 10: Brachiopod *Russiella* sp. 3D-model (with 80% transparency) of shell fragment with punctae (Upper Jurassic, Moscow).

Paleopathology

Sometimes in paleontological objects there are evidences of internal organs pathologies, growth interruptions and healed injuries. It is very important information on biology of extinction organisms. It is often paleontologists cannot study internal pathologies without destruction. In our case we found a belemnite rostrum with a growth interruption and a lamination (fig. 11).

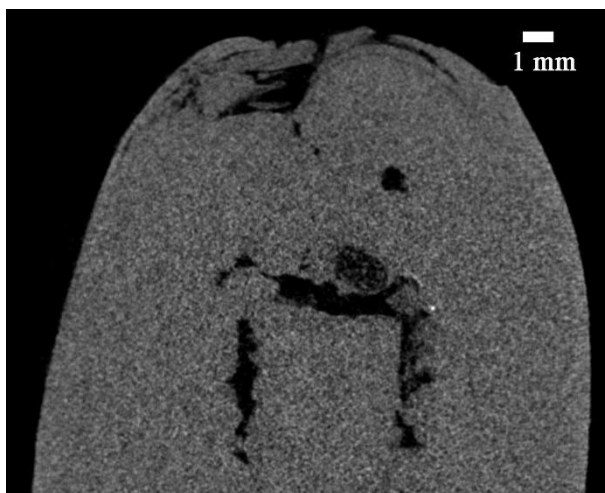


Figure 11: Growth pathology of belemnite rostrum (Upper Jurassic, Moscow region).

Conclusion

The presented investigation results, the ideas of further development of the X-ray microtomography directions are not reflect the whole range of studies, but are actual and perspective.

References:

1. Bryantseva A.V. and Rozhnov S.V., "Application of the Computer Microtomography Method for the Analysis of Echinoderms" Byull. Mosk. O-va Ispyt. Prir., Otd. Geol. V. 82. No 2, P. 81, 2007.
2. Gallagher W.B., Tumanova T.A., Dodson P., and Axel L., "CT Scanning Asian Ankylosaurs: Paleopathology in a *Tarchia* Skull" J. Vertebr. Paleontol. V. 18. No 3, P. 44A–45A, 1998.
3. Görög Á., Szinger B., Tóth E., Viskok J., "Methodology of the micro-computer tomography on foraminifera" Palaeontol. Electr. V. 15. Is. 1, 15p, 2012.
4. Kaloyan A.A., Kovalenko E.S., Pakhnevich A.V., Podurets K.M., Rozhnov S.V., and Somenkov V.A., "Synchrotron and neutron tomography for the Investigation of paleontological objects" J. Surf. Investig. X-ray, Synchrotron and Neutron Tech., V. 8. No. 6, P. 1093–1099, 2014.
5. Koromyslova A.V. and Pakhnevich A.V., "New Species of *Pachydermopora* Gordon, 2002 and *Beisselina* Canu, 1913 (Bryozoa: Cheilostomida) from a Campanian Erratic Block (Belarus) and Their Micro-CT Investigation", Paleontol. J. Vol. 50. No 1, P. 41–53, 2016
6. Kozlenko D.P., Kichanov S.E., Lukin E.V., Rutkauskas A.V., Bokuchava G.D., Savenko B.N., Pakhnevich A.V., Rozanov A.Yu., "Neutron Radiography Facility at IBR-2 High Flux Pulsed Reactor: First Results" Physics Procedia. V. 69, P. 87 – 91, 2015.
7. Pakhnevich A.V., "The Use of a Tomograph for the Analysis of Brachiopods" Modern Paleontology: Classical and New Methods: 3rd All-Russia Scientific School for Young Scientists–Paleontologists, October 3–5, 2006, Paleontological Institute RAS, Moscow, P. 48–50, 2006.

8. Pakhnevich A.V., "Study of Fossil and Recent Brachiopods, Using a Skyscan 1172 X-Ray Microtomograph" *Paleontol. J.*, V. 44. No 9, P. 1217–1230, 2010.
9. Pakhnevich A.V., "On the micro-ct investigation of the type specimens for example brachiopods" Micro-CT user meeting, Ostend, Belgium, 5th – 8th May 2014, P. 190-193, 2014.
10. Pérez-Huerta A., Cusack M., McDonald S., Marone F., Stamparoni M., MacKay S., "Brachiopod punctae: A complexity in shell biomineralisation" *J. Struct. Biol.* V. 167, P. 62–67, 2009.
11. Zhuravlev A.V., Vevel' Ya.A. "Possibilities of computed microtomography application in micropalaeontological and lithological studies" *Neftegasovaâ geologîâ. Teoriâ i praktika.* V. 7. No 2, 13 p., 2012.

Creation of dual-layer tissue engineering scaffolds with structural variation

Eleonora Vriend¹, Jennifer Shepherd^{1*}, David Shepherd¹, Serena Best¹, Ruth Cameron¹

¹Department of Materials Science and Metallurgy, University of Cambridge, 27 Charles Babbage Road Cambridge CB3 0FS

Aims

There is a tendency for tissue engineering scaffolds to demonstrate structural and chemical homogeneity, yet the native tissue we hope to replicate is often very far from homogeneous. Lyophilisation or freeze-drying is a technique to have received considerable attention in the production of relatively homogenous, highly interconnected collagen-based scaffold structures^{1,2}. We consider here, whether with careful modification, this technique could be used to construct more complex multi-region scaffolds with structural variation.

Method

Type I insoluble collagen from Bovine Dermis (Devro Medical) was swollen for 48 hours in 0.05M acetic acid at 4°C prior to blending (Waring commercial blender) and vacuum degassing in order to produce a 1wt% suspension. This suspension was pipetted into standard 48 well cell culture plates for lyophilisation.

During the freeze-drying process, a collagen suspension is frozen, forming an inter-penetrating network of ice crystals, with the collagen pushed out to the crystal boundaries. These ice crystals are then removed at low pressure through sublimation resulting in a highly porous interconnected structure. Freezing temperature and rate have a significant effect on the pore structure of lyophilised collagen scaffolds. Consequently these parameters were varied in the design of dual-layer scaffolds with structural variation. Combinations of freezing temperatures of -20, -40 and -80°C were considered. A layer of collagen suspension was frozen before a second layer pipetted on top and a second freezing profile applied. Application of a vacuum and sublimation was then carried out.

Samples were extensively analysed using Micro-CT (Skyscan 1172). Cylindrical samples were scanned in their entirety with a pixel size of 3 µm, an operating voltage of 25kV, 0.2° step size with frame averaging of 2 and 180° rotation. The resulting projections were processed into 3D data sets using a full cone beam Feldkamp reconstruction algorithm with NRecon software. Systematic regions of interest were selected through the scaffold structures and detailed three-dimensional pore analysis carried out in CTAn. The shrink-wrap feature was used in an analysis of scaffold interconnectivity, but additionally a percolation analysis was carried out¹. ROIs were modified to allow penetration only from the top x-y plane and the shrink wrap feature used to identify the volume accessible to a virtual object 'd'. This could be used to investigate the penetration of 'cell-sized' particles through the structure (particularly across interfaces) but could also be used in the calculation of a percolation diameter, a scalable measure of scaffold interconnectivity. By increasing the diameter of object 'd', the accessible pore volume could be investigated, the corresponding length of accessible pore volume 'l' in the z direction measured and this data plotted using the relationship from percolation theory in order to calculate the percolation diameter.

$$L = l_0 (d - d_c)^{-\nu}$$

where v is 0.88 for a 3D system². The percolation diameter is the diameter of the largest sphere able to penetrate through an infinitely large scaffold.

Results

Dual region structures with coherent interfaces were successfully produced using combinations of freezing temperatures of -20°C and -40°C and -80°C and -40°C. In both cases primary freezing of the base layer was carried out in a freezer where a largely uniform temperature through the collagen slurry could be assumed before directional solidification of the secondary layer.

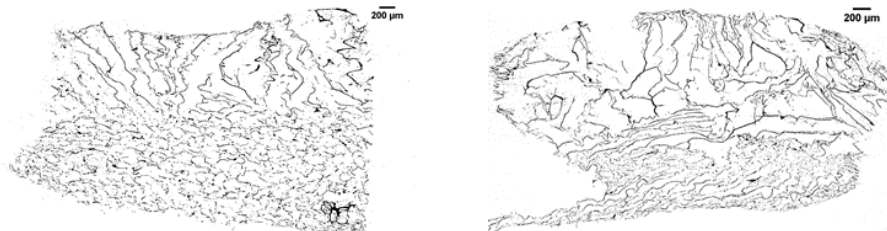


Figure 1: Sagittal slices (generated in dataviewer) demonstrate the clear dual-region nature of the lyophilized scaffolds. Structure (a) was produced with primary freezing of the base layer at -20°C followed by directional freezing of the top layer at -40°C, structure (b) with freezing of the base layer at -80°C then directional freezing of the top layer at -40°C.

The sagittal slices of Figure 2 clearly demonstrate the significant variation in pore structure between base and upper layers as well as the absence of any skin layer or other defect at the interface. Regions of interest were selected both around the interfacial region and within top and bottom layers and a three dimensional analysis of pore size (structural separation) carried out. Significant variation in pore size existed between top and bottom layers in both instances and freezing of the base layer at -80°C resulted in some decrease in pore size compared to -20°C. The generation of colour-coded models of structural separation (with reference to Bruker method note MN025) allowed for the clear pictorial representation of pore size distribution demonstrated in Figure 2.

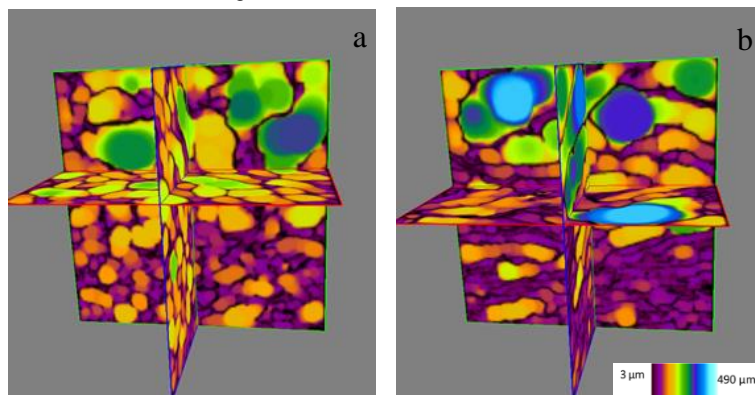


Figure 2: Colour coded models of structural separation for (a) -20, -40°C scaffolds and (b) -80, -40°C scaffolds

Calculation of percolation diameter demonstrated a reduced value for -80°C regions compared to -20°C . A pictorial representation of the directional shrink wrap analysis across the interfaces regions are shown in Figure 3 with a sphere of diameter $60\text{ }\mu\text{m}$. Both structures were observed to be highly accessible, with complete coherency of the interface observed.

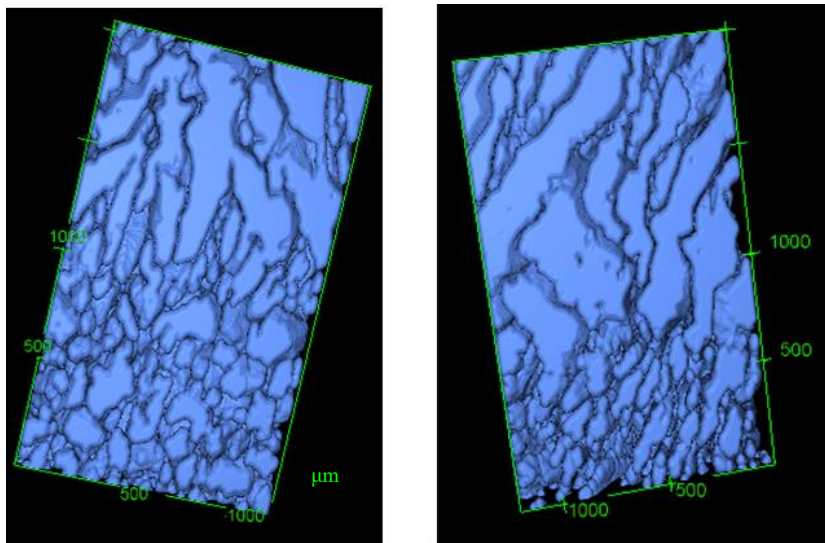


Figure 3: Percolation pathways across the interface of (a) a -20 , -40°C scaffold and (b) a -80 , -40°C scaffold

Conclusion

This work clearly demonstrates the potential of a lyophilisation technique in the production of structurally variable, highly interconnected structures for tissue engineering. It also demonstrates the significant role micro-CT can play in the analysis of such structures. One possible application of these structures may be to provide cell-sieving capabilities, so the next steps will be to compare this theoretical analysis with filtration of model micro-particles and finally to cell migration.

References:

1. Faraj, K.A., T.H. Van Kuppevelt, and W.F. Daamen, *Construction of collagen scaffolds that mimic the three-dimensional architecture of specific tissues*. Tissue engineering, 2007. **13**(10): p. 2387-2394.
2. Ko, Y.-G., et al., *Preparation of novel collagen sponges using an ice particulate template*. Journal of Bioactive and Compatible Polymers, 2010. **25**(4): p. 360-373.
3. Ashworth et al, *Cell Invasion in Collagen Scaffold Architectures Characterized by Percolation Theory*. Advanced Healthcare Materials, 2015. **4**(9): p. 1317-1321.
4. Sotta, P. and D. Long, *The crossover from 2D to 3D percolation: Theory and numerical simulations*. The European Physical Journal E, 2003. **11**(4): p. 375-388.

Analysis of Ceramic Materials by Computed Microtomography and X-ray Fluorescence

A. S. Machado¹, D. F. Oliveira^{1,2}, H. S. Gama Filho², R. Latini³, A. V. B. Bellido³, J. T. Assis⁴, M. J. Anjos² and R. T. Lopes¹

¹ Nuclear Instrumentation Laboratory, COPPE, Federal University of Rio de Janeiro, Brazil,

² Physics Institute, State University of Rio de Janeiro, Brazil

³ Chemistry Department, Federal Fluminense University, Brazil

⁴ Department of Mechanical Engineering and Energy, Polytechnic Institute, State University of Rio de Janeiro, Brazil

Aims

The analysis of ceramic materials has been proven to be an indispensable tool for indirectly approaching past people and societies through their cultural remnants, allowing inferences about their technology, and their interaction with their surrounding physical and social environments^{1,2}. Pottery products acquire their characteristic properties during the manufacture process. Compositional (mineralogical and chemical) and micro structural analyses have become an integral part of interdisciplinary archaeological research, underlining the importance of compositional and technological comparative studies. As damages must be avoided to the archeological artifacts under study, non-destructivity is an essential requirement for the scientific methods operating in this research field²⁻⁴. Therefore, the aim of this publication is to correlate two non-destructive techniques, namely computed microtomography (micro-CT) and X-ray microfluorescence (μ XRF) in the structural characterization and investigation of the elemental composition of ceramic samples.

Method

Two ceramic fragments from the same archaeological sites were analyzed. The ceramics samples IQ2AGH2 and L1CU1 (Figure 1) were found in located at the Purus basin, in the state of Acre, Brazil.

The μ XRF spectra of different regions of each sample were acquired with a μ XRF device (Bruker ARTAX 200) with a collimation size of 200 μ m, resulting in a point of analysis of approximately 500 μ m. For performing the measurements, the voltage of the X-ray tube was of 40 kV and the current was of 0.5 mA. The obtained X-ray microfluorescence spectra were evaluated by an AXIL software from the QXAS package for peak deconvolution and subtraction of the radiation background⁵.

Micro-CT images were obtained using the equipment Skyscan/Bruker, model 1173. Samples were placed in a polystyrene support and the system operated in a voltage and current range of 90 - 115 kV and 88 - 69 μ A, respectively. In order to reduce the contribution of low energy photons (beam hardening effect) a copper filter (0.50 mm of thickness) was used. The images were acquired with pixel sizes in a range of 30.00 - 33.50 μ m. A flat panel detector was used (2240 x 2240) to register the cone x-ray beam transmission. The projection images were taken over 360° at each step of 0.5° rotation. Subsequent to the acquisition, the images were reconstructed using Nrecon SkyScan - version 1.6.9.4. After the reconstruction, 3D models were built using CTVox and data was quantitatively analyzed using CTAn. All software used were proprietary form Bruker micro CT.



Figure 1: Ceramic samples, (a) IQ2AGH2 and (b) L1CU1

Results

A visual analysis of the samples IQ2AGH2 showed several external spots where different materials can be seen in ceramic matrix and two different tempers. In the μ XRF spectra for this sample, in three different spots, were found several chemical elements and concentrations, where it was possible to correlate these results with the low density (temper A) and high density (temper B) materials showed by the micro-CT images. The ceramic matrix is mainly composed by the elements Si, K, Ca, Ti, Mn, Fe, Zn, Rb, Sr, Y and Zr, whereas in the high density regions it was found the same elements, but in higher concentration. For the low density spots were found only the elements Si, Ti and Fe, and these last two in much smaller concentration than the ceramic matrix.

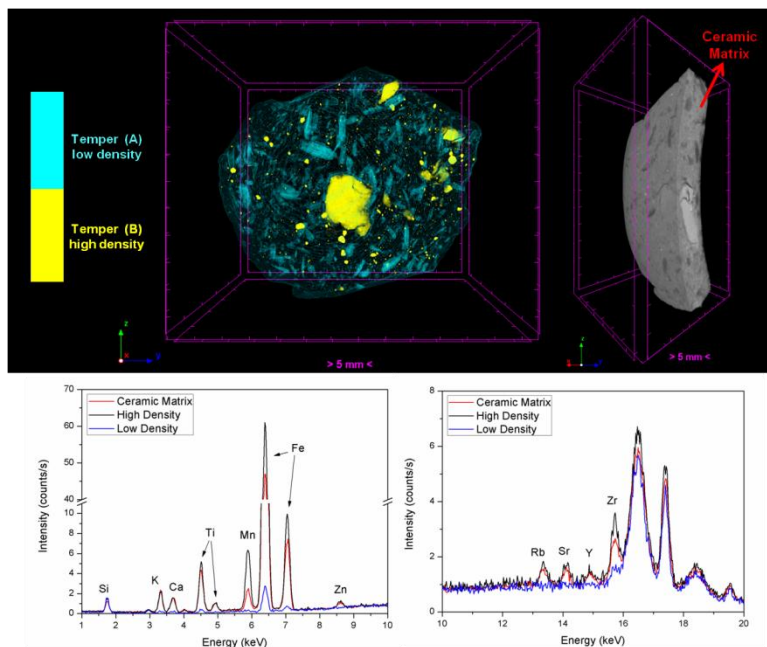


Figure 2: Micro-CT images and μ XRF spectra of the IQ2AGH2 sample.

In the micro-CT images of the sample L1CU1 can be visualized an inclusion of a high density material in the outer surface of the sample. The μ XRF spectra of this inclusion showed the elements Si, K, Ca, Ti, Cr, Mn, Fe, Cu, Zn, Pb and Y. These results suggest that it is an inclusion of an iron ore, caused during the manufacturing process of the ceramic.

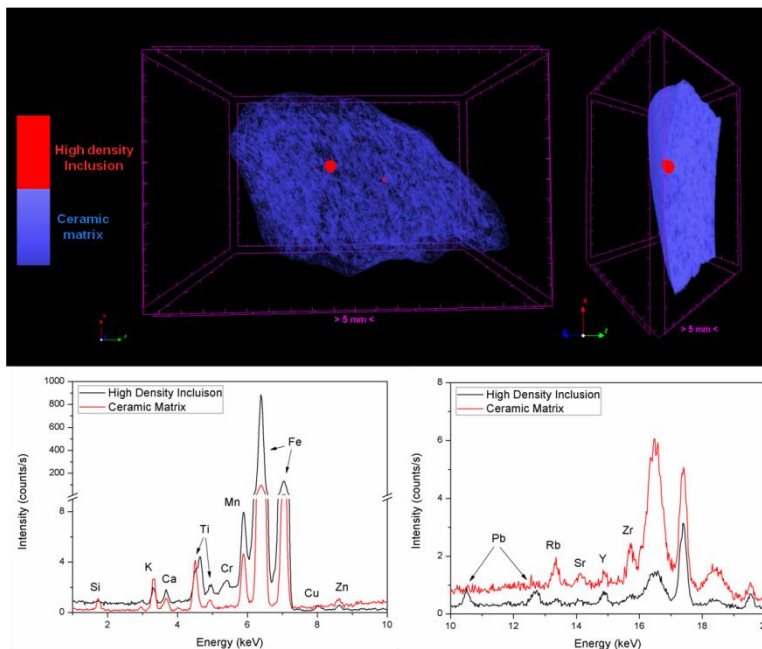


Figure 3: Micro-CT images and μ XRF spectra of the L1CU1 sample.

Conclusion

The study shows that both techniques proved to be valuable non-destructive tools for archeological ceramic characterization, since they can provide data on production materials and manufacturing techniques. The μ XRF technique helped in identifying elemental composition of the materials that constitute the samples how the ceramic matrix and the tempers/inclusions. In its turn, high resolution x-ray microtomography provided a three-dimensional view where the different mineralogical compositions could be observed. The results of this paper showed that the two techniques are powerful tools for characterizing archeological ceramic samples, with the advantage of being non-destructive and without requiring any previous preparation of the samples.

Acknowledgements

This work was partially supported by Conselho Nacional de Desenvolvimento Científico e Tecnológico (CNPq), Fundação de Amparo à Pesquisa do Estado do Rio de Janeiro (FAPERJ), Coordenação de Aperfeiçoamento de Pessoal de Nível Superior (CAPES) and Financiadora de Estudos e Projetos (FINEP).

References:

1. J. A. Barceló, Computational Intelligence in Archaeology. State of the art", Information Science Reference, Henshey, 11-21, 2009.
2. N. S. Müller, G. Vekinis, V. Kilikoglou, "Impact resistance of archaeological ceramics: The influence of firing and temper", J. Archeol. Sci. Rep., 519-525, 2016.
3. C. Reimann, P. Filzmoser, K. Fabian, K. Hron, M. Birke, A. Demetriades, E. Dinelli, A. Ladenberger, "The concept of compositional data analysis in practice--total major element concentrations in agricultural and grazing land soils of Europe", Sci. Total Environ., 196-210, 2012.
4. E. Charalambous, M. Dikomitou-Eliadou, G. M. Milis, G. Mitsis, D. G. Eliades, "An experimental design for the classification of archaeological ceramic data from Cyprus, and the tracing of inter-class relationships", J. Archeol. Sci. Rep., 465-471, 2016.
5. G. Bernasconi, A. Tajani, "Quantitative X-ray Analysis System (QXAS) Software", Package: Documentation Version 1.2, International Atomic Energy Agency, Vienna, 1996.

Application of the non-destructive methods to identify archaeological artefacts material

M. Wojtków¹, K. Winnicka², A. Nikodem¹

¹Department of Biomedical Engineering, Mechatronics and Theory of Mechanisms, ul. Łukasiewicza 7/9, 50-371 Wrocław, Poland,

²Institute of Archaeology, University of Wrocław, ul. Szewska 48, 50–139 Wrocław, Poland

Aims

Archaeology is a field of science whose main goal is to unveil the socio-cultural past of man based on the relicts found in the ground, on the ground or in water sources, archaeological, or material remains of human activities. These precious materials are often the only remnant of the ancient cultures and civilizations. These findings are therefore extremely valuable because they bring a lot of knowledge on various aspects of life of the people who inhabited the Earth at different times before us. This allows us to better understand the development and fate of different civilizations.

One of the most important directions of research in archeology is to determine the date and origin of archaeological sources obtained from excavations. Determination of the date of the excavations becomes possible by conducting studies to identify the raw material from which the source is created and information on the techniques of acquisition and production. Determination of the raw material from which archaeological artifacts are made is extremely difficult due to the fact that very often the excavations are highly degraded. This involves not only normal wear out resulting from subject use or its treatment during production, but also the erosion caused by the stay in the soil.

Macroscopic analysis conducted by archaeologists very often are not able to accurately identify the raw material (eg. bone, antler, dentin) from which the artifact was made. Moreover, the use of invasive methods for such identification is also not possible, due to the uniqueness and great value of the findings.

The latest non-invasive and non-destructive techniques, such as CT or x-ray microtomography, are extremely important in archaeology as they let to illustrate in detail the structure of the raw material, thus providing important information for identification. Ability to determine type and origin of bone (animal it belonged to) is especially important as it allows to determine the relationship between humans and animals in prehistory, eg. by recognizing the technology for the treatment of bone, which in turn is associated with an important problem of the craft and its role in the economy of the prehistory. Suitable artifacts that allow for such identification are everyday objects.

One example of such artifacts are buttons on the V-shaped perforations, which are commonly found in excavations throughout Europe, dating back to the late Stone Age and early Bronze Age [1,4,5]. Buttons are generally conical in shape and are characterized by a V-shaped hole that was used to attach the button to the clothes. Buttons were made of various materials, including stone (jet, amber), bones (bone, antler, ivory), and even metal (gold) [2,3]. The main goal of the presented study was to identify the raw material of V-shaped buttons found in the archaeological site of Sandomierz-Hill Zawichojskie (Poland). Particularly important here was to determine whether the buttons are made of a material commonly available (bones of domestic animals) or exotic (eg. ivory), which could indicate a supra-regional contact.

Method

The study material consisted of 5 V-shaped buttons found in the burial (dated 2203 ± 72 cal BC, or 3790 ± 40 BP) approx. 30-year-old woman in the loess hill in Poland. Buttons

found were heavily treated and consequently it was not possible to determine the raw material with macroscopic analysis.

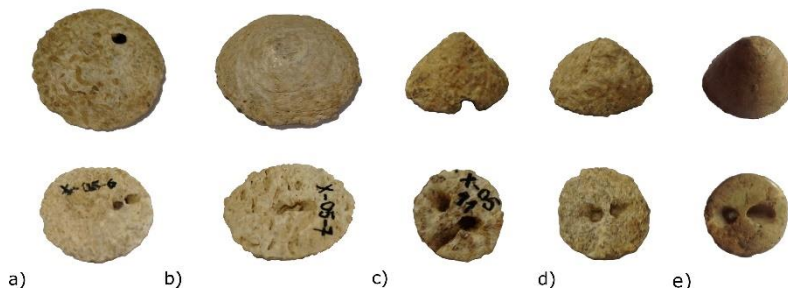


Figure 1: Pictures of each analyzed artefacts with V-perforations.

Therefore, several stages of nondestructive microscopic examination were carried out using: microscopic analysis (stereo microscope Olympus SZX9 and metallographic Nikon Eclipse LV 100), scanning electron microscopy (Hitachi S-400N cathode tungsten), x-ray microtomography computer (SkyScan 1172, Brucker). The final stage of the study was zooarcheology by mass spectrometry (ZooMS method).

Studies using X-ray microtomography image registration performed at a rate of radiation X-ray tube 89 kV voltage of 112 uA, using filter Al-Cu and the average scan resolution of 12 microns. Scanning was performed using a 360° rotation in increments of rotation of 0,4° and averaged scan window with two projections. Additionally, it reduced the occurrence of artifacts ring through the use of 10 random movements of the window.

The methods used were chosen to complement each other and ultimately allowed to fully identify the raw material from which the artefacts are made.

Results

The microscopic examination (microwear analysis) revealed histological means indicative of the fact that the buttons are made of bone tissue. However, they left serious doubts as to the type of tissue used. Both macroscopic analysis and SEM analysis allowed the exclusion of the raw material which could be dentine animal due to the observed channels, like in their dimensions and orientation to the bone channels (canaliculi). These channels are then identified as osteons, characteristic for the cortical bone forming the shafts of long bones, short and flat.

The use of microCT confirmed that the artifacts are made of compact tissue. The porosity of material Po(tot) was rated on 2.5%, and BV/TV amounted to 98%. Volume structural analysis enabled the observation of small foci of the spongy tissue, which probably narrowed areas used to produce the bone artifacts. It was found that buttons may have been made from animal bones with a thick layer of compact tissue, with a small share of cancellous bone- eg. the metaphyseal portion of long bones from large animals.

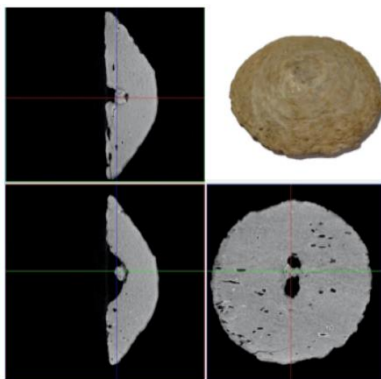


Figure 2: Cross-sections of sample artefact in ch-3 orthogonal planes (DataViewer®), along with a photography.

The final stage of the study was an analysis using ZooMs method. These studies helped confirm the previous findings obtained with earlier stages of research. Analysis of the resulting spectra showed that the raw material comes from cattle (Bos), but it was impossible to clarify whether it is domestic cattle (*Bos taurus*) and wild cattle (aurochs *Bos primigenius*).

Conclusion

Modern imaging methods having increasingly higher image resolution give undoubtedly more and more possibilities of description and characterization of structures including hard tissues. Archaeology and various other fields of science, opening up to these new techniques achieve enormous progress. The study allowed to conclude that the artefacts were produced of commonly available material, which confirms the prevalence of this material on the archaeological sites of the late Neolithic. The use of bovine bone was associated with their high availability and a good knowledge of the properties of this material.

References:

1. Aranda Jiménez, G., Montón Subías, S., Sánchez Romero, M., "The Archaeology of Bronze Age Iberia". Argaric Societies. Routledge, New York, 2014
2. Arnal, J., "Les boutons perforés en V", Bulletin de la Société Préhistorique Française, 51:255–268, 1954
3. Hájek, L., "Knoflíky středoevropské skupiny kultury zvoncovitých pohárů", Památky Archeologické, XLVIII (2):389–424, 1957
4. Makarowicz, P., "Northern and Southern Bell Beakers in Poland", (in:) J.Czebreszuk, M. Szmyt (ed.): The Northeast Frontier of Bell Beakers. Proceedings of the Symposium Held at the Adam Mickiewicz University, Poznań (Poland), May 26–29 2002 (British Archaeological Reports International Series 1155). Archaeopress, Oxford: 39–49, 2003
5. Pau, C., "Los botones campaniformes sardos y sus analogías con los adornos de la Península Ibérica y de otras zonas del Mediterráneo", SAGVNTVM (P.L.A.V.) 44:67–76, 2012

Micro-CT imaging and analysis for evaluating the quality of frozen food

M. Sadot¹, S. Chevallier¹, S. Curet-Ploquin¹, O. Rouaud¹ and M. Havet¹

¹ONIRIS, UMR 6144 GEPEA CNRS, 44322 Nantes, France

Aims

The quality of frozen food is linked with the ice crystal size as large crystals damage organic tissues. Fast freezing processes are known to provide smaller ice crystals so a better frozen product quality. X-ray micro-tomography is then an interesting method to observe crystal size distribution in order to determine the impact of freezing rate within the product on its quality.

Method

Sample preparation

Methylcellulose is used in this study because of these thermophysical properties close to those of meat. A sample (1) of 25 mm in height is placed in a cavity insulated by polystyrene (2). It is only frozen on its upper surface of 9 x 35 mm by gas nitrogen at -40°C with a heat transfer coefficient of close to 100 W.m⁻².K⁻¹. To accurately control the temperature of the nitrogen, a tank of liquid nitrogen (3) is put under pressure by a bottle of gaseous nitrogen (4). The liquid nitrogen is then pushed and vaporized in a heated pipe (5) with an output temperature regulation (Figure 1).

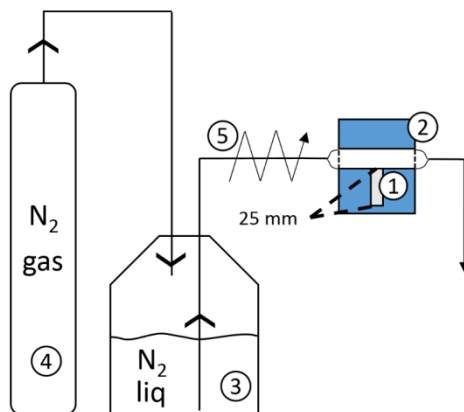


Figure 23. Freezing process

Temperature is measured inside the product at five different depths (2, 7, 12, 17 and 22 mm). When the temperature at 22 mm deep reaches -20°C (90 min), the sample is removed and directly placed in a freeze-dryer. After 24 h all the ice is sublimated which makes holes at the ice crystal locations. The sample is then cut to make a parallelepiped of 25 x 5 x 5 mm (Figure 2).

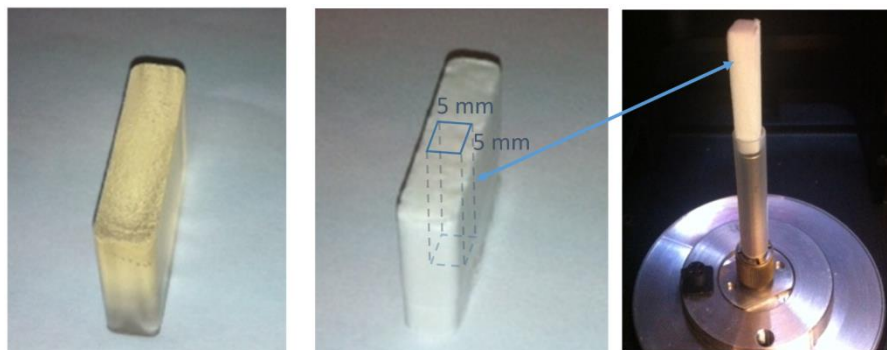


Figure 24. Methylcellulose gel. Left: fresh, Middle: freeze-dried, Right: sampled.

X-ray micro-tomography

The characterization of methylcellulose structure by X-ray micro-tomography was performed using the Skyscan 1174 (Brucker micro-CT, Kontich, Belgium). The sample was inserted in a plastic tube of 8 mm diameter which has a very low absorption coefficient and scanned at the best resolution. The source and the detector were fixed, while the sample was rotated during measurement. The acquisition and reconstruction parameters are reported in Table 1.

Table 1 Micro-tomography parameters for acquisition and reconstruction

Acquisition parameters	Value	Reconstruction parameters	Value
Image size (pixels)	1024*1304	Image size (pixels)	924*824
Expo.time (ms)	1600	# of sections	119 to 2383
Pixel size (μm)	6.46	Smoothing	0
Rot. step ($^{\circ}$)	0.1	Ring artifact reduction	20
Frame averaging	2		

The size of the gas cells which are the phantoms of the ice crystals was analyzed from reconstructed sections after an automatic thresholding to get binary images. The size of the ice crystals was derived from the local thickness calculation [1] i.e. the diameter of the largest sphere which encloses a point in the void and which is entirely bounded within the solid surfaces.

Results

A specific protocol had to be developed for the sample preparation because X-ray absorption coefficients for ice crystals and food matrix modelled by methylcellulose are too close to be differentiated on reconstructed images. The histogram exhibited a single peak for the sample pixels. Therefore, a freeze-drying step was conducted before the scanning in the micro-tomograph. No shrinkage of the samples was observed as can be seen on the images of Figure 2. Figure 3 presents some cross-sections taken at different depths of the sample corresponding to the temperature recording. It is not particularly obvious when observing these cross-sections, but the 3D calculation on the volumes of interest defined at the different depths exhibit significant discrepancies. The ice crystals volumes and the ice crystal sizes distributions evolve along the depth of the sample.

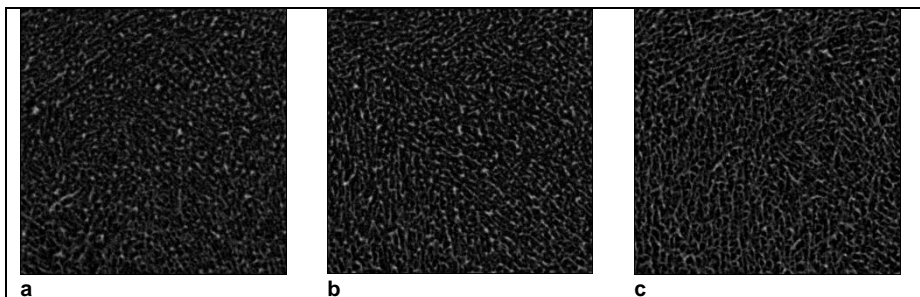


Figure 25. Cross-sections along the sample at (a) 2 mm, (b) 7 mm and (c) 12 mm.

Figure 4 illustrates the ice crystal sizes distribution at the different depths inside the sample. It can be observed that the ice crystal size is smaller near the surface exposed to the gas nitrogen and increases with the depth like in previous studies [2]. This can be explained by the decrease in freezing front rate with depth [3,4] as can be seen on Figure 5. In fact, frozen water fraction in food depends on the temperature [5]. So at a defined temperature for a larger number of crystals, their diameter is smaller. Classical nucleation theory assumes that the crystal size depends on two kinetics: nucleation rate which increases with the decrease in temperature and the crystal growth rate which increases with the number of liquid water molecules in contact to crystal surface. So the faster the temperature decreases the larger the number of crystals and the smaller the ice crystal size.

Distribution of ice crystal size

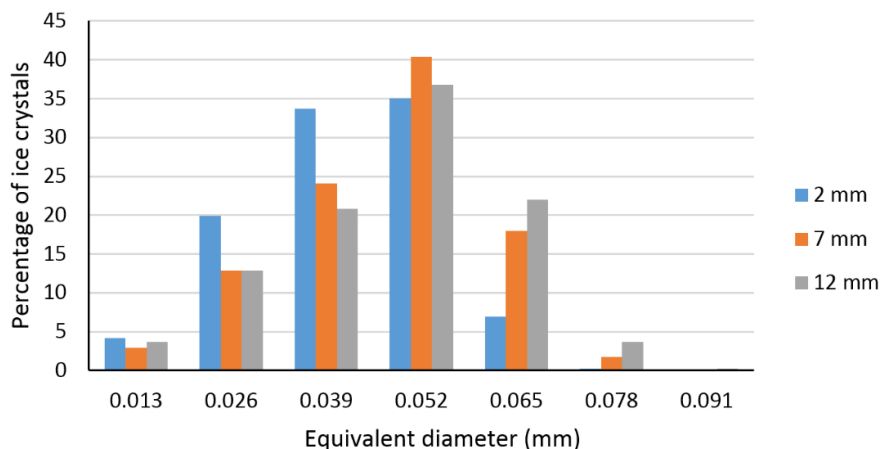


Figure 26. Distribution of ice crystal size as a function of product depth

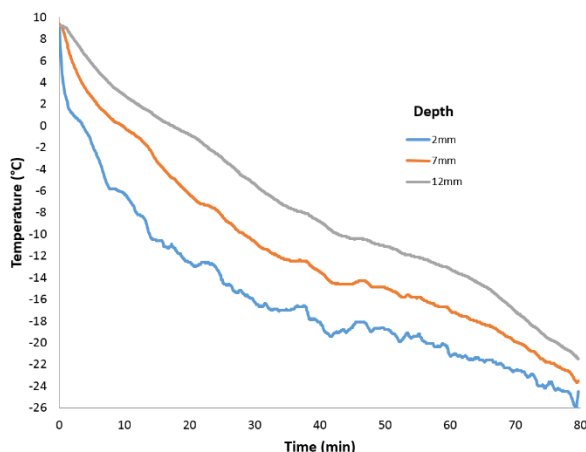


Figure 27. Evolution of temperature in the product as a function of time for different depths.

Conclusion

A protocol has been successfully developed for the study of frozen samples. X-ray microtomography has proven to be a powerful tool in characterizing the microstructure of freeze-dried samples, it gives access to the 3D structure that can be analyzed for the size distributions of the phantoms of the ice crystals and the matrix that describe the cellular structure. The investigation of the ice crystal sizes distributions within the volumes of interest at different depths in the sample allowed to correlate these sizes with the freezing rates. These data are expected to help the simulation of the heat and mass transfers occurring during freezing and the understanding of the implementation of structure during food processing.

References:

1. Hildebrand, T, Rüegsegger P, "A new method for the model-independent assessment of thickness in three-dimensional images" *Journal of Microscopy*, 67-75, 1997.
2. B. Woinet, J. Andrieu, M. Laurent, S.G. Min, Experimental and theoretical study of model food freezing. Part II. Characterization and modelling of the ice crystal size, *J. Food Eng.* 35 (1998) 395–407. doi:10.1016/S0260-8774(98)00036-3.
3. O. Miyawaki, T. Abe, T. Yano, Freezing and Ice Structure Formed in Protein Gels., *Biosci. Biotechnol. Biochem.* 56 (1992) 953–957. doi:10.1271/bbb.56.953.
4. E. Faydi, J. Andrieu, P. Laurent, R. Peczalski, Experimental study and modelling of the ice crystal morphology of model standard ice cream. Part II: Heat transfer data and texture modelling, *J. Food Eng.* 48 (2001) 293–300. doi:10.1016/S0260-8774(00)00166-7.
5. L. Wang, C.L. Weller, Thermophysical Properties of Frozen Foods, in: D.-W. Sun (Ed.), *Handb. Frozen Food Process. Packag.*, Boca Raton, 2012: pp. 101–127.

Obtaining Large Mixed Monocrystals in $\text{NH}_4\text{H}_2\text{PO}_4$ — KH_2PO_4 system

L.Yu. Kryuchkova, S.N. Bocharov, S.O. Saveliev

St. Petersburg State University, University Emb. 7/9, St. Petersburg, Russia, 199034

Aims

In the last decades much attention has been paid to obtaining mixed crystals of potassium-ammonium dihydrogen phosphate group ($\text{NH}_4\text{H}_2\text{PO}_4$ – KH_2PO_4 , hereafter ADP-KDP), as they are characterized by competing ferroelectric and antiferroelectric interactions that result in formation of so-called spin glass (also known as dipole or orientation glass) [1-3]. At the same time, despite the fact that ADP-KDP series forms ideal solid solutions, obtaining large high-quality monocrystals having intermediate compositions is quite a challenge. The main reason for the difficulties encountered is a significant difference in the a and c parameters of the tetragonal unit cells of the extreme members of the series ($\Delta a = 0.029 \text{ \AA}$ and $\Delta c = 0.575 \text{ \AA}$). If a crystal structure contains some areas that differ in their compositions, it becomes affected by high heterometric stresses with the magnitudes that exceed the limits of the yield stress and brittle deformation. That, in turn, results in cracking leading to formation of crystal blocks and fractured structures.

Techniques of growing large mixed monocrystals in the ADP-KDP system are chiefly based on the known methods used for growing large monocrystals of the extreme members of the series. These methods were useful in growing large mixed monocrystals with optical quality from aqueous solutions of ADP and KDP containing up to 10 % by weight of the opposite member [4-6]. When the solutions contained more than 10 % by weight of the opposite component, the crystals produced were intensely fractured and split growth was observed [4-6]. Such results show that the methods suitable for growing crystals of fixed composition are not useful for producing mixed crystals, since their growth is characterized by some distinct peculiarities [7, 8] unaccounted for by the principles of growing crystals of fixed composition.

The most important feature of the mixed crystal growth is, first of all, the presence of the metasomatic constituent of the growth process. It is characterized by simultaneous growth and dissolution of crystal areas, having the local compositions that are, respectively, in equilibrium and in non-equilibrium with the corresponding solution [7, 8]. Presence of the metasomatic constituent results in a specific volume distribution of the components, i.e. in microcluster compositional inhomogeneity [9, 10]. These inhomogeneities result from fluctuations in the growth conditions, such as temperature, driving force and composition of the aqueous media at the interface between solid solution and liquid solution. Another peculiarity can become evident when the distribution coefficient is not equal to 1. In this case, the process of growth of a large crystal causes gradual changes in the solution composition, i.e. solution starts to accumulate one of the components. That can lead to a significant change in solubility of any or both components and, consequently, to recrystallization of the growing crystal. In addition, it is to be kept in mind that the distribution coefficients of the components can vary in different sections of various simple forms. In the case of growing mixed ADP-KDP crystals this leads to fracturing with the cracks located, as a rule, in the plane that is perpendicular to the fourth order axis [4].

The above peculiarities of mixed crystal grows account for appearance of crystal areas differing in their compositions, such as zones, sections, and compositional microclusters that

create heteromeric stresses and, consequently, cause division of the crystal into blocks and formation of fractures. Considering all the points discussed above, it is possible to define some essential requirements for growing large mixed crystals, which are: minimal rates of growing, constant temperature, constant composition of the growth solution, and stirring the solution with the rates that can ensure stripping off the diffusion layer. Moreover, there are some restrictions imposed on the composition of a seeding crystal. The composition of the seed must be as close to that of the product monocrystal as possible.

The criteria listed above are met in a method of crystal growing, which involves isothermal evaporation of solvent from a stirred solution in the presence of previously spontaneously precipitated crystals, wherein the total volume of the spontaneously precipitated crystals must exceed the volume of the large crystal growing in the solution. Low growth rates ensure relaxation of composition of the near-surface layer, while high stirring rates facilitate decreasing the number of fluctuations. The previously spontaneously precipitated crystals serve as a buffer for solution composition, while their volume, which is considerably greater than that of the growing crystal, counter-balances changes in the solution composition. All the aforementioned techniques serve to lower the influence of a compositional microcluster inhomogeneity of a crystal upon volumetric distribution of isomorphic components.

Therefore, the purpose of the present article is to demonstrate a possibility of obtaining large monocrystals of ADP-KDP on the basis of the specially designed approaches and to analyze the volumetric distribution of the components

Method

Growing the crystals

The following proportions of the isomorphic components were used in the experiments, ADP:KDP (% by weight): 95:5, 90:10, 80:20, 75:25, 70:30, and 60:40. Reagents ADP and KDP with ACS purity and distilled water were used to grow crystals. The extreme member solutions were prepared to reach the saturation temperature of 50°C and then the solutions were filtrated through microporous filter (the pore size of 1.2 μm). Volumes of solutions containing pure extreme members were calculated to reach the desired proportions of the components. Pre-formulated solutions were transformed into 400ml beakers containing rods of magnetic stirrers. A beaker with solution was mounted onto a magnetic stirring unit and the unit with the beaker was put into a LOIP-47a thermostat maintaining the temperature of 45 ± 0.01 °C. The solution was kept in the thermostat for about 24 hours until spontaneous precipitation of crystals occurred. After that, a seeding crystal was introduced into the solution followed by addition of 0.5-1.0 ml of deionized water. Then the whole assemblage was covered with a cap that allowed controlling the rate of solvent evaporation, and the rate of stirring was set within the range of 100-110 rpm. The rate of solvent evaporation was regulated by adjusting the size of opening in the cap, which had to ensure that the growth rate in the [100]-direction did not exceed 100 $\mu\text{m}/24$ hours.

In the process of growing large monocrystals, Z-sections of ADP monocrystals were used for seeding solutions containing 5-10% by weight of KDP. When the KDP content in solutions was greater than indicated, the seeding was performed using high quality crystals spontaneously precipitated from solutions with the ADP:KDP ratios of 90:10 and 80:20 (% w/w).

X-ray microtomography

Volume distribution of components and defects in the crystals were qualitatively studied by means of X-ray microtomography using tomographs SkyScan 1074 and SkyScan 1072 (Bruker MicroCT, Belgium). The SkyScan 1174 settings were as follows: Cu radiation, acceleration voltage – 40 kV, aluminum filter, resolution – 6-10 μm (depending upon crystal size), crystal rotation angle – 0.2 grad., 5 scans in one position, exposure – 30 sec. The

SkyScan 1172 settings were as follows: Cu radiation, acceleration voltage – 100 kV, copper and aluminum filters, resolution – 2 μm , crystal rotation angle – 0.2 grad., 5 scans in one position, exposure – 1.2 sec. Microtomographic sections obtained were analyzed using DataViewer and CTAn (BrukerMicroCT), ImageJ (Rasband, NIH, 1997-2012), and Origin (OriginLab) software packages.

Electron microscopy

A Hitachi S-3400N electron microscope equipped with an Oxford X-Max accessory for energy-dispersive analysis was used for quantitative study of distribution of isomorphous elements in the grown crystals. For this study, thin sections cut from the monocrystals in the direction perpendicular to the fourth order axis were used. The sections were fixed in epoxy resin discs and were polished using kerosene. Uniformity of the component distribution in the crystal volume was derived from the images obtained in the back-scattered electrons.

Results

Seventeen mixed monocrystals with the sizes ranging from 5 x 5 x 65 mm to 25 x 25 x 60 mm were grown. Photos of six typical crystals are shown in Fig. 1.

Crystals grown from solutions with ADP:KDP ratios equal to 95:5 and 90:10 (% w/w) (Fig. 1a) had very high quality, i.e. did not contain any inclusions or fractures. Their faces were substantially free from any surface relief. Their *length* : *width* ratio ranged from 1:2 to 1:3, being standard for the KDP group crystals. In general, the mixed crystals obtained from solutions with low potassium content were similar to crystals formed by the extreme members of the series (ADP and KDP). When ADP:KDP ratio is equal to 80:20 (% w/w), the crystal quality deteriorates due to appearance of gas-liquid inclusions, but the crystals are still free of fractures. The surface relief becomes more prominent; the prism faces develop macrolayers. The *length* : *width* ratio becomes close to 1:3.

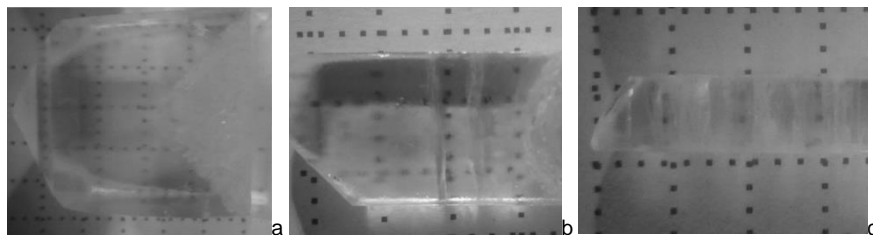


Fig. 1. Photographs of mixed ADP-KDP crystals grown from aqueous solutions having the following ADP:KDP ratios: 90/10 (a), 75/25 (b), and 60/40 (c) (% w/w). The frame size is 5 x 5 mm.

Further increasing KDP concentration in solution results in formation of cracks in the plane that is perpendicular to the fourth order axis. Gas-liquid inclusions still remain, but become smaller. These defects are observed when ADP:KDP ratio is, for example, 75:25 (% w/w) (Fig. 1b). At the same time, the crystals having the above proportion of the components still contain some areas that are free from cracks and inclusions and are large enough to be used for manufacturing optical elements. The *length* : *width* ratio increases and ranges from 1:5 to 1:6.

With increase of KDP percentage in solution, when ADP:KDP = 60:40 (% w/w) (Fig. 1c), the crystal quality substantially worsenes due to intensification of cracking. At the same time, the gas-liquid inclusions become more populated, but smaller in size in comparison to those trapped in the crystals containing less KDP. Consequently, defect-free volume of each crystal

becomes considerably smaller. The crystals also contain noticeable optically non-transparent regions, but splitting of the crystals is not observed. The crystals become longer, with the *length : width* ratio ranging from 1:13 to 1:16.

The authors think that formation of small gas-liquid inclusions is attributable to volumetric effect of recrystallization in the inner crystal regions due to leaking the solution into the crystal cracks [7, 8]. Our experimental results are, in general, in a good agreement with published data. Transition from optically pure crystals to those containing cracks and inclusions with increasing percentage of the potassium component in solution was observed by Zhong De-Gao et al. [4]. However, according to Zhong De-Gao et al., the transition takes place at a considerably lower KDP content, i.e. the crystals produced in solutions containing only 8% by weight of KDP were found to contain a noticeable amount of cracks and inclusions. This fact can be accounted for by their using another technique to obtain their experimental samples. Indeed, the authors of [4] applied the method of lowering the temperature with stirring at rather low rates, i.e. at 30 rpm. In our experiments, however, these rates ranged from 100 to 1100 rpm. Effect of relative elongation of crystals with increase of the opposite isomorphous component concentration in solution is also reported in published literature. The authors of [10] stated that with ADP:KDP = 50:50 (% w/w) the relative elongation of crystal expressed as the *length : width* ratio reached 1:22.

It is to be noted that crystals obtained in our experiments did not split during their growth. Splitting was observed only in the cases when stirring was stopped or the evaporation rate increased. The rate of growth in the direction perpendicular to [100]-plane was more than 100 μm per day. This confirms our suggestion that compositional heterogeneity of microclusters is the most important factor influencing the tendency of mixed crystals to split. A dramatic drop in quality of crystals, which were grown from solution with ADP:KDP = 60:40 (% w/w) (Fig. 1 c), was chiefly determined by intensive fracturing in the plane that was perpendicular to the fourth order axis. The probable factor triggering the fracturing can be a substantial difference between compositions of growth sectors of the pyramid and the prism of these crystals.

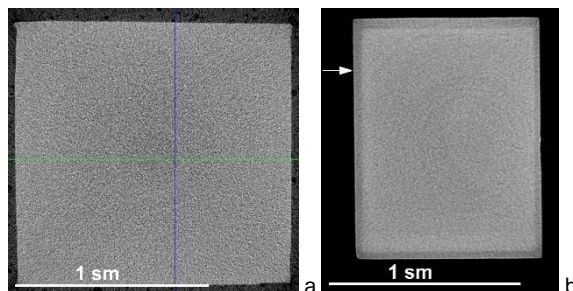


Fig. 2. X-ray microtomographic images of sections of ADP-KDP crystals grown from solutions having different ratios of isomorphous components ADP:KDP: 90/10 (a) and 75/25 (b) (% w/w), and with different rates of stirring: 400 rpm (a) and 600 rpm (b).

So, the reasonable conclusion is that splitting of crystals, their fracturing and occurrence of other volume defects is, chiefly, the result of non-uniform distribution of components in a crystal volume. Therefore, distribution of components in the mixed ADP-KDP crystals was studied by means of electron microscopy and computer X-ray microtomography.

X-ray microtomography study showed that non-split mixed crystals having the ADP/KDP ratios up to 90:10 (% w/w) had uniform component distribution throughout the crystal volume (Fig. 2a). Visible inhomogeneities, such as zonal or sectoral structures, were not found, but gas-liquid inclusions with the sizes up to 100 μm were observed.

Clearly visible sectoral structure and less prominent zonality were discerned in the mixed crystals containing more than 10% by weight of the potassium component (ADP/KDP = 80/20, 75/25, and 70/30% (w/w)). Fig. 2b shows X-ray tomographic image of a crystal section with clearly discernible zone of growth sector of the potassium-depleted prism faces (indicated by the arrow).

On the other hand, X-ray microtomography studies of split crystals grown from unstirred solutions containing from 10 to 30% by weight KDP demonstrated highly non-uniform component distribution throughout the crystal volume (Fig. 3). The non-uniformity is characterized by presence of large blocks, whose compositions differ from the average composition of the crystal. The white circle in Fig. 3 delineates the region of simultaneous growth of three differently oriented blocks. Two of them are characterized by only a slight deviation and grow in the direction of crystal elongation, i.e. in the direction that is substantially parallel to the line of growth of the main crystal. The third, comparatively more disoriented block is separated from the main crystal by large inclusions. These data confirm our assumption about correlation between the process of crystal splitting and geometry stresses caused by presence of different compositional regions in a mixed crystal volume.



Fig. 3. X-ray microtomographic image of a section of the ADP-KDP crystal grown from solution with ADP:KDP = 80:20 (% w/w). The solution was not stirred. The white circle denotes the area of the crystal splitting.

Electron microscopic study in backscattered electrons showed that the mixed crystals have zonal and sectoral distribution of their isomorphous components (Fig. 4). All the crystals have an outer zone, which is the prism growth sector. Results of quantitative analyses show that the growth sectors of the prism faces are depleted with the potassium component in comparison with those of the pyramid. A diagram showing the correlation between average concentrations

of potassium in various sectors of the mixed crystal and composition of the corresponding solution is presented in Fig. 5.

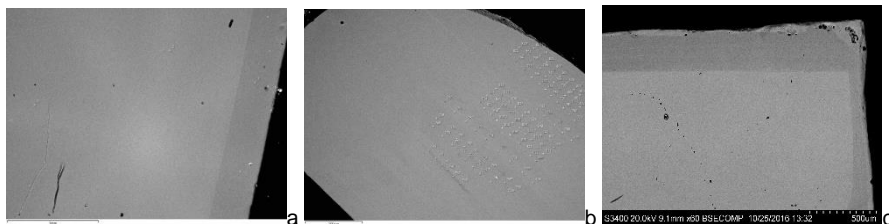


Fig. 4. Backscattered electron images of mixed crystals of the ADP-KDP series grown from solutions with the following ADP/KDP (% w/w): 90/10 (a), 80/20 (b) and 70/30 (c), and the following rotational rates of the magnetic stirrer (rpm): 400 (a), 600 (b), and 900 (c).

With increase of potassium concentration in solution, the difference between its content in the growth sector of the prism and that of the pyramid becomes more prominent. This difference increases from 0.9 to 8.2% by weight in the crystals grown from solutions containing 5 and 30 % by weight of KDP, respectively. When KDP content in solution reaches 20% by weight, the difference becomes significant (about 5% by weight in a crystal). This result correlates with substantial slowing down the growth of the prism faces and, correspondingly, with noticeable elongation of the crystals. So, the results of our X-ray microtomographic and microprobe investigations agree with the data obtained by Zhong De-Gao et al. [4], who, using another analytical method (X-ray diffraction), also found out that the prism growth sector differed in chemical composition from that of the pyramid.

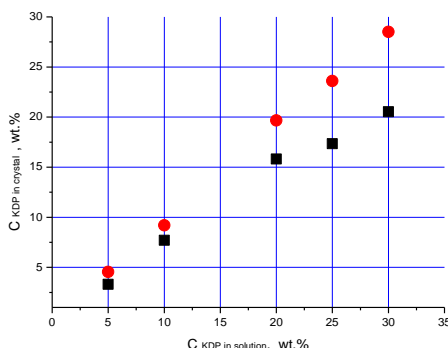


Figure 5: The average content of potassium in the growth sectors of the prism faces (squares) and those of the pyramid (circles) in the mixed crystals of the ADP-KDP series vs. KDP concentration in solution.

Conclusion

The proposed experimental techniques have been developed with bearing in mind the discussed peculiarities of mixed crystal growth that include the presence of metasomatic constituent. They allow to widen the compositional range of solutions suitable for growing high-quality mixed monocrystals. It appears that even in systems with substantially different

elemental cell parameters of the extreme members of the series it is possible to grow crystals that comprise several regions, which are free of defects and are sufficiently large to satisfy the requirements for the optical quality. In the ADP-KDP series, the crystals of the above quality can be produced from solutions containing up to 25% by weight of KDP. Conventional approaches do not give the same results. This conclusion is confirmed by the data obtained for distribution of the components within the crystal volume. Strictly speaking, zonality of the component distribution was clearly stated, but it is very weakly defined and compositional differences between the zones do not exceed the error of the microprobe analysis. On the other hand, compositional differences between the growth sectors of the prism and pyramid can be quite significant (up to 8.2% by weight) and can cause fracturing that would limit applicability of the method in producing of optically clear mixed monocrystals. In our opinion, growing large optically applicable monocrystals from solutions containing more than 25% of KDP is theoretically possible, if the growing is induced only in one growth sector. Of course, this assumption requires a thorough experimental verification.

Acknowledgements

The present work was supported by The Russian Foundation for Basic Research (projects Nos. 16-29-11727 and 16-05-00837). Experiments were performed in the Resource Centers "Geomodel", "X-Ray Diffraction Methods", and "Optical and Laser Investigative Methods" of Saint-Petersburg State University Scientific Park.

References:

1. Ishibashi Y. and Suzuki I. "On Phase Diagrams of Mixed Crystals of the KH_2PO_4 -Family." J. Phys. Soc. Jpn. 54, 1443, 1985.
2. Belushkin A.V., Tomkinson J., Shuvalov L.A., and Fedosyuk R.M. "Observation of the Increase in Atomic Mean Square Displacements upon Glass Formation: Inelastic Neutron Scattering Study of $\text{K}_{1-x}(\text{NH}_4)_x\text{H}_2\text{PO}_4$ Mixed Crystals." J. Phys. Soc. Jpn. 62, 403 1993.
3. Z. Trybula, S. Los, C.S. Tu, and V.H. Schmidt "The ferroelectric and proton glass coexistence region in $\text{K}_{0.77}(\text{NH}_4)_{0.23}\text{H}_2\text{AsO}_4$ detected by complex permittivity measurements." J. Phys. Cond. Matter 7, 947, 1995.
4. Zhong De-Gao, Teng Bing, Wang Shu-Hua, Jiang Xue-Jun, Li Ming, He Lin-Xiang and Huang Wan-Xia "Growth and characterization of $\text{K}_{1-x}(\text{NH}_4)_x\text{H}_2\text{PO}_4$ mixed crystals onto z-cut point seeds." Cryst. Res. Technol. 44, 925, 2009.
5. Rajesh P., Ramasamy P., Bhagavannarayana G. "Growth of ADP-KDP mixed crystal and its optical, mechanical, dielectric, piezoelectric and laser damage threshold studies." J. of Crystal Growth 362, 338, 2013.
6. Zhong De-Gao, Teng Bing, Yu Zheng-He, Ge Xiao-Hui, You Fei, Xu Hui, Zhang Shi-Ming, Yu Yue-Juan, and Ma Jiangtao "Structural, optical and dielectric studies on $\text{K}_{1-x}(\text{NH}_4)_x\text{H}_2\text{PO}_4$ mixed crystals grown from z-cut seeds." Cryst. Res. Technol. 45, 1127, 2010.
7. A.E. Glikin "Polyminal-Metasomatic Crystallogenesis" Springer Verlag, New York LLC, 2009.
8. Glikin A.E., Kryuchkova L.Y., Taratin N.V., Plotkina Y.V. "Micromosaic distribution of the components and peculiarities of mixed crystal origin in solutions." Doklady Earth Sciences, 433, 1, 894-896, 2010.
9. Vasilyeva N.A., Grigoryeva M.S., Grebenev V.V., Voloshin A.E. "Growth and properties of mixed $\text{K}_2\text{Ni}_x\text{Co}_{1-x}(\text{SO}_4)_2 \cdot 6\text{H}_2\text{O}$ crystals." Crystallography Reports, 58, 4, 646-650, 2013.
10. Srinivasan K., Cantoni A. and Bocelli G. "Compositional dependence of morphology and lattice parameters during growth of $\text{K}_{1-x}(\text{NH}_4)_x\text{H}_2\text{PO}_4$ mixed crystals." Cryst. Res. Technol, 45, 737, 2010.

Multidisciplinary investigation of archeological ceramics from Hlijeni-II site (Northern-Pontic region, 9-10 cc.BC)

A.M.Kulkov¹, M.A.Kulkova², M. Kashuba³, E. Kaizer⁴.

¹SPbSU, Uljanovskaja st.1, SPb, Russia,

²Herzen State Pedagogical University, Moika emb. 48, SPb, Russia

³Institute for the History of Material Culture, St.Petersburg

⁴Institut für Prähistorische Archaeologie, Freie Universität, Berlin

Aims

Archaeological ceramics are the important marker of the history of human development. The study of ceramics allows to define and clarify the cultural and economic relations within a human society. The new scientific technologies allow to determine the sources of ceramic raw materials and technology more accurately. The researchers reveal new patterns and technological features of pottery manufacturing. The m-CT method was used in combination with other methods to study processes of ceramic technology and to determine the different raw material sources. This work is devoted to studies of the archaeological ceramics from the site of Early Iron Age Hlijeni-II, located in the Northern Pontic region (Moldova).

Methods

The samples of Early Iron Age ceramics were scanned using the SkyScan 1172 device of the "Geomodel" Research Centrum of Saint-Petersburg University with a beam energy of 100 kV, a flux of 80 μ A and aluminum filter with a resolution of 4-6 μ m, performing a 180-degree rotation with a step size of 0.4 degrees. CTvox and CTan has been used for the visualization of a void caused by organic temper in fragments, shells, distribution of sand inclusions. The polarizing microscope "Leica 4500-P" was applied for the thin-section investigations. The chemical mapping of ceramic surfaces was provided by SEM-EDS method with help of the electronic microscope Hitachi S-3400N.

Results

Hlijeni II_2 (fig.1)

Thin walled ceramics (5 mm). The fabric is light-grey color covered with brown coating.

Paste composition: kaoline-carbonate clay with clustic material – 50%, grain sizes 0,02-0,08 mm, composition: feldspar, mica, amphibole, aqua organic inclusions, carbonate.

Temper:

1. Sand (8%): middle rounded grains (chalk, feldspar, gneiss), sizes of fragments of 0,2-1 mm.

2. Grog (25%) - crushed unfired ceramics of the different fabric compositions, sizes of fragments of 0,40-2 mm.

Porosity: 7%, pores of oval form and pores extended of length from 0,1 to 2 mm.

The firing temperature is 650-700°C, the carbonates and organics are unburned, short time.

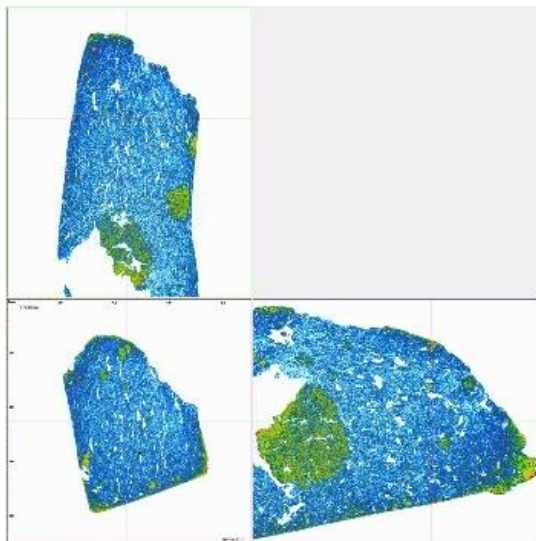


Fig.1 μ -CT visualization of ceramic paste of sample Hlijeni II_2

Hlijeni II_3 (fig. 2)

Thin walled ceramics (5 mm). The fabric is light-grey color covered with brown coating.

Paste composition: kaoline-carbonate clay with clustic material – 50%, grain sizes 0,02-0,08 mm, composition: feldspar, mica, amphibole, aqua organic inclusions, carbonate.

Temper:

1 .Sand (8%): middle rounded grains (chalk, feldspar, gneiss), sizes of fragments of 0,2-1 mm.

2. Grog (30%) - crushed unfired ceramics of the different fabric compositions, sizes of fragments of 0,40-2 mm.

Porosity: 7%, pores of oval form and pores extended of length from 0,1 to 2 mm.

The firing temperature is 650-700°C, the carbonates and organics are unburned, short time.

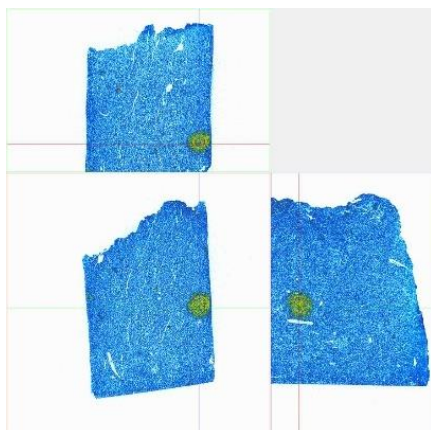


Fig.2 μ -CT visualization of ceramic paste of sample Hlijeni II_3

Hlijeni II_4 (fig. 3)

Thin walled ceramics (5 mm). The fabric is light-grey color covered with black coating.

Paste composition: smectite clay with clustic material – 50%, grain sizes 0,02-0,08 mm, composition: feldspar, mica, amphibole, aqua organic inclusions, carbonate.

Temper:

1. Crushed rocks of organic carbonate (20%): chalk or limestone with aragonite spheroids surround of calcite crystals and inclusions of fossils, sizes of fragments of 0,5-1,5 mm.
2. Grog (25%) - crushed ceramics of the same as fabric compositions, sizes of fragments of 0,40-2 mm.
3. Sand (5%): middle rounded grains (chalk, feldspar), sizes of fragments of 0,2-0,5 mm.

Porosity: 10%, pores of oval form and pores extended of length from 0,1 to 2 mm.

The firing temperature is 650-700°C, the carbonates and organics are unburned, short time, in reducing atmosphere.

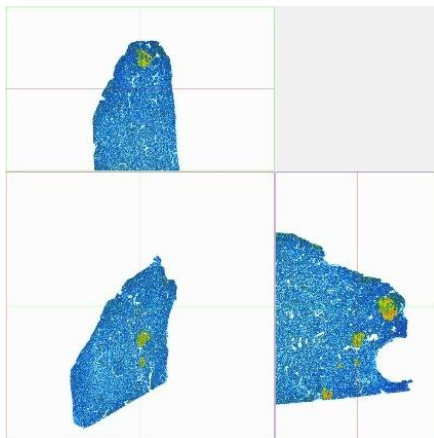


Fig.3 μ-CT visualization of ceramic paste of sample Hlijeni II_4

Hlijeni II_5 (fig. 4)

Thin walled ceramics (5 mm). The fabric is light-grey color covered with brown coating on the external surface and beige clay on the inner surface.

Paste composition: kaoline-carbonate clay with clustic material – 50%, grain sizes 0,02-0,08 mm, composition: feldspar, mica, amphibole, plant inclusions, carbonate.

Temper:

1. Sand (8%): poor rounded grains (chalk, feldspar, gneiss), sizes of fragments of 0,2-1 mm.
2. Grog (15%) - crushed unfired ceramics of the different fabric compositions, sizes of fragments of 0,40-2 mm.

Porosity: 7%, pores of oval form and pores extended of length from 0,1 to 2 mm.

The firing temperature is 650-700°C, the carbonates and organics are unburned, short time, reducing atmosphere.

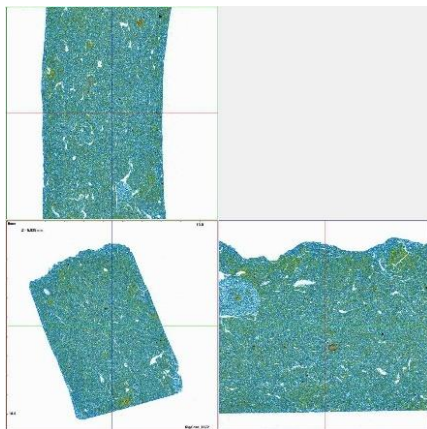


Fig.4 μ -CT visualization of ceramic paste of sample Hliljeni II_5

Hliljeni II_10 (fig. 5)

Thin walled ceramics (5 mm). The fabric is light-grey color with black burnished surface. Paste composition: smectite clay with clustic material – 50%, grain sizes 0,02-0,14 mm, composition: feldspar, mica, amphibole.

Temper:

1. Grog (25%) - crushed ceramics of the different compositions (with carbonate inclusions), sizes of fragments of 0,40-2 mm.

Porosity: 7%, pores of oval form and pores extended of length from 0,1 to 2 mm.

The firing temperature is 650-700°C, short time firing in reducing atmosphere.

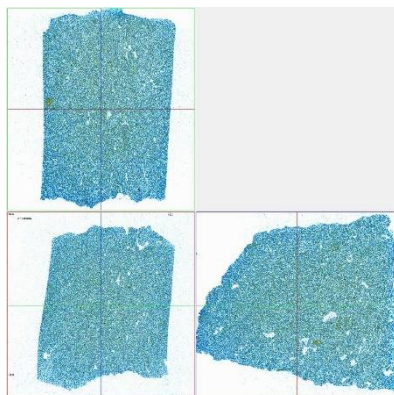


Fig.5 μ -CT visualization of ceramic paste of sample Hliljeni II_10

Hliljeni II_12 (fig. 6)

Thin walled ceramics (5 mm). The fabric is two layers with grey and beige color firing. The surface is covered by light-yellow clay.

Paste composition: smectite clay with clustic material – 20%, grain sizes 0,02-0,14 mm, composition: feldspar, mica, amphibole, aqua organic inclusions, rich of iron oxides (hematite).

Temper:

1. Crushed rocks of organic carbonate (8%): chalk or limestone with fossil, sizes of fragments of 0,2-0,7 mm.

2. Grog (35%) - crushed unfired ceramics of different composition, sizes of fragments of 0,40-2 mm.

Porosity: 7%, pores of oval form and pores extended of length from 0,1 to 2 mm.

The firing temperature is 650-700°C, the carbonates and organics are unburned, short time firing.

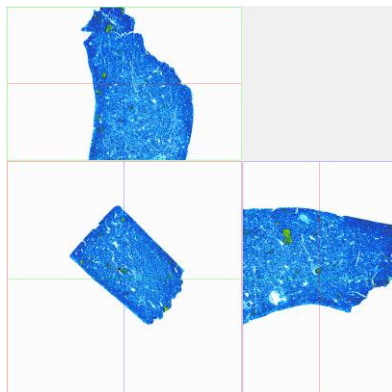


Fig.6 μ -CT visualization of ceramic paste of sample Hlijeni II_12

Hlijeni II_16 (fig. 7)

Thin walled ceramics (5 mm). The fabric is light-grey color covered with brown coating.

Paste composition: smectite-carbonate clay with clustic material – 40%, grain sizes 0,02-0,08 mm, composition: feldspar, mica, amphibole, charred aqua organic inclusions, carbonate (possible shells), rich of iron oxides.

Temper:

1. Sand (8%): middle rounded grains (chalk, feldspar), sizes of fragments of 0,2-1 mm.

2. Grog (25%) - crushed unfired ceramics of the different fabric compositions, sizes of fragments of 0,40-2 mm.

Porosity: 7%, pores of oval form and pores extended of length from 0,1 to 2 mm.

The firing temperature is 650-750°C, the carbonates and organics are unburned, short time.

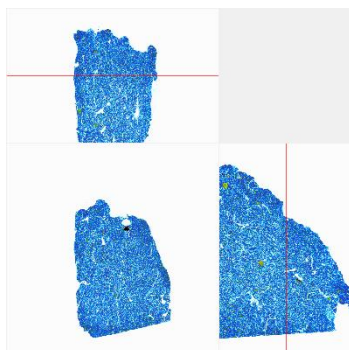


Fig.7 μ -CT visualization of ceramic paste of sample Hlijeni II_16**Table 1**

sample	porosity,%		carbonates,%	high density,%
	close	total		
Hlijeni II 2	2,1	5,3	4,2	1,5
Hlijeni II 3	1,3	8,5	5,7	0,15
Hlijeni II 4	1,4	7,7	4,1	0,1
Hlijeni II 5	2,5	7,3	0,2	0,02
Hlijeni II 10	1,5	4,4	5,5	0,9
Hlijeni II 12	1,6	5,6	5,2	0,1
Hlijeni II 16	2,8	4,6	2,3	0,2

Porosity data and concentrations of carbonate and high density inclusions presents in table 1.

Conclusion

All investigated samples were represented by the thin-walled shards of 5 mm, light-grey ceramics with brown or black coating. Ceramic pastes consist of mainly the smectite clay (except the sample 2, 3, 5 (kaoline-carbonate clay)). Some sherds have the carbonate inclusions or tempered by carbonate crushed rocks (Fig.8). The pore space mainly is presented by the linear cracks, the cracks around the grog inclusions and avoids from burning of aqua plants (fig.9) (except Hlijeni II 5 (there were avoids from moss [1]) (fig.10)).

Grain sizes of heavy minerals (zircon, hematite magnetite, rutile etc.), measured by the m-CT technique correlate with results of thin section analyses. If the sizes of heavy minerals particles less than 0,06 mm, they are the part of a clay composition, if they are more than 0,06 mm, they are belonged to the sand temper.

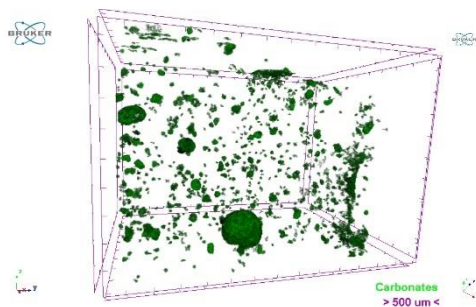


Fig. 8. Hlijeni II_3. Carbonate inclusions

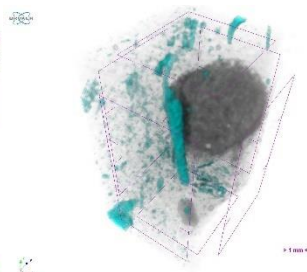


Fig. 9. Hlijeni II_3. Aqua plants traces (blue) and carbonate ovoid (grey)

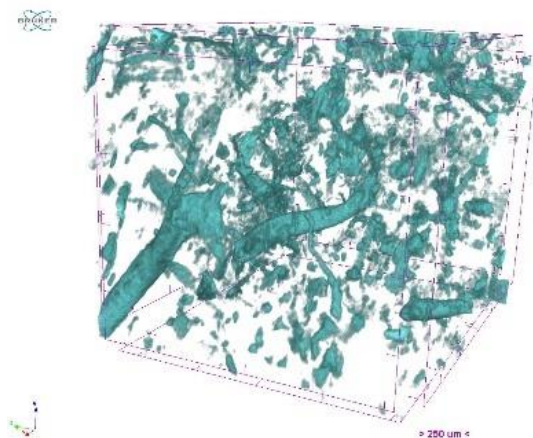


Fig. 10. Hlijeni II_5. Pore space

1. The method of m-CT analysis is important for analysis of the ratio of the open and closed porosity in the samples of ceramics.
2. 3D visualization of pore space allowed to determine the type of organic inclusions inside of the ceramics paste.
3. m-CT enable to analyze the particle size of carbonate minerals and minerals with high density. This is important for a suggestion about the anthropogenic or natural origin of sand and clay component of the ceramic paste.
4. m-CT investigations of the microstructure allows to conclude about the technology of pottery making (the paste composition, the different sources of raw materials) for small sizes of samples.

The researches were supported by Volkswagen Foundation, project № 90 216.

References:

1. D. Jan Author, "Petrographic study of vegetal temper in early and middle neolithic pottery in Lower Normandy (France)" Traditions and innovations in the study of earliest pottery. Materials of the International Conference. May 24-27, 2016, St. Petersburg, Russia, 2016, pp.71-75

A computed microtomographic study of the annular organism *Orbisiana* from Ediacaran deposits of East-European Platform (Russia)

Yulia Plotkina¹, Elena Golubkova¹, Alexander Kulkov², Ekaterina Kushim¹

¹ Institute of Precambrian geology and geochronology RAS, St. Petersburg, Russia,

² Research Center "Geomodel", St. Petersburg State University, Petergof, Russia

Aims

One of the inherent agent of Ediacaran (Upper Vendian in the Russian General stratigraphic scale) biota of East-European Platform (EEP) is a macroscopic fossil *Orbisiana*, which preserved as pyritized and limonitized forms on the surface of rock layering. The first finding of these organisms was in 1976 by B.S. Sokolov [1]. Nevertheless, nowadays the morphology, nature and stratigraphy location of these fossils in Vendian profile of EEP are not clear. Therefore, collection of annular fossils from borehole in Leningrad, Arkhangelsk and Yaroslavl' regions (European part of Russia) was detailed studied by optic and microCT.

Method

Orbisiana morphology was studied by optic microscope Olympus SZ 61. We had 6 samples of fossils for microtomography investigation. The Skyscan-1172 was used to scan the samples of fossils. In all cases used conditions are source voltage - 100 kV, source current - 100 μ A, Al filter, pixel size – 2.76 μ m, frame averaging - 4, rotation step - 0.2 deg.

Results

Optic and microCT complex study allows to select two groups of organisms.

The first group consists of double row sequence (Tabl.1 a, b), which was described earlier as *Orbisiana simplex*, and multi-row colony of annular cells (Tabl.1 c, d, e, f), which describe for the first time. The diameter of cells is 0.4-1.5 mm. The sequences are not regular and ramify dichotomously. The fragments of multi-row colony, were double row sequence begins to ramify, are identify as a *Orbisiana simplex*.

The second group consists of single line sequences with large cells (the diameter is 2-4 mm). These organisms are not ramifying and can be presented in form of isolated annular cells. This organism is comparable with species *Orbisiana linearis* (China) [2]. Perhaps originally the colonies of *O. linearis* was presented of ideal annular cells, but during burial process these cells was deformed in different directions. The horizontal compression could be lead to squashing of some parts of colony (Tabl.1 g, h). Besides the stretching could be lead to destruction of sequences with creation of isolated cells.

Microtomography investigation are shown that the all organisms have a similar structure of separated annular cells. The colonies with different morphology structures are formed by short tube (cylinders) opening to the external environment by two ends (Fig. 1). The cylinder segments of colony are locating on single layer and perpendicular to surface of the rocks stratification. The structure of these annular cells of our samples is analogically to single row sequences of *O. linearis* from Ediacaran of South China [2].

Based on the new paleontological data for *Orbisiana* (*O. simplex* and *O. linearis*) we can limit their distribution interval on the EEP by Redkino Regional Stage (~ 580 Ma).

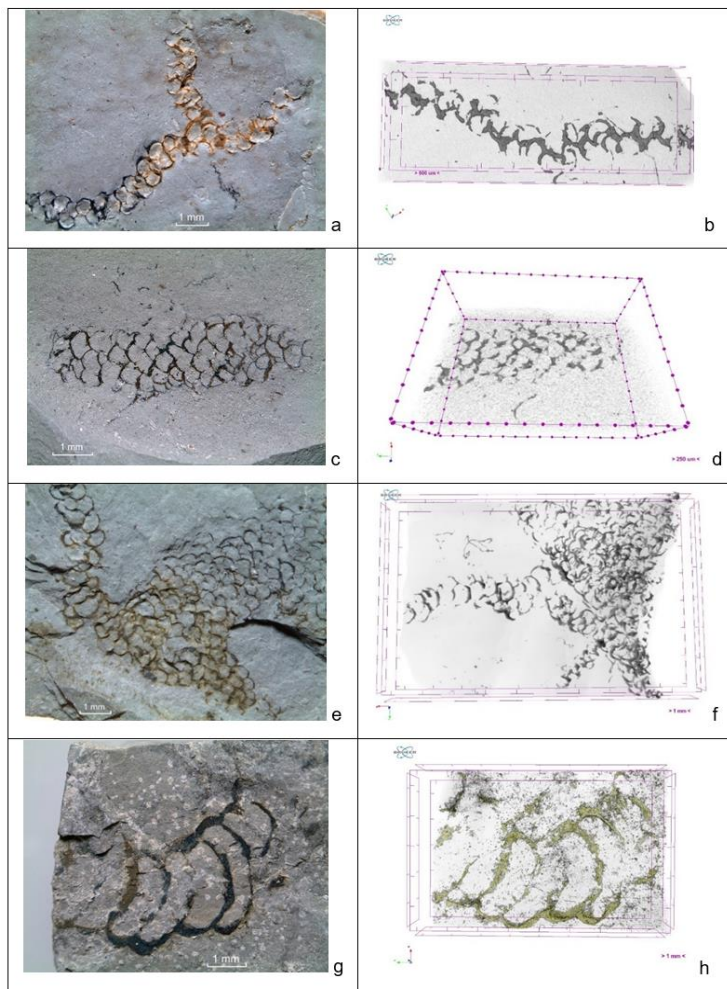


Table 1. Microfotographs and 3D model images of *Orbisiana* sp.: a-f - *O.simplex*; g, h - *O.linearis*.

Conclusion

We summarized the published and new data of *Orbisiana* organisms (morphology diversity, structure, vertical and lateral spreading) on the EEP. The double row sequences and multi-row colonies (*O.simplex*) as well as single line sequences (*O.linearis*) are identified within *Orbisiana* species. The fossils of *O.linearis* on the EEP was founded at the first time. Microtomography investigation shown that the colonies of different morphology have a similar structure of cells that allow us to unite them into same species. Our investigation was

demonstrated that microCT method is effective and prospective for micropaleontological study.

Acknowledgements

This project was financially supported by the Russian Fund of Basic Research (grant № 17-05-00498). We thank staff of Research Center "Geomodel" of St.Petersburg State University (Petergof, Russia) for microCT investigation and effective support.

References:

1. B.S.Sokolov The Earth's organic world on the path toward Phanerozoic differentiation / Vestn. Akademiy Nauk SSSR, 1, 1976, p. 126-143.
2. Bin Wan et al., *Orbisiana linearis* from the early Ediacaran Lantian Formation of South China and its taphonomic and ecological implications / Precambrian Research, 255, 2014, p. 266–275.

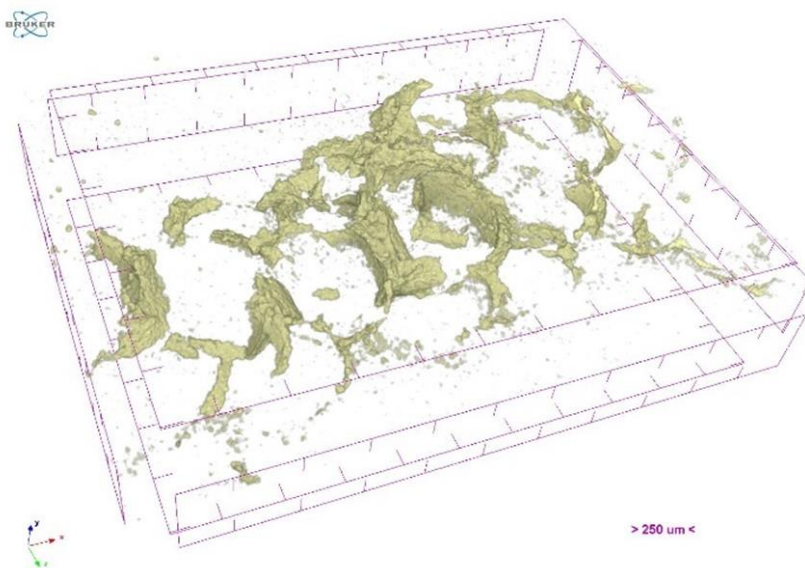


Fig. 1. 3D visualization of microCT images of *Orbisiana* sp.

Correlation of mCT analysis of vessel channels and blood vessel histology in a fracture repair model

J.L. Ramirez-GarciaLuna^{1,2}, R. Samberg¹, D. Chan¹, J.E. Henderson^{1,2}, P.A. Martineau^{1,2}

¹ Bone Engineering Labs, Research Institute-McGill University Health Centre Surgical Research, C10.160, Montreal General Hospital 1650 Cedar Ave, Montreal, Quebec, Canada H3G 1A4

² Experimental Surgery, Faculty of Medicine, McGill University. 3605 Rue de la Montaigne, H3G 2M1 Montreal, QC, Canada.

Aims

In a recent Bruker methods paper¹, an algorithm to identify and measure blood vessel channels encased in bone tissue was described. As neo-vascularization is one of the key components of the wound healing process, the aim of this study was to determine in a long bone fracture model the validity of the reconstruction of the blood vessel channels from mCT data by correlating them with the histological expression of CD34, which is a marker of endothelial cells.

Method

Bilateral 1x2mm defects were drilled on the anterolateral aspect of femurs of skeletally mature B16 mice. Cohorts were euthanized at 5, 14, 28 and 56-day post-operative. Femora were carefully dissected free of soft tissue before fixing for 24 hours in 4% paraformaldehyde. The bones were then rinsed x3 with sterile PBS and stored at 4°C until micro computed tomographic (micro CT) imaging.

Scans were performed on a Skyscan 1172 instrument with a 0.5 mm aluminium filter at a voltage of 50kV, a current of 200µA and a resolution of 5 µm/pixel. 2D images were reconstructed into 3D models using NRecon software v.1.6.10.4 (Bruker) and loaded into CTAn software v.1.16.4.1 (Bruker) for analysis. Two rectangular regions of interest (ROI) were drawn. The first in the Cortex opposite the defect, measuring 1.5 mm long, 0.9 mm wide and 0.6 mm in depth; and the second in the Defect/Medulla region measuring 1.5 mm long, 1.0 mm wide and 1.3 mm in depth. Bone was thresholded at 55-255 greyscale units and Bruker's protocol followed to reconstruct the blood vessel channels. Quantitative data for them includes channel volume/tissue volume (Ch/TV %), number of channels per mm (Ch.N. No./mm), and channel thickness (Ch.Th. mm x10⁻³).

Afterwards, bones were decalcified, embedded in in paraffin, and 5 µm sections were cut by the sagittal plane of the bone at the middle of the defect. Immunohistochemistry was used to identify vascular endothelial cells in bone and soft tissue in regenerating bone through CD34 staining (Abcam ab23830 1:300). Microscopic images were captured with a Zeiss Axioskop 40 microscope (Carl Zeiss, Toronto, ON, Canada) and stain intensity was measured and expressed as % of a matching ROI using ImageJ v.1.6.0 software (NIH, Bethesda, MD, USA).

Quantitative data is expressed as mean ± SD and the open source statistical program R v.3.3.0 (R Core Team, 2015) was used to obtain Spearman correlation coefficients at the 95% confidence level between the mCT parameters and the expression of CD34 (figure 1).

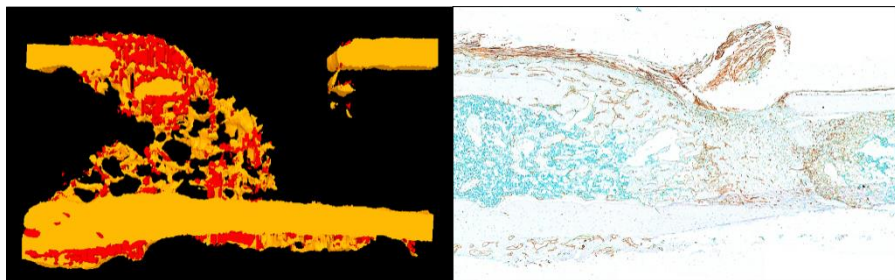


Figure 1: Comparison between blood vessel channels reconstructed by mCT and CD34 expression

Results

mCT values and CD34 expression are shown in table 1 and table 2. We found a correlation of $\rho = 0.61$, $p < 0.001$ between Ch.V and CD34 for the Defect/Medulla ROI and $\rho = 0.49$, $p < 0.001$ for the Cortex ROI (figure 2). Significant correlations were also found for Ch.N ($\rho = 0.62$, $p < 0.001$ for Defect/Medulla and $\rho = 0.40$, $p = 0.001$ for Cortex) and Cortex Ch.Th ($\rho = 0.44$, $p = 0.001$). No correlation was found for Defect/Medulla Ch.Th.

Variable	Day 5 PO (n = 8)	Day 14 Po (n = 10)	Day 28 PO (n = 7)	Day 56 PO (n = 6)
CD34 (%)	0.36 ± 0.31	9.1 ± 5.7	2.6 ± 2.1	1.5 ± 0.9
Ch.V (%)	6.8 ± 7.7	34.0 ± 11.4	9.0 ± 3.1	2.8 ± 1.1
Ch.N (No./mm)	3.3 ± 2.6	11.1 ± 3.3	3.3 ± 1.4	1.1 ± 0.4
Ch.Th (mm^{-3})	19.0 ± 6.1	28.7 ± 7.7	28.34 ± 8.5	26.6 ± 11.3

Table 1: Variables recorded for the Defect/Medulla ROI

Variable	Day 5 PO (n = 8)	Day 14 Po (n = 10)	Day 28 PO (n = 7)	Day 56 PO (n = 6)
CD34 (%)	0.29 ± 0.21	0.69 ± 0.32	0.98 ± 0.34	0.82 ± 0.32
Ch.V (%)	0.36 ± 0.31	9.1 ± 5.7	2.6 ± 2.1	1.5 ± 0.9
Ch.N (No./mm)	0.26 ± 0.4	2.5 ± 1.3	0.7 ± 0.5	0.4 ± 0.2
Ch.Th (mm^{-3})	19.8 ± 9.8	33.2 ± 8.2	33.3 ± 7.1	37.0 ± 11.5

Table 2: Variables recorded for the Cortex ROI

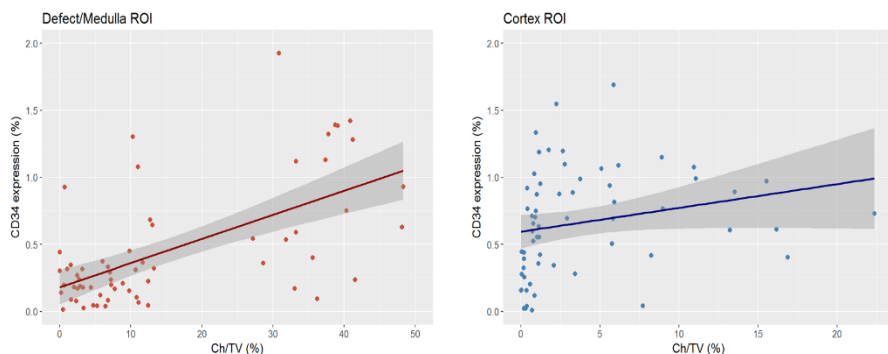


Figure 2: Correlation between Ch.TV and CD34 expression

Conclusion

Significant, albeit moderate correlation was found among all bone blood vessel channel mCT parameters and blood vessel histology for the Cortex; and between Ch.V and Ch.N with CD34 expression in the Defect/Medulla ROI. A plausible explanation for the relatively low correlation coefficients may be, first, that the algorithm is only capable of identifying blood vessel channels encased in bone, since it relies on the identification of a network of open pores. This is evident in figure 1, where no blood vessel channels can be observed in the distal (right) end of the mCT model, but are patent on the histology slide. These vessels lie in the soft tissue of the medullary bone, thus are not surrounded by regenerating bone. The second reason for moderate correlations may be that we analyzed the bones as a 2D object, but the mCT data as a 3D one. In the opinion of the authors, this is possible the greatest contribution of the algorithm to orthopedic research. Histology relies on the analysis of a 2D object, thus requiring considerable skill and resources to conduct a full 3D analysis of an object. This pitfall is easily overcome by mCT data and paves the way for more robust analyses. As correlations are consistent, we conclude the method has enough validity to consider it as an auxiliary for neovascularization quantification.

References:

1. Bruker micro CT academy. 2016;5(3).

